Universidade de Aveiro Departamento de Engenharia de Materiais e Cerâmica
2015

Vladislav Kolotygin

Materiais à Base de Óxidos com Estrutura do Tipo Perovskite e Compósitos como Ânodos de PCES

Propriedades Funcionais e Comportamento Eletroquímico em Células com Eletrólitos Sólidos à Base de Galatos e Silicatos

Tese apresentada à Universidade de Aveiro para cumprimento dos requisitos necessários à obtenção do grau de Doutor em Ciência e Engenharia de Materiais, realizada sob a orientação científica do Doutor Vladislav Kharton, Professor Associado Convidado do Departamento de Engenharia de Materiais e Cerâmica da Universidade de Aveiro

Apoio financeiro da FCT e do FSE no âmbito do III Quadro Comunitário de Apoio.

POPH QUALIFICAR É CRESCER. QREN QUADRO DE REFERÊNCIA ESTRATÉGICO NACIONAL PORTUGAL 2007.2013 GOVERNO DA REPÚBLICA PORTUGUESA UNIÃO EUROPEIA Fundo Social Europeu

o júri

presidente

Prof. Dr. José Carlos Esteves Duarte Pedro
Professor catedrático do Departamento de Eletrónica, Telecomunicações e Informática da Universidade de Aveiro

Prof. Dr. Albano Augusto Cavaleiro Rodrigues de Carvalho,
Professor Catedrático da Faculdade de Ciências e Tecnologia da Universidade de Coimbra

Prof. Dr. João António Labrincha Batista,
Professor Associado com agregação do Departamento de Engenharia de Materiais e Cerâmica da Universidade de Aveiro

Prof. Dr. João Carlos Bentes Waerenborgh,
Investigador Principal do Centro de Ciências e Tecnologias Nucleares, Instituto Superior Técnico da Universidade de Lisboa

Prof. Dr. Vladislav Vadimovich Kharton,
Professor Associado Convidado do Departamento de Engenharia de Materiais e Cerâmica da Universidade de Aveiro (**orientador**)

Prof. Dra. Elsa Maria Simões Branco Lopes,
Investigadora Auxiliar do Centro de Ciências e Tecnologias Nucleares, Instituto Superior Técnico da Universidade de Lisboa

acknowledgements

I would like to express my gratitude to my supervisor Dr. Vladislav V. Kharton for his assistance, useful recommendations and patience to my faults.

I am thankful to all my colleagues from the University of Aveiro, primarily to Dr. E.V. Tsipis, Dr. A.A. Yaremchenko, Dr. A.L. Shaula, Dr. E.N. Naumovich, Prof. J.R. Frade, Dr. S. Mikhalev, Dr. A.V. Kovalevsky, I.A. Antunes, Dr. E.V. Kiselev, Dr. Y.V. Pivak, Dr. M. Lü, for their invaluable help, discussions and experimental contributions. I wish also to thank all the technical and administrative staff of the Department, in particular Dr. A.S.V. Vale, M.L.P. Costa and T.S. Zhaludkevich.

I would like to express many thanks to my colleagues from other institutions, in particular, to Dr. J.C.B. Waerenborgh (Centro de Ciências e Tecnologias Nucleares, Instituto Superior Técnico, Universidade de Lisboa), Dr. S.N. Yarmolenko (North Carolina A&T State University), Prof. M.V. Patrakeev and Dr. A.A. Markov (Institute of Solid State Chemistry UB RAS), and Prof. S.I. Bredikhin, A.I. Ivanov, Yu. Fedotov and other colleagues from the Institute of Solid State Physics RAS in Chernogolovka, for their continuous collaboration and help.

Financial support from Fundação para a Ciência e Tecnologia (grant SFRH/BD/45227/2008 and project PEst-C/CTM/LA0011/2011), European project FP6-515960 “ULCOS”, and Ministry of Education and Science of the Russian Federation (project 14.B25.31.0018) is gratefully acknowledged.

I am sincerely thankful to my former teachers Dr. A.L. Podkorytov, Dr. E.V. Sokolova and Prof. L.K. Neudachina and to all my friends for their help and support. I am especially grateful to Koroleva I.E. for her continuous encouraging me and belief in my spirit.

Finally, and most importantly, I would like to acknowledge my parents and all my family for their breeding me and patience to my drawbacks.

palavras-chave

Pilhas de combustível de eletrólito sólido, ânodo, desempenho eletroquímico, condutividade mista, expansão térmica e química, polarização de elétrodo, modificação superficial

resumo

Este trabalho é dedicado à análise das propriedades de transporte, termomecânicas e eletroquímicas de materiais óxidos com estrutura do tipo perovskite e de compósitos para utilização como ânodo em pilhas de combustível de eletrólito sólido (PCES), com funcionamento a temperaturas intermédias, utilizando eletrólitos de galato e de silicato de lantânio. De entre os materiais estudados, destacam-se os sistemas à base das perovskites $A(Mn,Nb)O_{3-\delta}$ (A = Sr, Ca) e $(La,Sr)(Mn,Ti)O_3$, os cromitos de lantânio substituidos por catiões aceitadores de electrões e com valência mista e os compósitos do tipo "cermet" contendo Ni. É dada ênfase à estabilidade e estutura destes materiais, bem como à microestrutura das camadas porosas dos elétrodos e de cerâmicos densos, à condutividade eletrónica, ao coeficiente do Seebeck, à permeabilidade de oxigénio, à expansão térmica e química e à sobretensão anódica dos elétrodos depositados nas membranas de eletrólitos à base de $(La,Sr)(Ga,Mg)O_3$ e $La_{10}(Si,Al)_6O_{27}$. Numa seleção dos estudos efetuados incluiu-se a avaliação da difusão de oxigénio, do estado de oxidação dos catiões dos metais de transição relevantes para o transporte deeletrões, da atividade catalítica dos aditivos e das camadas protetorasde céria introduzidas no modelo das celulas eletroquímicas. A correlação entre as propriedades de transporte dos materiais de ânodo e o comportamento eletroquímico dos elétrodos porosos indica que os fatores principais, responsáveis pelo desempenho dos ânodos, incluem, em particular, a condutividade eletrónica das composições dos ânodos e a difusão de catiões entre as fases do eletrólito sólido e do elétrodo. Este último fator é especialmente crítico no caso das membranas à base de silicato de lantânio, prejudicando significativamente as propriedades dos ânodos, quando comparadas com as das células eletroquímicas fabricadas com galato de lantânio como o electrólito sólido. Os resultados obtidos neste trabalho permitem escolher as composições dos ânodos que possuem os valores da resistividade por área do eléctrodo mais baixos, comparativamente a alguns materiais análogos já estudados, tal como $(La,Sr)(Cr,Mn)O_{3-\delta}$.

keywords

Solid oxide fuel cell, perovskite, anode, electrochemical activity, mixed conductivity, thermal and chemical expansion, electrode polarization, surface modification

abstract

This work was focused on the analysis of transport, thermomechanical and electrochemical properties of a series of perovskite-like oxide materials and composites for potential applications as anodes of intermediate-temperature solid oxide fuel cells (SOFCs) with lanthanum gallate and silicate solid electrolytes. The primary attention was centered on $A(Mn,Nb)O_{3-\delta}$ (A = Sr, Ca) and $(La,Sr)(Mn,Ti)O_3$-based systems, lanthanum chromite substituted with acceptor-type and variable-valence cations, and various Ni-containing cermets. Emphasis was given to phase stability of the materials, their crystal structure, microstructure of porous electrode layers and dense ceramics, electronic conductivity, Seebeck coefficient, oxygen permeability, thermal and chemical induced expansion, and anodic overpotentials of the electrodes deposited onto $(La,Sr)(Ga,Mg)O_3$- and $La_{10}(Si,Al)_6O_{27}$- based electrolyte membranes. In selected cases, roles of oxygen diffusivity, states of the transition metal cations relevant for the electronic transport, catalytically active additives and doped ceria protective interlayers introduced in the model electrochemical cells were assessed. The correlations between transport properties of the electrode materials and electrochemical behavior of porous electrodes showed that the principal factors governing anode performance include, in particular, electronic conduction of the anode compositions and cation interdiffusion between the electrodes and solid electrolytes. The latter is critically important for the silicate-based electrolyte membranes, leading to substantially worse anode properties compared to the electrochemical cells with lanthanum gallate solid electrolyte. The results made it possible to select several anode compositions exhibiting lower area-specific electrode resistivity compared to known analogues, such as $(La,Sr)(Cr,Mn)O_{3-\delta}$.

Table of contents

Introduction

Solid oxide fuel cells (SOFC) provide advantages over other energy conversion engines due to high power output, fuel flexibility, environmental safety, capability to utilize exhaust heat etc. One of actual problems related with SOFCs is performance degradation attributable to high-temperature interaction between the cell components or microstructural instability of the electrode layers [1-6]. Consequently, reducing the operation temperature of the fuel cell is one of priority tasks. Since significant performance losses originate from insufficient electrochemical activity of the electrodes, especially pronounced at low temperatures due to high activation energies of rate-determining processes, significant efforts are focused on the search of optimum electrode compositions exhibiting high and stable performance. Conventional Ni-containing composite anodes suffer from chemical, mechanical and microstructural instability [1, 2, 4, 7] which requires search of alternative materials possessing high and stable performance. In last years, selected perovskite compositions have been proposed as promising candidates capable to substitute the cermets for electrochemical applications [8-13]. However, the information on relationships between the anode material composition, its functional characteristics and electrochemical activity is scarce and contradictive.

As discussed in Chapter 1, the choice of materials is restricted to oxide-based compositions, primarily those with the perovskite-like structure. The selection of the objects is associated with the stability, thermomechanical, transport and electrochemical characteristics of the materials as well a wide variety of dopants capable to modify their properties and optimize the anode behavior. Moreover, recent studies revealed a potential of so-called "symmetric cells" with the cathode and anode composed of the same material, in SOFC technology [9, 14]. In particular, fewer number of the materials utilized facilitates the procedure of the cell preparation, reduces the costs and enables to switch the cathode and anode atmosphere in order to eliminate carbonaceous species deposited in hydrocarbon-containing atmospheres while periodical alternation of $p(O_2)$ and current direction might avoid irreversible degradation of the electrode layer.

While promising characteristics have been observed on $(La,Sr)(Cr,Mn)O_{3-\delta}$, $(La,Sr)(Ti,Mn)O_{3-\delta}$, $(La,Sr)(Cr,Fe)O_{3-\delta}$, $(La,Sr)(Cr,Ni)O_{3-\delta}$, $(La,Sr)(Cr,Ru)O_{3-\delta}$ anodes [8, 10, 15-18], in most studies the anodes were covered with catalytically-active metal pastes which can barely be utilized in industrial scale. On the other hand, the presence of the additional layer obscures the electrochemical properties relevant to the oxide material and does not allow to evaluate the relationships between the anode performance and the bulk properties of the anode material. Selected compositions, such as Nb-doped manganites, are suggested to possess acceptable anode properties [19, 20], although no reports on their electrochemical behavior have been found. In a search of potential anode materials, the present study is focused on characterization and evaluation of the electrode activity of the relative compositions, such as $(La,Sr)(Mn,Cr,Ti)O_{3-\delta}$, $(La,Sr)(Mn,Ti)O_{3-\delta}$, $Sr(Mn,Nb)O_{3-\delta}$, $(La,Sr)(Cr,Fe)O_{3-\delta}$, $(La,Sr)(Cr,Mg,Ni)O_{3-\delta}$ and corresponding composites.

Another strategy of the work is to evaluate the potential of lanthanum silicate-based materials as solid electrolytes in SOFCs. In recent years this group of compositions with apatite-type structure has received much attention due to their satisfactory transport characteristics and low costs [21-24]. However, the

available information on electrochemical properties of apatite-based cells is scarce and requires further investigations, especially in terms of the long-term stability.

The present study is focused on synthesis, characterization and assessment of the electrode activity of perovskite-type chromite-, manganite- and titanate-based compositions and studying the relationships between the electrode properties and functional characteristics. With respect to the goals indicated above, the particular tasks are as follows:

1. Analysis of available data on the functional characteristics and electrochemical properties of chromite-, manganite- and titanate-based compositions.
2. Characterization of perovskite-like $(La,Sr)(Mn,Cr,Ti)O_{3-\delta}$, $(La,Sr)(Mn,Ti)O_{3-\delta}$, $Sr(Mn,Nb)O_{3-\delta}$, $(La,Sr)(Cr,Fe)O_{3-\delta}$, $(La,Sr)(Cr,Mg,Ni)O_{3-\delta}$ as potential electrode materials. Evaluation of electrochemical activity and stability of the perovskite-based cathodes and anodes.
3. Comparative assessment of the anode activity of cermet or oxide-based anodes in contact with apatite- and gallate-based solid electrolytes, evaluation of performance-determining factors.
4. Analysis of the correlation between stability, transport, thermomechanical properties of perovskite-based materials and performance of the corresponding anodes.

In accordance with the tasks of the study, the work is composed of five chapters. Chapter 1 is devoted to a survey of the available literature data on the possible groups of SOFC anode materials based on the binary oxides or oxide-based compositions, primarily with the perovskite-type structure. The stability and transport properties of the potential anode materials under operation conditions restrict their choice to chromites, titanates, selected manganites stabilized by introduction of donor-like cations as well as to some representatives of double perovskites, primarily based on molybdates. The overview of the electrode materials involves the consideration of the phase and structural relationships, mixed electronic and ionic conductivities, thermomechanical characteristics, analysis of the electrochemical behavior and the applicability of the corresponding anodes for practical utilization in hydrogen or natural gas-based fuels. Possible limitations associated with specific features of the given group of materials are considered as well.

The description of the experimental techniques, characteristics of the apparatus used, methods of synthesis of the materials studied and fabrication of the electrode layers is presented in Chapter 2. In this part the methods of calculation of physico-chemical parameters and routes of the treatment of the experimental data are also considered.

Chapters 3 and 4 are devoted to investigation of chromite- and manganite-based materials, respectively. The characterization includes structural and microstructural studies, assessment of the phase relationships associated with the behavior of the materials on thermal or redox cycling, evaluation of the parameters related to the mixed electronic and ionic conductivity. In terms of the electrode behavior, anodic and in some cases cathodic activity is considered, without any detailed analysis of the factors responsible for the electrochemical properties, routes of optimization of the anode performance etc.

Chapter 5 is focused on comparison of the anode properties of mixed-oxide and some metal-ceramic (cermet) anodes, assessment of the relationships between the electrode behavior and stability or transport properties of the anode/electrolyte materials. In order to provide more complete information on the phenomena related with the electrolyte utilized, a brief review of the stability and transport characteristics of

apatite- and gallate-based solid electrolytes known from the literature is presented. As a possible route to optimize the anode performance, selected electrode layers were impregnated with catalytically-active species; another approach involved preliminary deposition of the protective ceria-based layers on the electrolyte surface to avoid the interaction and cation exchange between the cell components.

The principal conclusions based on the results obtained are presented in a separate section. The symbols and abbreviations, as well as the references used are listed in the end of the work.

1. Literature review. Functional properties of chromite-, manganite- and titanate-based perovskite oxides for SOFC anode applications.

1.1. Stability limits and transport properties of transition metal oxide compounds: a brief overview

In order to achieve high and stable performance of the SOFC, the anode material should satisfy a list of requirements. These, primarily, include chemical and microstructural stability under the operation and fabrication conditions, high electronic and ionic conductivity, chemical and thermomechanical compatibility with solid electrolytes, high and stable electrochemical activity towards fuel oxidation and low cost [1-4]. By far, no ideal compound or composite material has been found to satisfy all the requirements.

In literature, one can found a large number of studies devoted to development of anodes alternative to commonly used Ni-containing cermets, mainly based on complex oxides possessing the perovskite-type structure. Prior to analyzing their behavior, it would be reasonable to consider some of characteristics of individual oxides, since the properties of the binary compounds may have a strong influence on the characteristics of their derivatives. Moreover, some of the individual oxides satisfy most of the requirements to the anodes and may be considered as the electrode component or a precursor for the electrode fabrication.

The advantage of individual oxides relates to their low cost and simplicity of production. Numerous oxides possess mixed electronic and ionic conduction which is beneficial for the electrochemical applications. Unfortunately, direct comparison of the functional characteristics, primarily conductivity and vapour pressure under operating conditions, is complicated due to poor availability of the literature data.

The comparison will be restricted by 3*d*, 4*d* and 5*d* transition metals and selected representatives of 4*f* elements. The most *s*- and *p*-elements are stable in an unique oxidation state ([25, 26] and references cited) and an acceptable level of the electronic conduction in these elements may be expected only in metallic state which cannot be attained under the anode environments. Another concern relates to a high tendency of these elements to form volatile products, especially in wet atmospheres [26-29].

Most oxides of elements of IIB, IIIB, IVB groups (Sc_2O_3, Y_2O_3, ZrO_2, ZnO etc.) as well as 4*f*- and 5*f*-elements are also stable in their maximum oxidation state in a wide domain of conditions [25, 26], with resultant negative effect on the electron transfer. Therefore, their transport properties are mainly determined by the presence of defects or impurities in the crystal lattice rather than by intrinsic properties of the parent oxide. On the other hand, these oxides and their derivatives may offer a relatively high level of the ionic conductivity [26, 30, 31]. Utilization of oxides of 4*f*- and 5*f*-elements as anodes is limited by their low availability, high prices and, in case of 5*f*-elements, complexity of production and nuclear instability.

Most elements of VIIIB group (Rh, Ru, Pt, Os, Ir, Pd) and IB group (Ag, Au) are characterized by stability in metallic state under a wide range of $p(O_2)$ [26, 32, 33]. Due to high electronic conductivity and, in some cases, electrochemical activity, some representatives have been assessed as components of composite anodes [32-35]. However, industrial application of these metals is restricted by their high price, low availability, tendency of metallic particles towards sintering and adsorption/dissolution of hydrogen with resultant deterioration of the transport, mechanical or electrochemical characteristics [15, 36-38].

Being stable under the anode conditions, metallic Fe, Co, Ni, Cu are susceptible to formation of oxides at higher $p(O_2)$ [25, 39-42]; the corresponding conditions of the oxidation are shown in Fig. 1.1.1. While oxides with low oxygen content ($FeO_{1\pm\delta}$, $Cu_2O_{1\pm\delta}$ etc.) still possess an acceptable level of the electronic conduction (Table 1.1.1), subsequent oxidation may deteriorate the transport properties and cause irreversible dimensional changes, microstructural degradation, etc. Another concern relates to fragility of Fe, Co, Ni in H_2 atmosphere [57-59].

$MnO_{1\pm\delta}$ is stable in a wide domain of conditions including the anode atmosphere. The composition exhibits the p-n transition in a broad $p(O_2)$ range (~10^{-10}-10^{-4}) atm [26] and an occasional oxidation is assumed not to influence critically the transport behavior. On the other hand, oxidation of $MnO_{1\pm\delta}$ into $Mn_3O_{4\pm\delta}$ occurring at 10^{-10}-10^{-11} atm at 1073 K (Fig. 1.1.1) is undesirable since the formation of the new phase may cause strong and irreversible volume changes. The processing conditions of $MnO_{1\pm\delta}$-based anodes are restricted by low melting point of metallic Mn (~1473 K at 10^{-19} atm [25]); this factor should also be accounted for when operating with unstable Mn-based compositions which produce $MnO_{1\pm\delta}$ under reducing conditions. At the same time, at small amounts of $MnO_{1\pm\delta}$ phase, the formation of the liquid phase may ensure the adhesion of the electrode to electrolyte. This indicates the preferability of manganites compared with pure $MnO_{1\pm\delta}$.

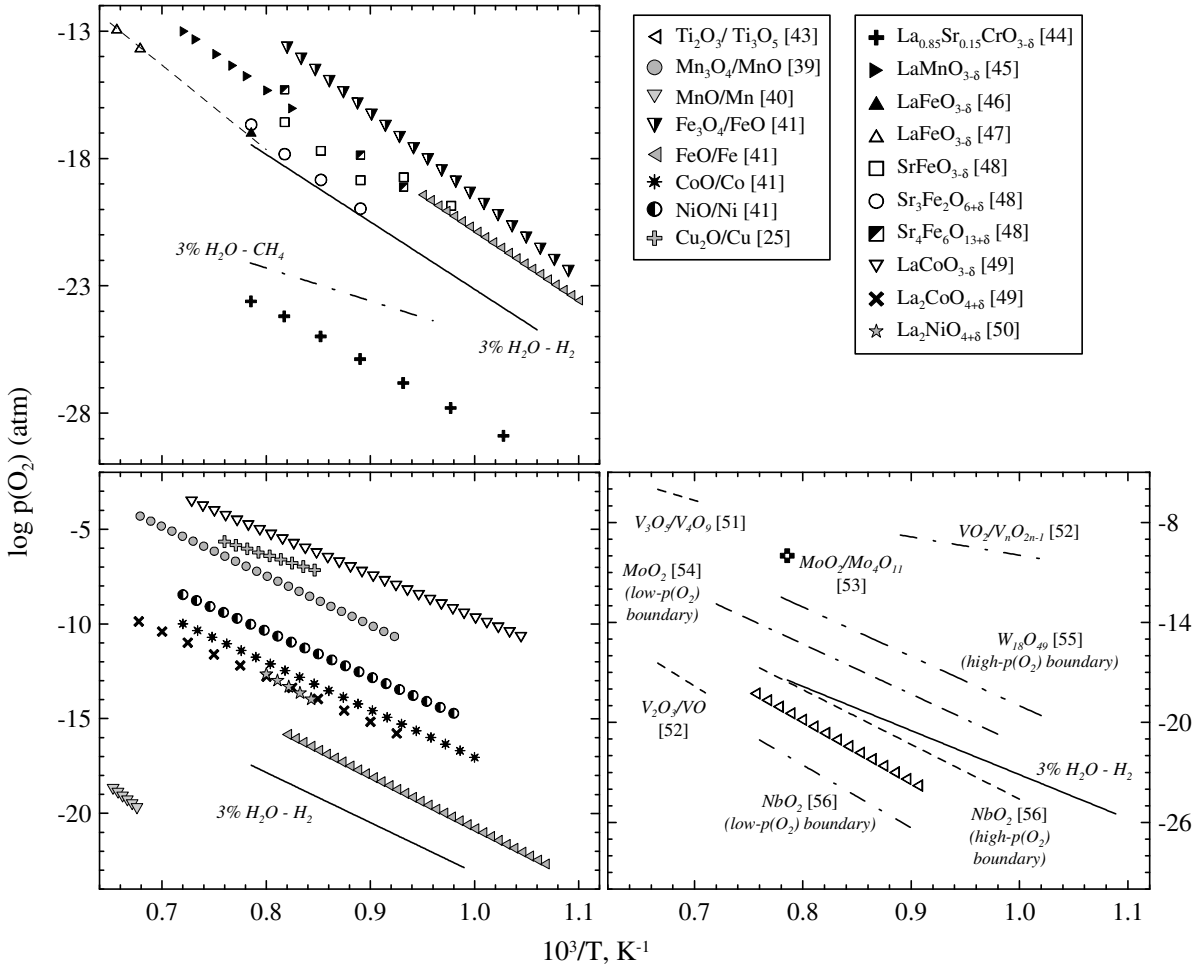

Fig. 1.1.1. Stability limits of selected binary oxides and oxide compounds

Table 1.1.1. Total conductivity of oxides of selected *d*- and *f*-elements

Composition	T, K	$p(O_2)$, atm	σ, S/cm	Reference
Sc_2O_3	1373	1.1×10^{-15}	7.2×10^{-7}	[26]
$TiO_{2-\delta}$	1373	3.8×10^{-14}	5.3	[26]
		5.9×10^{-11}	1.2	
		0.12	1.7×10^{-2}	
$Cr_2O_{3\pm\delta}$	1273	1.0×10^{-6}	9.0×10^{-3}	[60]
(single-crystal, oriented along a-axis)		1.0	1.3×10^{-2}	
	1373	1.0	2.2×10^{-2}	
$MnO_{1\pm\delta}$	1373	1.2×10^{-17}	3.7×10^{-2}	[26]
		1.2×10^{-9}	3.3×10^{-2}	
	1473	1.2×10^{-5}	0.61	
$FeO_{1\pm\delta}$	1273	2.0×10^{-15}	100	[61]
		1.3×10^{-13}	210	
	1373	8.5×10^{-12}	220	
$CoO_{1\pm\delta}$	1259	3.1×10^{-10}	0.14	[62]
		7.3×10^{-6}	0.69	
		0.17	9.2	
	1367	9.3×10^{-2}	10.0	
$NiO_{1\pm\delta}$	1273	1.6×10^{-5}	4.2×10^{-2}	[63]
		0.21	0.18	
	1273	6.7×10^{-4}	3.2×10^{-2}	[26]
	1373	7.0×10^{-4}	6.4×10^{-2}	
		0.31	0.29	
$Cu_2O_{1\pm\delta}$	1073	2.6×10^{-5}	0.37	[64]
	1173	1.4×10^{-5}	1.1	[26]
	1273	1.5×10^{-5}	1.9	
		8.1×10^{-2}	6.4	
Y_2O_3	1473	2.8×10^{-15}	6.9×10^{-6}	[26]
ZrO_2	1263	2.9×10^{-21}	3.7×10^{-6}	[26]
NbO_x	1043	3.2×10^{-3}	9.2×10^{-4}	[65]
		0.17	3.1×10^{-4}	
	1373	1.7×10^{-15}	32	[66]
		3.7×10^{-11}	0.52	
HfO_2	1273	1.1×10^{-19}	2.8×10^{-6}	[26]
$Ta_2O_{5-\delta}$	1247	4.3×10^{-19}	1.2×10^{-12}	[67]
WO_x	1023	6.6×10^{-19}	100	[68]
		8.2×10^{-11}	1.75	
		0.19	0.14	
La_2O_3	1300	1.1×10^{-5}	4.6×10^{-5}	[26]
CeO_2	1073	3.9×10^{-18}	0.21	[26]
		0.10	1.4×10^{-4}	
	1273	6.4×10^{-13}	0.94	

Cr_2O_3 is the unique Cr-O binary compound stable at elevated temperatures [25, 26, 42]. The conductivity is essentially $p(O_2)$-independent under oxidizing and moderately reducing conditions due to small variations of the oxygen content. At low oxygen partial pressures, the determination of the conductivity is complicated by a strong volatility of Cr-containing compounds and a slow equilibration between the solid and gas phase. Moreover, the conductivity behavior is strongly affected by the presence of donor- and acceptor-type impurities in Cr_2O_3; examples are shown in Table 1.1.2. Whatever the transport mechanism, basically the conductivity of Cr_2O_3-based materials does not exceed 1 S/cm which is insufficient for the

anode applications. Another concern is related with the vaporization of chromia-based compounds; this phenomenon and related problems will be discussed in Chapter 1.2.7.

A promising group of oxides for potential anode applications is represented by Ti, V, Nb, W oxides. Under extremely reducing conditions and elevated temperatures shown in Fig. 1.1.1, oxides $TiO_{1\pm\delta}$, $VO_{1\pm\delta}$, $NbO_{1\pm\delta}$ exhibit a metallic-like conduction, while in anode environments TiO_x, VO_x, NbO_x and WO_x are n-type conductors; both mechanisms are favorable for electrochemical applications. Similar to Cr_2O_3, the conductivity is strongly dependent of the presence of impurities in the cation sublattice. At the same time, the practical utilization of this group of oxides as well as studying their transport characteristics is complicated by a large variety of phases existing at different M:O ratio [26, 42, 66, 68, 69]. The phase transitions on oxidation (Fig. 1.1.1) are accompanied by strong irreversible drops of the conductivity (Fig. 1.1.2) and dimensional changes. Interaction of V-, Nb-, Ta-containing phases with hydrogen causes the deterioration of mechanical properties (toughness, plasticity) [59, 70, 71].

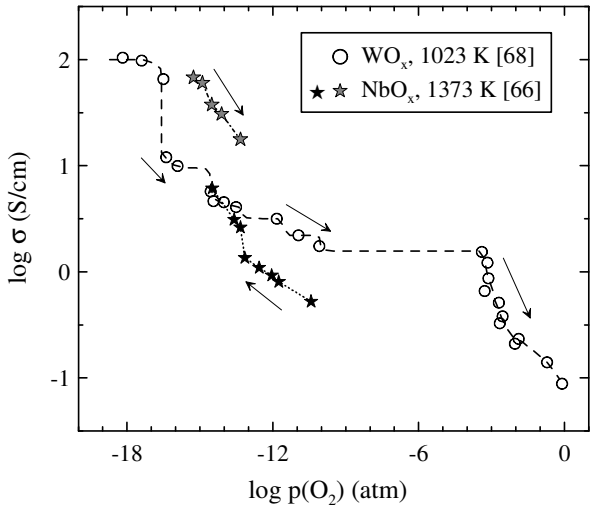

Fig. 1.1.2. Variation of total conductivity of NbO_x and WO_x on isothermal oxidation/reduction

Among 4*f*-elements, one may emphasize the behavior of $CeO_{2-\delta}$ and its derivatives due to promising combination of the stability, electronic and ionic transport properties and catalytic activity towards electrochemical processes. Pure and doped $CeO_{2-\delta}$ have been widely studied as individual anodes or as components of anode composites. Detailed characterization of the oxides may be found elsewhere [72-75]. One of the most critical disadvantages of doped $CeO_{2-\delta}$ for anode applications is insufficient electronic conductivity which requires the presence of metallic phase in the composite, and a high chemical expansivity on redox cycling which necessitates lowering its fraction in anodes [74, 76, 77].

The domain of operation conditions for most *d*-element oxides is restricted by the formation of volatile compounds. As evaluated by Sfeir at al. [44], the losses of a substance can be considered significant, if the partial pressure of volatile species exceeds 10^{-8} atm. The volatilization is essentially critical for Cu-, Ag-, Au-, MoO_x- and WO_x-containing anodes [27, 28, 78-80]. At the presence of VO_x- and Cr_2O_3-based phases, an oxidation of the anode material in wet atmosphere should be avoided [78, 79, 81-85]. In some extent, the volatilization of Mn-, Fe-, Co-, Ni-containing compounds might be problematic [27, 78, 80],

while electrodes containing NbO_x phase should be operated at temperatures lower than 1573-1673 K [86]. Apart from the loss of the material, the vaporization may result in microstructural degradation, especially for liquid phase-assisted processes. Subsequent precipitation of the volatile species into the electrode porous structure may block the pores or cause mechanical failure of the layer, while deposition from the gas phase onto the surface of other components of the cell may cause their poisoning; examples of chromia-related contamination will be presented in Chapter 1.2.7.

The functional characteristics of individual oxides may be modified by appropriate doping with donor- or acceptor-type cations. Among this group of materials, CeO_2- and ZrO_2-based materials have received much attention, since due to their adequate ionic conductivity, thermomechanical properties, contribution into the electrochemical processes, etc., the related oxides may be utilized both as electrolytes and constituents of the composite electrodes ([73, 87-89] and references cited). As for other oxide-based materials, one should mention the studies on NbO_x-, TiO_x-based solid solutions [90-92] which properties are, however, strongly affected by the processing conditions. Although their electrochemical activity has been reported to be insufficient for practical applications, one should not underestimate the potential of this type of materials since a wide choice of dopants enables to find an optimum combination of the stability, transport and mechanical properties.

Wide possibilities may be achieved by fabrication of oxide-based compositions with the structure of perovskite-related phases, spinels, pyrochlores, etc. Among possible combinations of mixed oxides composed of large-size cations in so-called A-sublattice (mainly alkali-earth or rare-arth cations) and small cations in B-sublattice (transition metal cations), we will briefly consider Ti-, Mn-, Fe-, Ni-, Co- Ti-, Nb- and W-based composition where the molar ratio A:B differs from 1. Characteristics of selected compositions in terms of stability, conductivity and electrode activity are presented in Fig. 1.1.1 and Tables 1.1.2, 1.1.3.

Although the reduction stability of manganites, ferrites and other oxides with Ruddlesden-Popper (RP) structure $(Ln,A)_{n+1}B_nO_x$ (where Ln is rare-earth metal, A is an alkali-earth metal and B is a transition metal element) is somewhat improved in comparison with perovskite analogues (Fig. 1.1.1), the level of the electronic and ionic conductivity is rather small to consider these materials as anodes [48, 93-95]. $(La,Ca,Sr,Ba)_{0.6}NbO_{3-\delta}$-based phases with tungsten bronzes-like structure generally exhibit sufficient level of the electronic conductivity which may even be superior compared with corresponding perovskites [96-98]. However, the performance of the bronze anodes studied in [98] is poor, while the problems associated with stability, interaction with YSZ, oxygen diffusion limitations associated with ordering phenomena due to high cation vacancy concentration, and extremely low TEC values [98] significantly constrict their utilization. Regardless these disadvantages, some research in the field of electrochemical characteristics of perovskite-related layered phases and tetragonal bronzes has been carried out [95, 99-101].

Pylochlore-type materials $(Gd,Ca)_2Ti_2O_{7-\delta}$ might be considered as an alternative to titanate perovskites due to their high stability in a wide $p(O_2)$ range which ensures their tolerance towards oxidation. The materials exhibit dominant oxygen ionic conductivity, while the comparatively low electronic contribution and catalytic activity necessitate distribution of metallic phases, ceria-based compositions, surface modification, etc. [108-102].

Table 1.1.2. Comparison of the total electrical conductivity of selected materials based on binary and ternary metal oxides

Composition	T, K	$p(O_2)$, atm	σ, S/cm	Reference
$Mg_{1.95}Ti_{0.95}Mn_{0.1}O_{4\pm\delta}$	1203	1.1×10^{-18}	1.1	[102]
$Mg_{1.95}Ti_{0.95}Fe_{0.1}O_{4\pm\delta}$	1203	1.3×10^{-18} 0.03	1.2 6.6×10^{-4}	[102]
$Mg_{1.95}Ti_{0.95}Co_{0.1}O_{4\pm\delta}$	1203	1.2×10^{-18}	0.94	[102]
$Cr_{0.99}Mg_{0.01}O_x$	1073	1.1×10^{-17} 0.21	5.6×10^{-2} 0.29	[90]
$Cr_{0.99}Ti_{0.01}O_x$	1073	1.1×10^{-18} 0.21	0.17 1.2×10^{-2}	[90]
$Cr_{0.5}Nb_{0.5}O_x$	1173	5% H_2 - Ar 0.21	6.3 2.5×10^{-2}	[91]
$Ti_{1.6}Cr_{0.2}Nb_{0.2}O_{4\pm\delta}$	1173	5% H_2 - Ar 0.21	21 1.5×10^{-2}	[91]
$Zr_{0.77}Y_{0.13}Ti_{0.1}O_{2-\delta}$	1273	H_2 0.21	3.9×10^{-2} 2.4×10^{-2}	[103]
$Nb_{1.33}Ti_{0.67}O_x$	1203	9.6×10^{-19} 6.6×10^{-13}	310 3.4	[92]
$NbTi_{0.5}Ni_{0.5}O_x$	1173	5% H_2 - Ar	280	[104]
$Sr_{0.9}La_{0.1}TiO_{3\pm\delta}$	1073	1.1×10^{-18} 0.20	78 3.7×10^{-3}	[105]
$Sr_3Ti_2O_{7-\delta}$	1173	wet H_2 wet air	3.4×10^{-2} 3.3×10^{-4}	[106]
$Gd_{1.86}Ca_{0.14}Ti_2O_{7-\delta}$	1073	1×10^{-20}	1.4×10^{-2}	[107, 108]
$Sr_3Ti_{1.8}Al_{0.2}O_{7-\delta}$	1073	2.0×10^{-18} 0.25	6.0×10^{-5} 3.3×10^{-4}	[109]
$Sr_3Ti_{1.8}Ga_{0.2}O_{7-\delta}$	1073	2.5×10^{-19}	4.3×10^{-5}	[109]
$Sr_3Ti_{1.9}In_{0.1}O_{7-\delta}$	1173	4.1×10^{-18}	9.2×10^{-4}	[106]
$Sr_2Ti_{0.93}In_{0.07}O_{4-\delta}$	1173	2.4×10^{-18} 0.15	1.1×10^{-4} 2.2×10^{-2}	[106]
$Ce_{0.8}Ca_{0.2}VO_{4-\delta}$	1073	1×10^{-20}	16	[110]
$CaV_{0.5}Mo_{0.5}O_{3-\delta}$	1123 973-1173	1.0×10^{-18} 0.21	320 10^{-5}-10^{-4}	[111]
$La_{0.8}Ca_{0.2}CrO_{3-\delta}$	1073	H_2	4.9	[112]
$La_{0.8}Sr_{0.2}Cr_{0.5}Mn_{0.5}O_{3-\delta}$	1073	wet 5% H_2-Ar	5.1	[113]
$La_{0.5}Sr_{1.5}MnO_{4-\delta}$	1073	9.4×10^{-16} 0.21	7.9 8.4	[94]
$La_{0.8}Sr_{0.2}FeO_{3-\delta}$	1123	1.7×10^{-18} 0.21	0.14 46	[114]
$Sr_3Fe_2O_{6-\delta}$	1123	1.5×10^{-18} 0.18	0.15 23	[115]
$LaSrFeO_{4-\delta}$	1073	1.1×10^{-15} 0.21	8.0×10^{-2} 0.84	[94]
$Sr_4Fe_6O_{13-\delta}$	1123	1.2×10^{-18} 1.3×10^{-5}	4.0 0.23	[115]
$SrFeCo_{0.5}O_x$	1173	H_2 0.21	0.49 22	[116]
$Sr_{0.25}Ba_{0.25}NbO_{3-\delta}$	1203	1.1×10^{-18} 1.0×10^{-2}	5.1 6.4×10^{-4}	[96]
$Sr_{0.6}Nb_{0.8}Ti_{0.2}O_{3-\delta}$	1203	1.2×10^{-18}	2.0	[96]
$Sr_{0.4}La_{0.2}Nb_{0.6}Ti_{0.4}O_{3-\delta}$	1203	1.3×10^{-18} 0.07	3.2 1.3×10^{-3}	[96]

Table 1.1.3. Examples of polarization resistance and polarization values under OCV conditions and 100 mA/cm^2 current, respectively, of selected perovskite and perovskite-like anodes

Composition	Electrolyte	T, K	Gas atmosphere or p(O_2), atm	R_η, Ohm×cm^2	η, mV (i=100 mA/cm^2)	Reference
$Gd_{1.86}Ca_{0.14}Ti_2O_{7-\delta}$ - Ni - CGO (30-50-20 wt.%) *c.c.: Pt gauze*	LSGM*	1073	wet 10% H_2 - 90% N_2		56	[107]
$Ce_{0.8}Ca_{0.2}VO_{3-\delta}$ - Ni - 8YSZ (30-50-20 wt.%) *c.c.: Pt gauze*	LSGM*	1073	wet 10% H_2 - 90% N_2		110	[107]
$La_{0.7}Sr_{0.3}VO_{3-\delta}$ *c.c: Pt mesh*	8YSZ*	1223	100% H_2	8.5		[117]
		1223	3% H_2S - 97% H_2	7.1		
$Ce_{0.9}Sr_{0.1}VO_{4-\delta}$ *c.c: Au wire*	8YSZ*	1223	5% H_2S - N_2	5.4		[111]
$SrCo_{0.8}Fe_{0.2}O_{3-\delta}$ *c.c.: Au grid*	YSZ**	1223	H_2		410	[101]
$La_{0.6}Sr_{0.4}Co_{0.2}Fe_{0.8}O_{3-\delta}$ *c.c.: Au grid*	YSZ**	1223	H_2		390	[101]
$La_{0.6}Sr_{0.4}Co_{0.2}Fe_{0.8}O_{3-\delta}$-YSZ (50-50 wt%) *c.c: Pt paste*	8YSZ*	1173	CH_4 - H_2 - Ar	3.0		[118]
$SrFeCo_{0.5}O_x$ *c.c.: Au grid*	YSZ**	1223	H_2		570	[101]
$SrFeCo_{0.5}O_x$ with Ni-YSZ anode layer *c.c.: Au grid*	YSZ**	1223	H_2		190	[101]
$Na_{0.8}WO_{3-\delta}$-YSZ (40-60 wt%) *c.c: Ag paste*	8YSZ*	973	3% H_2O - H_2	1.2		[100]
$Na_{0.8}WO_{3-\delta}$-YSZ (40-60 wt%) impregnated with Pd *c.c: Ag paste*	8YSZ*	973	3% H_2O - H_2	0.50		[100]

**LSGM corresponds to $(La_{0.9}Sr_{0.1})_{0.98}Ga_{0.8}Mg_{0.2}O_{3-\delta}$, 8YSZ corresponds to $Zr_{0.84}Y_{0.16}O_{2-\delta}$.*

***The cation composition of YSZ is not indicated*

The lattice of perovslites is tolerant towards cation substitution, while their transport properties are generally better compared with other families, like spinels, pyrochlores or garnets. Analysis of the low-p(O_2) stability limits (Fig. 1.1.1) restricts the choice of the perovskite-type anode materials to chromites, titanates, molybdates and vanadates. Moreover, appropriate doping of ferrites and manganites with a cation which ensures the low-p(O_2) stability without substantial deterioration of the transport and catalytic properties enables to consider these compounds as another group of potential anode materials.

Among the perovskite compounds, in the present study the primarily attention will be focused on chromite, titanate and manganite groups, since ferrites and cobaltites are insufficiently stable in fuel conditions [46-49]. Some authors report application of thermodynamically unstable perovskites such as $(La,Sr)(Co,Fe)O_{3-\delta}$ as SOFC anodes [101] or catalysts for hydrocarbon oxidation [118, 121]. One should note, however, that the requirements for catalyst materials differ from those to anodes, in particular in terms

of the electrocatalytic activity, compatibility with solid electrolytes, etc, while catalysts can generally be prepared and replaced by a simpler technology which imposes less stringent requirements to their stability.

Another large group of potential anodes includes vanadate-based perovskites [110, 111, 122] and the perovskites with large fraction (≥50 mol.%) of V, Mo, Nb. In particular, attractive characterisctics have been reported for $A_2(B,Mo)O_{6-\delta}$ ordered perovskites, where A is alkali-earth metal and B corresponds to Mg or transition metal cation [123-126]. Perovskite-type materials containing V, Mo, Nb etc. cations are regarded especially promising when working with S-containing fuels; however, their mechanical and transport characteristics are strongly susceptable to redox cycling [20, 111, 117, 127-130]. Nevertheless, a moderate content of these cations in chromites and manganites may ensure the optimum combination of the functional properties; the related compositions will be considered in the following sections.

1.2. Chromite-based perovskite solid solutions

1.2.1. Solubility of dopants

Solid solutions of perovskite $LnCrO_{3-\delta}$ are formed for Ln = La - Lu, Y, except for cerium which forms chromites stable only under reducing conditions [131]. In La_2O_3 - Cr_2O_3 system, $LaCrO_{3-\delta}$ is the only single phase compound [132]. The perovskite chromites of various lanthanides are similar to each other and are characterized by a relatively narrow field of the forming solid solutions [131]. The stability of $LnCrO_{3-\delta}$ decreases with lowering Ln ionic radius; the trend is especially obvious under reducing conditions [17].

Alkaline-earth cations are most common dopants for chromites, mainly due to their acting as electron acceptors on the Ln or Cr sites and resultant contribution to the p-type electronic conductivity. Among dopants, Ca, Sr and in some cases Ba were studied as A-site substitutions. Mg is more appropriate for B-site doping due to its smaller radius [133]. In accordance with [44, 132, 134], the solubility of Ca in $LaCrO_{3-\delta}$ varies from 12% at 923 K to 50% at 1673 K. Single phase perovskites may be synthesized at (La+Ca)/Cr ratio in the range of 0.96 - 1.04 [135]. Annealing at $p(O_2) = 10^{-9}$ atm at 1873 K decreases the solubility limit down to 22% [132]; the worse stability of $(La,Ca)CrO_{3-\delta}$ at low $p(O_2)$ is confirmed in [134]. Considering other lanthanide chromites, $Ln_{1-x}Ca_xCrO_{3-\delta}$ is stable at $0\le x\le 0.4$ for Ln = Pr, Nd, Sm, Eu, Gd, Y; $0\le x\le 0.2$ for Ln = Tb and $0\le x\le 0.15$ for Ln = Yb ([131, 136] and references therein).

An excess of Ca results in formation of La_2O_3, CaO, $CaCrO_4$, $Ca_3(CrO_4)_2$, $Ca_5(CrO_4)_3OH$ in air [44, 132]. The phases La_2O_3, CaO, β-$CaCr_2O_4$, $Ca(CrO_2)_4$ and RP-chromites ($(La,Sr)_2CrO_4$, $(La.Sr)_3Cr_2O_7$, $(La,Sr)_4Cr_3O_{10}$) were identified in Ca-rich $(La,Ca)CrO_{3-\delta}$ under reducing conditions [132]. Strong oxidation of $(La,Ca)CrO_{3-\delta}$ causes formation of Cr^{6+} species on the surface and segregation of La_2CrO_6 and $Ca_m(CrO_4)_n$ phases. The process is promoted by higher Ca content, lower temperature and higher $p(O_2)$ [132, 137, 138].

Sr is assessed to have worse solubility in $LaCrO_{3-\delta}$ than Ca, consistently with larger difference in ionic radii between La and alkali-earth cation. The data on solubility limit of Sr are more scattered, possibly due to discrepancies in the preparation procedure or slower equilibration in La_2O_3-SrO-Cr_2O_3 system compared with Ca-containing analogues [132, 139]. The latter factor can be attributed to smaller ionic radii and higher mobility of Ca cations [133, 140]. As reported by Peck et al. [139], Sr is soluble up to 10% at

1223 K in air, while other authors indicated a higher solubility of Sr: 15% at 1073 K [141] and 20% at 1173 K [138]. After sintering at elevated temperatures (1673 K) and subsequent quenching, the solubility limit of Sr increases up to 25% [44, 139]. $Ln_{1-x}Sr_xCrO_{3-\delta}$ are single phase perovskites at $0\leq x\leq 0.15$ for Ln=Pr, Eu and $0\leq x\leq 0.05$ for Ln = Tb, Y [131]. In opposite to Ca-doped chromites, Sr solubility is reported to increase on reduction from 10% in air to 31% at 10^{-9} atm (under strong vacuum conditions) [44, 139]; however, one should account for large difference between the synthesis temperature in both studies. The authors attribute the improved stability under low $p(O_2)$ to formation of RP-chromites which achieve a fast equilibrium with the perovskite phase, in contrast to $SrCrO_4$ and $Sr_{2.67}(CrO_4)_2$ phases dominant in air. The dominant secondary phases in $La_{1-x}Sr_xCrO_{3-\delta}$ are $SrCrO_4$, $Sr_{2.67}Cr_2O_8$, $La_{16}Cr_7O_{44}$, $Sr_5(CrO_4)_3OH$ in air [44, 139] and $La_2Sr_2O_5$, La_4SrO_7, Sr_2CrO_4, $Sr(CrO_2)_2$, $Sr(CrO_2)_4$ and RP-chromites at low $p(O_2)$ [139, 142].

Formation of single phase perovskites $Ln_{1-x}Ba_xCrO_{3-\delta}$ was observed at $0\leq x\leq 0.1$ for Ln = La, Pr; $0\leq x\leq 0.05$ for Ln = Eu, Gd, Tb, Y [131, 143]. The low solubility of Ba may be attributed to both large difference in ionic radii between Ba and Ln cations and high stability of $BaCrO_4$ and $BaCr_2O_4$ phases which are frequently present as impurities in Ba-rich chromites [143, 144].

Generally, $LnCrO_{3-\delta}$ are orthorhombic perovskites exhibiting a phase transition into the rhombohedral structure at ~563 K; no transition up to at least 1173 K was observed on $PrCrO_{3-\delta}$, $NdCrO_{3-\delta}$, $SmCrO_{3-\delta}$, $YCrO_{3-\delta}$ [131, 145-147]. Ca-doping allows to increase the transition temperature [131, 148]; this is consistent with the similarity of Ca^{2+} and La^{3+} ionic radii. Increasing Ca content in $La_{1-x}Ca_xCrO_{3-\delta}$ up to x = 0.5 is predicted to produce the cubic perovskite structure [135]. Introduction of large Sr and Ba atoms reduces the temperature of the orthorhombic-rhombohedral transition and promote the stabilization of the rhombohedral structure ($R\bar{3}c$) at room temperatures [131, 143, 149].

Due to the small radius, Mg is incorporated into B-sublattice; attempts to obtain A-site substituted $(Ln,Mg)CrO_{3-\delta}$ result in formation of $MgCr_2O_4$ spinel [143]. Depending on Ln cation radius and preparation conditions, the solubility limit of Mg in $LnCr_{1-x}Mg_xO_{3-\delta}$ is assessed to be $0\leq x\leq 0.4$ ([131] and references therein). For $LaCr_{1-x}Mg_xO_{3-\delta}$ the maximum Mg content was found to be 46% in air and 7.5% at $p(O_2) = 10^{-16}$ atm at 1573 K [142], while for $NdCrO_{3-\delta}$ the limit is 25% at 1173 K [150]. At least 20% of Mg can be introduced into $La_{0.8}Sr_{0.2}Cr_{1-x}Mg_xO_{3-\delta}$ [151]. An excessive Mg content may cause precipitation of MgO phase at the grain boundaries [142]. Under reducing conditions, Mg solubility in $LaCrO_{3-\delta}$ is evaluated as >10% [17]. Mg-doped chromites generally possess the orthorhombic struture [142, 150] transforming into the rhombohedral symmetry on reduction [112].

The series of $La_{0.9}Ca_{0.1}Cr_{1-x}Al_xO_{3-\delta}$ with $0\leq x\leq 0.9$ was studied in the $p(O_2)$ region 10^{-21} - 1 atm [152], while the electrochemical properties of $La_{0.75}Sr_{0.25}Cr_{0.5}Al_{0.5}O_{3-\delta}$ were studied in air and in wet 5% H_2 [9], with no emphasis on the phase stability. In $YbCrO_{3-\delta}$ Al is soluble up to 0.35 [131]. Doping with Al enables to stabilize the rhombohedral structure at low temperatures [153, 154].

Ti has unlimited solubility in B-sublattice of $(La,A)(Cr,Ti)O_{3-\delta}$ (A = Ca, Sr), provided that the introduction of Ti is compensated by appropriate acceptor doping or creation of A-site vacancies [155-157]. At Ca:Ti <1, the formation of secondary intergrowth phase $La_n(Ti,Cr)_nO_{3n+2}$ can be observed. The materials are orthorhombic perovskites (S.G.: *Pbnm*) for Ca(Sr) and Ti content lower than 60 - 70 mol.% [156, 158] and exhibit a stability at least down to 10^{-21} atm, with Ti solubility increasing on reduction [146, 155, 159].

At least 5 mol. % of V can be doped into $La_{0.85}Sr_{0.15}Cr_{1-x}V_xO_{3-\delta}$ [160] and $La_{0.8}Ca_{0.15}Sr_{0.05}Cr_{1-x}V_xO_{3-\delta}$ [161] forming perovskites with rhombohedrally-distorted structure. The solubility of V may be enhanced by reduction or acceptor doping. The formation of single phase $Ce_{0.75}Sr_{0.25}Cr_{0.5}V_{0.5}O_{3-\delta}$ under low $p(O_2)$ with tetragonal structure was reported. However, high V content may induce phase transitions on oxidation or reduction, detrimental for the electrochemical applications [162]. An excess of V in $(La,A)(Cr,V)O_{3-\delta}$ (A = Ca, Sr) causes formation of $A_3(VO_4)_2$-based phases [160, 161, 163].

Mn, Fe and Co have been reported to have unlimited solubility in $LaCrO_{3-\delta}$ or in $(La,A)CrO_{3-\delta}$ under atmospheric conditions and with moderate amount of alkali-earth dopants [131, 164-166]. The composition $LaCr_{0.8}Co_{0.2}O_{3-\delta}$ was shown to consist of a mixture of orthorhombic $LaCrO_{3-\delta}$- and rhombohedral $LaCoO_{3-\delta}$-based phases [167], while at other ratios Cr/Co single phase perovskites are produced. Similar mixtures of the orthorhombic and rhombohedral phases were found for $LaCr_{0.4}Mn_{0.6}O_{3-\delta}$ [168] and for $La_{0.33}Sr_{0.67}Cr_{0.33}Fe_{0.67}O_{3-\delta}$ [169].

Mn-, Fe-, Co-substituted chromites are unstable towards high content of alkali-earth dopants or oxygen deficiency. Depending on the cation composition, the stability limits may be located close to anodic conditions. In most studies, the decomposition or low-$p(O_2)$ equilibration is hindered kinetically which results in discrepancies between the literature data on the phase stability or crystal structure. As an example, a precipitation of metallic Co from $LaCr_{0.9}Co_{0.1}O_{3-\delta}$ at 10^{-18} - 10^{-16} atm at 1273 K was reported [146], while no decomposition of $La_{0.7}Ca_{0.3}Cr_{0.8}Co_{0.2}O_{3-\delta}$ was detected under similar conditions [170], although the high quantities of Ca and Co should destabilize the structure. While $LaCr_{0.5}Mn_{0.5}O_{3-\delta}$ exhibits a separation of traces of La_2O_3 in wet H_2 [171], $(La,Sr)(Cr,Mn)O_{3-\delta}$ are stable in typical anode atmospheres [8, 10], despite the expected destabilization induced by introduction of Sr.

$LaCr_{1-x}Mn_xO_{3-\delta}$ preserve the orthorhombically-distorted structure for $0\leq x\leq 0.5$, while for $x\geq 0.7$ the material adopts the rhombohedral symmetry [168, 171]. The data on the crystal structure of reduced $LaCr_{1-x}Mn_xO_{3-\delta}$ are scarce due to insufficient phase stability; according to Deleebeck et al. [171], in wet H_2 $LaCr_{0.5}Mn_{0.5}O_{3-\delta}$ becomes cubic. $LaCr_{1-x}Fe_xO_{3-\delta}$ perovskites form a series of solid solutions with orthorhombic crystal lattice in air, typical for both end members [172, 173].

Increasing Co content in $LaCr_{1-x}Co_xO_{3-\delta}$ above x = 0.25 causes rhombohedral distortion of the structure [167, 173]; the behavior of Mn- or Co-doped chromites is consistent with the symmetry of orthorhombic $LaCrO_{3-\delta}$ and rhombohedral $LaMnO_{3-\delta}$ and $LaCoO_{3-\delta}$ [49, 131, 174, 175]. The orthorhombic and rhombohedral structure is preserved on reduction of $LaCr_{1-x}Co_xO_{3-\delta}$ with $0\leq x\leq 0.15$ and $0.25\leq x\leq 0.4$, correspondingly, while for $0.5\leq x\leq 0.8$, high oxygen losses induce formation of cubic perovskites [167].

Similar to $(La,Sr)CrO_{3-\delta}$, $La_{0.75}Sr_{0.25}Cr_{0.9}B_{0.1}O_{3-\delta}$ (B = Mn, Fe, Co) are rhombohedral perovskites [176]. Increasing Mn content up to 50 mol. % preserves the rhombohedral structure [9, 113, 131, 177], while for Fe-doped analogues, the symmetry transforms into the orthorhombic one [9, 178].

A gradual phase transition rhombohedral-cubic is observed for $La_{0.75}Sr_{0.25}Cr_{0.5}Mn_{0.5}O_{3-\delta}$ at 770 - 1270 K [177]. The rhombohedral structure of $La_{1-x}Sr_xCr_{0.5}Mn_{0.5}O_{3-\delta}$ with x = 0.2 is maintained on reduction in wet 5% H_2, while the compositions with x = 0.25 and x = 0.3 exhibit a transformation into the orthorhombic and cubic structure, respectively [113]. $La_{0.75}Sr_{0.25}Cr_{0.5}Fe_{0.5}O_{3-\delta}$ is orthorhombic in air. On reduction, traces of metallic Fe can be detected, while the perovskite adopts the rhombohedral symmetry [9,

178]. Increasing Cr content in $La_{0.3}Sr_{0.7}Fe_{1-x}Cr_xO_{3-\delta}$ above 33% may induce formation of $SrCrO_4$. Subsequent reduction results in dissolution of $SrCrO_4$ phase, with simultaneous formation of $Fe(Fe,Cr)_2O_4$ spinel and precipitation of metallic Fe [169, 179].

Ni has a limited solubility in chromites which increases at lower T and higher $p(O_2)$ [131]. The composition with ~60 mol. % of Ni was found to consist of $LaCrO_{3-\delta}$- and $LaNiO_{3-\delta}$-based phases [180]. In $LnCr_{1-x}Ni_xO_{3-\delta}$ (Ln = Gd, Yb), Ni can be dissolved up to x = 0.15 [131]. The stability of $La(Cr,Ni)O_{3-\delta}$ under reducing conditions is reported for 50 - 60 mol.% of Ni at 1173 - 1273 K [181, 182], although the phase may be stabilized kinetically. $LaCr_{1-x}Ni_xO_{3-\delta}$ are orthorombic perovskites at $x<0.6$ and rhombohedral at $x>0.7$ at room temperature [181]. The phase transition shifts to lower temperatures on Ni-doping [183]. Introduction of A-site acceptor-type dopants and/or reduction decrease the solubility of Ni in $(Ln,A)(Cr,Ni)O_{3-\delta}$ down to 10 - 20 mol. % [184, 185]. Reduction induces subsequent lowering of Ni solubility, although the determination of exact values is difficult due to kinetic reasons. The formation of submicron Ni particles at low $p(O_2)$ is important in terms of potential electrochemical applications [17, 184, 186]. For $La_{1-x}Sr_xCr_{1-y}Ni_yO_{3-\delta}$, the transition orthorombic-rhombohedral occurs at x = 0.2 - 0.25 and y = 0.05 - 0.1 under ambient conditions [176, 187].

Similar to Ni-doped chromites, an attention was attracted by Ru-containing analogues due to their electrocatalytic activity. Up to 20 - 25 mol.% of Ru can be accommodated by $La_{0.8}Sr_{0.2}Cr_{1-x}Ru_xO_{3-\delta}$ [15, 188].

1.2.2. Key defect chemistry mechanisms

The basic relationships of the defect chemistry of chromites can be found elsewhere [134, 146, 189, etc.]. Here, 3 simplified possibilities will be considered which include $(La,A)CrO_{3-\delta}$ and $La(Cr,B)O_{3-\delta}$ perovskites where A and B are dopant cations with a fixed oxidation state, and $La(Cr,B)O_{3-\delta}$ where B is a transition metal cation with variable valence.

Replacement of 3-fold charged lanthanum cations $La_{La}^{\times}$ with 2-fold charged cations of the dopant A'_{La} necessitates charge compensation realized by formation of equivalent amount of oxygen vacancies $V_O^{\bullet\bullet}$ or increasing the fraction of Cr^{4+} species ($Cr_{Cr}^{\bullet}$). Therefore, the predominant defects in $La_{1-x}A_xCrO_{3-\delta}$ are A'_{La}, $V_O^{\bullet\bullet}$ and $Cr_{Cr}^{\bullet}$. The distribution of the defects in the chromite crystal lattice is considered to be random, in accordance with [152, 190], while no structural transitions are taken into account. Although in literature one can find a possibility of existence of chromium or oxygen interstitials or cation vacancies ([131, 191, 192] and references cited) in chromites, these aspects will not be addressed.

The charge compensation via formation of $Cr_{Cr}^{\bullet}$ species is realized in a wide $p(O_2)$ range, including the atmospheric conditions, while the formation of oxygen vacancies dominates at lower $p(O_2)$. The relationship between the defects can thus be expressed by equation of charge conservation: $2\delta + p = x$, where δ, p and x correspond to the concentration of $V_O^{\bullet\bullet}$, $Cr_{Cr}^{\bullet}$ and A'_{La}, respectively. Taking into account lattice site

conservation condition, the concentration of $Cr_{Cr}^{\times}$ and $O_O^{\times}$ may be expressed as (1-*p*) and (3-δ), respectively. The oxygen exchange between the perovskite and gas phase induced by reduction of the material may be described by equation

$$1/2O_2 + V_O^{\cdot\cdot} + 2Cr_{Cr}^{\times} = O_O^{\times} + 2Cr_{Cr}^{\cdot} \qquad \textbf{(Eq. 1.2.1)}$$

Taking into account the conditions of charge and lattice site conservation, the equilibrium constant of the process described by Eq. (1.2.1) may be formulated as

$$K_1 = p(O_2)^{-1/2}\left(\frac{3-\delta}{\delta}\right)\left(\frac{x-2\delta}{1-x+2\delta}\right)^2 \frac{\gamma_2^2\gamma_3}{\gamma_1^2\gamma_4} \qquad \textbf{(Eq. 1.2.2)}$$

where $\gamma_1, \gamma_2, \gamma_3, \gamma_4$ correspond to the activity coefficients of $Cr_{Cr}^{\times}, Cr_{Cr}^{\cdot}, O_O^{\times}$ and $V_O^{\cdot\cdot}$. Due to the high ionic strength in the crystal [189], the activity coefficients are considered independent of the defect concentrations.

Eq. (1.2.2) assumes a linear relationship between log δ and log $p(O_2)$ for $\delta << x/2$, with the proportionality coefficient equal to -½, as shown on the inset in Fig. 1.2.1. Since variations of the oxygen deficiency in oxidative atmospheres are below 10^{-2}, the absolute value of the oxygen content is nearly $p(O_2)$-independent in a wide range of oxygen pressures. Therefore, the electronic conductivity in this domain of $p(O_2)$ is essentially unaffected by reduction while the the ionic conduction and chemically-induced strains which are proportional to the deficiency, are low. Further reduction induces a gradual decrease of the oxygen content; the proportionality between log δ and log $p(O_2)$ is preserved. The onset of extensive oxygen losses is determined by the nature and amount of A-site dopants and by temperature, being shifted to more oxidative conditions on heating or increasing the dopant content.

As shown in Fig. 1.2.1, the oxygen losses observable on Ca- and Sr-doped chromites are close, with $(La,Sr)CrO_{3-\delta}$ exhibiting slightly larger oxygen deficiency [134, 190]. This may be attributed to a larger cell volume of Sr-substituted chromites which facilitates the oxygen losses, or stronger tendency of rhombohedral structure to the formation of oxygen vacancies. At extremely low $p(O_2)$, the dependence log δ vs. log $p(O_2)$ deviates from the linearity, while the absolute value of oxygen content approaches the value corresponding to complete reduction of Cr into 3+. Obviously, for $La_{1-x}A_xCrO_{3-\delta}$ the limiting value of oxygen nonstoichiometry should be equal to x/2. However, in practice, this saturation for most chromites occurs in a region of extremely low $p(O_2)$ located beyond the experimental conditions (unless B-site substituted chromites are reduced) or stability domain of the perovskites.

The equilibrium constant in Eq. (1.2.2) may be expressed by the concentration of $Cr_{Cr}^{\cdot}$ species:

$$K_1^* = p(O_2)^{-1/2}\left(\frac{6-x-p}{x-p}\right)\left(\frac{p}{1-p}\right)^2 \qquad \textbf{(Eq. 1.2.3)}$$

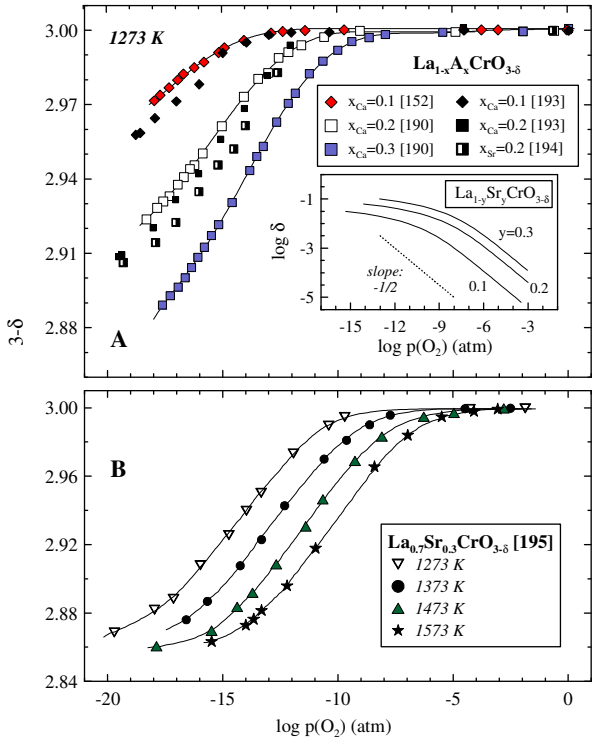

Fig. 1.2.1. Isothermal dependencies of oxygen content in selected alkali-earth metal-doped chromites vs. $p(O_2)$. The inset shows the $p(O_2)$ dependence of delta in the logarithmic scale, calculated using the modelling parameters estimated in [195].

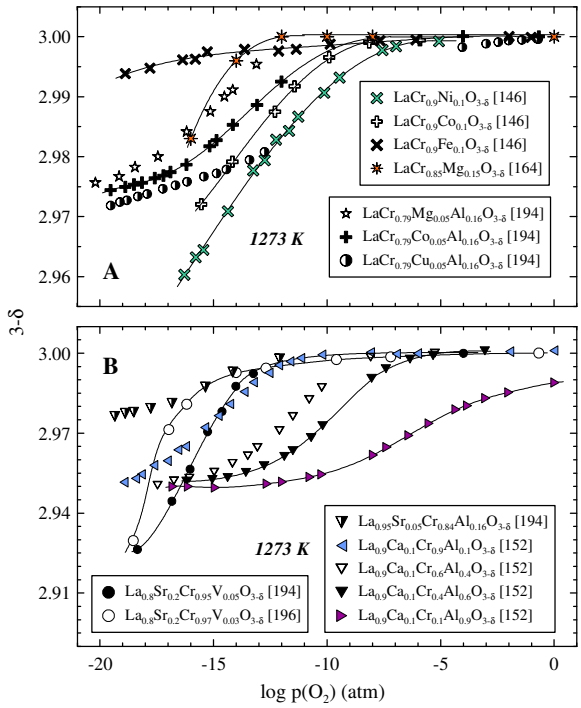

Fig. 1.2.2. Isothermal dependencies of oxygen content in selected B-site doped chromites vs. $p(O_2)$

On approaching the low-$p(O_2)$ limit of the oxygen deficiency, the amount of $Cr_{Cr}^{\bullet}$ becomes negligible in comparison with $V_O^{\bullet\bullet}$ and $A_{La}^{\prime}$, while the concentration of $Cr_{Cr}^{\times}$ is hardly affected by $p(O_2)$ variations. This yields a linear relationship $p = k \times p(O_2)^{1/4}$, where k is constant involving the equilibrium constant and equilibrium concentrations of $A_{La}^{\prime}$, $O_O^{\times}$ and $Cr_{Cr}^{\times}$. As shown in following sections, the electronic conductivity of chromites is determined by the population of Cr^{4+} species. Therefore, in the region of large oxygen losses, a linear relationship between log σ and log $p(O_2)$ with the slope +1/4 is expected.

If $LaCrO_{3-\delta}$ is doped into B-sublattice by a 2-fold charged cation, with the oxidation state stable within the experimental conditions (i.e. Mg^{2+}), the basic equations are similar to $(La,Sr)CrO_{3-\delta}$. In accordance with the coexistence of 3 types of species (Cr^{3+}, Cr^{4+} and B^{2+}), the equilibrium constant of the process Eq. (1.2.2) adopts the form (assuming that the activity coefficients are $p(O_2)$-independent)

$$K_1 = p(\mathrm{O}_2)^{-1/2}\left(\frac{3-\delta}{\delta}\right)\left(\frac{y-2\delta}{1-2y+2\delta}\right)^2 \qquad \textbf{(Eq. 1.2.4)}$$

The similarity between Eqs. (1.2.2) and (1.2.4) assumes that the behaviour of Mg-doped chromites should not essentially differ from that of A-site substituted $(La,A)CrO_{3-\delta}$ considered previously. The nonstoichiometry curve still exhibits 2 saturations and one continuous drop of oxygen content. Similar to the

1st situation, the low-p(O_2) saturation corresponds to complete reduction of Cr into 3+ state, with the corresponding assymptotic value of oxygen deficiency equal to y/2.

B-site doping induces larger variations of the oxygen content variations then substitutions into A-sublattice (Fig. 1.2.2). Even doping of cations with relatively high oxidation state accompanied by equivalent introduction of acceptor-type dopants shifts the onset of oxygen losses to higher p(O_2) [152, 191]. This may be attributed to comparatively weak B-O bond strength and more significant destabilization of the structure by B-site doping. Obviously, replacement of Cr with cations stable with oxygen coordination lower than octahedral should increase the effect of the doping.

The last case considered involves the situation when both B-site cations possess variable oxidation state under working conditions. For simplicity, the situation when only 2 oxidation states can be realized for both cations will be considered. Apart from the relationships valid for the previous situations, the transition metal cations participate in the process of electrone exchange with the equilibrium constant

$$K_2^* = \frac{[B'_{Cr}][Cr^{\bullet}_{Cr}]}{[B^{\times}_{Cr}][Cr^{\times}_{Cr}]} \qquad \textbf{(Eq. 1.2.5)}$$

Combination of Eqs. (1.2.2) and (1.2.5) with modified conditions of lattice site and charge concervation yields 6 equations with 6 variables. The system can be solved analytically, but the final expression is rather complex. In practice, the proposed model is generally complicated by numerous factors; among those one may emphasize the following:

1. Most *d*-elements may adopt more than 2 oxidation states, involving the process of charge disproportionation under the experimental conditions [10, 191, 194].
2. Extensive oxygen losses may induce phase decomposition or structural transformations, while the coexistence of 2 or more phases significantly affects the equilibration kinetics [146, 191].
3. The presence of lattice defects may impose constrictions on their cation or anion environment due to electrostatic or steric factors [152].

In some studies, the defect model of chromites doped with transition metals is simplified; the most common assumption relates to neglecting the electron exchange and considering chromium or the dopant cation to be stable in a definite oxidation state. Although this approach satisfactory describes the data presented in works [191, 196, 197], more studies on perovskite systems are required in order to make certain conclusions about the processes responsible for the behavior of doped chromites.

1.2.3. Total conductivity

The conductivity in $LnCrO_{3-\delta}$ is essentially electronic; the ionic transference numbers are less than 10^{-4} [131, 198]. The electronic transport in chromites proceeds by hopping electron holes along Me-O-Me network in B-sublattice (p-type conductivity). Chromites are characterized by relatively strong electron localization on Cr atoms [199] which favors small polaron conduction and enhanced activation energies of the hole mobility. In the absence of structural transformations, the isothermal conductivity should be

governed by the population of charge carriers which is equivalent to the concentration of $Cr_{Cr}^{\cdot}$. Correspondingly, the basic trends shown in the previous section can be applied for characterization of the electronic transport behavior.

Preparation conditions strongly affect the transport properties. This may originate from incomplete synthesis, oversintering, volatilization of Cr-containing species at high temperatures ([131, 134] and references therein). The scattering between the literature data is especially strong for undoped $LnCrO_{3-\delta}$, where the content of charge carriers is mainly governed by the presence of impurities [200]. $LaCrO_{3-\delta}$-based materials exhibit a degradation of the conductivity [141, 201], especially pronounced at low $p(O_2)$.

$LaCrO_{3-\delta}$-based perovskites generally exhibit larger conductivity under ambient conditions compared with other lanthanides, as shown in Fig. 1.2.3. The conductivity of $LnCrO_{3-\delta}$ decreases in the row La>Nd>Y>Sm [131]. This behavior correlates with the corresponding activation energies and is attributed to higher overlapping integral of the *d*- and *p*-orbitals of chromium and oxygen atoms, respectively, and faster hole mobility for larger Ln radius. Kunifusa et al. [150] reported the conductivity of $NdCrO_{3-\delta}$ to be significantly higher compared with $LaCrO_{3-\delta}$ [199] and $YCrO_{3-\delta}$ [202], although the activation energy is minimum for $LaCrO_{3-\delta}$ (0.20 eV vs. 0.22 - 0.23 eV for other chromites). In some studies, a higher conductivity of $PrCrO_{3-\delta}$-based perovskites in comparison with other $LnCrO_{3-\delta}$ analogues in air or under reducing conditions was reported [136, 184].

Ce-containing chromites show a drastic change of the activation energy of the electronic conductivity in air with temperature (0.15 eV in low-temperature vs. 0.20 - 0.25 eV in the high-temperature region) [203]. The difference in the slopes decreases on introducing Ca, presumably due to an effect of the equilibrium between $Ce^{4+/3+}$ and $Cr^{4+/3+}$ on variations of the temperature and resultant change of the content of mobile charge carriers, although the low stability of Ce-containing chromites in air and the possibility of the phase transition should also be considered [131, 204].

The conductivity of $(Ln,A)CrO_{3-\delta}$ where A is an alkali-earth metal gradually increases with the acceptor dopant amount. This trend is limited by separation of secondary non-conductive phases at high doping levels, in particular those containing Cr^{6+} species [132, 134, 139]. The conductivity of Ca-doped chromites is generally slightly higher as compared with Sr-doped analogues [112, 134, 143] (Fig. 1.2.3). Ba-doping seems to result in strong lattice strains which hamper the electronic transfer [143] compared with Ca- or Sr-doped counterparts. This behavior is consistent with the ionic radii of the alkali-earth metals, with Ca possessing the radius close to that of La^{3+} and smaller resultant lattice distortions [133, 134, 143].

Mg-doping enhances the conductivity, although the effect is smaller compared with Sr and Ca. Apart from increasing the amount of p-type charge carriers, introduction of Mg results in lower content of Cr atoms available for the electron transfer and blocks Cr-O-Cr bonds [114, 134].

Al-doping suppresses the conduction of chromites due to blocking of conductive Cr-O-Cr paths and by facilitating oxygen removal from chromites on reduction [152, 153, 205]. On the other hand, Al-doping into acceptor-rich chromites should increase the amount of Cr^{4+} species. As an example, introduction of 12 mol. % of Al into $La_{0.75}Ca_{0.25}Cr_{0.92-x}Co_{0.08}Al_xO_{3-\delta}$ slightly enhances the conductivity in air and reduces the E_a down to 0.11 eV [154], possibly due to structural factors.

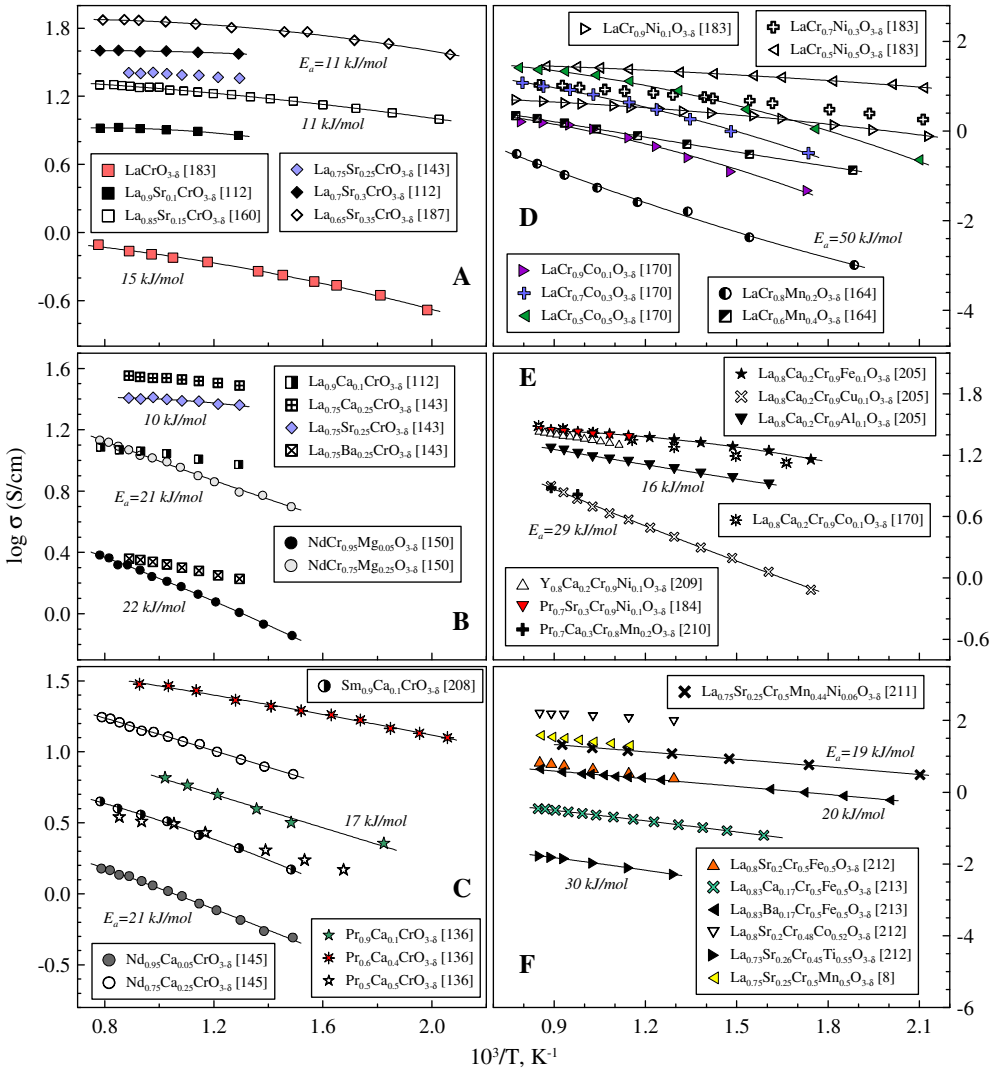

Fig. 1.2.3. Temperature dependencies of total conductivity of chromites in air

The effect of introduction of transition metal (Mn, Co, Fe, Ni, Cu) into B-sites of chromites on the electronic transport is controversial, while the approaches to describe the electronic state of transition metal cations are significantly different. Basically, available data on the total conductivity, Seebeck coefficient, oxygen nonstoichiometry, XPS studies suggest that the electronic transfer either dominates by hole migration over B-O-B network (where B is the transition metal dopant) with preservation of the stable state Cr^{3+} [113, 167, 189, 191] or involves participation of chromium species in the redox equilibrium [10, 17, 164-166, 170, 189, 206, 207]. In particular, slight doping $LaCrO_{3-\delta}$ and $(La,Sr)CrO_{3-\delta}$ with Mn/Co sharply decreases the conductivity in air and enhances the corresponding activation energy [164-166, 170]. This behavior assumes that the hole transfer in moderately doped chromites proceeds over Cr atoms while isolated Mn^{3+}/Co^{2+} cations act as hole traps. At higher Mn or Co content (~30% for $La(Cr,Mn)O_{3-\delta}$) Mn-O-Mn paths become percolating which increases the conductivity and diminishes the corresponding activation energy. The equilibrium between Cr^{4+}/Cr^{3+} and $Mn^{4+}/Mn^{3+}/Mn^{2+}$ species was considered to analyze the temperature and $p(O_2)$ dependence of the conductivity and Seebeck coefficient of $(Ln,Sr)(Cr,Mn)O_{3-\delta}$ [10]. In $(Ce,Sr)(Cr,Mn)O_{3-\delta}$, Cr atoms are regarded as only hole traps, without significant contribution into the

electronic transport [207]. Whatever the transport mechanism, the conductivity values in air exceed 10 - 20 S/cm at 973 K for (Ln,A)(Cr,Mn)$O_{3-\delta}$ with Mn content above 40 - 50% and for (Ln,A)(Cr,Co)$O_{3-\delta}$ with Co content higher than 10% [8, 10, 164-166, 170] (Fig. 1.2.3). Introduction of Ni or Fe into $LaCrO_{3-\delta}$ or (La,A)$CrO_{3-\delta}$ monotonously increases the conductivity in air and decreases the activation energy [131, 183], although the stability of Ni-rich chromites is arguable [131] and the corresponding data were obtained in O_2 [183]. Cu-doping within the solubility limit also increases the conductivity in air [131, 134].

In view of potential anode applications, much attention is focused on low-p(O_2) conductivity, since the electrocatalytic properties are generally governed by the transport characteristics. The conduction at reduced p(O_2) is determined by both the conductivity in air and the reducibility of the composition and resultant drop of the amount of charge carriers; selected examples are shown in Figs. 1.2.4, 1.2.5 and Table 1.2.1. Obviously, in order to achieve a reasonable low-p(O_2) conductivity, one should find the optimum content for each dopant to ensure the high concentration of the charge carriers and moderate reducibility of the perovskite. Because of differences in the preparation conditions of the materials, measuring procedure, uncertainties in the literature data, we will give only a brief overview of basic trends observed on reduced chromites, and discuss their applicability as anodes in terms of the electronic transport.

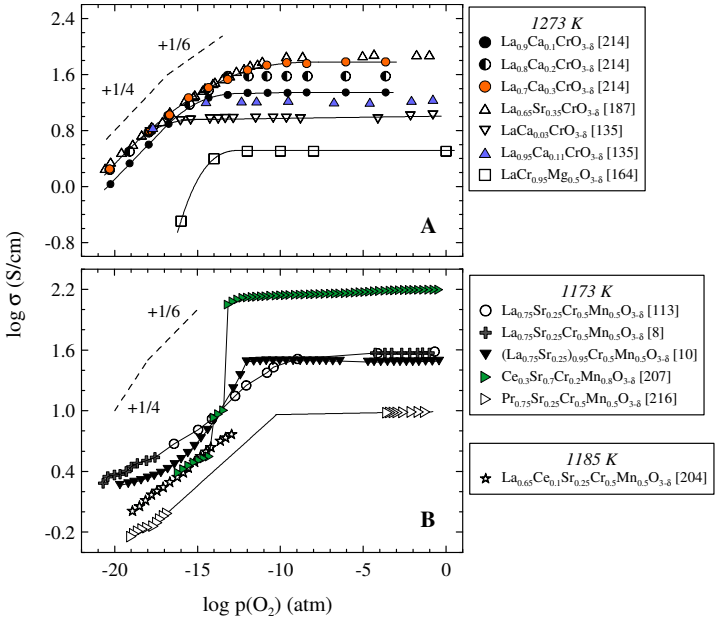

Fig. 1.2.4. Isothermal dependencies of the total conductivity of selected (La,A)$CrO_{3-\delta}$ (A) and (Ln,Sr)(Cr,Mn)$O_{3-\delta}$-based compositions (B) vs p(O_2)

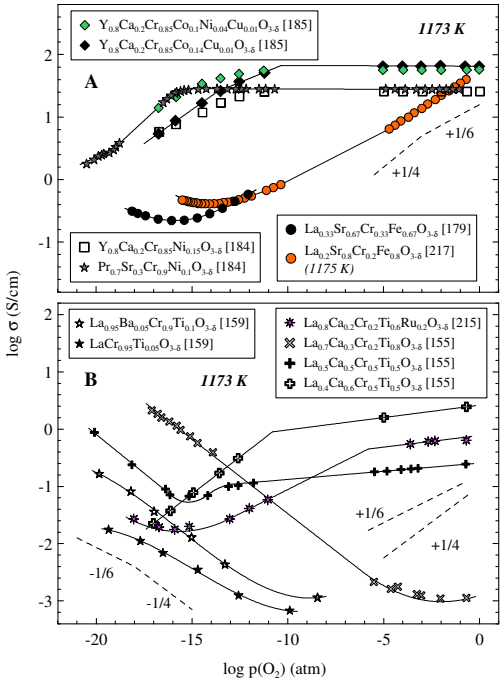

Fig. 1.2.5. Isothermal dependencies of total conductivity of selected B-site doped chromites vs. p(O_2)

Consistently with the trends in the nonstoichiometry, the electronic conductivity of $LaCrO_{3-\delta}$-based perovskites shows a p(O_2)-independent behavior in oxidizing and moderately reducing atmospheres; for chromite perovskites with a modest degree of substutution, the sufficient level of the electronic transport may be extended down to the anodic conditions [112, 135, 184, 214]; in particular, the onset of $LaCrO_{3-\delta}$

Table 1.2.1. Total conductivity of chromites in reducing atmospheres

Composition	Oxygen partial pressure (atm) or gas mixture	$\sigma_{873\ K}$, S/cm	$\sigma_{1073\ K}$, S/cm	Reference
$LaCrO_{3-\delta}$	10% H_2 - 90% N_2	4.6×10^{-3}	5.4×10^{-3}	[143]
$La_{0.9}Ca_{0.1}CrO_{3-\delta}$	H_2	1.5	2.3	[112]
$La_{0.8}Ca_{0.2}CrO_{3-\delta}$	H_2	3.6	4.8	[112]
$La_{0.7}Ca_{0.3}CrO_{3-\delta}$	H_2	3.3	4.3	[112]
$La_{0.7}Ca_{0.3}CrO_{3-\delta}$	10% H_2 - 90% N_2	2.0	3.1	[143]
$La_{0.9}Sr_{0.1}CrO_{3-\delta}$	H_2	0.80	1.7	[112]
$La_{0.8}Sr_{0.2}CrO_{3-\delta}$	H_2	4.7	6.2	[112]
$La_{0.7}Sr_{0.3}CrO_{3-\delta}$	H_2	4.4	4.7	[112]
$La_{0.7}Ba_{0.3}CrO_{3-\delta}$	10% H_2 - 90% N_2	8.6×10^{-3}	6.8×10^{-2}	[143]
$LaCr_{0.9}Mg_{0.1}O_{3-\delta}$	H_2	3.4×10^{-2}	0.12	[112]
$LaCr_{0.8}Mg_{0.2}O_{3-\delta}$	H_2	3.9×10^{-2}	0.17	[112]
$LaCr_{0.95}Ti_{0.05}O_{3-\delta}$	3.3×10^{-22}		7.6×10^{-3}	[159]
$LaCr_{0.9}Ti_{0.1}O_{3-\delta}$	4.5×10^{-21}		4.6×10^{-2}	[159]
$La_{0.95}Ba_{0.05}Cr_{0.9}Ti_{0.1}O_{3-\delta}$	1.1×10^{-22}		7.5×10^{-2}	[159]
$La_{0.7}Ca_{0.3}Cr_{0.5}Ti_{0.5}O_{3-\delta}$	4% H_2 - Ar	1.3×10^{-2}	2.1×10^{-2}	[163]
$La_{0.73}Sr_{0.26}Cr_{0.45}Ti_{0.55}O_{3-\delta}$	5% H_2 - Ar	1.9×10^{-3}	4.0×10^{-3}	[212]
$La_{0.85}Sr_{0.05}Ca_{0.1}Cr_{0.95}V_{0.05}O_{3-\delta}$	1.3×10^{-10}		3.5	[161]
$La_{0.8}Sr_{0.2}Cr_{0.5}Mn_{0.5}O_{3-\delta}$	wet 5% H_2 - Ar	3.2	5.1	[113]
$La_{0.75}Sr_{0.25}Cr_{0.5}Mn_{0.5}O_{3-\delta}$	5% H_2 - Ar	0.29	0.93	[8]
$La_{0.75}Sr_{0.25}Cr_{0.5}Mn_{0.5}O_{3-\delta}$	H_2	9.0×10^{-2}	0.29	[218]
$La_{0.75}Sr_{0.25}Cr_{0.5}Mn_{0.5}O_{3-\delta}$	CH_4	0.16		[218]
$La_{0.75}Sr_{0.25}Cr_{0.5}Mn_{0.5}O_{3-\delta}$	10% H_2S - H_2	0.28	1.0	[219]
$La_{0.75}Sr_{0.25}Cr_{0.5}Mn_{0.44}Ni_{0.06}O_{3-\delta}$	5% H_2 - Ar	0.66	1.4	[211]
$La_{0.75}Sr_{0.25}Cr_{0.5}Mn_{0.44}Ni_{0.06}O_{3-\delta}$	wet 5% H_2 - Ar	0.82	1.47	[211]
$La_{0.75}Sr_{0.25}Cr_{0.5}Mn_{0.3}Ni_{0.2}O_{3-\delta}$	5% H_2 - Ar	5.1×10^{-2}	0.18	[211]
$La_{0.75}Sr_{0.25}Cr_{0.5}Mn_{0.3}Ni_{0.2}O_{3-\delta}$	wet 5% H_2 - Ar	8.6×10^{-2}	0.28	[211]
$La_{0.7}Sr_{0.3}Cr_{0.5}Mn_{0.5}O_{3-\delta}$	wet 5% H_2 - Ar	2.0	4.4	[113]
$La_{0.83}Ca_{0.17}Cr_{0.5}Fe_{0.5}O_{3-\delta}$	dry 5% H_2 - Ar	3.9×10^{-3}	2.1×10^{-2}	[213]
$La_{0.8}Sr_{0.2}Cr_{0.5}Fe_{0.5}O_{3-\delta}$	5% H_2 - Ar	4.7	6.3	[212]
$La_{0.33}Sr_{0.67}Cr_{0.33}Fe_{0.67}O_{3-\delta}$	8.4×10^{-21}		0.14	[179]
$La_{0.2}Sr_{0.8}Cr_{0.2}Fe_{0.8}O_{3-\delta}$	1.1×10^{-16}		0.20	[217]
$La_{0.83}Ba_{0.17}Cr_{0.5}Fe_{0.5}O_{3-\delta}$	wet 5% H_2 - Ar	3.9×10^{-2}	0.12	[213]
$La_{0.75}Ca_{0.25}Cr_{0.9}Co_{0.08}Al_{0.02}O_{3-\delta}$	5% H_2 - 95% Ar	0.71	1.0	[154]
$La_{0.85}Sr_{0.05}Ca_{0.1}Cr_{0.9}Ni_{0.1}O_{3-\delta}$	1.3×10^{-10}		0.82	[161]
$La_{0.7}Ca_{0.3}Cr_{0.95}Zn_{0.05}O_{3-\delta}$	H_2	3.6	6.1	[220]
$Sr_2CrNbO_{6-\delta}$	CO	3.1×10^{-3}	1.5×10^{-2}	[221]
$Ce_{0.9}Sr_{0.1}Cr_{0.5}V_{0.5}O_{3-\delta}$	10% H_2 - N_2	0.46	0.52	[162]
$Ce_{0.9}Sr_{0.1}Cr_{0.5}V_{0.5}O_{3-\delta}$	10% H_2S - N_2	42	44	[162]
$Ce_{0.3}Sr_{0.7}Cr_{0.2}Mn_{0.8}O_{3-\delta}$	6.7×10^{-19}		4.8	[207]
$La_{0.65}Ce_{0.1}Sr_{0.25}Cr_{0.5}Mn_{0.5}O_{3-\delta}$	3% H_2O - H_2	0.19	0.73	[222]
$Ce_{0.9}Sr_{0.1}Cr_{0.5}Fe_{0.5}O_{3-\delta}$	5% H_2S - N_2	0.64	3.0	[223]
$Pr_{0.75}Sr_{0.25}Cr_{0.5}Mn_{0.5}O_{3-\delta}$	5% H_2 - Ar	6.2×10^{-2}	0.28	[216]
$Pr_{0.7}Ca_{0.3}Cr_{0.8}Mn_{0.2}O_{3-\delta}$	wet 5% H_2 - Ar		6.5×10^{-2}	[210]
$Pr_{0.7}Ca_{0.3}Cr_{0.6}Mn_{0.4}O_{3-\delta}$	wet 5% H_2 - Ar		0.23	[210]
$Pr_{0.7}Ca_{0.3}Cr_{0.4}Mn_{0.6}O_{3-\delta}$	wet 5% H_2 - Ar	0.25	0.70	[210]
$Pr_{0.7}Ca_{0.3}Cr_{0.9}Ni_{0.1}O_{3-\delta}$	5% H_2	0.39	0.98	[184]
$YCrO_{3-\delta}$	6.3×10^{-11}	1.2×10^{-4}	2.3×10^{-3}	[224]

decomposition is observed at ~10^{-21} atm at 1273 K [46]. This region is followed by the conductivity drop characterized by the proportionality between the conductivity and $p(O_2)^{1/4}$. The slope may be reduced for

transition metal-doped chromites (Figs. 1.2.4 - 1.2.5) in the case of electron exchange between the corresponding redox couples [8, 113, 184, 209]. The onset of the drop is determined by the nature and amount of dopants and temperature.

The maximum low-p(O_2) conductivity of (La,Ca)$CrO_{3-\delta}$ and (La,Sr)$CrO_{3-\delta}$ is observed for ~20 mol.% of the acceptor (Table 1.2.1) [112], although the exact knowledge of p(O_2) is required for more accurate conclusions. For slightly doped (La,A)$CrO_{3-\delta}$, the conductivity of Ca-containing chromites is somewhat higher, while doping above 10% results in higher conduction of (La,Sr)$CrO_{3-\delta}$ [112, 143]. The conductivity of Ba-substituted $LaCrO_{3-\delta}$ is substantially lower; taking into account the poor stability [143], this material is inappropriate for anode utilization.

Mg-doping negatively influences the low-p(O_2) transport properties due to a substantial conductivity drop originating from extensive oxygen losses [112]. On the other hand, introduction of bivalent Mg atoms may improve the oxygen ionic conduction and suppress the chemical expansion. Introduction of small amounts of Ni, Co, Fe, Mn or noble metals is considered to be a promising way to improve the electrocatalytic activity, since the conductivity remains on the level 1 - 10 S/cm at partial oxygen pressure of 10^{-20} - 10^{-15} atm (as shown in Table 1.2.1), while formation of small quantities of metallic or oxide phases should not be detrimental for the electron transport characteristics (Table 1.1.1). High amounts of the dopants result in a degradation of the conductivity with time, possibly associated with phase instability [17, 210].

The donor dopants decrease the high-p(O_2) conductivity and may annihilate the positive effect induced by the presence of acceptor cations [155, 157, 159, 215]. At the same time, the introduction of donors may improve the low p(O_2) transport. For example, the conductivity of $(La_{1-x}Ca_x)_yCr_{1-z}Ti_zO_{3-\delta}$ is significantly influenced by Ca:Ti ratio. Unless affected by kinetic factors, the conductivity basically exhibits a p-n transition: in the high p(O_2) region Ti is essentially in +4 state while the electron transport proceeds via hole hopping over Cr^{3+} and Cr^{4+} species. On further reduction, the formation of Ti^{3+} starts contributing while Cr is essentially in +3 state; this combination provides the n-type transport behavior, although the existence of equilibrium amounts of Ti^{3+} and Cr^{4+} in the high- and low-p(O_2) range, respectively, should also be accounted for more accurate analysis of the conductivity mechanism. Increasing La or Ti content or lowering the A-site deficiency results in shifting the p-n transition to more oxidative region. However, these trends may be obscured by the slow equilibration kinetics, especially typical for Ti-rich perovskites. The n-type conductivity, typical for ferrites, was also observed on Fe-doped chromites with large quantities of Fe at low p(O_2), when the contribution of Fe^{3+}/Fe^{2+} couple is realized (Fig. 1.2.5). Depending on the composition and experimental conditions, the conductivity of (La,A)(Cr,Fe)$O_{3-\delta}$ may achieve 5 - 10 S/cm at low p(O_2) [212].

1.2.4. Thermal and chemical expansion

The data of the thermal expansion of chromites are contradictory; this primarily relates to undoped $LnCrO_{3-\delta}$ perovskites (Table 1.2.2) since their functional properties are strongly affected by the preparation technique, measurement procedure, purity of the material and other factors. Basically, in $LnCrO_{3-\delta}$ series the thermal expansivity behavior is consistent with Ln radii [131, 185, 203] showing the maximum thermal expansion coefficients (TEC) for $LaCrO_{3-\delta}$.

Table 1.2.2. Thermal expansion coefficients of chromite-based ceramics

Composition	T, K	Oxygen partial pressure (atm) or gas mixture	TEC×10^6, K^{-1}	Reference
$LaCrO_{3-\delta}$	540 - 1020	0.21	9.5	[131]
$LaCrO_{3-\delta}$	570 - 1270	0.21	11.3	[143]
$LaCrO_{3-\delta}$	320 - 1270	wet air	8.0	[112]
$LaCrO_{3-\delta}$	320 - 1270	wet H_2	8.2	[112]
$La_{0.9}Ca_{0.1}CrO_{3-\delta}$	320 - 1270	wet air	9.0	[112]
$La_{0.9}Ca_{0.1}CrO_{3-\delta}$	320 - 1270	wet H_2	8.5	[112]
$(La_{0.8}Ca_{0.2})_{1.01}CrO_{3-\delta}$	300 - 1470	0.21	10.0	[203]
$La_{0.7}Ca_{0.3}CrO_{3-\delta}$	570 - 1270	0.21	11.5	[143]
$La_{0.9}Sr_{0.1}CrO_{3-\delta}$	320 - 1270	0.21	10.0	[153]
$La_{0.9}Sr_{0.1}CrO_{3-\delta}$	320 - 1270	wet air	9.2	[112]
$La_{0.9}Sr_{0.1}CrO_{3-\delta}$	320 - 1270	wet H_2	9.8	[112]
$La_{0.75}Sr_{0.25}CrO_{3-\delta}$	570 - 1270	0.21	11.6	[143]
$La_{0.85}Sr_{0.1}Ca_{0.05}CrO_{3-\delta}$	320 - 1070	0.21	10.3	[230]
$La_{0.7}Ba_{0.3}CrO_{3-\delta}$ ($BaCrO_4$ impurity)	570 - 1270	0.21	12.5	[143]
$LaCr_{0.9}Mg_{0.1}O_{3-\delta}$	320 - 1270	wet air	8.4	[112]
$LaCr_{0.9}Mg_{0.1}O_{3-\delta}$	320 - 1270	wet H_2	8.4	[112]
$La_{0.9}Sr_{0.1}Cr_{0.95}Al_{0.05}O_{3-\delta}$	320 - 1270	wet H_2	10.8	[153]
$La_{0.7}Ca_{0.3}Cr_{0.8}Ti_{0.2}O_{3-\delta}$	300 - 1270	0.21	10.4	[231]
$La_{0.7}Ca_{0.3}Cr_{0.5}Ti_{0.5}O_{3-\delta}$	300 - 1270	0.21	10.1	[227]
$La_{0.7}Sr_{0.3}Cr_{0.8}Ti_{0.2}O_{3-\delta}$	300 - 1270	0.21	10.4	[231]
$La_{0.85}Sr_{0.15}Cr_{0.95}V_{0.05}O_{3-\delta}$	300 - 1270	0.21	9.9	[232]
$La_{0.75}Sr_{0.25}Cr_{0.5}Mn_{0.5}O_{3-\delta}$	570 - 1270	0.21	12.0	[143]
$(La_{0.75}Sr_{0.25})_{0.95}Cr_{0.5}Mn_{0.5}O_{3-\delta}$	920 - 1220	0.21	12.7	[10]
$(La_{0.75}Sr_{0.25})_{0.95}Cr_{0.5}Mn_{0.5}O_{3-\delta}$	920 - 1220	5×10^{-21}-3×10^{-14}	11.7	[10]
$La_{0.7}Sr_{0.3}Cr_{0.8}Fe_{0.2}O_{3-\delta}$	300 - 1270	0.21	11.1	[163]
$La_{0.33}Sr_{0.67}Cr_{0.33}Fe_{0.67}O_{3-\delta}$	970 - 1120	0.21	19.3	[179]
$La_{0.33}Sr_{0.67}Cr_{0.33}Fe_{0.67}O_{3-\delta}$	970 - 1120	He	20.7	[179]
$La_{0.9}Sr_{0.1}Cr_{0.95}Co_{0.05}O_{3-\delta}$	320 - 1270	0.21	11.4	[153]
$La_{0.9}Sr_{0.1}Cr_{0.95}Co_{0.05}O_{3-\delta}$	320 - 1270	wet H_2	10.6	[153]
$La_{0.7}Sr_{0.3}Cr_{0.5}Co_{0.5}O_{3-\delta}$	470 - 870	0.21	19.0	[131]
$La_{0.75}Ca_{0.25}Cr_{0.9}Co_{0.08}Al_{0.02}O_{3-\delta}$	300 - 1270	0.21	10.6	[154]
$LaCr_{0.9}Ni_{0.1}O_{3-\delta}$	600 - 1320	0.21	10.1	[229]
$LaCr_{0.7}Ni_{0.3}O_{3-\delta}$	630 - 1310	0.21	11.8	[229]
$La_{0.85}Sr_{0.15}Cr_{0.9}Ni_{0.1}O_{3-\delta}$	300 - 1270	0.21	10.3	[232]
$La_{0.85}Sr_{0.15}Cr_{0.98}Cu_{0.02}O_{3-\delta}$	300 - 1270	0.21	10.2	[232]
$La_{0.7}Ca_{0.3}Cr_{0.95}Zn_{0.05}O_{3-\delta}$	470 - 1270	0.21	11.5	[220]
$Sr_{0.7}Ce_{0.3}Cr_{0.5}Mn_{0.5}O_{3-\delta}$	950 - 1370	0.21	15.8	[207]
$La_{0.65}Ce_{0.1}Sr_{0.25}Cr_{0.5}Mn_{0.5}O_{3-\delta}$	300 - 1790	0.21	11.5	[222]
$PrCrO_{3-\delta}$	300 - 1180	0.21	8.5	[131]
$(Pr_{0.85}Ca_{0.15})_{1.01}CrO_{3-\delta}$	300 - 1470	0.21	9.0	[203]
$Pr_{0.75}Sr_{0.25}Cr_{0.5}Mn_{0.5}O_{3-\delta}$	820 - 1170	0.21	9.5	[216]
$NdCrO_{3-\delta}$	300 - 1180	0.21	8.3	[131]
$(Nd_{0.85}Ca_{0.15})_{1.01}CrO_{3-\delta}$	300 - 1470	0.21	9.7	[203]
$SmCrO_{3-\delta}$	300 - 1180	0.21	8.6	[131]
$GdCrO_{3-\delta}$	300 - 1180	0.21	7.0	[131]
$YCrO_{3-\delta}$	300 - 1180	0.21	7.9	[131]
$Y_{0.8}Ca_{0.2}CrO_{3-\delta}$	370-1170	0.21	9.7	[209]
$Y_{0.8}Ca_{0.2}Cr_{0.9}Co_{0.1}O_{3-\delta}$	300-1170	0.21	10.7	[185]
$Y_{0.8}Ca_{0.2}Cr_{0.9}Ni_{0.1}O_{3-\delta}$	370-1170	0.21	11.0	[209]

The values of TEC of $LaCrO_{3-\delta}$ are ~6.7×10^{-6} K^{-1} for the orthorhombic phase while for the rhombohedral modification those vary in the range (8.0 - 11.3)$\times10^{-6}$ K^{-1} (Table 1.2.2). Although the expansion behavior of undoped $LnCrO_{3-\delta}$ is expected to be $p(O_2)$-independent [112] due to negligible oxygen losses, the thermomechanical properties may be affected by other factors influenced by $p(O_2)$, such as the presence of minor amounts of transition metals, temperature- or $p(O_2)$-induced phase transitions, Cr volatilization in oxidative or H_2O-rich atmospheres, formation of Cr^{6+} species in oxidizing conditions, etc.

Introduction of alkali-earth cations into A-sublattice increases TECs, as shown in Table 1.2.2. Since the radius of Ca ions is close to that of La, the higher expansion may be related with the phase transition or more extensive oxygen losses [131, 225]. The effect of facilitated formation of oxygen vacancies on thermal expansion is consistent with the correlation observed between the TEC and oxygen nonstoichiometry [131, 194, 226]. The same factors should also contribute to the expansion of Sr- and Ba-doped chromites; in combination with their larger ionic radii and shifting the phase transition to lower temperature, the TEC values are higher compared with Ca-doped analogues. The expansivity is partially suppressed by increasing fraction of relatively small Cr^{4+} ions with alkali-earth dopant content; this is supported by a decrease of the cell parameters of A-site doped chromites at room-temperature on doping [112, 143, 153].

Mg introduction into B-sublattice of $LaCrO_{3-\delta}$ increases the thermal expansion, consistently with larger ionic radius of Mg^{2+} in comparison with Cr^{3+} and Cr^{4+} [112]. The TECs of chromites doped with alkali-earth cations are in the range (8.0 - 12.0)$\times10^{-6}$ K^{-1}, which is close to those of commonly used solid electrolytes [72, 227, 228]. Introduction of transition metal cations into B-cites of perovskite lattice of chromites basically results in an enhanced thermal expansion (Table 1.2.2); this may be attributed to larger ionic radii of the guest ions, structural transitions, easier reducibility of the corresponding cations or that of Cr^{4+} [8, 153, 179, 229]. The expansion behavior may also be influenced by electron exchange between the transition metal cations [10, 207], variations of the spin state of cations [153] or other factors. Whatever the effect, the TECs remain moderate on doping with Al, Ti, Mn. Limited solubility of Ni, Cu, Zn in chromites [131, 181] also enables to keep the expansion below the critical level. Introduction of large amounts of easily reducible Fe and Co atoms in combination with A-site acceptor doping may increase TECs above 20×10^{-6} K^{-1} [131, 179, 213] which is inappropriate for fuel cell applications.

Similar to other perovskite groups containing transition metal cations, chromites generally exhibit an expansion on reduction. The isothermal expansion behavior of chromites was studied by numerous authors; the volume changes were attributed to increasing coulombic repulsion between charged cations close to a vacancy [194, 233], variation of the radius of transition metal ions [194, 196, 234-236], phase transitions [8, 236], microstructural phenomena or segregation/dissolution of impurities [169, 233, 235].

In subsequent equations, the value of absolute oxygen deficiency δ will be used instead of more correct $\Delta\delta$ which characterizes relative changes of the oxygen content. This simplification is based on observations that chromites are nearly stoichiometric under high-$p(O_2)$ conditions [190, 197]. As observed in numerous studies, the chemical expansion ε_{ch} exhibits nearly linear dependence on the oxygen deficiency δ, with the proportionality factor k represented by averaged linear expansion coefficient:

$$\varepsilon_{ch} = \frac{\Delta L}{L_0} = k\delta \qquad \textbf{(Eq. 1.2.6)}$$

In the model proposed in [234], following assumptions were suggested: 1. mobile holes are located on transition metal cations; 2. a closely packed lattice of oxides is formed by ions with rigid spheres; 3. the expansion is isotropic in each of 3 directions. According to this approach, the generalized equation for the expansion is as follows

$$\varepsilon_{ch} = \frac{\sum_i (c_i r_i - c_{i0} r_i)}{\sum_i c_{i0} r} \qquad \textbf{(Eq. 1.2.7)}$$

where c_i and r_i are the concentration and ionic radii, correspondingly, of i^{th} ion of $ABO_{3-\delta}$ perovskite. The subscript 0 relates to the reference state (which generally corresponds to the stoichiometric compound for chromites) at given temperature.

In accordance with [196, 234], the value ε_{ch}/δ should be essentially independent on temperature and alkali-earth dopant nature and amount. Indeed, as shown in Fig. 1.2.6, the expansion behavior vs. δ is temperature-independent within the experimental errors. However, comparison of $(La,Sr)CrO_{3-\delta}$ and $(La,Ca)CrO_{3-\delta}$ shows that the strains are slightly larger for Ca-substituted chromites and enhance with dopant level. In framework of the model in [234], the effect of dopant nature may be attributed to larger Sr radius compared with Ca, while higher dopant amount yields more Cr^{4+} species in stoichiometric perovskites. Both factors decrease the denominator in Eq. (1.2.7) for higher dopant content and for Sr-substituted chromites.

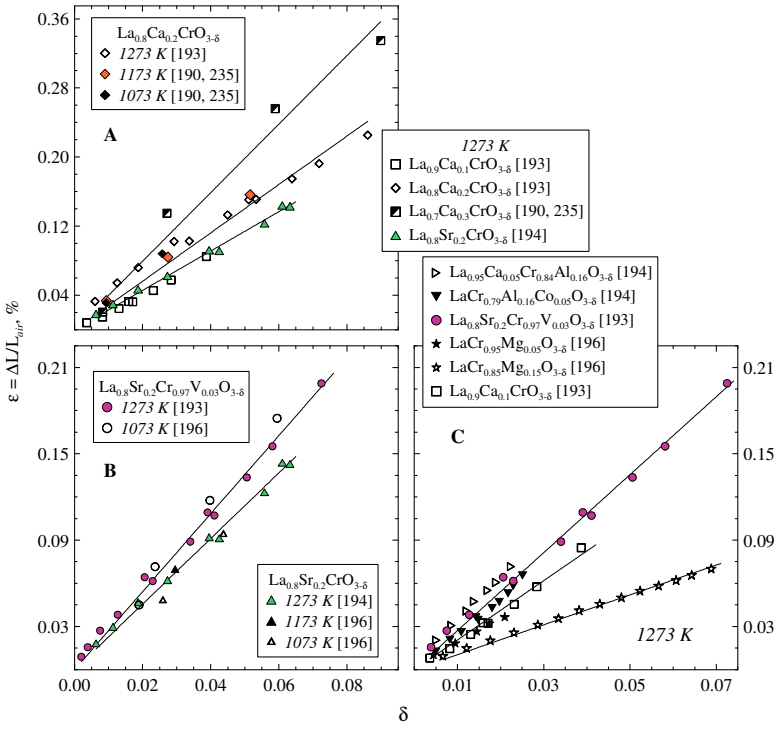

Fig. 1.2.6. Isothermal dependencies of relative elongation of chromite-based ceramics vs. oxygen deficiency

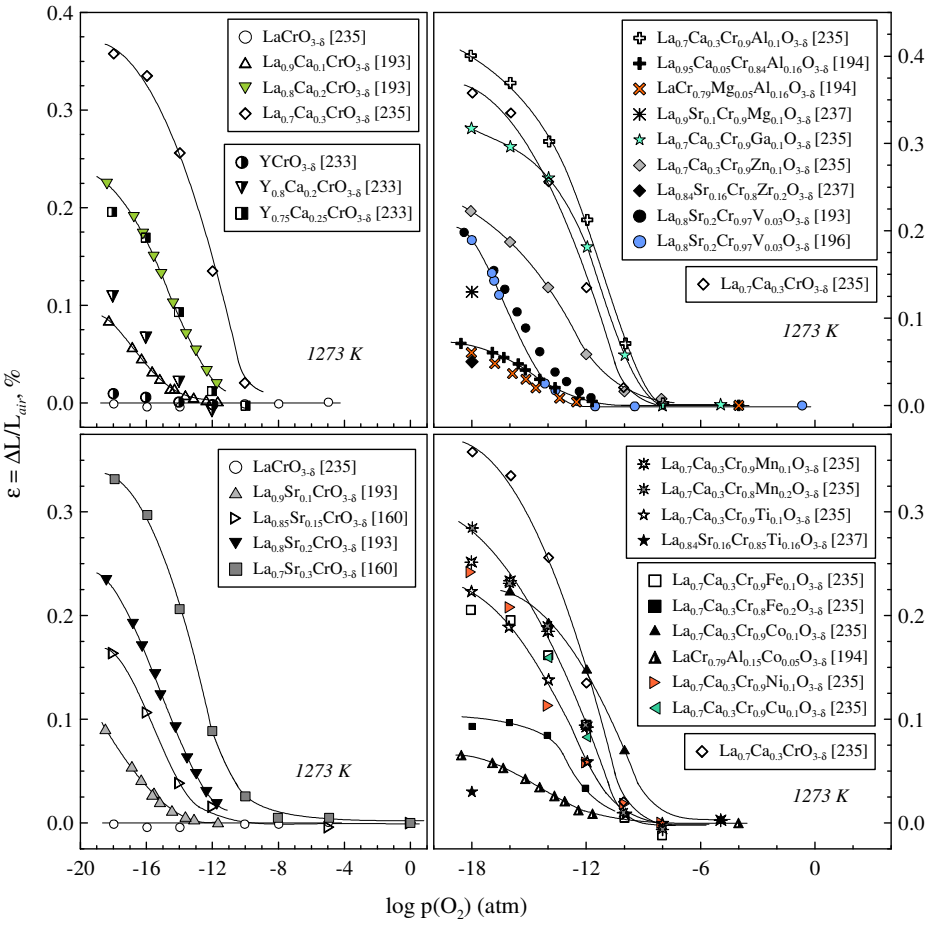

Fig. 1.2.7. Isothermal dependencies of relative elongation of chromite-based ceramics vs. $p(O_2)$

Regardless of the effects indicated, the difference between the value ε_{ch}/δ for the examples above is not substantial, and the expansion behavior should generally correlate with that of oxygen nonstoichiometry variations. As shown in Figs. 1.2.6 - 1.2.7, the expansion is promoted by higher acceptor content and elevated temperature. $LaCrO_{3-\delta}$-based materials exhibit larger expansivity compared with other $LnCrO_{3-\delta}$ counterparts [160, 193, 233]. An exception was observed on Ce-doped chromites, where reduction of Cr^{4+} is suppressed by formation of Ce^{3+}. As the influence of changes in A-site cation radii on the expansion is smaller, the presence of Ce^{4+}/Ce^{3+} couple is suggested to have a buffering effect on the expansivity [203].

As follows from Eq. (1.2.7), the value ε_{ch}/δ decreases on introduction of Mg or other acceptor-type dopants into B-sublattice. The effect of B-site doping into chromites on the expansion behavior is more substantial compared with substitutions in A-sublattice, as shown in Figs. 1.2.6 - 1.2.7. Al, Ga-doping into chromites shifts the onset of the expansion towards oxidative conditions, consistently with facilitated oxygen losses [152, 235] (Fig. 1.2.7).

The effect of doping with cations with strong reducibility is less obvious. Basically, the preference of a dopant to lower oxidation state is expected to provide larger oxygen losses and expansivity, as was observed for Mn-, Co-, Ni-, Cu-doped chromites. On the other hand, Fe-doped chromites exhibit surprisingly lower chemically-induced strains decreasing with Fe content. Apart from possible experimental errors, the effects of the electron exchange between the cations, charge disproportionation, ordering phenomena, phase

transformations or spin state transitions on reduction [8, 10, 207, 237, 238] could also be responsible for the behaviour observed. One should also account for possible formation or dissolution of secondary phases and microstructural factors, which result in slow equilibration or mechanical failure [163, 169]. Whatever the expansion-determining factors, introduction of reducible cations into chromites suppresses the expansivity of (La,A)$CrO_{3-\delta}$. On the other hand, doping with B-site cations shifts the onset of the length changes towards oxidative conditions (Fig 1.2.7).

The data on the expansion of chromites indicate that this group of perovskite materials possesses a moderate level of the thermally- and chemically-induced strains, in comparison with conventional Ni-YSZ anodes [239-241]. The parameter $\varepsilon_{chem}/\delta$ in chromites is basically lower compared with fluorites [237] which ensures their lower sensitivity to nonstoichiometry variations caused by $p(O_2)$ changes or polarization, in comparison with, for example, CeO_2-based cermet anodes. Taking tensile modulus of chromites as 150-200 GPa and Poisson ratio as 0.3 [242], an expansion of 0.25 - 0.3% in isothermal conditions will cause the stresses 500 - 800 MPa, increasing on reduction [194]. Obviously, application of chromite-based anodes ensures their better chemical and thermomechanical compatibility with chromite interconnects.

1.2.5. Oxygen diffusivity

The process of the oxygen ionic transfer in perovskites $ABO_{3-\delta}$ is governed by the passage of an oxygen anion through a bottleneck formed by a triangle A-B-A with A and B atoms located in the neighboring positions ([243] and references cited). The diffusion coefficient of oxygen atoms D_O may be schematically expressed as

$$D_{\mathrm{O}} \sim \left[\mathrm{V}_{\mathrm{O}}^{\bullet\bullet}\right] \cdot a^2 \cdot e^{\frac{\Delta H_f + \Delta H_m + \Delta H_a}{R \cdot T}} \qquad \textbf{(Eq. 1.2.8)}$$

where a stands for pseudocubic cell parameter and the temperature dependence of the diffusion coefficient is determined by thermal effect of the formation of oxygen vacancies (ΔH_f), their migration (ΔH_m) and association (ΔH_a). Generally, the vacancy formation term dominates among the enthalpies, since this value involves breaking of B-O bonds and lowering the coordination of B-cation. The energy required for the breaking of B-O bond decreases in the sequence Ti>Cr>Mn>Cu>Fe>Co [17, 146, 244]. The migration enthalpy of oxide ions is essentially governed by their facility to pass through the triangle A-B-A and is influenced by the nature (electronic structure, dimension etc.) of large A-site cations and lattice distortions; the minimum energy required to penetrate through the triangle is expected for cubic perovskites. The defect association-related phenomena are basically observed at high oxygen deficiency; examples include vacancy ordering, coulombic interaction between the defects, etc. [243, 245, 246].

Oxygen ionic transport in chromites is slow due to small oxygen vacancy concentration and the strong preferability of Cr atoms to octahedral environment with oxygen atoms [46, 149], while the presence of Co, Mn, Ga and other cations with a flexible coordination number in B-sublattice promotes the formation and transfer of oxygen vacancies [247-249].

Table 1.2.3. Oxygen ionic conductivity and chemical or oxygen vacancy diffusion coefficients of chromites

Composition	T, K	$p(O_2)$, atm	D_{chem} or D_V, cm^2/s	σ_O, S/cm	Method	Reference
$La_{0.9}Ca_{0.11}CrO_{3-\delta}$	1273	10^{-10}-10^{-5}	$D_V = 1.5\times10^{-6}$		Oxygen permeation	[254]
$La_{0.9}Ca_{0.1}CrO_{3-\delta}$	1273	10^{-13} 10^{-15}	$D_V = 3.1\times10^{-6}$		Conductivity relaxation	[251]
$La_{0.9}Ca_{0.1}Cr_{1.03}O_{3-\delta}$	1288 1288	1×10^{-10} 1×10^{-15}	$D_V = 1.7\times10^{-8}$	2.2×10^{-6} 2.6×10^{-5}	Electron-blocking	[198]
$La_{0.87}Sr_{0.13}Cr_{1.03}O_{3-\delta}$	1288 1288	1×10^{-10} 1×10^{-15}	$D_V = 1.1\times10^{-5}$	1.1×10^{-6} 1.9×10^{-5}		
$La_{0.8}Ca_{0.2}CrO_{3-\delta}$	1273	6.5×10^{-12} 10^{-15}	$D_V = 6.8\times10^{-6}$ $D_V = 1.0\times10^{-5}$		Conductivity relaxation	[251]
$La_{0.7}Ca_{0.3}CrO_{3-\delta}$	1273	10^{-6}-10^{-3}	$D_V = 8.1\times10^{-6}$		Oxygen permeation	[257]
$La_{0.7}Ca_{0.3}CrO_{3-\delta}$	1273 1173	1.1×10^{-11} 10^{-15} 10^{-15}			Conductivity relaxation	[251]
$La_{0.65}Sr_{0.35}CrO_{3-\delta}$	1273 1173	7.0×10^{-12} 2.5×10^{-15} 2.0×10^{-15}	$D_{chem} = 1.4\times10^{-5}$ $D_{chem} = 2.5\times10^{-5}$ $D_{chem} = 2.8\times10^{-6}$		Conductivity relaxation	[187]
$(La_{0.75}Sr_{0.25})_{0.95}Cr_{0.5}Mn_{0.5}O_{3-\delta}$	1223 1223 1273	0.21 1.1×10^{-15} 0.21		3.0×10^{-5} 3.5×10^{-4} 8.2×10^{-5}	Faradaic efficiency	[10]
$La_{0.33}Sr_{0.67}Cr_{0.33}Fe_{0.67}O_{3-\delta}$	1023 1173			2.9×10^{-2} 0.12	Conductivity vs. $p(O_2)$ [a]	[179]
$La_{0.33}Sr_{0.67}Cr_{0.1}Fe_{0.9}O_{3-\delta}$	1023			3.1×10^{-2}	Conductivity vs. $p(O_2)$ [a]	[179]
$La_{0.8}Sr_{0.2}Cr_{0.95}Ni_{0.05}O_{3-\delta}$	1223	oxidizing conditions ($\delta\approx0$)	$D_V = 1.1\times10^{-6}$		Conductivity relaxation [b]	[187]
	1273	oxidizing conditions ($\delta\approx0$)	$D_V = 1.3\times10^{-6}$			
	1223	4.5×10^{-19} 1.1×10^{-12}	$D_{chem} = 5.7\times10^{-6}$ $D_{chem} = 2.0\times10^{-6}$			
	1273	1.2×10^{-12}	$D_{chem} = 2.7\times10^{-6}$			
$Sr_{0.3}Ce_{0.7}Cr_{0.2}Mn_{0.8}O_{3-\delta}$	1248	1.7×10^{-2}		4.6×10^{-4}	Oxygen permeation	[207]
$Y_{0.8}Ca_{0.2}Cr_{0.85}Ni_{0.15}O_{3-\delta}$	1023 1173	gradient 0.21 vs. 10^{-20}		4.2×10^{-6} 2.2×10^{-5}	Oxygen permeation [c]	[187]

[a] *σ_O is suggested to be $p(O_2)$-independent*
[b] *D_v is suggested to be $p(O_2)$-independent in oxidizing conditions*
[c] *Surface limitations are neglected; σ_O is suggested to be $p(O_2)$-independent*

The ionic conductivity of Cr-rich perovskites does not exceed 3×10^{-5} S/cm (Table 1.2.3); for comparison, the ionic conductivity of ferrite perovskites are ~4 orders of magnitude higher [114, 250]. The activation energies of the chemical diffusion or ionic conductivity in $(Ln,A)CrO_{3-\delta}$ are assessed as 100 - 160 kJ/mol decreasing on B-site doping with Fe or Ni [198, 251, 252]. The diffusivity of oxygen vacancies in chromites is, however, assessed to be comparable to that in cobaltites and ferrites [251] which indicates that

the difference in the ionic conduction is primarily associated with much smaller oxygen deficiency and its low sensitivity towards variations in oxygen chemical potential.

On the other hand, small oxygen deficiency in chromites allows to avoid the ordering phenomena typical for ferrites and cobaltites [114, 245, 246, 251]. Even Cr content as low as y = 0.1 in $La_{0.33}Sr_{0.67}Fe_{1-y}Cr_yO_{3-\delta}$ make it possible to prevent the ordering of oxygen vacancies due to random distribution of Cr atoms in B-sublattice and suppressed formation of FeO_4 tetrahedra [179]. Increasing concentration of oxygen vacancies via acceptor doping or by reducing $p(O_2)$ ensures a higher level of the ionic transport in chromites, as shown in Tables 1.2.3 - 1.2.4. This behavior is in accordance with a general observation that the ionic transport correlates with the expansion behaviour of perovskites [226, 253]. However, the increased oxygen diffusivity should be compromised by worse stability, enhanced expansion and lower electronic conductivity in reducing atmospheres.

Table 1.2.4. Isotopic oxygen diffusion and surface exchange coefficients for chromites

Composition	T, K	$p(O_2)$, atm	D*, cm^2/s	k*, cm/s	E_a of D*, kJ/mol	Reference
$La_{0.9}Ca_{0.12}CrO_{3-\delta}$	1273	0.2	1.57×10^{-13}			[254]
$La_{0.8}Ca_{0.22}CrO_{3-\delta}$	1273	0.2	1.92×10^{-13}			[254]
$La_{0.7}Ca_{0.3}CrO_{3-\delta}$	1273	0.2	2.2×10^{-12}			[257]
$(La_{0.75}Sr_{0.25})_{0.95}Cr_{0.5}Mn_{0.5}O_{3-\delta}$	1185 1168	0.2 2.0×10^{-17}	1.1×10^{-10} 1.9×10^{-8}	9.7×10^{-9} 9.2×10^{-8}	70	[258]
$La_{0.8}Sr_{0.2}Cr_{0.2}Fe_{0.8}O_{3-\delta}$	1185 1033 1171	0.2 0.2 2.1×10^{-16}	9.4×10^{-10} 2.5×10^{-11} 2.3×10^{-7}	2.0×10^{-6} 1.1×10^{-11} 6.6×10^{-6}	240	[237]
$La_{0.8}Sr_{0.2}Cr_{0.2}Fe_{0.8}O_{3-\delta}$ $La_{0.6}Sr_{0.4}Cr_{0.2}Fe_{0.8}O_{3-\delta}$ $La_{0.4}Sr_{0.6}Cr_{0.2}Fe_{0.8}O_{3-\delta}$	1174 1171 1158 1164	0.21 0.2 0.21 1.4×10^{-16}	9.6×10^{-10} 1.9×10^{-8} 8.2×10^{-8} 3.1×10^{-7}	3.3×10^{-7} 4.1×10^{-7} 1.3×10^{-6} 1.3×10^{-6}	210 160 120	[252]
$La_{0.2}Sr_{0.8}Cr_{0.2}Fe_{0.8}O_{3-\delta}$ [a]	1123	20% O_2 10% CO - 10% CO_2 - Ar	1.2×10^{-6}	3.9×10^{-5} 1.5×10^{-5}		[259]
$La_{0.2}Sr_{0.8}Cr_{0.2}Fe_{0.8}O_{3-\delta}$ [b]	1173	gradient: air vs. CO-CO_2-He (45 - 5 - 50 %)	7.3×10^{-7}			[260]

[a] *Redox exchange mechanism is suggested*
[b] *D* is averaged across membrane*

The ionic diffusion in chromites was shown to be strongly contributed by grain boundary mechanism, especially under oxidizing conditions ([112, 254] and references cited). This factor, in particular, might induce an increase of the ionic conductivity proportionally to $p(O_2)^{1/2}$ in high-$p(O_2)$ range [192, 198].

The surface exchange rates over chromites basically correlate with the ionic diffusion, assuming a major role of oxygen vacancies in the surface kinetics [252, 255]. However, the results are strongly susceptible to material processing and experimental conditions, while slow equilibration results in a strong scattering of the data. As observed in Table 1.2.4, the exchange coefficients exhibit lower activation energies compared with the diffusion coefficients and are less sensitive to $p(O_2)$ variations or acceptor doping. This

indicates that the role of the surface-related limitations is expected to be more pronounced at lower temperatures [252, 256], more reducing conditions [192] or higher content of dopants in A or B-sublattice [173, 252]. Irrespective of the trends observed, the low level of the ionic conductivity and slow surface exchange for $LaCrO_{3-\delta}$-based materials does not allow to expect any substantial contribution of the bulk phase of the anode to the electrochemical process. This necessitates an optimization of the electrode morphology or addition of ion-conductive components into the anode.

1.2.6. Electrode performance

The electrochemical activity of chromite anodes strongly depends on the processing conditions, while comparison of experimental data is complicated by the lack of information on such important details as the composition of the solid electrolyte, fuel gas atmosphere, fractions of the components in composite electrode, etc. In most studies the perovskite anodes are covered with a layer of dispersed metallic particles sputtered or coated in form of paste, inks, etc. Althouth these particles are suggested to serve only as an electron-conductive component, without any effect on the activity, the contribution of metal-containing components can be neglected only when no surface spreading or metal penetration into the electrochemically active zone occurs. As shown by previous studies [261-263], Pt, Ag, Au and other noble metals possess non-negligible catalytic activity which may be significantly higher compared to that of chromites. A wide utilization of noble metals in industrial scales is limited by high costs, while conventional current collectors made of stainless steels or $LaCrO_{3-\delta}$-based ceramics have significantly higher bulk and contact resistance.

Pure or A-site doped $LaCrO_{3-\delta}$ basically possess extremely low electrochemical activity (Table 1.2.5); for instance, the polarization resistance of $La_{0.7}Cr_{0.32}CrO_{3-\delta}$ anode is reported to be ~86 Ohm×cm^2 at 1123 K [201]. Therefore, chromites basically serve as chemically and mechanically stable electron conductive matrix in combination with ionic conductors (CeO_2-, ZrO_2-based oxides) or catalytically-active components (Ni, Pd, VO_x). A large fraction of the stable perovskite phase diminishes risks of microstructural changes occurring on the additional components. Obviously, compared with conventional Ni-YSZ anodes, chromites are less susceptible to contamination with Cr species originating from the contact with interconnect materials. The activity can be to some extent improved by introducing A- or B-site dopants, especially those which form catalytically-active centres on the perovskite surface (Mn, Fe, etc.) or dispersed metallic particles (Ni, Ru). Extensive doping may induce a destabilization of the perovskite phase and enhance the chemical expansion [17, 146, 264, 265].

The electronic conductivity is one of critical factors determining the activity of perovskite-based anodes for hydrogen or hydrocarbon oxidation [10, 14, 265, 266]. As shown in Table 1.2.1, the conductivity is significantly reduced under anode conditions below 1 - 5 S/cm. Accounting for the porous microstructure of the electrode layer, the role of the current collector and addition of metallic or other electron conductive phases in most cases becomes more substantial than the intrinsic properties of the perovskite phase. On the other hand, appropriate A- or B-site doping may modify the transport and electrochemical properties.

Table 1.2.5. Polarization resistances of selected chromite-based anodes under zero current

Anode	Electrolyte	Fuel	T, K	R_η (i=0), Ohm×cm^2	E_a, kJ/mol	Reference
$La_{0.7}Sr_{0.32}CrO_{3-\delta}$ ***c.c.: Au paste***	8YSZ	wet H_2	1123	86		[201]
$La_{0.75}Sr_{0.35}Cr_{0.5}Al_{0.5}O_{3-\delta}$ ***c.c.: Pt paste***	LSGM9182	wet 5% H_2 - Ar	1123	0.33	57	[9]
$La_{0.7}Sr_{0.3}Cr_{0.8}Ti_{0.2}O_{3-\delta}$ ***c.c.: not indicated***	8YSZ	wet 100% H_2	1130	33		[163]
$La_{0.8}Sr_{0.2}Cr_{0.97}V_{0.03}O_{3-\delta}$ [a] ***c.c.: Au paste***	8YSZ	wet H_2	1123	4.1		[201]
$La_{0.8}Sr_{0.2}Cr_{0.97}V_{0.03}O_{3-\delta}$ [b] ***c.c.: Au paste***	8YSZ	wet H_2	1123	11		[201]
$La_{0.8}Sr_{0.2}Cr_{0.97}V_{0.03}O_{3-\delta}$ - YSZ [b] (50-50 wt.%) ***c.c.: Au paste***	8YSZ	wet H_2	1123	4.2		[201]
$La_{0.8}Sr_{0.2}Cr_{0.97}V_{0.03}O_{3-\delta}$ - Ni [c] (99.7-0.3 wt.%) ***c.c.: Au paste***	8YSZ	wet H_2	1123	2.1		[201]
$La_{0.8}Sr_{0.2}Cr_{0.97}V_{0.03}O_{3-\delta}$ - CGO10 -Ni (47.5-47.5-5 wt.%) ***c.c.: Au paste***	CGO10	wet 100% H_2	1023	0.46	13	[11]
$La_{0.75}Sr_{0.25}Cr_{0.5}Mn_{0.5}O_{3-\delta}$-YSZ (graded) ***c.c.: Au paste***	YSZ	wet 5% H_2 - Ar	1123	0.59	32	[8]
$La_{0.75}Sr_{0.25}Cr_{0.5}Fe_{0.5}O_{3-\delta}$ ***c.c.: Au paste***	YSZ	wet H_2	1123	1.2	35	[177]
$La_{0.75}Sr_{0.25}Cr_{0.5}Fe_{0.5}O_{3-\delta}$ ***c.c.: Au paste***	YSZ	wet 5% H_2 - Ar	1123	1.8		[177]
$La_{0.75}Sr_{0.25}Cr_{0.5}Fe_{0.5}O_{3-\delta}$ ***c.c.: Pt paste***	LSGM9182	wet 5% H_2 - Ar	1123	1.2	58	[9]
$La_{0.75}Sr_{0.25}Cr_{0.5}Fe_{0.5}O_{3-\delta}$ ***c.c.: Pt paste***	LSGM9182	dry 5% H_2 - Ar	1123	2.8	83	[9]
$La_{0.33}Sr_{0.67}Cr_{0.33}Fe_{0.67}O_{3-\delta}$ - CGO10 (50-50 wt.%) with $La_{0.6}Ce_{0.4}O_{2-\delta}$ sublayer ***c.c.: Au ink***	LSGM9182	wet 100% H_2	1073	0.32 [d]		[18]
$La_{0.33}Sr_{0.67}Cr_{0.33}Fe_{0.67}O_{3-\delta}$- CGO10 with CGO10 sublayer ***c.c.: Au grid (printed)***	LSGM9182	wet 100% H_2	1073	0.29 [e]		[264]
$Pr_{0.7}Sr_{0.3}Cr_{0.9}Ni_{0.5}O_{3-\delta}$ ***c.c.: not indicated***	YSZ	wet H_2	1173	1.0	92	[184]
		wet 5% H_2	1173	2.4		
$La_{0.7}Sr_{0.3}Cr_{0.95}Ru_{0.05}O_{3-\delta}$ ***c.c.: Au mesh***	YSZ	H_2 - H_2O (40-60%)	1023	17		[186]
$La_{0.7}Sr_{0.3}Cr_{0.95}Ru_{0.05}O_{3-\delta}$-YSZ (graded) with CGO10 sublayer ***c.c.: Au mesh***	YSZ	H_2 - H_2O (40-60%)	1023	3.7		[186]
$La_{0.8}Sr_{0.2}Cr_{0.82}Ru_{0.18}O_{3-\delta}$- CGO10 (50-50 wt.%) ***c.c.: Au grid (printed)***	LSGM9182	wet H_2	1073	0.23 [f]		[15]

[a] pre-annealed at 1273 K, fired at 1373 K; [b] pre-annealed at 1573 K, fired at 1373 K; [c] pre-annealed at 1623 K, fired at 1373 K; [d] measured 20 hours after inlet of PH_3; [e] R_η includes LSCF-CGO cathode; [f] measured under 0.5 V polarization

Table 1.2.6. Power densities of selected cells with chromite-based anodes in H_2-containing fuels

Anode	Electrolyte (thickness, μm)	Cathode	Fuel	T, K	P_{max}, mW/cm^2	Reference
$La_{0.85}Sr_{0.15}CrO_{3-\delta}$ ***c.c.: not indicated***	YSZ	not indicated	H_2	1173	70	[17]
$La_{0.7}Ca_{0.3}CrO_{3-\delta}$ impr.with CGO10 ***c.c.: Ag paste***	LSGM9182 (300)	Symmetrical	dry H_2	1173 1073	640 390	[268]
$La_{0.8}Sr_{0.2}CrO_{3-\delta}$ - CGO10 (50 - 50 wt.%) ***c.c.: printed Au grids***	LSGM9182 (400)	$La_{0.6}Sr_{0.4}Co_{0.2}Fe_{0.8}O_{3-\delta}$ - CGO10	wet H_2	1073	200	[15]
$La_{0.8}Sr_{0.2}Cr_{0.82}Ru_{0.18}O_{3-\delta}$ - CGO10 (50 - 50 wt.%) ***c.c.: printed Au grids***	LSGM9182 (400)	$La_{0.6}Sr_{0.4}Co_{0.2}Fe_{0.8}O_{3-\delta}$ - CGO10	wet H_2	1073	260	[15]
$La_{0.7}Sr_{0.3}CrO_{3-\delta}$ -YSZ (50-50 wt.%) ***c.c.: Pt-based ink***	YSZ (2000)	Symmetrical	wet 100% H_2	1223	110	[269]
$La_{0.7}Sr_{0.3}CrO_{3-\delta}$ - CeO_2 - Ni (51 - 39 - 10 wt.%) ***c.c.: Ag paste***	8YSZ (300)	$La_{0.8}Sr_{0.2}MnO_{3-\delta}$ - 8YSZ (60 - 40 wt.%)	H_2 - H_2O (97 - 3%)	1073	80	[270]
$La_{0.7}Sr_{0.3}CrO_{3-\delta}$ - CGO20 (80 - 20 wt.%) ***c.c.: Ag paste***	LSGM9182 (300)	LSM	H_2	1173 1073	570 210	[271]
$La_{0.7}Sr_{0.3}CrO_{3-\delta}$ - CGO20 (70 - 30 wt.%) ***c.c.: Ag paste***	LSGM9182 (300)	LSM	H_2	1173 1123 1073	480 360 200	[271]
$La_{0.7}Sr_{0.3}CrO_{3-\delta}$ - CeO_2 - Ni (25 - 37.5 - 37.5 mol.%) ***c.c.: not indicated***	8YSZ (350)	$La_{0.8}Sr_{0.2}MnO_{3-\delta}$ - 8YSZ (50 - 50 wt.%)	H_2 - H_2O (97 - 3%)	1073 973	130 70	[272]
$La_{0.75}Sr_{0.25}Cr_{0.5}Al_{0.5}O_{3-\delta}$ ***c.c.: Pt paste***	LSGM9182 (1500)	$Ba_{0.5}Sr_{0.5}Co_{0.8}Fe_{0.2}O_{3-\delta}$	wet 5% H_2 - Ar	1073	80	[9]
$La_{0.73}Sr_{0.26}Cr_{0.45}Ti_{0.55}O_{3-\delta}$ -CGO20 (50 - 50 wt.%) ***c.c.: Au paint***	8YSZ (300)	Pt	H_2	1123	20	[212]
$La_{0.8}Sr_{0.2}Cr_{0.98}V_{0.02}O_{3-\delta}$ - CGO10 - Ni (48 - 48 - 4 wt.%) ***c.c.: Au paste***	CGO10 (300)	$La_{0.6}Sr_{0.4}Co_{0.2}Fe_{0.8}O_{3-\delta}$ - CGO10 (50 - 50 wt.%)	H_2 - H_2O (97 - 3%)	1073 1023	270 150	[11]
$La_{0.75}Sr_{0.25}Cr_{0.5}Fe_{0.5}O_{3-\delta}$ ***c.c.: Pt paste***	LSGM9182 (1500)	$Ba_{0.5}Sr_{0.5}Co_{0.8}Fe_{0.2}O_{3-\delta}$	wet 5% H_2 - Ar	1073	50	[9]
$La_{0.33}Sr_{0.67}Cr_{0.33}Fe_{0.67}O_{3-\delta}$ -CGO10 (50 - 50 wt.%), $La_{0.4}Ce_{0.6}O_{2-\delta}$ sublayer ***c.c.: Au ink, Pt paste***	LSGM9182	$La_{0.6}Sr_{0.4}Co_{0.8}Fe_{0.2}O_{3-\delta}$ - CGO10 (graded)	dry H_2	1073	350	[18]
			H_2 - H_2O (97 - 3%)	1073	340	
$La_{0.8}Sr_{0.2}Cr_{0.5}Fe_{0.5}O_{3-\delta}$ - CGO20 (50 - 50 wt.%) ***c.c.: Au paint***	8YSZ (300)	Pt	H_2	1123	250	[212]
$La_{0.33}Sr_{0.67}Cr_{0.33}Fe_{0.67}O_{3-\delta}$ -CGO10 (50 - 50 wt.%) ***c.c.: printed Au grids***	CGO10 (300)	$La_{0.6}Sr_{0.4}Co_{0.8}Fe_{0.2}O_{3-\delta}$ - CGO10 (50 - 50 wt.%)	H_2 - H_2O (97 - 3%)	1073 973	300 150	[264]
$La_{0.33}Sr_{0.67}Cr_{0.33}Fe_{0.67}O_{3-\delta}$ -CGO10 (50 - 50 wt. %), with CGO10 sublayer ***c.c.: printed Au grids***	LSGM9182 (400)	$La_{0.6}Sr_{0.4}Co_{0.8}Fe_{0.2}O_{3-\delta}$ - CGO10 (50 - 50 wt.%)	H_2 - H_2O (97 - 3%)	1073	360	[264]
$La_{0.8}Sr_{0.2}Cr_{0.48}Co_{0.52}O_{3-\delta}$ -CGO20 (50 - 50 wt.%) ***c.c.: Au paint***	8YSZ (300)	Pt	H_2	1123	140	[212]
$La_{0.85}Sr_{0.15}Cr_{0.9}Ni_{0.1}O_{3-\delta}$ ***c.c.: not indicated***	YSZ	not indicated	H_2	1173	140	[17]
$La_{0.8}Sr_{0.2}Cr_{0.82}Ru_{0.18}O_{3-\delta}$ -CGO10 (50 - 50 wt. %) ***c.c.: printed Au grids***	LSGM9182 (400)	$La_{0.6}Sr_{0.4}Co_{0.8}Fe_{0.2}O_{3-\delta}$ - CGO10	wet H_2	1073 1023	390 300	[188]
$La_{0.8}Sr_{0.2}Cr_{0.82}Ru_{0.18}O_{3-\delta}$ -CGO10 (50 - 50 wt. %) ***c.c.: printed Au grids***	LSGM9182 (400)	$La_{0.6}Sr_{0.4}Co_{0.8}Fe_{0.2}O_{3-\delta}$ - CGO10	wet H_2	1073	460	[15]

Table 1.2.7. Power densities of selected cells with chromite-based anodes in CO-, hydrocarbon- or H_2S-containing fuels

Anode	Electrolyte (thickness, μm)	Cathode	Fuel	T, K	P_{max}, mW/cm^2	Reference
$LaCrO_{3-\delta}$ - VO_x - 8YSZ (40- 40 - 20 wt.%) ***c.c.: Au mesh***	8YSZ (300)	Pt	H_2 - CO (40 - 60%) + 5000 ppm H_2S	1173 1123	260 190	[273]
			H_2 + 5000 ppm H_2S	1173	170	
			H_2 - N_2 (40 - 60%) + 5000 ppm H_2S	1173	130	
			CO	1173	130	
$La_{0.7}Ca_{0.3}CrO_{3-\delta}$ impr. with CGO10 ***c.c.: Ag paste***	LSGM9182 (300)	Symmetrical	commercial city gas	1173	490	[268]
$La_{0.85}Sr_{0.15}CrO_{3-\delta}$ ***c.c.: not indicated***	YSZ	not indicated	CH_4 - Ar - H_2O (56 - 41 - 3%)	1173	140	[17]
$La_{0.7}Sr_{0.3}CrO_{3-\delta}$ - YSZ (50-50 wt.%) ***c.c.: Pt-based ink***	YSZ (2000)	Symmetrical	wet 100% CH_4	1223	25	[269]
$La_{0.7}Sr_{0.3}CrO_{3-\delta}$ - CGO20 (80 - 20 wt.%) ***c.c.: Ag paste***	LSGM9182 (300)	LSM	commercial city gas	1173	330	[271]
$La_{0.73}Sr_{0.26}Cr_{0.45}Ti_{0.55}O_{3-\delta}$ ***c.c.: Au paint***	8YSZ (300)	Pt	0.5% H_2S - CH_4	1173 1123 1073	140 55 20	[212]
$La_{0.73}Sr_{0.26}Cr_{0.45}Ti_{0.55}O_{3-\delta}$ - CGO20 (50 - 50 wt.%) ***c.c.: Au paint***	8YSZ (300)	Pt	0.5% H_2S - CH_4	1123	120	[212]
$La_{0.8}Sr_{0.2}Cr_{0.98}V_{0.02}O_{3-\delta}$ - CGO10 - Ni (48 - 48 - 4 wt.%) ***c.c.: Au paste, Ag paint***	CGO10 (300)	LSCF6428 - CGO10 (50 - 50 wt.%)	3% H_2O - CH_4	973	110	[274]
			3% H_2O - C_2H_6	973	100	
			3% H_2O - C_3H_8	973	130	
			3% H_2O - C_4H_{10}	973	80	
$Ce_{0.9}Sr_{0.1}Cr_{0.5}V_{0.5}O_{3-\delta}$ ***c.c.: Au paste***	8YSZ (300)	Pt	0.5% H_2S - N_2	1123	80	[162]
			0.5% H_2S - CH_4	1123	70	
$Ce_{0.9}Sr_{0.1}Cr_{0.5}V_{0.5}O_{3-\delta}$ - 8YSZ - Ni (47.5 - 47.5 - 5 wt.%) ***c.c.: Au paste***	8YSZ (300)	Pt	0.5% H_2S - N_2	1123	100	[162]
$La_{0.8}Sr_{0.2}Cr_{0.5}Fe_{0.5}O_{3-\delta}$ ***c.c.: Au paint***	8YSZ (300)	Pt	CH_4	1173	80	[212]
			0.5% H_2S - CH_4	1173	150	
$La_{0.33}Sr_{0.67}Cr_{0.33}Fe_{0.67}O_{3-\delta}$ - CGO10 (50 - 50 wt.%) $La_{0.4}Ce_{0.6}O_{2-\delta}$ sublayer ***c.c.: Au ink, Pt paste***	LSGM9182	LSCF6482 - CGO10 (graded)	H_2 - H_2O - CO - CO_2 (30 - 26 - 23 - 21%)	1073	220	[18]
$La_{0.8}Sr_{0.2}Cr_{0.5}Fe_{0.5}O_{3-\delta}$ - CGO20 (50 - 50 wt.%) ***c.c.: Au paint***	8YSZ (300)	Pt	CH_4	1123	70	[212]
			0.5% H_2S - CH_4	1123	150	
$Ce_{0.9}Sr_{0.1}Cr_{0.5}Fe_{0.5}O_{3-\delta}$ - SDC20 (80 - 20 wt.%) ***c.c.: Pt paste***	SDC20 (800)	Ag (from epoxy adhesive)	5% H_2S - N_2	873	20	[223]
$La_{0.8}Sr_{0.2}Cr_{0.48}Co_{0.52}O_{3-\delta}$ - CGO20 (50 - 50 wt.%) ***c.c.: Au paint***	8YSZ (300)	Pt	CH_4	1123	50	[212]
			0.5% H_2S - CH_4	1123	100	
$La_{0.85}Sr_{0.15}Cr_{0.9}Ni_{0.1}O_{3-\delta}$ ***c.c.: not indicated***	YSZ	not indicated	CH_4 - Ar - H_2O (56 - 41 - 3%)	1173	140	[17]

** LSCF6428 corresponds to $La_{0.6}Sr_{0.4}Co_{0.2}Fe_{0.8}O_{3-\delta}$, LSCF6482 corresponds to $La_{0.6}Sr_{0.4}Co_{0.8}Fe_{0.2}O_{3-\delta}$*

One of the most widely studied chromite-based anodes is $La_{0.75}Sr_{0.25}Cr_{0.5}Mn_{0.5}O_{3-\delta}$ and its derivatives [8, 10, 210]. Detailed description of the corresponding anodes and relationships between their functional properties and electrochemical performance will be presented in a separate section. One should

note that basically increasing the electronic transport in $(Ln,A)(Cr,Mn)O_{3-\delta}$ perovskite results in higher catalytic or electrocatalytic activity, emphasizing the role of the electronic conduction. Similar observations were made for $(La,Sr)(Cr,Fe)O_{3-\delta}$-based perovskite anodes. The performance generally increases with Fe content, possibly due to better electronic conductivity and improved ionic transport. The polarization resistances for $(Ln,A)(Cr,Mn)O_{3-\delta}$ and $(Ln,A)(Cr,Fe)O_{3-\delta}$ are comparable, although the results in various studies are contradictory [9, 212].

Dissolution of Ni or Ru cations in the perovskite phase with their subsequent segregation on reduction allows to produce submicron dispersed metallic particles which possess a high catalytic activity. One of benefits of such an approach relates to partial or complete dissolution of the metals on oxidation [15, 201] which improves the stability of the anodes on redox cycling. The precipitation of the metallic phases from the perovskite structure provides better electrochemical performance than preparation of mechanical mixtures with similar fraction of perovskite and metal [15]. In terms of microstructural stability, Ru-doping is more preferable compared with Ni due to higher melting point of Ru and, as a result, its suppressed vaporization and sintering [188, 267]. In $La_{1-x}Sr_xCr_{1-y}Ru_yO_{3-\delta}$, the compromise between the optimum electrochemical activity and stability was achieved for x = 0.3 and y = 0.08 [15]; this composition is close to $La_{0.7}Sr_{0.3}Cr_{0.95}Ni_{0.05}O_{3-\delta}$ which exhibited the maximum CH_4 conversion compared with other $(La,Sr)(Cr,Ni)O_{3-\delta}$ catalysts [265].

Apart from the electrochemical activity of chomite electrodes, one should take into account their compatibility with solid electrolytes. As the reactivity of electrode materials is governed by their stability, the chemical compatibility of chromites with commonly used solid electrolytes is generally better than that of cobaltites, ferrites and manganites. Interaction of Ca- or Sr-doped $LaCrO_{3-\delta}$ with solid electrolytes is strongly associated with cation demixing and formation of Ca-Cr-O or Sr-Cr-O secondary phases [141]. $(La,Sr)CrO_{3-\delta}$ are basically more compatible with YSZ electrolytes [134, 138, 275]. Reactivity of Ca-doped $LaCrO_{3-\delta}$ with YSZ originates from formation of CaO, $Ca_m(CrO_4)_n$ phases [143], which are in most cases segregated at high temperatures during synthesis of the chromite perovskites, or from high diffusivity and solubility of Ca in the fluorite structure [154, 276]. Obviously, A-site deficiency suppresses the formation of $Ln_2Zr_2O_{7-\delta}$, $SrZrO_{3-\delta}$ or $CaZrO_{3-\delta}$ phases [134]. The cation demixing may be promoted by exposure of the electrode to hydrocarbon- or CO/CO_2-containing atmospheres or by polarization ([44, 259] and references cited).

The presence of Sr_2VO_4 and Sr_2CrO_4 impurities in $(La,Sr)(Cr,V)O_{3-\delta}$ enhances the reactivity of the anode with YSZ at temperatures as low as 1273 K in both oxidizing and reducing atmospheres, which is inappropriate for SOFC applications [231]. The chemical compatibility of $(La,Ca)(Cr,Ti)O_{3-\delta}$ [155], $La_{0.75}Sr_{0.25}Cr_{0.5}Mn_{0.5}O_{3-\delta}$ [8, 277], $Pr_{0.7}Ca_{0.3}(Cr,Mn)O_{3-\delta}$ [210] and $(La,Sr)(Cr,Ru)O_{3-\delta}$ [186] with YSZ electrolytes was observed at least up to 1573, 1573, 1473 and 1373 K.

The interaction with $LaGaO_{3-\delta}$-based electrolytes is primarily associated with a high tolerance of gallate phases towards B-site substitution and a gradient of La chemical potential between the components inducing La diffusion and formation of interfacial $LaSrGaO_4$ and $LaSrGa_3O_7$ phases with low ionic conductivity [278-280]. With respect to anode materials, the presence of Fe, Ni, Co-containing compositions in direct contact with LSGM is undesirable [9, 10, 278]. For example, the onset of interaction between $(La,Sr)(Cr,Fe)O_{3-\delta}$ and LSGM is located at relatively low temperatures (1073 - 1173 K) resulting in cation

exchange [278] or formation of $LaSrGa_3O_7$ [264]. The interaction of $La_{0.75}Sr_{0.25}Cr_{0.5}Al_{0.5}O_{3-\delta}$ with LSGM starts at 1473 K producing $SrCrO_4$, $LaCrO_{3-\delta}$ and $LaGaO_{3-\delta}$-based phases and causing the electrode delamination [9]. $La_{0.75}Sr_{0.25}Cr_{0.5}Mn_{0.5}O_{3-\delta}$ reacts with LSGM at temperatures as high as 1623 - 1673 K with formation of $LaSrGaO_4$ and $LaSrGa_3O_7$ [279, 280]. Similar to LSGM, the compatibility of $CeO_{2-\delta}$-based electrolytes is determined by solubility and mobility of cations in the fluorite structure. $La_{0.7}Ca_{0.3}CrO_{3-\delta}$ was reported to be compatible with CGO [268] at 1473 K. No chemical interaction between $(La,Sr)CrO_{3-\delta}$ and CGO was reported up to 1873 K, however, the presence of $CaCrO_4$, $SrCrO_4$ or Cr_2O_3 impurities causes a strong cation interdiffusion and formation of new phases [281]. No interaction of $Ce_{0.9}Sr_{0.1}Cr_{0.5}Fe_{0.5}O_{3-\delta}$ with $Ce_{0.8}Sm_{0.2}O_{2-\delta}$ was found at 1173 K in N_2 [223].

Apart from the interaction with electrolyte material, the long-term performance of chromite-based anodes is strongly affected by the presence of components with low chemical and/or microstructural stability (metallic phase, VO_x, doped $CeO_{2-\delta}$, etc.) which may undergo a loss of catalytic activity, vaporization, changes in porous anode microstructure due to sintering and lowering the active electrode surface area, blocking the pores, strong volume changes, cracking of the electrode layer or its delamination from the electrolyte. As an example, stable operation was found in H_2 and CH_4 for $La_{0.7}Sr_{0.3}Cr_{0.95}Ru_{0.05}O_{3-\delta}$ - YSZ [186], while increasing Ru fraction results in a coalescence of the metallic particle and reduces the activity [15, 188]. While the performance of $Ce_{0.9}Sr_{0.1}Cr_{0.5}V_{0.5}O_{3-\delta}$ anode was stable in H_2S - CH_4 for more than 15 hours at 1123 K, the composite $Ce_{0.9}Sr_{0.1}Cr_{0.5}V_{0.5}O_{3-\delta}$ - YSZ - Ni showed a degradation rate of 10% per 15 hours at the same conditions [162]. Comparable degradation rate was detected for $La_{0.8}Sr_{0.2}Cr_{0.98}V_{0.02}O_{3-\delta}$ - CGO - Ni (48 - 48 - 4 wt. %) in hydrocarbon atmosphere at 873 - 1023 K [274], while no drop of the performance was observed for anode $La_{0.8}Sr_{0.2}Cr_{0.97}V_{0.03}O_{3-\delta}$ - CGO (75 - 25 wt.%) impregnated with Ru (1 mg/cm^2) in wet CH_4 [282]. This observation confirms that the stability is mainly governed by the nature and amount of metallic or other microstructurally-unstable phases rather than by the perovskite degradation. B-site doping of chromites with transition metals may also promote the degradation processes; in particular, the initial high performance of Mn-, Fe-, Ni- and Ru-doped chromite anodes is in most cases followed by a rapid decay [186, 212, 283].

Other factors which influence the stable operation of chromite electrodes are thermal or redox cycling; the latter may be induced by changing the gas environment or by oscillating polarization. As the elementary electrode steps are affected by $p(O_2)$ by various manner, the final result is not obvious. For example, the polarization resistance of $La_{0.8}Sr_{0.2}Cr_{0.97}V_{0.03}O_{3-\delta}$ anode decreased after reoxidation in air [201], while $La_{0.8}Sr_{0.2}Cr_{0.98}V_{0.02}O_{3-\delta}$ - CGO - Ni showed a drop of activity on oxidation in air, followed by a rapid recovery after switching back to H_2 or C_3H_8. This composite anode could withstand up to 11 redox cycles of 1 hour [274]. In [283], the performance of $La_{0.75}Sr_{0.25}Cr_{0.5}Mn_{0.5}O_{3-\delta}$ - YSZ composite anode was deteriorated on cycling in wet H_2 - reformate - wet O_2 at 1173 K by 15% per 4 cycles; however, the initial performance drop was followed by subsequent stabilization. The performance of $La_{0.75}Sr_{0.25}Cr_{0.5}Mn_{0.5}O_{3-\delta}$ - CGO (33 - 67 wt. %) showed a slight (3%) decrease after cycling in wet CH_4 at 1123 K for 50 hours under currents oscillating in the range 200 - 400 mA/cm^2 [284].

1.2.7. Cr-poisoning phenomena in SOFCs

This section is devoted to the phenomena of contamination of SOFC components with Cr species. The poisoning is mainly associated with application of Cr-containing interconnect materials. The primary function of interconnects is to ensure mechanical and electrical contact between the cathode/anode of adjacent cells and to provide the separation of the fuel gas from the oxidant. This imposes stringent requirements on the interconnect material such as chemical stability towards oxidative and reductive atmospheres, impremeability of gases, high electronic and negligible ionic conduction, chemical and mechanical compatibility with SOFC components, low costs [3, 6].

Currently, 2 types of interconnect materials are employed. One group is represented by metallic alloys, mainly Fe-based materials due to their low costs and relatively high tolerance towards oxidation due to formation of Cr_2O_3-based scales on the surface. The oxidation resistance as well as mechanical properties may be tuned by addition of Al, Cr, Si, Mo and other elements. The percentage of Cr in metal-based interconnect materials is basically higher than 10 wt.%, although this amount should not overcome 26 wt.% to avoid formation of brittle phases [285].

Ceramics with acceptable electronic conductivity compose the other group of interconnect materials. As shown in previous sections, the characteristics of $LnCrO_{3-\delta}$-based materials satisfy the most requirements; in particular, the negligible ionic conductivity of chromites is more advantageous for interconnects rather than for anodes. However, poor thermal conductivity, possibility of cracking and insufficient density restricts the application of chromites as interconnects. Generally, the choice of interconnect material is determined by the range of working and fabrication temperatures. While metal-based interconnects suffer from oxidation at high temperatures, chromite-based ceramic materials are stable in a wide $p(O_2)$ range ([46, 134] and references therein). On the other hand, the conductivity of chromites is substantially activated by temperature [112, 160, 187]; consequently, this group of interconnects is mainly considered for high-temperature utilization. Decreasing the temperature reduces the risk of oxidation of metallic interconnects which makes these more appropriate for intermediate- and low-temperature electrochemical cells.

Irrespective of the type of the interconnect, most materials contain substantial amount of Cr which can cause contamination of other SOFC components and subsequent degradation of the performance. Even if Cr content in interconnect is moderate and its reactivity is suppressed by binding to a stable composition or application of protective layers, Cr penetration into electrode compartments may proceed via flowing in gas phase from upstream cell components like manifolds, heat exchangers, etc.

As reported above, for Cr-containing alloys, protective Cr_2O_3-based scales are formed on the surface. The formation was observed under both cathode and anode conditions, although in the latter case, the growth rate was much lower. In numerous cells, the Cr_2O_3 layer is the most resistant component, while its continuous enlargement results in a progressive increase of Ohmic losses [286]. In contact of Cr_2O_3 with Co, Fe, Mn, Ni-containing electrodes, the formation of spinel phases $(Cr,M)_3O_4$ was observed [241, 285, 287]. These phases are more preferable in comparison with Cr_2O_3 in terms of conductivity, especially Co-rich ones [241], although the resistance is still too high for achieving reasonable power densities of the cell, while the depletion of the electrode with a transition metal may reduce the catalytic activity.

One of the most detrimental phenomena in terms of the cell degradation is Cr penetration into the electrode layers. In literature, two ways of Cr incorporation are discussed: surface diffusion and deposition from the gas phase. The diffusion was shown to be strongly promoted by the presence of Co-, Mg-, Mn-, Sr-, and Au-containing species [285, 288, 289]. Among cathode materials, the most susceptible ones to diffusion-related Cr contamination are manganite- and cobaltite-based compositions [285].

Another mechanism Cr poisoning processes involves chromia vaporization and subsequent deposition on the surface of cell components [82-85]. The latter process is especially pronounced at elevated temperatures due to enhanced activation energy [285]. As shown in Figs. 1.2.8 - 1.2.9, the most abundant Cr-containing species in gas phase are CrO_3, $CrO_2(OH)_2$ and $CrO_2(OH)$. Occasional penetration of water vapors into the cathode compartment results in an enrichment of the atmosphere with Cr oxihydroxides. The presence of Cr-containing volatile species may subsequently result in their reduction and deposition on the cathode or electrolyte surface or at the interface cathode-electrolyte.

The deposition of Cr-containing compounds from the gas phase may be catalyzed electrochemically [85, 290], by reduction in oxygen-depleted atmosphere near the triple phase boundary (TPB) [83, 290] or chemically; in the latter case, the deposition is ensured by the presence of catalytically-active species (i.e. Mn^{2+}, Co^{2+} or SrO) [84, 285, 291]. The latter mechanism is confirmed by the fact that in manganite- and cobaltite-based cathodes, the deposition proceeds in the entire electrode layer.

Basically, Cr is deposited in form of spinel phase; examples of the chemical reduction processes are shown in Eqs. (1.2.9) - (1.2.12):

$$2CrO_3(g) = Cr_2O_3(s) + 3/2\,O_2(g) \qquad \textbf{(Eq. 1.2.9)}$$

$$2CrO_2(OH)_2(g) = Cr_2O_3(s) + 2H_2O(g) + 3/2\,O_2(g) \qquad \textbf{(Eq. 1.2.10)}$$

$$La_{1-x}Sr_xMnO_{3-\delta}(s) + 1/2\,Cr_2O_3(s) = La_{1-x}Sr_xMn_{1-y}Cr_yO_{3-\delta'}(s) + (Cr_{1-y}Mn_y)O_{4/3-\delta''}(s) + \\ + (1/6 + \delta' + \delta'' - \delta)/2\,O_2(g) \qquad \textbf{(Eq. 1.2.11)}$$

$$La_{1-x}Sr_xMnO_{3-\delta}(s) + yZrO2 + (1-y)/2\,Cr_2O_3(s) = La_{1-x}Sr_xMn_{1-y}Zr_yO_{3-\delta'}(s) + \\ + (Cr_{1-y}Mn_y)O_{4/3-\delta''}(s) + (1/6 + \delta' + \delta'' - \delta + y/2)/2\,O_2(g) \qquad \textbf{(Eq. 1.2.12)}$$

Deposition of Cr_2O_3 causes lowering the pressure of Cr-containing phases which favors subsequent vaporization of Cr from interconnect and resultant depletion with chromium. Accumulation of the spinel phase results in gradually increasing concentration polarization, while the volume changes may cause a propagation of cracks [83, 290].

The electrochemically-assisted deposition process is supported by observations that cathodic polarization promotes the degradation, while the formation of spinel phase takes place predominantly near cathode-electrolyte interface [82, 83, 290]. The electrochemical reactions can be briefly formulated as:

$$CrO_3(g) + 3\overline{e} = 1/2\,Cr_2O_3(s) + 3/2\,O^{2-} \qquad \textbf{(Eq. 1.2.13)}$$

$$CrO_2(OH)_2(g) + 3\overline{e} = 1/2\,Cr_2O_3(s) + H_2O(g) + 3/2\,O^{2-} \qquad \textbf{(Eq. 1.2.14)}$$

$$CrO_2(OH)(g) + 2\overline{e} = 1/2\,Cr_2O_3(s) + 1/2\,H_2O(g) + O^{2-} \qquad \textbf{(Eq. 1.2.15)}$$

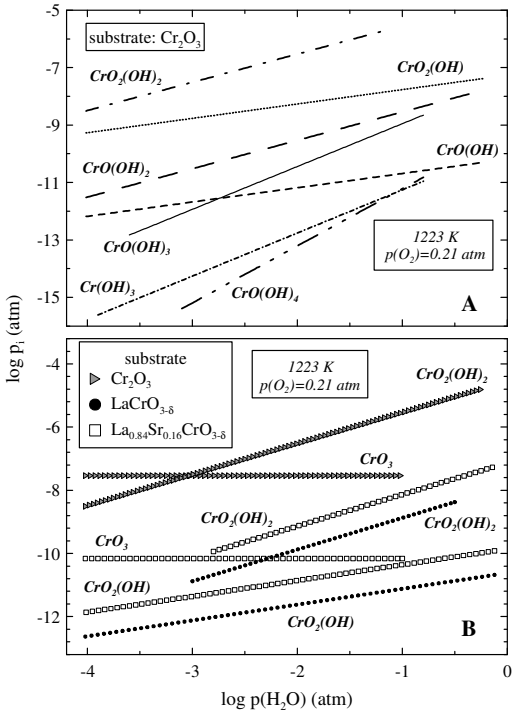

Fig. 1.2.8. Isothermal dependencies of partial pressure of selected Cr-containing gaseous species over solid Cr_2O_3 and chromites vs. $p(H_2O)$. The data are taken from [82].

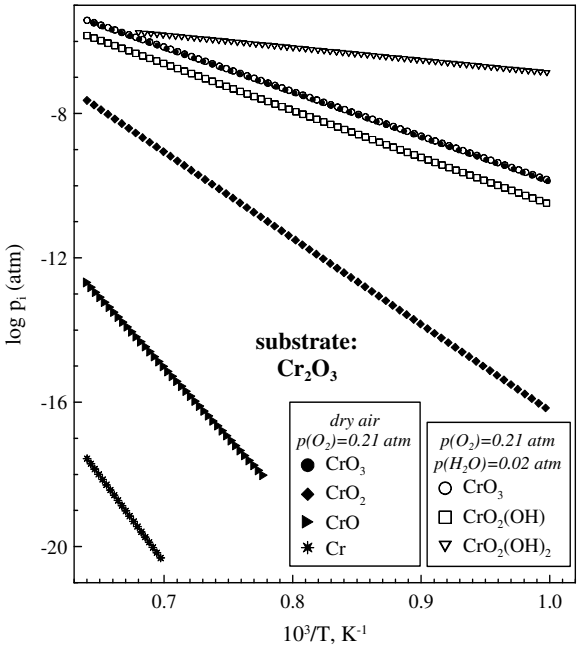

Fig. 1.2.9. Temperature dependencies of selected Cr-containing gaseous species over solid Cr_2O_3. The data are taken from [82].

The deposition of Cr_2O_3 and subsequent interaction with cathode and electrolyte materials (Eqs. (1.2.11), (1.2.12)) result in blocking TPB by the products, while the participation of electrons in the secondary processes reduces the efficiency of the cell. Estimations carried out in [82] showed that under working conditions, the deposition rate of chromia at the cathode exceeds 8×10^{-9} g/m$^2\times$s, i.e., considering the total cathode surface, this value corresponds to formation of a Cr monolayer in 2.4 s.

Similar to the surface diffusion, the maximum Cr deposition from the gaseous phase was observed on (La,Sr)$MnO_{3-\delta}$ and (La,Sr)(Co,Fe)$O_{3-\delta}$-based cathodes [285, 291, 292]. A strong tendency of Fe-containing cathodes, i.e $La_{0.8}Sr_{0.2}Co_{0.75}Fe_{0.25}O_{3-\delta}$, $LaNi_{0.6}Fe_{0.4}O_{3-\delta}$, $La_{0.8}Sr_{0.2}FeO_{3-\delta}$ to degradation in contact with Cr-containing materials was reported by Montero et al. [293], although in other publications, La(Ni,Fe)$O_{3-\delta}$ compositions were found to be tolerant towards Cr contamination [285, 294]. At high content of alkali-earth cations in cathode material, the phases $CaCrO_4$, $SrCrO_4$ or $BaCrO_4$ can be formed at the interface cathode-interconnect or on the cathode surface [44, 293] with resultant deterioration of transport and mechanical properties or loss of the electrochemical activity.

The anode conditions are generally not favorable for Cr vaporization and a substantial enrichment of the gas atmosphere with Cr species may be only as a result of an occasional penetration from other compartments of the cell or by an accidental oxidation of Cr-containing anodes. Moreover, the electrochemical oxidation at the anode side should suppress the processes Eqs. (1.2.13) - (1.2.15). Possibly, one should take precautions with Cr chemical deposition on the anode surface, in particular when operating with Mn-containing since the presence of Mn^{2+} or MnO species and low $p(O_2)$ may induce the reduction of gaseous Cr^{6+}-containing species and their deposition. However, such phenomena have not been found in

literature. More concerns are related with Cr, Fe and Ni interdiffusion between the anode and interconnect materials resulting in formation of insulating Cr_2O_3, $(Cr,Ni)_3O_4$ and FeO phases [288, 293, 295, 296]. One should notice that Cr_2O_3-based phases possess a worse conductivity under low-$p(O_2)$ conditions [115, 288] which may be caused by H_2 dissolution in chromia [297]. Similar to cathode degradation process, the formation of the secondary phases may result in blocking pores in the top layers of the electrode, and risks of mechanical failure due to chemical expansion [296].

Among solid electrolytes, gallate-based perovskites are strongly susceptible to deposition of chromia onto the surface from the vapour phase or to the surface diffusion in contact with an interconnect [285]. A slight bulk diffusion of Cr and Mn from $(La,Sr)(Cr,Mn)O_{3-\delta}$-based electrodes into LSGM was reported [10, 218]. The poisoning effect of Cr on fluorite-type electrolytes is less studied. A slight diffusion of Cr along the surface of YSZ and CGO was observed, without any traces of Cr_2O_3 precipitated from the gas phase [285], in contrast to the mechanism expressed by Eq. (1.2.12) [82]. The contamination of the electrolytes is attributed to catalyzing effect of Y_2O_3 and Gd_2O_3 additions, while the parent phases ZrO_2 and CeO_2 are insusceptible towards Cr penetration [285].

In order to prevent the problems associated with the contamination of SOFC components with Cr, several modifications were undertaken, with the primary focus on inhibition of volatilization of Cr-containing compounds or suppressing the diffusion. In particular, the vaporization may be suppressed by utilization of ceramic chromite-based interconnects. As shown in Fig. 1.2.8, the partial pressure of CrO_3, $CrO_2(OH)_2$ and $CrO_2(OH)$ over chromite perovskites are 3 - 4 orders lower than over Cr_2O_3, although their behavior with changes of $p(H_2O)$ or temperature is similar. A positive effect may be achieved by reducing the operation temperature. One should note that most studies on Cr vaporization or diffusion phenomena from metallic interconnects have been carried out at the temperatures above 973 K, while the Cr-containing alloys are designed for operation in the intermediate- or low-temperature ranges.

In $LnCrO_{3-\delta}$-based interconnects, the vaporization of chromia during preparation or operation procedure was shown to be suppressed by creation of Cr deficiency in the perovskite [135], appropriate doping into A- or B-sublattice [153, 189, 209] or introduction of components ensuring better densification [160]. Thin layers of $LaCrO_{3-\delta}$- or $LaMnO_{3-\delta}$-based perovskites ([288, 290] and references cited), spinel-type $(Mn,Co,Cr)_3O_4$ [293, 296] or CeO_2-based materials [296] were shown to prevent the interdiffusion between the corresponding materials or to suppress chromia vaporization from the surface, although their application may result in increasing Ohmic drops of the cell.

Finally, one should notice that Cr is not the unique component which causes the cell degradation. Fe-diffusion from interconnects is stronger than that of Cr, and may also cause the formation of insulating phases [288, 296]. Numerous interconnect alloys contain Mo-, Si- and other elements capable to generate volatile compounds with more detrimental effect on the properties of SOFC components.

1.3. Manganite-based perovskites and their limitations

Manganite-based perovskites have been widely studied as cathode materials due to their high electronic conductivity, moderate thermal expansion, acceptable catalytic activity and suppressed (in

comparison with other cathodes) interaction with SOFC components. Reduction of manganites, although being attractive in terms of an improvement of the ionic transport and mofification of the electrochemical properties, results in destabilization of the perovskite phase. On the other hand, the number of studies devoted to assessment of manganites as anode materials or evaluation of their low-p(O_2) characteristics has been growing in recent years. The present section is focused on comparison of manganite perovskite as potential anode materials, with a primary attention on their tolerance towards reducing atmospheres.

1.3.1. Thermodynamic stability

The behavior of manganite perovskites in terms of the defect equilibrium is generally similar to that of chromite analogues, and most equations described in the corresponding section may be applied for $LnMnO_{3\pm\delta}$-based compositions. However, manganite perovskites exhibits some peculiarities:

1. High flexibility of Mn cations in terms of the oxygen coordination and the capability to adopt the oxidation state +2 significantly increase the oxygen nonstoichiometry of manganites in comparison with chromite analogues. The stability of Mn in +2, +3 and +4 oxidation states makes it necessary to account for the process of Mn^{3+} disproportionation in modeling the defect equilibrium.

2. Manganites are capable to accommodate excessive oxygen in the crystal lattice. Since the perovskite structure is not tolerant to incorporation of oxygen into the interstitial sites, the overstoichiometry is accompanied by generation of cation vacancies [298-300]. Although at low p(O_2) the cation vacancies disappear, the processes associated with variations of oxygen content may be characterized by phase transitions and dimensional changes which should be taken into account when fabricating the anode layers.

Defect models explaining the behavior of manganite perovskites have been elaborated in numerous studies [234, 244, 300-305]. In [303], a model which included the coexistence of 9 type of lattice defects in La, Mn and O sublattices in p(O_2) range of 10^{-30} - 10^{-5} atm was proposed using numerical methods of calculation. Selected approaches involved consideration of the interactions between the defect species, formation of defect clusters, etc [224, 304, 305]. In the model elaborated by Mizusaki et al. [300] for Sr-substituted manganites, the energy levels of the states Mn'_{Mn}, $Mn^{\times}_{Mn}$, $Mn^{\cdot}_{Mn}$ are assumed to be close, and the thermodynamic parameters are governed essentially by the average Mn oxidation state. However, this approach is valid only in a limited range of Mn oxidation states, where the concentrations of Mn species may be considered comparable. Moreover, the model does not describe adequately the experimental data.

Regardless the approach describing the behavior of manganite perovskites, the stability of Mn in 2+ state significantly enhances the maximum oxygen deficiency in comparison with chromites. While $La_{1-x}A_xCrO_{3-\delta}$ shows the high- and low-p(O_2) saturations at $\delta = 0$ and $x/2$, for manganite-based analogues these regions are expected to transform into a plateau-like dependencies, followed by subsequent variations of oxygen content [303]. The width of the low-p(O_2) plateau is determined by the equilibrium constant of Mn^{3+} disproportionation. In practice, no plateau-like behavior at $\delta = x/2$ has been observed, as shown in Fig. 1.3.1. For most compositions, this phenomenon is associated with low tolerance of the perovskite structure towards extensive oxygen losses, preventing formation of large quantities of Mn^{2+} species.

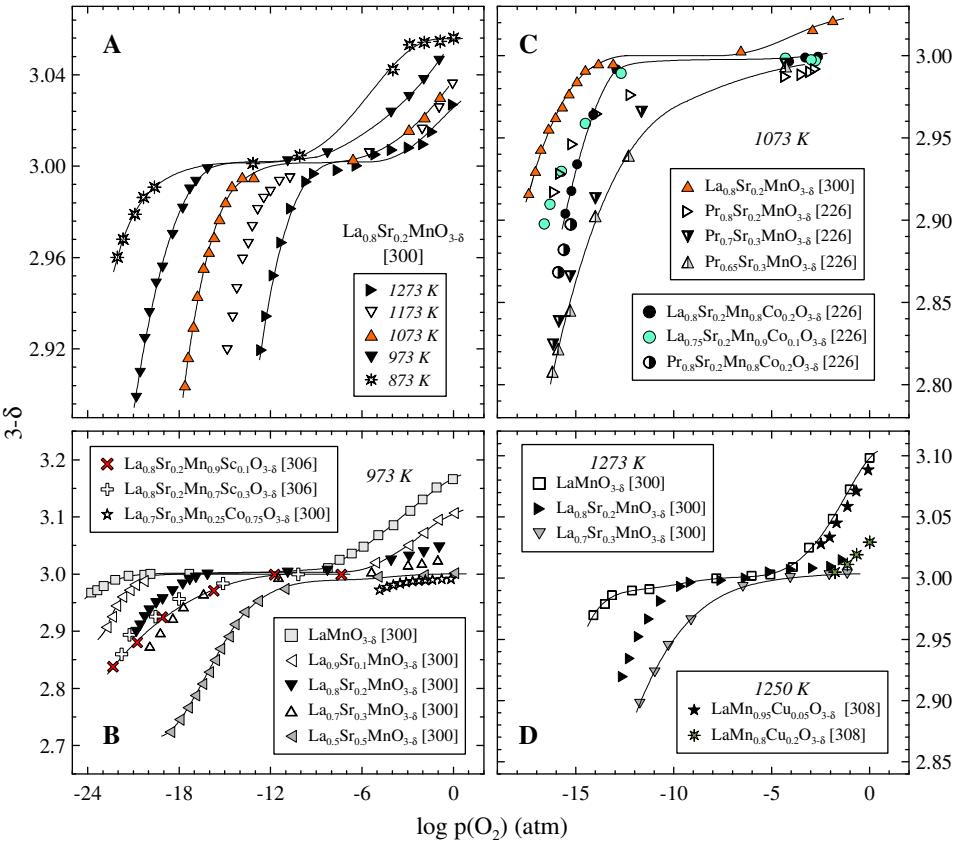

Fig. 1.3.1. Isothermal dependencies of oxygen content in manganites vs. $p(O_2)$

Approximate phase boundaries of selected manganite-based perovskites are shown in Fig. 1.3.2 and Table 1.3.1. Consistently with the defect model, alkali earth dopants enlarge the oxygen losses and reduce the stability of manganites. Depending on the doping level, decomposition of $(La,Sr)MnO_{3\pm\delta}$ leads to formation of MnO, $SrMnO_{3-\delta}$ and $(La,Sr)_2MnO_{4\pm\delta}$ phases, with La:Sr ratio similar or somewhat lower (for La-rich compositions) than that in the parent perovskite [309, 310]. On increasing Sr content, an enrichment of the surface with Sr was observed, promoted by low $p(O_2)$ [311-313]. The stability of $LnMnO_{3\pm\delta}$ decreases with lowering the radius of A-cation [45], as shown in Fig. 1.3.2.

While replacement of chromium in $LnCrO_{3\pm\delta}$-based perovskites promotes oxygen losses even when the doping cations are stable towards reduction, the effect of B-site cation substitution in manganites is less obvious. Introduction of easily reducible Fe, Co, Ni, Cu enhances the oxygen losses and deteriorates the stability of the manganites towards reduction; selected examples of variations of the oxygen content in Co-doped manganites are presented in Fig. 1.3.1. [226, 307, 308].

Introduction of 3-fold charged cations, like Sc, has no obvious effect on the oxygen nonstoichiometry [306], although more results for B-site substituted manganites are required for more certain conclusions. Doping of $PrMnO_{3\pm\delta}$-based compositions with In diminishes oxygen losses on reduction at 973 K compared with In-free analogue, while at 1273 K the trend is opposite [314]. This might indicate a strong effect of the substituents on the enthalpy of vacancy formation, kinetic factors or individual peculiarities of doping cations with respect to oxygen environment.

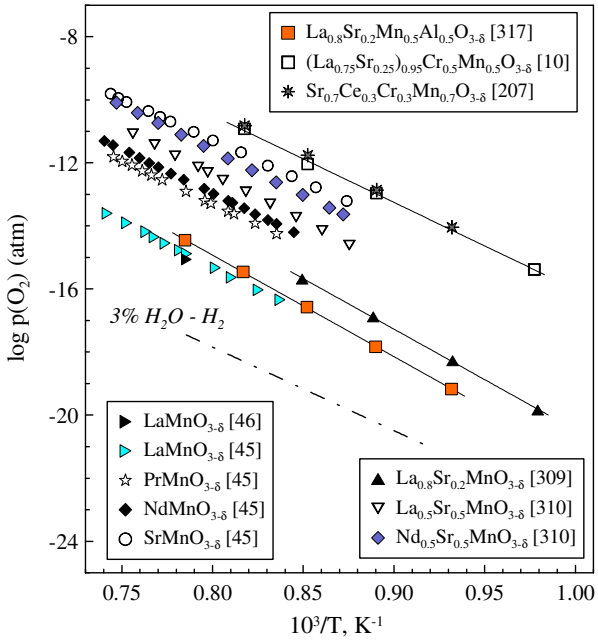

Fig. 1.3.2. Stability limits of manganite perovskites

Introduction of 3+, 4+, 5+-charged cations generally results in thermodynamic or kinetic stabilization of manganites at low $p(O_2)$, as shown in Table 1.3.1. Single-phase $LnMnO_{3\pm\delta}$-based perovskites were detected at $p(O_2)$ as low as 10^{-20} atm at 973 - 1173 K, which is quite acceptable for the anode applications. One may observe contradictions between the results presented in Table 1.3.1. In particular, $La_{0.75}Sr_{0.25}Cr_{0.5}Mn_{0.5}O_{3-\delta}$ is reported to decompose at 10^{-20} atm at 1173 K [191], although in [8] the stability of the perovskite phase was observed down to at least 10^{-21} atm. While $Pr_{0.7}Ca_{0.3}Cr_{0.4}Mn_{0.6}O_{3-\delta}$ was found to be stable in dry 5% H_2 - Ar [210], a similar composition doped with 25% of Sr and 50% of Mn showed insufficient stability in more mild reducing atmospheres [8], although the lower content of the alkali earth cation and Mn are expected to improve the tolerance towards reduction. $La_{0.8}Sr_{0.2}Mn_{0.8}Sc_{0.2}O_{3-\delta}$ is stable at 1123 K in H_2 - Ar mixture with $p(O_2) = 10^{-21}$ atm and in wet CH_4 ($p(O_2) = 10^{-23}$ atm) [315]. On the other hand, in CO - CO_2 atmosphere with $p(O_2) = 10^{-18}$ atm at 1123 K the same material shows the formation of secondary phases [316]. In the latter case, the presence of CO or CO_2 might promote the decomposition of the perovskite while poor conversion of CH_4 over the perovskite might ensure insufficiently reductive atmosphere, thus maintaining its stability.

In the high $p(O_2)$ range, manganites with moderate quantities of acceptor-type substituents exhibit a so-called oxygen overstoichiometry ($LnMnO_{3+\delta}$), presumably due to preferability of formation of the vacancies in A- or B-sublattice is arguable. Small size of B-cations favors their incorporation into A-sublattice, which, on the other hand, is hindered by strong bonds B-O. In literature, the equivalent concentration of A- and B-site vacancies as well as their dominant formation in one of the sublattices can be found [298-300, 321, 322]; currently, most approaches consider the preferability of the formation of A-site vacancies [298-300]. The cation exchange between A and B-perovskite positions enlarges the range of acceptable Ln:Mn ratios; for $LaMnO_{3\pm\delta}$, formation of single phase was observed for Mn/(La+Mn) of 0.45 - 0.52 at 1123 K, the region expanding on cooling [302].

Table 1.3.1. Stability of selected manganite perovskites under reducing conditions

Composition	T, K	Atmosphere or $p(O_2)$, atm	Stability	Examination method	Products of decomposition	Reference
$LaMnO_{3-\delta}$	1273	9×10^{-16}	Start of decomposition	TGA	La_2O_3, MnO	[46]
$La_{0.8}Sr_{0.2}MnO_{3-\delta}$	1173	4×10^{-17}	Start of decomposition	EMF	$(La,Sr)_2MnO_4$, MnO	[310]
$SrMnO_{3-\delta}$	1173	2×10^{-13}	Start of decomposition	EMF	$Sr_2MnO_{3.5}$	[310]
$La_{0.8}Sr_{0.2}Mn_{0.5}Al_{0.5}O_{3-\delta}$	1123	1×10^{-18}	Start of decomposition	XRD	$(La,Sr)_2MnO_4$, $(La,Sr)AlO_3$, MnO	[317]
$La_{0.8}Sr_{0.2}Mn_{0.9}Sc_{0.1}O_{3-\delta}$	973	H_2	Stable	XRD	-	[306]
$La_{0.8}Sr_{0.2}Mn_{0.8}Sc_{0.2}O_{3-\delta}$	1423	H_2 (1×10^{-18})	Stable	XRD	-	[316]
	1123	CO (1×10^{-17})	Stable	XRD	-	
	1123	CO (1×10^{-18})	Unstable	XRD, fuel cell tests	not indicated	
$La_{0.8}Sr_{0.2}Mn_{0.8}Sc_{0.2}O_{3-\delta}$	1123	dry 5% H_2 - Ar (1×10^{-21})	Stable	XRD	-	[315]
	1123	wet CH_4 (1×10^{-23})	Stable	XRD	-	
	1123	dry CH_4	Unstable	XRD	not indicated	
$La_{0.8}Sr_{0.2}Mn_{0.7}Sc_{0.3}O_{3-\delta}$	973	H_2	Stable	XRD	-	[306]
$La_{0.4}Sr_{0.6}Mn_{0.6}Ti_{0.4}O_{3-\delta}$	1123	2×10^{-16}	Stable	XRD	-	[16]
	1123	1×10^{-23}	Unstable	XRD	$(La,Sr)_2MnO_4$, MnO	
$La_{0.4}Sr_{0.6}Mn_{0.4}Ti_{0.6}O_{3-\delta}$	1123	1×10^{-23}	Stable	XRD	-	[16]
$La_{0.75}Sr_{0.25}Cr_{0.5}Mn_{0.5}O_{3-\delta}$	1173	1×10^{-21}	Stable; phase transition	XRD	-	[8]
$La_{0.75}Sr_{0.25}Cr_{0.5}Mn_{0.5}O_{3-\delta}$	1173	1×10^{-20}	Unstable	XRD, TGA	$(La,Sr)_2MnO_4$, MnO	[191]
$La_{0.75}Sr_{0.25}Cr_{0.3}Mn_{0.5}Ni_{0.2}O_{3-\delta}$	1073	wet 5% H_2 - Ar	Unstable	TEM	Ni particles	[211]
$La_{0.6}Sr_{0.4}Mn_{1-x}Ni_xO_{3-\delta}$ (x = 0 - 0.5)	1123	7×10^{-18}	Unstable	XRD	$(La,Ca)_2MnO_4$, MnO, Ni	[318]
$La_{0.9}Sr_{0.1}Mn_{0.43}Ga_{0.57}O_{3-\delta}$	1023	H_2	Stable	XRD	-	[319]
$SrMn_{0.5}Nb_{0.5}O_{3-\delta}$	1173	H_2 - Ar (5 - 95%)	Stable; phase transition	XRD	-	[20]
$Sr_{0.7}Ce_{0.3}Mn_{0.9}Al_{0.1}O_{3-\delta}$	1173	3×10^{-14}	Start of decomposition	XRD, conductivity	CeO_2, $SrMn_3O_6$	[320]
$Sr_{0.7}Ce_{0.3}Cr_{0.5}Mn_{0.5}O_{3-\delta}$	1223	2×10^{-11}	Stable	XRD	-	[207]
	1223	2×10^{-13}	Unstable	XRD	Sr_2MnO_4, $CeCrO_3$, MnO	
$PrMnO_{3-\delta}$	1173	2×10^{-15}	Start of decomposition	EMF	Pr_2O_3, MnO	[45]
$Pr_{0.75}Sr_{0.25}Cr_{0.5}Mn_{0.5}O_{3-\delta}$	1173	5% H_2 - Ar	Unstable	XRD	$(Pr,Sr)_2MnO_4$, Pr_2O_3	[216]
$Pr_{0.7}Ca_{0.3}Cr_{0.4}Mn_{0.6}O_{3-\delta}$	1223	dry 5% H_2 - Ar	Stable	XRD	-	[210]
$ScMnO_{3-\delta}$	1173	1×10^{-6}	Start of decomposition	EMF	Sc_2O_3, Mn_3O_4	[45]

Mizusaki et al. [300] detected a tendency towards saturation of the oxygen overstoichiometry, close to $3+\delta\approx3.2$ for $LaMnO_{3+\delta}$ and decreasing with Sr content. The limit is especially pronounced at temperatures lower than 700 - 800 K and Sr-substituted manganites. The maximum amount of the cation vacancies is evaluated to be 1/9 which corresponds to $LaMnO_{3.19}$ [300]. Alkali-earth doping results in a linear decrease of the maximum oxygen content which the perovskite structure may accommodate; at doping level higher than ~30%, the oxygen excess disappears. These results as well as the corresponding defect model should be

considered with precautions due to hindered mobility of the cation vacancies, especially at lowered temperatures, retarding the equilibration kinetics. This causes a wide scattering between the experimental data; in particular, under $p(O_2)$ = 200 bar at low temperatures formation of $LaMnO_{3.29}$ was reported [322].

Irrespective to the oxygen excess, the transport behavior of manganites is essentially unaffected by $p(O_2)$ variations in oxidative atmospheres [301, 323]. According to [300, 323], an electron from a sublevel belonging to an oxygen atom is suggested to hop into a t_{2g} level of Mn and the hole remaining in the oxygen sublevel is excluded from the transfer mechanism. Another possibility is associated with the fact that the charge transport proceeds along Mn-O-Mn paths and formation of cation vacancies in B-sublattice compensates the increase in hole concentration [322].

In terms of potential anode applications, consideration of the functional properties will be focused primarily on the behavior at low $p(O_2)$. Therefore, the choice of the manganite perovskites will be limited by the materials stable under reducing conditions.

1.3.2. Mixed electronic-ionic conductivity in reducing atmospheres and thermomechanical properties

In the present section, available data on the behavior of manganites under low oxygen pressures will be overviewed, with a brief discussion of selected properties of the materials under atmospheric $p(O_2)$ and their behavior on reduction. More detailed characterization of Mn-rich perovskites under atmospheric conditions can be found elsewhere ([4, 131, 266, 323, 324] and references cited]).

Similar to $LnCrO_{3-\delta}$ perovskites, manganites are electronic conductors with a minor contribution of the oxygen ionic transport. The conductivity behavior of manganites with a moderate (<50%) content of acceptor-type dopants in A-sublattice shows trends typical for p-type electronic conductors. According to the transport model proposed by Mizusaki et al. [300, 323], the electron transfer is promoted by participation of a vacant e_g sublevel in 3*d*-level of $Mn^{\cdot}_{Mn}$. The conductivity of $(La,Sr)MnO_{3\pm\delta}$ in air increases with acceptor content, achieving the maximum for doping level of 20 - 50 mol.% [266, 323, 324]. As discussed in the previous section, no effect of excessive oxygen content on the transport properties has been found. Formation of Mn^{2+} species does not result in a noticeable contribution of n-type conductivity, and the total conductivity is substantially suppressed under reducing conditions, as shown in Figs. 1.3.3 - 1.3.5. Due to substantial oxygen losses and worse stability of manganites doped with alkali-earth cations, the effect of the acceptor content under low $p(O_2)$ conditions is not obvious; examples are shown in Table 1.3.2 and Fig. 1.3.3.

In terms of the total conductivity, manganites seem more preferable in comparison with chromite analogues; the values of the electronic transport of $(La,Sr)MnO_{3\pm\delta}$ may be as high as 50 - 100 S/cm at $p(O_2) = 10^{-18}$ -10^{-15} atm [323]. One should note that the $p(O_2)$ range indicated is located close to the decomposition boundary and the high level of the electronic transport may be attributed to kinetic stabilization of the perovskite phase or a contribution of the decomposition products into the overall conductivity. Therefore, long-term tests are required to assess the stability of the transport characteristics of manganites.

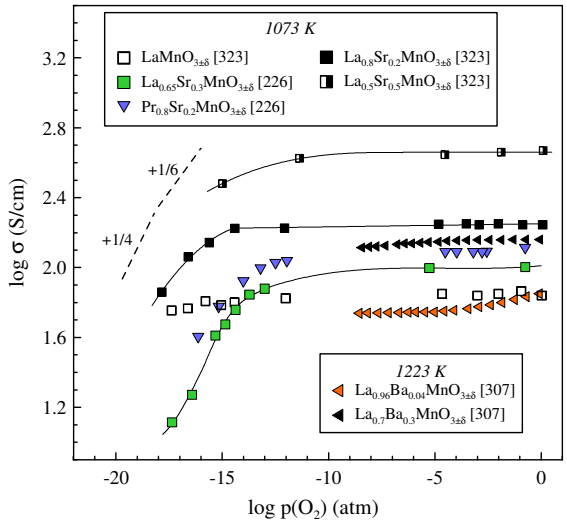

1.3.3. Isothermal $p(O_2)$-dependencies of the total conductivity of selected A-site doped manganites

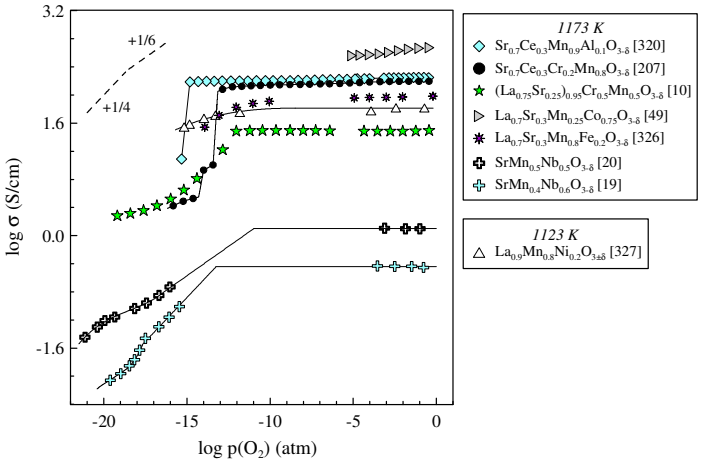

Fig. 1.3.4. Isothermal $p(O_2)$-dependencies of the total conductivity of selected manganites

More reliable seem the data for manganites stabilized with dopants in B-sublattice. As a general rule, increasing the content of stabilizing dopant (Cr, Ti, Sc, Ga, Al etc.) reduces the conductivity in both oxidizing and reducing conditions [16, 315, 319], attributable to a decrease of the concentration of sites available for the electronic transport. No contribution of n-type conductivity has been found for Ti- or Nb-doped manganites [16, 19, 20] which indicates that a preliminary reduction step might be required to activate electron charge carriers, similar to other Ti- or Nb-rich compositions [73, 97, 98, 105].

Table 1.3.2. Total conductivity of selected manganite perovskites in reducing atmospheres

Composition	Oxygen partial pressure (atm) or gas mixture	σ_{873}, S/cm	σ_{1073}, S/cm	Reference
$LaMnO_{3-\delta}$	4.1×10^{-18}		57	[323]
$La_{0.9}Sr_{0.1}MnO_{3-\delta}$	3.3×10^{-19}		81	[323]
$La_{0.8}Sr_{0.2}Mn_{0.3}Al_{0.7}O_{3-\delta}$	4% H_2 - 9.5% H_2O - Ar	3.4×10^{-2}	6.4×10^{-2}	[325]
$La_{0.8}Sr_{0.2}Mn_{0.5}Al_{0.5}O_{3-\delta}$	4% H_2 - 9.5% H_2O - Ar	1.1	1.5	[325]
$La_{0.8}Sr_{0.2}Mn_{0.8}Sc_{0.2}O_{3-\delta}$	wet H_2	3.0	5.1	[315]
$La_{0.8}Sr_{0.2}Mn_{0.8}Sc_{0.2}O_{3-\delta}$	dry H_2	1.6	3.8	[315]
$La_{0.4}Sr_{0.6}Mn_{0.2}Ti_{0.8}O_{3-\delta}$	wet 4% H_2-Ar	1.2×10^{-2}	9.5×10^{-2}	[16]
$La_{0.4}Sr_{0.6}Mn_{0.4}Ti_{0.6}O_{3-\delta}$	wet 4% H_2-Ar	1.9×10^{-2}	8.7×10^{-2}	[16]
$La_{0.4}Sr_{0.6}Mn_{0.6}Ti_{0.4}O_{3-\delta}$	wet 4% H_2-Ar	0.62	1.3	[16]
$La_{0.8}Sr_{0.2}Cr_{0.5}Mn_{0.5}O_{3-\delta}$	wet 5% H_2-Ar	3.2	5.2	[113]
$La_{0.75}Sr_{0.25}Cr_{0.5}Mn_{0.5}O_{3-\delta}$	5% H_2-Ar	0.29	0.93	[8]
$La_{0.7}Sr_{0.3}Cr_{0.5}Mn_{0.5}O_{3-\delta}$	wet 5% H_2-Ar	2.0	4.4	[113]
$La_{0.9}Sr_{0.1}Mn_{0.2}Ga_{0.8}O_{3-\delta}$	H_2	6.1×10^{-2}	0.10	[328]
$La_{0.9}Sr_{0.1}Mn_{0.43}Ga_{0.57}O_{3-\delta}$	H_2	0.26	0.38	[319]
$SrMn_{0.5}Nb_{0.5}O_{3-\delta}$	wet 5% H_2-Ar	1.8×10^{-2}	4.4×10^{-2}	[20]
$SrMn_{0.5}Nb_{0.5}O_{3-\delta}$	5% H_2-Ar	4.7×10^{-3}	1.7×10^{-2}	[105]
$Sr_{0.7}Ce_{0.3}Mn_{0.8}Cr_{0.2}O_{3-\delta}$	6.7×10^{-19}		4.8	[207]
$La_{0.65}Ce_{0.1}Sr_{0.25}Cr_{0.5}Mn_{0.5}O_{3-\delta}$	3% H_2O - H_2	0.20	0.73	[222]
$Pr_{0.75}Sr_{0.25}Cr_{0.5}Mn_{0.5}O_{3-\delta}$	5% H_2-Ar	6.2×10^{-2}	0.28	[216]
$Pr_{0.7}Ca_{0.3}Cr_{0.4}Mn_{0.6}O_{3-\delta}$	wet 5% H_2-Ar	~0.25	~0.70	[210]

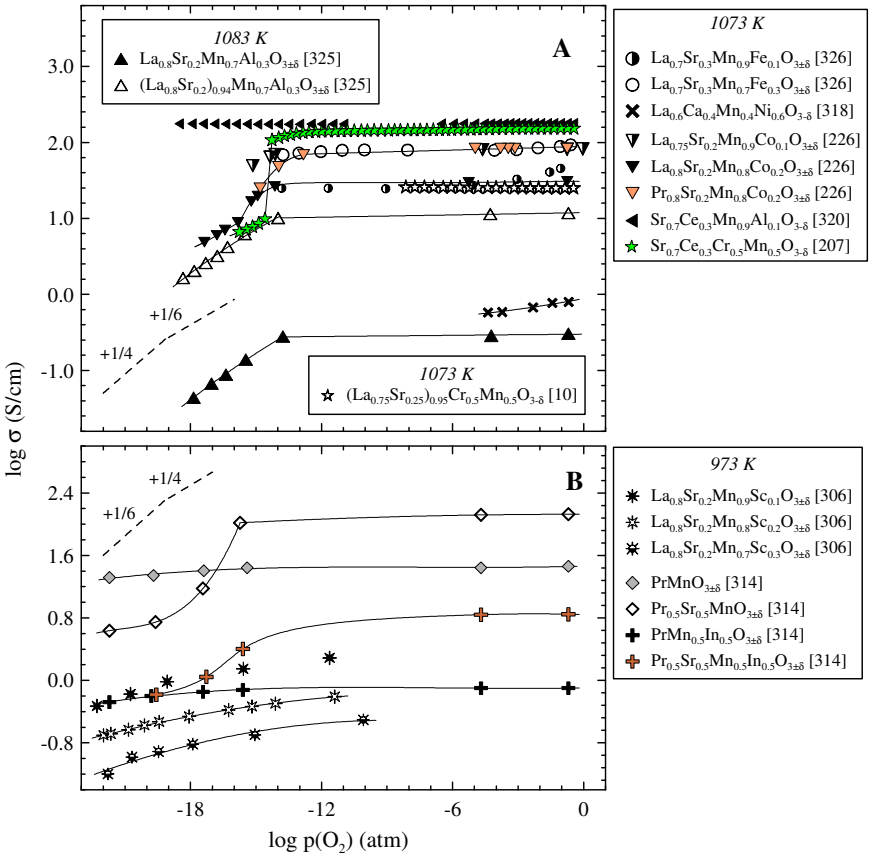

Fig 1.3.5. Isothermal dependencies of the total conductivity of selected manganites vs $p(O_2)$ at 973 - 1223 K

In case of decomposition of stabilized manganites, formation of phases enriched with Al, Ga, Ti, etc. with high resistivity is expected which may be more detrimental in terms of the transport properties and catalytic activity than formation of RP-manganites or MnO. As shown in $p(O_2)$ dependencies of the conductivity (Figs. 1.3.3 -1.3.5), larger values of the electronic transport were exhibited by (La,Sr)$MnO_{3\pm\delta}$ or manganites substituted by Fe, Co or Ni cations, despite their insufficient stability. Therefore, one should find the compromise between the transport properties, stability and other characteristics.

Another limitation of manganite-based anodes, especially those stabilized by cations in B-sublattice relates to their enhanced activation energy at low $p(O_2)$ which amounts to 30 - 50 kJ/mol for perovskites with ~50 mol.% of Mn and increases with the concentration of B-site dopant [16, 20, 319, 325]. This necessitates application of high temperatures to achieve reasonable anode performances, with a risk to promote the interaction between the cell components.

Dilatometric curves of $LaMnO_{3\pm\delta}$ in air exhibit a change in slope on heating at 550 - 600 K, possibly associated with the onset of oxygen losses and resultant transformation of the low-temperature orthorhombic structure into the rhombohedral symmetry [131, 299]. Doping with alkali-earth cation increases the TEC (Table 1.3.3), more pronounced for the dopants with larger ionic radii. Detailed information on the effect of B-site dopant on the thermomechanical properties can be found elsewhere ([131, 238, 266, 324, 326] and references cited). Nevertheless, the thermal expansion of manganite perovskites is quite appropriate for fabrication of the electrode layers, except for $CaMnO_{3-\delta}$- and $SrMnO_{3-\delta}$-based compositions.

Table 1.3.3. Thermal expansion coefficients of selected manganites

Composition	T, K	$p(O_2)$, atm	TEC×10^6, K^{-1}	Reference
$LaMnO_{3\pm\delta}$	320-580	0.21	7.7	[131]
$LaMnO_{3\pm\delta}$	580-1100	0.21	11.8	[131]
$La_{0.8}Ca_{0.2}MnO_{3\pm\delta}$	not indicated	0.21	10.0	[324]
$CaMnO_{3-\delta}$	not indicated	0.21	17.5	[324]
$La_{0.9}Sr_{0.1}MnO_{3\pm\delta}$	300-1270	0.21	9.9	[329]
$La_{0.8}Sr_{0.2}MnO_{3\pm\delta}$	300-1270	0.21	11.2	[329]
$La_{0.7}Sr_{0.3}MnO_{3\pm\delta}$	300-1270	0.21	11.7	[329]
$La_{0.7}Sr_{0.3}MnO_{3\pm\delta}$	300-1220	0.21	12.2	[326]
$La_{0.65}Sr_{0.3}MnO_{3\pm\delta}$	300-1270	0.21	12.3	[227]
$La_{0.5}Sr_{0.5}MnO_{3\pm\delta}$	320-1100	0.21	12.3	[131]
$SrMnO_{3-\delta}$	970-1270	0.21	15.7	[314]
$SrMnO_{3-\delta}$	970-1270	~10^{-5}	17.2	[314]
$La_{0.8}Pb_{0.2}MnO_{3\pm\delta}$	300-1100	0.21	11.9	[131]
$La_{0.8}Sr_{0.2}Mn_{0.9}Mg_{0.1}O_{3\pm\delta}$	320-1170	0.21	11.5	[238]
$La_{0.8}Sr_{0.2}Mn_{0.5}Al_{0.5}O_{3\pm\delta}$	300-1270	0.21	11.5	[317]
$La_{0.8}Sr_{0.2}Mn_{0.9}Ti_{0.1}O_{3\pm\delta}$	320-1170	0.21	12.8	[238]
$La_{0.4}Sr_{0.6}Mn_{0.6}Ti_{0.4}O_{3\pm\delta}$	300-1270	0.21	11.9	[16]
$La_{0.8}Sr_{0.2}Cr_{0.1}Mn_{0.9}O_{3\pm\delta}$	320-1170	0.21	11.6	[238]
$La_{0.75}Sr_{0.25}Cr_{0.5}Mn_{0.5}O_{3\pm\delta}$	800-1230	0.21	10.1	[8]
$La_{0.7}Sr_{0.3}Mn_{0.9}Fe_{0.1}O_{3\pm\delta}$	300-1220	0.21	11.2	[326]
$La_{0.7}Sr_{0.3}Mn_{0.7}Fe_{0.3}O_{3\pm\delta}$	300-1220	0.21	14.2	[326]
$La_{0.65}Sr_{0.3}Mn_{0.8}Co_{0.2}O_{3\pm\delta}$	300-1370	0.21	11.7	[227]
$La_{0.8}Sr_{0.2}Mn_{0.9}Ni_{0.1}O_{3\pm\delta}$	320-1170	0.21	11.5	[227]
$La_{0.6}Sr_{0.4}Mn_{0.8}Ni_{0.2}O_{3\pm\delta}$	350-1100	0.21	12.7	[131]
$SrMn_{0.5}In_{0.5}O_{3-\delta}$	970-1270	0.21	14.1	[314]
$SrMn_{0.5}In_{0.5}O_{3-\delta}$	970-1270	~10^{-5}	14.0	[314]
$Sr_{0.7}Ce_{0.3}MnO_{3-\delta}$	320-1370	0.21	10.1	[330]
$Sr_{0.7}Ce_{0.3}MnO_{3-\delta}$	460-1100	0.21	11.8	[320]
$Sr_{0.7}Ce_{0.3}Mn_{0.9}Al_{0.1}O_{3-\delta}$	370-1090	0.21	10.8	[320]
$Sr_{0.7}Ce_{0.3}Cr_{0.1}Mn_{0.9}O_{3-\delta}$	950-1370	0.21	15.1	[207]
$PrMnO_{3\pm\delta}$	920-1270	0.21	9.8	[314]
$PrMnO_{3\pm\delta}$	920-1270	~10^{-5}	9.6	[314]
$Pr_{0.7}Ca_{0.3}MnO_{3\pm\delta}$	570-1270	0.21	11.9	[207]
$Pr_{0.65}Sr_{0.3}MnO_{3\pm\delta}$	300-1270	0.21	11.6	[227]
$Pr_{0.6}Sr_{0.4}MnO_{3\pm\delta}$	300-1270	0.21	11.6	[329]
$Pr_{0.5}Sr_{0.5}MnO_{3\pm\delta}$	300-1270	0.21	12.2	[329]
$Pr_{0.5}Sr_{0.5}MnO_{3\pm\delta}$	970-1270	0.21	13.9	[314]
$Pr_{0.5}Sr_{0.5}MnO_{3\pm\delta}$	970-1270	~10^{-5}	13.8	[314]
$Pr_{0.8}Sr_{0.2}Mn_{0.8}Co_{0.2}O_{3\pm\delta}$	300-1270	0.21	10.9	[227]
$PrMn_{0.5}In_{0.5}O_{3\pm\delta}$	970-1270	0.21	10.5	[314]
$PrMn_{0.5}In_{0.5}O_{3\pm\delta}$	970-1270	~10^{-5}	10.5	[314]
$Pr_{0.5}Sr_{0.5}Mn_{0.5}In_{0.5}O_{3\pm\delta}$	970-1270	0.21	12.3	[314]
$Pr_{0.5}Sr_{0.5}Mn_{0.5}In_{0.5}O_{3\pm\delta}$	970-1270	~10^{-5}	12.5	[314]
$Nd_{0.5}Ca_{0.5}MnO_{3\pm\delta}$	500-1200	0.21	11.3	[131]
$Nd_{0.8}Sr_{0.2}MnO_{3\pm\delta}$	300-1270	0.21	9.6	[329]
$Nd_{0.65}Sr_{0.3}Mn_{0.8}Co_{0.2}O_{3\pm\delta}$	300-1370	0.21	10.8	[227]
$Sm_{0.7}Sr_{0.3}MnO_{3\pm\delta}$	300-1270	0.21	9.9	[329]
$Sm_{0.6}Sr_{0.4}MnO_{3\pm\delta}$	300-1270	0.21	10.4	[329]
$Gd_{0.7}Sr_{0.3}MnO_{3\pm\delta}$	300-1270	0.21	9.5	[329]
$Gd_{0.8}Sr_{0.2}Mn_{0.8}Co_{0.2}O_{3\pm\delta}$	300-1370	0.21	10.2	[227]
$YbMnO_{3\pm\delta}$	300-1100	0.21	8.6	[131]
$Yb_{0.6}Ca_{0.4}MnO_{3\pm\delta}$	700-1100	0.21	8.0	[131]

More concerns are related with large expansivity of manganite perovskites in reducing atmospheres. As shown in Table 1.3.4, the chemically-induced elongation of most manganites is as high as 0.4 - 0.7%, which significantly exceeds that of chromite analogues, presumably due to increased oxygen losses and generation of large Mn^{2+} species. While the chemical strains in $LaCrO_{3-\delta}$ are essentially negligible within the uncertainties of the experimental technique, $LaMnO_{3\pm\delta}$ on reduction exhibits the expansion up to 0.1%. Consistently, among the perovskites with substantial amount of Mn, the lowest strains were found for $(La,Sr)(Cr,Mn)O_{3-\delta}$-based compositions. In the oxygen-deficient region, the thermomechanical behavior of manganites is governed by relationships similar to those described in the corresponding section for chromites [234, 236]. In some cases, redox cycling of manganites is accompanied by irreversible microstructural changes, resulting in mechanical degradation [16, 317].

The expansion behavior of manganites in oxygen-excessive region is less obvious. Appart from the common factors responsible for the thermomechanical properties of most perovskites, such as variations of the oxidation state of Mn species, generation of cation vacancies leading to an enhancement of the number of unit cells [331-334], the expansivity of manganites may be influenced by slow equilibration, ceramics densification, cracking, etc [16, 238, 335].

The dimensional instability in the high $p(O_2)$ range makes it necessary to suppress the oxygen overstoichiometry. Even if the reduction of oxygen-rich manganites causes a shrinkage which might compensate the subsequent low-$p(O_2)$ expansion, exposure of the material to periodic volume changes may be detrimental for the mechanical integrity of the anode layers. While chromites show nearly linear relationship between the amount of alkali-earth dopant and chemical strains on reduction, for manganite perovskites the presence of moderate quantities of acceptor dopants is beneficial which, however, should be compromised by stability and dimensional behavior at low $p(O_2)$.

Table 1.3.4. Chemical expansion of manganites determined by dilatometry

Composition	T, K	$p(O_2)_{initial}$, atm	$p(O_2)_{final}$ (atm) or gas mixture	$\Delta L/L_{initial}$, %	Reference
$LaMnO_{3\pm\delta}$	1373 1273	0.21	1.0×10^{-12} 3.1×10^{-14}	0.081 0.044	[234]
$LaMnO_{3\pm\delta}$	1273 1073	0.21	2.5×10^{-14} 1.3×10^{-20}	0.041 0.10	[236]
$LaMnO_{3\pm\delta}$	1273 1273	0.21 10^{-4}	10^{-4} 10^{-2}	-0.35 0.11	[334]
$La_{0.8}Sr_{0.2}Mn_{0.5}Al_{0.5}O_{3\pm\delta}$	1273 1123	0.21	4% H_2-Ar 3% H_2O-4% H_2-Ar	0.68 0.52	[317]
$La_{0.4}Sr_{0.6}Mn_{0.6}Ti_{0.4}O_{3\pm\delta}$	1090	0.21	wet 4% H_2-Ar	0.61	[16]
$La_4Sr_8Ti_{11}MnO_{38-\delta}$	1123 1023	0.21	5% H_2-Ar	0.07 0.05	[335]
$La_4Sr_8Ti_{11}Mn_{0.5}Ga_{0.5}O_{38-\delta}$	1123 1023	0.21	5% H_2-Ar	0.18 0.13	[335]
$(La_{0.75}S_{0.25})_{0.95}Cr_{0.5}Mn_{0.5}O_{3-\delta}$	1223 1023	0.21	3×10^{-13} 6×10^{-18}	0.20 0.22	[10]
$Sr_{0.7}Ce_{0.3}Mn_{0..9}Cr_{0.1}O_{3-\delta}$	1223 1023	0.21	2.3×10^{-11} 4.4×10^{-14}	0.68 0.65	[207]
$Sr_{0.7}Ce_{0.3}Mn_{0..5}Cr_{0.5}O_{3-\delta}$	1223 1023	0.21	2.3×10^{-11} 4.4×10^{-14}	0.47 0.45	[207]

Oxygen ionic conductivity in manganites in oxygen deficient region shows the features typical for most perovskites. The ionic transfer proceeds via vacancy mechanism, and the diffusivity may to some extent be enhanced by formation of oxygen vacancies generated by introduction of alkali-earth cations or reduction, as shown in Tables 1.3.5 - 1.3.6. However, under low $p(O_2)$ conditions, the effect of acceptor content is weak [305]. Generation of A-site deficiency basically has no substantial effect on the ionic transport which may indicate the defect association or that the charge compensation in the latter case is realized by Mn oxidation rather than by the formation of oxygen vacancies [336].

A correlation between the chemical diffusion and surface exchange kinetics for $(La,Sr)(Mn,Co)O_{3-\delta}$ perovskites was found [337, 338] indicating that the oxygen exchange processes are governed by the availability of the oxygen vacancies on the surface. Although the oxygen ionic transport in manganites is higher in comparison with chromite analogues, this level is still insufficient to expect a substantial promotion of the electrochemical processes; for example, the ionic conductivity of $La_{1-x}Sr_xMnO_{3-\delta}$ (x = 0.05 - 0.2) is as low as 10^{-7}-10^{-6} S/cm at 1273 K under oxidizing conditions. Similar to chromites, the diffusion may be contributed by oxygen transport along the grain boundaries [336, 339].

The values of the activation energy of the chemical or oxygen vacancy diffusion in manganites are generally larger (200 - 300 kJ/mol) in comparison with those for chromite analogues. Such a difference is attributed to high enthalpies of the vacancy formation in manganites [338], variations in Mn-O bond strength owing to variations in Mn oxidation state [336], or defect interactions [305, 327, 336, 340]. The dominant contribution of the enthalpy of oxygen vacancy formation into the activation energy was confirmed by increasing activation energy with Sr-doping [336, 338], while facilitation of oxygen release by introduction of Fe or Co results in lower activation energies [338, 339].

Table 1.3.5. Isotopic diffusion and surface exchange coefficients of manganites

Composition	T, K	$p(O_2)$, atm	D*, cm^2/s	k*, cm/s	E_a of D*, kJ/mol	Reference
$LaMnO_{3\pm\delta}$	979 1169	1.0 1.0	8.7×10^{-16} 1.2×10^{-13}	2.6×10^{-9} 4.8×10^{-8}	240	[336]
$La_{0.92}MnO_{3\pm\delta}$ (annealed at 1273 K)	1073	~0.1	2.5×10^{-13}	7.5×10^{-8}		[341]
$La_{0.9}MnO_{3\pm\delta}$	1170	1.0	2.0×10^{-13}	7.7×10^{-9}	294	[336]
$La_{0.95}Sr_{0.05}MnO_{3\pm\delta}$	1173	0.13	2.4×10^{-13}		260	[342]
$La_{0.9}Sr_{0.1}MnO_{3\pm\delta}$	1273	0.13	4.8×10^{-12}		280	[342]
$La_{0.8}Sr_{0.2}MnO_{3\pm\delta}$	1173	0.13	1.3×10^{-12}		300	[342]
$La_{0.8}Sr_{0.2}MnO_{3\pm\delta}$	973 1173 1273	~1.0 ~1.0 ~1.0	3.1×10^{-16} 1.6×10^{-13} 6.6×10^{-13}	1.1×10^{-9} 7.3×10^{-9} 1.1×10^{-7}	270	[337, 338]
$La_{0.5}Sr_{0.5}MnO_{3\pm\delta}$	973 1173 1273	1.0 1.0 1.0	1.4×10^{-15} 9.2×10^{-13} 1.8×10^{-11}	2.7×10^{-9} 5.4×10^{-8} 1.3×10^{-6}	360	[338]
$(La_{0.75}Sr_{0.25})_{0.95}Cr_{0.5}Mn_{0.5}O_{3-\delta}$	989 1185 1168	0.2 0.2 2.0×10^{-17}	7.0×10^{-11} 1.1×10^{-10} 1.9×10^{-8}		80 180	[279]
$La_{0.8}Sr_{0.2}Mn_{0.8}Co_{0.2}O_{3\pm\delta}$	1173	1.0	4.1×10^{-13}	1.3×10^{-8}	340	[338]
$La_{0.5}Sr_{0.5}Mn_{0.8}Co_{0.2}O_{3\pm\delta}$	1173	1.0	2.1×10^{-11}	2.8×10^{-8}	270	[338]
$La_{0.8}Sr_{0.2}Mn_{0.5}Co_{0.5}O_{3\pm\delta}$	1173	1.0	5.0×10^{-12}	1.2×10^{-7}	260	[338]

Table 1.3.6. Oxygen ionic conductivity and chemical diffusion coefficients of manganites

Composition	T, K	$p(O_2)$, atm	D_{chem}, cm^2/s	σ_O, S/cm	Method	Reference
$La_{0.95}Sr_{0.05}MnO_{3\pm\delta}$	1273	4.0×10^{-14}	3.1×10^{-4}		Conductivity relaxation	[305]
$La_{0.9}Sr_{0.1}MnO_{3\pm\delta}$	1273	1.0×10^{-14}	2.0×10^{-4}		Conductivity relaxation	[305]
$La_{0.85}Sr_{0.15}MnO_{3\pm\delta}$	1273	2.5×10^{-15}	2.6×10^{-4}		Conductivity relaxation	[305]
$La_{0.8}Sr_{0.2}MnO_{3\pm\delta}$	1173	high $p(O_2)$	6.4×10^{-6} *		Conductivity relaxation	[305]
$La_{0.8}Sr_{0.2}MnO_{3\pm\delta}$	1173 1273	1.5×10^{-14} 4.2×10^{-14}	2.1×10^{-5} 1.7×10^{-4}		Conductivity relaxation	[305]
$La_{0.7}Sr_{0.3}MnO_{3\pm\delta}$	1073	0.21		6.3×10^{-4}	Electron-blocking	[343]
$La_{0.65}Sr_{0.3}MnO_{3\pm\delta}$	1073	gradient air/Ar		1.7×10^{-4}	Oxygen permeation**	[226]
$La_{0.75}Sr_{0.2}Mn_{0.5}Co_{0.5}O_{3\pm\delta}$	1073	gradient air/Ar		3.1×10^{-5}	Oxygen permeation**	[226]
$Pr_{0.65}Sr_{0.3}MnO_{3\pm\delta}$	1073	gradient air/Ar		3.4×10^{-4}	Oxygen permeation**	[226]
$Pr_{0.8}Sr_{0.2}Mn_{0.8}Co_{0.2}O_{3\pm\delta}$	1073	gradient air/Ar		3×10^{-5}	Oxygen permeation**	[226]
$Pr_{0.7}Sr_{0.3}Mn_{0.8}Co_{0.2}O_{3\pm\delta}$	1073	gradient air/Ar		4.4×10^{-5}	Oxygen permeation**	[226]
$Sr_{0.7}Ce_{0.3}Mn_{0.9}Al_{0.1}O_{3-\delta}$	1173 1248	2.1×10^{-2} 2.1×10^{-2}		4.5×10^{-4} 2.2×10^{-3}	Oxygen permeation	[320]
$Sr_{0.7}Ce_{0.3}Cr_{0.2}Mn_{0.8}O_{3-\delta}$	1248	1.7×10^{-2}		4.6×10^{-4}	Oxygen permeation	[207]

** - extrapolated to high-$p(O_2)$ region where enhancement factor is equal to 1*
*** - surface limitations are neglected, σ_O is considered $p(O_2)$-independent*

The ionic transport characteristics may be improved by introduction of cations with stable oxidation state (basically +3) in B-sublattice [320, 328]; in combination with better chemical stability, this route seems promising for anode applications, although one should account for the decrease in the electronic conductivity. The presence of reducible substituents in B-sublattice is less preferable, since apart from the worse stability towards reduction, the defect interactions retard the ionic mobility and surface exchange [131, 338].

Under oxidizing conditions, the behavior Ln- and Mn-enriched perovskites is strongly influenced by the presence of cation vacancies. As discusses above, the equilibration in this domain of conditions is slow, and the experimental results are affected by material preparation route and experimental procedure. Therefore, direct comparison of the experimental data under high $p(O_2)$ is complicated (Table 1.3.5).

1.3.3. Electrochemical behavior in reducing atmospheres

Comparing the polarization resistance and power densities of electrochemical cells based on manganite anodes (Fig. 1.3.6 and Table 1.3.5) with those for chromite analogues, one may notice a somewhat superior activity of the manganites. In particular, while non-modified $La_{0.85}Sr_{0.15}CrO_{3-\delta}$ anode showed

extremely low electrode performance [17], a satisfactory anode activity was detected for $La_{1-x}Sr_xMnO_{3-\delta}$ anodes, increasing with Sr content up to 630 mW/cm^2 for x = 0.5 at 1273 K in 3% H_2O - H_2 [95]. However, no compositional or microstructural modifications or anode current collectors were indicated in both cases which complicates the comparison. Higher Sr content in manganites allows to reduce Ohmic and polarization losses; both contributions to the overall resistance show a correlation with the electronic conductivity of the perovskites in oxidative atmospheres indicating that the phase decomposition of $(La,Sr)MnO_{3-\delta}$ expected under anode conditions might be hindered by kinetic reasons. The electrodes are tolerant towards one redox cycle, although more severe stability tests are necessary, especially accounting for the large chemical expansivity of the materials.

For Al, Sc, Ti, Ga-doped manganites, the performance is basically better for Mn-enriched electrode compositions. The preferability of Mn-rich perovskites as well as higher activity of manganites over other perovskite anodes such as chromites and titanates may be associated with the following factors:

1. High Mn content ensures enhanced electronic conductivity (compare the data in Table 1.3.2 and Table 1.2.1) and promotes higher oxygen diffusion under reducing conditions, although the presence of moderate amounts of 3-valent cations in B-sublattice is also favorable for the ionic transport [320, 328]. The sufficient level of the electronic and ionic conductivity provides a reasonable rate of supply/removal of electrons, oxygen vacancies to/from the electrochemically active sites on the electrode surface or at the TPB.

2. Mn cations are stable in multiple oxidation states (+2, +3 and +4), as discussed in Chapter 1.3.1 [234, 300, 324], and may adopt various oxygen coordination (tetrahedral, square pyramidal, octahedral) (examples may be found in [249, 344-346] and references cited). This favors stabilization of numerous forms of Mn-containing species participating in the electrochemical processes and allows to maintain catalytically-active species on the anode surface. By far, the information on the role of Mn species in oxidation processes is scarce [258, 279, 347, 348] which does not allow to elucidate a certain mechanism of the electrochemical processes over manganite anodes.

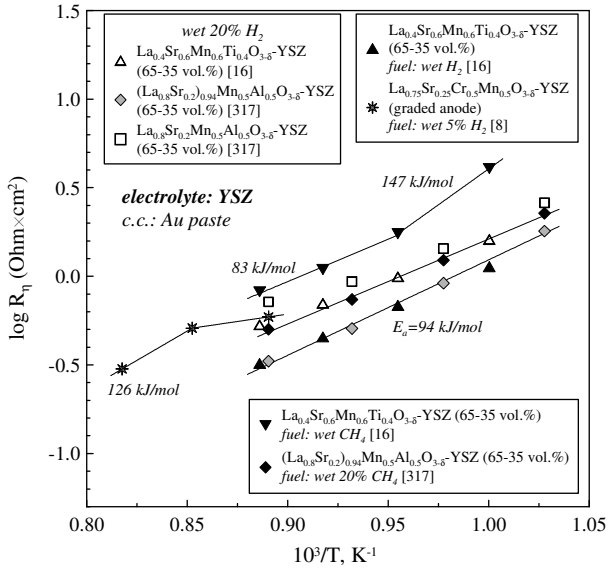

Fig. 1.3.6. Temperature dependencies of polarization resistance of manganite-based anodes under zero current

Table 1.3.7. Power density of cells with manganite-based anodes

Anode	Electrolyte* (thickness, μm)	Cathode*	Fuel	T, K	P_{max}, mW/cm^2	Reference
$LaMnO_{3-\delta}$ ***c.c.: not indicated***	LSGMNi (300)	LBCo	3% H_2O - H_2	1273	60	[95]
$La_{0.8}Sr_{0.2}MnO_{3-\delta}$ ***c.c.: not indicated***				1273	240	
$La_{0.5}Sr_{0.5}MnO_{3-\delta}$ ***c.c.: not indicated***				1173 1273	450 630	
$La_{0.4}Sr_{0.6}MnO_{3-\delta}$ ***c.c.: not indicated***				1273	320	
$SrMnO_{3-\delta}$ ***c.c.: not indicated***				1273	20	
$La_{0.8}Sr_{0.2}Mn_{0.9}Sc_{0.1}O_{3-\delta}$ impreg. into 8YSZ (40-60 wt.%) ***c.c.: Ag paste***	8YSZ (85)	LSF - 8YSZ	3% H_2O - H_2	973	220	[306]
$La_{0.8}Sr_{0.2}Mn_{0.9}Sc_{0.1}O_{3-\delta}$ -CeO_2-Pd impreg. into 8YSZ (40-10-1-49 wt.%) ***c.c.: Ag paste***	8YSZ (85)	LSF - 8YSZ	3% H_2O - H2 3% H_2O - CH_4	973 1073 973 1073	400 700 340 450	[306]
$La_{0.8}Sr_{0.2}Mn_{0.8}Sc_{0.2}O_{3-\delta}$ ***c.c.: Au***	ScSZ (200)	Symmetr.	3% H_2O - H_2 CO	1173 1173	170 110	[316]
$La_{0.8}Sr_{0.2}Mn_{0.8}Sc_{0.2}O_{3-\delta}$ ***c.c.: Au paste***	ScSZ (300)	Symmetr.	3% H_2O - H_2 3% H_2O - CH_4	1123 1123	220 100	[315]
$La_{0.8}Sr_{0.2}Mn_{0.8}Sc_{0.2}O_{3-\delta}$ -CeO_2-Pd impreg. into YSZ (40-10-1-49 wt.%) ***c.c.: Ag paste***	8YSZ (85)	LSF - 8YSZ	3% H_2O - H_2 3% H_2O - CH_4	973 1073 1073	350 550 420	[306]
$La_{0.8}Sr_{0.2}Mn_{0.7}Sc_{0.3}O_{3-\delta}$ -CeO_2-Pd impreg. into YSZ (40-10-1-49 wt.%) ***c.c.: Ag paste***	8YSZ (85)	LSF - 8YSZ	3% H_2O - H_2	1073	280	[306]
$La_{0.4}Sr_{0.6}Mn_{0.6}Ti_{0.4}O_{3-\delta}$ -8YSZ (50-50 wt.%) ***c.c.: Au paste***	8YSZ (200)	LSM - 8YSZ	wet H_2 wet CH_4	1081 1129 1129	250** 360** 50**	[16]
$La_{0.4}Sr_{0.6}Mn_{0.2}Ti_{0.8}O_{3-\delta}$ -CeO_2-Pd impreg. into 8YSZ (50-10-1-39 wt.%) ***c.c.: Ag paste***	8YSZ (50)	LSM82 - 8YSZ	3% H_2O - H_2	1123	210	[350]
$La_{0.9}S_{0.1}Mn_{0.8}Ga_{0.2}O_{3-\delta}$ ***c.c.: porous Pt***	LSGM (1650)	LSCoGa	2% H_2O - H_2	1073 1123	60 90	[328]
$La_{0.9}S_{0.1}Mn_{0.8}Ga_{0.2}O_{3-\delta}$ ***c.c.: not indicated***	LSGM (800)	LSCF	3% H_2O - H_2	1073	110	[319]
$La_{0.9}S_{0.1}Mn_{0.57}Ga_{0.43}O_{3-\delta}$ ***c.c.: not indicated***	LSGM (800)	LSCF	3% H_2O - H_2	1073	180	[319]
CGO10-Ni (66-34 wt.%) on $La_{0.9}Mn_{0.8}Ni_{0.2}O_{3-\delta}$ ***c.c.: Ni gauze***	3YSZ (90)	LSM -8YSZ (graded)	H_2O - H_2 (50 - 50) %	1123	170**	[327]
$Pr_{0.6}Sr_{0.4}MnO_{3-\delta}$ ***c.c.: not indicated***	LSGMNi (300)	LBCo	3% H_2O - H_2	1273	270	[95]

**The results were obtained using the following electrolytes and cathodes: $Zr_{0.94}Y_{0.06}O_{2-\delta}$ [327], $Zr_{0.84}Y_{0.16}O_{2-\delta}$ [16, 306, 350], $Zr_{0.82}Sc_{0.18}O_{2-\delta}$ [315, 316], $La_{0.9}Sr_{0.1}Ga_{0.8}Mg_{0.2}O_{3-\delta}$ [319, 328], $La_{0.8}Sr_{0.2}Ga_{0.8}Mg_{0.15}Ni_{0.05}O_{3-\delta}$ [95]; $La_{0.4}Ba_{0.6}CoO_{3-\delta}$ [95], $La_{0.8}Sr_{0.2}FeO_{3-\delta}$ infiltrated into 8YSZ [305], $La_{0.8}Sr_{0.2}Mn_{0.8}Sc_{0.2}O_{3-\delta}$ [315, 316], $La_{0.65}Sr_{0.3}MnO_{3-\delta}$ -8YSZ [16, 327], $La_{0.8}Sr_{0.2}MnO_{3-\delta}$ impregnated into 8YSZ [350], $La_{0.9}Sr_{0.1}Co_{0.8}Ga_{0.2}O_{3-\delta}$ [328], $La_{0.6}Sr_{0.4}Co_{0.2}Fe_{0.8}O_{3-\delta}$ [319]*

*** Under cell voltage of 0.7 V*

3. High solubility of Mn in zirconia provides good adhesion of the manganite electrode layers to ZrO_2-based electrolytes which may contribute the performance due to microstructural factors, especially in YSZ-containing composites [306, 349-352].

In accordance with the factors listed above, promising power densities were produced for $La_{0.8}Sr_{0.2}Mn_{0.9}Sc_{0.1}O_{3-\delta}$ perovskite anode activated by CeO_2, Ag, Pd and impregnated into YSZ scaffolds (~700 mW/cm^2 in 3% H_2O - H_2 and 450 mW/cm^2 in 3% H_2O - CH_4 at 1073 K) [306]. The power density as high as ~360 mW/cm^2 at 1129 K in wet H_2 was yielded for $La_{0.4}Sr_{0.6}Mn_{0.6}Ti_{0.4}O_{3-\delta}$ - YSZ (50 - 50 wt.%) with YSZ electrolyte of 200 μm thickness. This value of the power density is not a limit for this cell, since it corresponds to the voltage of 0.7 V. The result is, however, interfered by the presence of Au paste. The anode polarization resistance under given conditions is ~0.3 Ohm×cm^2 [16]; a close value was obtained for A-deficient $(La_{0.8}Sr_{0.2})_{0.94}Mn_{0.5}Al_{0.5}O_{3-\delta}$ - YSZ (65 - 35 vol.%) composite anode covered with Au paste [317]. The level of the polarization resistances observable for manganite anodes studied in the present section is somewhat higher in comparison with Cr-substituted manganites. One should note that the latter group of compositions has been studied more extensively and more compositional and microstructural improvements have been elaborated.

The insufficient stability of manganites, large chemical expansion and strong reactivity with electrolytes make the problem of long-term performance critical for their practical applications as anodes. While the anode $La_{0.4}Sr_{0.6}Mn_{0.6}Ti_{0.4}O_{3-\delta}$ - YSZ showed only a slight initial increase in polarization and Ohmic resistance in H_2 at 1068 K (~10% per 200 hours) [16], the degradation rate for $La_{0.8}Sr_{0.2}Mn_{0.5}Al_{0.5}O_{3-\delta}$ - YSZ under similar condition was more than 100% in terms of the overvoltage for 100 hours of testing. While the Ohmic drop might be recovered by redox cycling, the increase in the polarization resistance was irreversible, apparently due to mechanical degradation [317].

$La_{0.8}Sr_{0.2}Mn_{0.8}Sc_{0.2}O_{3-\delta}$ exhibited a rapid degradation of performance (70%/3 hours) in CO under open circuit voltage (OCV) while oxidation of the anode induced by anodic polarization or addition of CO_2 into the fuel allowed to suppress the drop of the power density indicating that the material is close to the phase boundary under anode environments [316]. However, similar anode material showed a satisfactory stability towards fuel cell tests in CH_4 [315], possibly due to inhibited methane reforming over the manganite which enables to preserve the local oxygen pressure high enough to stabilize the perovskite.

Summarizing the results observable on manganite-based anodes one should note that the dominant part of the electrodes studied contains large amounts of additives, in particular a layer of metal-containing paste. These modifications do not allow to evaluate the applicability of manganite-based anodes in industrial scale. One should take into account that high-temperature utilization of manganites may be detrimental in terms of poor chemical stability, drop in the electronic conductivity, microstructural changes and mechanical degradation of the electrode layers. Therefore, for industrial application of $(La,A)MnO_{3-\delta}$-based anodes without expensive modifications one should achieve reasonable performances at comparatively low temperatures (950 - 1100 K). Reviewing the available data on manganites, no proper anode composition has been found by far. At the same time, the attractive characteristics of manganite perovskites offer many possibilities to improve both activity and stability by compositional modifications.

1.4. La(Cr,Mn)$O_{3-\delta}$-based electrode materials

A brief description of (Ln,A)(Cr,Mn)$O_{3-\delta}$-based materials (LnACM) and corresponding anodes has been given in the sections devoted to chromites and manganites. One of the most widely studied representatives is $La_{0.75}Sr_{0.25}Cr_{0.5}Mn_{0.5}O_{3-\delta}$, since this material possesses a good combination of the chemical and thermomechanical properties, electronic transport and catalytic activity. On the other hand, further optimization of the composition can be achieved. This material and its derivatives are characterized by a structural transition on heating or reduction which, however, has no detrimental effects on the transport or thermomechanical properties [113, 177]. In reducing atmospheres, small quantities of MnO and Ln_2O_3 or RP-phases may be separated [207, 216, 222], while Ruiz-Morales et al. reported a possibility of formation of ordered structures, which, however, might also relate to the RP-manganites [353]. While under oxidizing conditions the conductivity increases on A-site doping (Ca>Sr>Ba) [144] and with Mn content [210], in anodic atmospheres this trend depends on the facility and kinetics of the oxygen losses, as shown in Fig. 1.2.4 and Table 1.2.1. The conductivity of LnACM materials at low $p(O_2)$ varies in the range 0.2 - 5 S/cm, close to the minimum acceptable for the anode application.

The thermal expansion coefficients of LnACM are close or slightly higher than those of SOFC electrolytes or interconnects. The chemical expansivity for Ln = La is 0.2 - 0.3 % at 1073 - 1273 K, $p(O_2) = 10^{-18}$ - 10^{-13} atm [10, 235]. Replacement of La by Ce increases the expansion up to 0.45 - 0.7% on mild reduction and causes the phase decomposition at $p(O_2)$ lower than 10^{-14} - 10^{-11} atm [207]. Due to variations of ionic radii of the B-cations, different reducibility and electron exchange between Cr and Mn species and Mn^{3+} disproportionation, the effect of Mn:Cr ratio at various cation compositions on the expansion may be opposite [10, 207, 235]. Despite the moderate expansivity, poor adhesion of $La_{0.75}Sr_{0.25}Cr_{0.5}Mn_{0.5}O_{3-\delta}$ to YSZ was reported [354]; this drawback can be solved by fabrication of composites.

In comparison with Cr-rich perovskites, the ionic transport and surface kinetics are substantially enhanced for LnACM, especially under reducing conditions [10, 258]. This is attributed to higher tendency of Mn-containing perovskites towards formation of oxygen vacancies [8]. The presence of Mn is expected to promote participation of bulk oxygen in oxidation processes [347]. At the same time, the ionic transport is obviously insufficient for adequate performance; in particular, this is reflected by reducing the polarization for composites of LnACM with ionic conductors (Figs. 1.4.1 - 1.4.2, Table 1.4.1)

$La_{0.75}Sr_{0.25}Cr_{0.5}Mn_{0.5}O_{3-\delta}$ and $Pr_{0.7}Ca_{0.3}(Cr,Mn)O_{3-\delta}$ are chemically compatible with YSZ at 1573 and 1473 K, respectively [8, 210, 277]. Despite the decreased phase stability, the presence of Ce ensures better chemical compatibility with YSZ in air, while in Ar or H_2, formation of $SrZrO_3$ and strong interdiffusion were observed [222]. In contact of $La_{0.75}Sr_{0.25}Cr_{0.5}Mn_{0.5}O_{3-\delta}$ with LSGM, the interaction was observed at 1623 - 1673 K [279, 280]. No interaction or interdiffusion between $La_{0.75}Sr_{0.25}Cr_{0.5}Mn_{0.5}O_{3-\delta}$ and Co-substituted LSGM was detected up to 1573 K [355]; the anode material exhibited also the chemical compatibility with Ni at 1673 K which facilitates the fabrication of composites.

On the other hand, Mn possesses enhanced diffusivity [324, 356], and analogously with manganite-based electrodes, application of LnACM necessitates application of buffer layers between the electrode and electrolyte. The diffusivity of Mn is promoted by A-cation deficiency; however, one should take into account

that for cation-stoichiometric perovskites, depletion with Mn induces phase decomposition with formation of phases enriched with A-cations. Since electrodes based on cation-stoichiometric perovskites basically require elevated preparation temperatures [357] and are more susceptible towards the high-temperature interdiffusion or decomposition, application of A-deficient perovskite electrodes may be beneficial.

One of advantages of LnACM-based compositions is some catalytic activity towards oxidation processes; this makes the materials attractive as a component of catalysts or anodes in hydrocarbon fuels. In particular, higher content of $La_{0.75}Sr_{0.25}Cr_{0.5}Mn_{0.5}O_{3-\delta}$ in composite with CGO increases the open circuit voltage of a cell with CH_4-containing atmosphere on the anode side, indicating an enhanced conversion over $La_{0.75}Sr_{0.25}Cr_{0.5}Mn_{0.5}O_{3-\delta}$ [284]. As suggested in [348, 358], Mn-doping into LnACM promotes the oxidation processes which proceed via Mars-van-Krevelen mechanism where the bulk oxygen ions participate in the oxidation; the activity is higher for Mn-enriched perovskites [347]. The effect of Mn species originates from the capability of Mn^{3+} species to accept electrons in chemisorption step producing low-coordinated Mn^{2+} and release CO_2 and H_2O [218]. In H_2, the oxidation process is considered to be limited by the chemisorption step rather than by diffusion of O^{2-} and subsequent oxidation of Mn^{2+}. Formation of Mn^{2+} reduces the electronic conduction and decreases the number of available sites for chemisorption [218]. This behaviour is consistent with observation of McIntosh et al [347] where formation of oxygen vacancies reduces CH_4 conversion over $La_{0.75}Sr_{0.25}Cr_{0.5}Mn_{0.5}O_{3-\delta}$ and increases the fraction of CO in the product mixture. The material promotes essentially partial oxidation and dry reforming, while the rate of the wet reforming is slow.

Whatever the oxidation mechanism, the catalytic activity of pure LnACM perovskites is insufficient for utilizing these materials as individual anode [348]; in combination with the disadvantages caused by the transport properties, compositional modifications of the electrodes are required. Positive effects of additions of Pd, Rh, Fe, Ni or ceria have been demonstrated [10, 14, 359, 360], possibly due to improved catalytic activity. In particular, surface modification of the perovskite electrodes with Pd was shown to improve the activity in CH_4 and ethanol, without significant effect on the performance in H_2 [361-363].

At the same time, the most important factor determining the performance of LnACM anodes is insufficient electronic conductivity. In particular, for non-modified $La_{0.7}A_{0.3}Cr_{0.5}Mn_{0.5}O_{3-\delta}$ anodes, the performance increased in the order Ba<Sr<Ca, consistently with the electronic conduction and stability of the materials [144]. A similar correlation was observed for $LaCr_{0.5}Mn_{0.5}O_{3-\delta}$ and $La_{0.8}Sr_{0.2}Cr_{0.5}Mn_{0.5}O_{3-\delta}$ anodes, where the former composition possesses higher electronic conduction and catalytic activity at low $p(O_2)$ [171]. Analogously, increasing Mn content in $Pr_{0.7}Ca_{0.3}Cr_{1-x}Mn_xO_{3-\delta}$ from x = 0.2 to 0.8 leads to ~1 order enhancement of the conductivity and anode performance [210]. Apart from increasing the polarization resistance, the insufficient conductivity leads to higher Ohmic drops [171]. On the other hand, the anodic polarization may induce partial oxidation of the perovskite resulting in higher electronic transport.

The role of the electronic conductivity of LnACM in the electrochemical processes is also confirmed by positive effects of addition of metallic phase or optimization of the current collector on the polarization. In particular, an improvement of the anode performance by impregnation of $La_{0.75}Sr_{0.25}Cr_{0.5}Mn_{0.5}O_{3-\delta}$ with Cu was demonstrated in [218, 361, 353, 364]. Since contribution of Cu into the catalytic activity is suggested to be insignificant [353, 364, 365], the smaller polarization losses are attributed to the improved electronic transport.

Table 1.4.1. Power densities of cells with (Ln,A)(Cr,Mn)$O_{3-\delta}$ anodes

Anode	Electrolyte (thickness, μm)	Cathode	Fuel	T, K	P_{max}, mW/cm^2	Reference
$La_{0.82}Sr_{0.18}Cr_{0.44}Mn_{0.56}O_{3-\delta}$ ***c.c.: Au paint***	8YSZ (300)	Pt	H_2	1223	75	[212]
			0.5% H_2S - CH_4	1223	120	
$La_{0.75}Sr_{0.25}Cr_{0.5}Mn_{0.5}O_{3-\delta}$ ***c.c.: Au ink***	LSGM (600)	PrCM	wet H_2	1123	160	[368]
$La_{0.75}Sr_{0.25}Cr_{0.5}Mn_{0.5}O_{3-\delta}$ ***c.c.: Pt paste***	LSGM (1500)	BSCF	wet 5% H_2 - Ar	1073	120	[9]
$La_{0.75}Sr_{0.25}Cr_{0.5}Mn_{0.5}O_{3-\delta}$ ***c.c.: Pt mesh***	LSGM (250)	SCF	dry H_2	1073	170	[218]
			dry CH_4	1123	250	
$La_{0.75}Sr_{0.25}Cr_{0.5}Mn_{0.5}O_{3-\delta}$ ***c.c.: Au paste***	LSGM (2000)	LSM	H_2 - H_2O (97 - 3%)	1073	570	[279]
$La_{0.75}Sr_{0.25}Cr_{0.5}Mn_{0.5}O_{3-\delta}$ ***c.c.: Pt mesh***	8YSZ (250)	LSM	H_2	1223	370	[219]
				1073	110	
$La_{0.75}Sr_{0.25}Cr_{0.5}Mn_{0.5}O_{3-\delta}$ - YSZ (graded) ***c.c.: Au paste***	YSZ (200)	Symmetrical	H_2 - H_2O (97 - 3%)	1173	300	[283]
			wet 5% H_2	1173	170	
			wet CH_4	1173	230	
$La_{0.75}Sr_{0.25}Cr_{0.5}Mn_{0.5}O_{3-\delta}$ -YSZ (graded) ***c.c.: Au paste***	YSZ (300)	LSM	wet 5% H_2 - Ar	1173	290	[8]
			wet H_2	1173	470	
			wet CH_4	1173	200	
$La_{0.82}Sr_{0.18}Cr_{0.44}Mn_{0.56}O_{3-\delta}$ - CGO20 (50-50 wt.%) ***c.c.: Au paint***	8YSZ (300)	Pt	H_2	1123	180	[212]
			CH_4	1123	15	
			0.5% H_2S - CH_4	1123	120	
$La_{0.75}Sr_{0.25}Cr_{0.5}Mn_{0.5}O_{3-\delta}$ - CGO20 - YSZ (50 - 25 - 25 wt.%), ***c.c.: Pt-based ink***	YSZ (180)	Symmetrical	100% H_2	1223	400	[370]
			100% CH_4	1223	130	
$La_{0.75}Sr_{0.25}Cr_{0.5}Mn_{0.5}O_{3-\delta}$ - YSZ (50 - 50 wt. %), impreg. with CGO20; ***c.c.: Pt mesh***	8YSZ (~50)	Symmetrical	H_2 - H_2O (97 - 3%)	1123	270	[277]
				1073	250	
$La_{0.75}Sr_{0.25}Cr_{0.5}Mn_{0.5}O_{3-\delta}$ impreg. with Pt and Cu ***c.c.: Pt mesh***	LSGM (250)	SCF	dry H_2	1123	850	[218]
				1073	520	
			dry CH_4	1073	450	
$La_{0.75}Sr_{0.25}Cr_{0.5}Mn_{0.5}O_{3-\delta}$ - Cu - YSZ (8 - 35 - 57 wt%) ***c.c.: Au paste***	YSZ (50)	LSM - YSZ	H_2	973	130	[347]
			CH_4	973	20	
			C_4H_{10}	973	50	
$La_{0.75}Sr_{0.25}Cr_{0.5}Mn_{0.5}O_{3-\delta}$ - YSZ (50 - 50) impreg. with Pt ***c.c.: Pt paste***	YSZ (250)	Symmetrical	wet pure H_2	1223	550	[366]
			wet 5% H_2	1223	330	
			wet pure CH_4	1223	350	
$La_{0.8}Sr_{0.2}Cr_{0.8}Mn_{0.2}O_{3-\delta}$ - CGO10 - Ni (48 - 48 - 4 wt.%) ***c.c.: Ag or Pt paint***	CGO10 (400 - 600)	LSCF - CGO10 (50 - 50 wt.%)	wet H_2	1023	150	[367]
			wet CH_4	1023	120	
			wet C_3H_8	1023	140	
$Pr_{0.7}Ca_{0.3}Cr_{0.6}Mn_{0.4}O_{3-\delta}$ ***c.c.: Pt-based ink***	8YSZ (~370)	Symmetrical	wet 100% H_2	1223	250	[210]
$Pr_{0.7}Ca_{0.3}Cr_{0.2}Mn_{0.8}O_{3-\delta}$ ***c.c.: Pt-based ink***	8YSZ (~370)	Symmetrical	wet 100% H_2	1223	300	[210]
			wet 100% CH_4	1223	200	
$(Pr_{0.75}Sr_{0.25})_{0.95}Cr_{0.5}Mn_{0.5}O_{3-\delta}$ - YSZ (graded), ***c.c.: Au paste***	YSZ (300)	LSM –YSZ (graded)	wet 5% H_2	1184	180	[216]
				1129	130	

The results were obtained using the following electrolyte and cathode materials: $Zr_{0.84}Y_{0.16}O_{2-\delta}$ [210, 212, 219, 277], $La_{0.8}Sr_{0.2}Ga_{0.83}Mg_{0.17}O_{3-\delta}$ [218], $La_{0.8}Sr_{0.2}Ga_{0.8}Mg_{0.2}O_{3-\delta}$ [368], $La_{0.9}Sr_{0.1}Ga_{0.8}Mg_{0.2}O_{3-\delta}$ [9, 279], $Ce_{0.9}Gd_{0.1}O_{2-\delta}$ [367]; $La_{0.8}Sr_{0.2}MnO_{3-\delta}$ [8, 279], $La_{0.8}Sr_{0.2}MnO_{3-\delta}$ - YSZ [217], $La_{0.75}Sr_{0.25}MnO_{3-\delta}$ - YSZ [347], $(Pr_{0.7}Ca_{0.3})_{0.95}MnO_{3-\delta}$ [368], $SrCo_{0.8}Fe_{0.2}O_{3-\delta}$ [218], $La_{0.6}Sr_{0.4}Co_{0.2}Fe_{0.8}O_{3-\delta}$ - CGO10 [367], $Ba_{0.5}Sr_{0.5}Co_{0.8}Fe_{0.2}O_{3-\delta}$ [9].

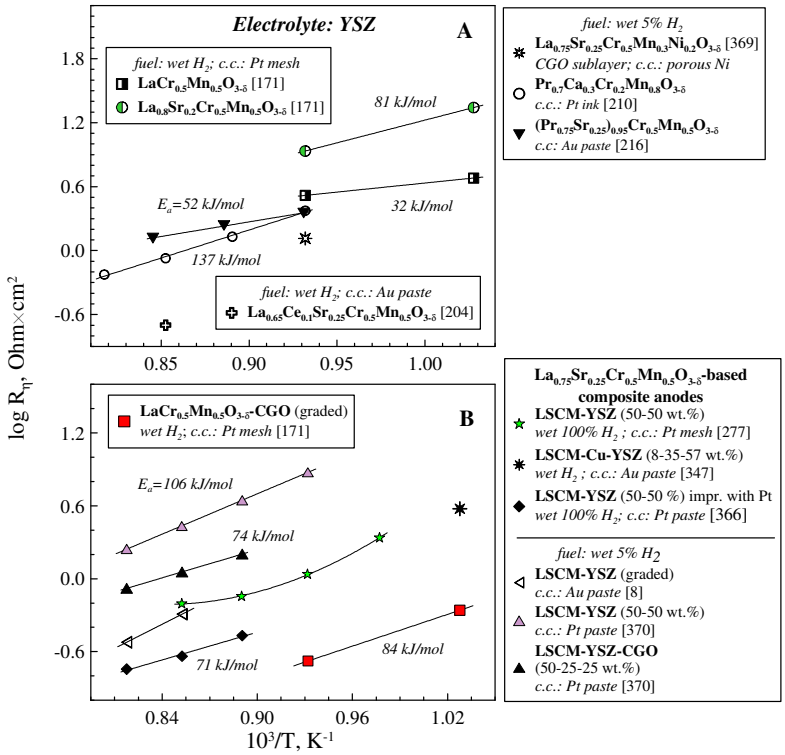

Fig. 1.4.1. Temperature dependencies of polarization resistances of (Ln,A)(Cr,Mn)$O_{3-\delta}$ anodes under zero current

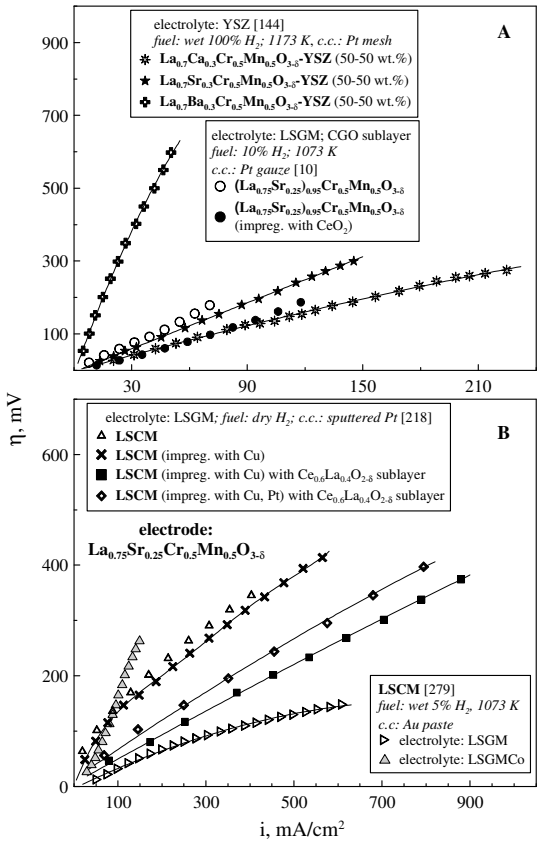

Fig. 1.4.2. Current - overvoltage dependencies of selected (Ln,A)(Cr,Mn)$O_{3-\delta}$ anodes.

Enhancing the electronic conductivity by introduction of metallic phase or compositional modifications generally reduces the activation energy of the electrochemical performance, as shown in Fig. 1.4.1. The presence of $CeO_{2-\delta}$-based phases in the composite anode also diminishes the E_a, possibly due to contribution to the electronic transport, although increased ionic conduction or catalytic activity may have the activating effect as well. At the same time, introducing YSZ into the anode increases the activation energy attributable to worse percolation of the electron-conductive paths in the composite or to a change of the electrode mechanism.

The anode $La_{0.75}Sr_{0.25}Cr_{0.5}Mn_{0.5}O_{3-\delta}$ with Au paste current collector exhibited quite reasonable power densities (400 - 600 mW/cm^2 at 1073 K) in H_2 - H_2O - Ar fuel with LSGM electrolyte as thick as 2 mm; however, no stability was checked in the study [279]. Impregnation of the anode with Pt and Cu allows to achieve power densities as high as 850 mW/cm^2 in dry H_2 at 1123 K and 450 mW/cm^2 in dry CH_4 at 1073 K [218]. Stable performance (for at least 24 hours) of 320 - 550 mW/cm^2 and R_η of 0.18 - 0.29 Ohm×cm^2 at 1223 K was observed for $La_{0.75}Sr_{0.25}Cr_{0.5}Mn_{0.5}O_{3-\delta}$ - YSZ - Pt composite electrode in wet H_2 atmospheres, while in wet CH_4, the power density and R_η were 350 mW/cm^2 and 0.26 Ohm×cm^2, respectively [366]. Composite anodes based on $(La,Sr)(Cr,Mn)O_{3-\delta}$ showed a noticeable activity towards conversion of wet C_3H_8 [367], wet ethanol [368] (stable for 60 hours), 0.5% H_2S - CH_4 [212]. The preferability of $La_{0.75}Sr_{0.25}Cr_{0.5}Mn_{0.5}O_{3-\delta}$ - Cu anodes over analogous CGO - Cu cermets was reported [364].

1.5. Perovskite-related titanates with high electronic conductivity

The present section concerns phase and structural relationships, their influence on the electronic, oxygen- and hydrogen ionic conductivity as well as on the thermomechanical and electrochemical behaviour. A particular attention is focused on kinetic factors which are essentially important for titanate-based materials. Although Ti-enriched solid oxides include several structural groups such as pyrochlores, tungsten bronzes, spinels, etc. which may also be regarded as potential candidates for the anode utilization ([7, 14, 91, 102, 103] and references cited), the present consideration will be restricted by $ATiO_{3-\delta}$ (A = Ca, Sr, Ba) compositions and their derivatives possessing the perovskite structure.

1.5.1. Defect chemistry mechanisms under oxidizing and reducing conditions

The defect structure of titanate-based compositions significantly differs from that of previously considered perovskites. Since Cr and Mn can exist in 4+/3+ or 4+/3+/2+ oxidation state, respectively, in a wide operational range of oxygen pressures, the corresponding compositions are tolerant towards reasonable introduction of aliovalent dopants, without any significant formation of secondary phases, while the functional characteristics of the materials continuously change with the concentration of the substituent. In titanates, Ti^{4+} dominates under oxidizing conditions; the onset of generation of noticeable fractions of Ti^{3+} is located at $p(O_2)<10^{-7}$ atm at 1473 K [371]. Therefore, titanates are much less flexible towards doping in terms of the phase purity, and their defect chemistry is strongly related with variations in the phase

composition. For simplicity, the basic relationships of the defect chemistry will be given for model composition $SrTiO_{3-\delta}$ and its derivatives, although similar equations are also relevant for $CaTiO_{3-\delta}$- and $BaTiO_{3-\delta}$-based analogues.

Generalized approaches consider that the defect species in undoped $SrTiO_{3-\delta}$ are electrons (e'), holes ($h^{\cdot}$) and vacancies in Sr, Ti and O sublattices, denoted as V''_{Sr}, V'''_{Ti} and $V^{\cdot\cdot}_{O}$. The corresponding concentrations are denoted as n, p, $[V''_{Sr}]$, $[V'''_{Ti}]$ and $[V^{\cdot\cdot}_{O}]$. Moreover, most titanates are susceptible towards minor amounts of acceptor-type impurities [372-375] and the conductivity trends may adequately be described only assuming the presence of acceptor cations in A or B sublattice, schematically denoted as A'_C with the concentration $[A'_C]$. Within the model considered below, the distribution of the acceptor between A- and B-sublattices is considered to be non-important in terms of the transport properties.

The defect chemistry in undoped $SrTiO_{3-\delta}$ is associated with the processes of oxygen vacancy formation and dissolution of SrO in the perovskite structure, with the expression of the equilibrium constants:

$$K_{re}=[V^{\cdot\cdot}_{O}]n^2p(O_2)^{+1/2} \qquad \textbf{(Eq. 1.5.1)}$$

$$K_B=\frac{[Sr^{\times}_{Sr}][O^{\times}_{O}][V'''_{Ti}][V^{\cdot\cdot}_{O}]^2}{a_{SrO}} \qquad \textbf{(Eq. 1.5.2)}$$

The equilibrium is governed by the electron-hole generation and the processes of Shottky-disorder as:

$$K_i=np \qquad \textbf{(Eq. 1.5.3)}$$

$$K_S=[V''_{Sr}][V'''_{Ti}][V^{\cdot\cdot}_{O}]^3 \qquad \textbf{(Eq. 1.5.4)}$$

Depending on the values of the equilibrium constants and the level of intentionally introduced or background impurities $[A'_C]$, the compensation mechanism is strongly affected by the cation stoichiometry and oxygen pressure. Selected examples of the compensation mechanisms for $BaTiO_{3-\delta}$ as well as the slopes of the fraction of p- and n-type carriers vs. $p(O_2)$ (in logarithmic scale) are shown in Fig. 1.5.1.

One of peculiarities of titanate-based perovskites is the appearance of p-type and n-type branches of the total conductivity, observable even on undoped titanates. The generation of large amounts of holes is compensated by formation of cation vacancies in A- or B-sublattice. In accordance with the diagram, the slopes in the logarithmic plot of the total conductivity vs. $p(O_2)$ for $SrTiO_{3-\delta}$ should change in the order -1/6, -1/4, +1/4, +1/6 upon oxidation, assuming comparable mobilities of p- and n-type electronic carriers. In practice, the value of $p(O_2)$ corresponding to the change in the value of the positive slope is generally located beyond the experimental conditions. Increasing the temperature favors the formation of oxygen vacancies and thus shifts the changes in the compensation mechanisms to higher values of $p(O_2)$. Although the oxygen deficiency as large as 0.28 was observed in $SrTiO_{3-\delta}$ [376], under typical experimental conditions variations in the oxygen content on redox cycling in $SrTiO_{3-\delta}$ and $BaTiO_{3-\delta}$ do not exceed 0.002 - 0.004 per perovskite formula unit [248, 377-379]. Nevertheless, even such negligible changes in the defect concentration cause a ~2-fold enhancement of the n-type conductivity.

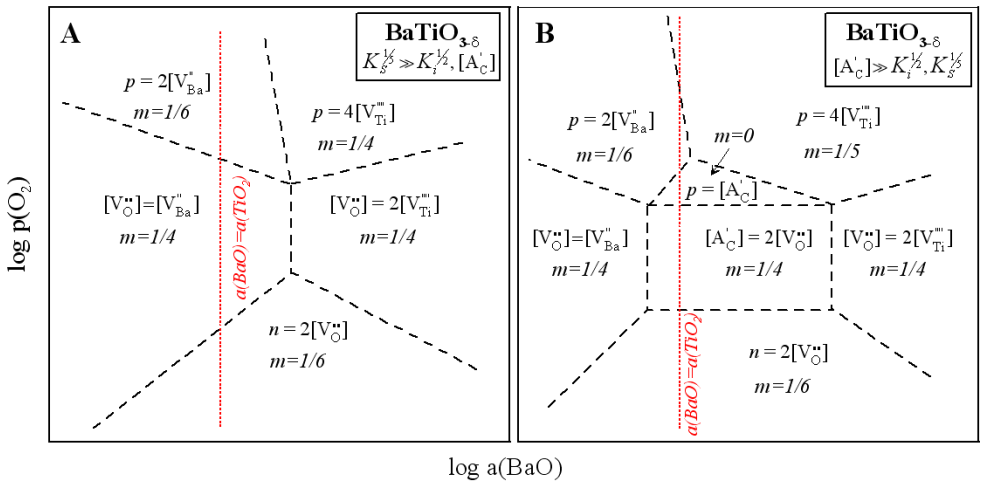

Fig. 1.5.1. Diagrams showing the defect equilibria in $BaTiO_{3-\delta}$ [372] depending on the equilibrium constants, content of acceptor-type dopant, $p(O_2)$ and activity of BaO. The equations correspond to the compensation mode; *m* is the slope of the dependencies log *p* = m log $p(O_2)$ and log *n* = -m log $p(O_2)$ under given conditions. Red lines correspond to cation-stoichiometric composition.

In accordance with the diagrams (Figs. 1.5.1 - 1.5.2) even minor deviations from the cation stoichiometry or a contamination of titanates with donor- or acceptor-type impurities significantly affects the defect equilibrium ([372, 373, 380] and references cited). This leads to large discrepancies between the data on the total conductivity obtained in various studies; the difference is especially pronounced in the range of p-n transition and on the branch of p-type conductivity, due to a relatively small concentration of the charge carriers and their strong susceptibility towards the factors discussed above.

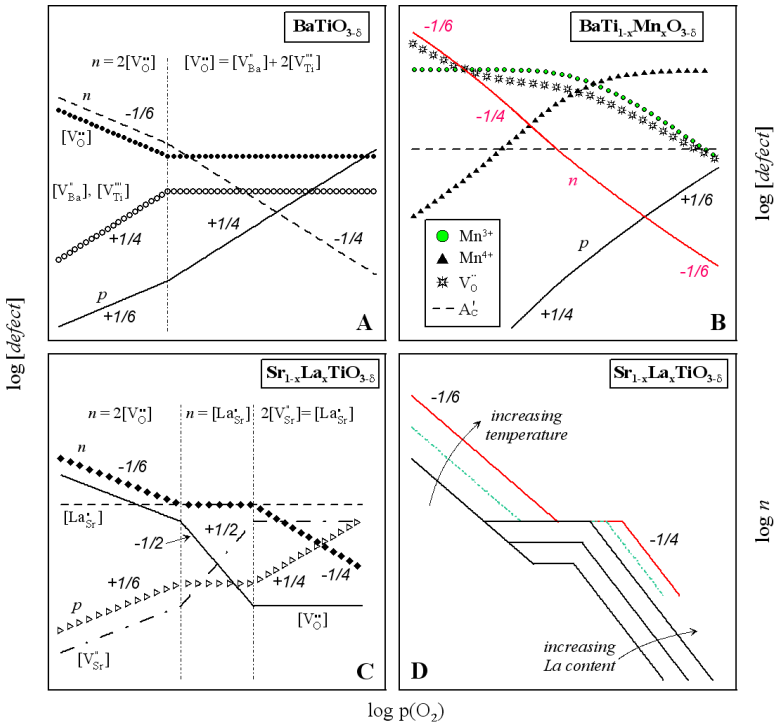

Fig. 1.5.2. Isothermal dependencies of equilibrium dopant concentrations (A, B, C) and n-type charge carriers concentration (D) vs. $p(O_2)$ for selected titanates. The diagrams are taken from [374, 381, 382]

Due to relatively small cation radii of Ca and Sr, the formation of A-site cation vacancies dominates in $CaTiO_{3-\delta}$ and $SrTiO_{3-\delta}$ [381, 383-385]. Whenever the cation vacancy compensation mechanism is realized in $CaTiO_{3-\delta}$ or $SrTiO_{3-\delta}$, this results in separation of Ca- or Sr-enriched phases or, more likely, generation of domains of RP-intergrowths in the perovskite structure [375, 381, 385]. The ratios of Ca:Ti or Sr:Ti where single perovskite phase exists are scattered in the literature and strongly depend on the processing conditions. The acceptable level of Ca- or Sr-deficiency varies in the range 0.1 - 10% [376, 386-390], while Sr:Ti ratio as low as 0.8:1 causes formation of superstructures with ordering in A- and O-sublattice [391]. For $Ca_{1+x}TiO_{3-\delta}$, the maximum acceptable value of x was assessed up to 0.01% [392]; similar value for $Sr_{1+x}TiO_{3-\delta}$ was evaluated as 0.2% [390].

In contrast, the high-$p(O_2)$ charge compensation in $BaTiO_{3-\delta}$ is accompanied by dominating formation of Ti vacancies [371, 393, 394] causing separation of Ti-enriched phases, such as $BaTi_2O_5$, $Ba_6Ti_{11}O_{40}$, etc. [371, 381, 382, 395]. The perovskite phase exists in a narrow domain of Ba:Ti ratio; the excess of Ba or Ti should not exceed 0.1 - 1 mol.% [382, 396]. No formation RP-phases has been reported for $BaTiO_{3-\delta}$ [381, 397]. On the other hand, an enrichment of $BaTiO_{3-\delta}$ with rare-earth cations allows to stabilize the RP-structures [398].

An important feature of the titanates of alkali-earth metals is their complex structural behavior. $CaTiO_{3-\delta}$ is orthorhombically-distorted perovskite (S.G.: *Pbmn*) adopting the tetragonal perovskite structure at 1500 - 1600 K, followed by the transformation into the cubic symmetry at 1635 K [399, 400]. On heating from the room temperature, $BaTiO_{3-\delta}$ consequently exhibits transformations from tetragonal (S.G.: *P4mm*) into cubic (393 K) and into hexagonal structure (~1700 K) possessing S.G.: *P6₃/mmc* [401, 402]. In terms of the structural stability, $SrTiO_{3-\delta}$ is more preferable for the high-temperature applications, since this perovskite exists in the cubic modification ($Pm\bar{3}m$) at T>105 K, without transformations on heating [403, 404].

Introduction of nonreducible rare-earth donor cations (i.e. Ln) into A-sublattice is accompanied by either electronic compensation at low $p(O_2)$ or cation vacancy formation taking place under oxidizing conditions [388, 405]. The 3rd possibility involving the formation of ordered structures where Ti may be stabilized in 3+ state at atmospheric oxygen pressure is beyond the present consideration. If the cation stoichiometry does not support any of the mechanisms, the compensation is accompanied by the formation of secondary phases. For example, stoichiometric $(Sr,La)TiO_{3-\delta}$ may be synthesized at low $p(O_2)$ due to equivalent formation of Ti^{3+} species; however, their oxidation destabilizes the perovskite structure with resultant formation of Sr-enriched impurities or, as a particular case, RP-titanate intergrowths in the perovskite structure (schematically denoted as SrO) [406, 407]:

$$\frac{2}{2-x}\,Sr_{1-x}La_xTiO_3 + \frac{x}{4}\,O_2 = Sr_{\frac{1-3x}{2}}La_xTiO_3 + \frac{x}{2}\,SrO \qquad \textbf{(Eq. 1.5.5)}$$

In contrast, generation of appropriate amounts of cation vacancies results in stabilization of titanates in air. However, the coexistence of vacancies in A- and O-sublattice in reducing atmospheres makes the excess of Ti unfavorable in terms of the phase stability which results in separation of Magneli phases Ti_nO_{2n-1}, Magneli layers accommodated into the perovskite structure or other Ti-rich compositions [377, 388, 406]:

$$\frac{2}{2\text{-}x}\ Sr_{\frac{2-3x}{2}}La_xTiO_3 = Sr_{\frac{2-3x}{2-x}}La_{\frac{2x}{2-x}}TiO_3 + \frac{x}{2-x}\ TiO_2 + \frac{x}{4-2x}\ O_2 \qquad \textbf{(Eq. 1.5.6)}$$

Similar relationships were observed on introduction of donor dopants into B-sublattice. In particular, Nb^{5+} is less reducible in comparison with Ti^{4+}, and Nb-substitution into $BaTiO_{3-\delta}$ with overall deficiency of B-cations results in formation of single phase perovskite in air and segregation of Ba-enriched impurities in N_2. In contrast, $BaTi_{0.94}Nb_{0.06}O_{3-\delta}$ is single phase perovskite when prepared in N_2, while oxidation provokes generation of Ti-vacancies in the perovskite and decomposition into Ti-enriched compounds. Such a behavior is consistent with the examples presented for $(Sr,La)TiO_{3-\delta}$ system, with the exception that $BaTiO_{3-\delta}$ shows the tendency towards Ti vacancy formation ([395] and references cited).

Whatever the phase relationships, donor doping into $ATiO_{3-\delta}$ induces the appearance of a region where the amount of charge carriers (and, consequently, the electronic conductivity) is independent of $p(O_2)$ (Fig. 5.2). One should note that within the defect model considered by most authors ([381, 395] and references therein), the defect concentration is considered to be independent of Ln content under fixed $p(O_2)$ in the low oxygen pressure region. However, such a simplification assumes an equal level of the oxygen deficiency for titanates with various donor amounts. Analysis of the literature data on reducibility does not allow to verify this suggestion since apparent variations of oxygen content upon redox cycling might be attributed to formation/dissolution of the secondary phases capable to accommodate/release large oxygen amounts [247, 248, 408-410].

Higher amounts of donor dopants increase the n-type conductivity in the intermediate- and high-$p(O_2)$ regions and expand the domain of $p(O_2)$-independent conductivity. Considering the behavior of Nb- or V-doped titanates, one should mention that under severe high-temperature reducing conditions Ti^{3+} coexists with the corresponding cations in low oxidation states. This leads to a substantial oxygen uptake observable on oxidation (0.05 - 0.1 per perovskite formula unit) in comparison with other titanate materials [410, 411] and may cause significant irreversible changes of the functional properties.

Reduction of cation stoichiometric $Sr_{1-x}La_xTiO_{3-\delta}$ enables to dissolve up to x = 0.3 - 0.4 with preservation of single cubic perovskite structure [412, 413]. In air, the solubility drops down to 4% [414, 415]; on further doping, $La_2Ti_2O_7$ is separated. A possibility of preparation of heavily-doped (30 - 40%) $Sr_{1-x}La_xTiO_{3-\delta}$ in air has been reported [105, 409]; in [105], the cubic perovskite phases were stable on annealing at 1923 K in air and under reducing conditions. These results seem to be affected by kinetic stabilization or low sensitivity of the examination techniques towards formation of impurities or superstructures, since $Sr_{0.6}La_{0.4}TiO_{3-\delta}$ should contain at least 40% of Ti^{3+}, which is hardly possible in oxidizing atmospheres. More reliable in this respect seems the separation of Sr-rich phases which forms Sr-O layers in the perovskite structure with A-site deficiency, similar to RP-phases (mainly, $Sr_2TiO_{4-\delta}$, $Sr_3Ti_2O_{7-\delta}$, etc.) [408, 416, 417]. Such a structure enables to accommodate both Sr vacancies (in perovskite blocks) and excessive oxygen and strontium (in Sr-O planes) and thus realize the charge compensation in air.

Introducing equivalent amounts of A-site cation vacancies in $Sr_{1-3x/2}La_xTiO_{3-\delta}$ ensures La solubility up to x = 0.4 in air [377, 418] with the preservation of the cubic structure; further generation of cation vacancies induces short- or long-range ordering in A-sublattice [96, 418, 419]. $Sr_{0.7}La_{0.2}TiO_{3-\delta}$ was reported

to be stable under reducing and oxidizing conditions [420], possibly due to kinetic factors. Increasing La content up to 20 - 40% promotes the transition tetragonal-cubic at 300 - 450 K on heating in air [418].

The solubility of Y in cation-stoichiometric $SrTiO_{3-\delta}$ is as low as 1% [414]; reduction allows to accommodate up to 7% of Y without destabilization of the cubic perovskite structure. On the other hand, according to Das et al. [421], $Ca_{1-x}Y_xTiO_{3-\delta}$ and $Sr_{1-x}Y_xTiO_{3-\delta}$ solid solutions exist in the entire compositional range. The maximum content of Y in A-site vacancy-compensated $(Sr,Y)TiO_{3-\delta}$ is assessed to be 4 - 8% [406, 410, 414] and may be preserved down to reducing conditions. Exceeding Y content results in separation of $Y_2Ti_2O_7$ and TiO_2 rather than to generation of RP-phases [406, 414, 422].

$CaTiO_{3-\delta}$-based perovskites exhibit essentially the same phase relationships as $SrTiO_{3-\delta}$-based analogues. $Ca_{1-x}La_xTiO_{3-\delta}$ might be produced single-phase in air with presumably $GdFeO_3$-like orthorhombic structure (S.G.: *Pbnm*) in the range $0 \le x \le 0.3$ [423]. Further enrichment with La results in transition into the $R\bar{3}c$ symmetry and a gradual accumulation of $Ca_2La_4Ti_6O_{20}$ and $CaLa_4Ti_5O_{17}$ phases [423]. Similar to Sr- or La-rich $(Sr,La)TiO_{3-\delta}$, formation of RP-titanate superstructures is also relevant to $(Ca,La)TiO_{3-\delta}$ [380, 392]. For A-site deficient $Ca_{1-3x/2}La_xTiO_{3-\delta}$, simple orthorhombic perovskite phase, slightly contaminated by TiO_2, was obtained up to x = 0.33 exhibiting a phase transition on La-doping owing to tilting the octahedra or cation vacancy ordering [424]. $Ba_{1-x}La_xTiO_{3-\delta}$ may accommodate as much as 3% of La in air, the symmetry increasing with La content [371, 425]. At higher La amounts, phases like $Ba_6Ti_{11}O_{40}$ or $Ba_6La_8Ti_{18}O_{54}$ are separated confirming the preferential formation of Ti vacancies in $BaTiO_{3-\delta}$-based perovskites.

Nb solubility in air without intentional creation of cation vacancies may be accomplished up to 2% in $SrTi_{1-x}Nb_xO_{3-\delta}$ [426]; the excessive amount is separated as Sr_2NbO_4 phase. On the other hand, Nb can be stabilized in the titanate structure by Ti/Nb reduction at low $p(O_2)$ or enhanced temperatures; in the latter case, formation of $Sr(Ti,Nb)O_{3-\delta}$ may be achieved in air up to 9% Nb even with 1% deficiency in B-sublattice [413]. The cubic structure of $Sr(Ti,Nb)O_{3-\delta}$ is maintained on Nb-doping within the solubility domain. Introducing Nb with simultaneous generation of cation vacancies ($Sr_{1-x/2}Ti_{1-x}Nb_xO_{3-\delta}$) allows to substitute up to 40% of Ti; the materials are stable in air and under reducing conditions [96, 97]. Further enrichment with Nb necessitates an additional amount of A-site vacancies for charge compensation, which causes formation of secondary phase with tetragonal tungsten bronze structure [96, 97]. For Nb-doped $BaTiO_{3-\delta}$, Ti deficiency is necessary for Nb dissolution; the composition $BaTi_{0.926}Nb_{0.06}O_{3-\delta}$ was found to be stable in air forming Ba-rich phase on reduction [395].

Comparing the behavior of acceptor-doped and so-called pure $SrTiO_{3-\delta}$ (Fig. 1.5.1), one may conclude that the presence of acceptors shifts the p-n transition of the total conductivity towards more reducing conditions and introduces an additional domain in the p-type conductivity branch, where the concentration of charge carriers is essentially determined by the concentration of acceptor cations, i.e. the conductivity is $p(O_2)$-independent. However, under experimental conditions, any accurate separation of the compensation regimes is complicated by kinetic factors and a strong contribution of the ionic conductivity. Thus, typical $p(O_2)$ dependencies of the conductivity exhibit a wide p-n transition, where the conductivity remains on a nearly constant low level.

The presence of transition metal cations which vary their oxidation state under operation conditions may have a multiple effect on the defect chemistry of titanates, depending on the redox potential,

concentration, the presence of irreducible acceptor or donor atoms (including impurities), defect interactions etc. As shown in Fig. 1.5.2, in Mn-doped $BaTiO_{3-\delta}$, Mn species in the oxidation state +3 and +4 may coexist with the electrons delocalized in 3*d*-conduction band of Ti atoms. Details of the defect equilibrium for $(A,Ln)(Ti,B)O_{3-\delta}$ systems (A = Ca, Sr, Ba, B = Cr, Mn, Fe, Co, Ni) may be found elsewhere [155, 372, 374, 412, 427-431]. Generally, the p-n transition also shifts to lower $p(O_2)$ attributable to increasing contribution of electron holes. Doping of reducible Mn, Fe, Co, Ni, Cu promotes higher oxygen losses (0.03 - 0.05 per perovskite formula unit) [247, 335] and may significantly affect the behavior of the parent compositions.

The solubility of acceptor-type dopants with a fixed or variable oxidation state in $CaTiO_{3-\delta}$, $SrTiO_{3-\delta}$, $BaTiO_{3-\delta}$ has been studied in [432-439] and references cited. Depending on the oxidation state, reducibility and ionic radius of the guest atom as well as on the nature of A-cation in the titanate, the solubility of the acceptor-type cations varies in the range 5 - 40 mol. %. For example, up to 40% Al might be incorporated into $CaTiO_{3-\delta}$, while for $SrTiO_{3-\delta}$ analogue the solubility was limited only by 20%, possibly due to comparatively small radius for Al^{3+} and Ca^{2+} cations ensuring the optimum tolerance factor. At the same time, both $Ca(Ti,Fe)O_{3-\delta}$ and $Sr(Ti,Fe)O_{3-\delta}$ form a continuous series of solid solutions, with formation of ordered structures at 40 - 50% of the dopant [428, 440-442]. The solubility of acceptors in titanates as well as their phase and structural stability may be modified by the presence of appropriate quantities of Ln^{3+}, Nb^{5+} or other donor-type cations [16, 429, 431, 443, 444]. Depending on the cation ratios and synthesis conditions, single phase perovskites $(A,La)(Ti,B)O_{3-\delta}$ (A = Ca, Sr, B = Cr, Mn, Fe, Co) may be produced in the entire range of Ti:B ratios, especially when Sr(Ca):Ti ratio is preserved close to 1. The crystal structure exhibits orthorhomic distortions on increasing Fe or Cr amount, while Mn- promotes the transition to rhombohedral symmetry. For Co-doped $(Sr,La)TiO_{3-\delta}$ the structure was refined to be orthorhombic or rhombohedral, depending on La and Co content [12, 16, 156, 158, 352, 431, 444, 445]. In terms of the application in a wide $p(O_2)$ and temperature range, one should take into account possible phase decomposition and structural transformations on thermal or redox cycling observable for Mn, Fe, Co or Ni-substituted titanates at low $p(O_2)$ [16, 372, 429, 437, 440-442, 446].

On the other hand, the presence of acceptor-type dopants increases the solubility limit of donor substituents which enables to tune the functional properties of titanates. In particular, doping of $(Sr,La)TiO_{3-\delta}$ with Sc enables to introduce larger quantities of La with preserving the cubic perovskite structure [447]. Similar improvement of the solubility of donor-type cations was observed for $Sr_{0.9}(Ti,Ga,Nb)O_{3-\delta}$ and $(Ca,Na)(Ti,Ta)O_{3-\delta}$ perovskites; in the latter case, co-introduction of Na and Ta into A- and B-sublattice of $CaTiO_{3-\delta}$ allows to stabilize the composition up to the complete substitution in both sublattices [448, 449].

1.5.2. Redox kinetics

One of most important factors influencing the functional characteristics of titanate perovskites is a strong effect of the relaxation kinetics upon $p(O_2)$ changes on the functional properties. An incomplete equilibration causes a poor reliability of the experimental results, large scattering between literature data, hysteresis behavior of the material properties on redox cycling and their strong dependence on the synthesis conditions and measurement procedure; examples of such a behavior are presented in Fig. 1.5.3. The kinetics

strongly depends on the ceramics microstructure. Equilibration of porous ceramics proceeds faster, due to large surface area and shorter distances from the surface to the bulk phase [247, 377, 420]. However, utilization of porous ceramic samples is inappropriate for determination of the ionic conductivity while the total conductivity requires a correction for the porosity. At the same time, for porous anode layers, the equilibration is expected to proceed in a reasonable period. The grain size, utilization of single crystal or film samples has also a great influence on the relaxation indicating a different rate of the bulk- and grain boundary-related processes [247, 248, 377, 450].

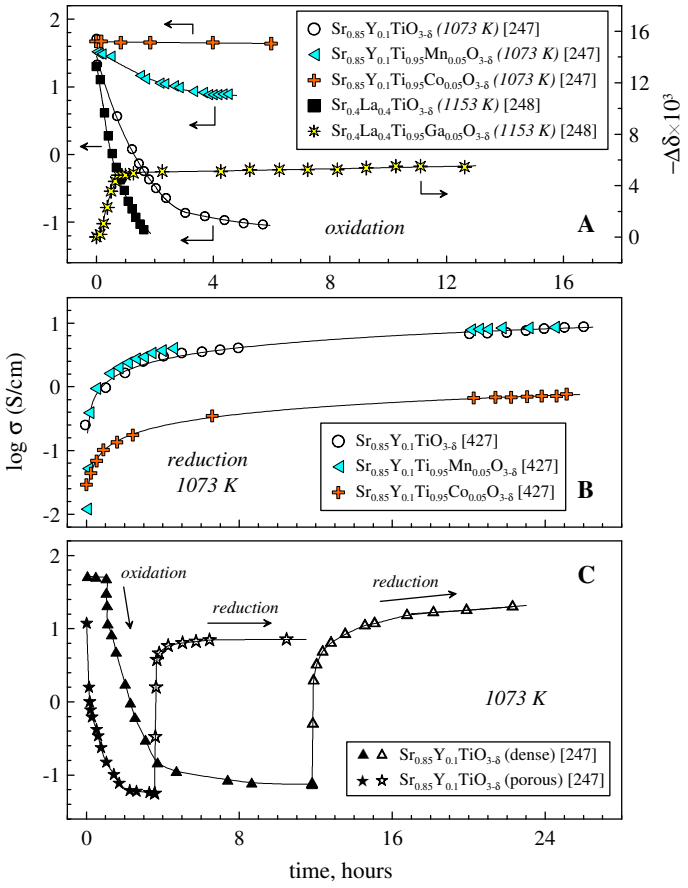

Fig. 1.5.3. Equilibration of the total conductivity and oxygen content variations for selected titanates upon $p(O_2)$ changes

In accordance with most studies, the redox kinetics for dense ceramic titanate-based materials is governed by slow oxygen diffusion in the bulk [247, 248, 377, 414]. Correspondingly, the basic trends in the equilibration rate and mechanism of the relaxation are generally consistent with the behavior of the oxygen ionic conductivity. Analysis of the literature data does not allow to make a conclusion whether the rate of oxidation is superior to that of reduction or contrary [105, 247, 249, 411, 420]; the faster kinetics of any of the processes is primarily associated with individual characteristics of the sample rather than with general trends. Most authors note that both processes proceed rapidly on the initial stage followed by subsequent drift with much slower rate. Such a behavior indicates that oxygen incorporation/elimination into/from ceramics

proceeds in several steps. A possible mechanism suggests that the penetration of oxygen initially occurs into regions at the interfaces between the grains. In accordance with the defect model of titanates, this results in a drop of the population of oxygen vacancies and n-type carriers in the oxidized regions of the ceramics causing a sharp initial decrease of the electronic conductivity. Subsequent oxidation of the material is determined by oxygen exchange between the oxidized exterior zone and reduced grain core. Although the process is driven by a large gradient in oxygen chemical potential between these states, the rate of the latter process is much lower [247, 248, 377, 414].

Analogously, on the onset of supply of reductive atmosphere to preliminary oxidized titanate-based materials, fast reduction of the layers close to the surface of the sample or grain boundaries provides percolative paths for the electronic transport thus ensuring the initial rise of the total conductivity. Further propagation of reducing front into the grain is limited by slow oxygen diffusivity of the oxidized domains, while the contribution from deeper layers into the total conductivity is less significant. The decaying kinetics is also affected by increasing distance from the grain surface to the reductive front [377, 247].

In accordance with higher oxygen vacancy concentration, an acceleration of the redox processes for $(Sr,Ln)TiO_{3-\delta}$ was observed upon introduction of low-valent Ga, Al, Sc, Fe, Co or Cu, while decreasing the oxygen deficiency on V-, Nb-, La-doping inhibits the oxygen diffusion-related processes thus suppressing the equilibration rates [247, 380, 414, 447]. As a particular example, introduction of Ga into $(Sr,La)TiO_{3-\delta}$ promotes the reducibility of the parent composition due to lower oxidation state of Ga and its flexibility towards variations in the oxygen environment. On the other hand, evaporation of Ga in reductive atmospheres results in formation of Ga-depleted layer on the surface with a poor oxygen ionic conductivity, thus making the material more tolerant towards oxidation [248].

Another important factor affecting the redox kinetics is associated with formation/dissolution of secondary phases induced by variations of oxygen pressure. Basically, variations in the phase composition are accompanied by appearance of large stresses in the material structure or microstructure; therefore, the processes described by Eqs (1.5.5) - (1.5.6) proceed with inhibited rates. Moreover, the secondary phase-related proceses are determined by cation diffusion which is low in titanates [395, 406]. The slow rate of formation/dissolution of the impurities as well as phase transitions on redox cycles may lead to formation of inhomogeneous zones where the local composition deviates from the average one (donor-rich regions, domains with ordered oxygen vacancies, etc.) [371, 413, 451].

Slow equilibration may significantly affect the theoretically expected behaviour, primarily in terms of electronic transport. Generally, most $p(O_2)$ dependencies of the conductivity are affected by the degree of oxidation or reduction in each point rather than by the variations in the charge carrier concentration predicted by the defect model; the influence of parameters determining the kinetics on the transport properties is demonstrated in Fig. 1.5.4.

In terms of anode applications, the slow equilibration kinetics necessitates a preliminary high-temperature reduction of titanate-based anodes in order to achieve maximum electronic and ionic conductivity of the material. On the other hand, the susceptibility of titanates towards oxidation and resultant irreversible drop of the conductivity (Fig. 1.5.3), necessitates to avoid an occasional oxidation of the anodes. These requirements represent one of the most serious disadvantages of titanate anodes [105, 411, 452].

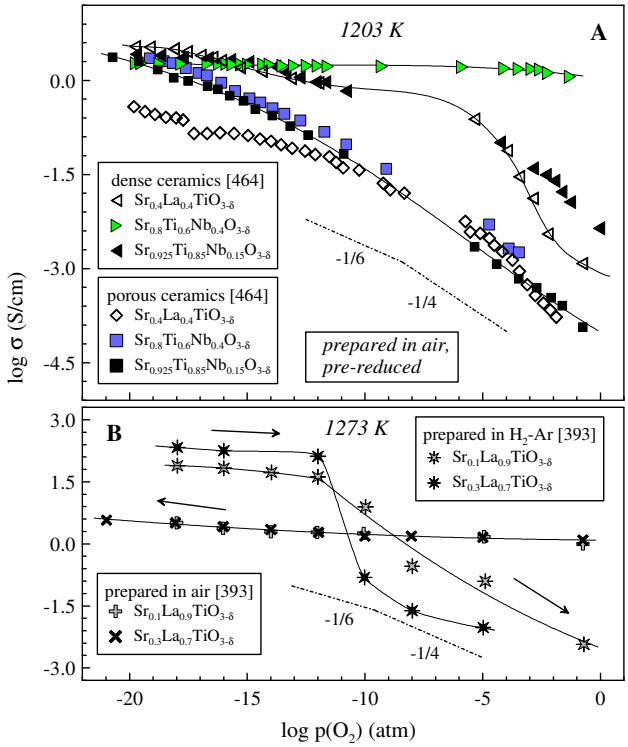

Fig. 1.5.4. Isothermal dependencies of the total conductivity vs. $p(O_2)$ of selected titanates as a function of the preparation conditions and ceramics porosity.

1.5.3. Total conductivity

Depending on the composition, structural or microstructural characteristics, preparation conditions and measurement procedure, titanate materials may exhibit dielectric, semiconducting, metallic-like, superconducting or ferroelectric properties [453-456]. The present consideration will be restricted primarily by the behaviour in the high-temperature interval.

In cubic perovskite lattice, Ti atom is located in the octahedral environment with oxygen. This results in splitting of the orbitals in 3*d*-level of Ti into e_g and t_{2g} sublevels, while 2*p* orbitals from oxygen split into high-energy $2p(\pi)$ and low-energy $2p(\sigma)$ levels. The overlap between $3e_g$ and $2p(\sigma)$ as well as between $3t_{2g}$ and $2p(\pi)$ orbitals causes formation of σ- and π-like bands in the electronic structure of the titanates. The electrons of alkali earth metals occupy preferentially low-energy bands, since the bands associated with the corresponding cations are characterized by significantly higher energies [457, 458]. Such electron structure of the titanate-based compositions ensures location of Fermi level between the completely occupied bonding P_π band and shallow $\pi^*(t_{2g})$ band. The bandgap of "ideal" $SrTiO_{3-\delta}$ is as large as 3.1 - 3.8 eV which ensures the insulating nature of the material [458, 459]. On the other hand, reduction of Ti induced by formation of oxygen vacancies or introduction of donor cations results in a partial occupation of the $\pi^*(t_{2g})$ conduction band with electrons and appearance of band-type conduction mechanism which is especially pronounced under reducing conditions. The electron mobilities are proportional to T^{-M}, where M varies from 2.7 at room temperature down to 1.5 - 2 at 1000 K [381, 457, 460].

Variations in the charge carrier concentration or band structure may induce changes in the effective mass of the electrons and partial localization of the electrons ensuring large polaron or small polaron conduction mechanism, while the electron transport changes from the metallic-like to semiconducting behavior. One should note that the Arrhenius-like behavior, typical for semiconductors and observable on titanates under oxidizing conditions might also be associated with temperature-induced minor oxygen losses leading to generation of additional electrons. Whatever the mechanism of the charge carrier formation and their transport, the conductivity of undoped or donor-doped $ATiO_{3-\delta}$ (A = Ca, Sr, Ba) under reducing conditions may exceed 100 - 1000 S/cm and slightly increases on cooling, beneficial for the IT-SOFC applications. Kinetic limitations may induce deviations between the experimental results and theoretically predicted dependencies; selected examples are presented in Fig. 1.5.4. Such a behavior complicates comparison of the literature data and only outlines the basic trends typical for titanates.

In accordance with the defect model, in the high-$p(O_2)$ range, titanate-based materials are characterized by p-type electronic conduction, attributable to the formation of cation vacancies and equivalent generation of electron holes. One should note that the appearance of the p-type conductivity branch in oxidizing atmospheres with the same slope has been observed on doped ZrO_2, HfO_2 and related compositions [26, 461, 462].

The intrinsic conductivity in "pure" $ATiO_{3-\delta}$ (A = Ca, Sr, Ba) in the region of p-n transition is negligible due to the low concentration of charge carriers. In practice, however, the materials are strongly susceptible to the presence of impurities, self-disordering and other factors which induce the excitation of charges. This results in huge discrepancies between the experimental data, much more pronounced in comparison with $LaCrO_{3-\delta}$, $LaMnO_{3-\delta}$ and other p-type conductors, possessing non-negligible levels of intrinsic charge carriers without intentional doping. Another consequence of the low concentration of the charge carriers in titanates relates to a strong effect of minor (1 - 2 mol.%) quantities of acceptor- or donor-type dopants on the level of the total conductivity and the transport mechanism, as shown in Fig. 1.5.5.

Consistently with the relationships presented in the defect model, donor-doped titanates exhibit the n-type conductivity in a wide $p(O_2)$ range. Upon reduction, the interval characterized by the slope of the conductivity vs. $p(O_2)$ in the logarithmic scale equal to -1/4 transforms into the region where the conductivity weakly depends on $p(O_2)$ followed by the domain with the slope of -1/6. As expected from the model, the intermediate-$p(O_2)$ region, where a weak influence of the oxygen pressure on the conductivity is observed, expands on donor-doping (Fig. 1.5.5). The concentration of mobile charge carriers in the intermediate $p(O_2)$ range is suggested to be temperature-independent [381, 460].

As follows from the defect model, in the low-$p(O_2)$ region the conductivity should be independent of the donor content under fixed $p(O_2)$, and the $p(O_2)$-dependencies of the conductivity for titanates with various dopant level should converge into a single line (Fig. 1.5.2). This behavior cannot be verified due to the lack of experimental data in extremely reducing atmospheres, where such a regime should be realized. In oxidizing and moderately reducing conditions, the presence of donor-like dopants increases the fraction of the electrons in the conduction band, shifts the Fermi level and causes the appearance of additional levels in the bandgap facilitating the electron transitions [105, 381, 406, 412, 414, 460].

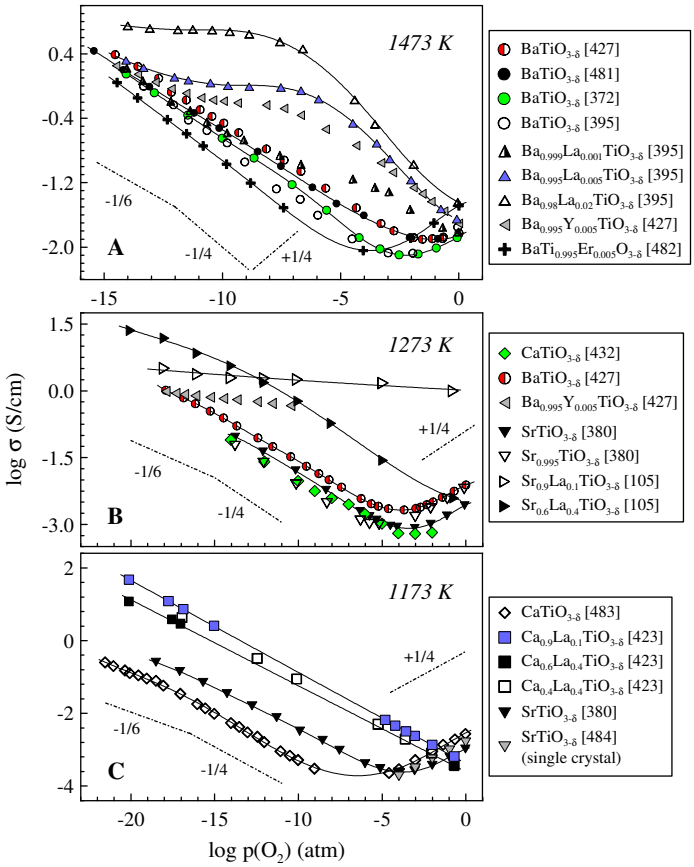

Fig. 1.5.5. Isothermal dependencies of the total conductivity vs. $p(O_2)$ of selected titanates prepared in air

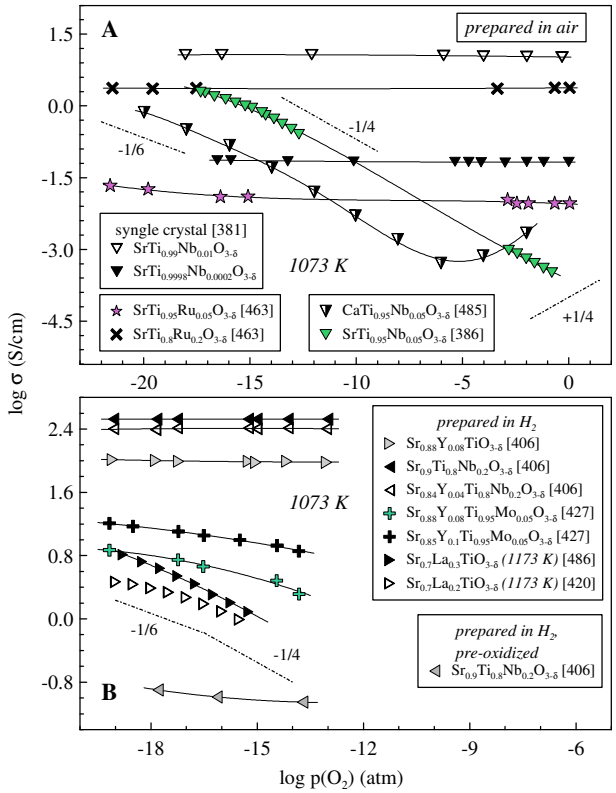

Fig. 1.5.6. Isothermal dependencies of the total conductivity vs. $p(O_2)$ of selected titanates with donor-type dopants in A- or B-sublattice

In this respect, the maximum effect is observed on doping with Nb cations, since the orbitals of 4*d* level of Nb have comparable energies to those of 3*d* level of Ti, which ensures a contribution of Nb species into the electron transfer, improves the overlapping between Ti 3*d* and O 2*p* orbitals and induces more significant modifications in the band structure, in particular shifts the conduction band towards lower energies [406, 407, 413]. Ru-doping has also been shown to improve the electron transport, possibly due to donation of an electron from Ru^{4+} to generate Ti^{3+} (Fig. 1.5.6) [463].

According to the defect model of titanates doped with irreducible acceptor-type cations, the p-n transition should be shifted towards reducing conditions, while in the oxidative domain a region of $p(O_2)$-independent electronic conductivity should appear on the high-$p(O_2)$ branch. In practice such a behavior is generally obscured by slow equilibration and dominating oxygen ionic conductivity which may exceed 80 - 90% of the total one. As a result, such materials exhibit an extended (~10 orders of $p(O_2)$) domain where the total conductivity is preserved on nearly constant low level (10^{-4} - 10^{-2} S/cm) (Fig. 1.5.7). The effect of acceptor content on the magnitude of the electronic conductivity may be multiple; as a general rule, the p-n transition shifts to lower $p(O_2)$ upon doping, while replacement of Ti with inert cations above a definite level hampers the electron mobility due to a smaller degree of overlapping between Ti 3*d* and O 2*p* orbitals.

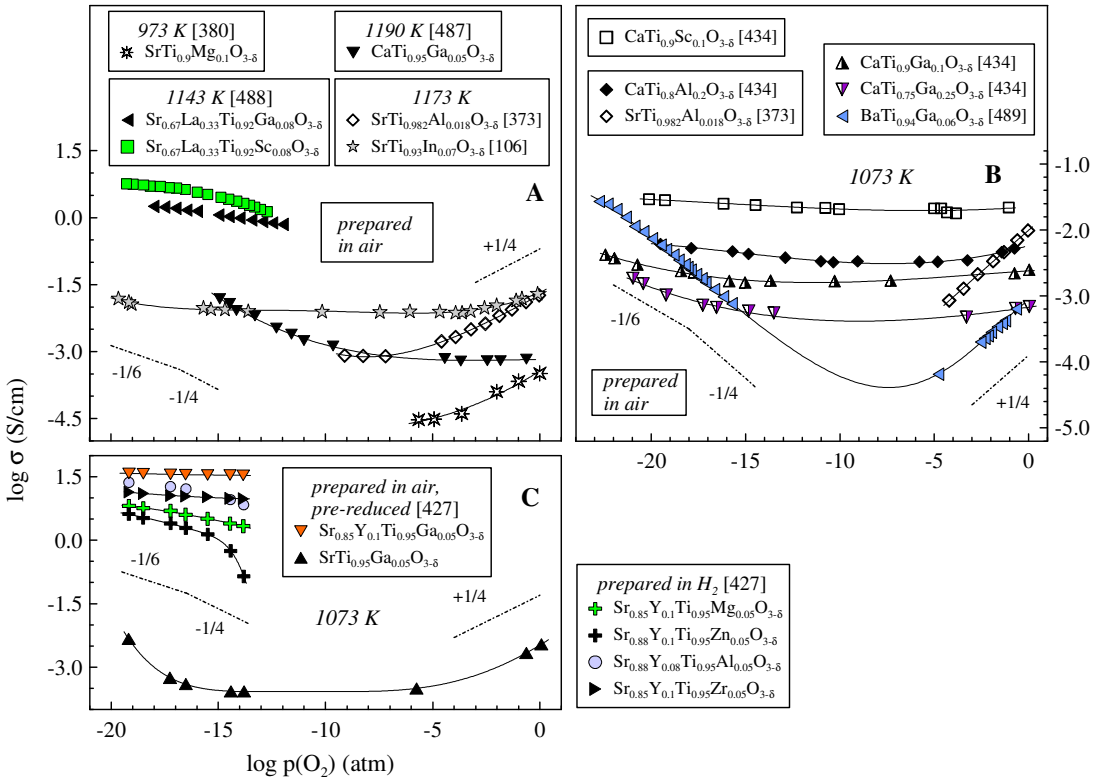

Fig. 1.5.7. Isothermal dependencies of the total conductivity vs. $p(O_2)$ of selected titanates substituted with acceptor-type dopants with a fixed oxidation state

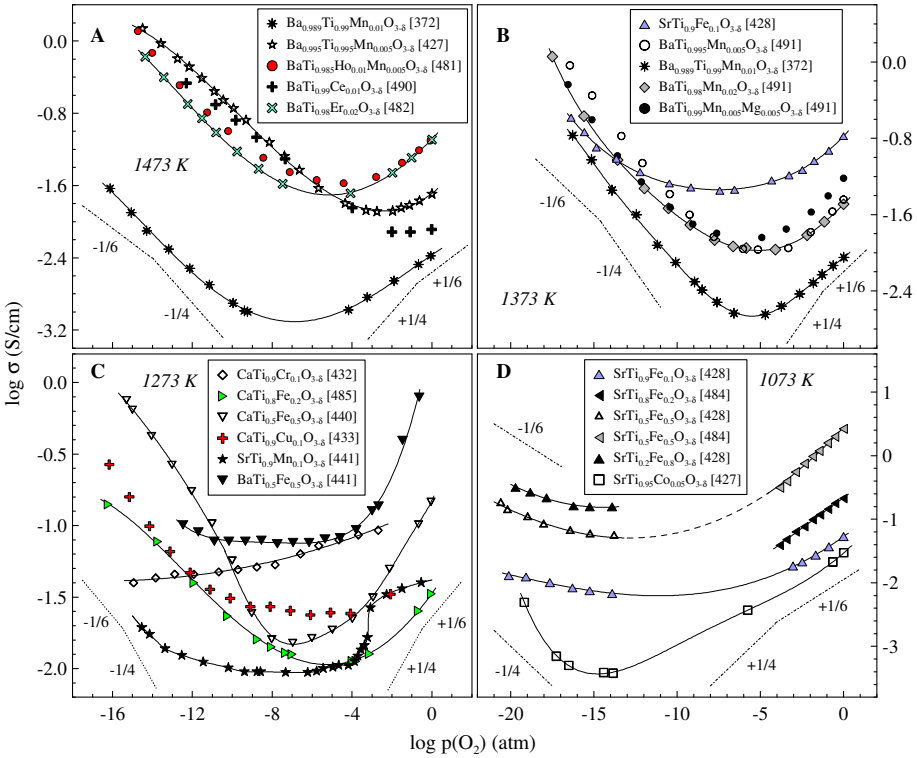

Fig. 1.5.8. Isothermal dependencies of the total conductivity vs. $p(O_2)$ of selected $ATiO_{3-\delta}$-based compositions substituted with acceptor-type dopants with variable oxidation state, prepared in air

A significant improvement was observed on introduction of cations with variable oxidation state, especially in the high-$p(O_2)$ range due to a stronger contribution of the p-type conductivity. As shown in Fig. 1.5.8, the compositions exhibit a definite p-n transition, possibly due to faster equilibration or larger electronic transference numbers, whereas the behavior in the p- and n-conductivity branches depends on the nature and content of the dopant cation [155, 159, 372, 427, 428, 441, 443, 444]. The conductivity of $A(Ti,B)O_{3-\delta}$ (A = Ca, Sr, Ba, B = Cr, Mn, Fe, Co, Ni, Cu) in the low $p(O_2)$ range is within 1 - 5 S/cm, but may be substantially increased by simultaneous donor-doping (Fig. 1.5.9.). In particular, Ga-, Mn-, Fe- or Co-doped $(Sr,Y)TiO_{3-\delta}$ or $(Sr,La)TiO_{3-\delta}$ are considered as promising materials for low-$p(O_2)$ applications, due to acceptable (up to 100 S/cm) electronic conductivity and sufficient tolerance towards moderate oxidation [247, 248, 335, 427].

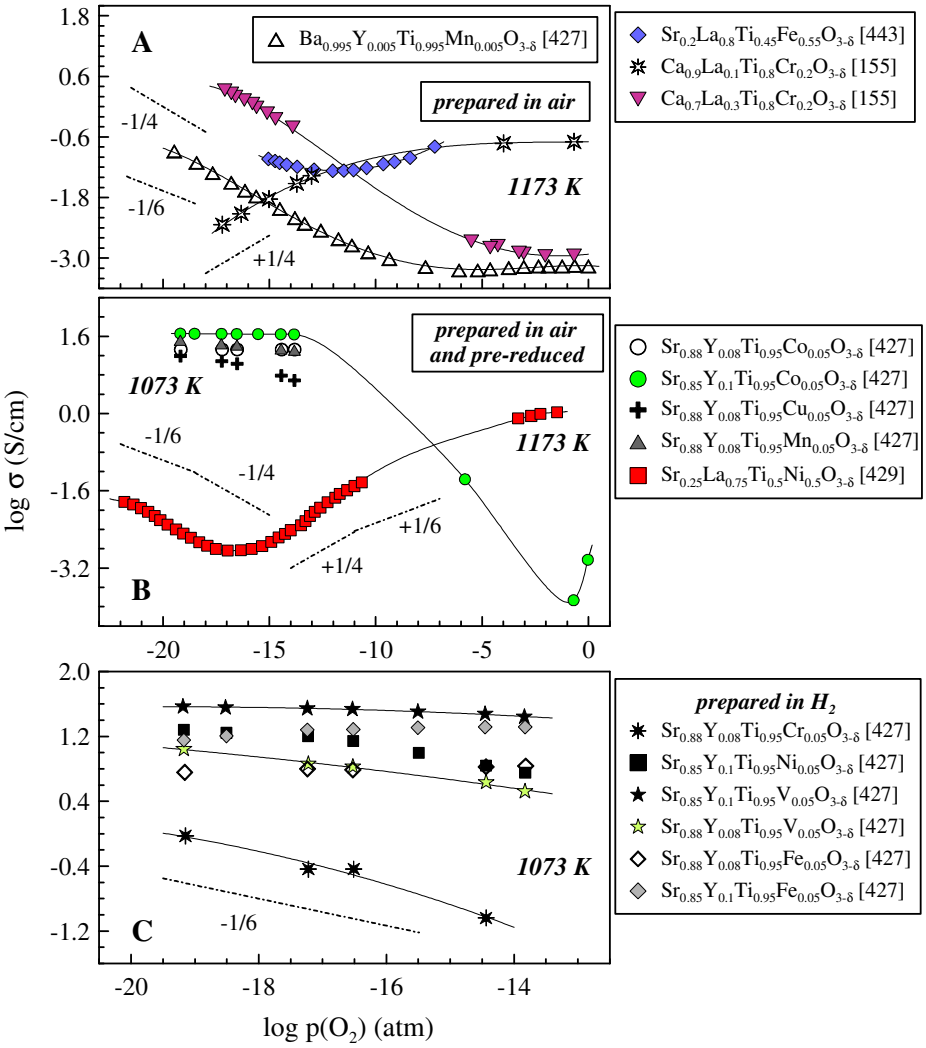

Fig. 1.5.9. Isothermal dependencies of the total conductivity vs. $p(O_2)$ of selected $(A,Ln)TiO_{3-\delta}$-based compositions substituted with acceptor-type dopants with variable oxidation state

The transport properties of titanate-based ceramics are substantially governed by microstructural characteristics, essentially pronounced at reduced temperatures. As can be inferred from literature data, the conductivity behavior for single crystal, film or ceramic materials with various grain size may be quite different [248, 380, 381, 465-467]; selected examples are shown in Fig. 1.5.5. One of the most common origins of the complex behavior is a non-uniform cation or defect distribution over the grain, such as an enrichment of the grain surface with Ti or acceptor-type dopants [451, 468, 469]. Slow oxygen diffusion into/out of the bulk phase on redox cycling also causes compositional differences over the grain, varying with time [247, 377]. Accumulation of immobile charges at the boundaries results in non-uniform distribution of electrons, holes or oxygen vacancies over the grain, deformation of the valence and conduction band with subsequent changes in their occupation with electrons and in the width of the bandgap [468, 470-472]. The factors indicated significantly affect the resistive properties of the grain exterior layers, while their large capacitance may cause trapping of the mobile charge carriers [384, 468, 473]. In particular, the conductivity of Ni-doped $SrTiO_{3-\delta}$ within a layer of the thickness of 30 - 200 nm at the grain interface was found to be 4 orders lower compared with that in the bulk phase. Apart from the non-uniform cation distribution, formation of defect clusters [413, 474, 475] and phase separation at the grain boundaries were reported [371, 409, 413]. One should note that the grain surface-related limitations are typical for most mixed ionic/n-type conductors [30, 72, 476-478] and their effect reduces at elevated temperatures. More details on the grain boundary contribution into the electronic transport in titanates may be found in [380, 451, 468, 471, 479, 480] and references cited.

1.5.4. Oxygen ionic and protonic conductivity: selected examples

Due to complex defect chemistry of titanates and multiple transitions of the compensation mechanism, the chemical diffusion coefficient is strongly affected by changes in the concentration of p-, n-, $V_O^{\cdot\cdot}$ and other charge carriers on variations of $p(O_2)$ or temperature, with resultant influence on the enhancement factor. In particular, in the region of p-n transition, the ionic conductivity becomes comparable or even higher than the electronic contribution (Table 1.5.1), while the ambipolar diffusion becomes limited by both ionic and electronic transport. Such a behavior is different from that of chromites and manganites, where the electronic transference number are close to unity in the entire $p(O_2)$ range. Basically, in the region of p-type conductivity, the chemical diffusion in titanates increases on reduction, exhibiting a maximum within the p-n transition region. Subsequent decrease in $p(O_2)$ reduces the diffusivity due to lowering the enhancement factor, while in the low-$p(O_2)$ range, the behavior is more scattered [492-494]. Such a complex behavior of the diffusion coefficients yields large discrepancies between experimental data which achieve 2-3 orders of magnitude (Tables 1.5.2 - 1.5.3). In combination with incomplete equilibration and grain boundary-related effects, the ionic transport becomes strongly influenced by preparation conditions, measurement procedure or the microstructure of the sample. Moreover, large variety of the experimental techniques and testing conditions complicates a direct comparison of the data on diffusion in titanates with those obtained for other perovskite groups.

Table 1.5.1. Oxygen ionic transference numbers for titanates

Composition	T, K	$p(O_2)$, atm	t_O	Method	Reference
$Sr_{0.7}La_{0.3}TiO_{3-\delta}$*	1273	wet 5% H_2-Ar (~1×10^{-18} at 1073 K)	3.4×10^{-5}	Electron-blocking	[412]
	1073		1.3×10^{-5}		
$CaTi_{0.95}Mg_{0.05}O_{3-\delta}$	1315	gradient dry air/ dry O_2	0.70	Electromotive force	[495]
	1233		0.68		
	1273	fuel cell gradient	0.80	Electromotive force	
	1073		0.91		
	973		0.94		
$CaTi_{0.7}Al_{0.3}O_{3-\delta}$	1273	gradient dry air/ dry O_2	0.85	Electromotive force	[495]
	1167		0.73		
	973		0.48		
	1273	fuel cell gradient	0.91		
	973		0.93		
$SrTi_{0.9}Al_{0.1}O_{3-\delta}$	1333	gradient dry air/ dry O_2	0.20	Electromotive force	[495]
	1003		0.16		
	1273	fuel cell gradient	0.65		
	1073		0.78		
	923		0.84		
$CaTi_{0.9}Sc_{0.1}O_{3-\delta}$	1273	gradient dry air/ dry O_2	0.87	Electromotive force	[434]
	1073		0.37		
	1273	gradient wet H_2/ dry O_2	0.94		
	873		0.71		
$Sr_{0.7}La_{0.3}Ti_{0.9}Sc_{0.1}O_{3-\delta}$*	1223	wet 5% H_2-Ar	2.1×10^{-4}	Electron-blocking	[509]
$Sr_{0.97}Ti_{0.6}Fe_{0.4}O_{3-\delta}$	1223	0.21	4.1×10^{-2}	Faradaic efficiency	[501]
	1073		9.0×10^{-3}		
	973		5.0×10^{-3}		
$Sr_{0.9}Ti_{0.6}Fe_{0.4}O_{3-\delta}$	1173	0.21	2.7×10^{-3}	Faradaic efficiency	[501]
	1073		8.6×10^{-4}		
$Sr_{0.7}La_{0.2}Ti_{0.6}Fe_{0.4}O_{3-\delta}$	1223	0.21	5.0×10^{-3}	Faradaic efficiency	[501]
	1173		2.8×10^{-3}		
$Sr_{0.7}La_{0.3}Ti_{0.95}Co_{0.05}O_{3-\delta}$*	1273	wet 5% H_2-Ar (~1×10^{-18} at 1073 K)	1.5×10^{-4}	Electron-blocking	[412]
	1073		5.9×10^{-5}		
$SrTiO_{3-\delta}$ + Ni (10^{18}/cm^3) single-crystal	665	not indicated	3.4×10^{-2}	Wagner-Hebb polarization	[451]
$CaTi_{0.85}Ga_{0.15}O_{3-\delta}$	1273	gradient dry air/ dry O_2	0.87	Electromotive force	[434]
	1273	gradient wet H_2/ dry O_2	0.84		
$SrTi_{0.95}Ru_{0.05}O_{3-\delta}$	1073	gradient H_2 (1 atm)/H_2-Ar ($p(H_2) \approx 0.4$ atm)	1.2×10^{-2}	Electromotive force**	[463]
$SrTi_{0.93}In_{0.07}O_{3-\delta}$	1173	gradient dry air/dry O_2	0.02	Electromotive force	[106]
	1073		0.08		

* *Prepared in 5% H_2-Ar*
** *Protonic transport and polarization are neglected*

Due to negligible concentration of electron-type charge carriers in the range of p-n transition, most titanates exhibit dominating oxygen ionic conduction in the intermediate-$p(O_2)$ range (Table 1.5.1). Selected titanates have been tested as solid electrolyte materials (in particular, the power density of 140 mW/cm^2 was achieved for a cell with $CaTi_{0.7}Al_{0.3}O_{3-\delta}$ electrolyte membrane (350 μm) [495]), although their application as pure ionic conductor is limited by a narrow interval of $p(O_2)$ where the electronic contribution is negligible.

Table 1.5.2. Diffusion and surface exchange coefficients of titanates determined by isotope diffusion technique (all the samples were prepared or pre-annealed under oxidizing conditions)

Composition	T, K	$p(O_2)$, atm	D*, cm^2/s	E_a for D*, kJ/mol	k*, cm/s	Reference
$SrTiO_{3-\delta}$ single crystal	1482 1381	0.21	~1.2×10^{-9} ~7.7×10^{-10}	95		[450]
$SrTiO_{3-\delta}$	1471	0.21	~1.1×10^{-9}	70		[450]
$BaTiO_{3-\delta}$ [a]	1273	~1	3.2×10^{-13}	50		[497]
0.3% La-doped $SrTiO_{3-\delta}$ single crystal	1173	O_2 (pre-annealed)	1.3×10^{-13}	160	4×10^{-10} - 8×10^{-8}	[500]
1% Gd-doped $SrTiO_{3-\delta}$ (single crystal)	1373 1273	0.21	4.3×10^{-11} 2.1×10^{-11}	100		[450]
0.4% Dy-doped $SrTiO_{3-\delta}$	1488	0.21	8.5×10^{-10}	160		[450]
0.8% Dy-doped $SrTiO_{3-\delta}$	1433	0.21	2.8×10^{-10}	170		[450]
1.0% Dy-doped $SrTiO_{3-\delta}$	1521	0.21	1.3×10^{-10}	260		[450]
$Ba_{0.9}La_{0.0667}TiO_{3-\delta}$ [a]	1273	~1	8.3×10^{-15}	430		[497]
$Ba_{0.676}La_{0.1}TiO_{3-\delta}$ [a]	1273 1073	~1	7.1×10^{-15} 6.2×10^{-17}	410		[497]
$SrTiO_{3-\delta}$ + Fe ($4\times10^{18}/cm^3$) single-crystal [b]	1073 873	~1 ~1			1.3×10^{-8} 2.0×10^{-11}	[510]
$SrTiO_{3-\delta}$ + Fe ($5\times10^{19}/cm^3$) single-crystal [b]	1073	~1			7.2×10^{-7}	[510]
$SrTi_{0.9998}Nb_{0.0002}O_{3-\delta}$ (single crystal)	873	~0.1	4.2×10^{-16}		1.1×10^{-10} cm^3/s	[511]

[a] *Ceramics with various grain size*
[b] *Surface (100)*

Introduction of Ln cations basically reduces the ionic conduction and increases the corresponding activation energy. This trend is clearly demonstrated for Dy-doped $SrTiO_{3-\delta}$ [450]. One should note introduction of Ln cations into $(A,Ln)TiO_{3-\delta}$ may be accompanied by equivalent introduction of cation vacancies which might also be responsible for smaller diffusion coefficients and larger activation energies observed [377, 496-498].

Obviously, the ionic conductivity should be promoted by the presence of acceptor-type cations in B-sublattice, with fixed or variable oxidation state [412, 428, 434, 441, 495, 499-501]. The effect of acceptor doping originates from lowering average oxidation state of B-site cations, weaker B-O bonds and more flexible oxygen coordination around cations in B-sublattice which facilitates formation of oxygen vacancies.

Generally, the oxygen diffusivity proportionally increases with the dopant amount up to a definite level, while further doping induces the separation of secondary phases, structural transformations, defect interactions and formation of vacancy-ordered superstructures; two latter phenomena are especially pronounced for titanates enriched with Fe, Co, Ni or cations with the oxidation state lower than +3 [428, 434, 436, 439, 441, 499, 501-503]. In accordance with calculations [441], the maximum oxygen diffusivity is expected for titanates doped with 20% of Fe; this doping level was confirmed by experimental data [441, 503, 504]. Co-introduction of donor- and acceptor-type dopants into titanates has 2 opposite effects on the oxygen deficiency and ionic transport [427, 448, 501]; on the other hand, the presence of Ln-cations in A-sublattice improves the stability and suppresses the vacancy ordering [501].

Table 1.5.3. Oxygen ionic conductivity, chemical diffusion and surface exchange coefficients of titanates

Composition	T, K	$p(O_2)$, atm	D_{chem}, cm^2/s	σ_O, S/cm	k, cm/s	Method	Reference
$CaTiO_{3-\delta}$	1273	1.2×10^{-4}	7.5×10^{-6}			Conductivity relaxation [b]	[512]
	1073	1.5×10^{-4}	6.3×10^{-7}				
$SrTiO_{3-\delta}$ (single crystal)	1073	$10^{-2}\rightarrow10^{-4}$	7.5×10^{-6}			Conductivity relaxation	[376]
$SrTiO_{3-\delta}$	1273	$\sim10^{-7}$-10^{-6}		8.0×10^{-4}		Conductivity vs. $p(O_2)$ [c]	[386]
$Sr_{0.975}TiO_{3-\delta}$	1273	$\sim10^{-6}$-10^{-4}		2.5×10^{-4}		Conductivity vs. $p(O_2)$	[386]
$BaTiO_{3-\delta}$	1273	5.9×10^{-12}	3.5×10^{-4}		3.0×10^{-2}	Conductivity relaxation	[493]
$Sr_{0.7}La_{0.3}TiO_{3-\delta}$ [a]	1273	wet 5% H_2-Ar $\sim10^{-18}$ at 1073 K		5.7×10^{-3}		Electron-blocking	[412]
$Ba_{0.992}La_{0.01}TiO_{3-\delta}$	1473	3.9×10^{-14}	4.8×10^{-5}		3.5×10^{-3}	Conductivity relaxation	[496]
$SrTi_{0.95}Mg_{0.05}O_{3-\delta}$	1073	H_2 - H_2O - Ar 0.1 - 2.4 - 97.5%		9.9×10^{-4}		Electromotive force	[513]
	973			4.7×10^{-4}			
$BaTi_{0.95}Mg_{0.05}O_{3-\delta}$	1073	H_2 - H_2O - Ar 0.1 - 2.4 - 97.5%		4.7×10^{-5}		Electromotive force	[513]
$SrTi_{0.982}Al_{0.018}O_{3-\delta}$	1273	0.24→0.05	4.9×10^{-4}		1.4×10^{-3}	Conductivity relaxation	[373]
$La_{0.683}Ti_{0.95}Al_{0.05}O_{3-\delta}$	1373	O_2→air	6.2×10^{-8}			Conductivity relaxation [d]	[505]
$SrTi_{0.95}Sc_{0.05}O_{3-\delta}$	1073	H_2 - H_2O - Ar 0.1 - 2.4 - 97.5%		1.9×10^{-3}		Electromotive force	[513]
	973			5.8×10^{-4}			
$Sr_{0.7}La_{0.3}Ti_{0.9}Sc_{0.1}O_{3-\delta}$ [a]	1223	wet 5% H_2-Ar		1.0×10^{-2}		Electron-blocking	[509]
$La_{0.3}Ca_{0.4}Ti_{0.8}Cr_{0.2}O_{3-\delta}$	1173	$9\times10^{-3}\rightarrow0.21$	$\sim7\times10^{-9}$			Conductivity relaxation	[156]
$CaTi_{0.9}Fe_{0.1}O_{3-\delta}$	1273	$\sim10^{-10}$-10^{-2}		4.8×10^{-2}		Conductivity vs. $p(O_2)$	[441]
$SrTi_{0.9}Fe_{0.1}O_{3-\delta}$	1273	$\sim10^{-11}$-10^{-3}		1.8×10^{-2}		Conductivity vs. $p(O_2)$	[441]
$Sr_{0.97}Ti_{0.6}Fe_{0.4}O_{3-\delta}$	1173	0.21		3.1×10^{-2}		Faradaic efficiency	[501]
	1073			8.5×10^{-3}			
$Sr_{0.9}Ti_{0.6}Fe_{0.4}O_{3-\delta}$	1173	0.21		2.2×10^{-3}		Faradaic efficiency	[501]
$BaTi_{0.9}Fe_{0.1}O_{3-\delta}$	1273	$\sim10^{-8}$-10^{-3}		2.5×10^{-3}		Conductivity vs. $p(O_2)$	[441]
$Sr_{0.7}La_{0.2}Ti_{0.6}Fe_{0.4}O_{3-\delta}$	1173	0.21		2.7×10^{-3}		Faradaic efficiency	[501]
$Sr_{0.7}La_{0.3}Ti_{0.95}Co_{0.05}O_{3-\delta}$ [a]	1273	wet 5% H_2-Ar ($\sim10^{-18}$ at 1073 K)		1.2×10^{-2}		Electron-blocking	[412]
	1073			6.2×10^{-3}			
$Sr_{0.7}La_{0.3}Ti_{0.93}Co_{0.07}O_{3-\delta}$ [a]	1273	wet 5% H_2-Ar		1.8×10^{-2}		Electron-blocking	[412]
$SrTi_{0.95}Nb_{0.05}O_{3-\delta}$	1273	$10^{-22}\rightarrow0.21$	1.7×10^{-6}			Conductivity relaxation	[386]

[a] *materials were prepared in 5% H_2 - Ar;*
[b] *all the data on conductivity relaxation were obtained on reduction runs, unless indicated;*
[c] *in conductivity vs. $p(O_2)$ tests σ_O is considered $p(O_2)$-independent;*
[d] *surface limitations are neglected*

The reports on the exchange kinetics in titanates are scarce. This might be associated with wide uncertainties in the determination of the surface kinetics-related parameters due to dominant limitations by the bulk diffusion [247, 377, 492, 497, 505]. Ti atoms located at the surface significantly differ from those in the bulk phase in terms of crystal symmetry, oxygen coordination, strength of B-O bonds etc., which ensures faster rates of the surface processes [506, 507]. Selected experimental results presented in Tables 1.5.2 - 1.5.3 and the equilibration behavior of titanates discussed earlier confirm accelerated rates of the oxygen exchange. Substitution of transition metal cations for titanium increases the contribution of the surface limitations which become essentially pronounced at elevated temperatures [439, 499, 508] due to more substantial improvement of the bulk ionic transport in comparison with the surface exchange.

Finally, one should briefly consider a possible contribution of the protonic conduction into the overall ionic transport in titanates. The proton transport in most perovskites proceeds via so-called Grotthus mechanism which involves hopping of proton species from OH^- groups located in the oxygen sites of the perovskite lattice to neighboring oxygen atoms ([514, 515] and references cited). Nevertheless, the nature of the protonic charge carriers in titanate-based perovskites is arguable. In particular, temperature- and $p(O_2)$-dependent behavior of the electromotive force (e.m.f) across a titanate-based membrane was attributed to migration of hydride species (H^-) or associates of neutral hydrogen atoms or protons with electrons [514]. Although such a possibility was predicted from molecular dynamic simulations [516], formation of substantial amounts of hydride ions may be achieved only at extremely low $p(O_2)$ ($<10^{-20}$ atm), located beyond testing conditions. Moreover, most cations, in particular Ti^{4+}, cannot coexist with hydride species which may cause decomposition of the perovskite phase [517]. More reliable seems the assumption of participation of OH^- groups in the protonic transfer mechanism. Generation of $OH_O^{\bullet}$ species in the oxygen sublattice proceeds in accordance with the process [502, 514, 515]:

$$H_2O + V_O^{\bullet\bullet} + O_O^{\times} = 2OH_O^{\bullet} \qquad \textbf{(Eq. 1.5.7)}$$

The protonic conductivity of an acceptor-doped titanate may be formulated as

$$\sigma_H \sim [A'_{Ti}]^{1/2} p_{H_2O}^{1/2} (1/T) e^{\frac{\Delta S_w}{2R}} e^{\frac{-(\Delta H_w + 2\Delta H_m)}{2RT}} \qquad \textbf{(Eq. 1.5.8)}$$

As follows from Eq. (1.5.8), the protonic diffusion is determined by proton migration enthalpy ΔH_m and solubility of water in the perovskite structure. Since the enthalpy of the hydration process ΔH_w is negative, the term ($\Delta H_w + 2\Delta H_m$) may adopt both positive and negative value; in the latter case, the protonic conduction should decrease on heating.

Localization of protons on oxygen sites is considered to promote the transfer of $OH_O^{\bullet}$ species due to their smaller charge and ionic radius in comparison with $O_O^{\times}$. On the other hand, formation of $OH_O^{\bullet}$ groups induces lattice deformations, i.e. elongation of Ti-OH bonds and reduction of O-OH bonds in comparison with proton-free perovskite structure which causes additional stresses contributing into the overall activation energy of the protonic migration [518-520]. As shown by molecular dynamic simulations [518], $CaTiO_{3-\delta}$- and $SrTiO_{3-\delta}$-based perovskites support both the mechanism of the protonic hopping between two adjacent

oxygen atom within the same octahedron (intra-octahedral mechanism) and the mechanism involving participation of next-nearest neighboring O positions (inter-octahedral mechanism).

Regardless of the specific mechanism of the migration, the protonic conductivity in titanates is rather low (10^{-5} - 10^{-4} at 873 - 1073 K, as can be observed from Table 1.5.4), which is primarily associated with low water solubility in titanates (<1 mol.% [521]).

Table 1.5.4. Protonic conductivity of selected titanate-based materials, determined by EMF technique

Composition	Sweeping gas atmosphere	σ_H, S/cm (1073 K)	σ_H, S/cm (873 K)	E_a, kJ/mol	Reference
$SrTiO_{3-\delta}$ *	H_2-H_2O-Ar ($p(O_2) = 1.3\times10^{-14}$, $p(H_2O) = 1.7\times10^{-4}$ atm at 1073 K)	1.3×10^{-6}	1.4×10^{-6}		[514]
$SrTiO_{3-\delta}$*	H_2-H_2O-Ar ($p(O_2) = 1.3\times10^{-14}$, $p(H_2O) = 0.013$ atm at 1073 K)	1.4×10^{-5}	1.4×10^{-5}		[514]
$SrTi_{0.95}Mg_{0.05}O_{3-\delta}$ **	H_2O-saturated air	4.8×10^{-5}	3.8×10^{-5}		[502]
$SrTi_{0.95}Mg_{0.05}O_{3-\delta}$ **	0.123% H_2 - 2.4% H_2O - Ar	3.7×10^{-5}	1.1×10^{-4}		[513]
$SrTi_{0.95}Mg_{0.05}O_{3-\delta}$ ***	0.123% H_2 - 2.4% H_2O - Ar	5.5×10^{-4}	1.7×10^{-4}	60	[513]
$BaTi_{0.95}Mg_{0.05}O_{3-\delta}$	H_2O-saturated air	2.1×10^{-5}	7.6×10^{-6}	48	[502]
$BaTi_{0.95}Mg_{0.05}O_{3-\delta}$ **	0.123% H_2 - 2.4% H_2O - Ar	2.7×10^{-5}	8.8×10^{-6}		[513]
$BaTi_{0.95}Mg_{0.05}O_{3-\delta}$ ***	0.123% H_2 - 2.4% H_2O - Ar	5.2×10^{-5}	3.1×10^{-5}	72	[513]
$SrTi_{0.9}Al_{0.1}O_{3-\delta}$*	H_2-H_2O-Ar ($p(O_2) = 1.6\times10^{-19}$, $p(H_2O) = 0.015$ atm at 1073 K)	1.92×10^{-4}	8.3×10^{-6}	122	[516]
$CaTi_{0.95}Sc_{0.05}O_{3-\delta}$ **	0.123% H_2 - 2.4% H_2O - Ar		6.7×10^{-5}		[513]
$CaTi_{0.95}Sc_{0.05}O_{3-\delta}$	0.123% H_2 - 2.4% H_2O - Ar		7.0×10^{-4}	56	[513]
$SrTi_{0.95}Sc_{0.05}O_{3-\delta}$	H_2O-saturated air	7.6×10^{-5}	8.1×10^{-5}	20	[502]
$SrTi_{0.95}Sc_{0.05}O_{3-\delta}$ **	0.123% H_2 - 2.4% H_2O - Ar	1.2×10^{-4}	1.8×10^{-4}		[513]
$SrTi_{0.95}Sc_{0.05}O_{3-\delta}$ ***	0.123% H_2 - 2.4% H_2O - Ar	1.1×10^{-3}	2.1×10^{-4}	79	[513]
$SrTi_{0.9}Fe_{0.1}O_{3-\delta}$	H_2-H_2O-Ar ($p(O_2) = 1.0$, $p(H_2O) \approx 1.6\times10^{-4}$ atm)	1.6×10^{-6}	7.1×10^{-7}	40	[514]
$SrTi_{0.9}Fe_{0.1}O_{3-\delta}$	H_2-H_2O-Ar ($p(O_2) = 1.0$, $p(H_2O) = 0.013$ atm)	3.1×10^{-5}	6.9×10^{-6}	67	[514]
$SrTi_{0.6}Fe_{0.4}O_{3-\delta}$	wet O_2	1.0×10^{-4}		90	[514]

** H^+ charge carriers are suggested; ** OH^- transfer is neglected; *** O^{2-} flux is neglected, OH^- transfer dominates*

1.5.5. Thermomechanical behavior

Similar to other characteristics of $ATiO_{3-\delta}$-based compositions, the behaviour of thermal expansion coefficients is strongly influenced by synthesis and measuring conditions. Since most available literature data on the expansion of titanates are essentially presented by those, obtained by XRD studies, and relate to quite various temperature ranges, direct comparison of the TEC values is unreasonable. For example, depending on the temperature interval studied, $BaTiO_{3-\delta}$ has been reported to have extremely low TEC values (~3×10^{-6} K^{-1} at 300 - 500 K [522]) and even exhibits a negative expansion at the conditions where the phase transformations occur [523]. As shown in Table 1.5.5, the relative expansivity for two various samples of $CaTiO_{3-\delta}$ tested under analogous conditions differs by 10 - 20% [524-526].

Table 1.5.5. Thermal expansion coefficients of titanate-based ceramics determined by dilatometry

Composition	T, K	p(O_2), atm	TEC×10^6, K^{-1}	Reference
$CaTiO_{3-\delta}$	300-1273	0.21	13.4	[524]
$CaTiO_{3-\delta}$	300 - 1000	0.21	10.8	[526]
$CaTiO_{3-\delta}$	300-973	0.21	12.2	[525]
$CaTiO_{3-\delta}$ (single crystal)	300-973	0.21	11.1	[525]
$SrTiO_{3-\delta}$	423-1273	0.21 H_2	11.0 10.9	[529]
$Ca_{0.4}La_{0.4}TiO_{3-\delta}$	873-1273	0.21	~11.2	[423]
$Sr_{0.8}La_{0.2}TiO_{3-\delta}$	333-1273	30% H_2-N_2	12.5	[530]
$Sr_{0.7}La_{0.2}TiO_{3-\delta}$	300-1273 300-1273	0.21 5% H_2 - Ar	8.6 9.5	[420]
$Sr_{0.95}Ce_{0.05}TiO_{3-\delta}$	853 - 1373 923 - 1223	0.21 4.2×10^{-19} - 2.9×10^{-13}	12.1 11.7	[527]
$Sr_{0.925}Ce_{0.05}TiO_{3-\delta}$	853 - 1373	0.21	12.0	[527]
$Sr_{0.88}Y_{0.08}TiO_{3-\delta}$	300-1373	0.21	12.0	[247]
$Sr_{0.85}Y_{0.1}Ti_{0.95}Al_{0.05}O_{3-\delta}$	300-1373	0.21	11.2	[247]
$La_{0.7}Ca_{0.3}Ti_{0.8}Cr_{0.2}O_{3-\delta}$	300-1273	0.21	11.5	[231]
$Sr_{0.67}La_{0.33}Ti_{0.92}Mn_{0.08}O_{3-\delta}$	323-1123	0.21 5% H_2-Ar	12.3 13.8	[335]
$Sr_{0.97}Ti_{0.6}Fe_{0.4}O_{3-\delta}$	723-1123	0.21	16.1	[501]
$Sr_{0.9}Ti_{0.6}Fe_{0.4}O_{3-\delta}$	723-1123	0.21	17.2	[501]
$Sr_{0.8}La_{0.2}Ti_{0.6}Fe_{0.4}O_{3-\delta}$	723-1123	0.21	12.0	[501]
$Sr_{0.8}La_{0.2}Ti_{0.45}Fe_{0.55}O_{3-\delta}$	300-1473	0.21	9.3	[531]
$Sr_{0.92}Y_{0.08}Ti_{0.95}Fe_{0.05}O_{3-\delta}$	673-1273	0.21	11.8	[528]
$Sr_{0.85}Y_{0.1}Ti_{0.95}Co_{0.05}O_{3-\delta}$	300-1373	0.21	12.0	[247]
$La_{0.95}Ti_{0.5}Ni_{0.5}O_{3-\delta}$	800-1200	0.21	10.0	[532]
$Sr_{0.67}La_{0.33}Ti_{0.92}Ga_{0.08}O_{3-\delta}$	323-1123	0.21 5% H_2-Ar	7.0 7.9	[335]
$Sr_{0.67}La_{0.33}Ti_{0.92}Mn_{0.04}Ga_{0.04}O_{3-\delta}$	323-1123	0.21 5% H_2-Ar	11.2 13.2	[335]
$Sr_{0.94}Ti_{0.9}Nb_{0.1}O_{3-\delta}$	573-1173	9% H_2-Ar	12.1	[407]

Introducing Ln cations into $Sr_{1-x}Ln_xTiO_{3-\delta}$ under oxidizing conditions results in formation of ordered intergrowths rather than in generation of Ti^{3+} cations. In this respect, the expansion behavior of doped titanates is less obvious in comparison with the perovskites enriched with easily reducible cations. For example, no obvious compositional dependence of the thermally-induced strains was detected for $Sr_{1-x}La_xTiO_{3-\delta}$ series [105]. Generation of A-site cation vacancies basically results in lower TECs [420, 527] due to hindered oxygen losses or suppressed formation of RP-phases (Table 1.5.5).

On the other hand, a decrease in TEC on Ln doping is well pronounced for transition metal-substituted titanates, where the electronic compensation of the variations in cation composition may be realized [501]. Introduction of reducible cations generally increases the thermally-induced strains; such a behavior is consistent with lower TECs of Ti-substituted ferrites, manganites, cobaltites, etc. and is primarily associated with the contribution of the oxygen losses into the overall dimensional changes [438, 501, 528].

Larger ionic radius of Ti^{3+} compared with that of Ti^{4+} (0.67 vs 0.605 Å in 6-fold coordination [133]) is expected to enlarge the cell volume with oxygen losses on reduction. Indeed, an enhancement of the cell parameters of the perovskite phase upon reduction has been observed on numerous titanate-based

compositions [16, 377, 414, 422]. On the other hand, similar to manganite perovskites, formation of cation vacancies induced by oxidation may generate additional unit cells with resultant increasing of the total volume [529, 533]. Furthermore, the thermomechanical behavior of $ATiO_{3-\delta}$-based systems is in most cases interfered by slow equilibration, formation or dissolution of secondary phases on redox cycling, while accumulation of stresses in the perovskite lattice may provoke formation and propagation of cracks. These factors lead to large discrepancies between the experimental results which obscure the comparison of the literature data. Therefore, no unambiguous correlation between the defect equilibria and chemical expansion behavior has been found [70, 527, 529, 533].

For pre-oxidized samples, the volume changes generally occur towards a slight expansion on decreasing $p(O_2)$ due to an enlargement of Ti cations upon reduction, although densification of initially porous specimens as well as kinetics or secondary phase-related factors may result in a slight shrinkage, as shown in Table 1.5.6. The linear expansivity of air-sintered $(Sr,Ln)TiO_{3-\delta}$ on reduction is generally within 0.02 - 0.03% [105, 527, 529], while the presence of reducible cations basically induces more substantial dimensional variations [16, 531]; in the latter case, the thermomechanical behaviour is determined by the reducibility of the corresponding cations.

Table 1.5.6. Relative length changes of titanate ceramics on isothermal redox cycling

Composition	T, K	Initial atmosphere or $p(O_2)$, atm	Final atmosphere or $p(O_2)$, atm	$\Delta L/L_0$, %	Reference
$Sr_{0.9}La_{0.1}TiO_{3-\delta}$ [a]	1273	0.21	10^{-18}	0.01	[105]
$Sr_{0.7}La_{0.3}TiO_{3-\delta}$ [a]	1273	0.21	10^{-18}	-0.01	[105]
$Sr_{0.7}La_{0.3}TiO_{3-\delta}$ [b]	1273 1273	9.9×10^{-17} 9.9×10^{-17}	0.21 9.9×10^{-11}	0.51 0.46	[533]
$Sr_{0.6}La_{0.4}TiO_{3-\delta}$ [a]	1273	0.21	10^{-18}	-0.02	[105]
$Sr_{0.95}Ce_{0.05}TiO_{3-\delta}$ [a]	1173	0.21	2.7×10^{-14}	0.01	[527]
$Sr_{0.925}Ce_{0.05}TiO_{3-\delta}$ [a]	1173 973	0.21 0.21	2.7×10^{-14} 1.9×10^{-14}	0.01 0.02	[527]
$Sr_{0.93}Y_{0.07}TiO_{3-\delta}$ [c]	1103	wet 4% H_2-Ar ($\sim1\times10^{-18}$)	0.2	0.13-0.15	[13]
$Sr_{0.93}Y_{0.07}TiO_{3-\delta}$ - 8YSZ (65-35 vol.%) [c]	1103	wet 4% H_2-Ar ($\sim1\times10^{-18}$)	0.2	0.05	[13]
$Sr_{0.94}Y_{0.04}TiO_{3-\delta}$ - $CeO_{2-\delta}$ (50-50 wt.%) [d]	1173	8% H_2-Ar	0.21	0.13	[534]
$La_{0.7}Ca_{0.3}Ti_{0.5}Cr_{0.5}O_{3-\delta}$ [a]	1273 1073	0.21 0.21	4% H_2-Ar 4% H_2-Ar	within exper. error within exper. error	[163]
$La_{0.4}Sr_{0.6}Ti_{0.4}Mn_{0.6}O_{3-\delta}$ [a]	1090	0.21	wet 4% H_2 - Ar	0.61	[16]
	1090	0.21	20% O_2-Ar (after wet 4% H_2-Ar)	0.42	
$La_{0.2}Sr_{0.8}Ti_{0.7}Fe_{0.3}O_{3-\delta}$ [a]	not indicated	0.21	4% H_2 - 96% N_2	0.10	[535]
$La_{0.2}Sr_{0.8}Ti_{0.5}Fe_{0.5}O_{3-\delta}$ [a]	not indicated	0.21	4% H_2 - 96% N_2	0.10	[535]
$La_{0.2}Sr_{0.8}Ti_{0.45}Fe_{0.55}O_{3-\delta}$ [a]	1271 1170	0.21 0.21	2.5×10^{-4} 2.5×10^{-4}	0.15 0.18	[531] [531]

Preparation conditions: [a] 0.21 atm; [b] 10^{-10} atm, 1773 K; [c] in a flow 4% H_2 - Ar, 1573 K; [d] in a flow 8% H_2 - Ar, 1573 - 1673 K

On the other hand, preliminary generation of a large quantity of oxygen vacancies achieved at elevated temperatures under low $p(O_2)$ conditions and subsequent oxidation of the perovskite induces a dramatic enhancement of the dimensions which may amount to 0.1 - 0.5% in the linear scale. The origins of

such a behaviour may be complex and are associated with a slow re-distribution of the defects in the perovskite structure which may delay from fast $p(O_2)$ variations, cracking or contribution of secondary phases/ordered domains at high $p(O_2)$ into the volume changes. In accordance with large variations in the oxygen nonstoichiometry, pre-reduced titanates doped with donor-like Ln or Nb cations show larger volume changes, at least in terms of the cell parameters [407, 464, 529].

As discussed in previous sections, a preliminary step of high-temperature reduction is generally required in order to improve the transport and electrocatalytic properties of titanates. Therefore, any oxidation of preliminary reduced anode material should be avoided; in particular, $p(O_2)$ changes in the range ~10^{-16} - 10^{-10} atm induce ~0.5% linear strain of pre-reduced $Sr_{0.7}La_{0.3}TiO_{3-\delta}$, unacceptable for the electrochemical applications [533].

1.5.6. Electrochemical properties

Analogously with other perovskite-based anodes, the electrochemical performance of titanates is strongly influenced by preparation and testing conditions. Apart from the common origins of the discrepancies, for the present system the behavior is complicated by the slow equilibration kinetics, and a comparison of results obtained for different titanate-based anodes in various studies is in most cases unreasonable.

Selected results on the electrochemical behaviour of titanate-based anodes and related composites are shown in Figs. 1.5.10 - 1.5.12 and Table 1.5.7. Despite the high electronic conductivity of $ATiO_{3-\delta}$-based perovskites under low-$p(O_2)$ conditions (above 100 - 1000 S/cm) reported in numerous studies [13, 105, 406, 460], most titanate anodes are coated with Pt, Au or other metallic paste. Comparing the level of the polarization resistances obtained for the covered anodes with a few data for uncoated ones, one may conclude that such a modification indeed results in a strong improvement of the electrochemical performance, primarily due to a promotion of elementary steps involved in the oxidation process [7, 388, 416, 536].

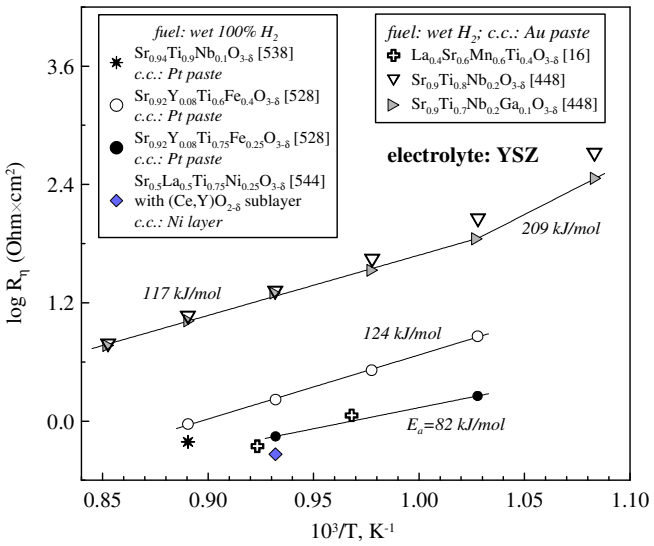

Fig. 1.5.10. Polarization resistance of selected titanate-based anodes deposited onto YSZ electrolyte

Table 1.5.7. Power densities of selected cells with titanate-based anodes

Anode	Electrolyte (thickness, μm)	Cathode	Fuel	T, K	P_{max}, mW/cm^2	Reference
$Sr_{0.8}La_{0.2}TiO_{3-\delta}$-CGO20 (50:50 wt.%), impreg. with Ni ***c.c.: Pt paste***	LSGM (500)	BSCF	H_2 - H_2O (97-3%)	1073	270	[547]
Layered $Sr_{0.8}La_{0.2}TiO_{3-\delta}$ / Ni-CSO20 (50:50 wt.%) / Ni-YSZ (50:50 wt.%)	YSZ (~10)	LSM – YSZ (graded)	dry H_2	1073	850	[545]
			dry H_2 + H_2S (100 ppm)	1073	700	
$Sr_{0.7}La_{0.2}TiO_{3-\delta}$ impreg. with CGO20 and Cu; ***c.c.: Ag paste***	8YSZ (75)	LSCo impreg. into 8YSZ	wet pure H_2	1023	400	[420]
				873	150	
$Sr_{0.75}La_{0.25}TiO_{3-\delta}$-8YSZ (50-50%), ***c.c.: Au mesh***	8YSZ (~2000)	LSM - 8YSZ (graded)	H_2	1173	110	[416]
$Sr_{0.71}La_{0.29}TiO_{3-\delta}$-8YSZ (50-50%), ***c.c.: Au mesh***	8YSZ (~2000)	LSM - 8YSZ (graded)	H_2	1173	120	[416]
			wet 5% H_2-Ar	1173	60	
$Sr_{0.6}La_{0.4}TiO_{3-\delta}$ ***c.c.: Pt paste***	YSZ (160)	LSM	H_2 - H_2O (97-3%)	1273	340 (initial)	[105]
$Sr_{0.895}Y_{0.07}TiO_{3-\delta}$ - NiO - 8 YSZ (graded) ***c.c.: not indicated***	8YSZ (~14) sublayer CGO20	LSCo - 8YSZ (67 - 33 vol.%)	dry H_2	1123	1400	[452]
				1073	850	
$Sr_{0.88}Y_{0.08}TiO_{3-\delta}$-8YSZ (50-50 wt.%) , impreg. with CeO_2 and Ru, ***c.c.: Pt mesh***	8YSZ (~10)	LSM - YSZ (50 - 50 wt.%)	H_2O - H_2 - Ar (3 - 4 - 93%)	1073	510	[548]
				873	240	
$Sr_{0.88}Y_{0.08}TiO_{3-\delta}$ - $Ce_{0.6}La_{0.4}O_{2-\delta}$ - Pd (49.25-49.25-1.5 wt.%) ***c.c.: Au paste***	LSGM (300) Sublayer CLO40	SmSCo	dry H_2	1123	1000	[539]
				1073	580	
$Sr_{0.88}Y_{0.08}TiO_{3-\delta}$-$CeO_{2-\delta}$ (50-50 wt.%); ***c.c.: Au paste***	8YSZ (300)	LSM - 10ScYSZ (70 - 30 wt.%)	3% H_2O- H_2	1173	160	[549]
			3% H_2O- CH_4	1173	140	
$Sr_{0.67}La_{0.33}Ti_{0.95}Sc_{0.05}O_{3-\delta}$-YSZ (graded) ***c.c.: Au paste***	YSZ (2000)	Pt	H_2 - H_2O (97-3%)	1173	130	[447]
			CH_4 - H_2O (97-3%)	1173	120	
$Sr_{0.67}La_{0.33}Ti_{0.92}Sc_{0.08}O_{3-\delta}$-YSZ (graded); ***c.c.: Au paste***	YSZ (2000)	Pt	H_2 - H_2O (97-3%)	1173	110	
$La_{0.73}Sr_{0.26}Cr_{0.45}Ti_{0.55}O_{3-\delta}$ - CGO20 (50-50 wt.%) ***c.c.: Au paint***	8YSZ (300)	Pt	0.5% H_2S - CH_4	1123	120	[212]
$La_{0.4}S_{0.6}Mn_{0.6}Ti_{0.4}O_{3-\delta}$ - 8YSZ (50-50 wt.%), ***c.c.: Au paste***	8YSZ (200)	LSM - 8YSZ	wet H_2	1129	360 (0.7 V)	[16]
$CaTi_{0.9}Fe_{0.1}O_{3-\delta}$-Ni (20-80 wt.%); ***c.c.: not indicated***	8YSZ (500)	LSM	wet H_2	1273	220 (0.6 V)	[550]
$Sr_{0.67}La_{0.33}Ti_{0.92}Mn_{0.04}Ga_{0.04}O_{3-\delta}$-8YSZ (graded), ***c.c.: Au paste***	8YSZ (330)	LSM	wet H_2	1223	500	[540]
			wet 5% H_2 - Ar	1223	160	
			wet CH_4	1223	350	
$Sr_{0.9}Ti_{0.7}Ga_{0.1}Nb_{0.2}O_{3-\delta}$-8YSZ (70-30 wt.%); ***c.c.: Au paste***	8YSZ (300)	LSM - 8YSZ (50 - 50 wt.%)	3% H_2O-H_2	1073	70	[448]

The results were obtained with the following electrolytes and cathodes: $Zr_{0.84}Y_{0.16}O_{2-\delta}$ [16, 212, 416, 420, 448, 452, 540, 548-550], $La_{0.8}Sr_{0.2}Ga_{0.83}Mg_{0.17}O_{3-\delta}$ [539], $La_{0.9}Sr_{0.1}Ga_{0.8}Mg_{0.2}O_{3-\delta}$ [547], $La_{0.6}Sr_{0.4}MnO_{3-\delta}$ [550], $La_{0.8}Sr_{0.2}MnO_{3-\delta}$-YSZ [416, 545], $La_{0.8}Sr_{0.2}MnO_{3-\delta}$-10ScSZ [549], $(La_{0.75}Sr_{0.25})_{0.95}MnO_{3-\delta}$-8YSZ [448], $La_{0.65}Sr_{0.3}MnO_{3-\delta}$ - 8YSZ [16], $La_{0.6}Sr_{0.3}MnO_{3-\delta}$-YSZ [548], $La_{0.6}Sr_{0.4}CoO_{3-\delta}$ - 8YSZ [420, 452], $Sm_{0.5}Sr_{0.5}CoO_{3-\delta}$ [539], $Ba_{0.5}Sr_{0.5}Co_{0.8}Fe_{0.2}O_{3-\delta}$ [547].

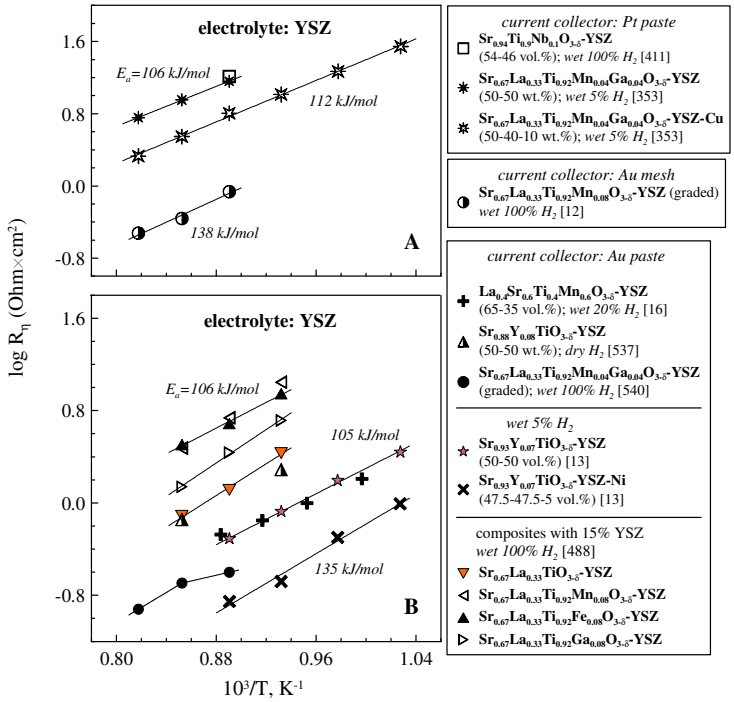

Fig. 1.5.11. Polarization resistance of selected titanate-based composite anodes deposited onto YSZ electrolyte

As a confirmation of the small effect of the electronic conductivity on the electrochemical performance, highly-conductive donor-doped titanates show extremely poor performances [215, 411, 537], in accordance with lowering the oxygen ionic conduction on increasing dopant amount [407, 450, 501]. Moreover, the characteristics of such electrodes are strongly related with the conditions of the electrode processing. In particular, individual anodes $Sr_{0.94}Ti_{0.9}Nb_{0.1}O_{3-\delta}$ deposited onto YSZ and covered with Pt paste, showed polarization resistance in the range 0.5 - 160 Ohm×cm^2 at 1123 K, depending on the sequence of reduction or oxidation runs [411, 538].

The anode characteristics can be improved by fabrication of composite anodes (Fig. 1.5.11, Table 1.5.7). For example, the anode $Sr_{0.88}Y_{0.08}TiO_{3-\delta}$ - $Ce_{0.5}La_{0.5}O_{2-\delta}$ (50 - 50 wt.%) deposited onto LSGM electrolyte with $Ce_{0.5}La_{0.5}O_{2-\delta}$ buffer layer showed the power density in dry H_2 at 1123 K as high as 450 mW/cm^2, which might be enhanced up to 1000 mW/cm^2 by Pd impregnation into the anode, in accordance with improved catalytic activity [539]. Composite anodes (Sr,La)$TiO_{3-\delta}$ - YSZ (50-50 wt.%) covered with Au paste rendered the polarization resistances in the range 0.9 - 1.3 and 2.0 - 2.5 Ohm×cm^2 at 1173 K in wet H_2 and CH_4, respectively. Power densities observable on cells with the corresponding anodes were as high as 100 - 120 mW/cm^2 at 1173 K with pure hydrogen as fuel; the major performance losses were associated with a large electrolyte thickness (2 mm). Although the results obtained for anode compositions with various doping level were scattered, somewhat better results were obtained for 25 - 29% of La [416]. This amount of donor atoms was shown to be acceptable to ensure a high level of the electronic conduction, while further La-doping might induce formation of ordered domains and hamper the ionic conduction.

Nevertheless, most studies have been carried out with derivatives of $Sr_{0.67}La_{0.33}TiO_{3-\delta}$, containing a larger amount of donor cations (Figs. 1.5.11 - 1.5.12). Such a choice was related with the necessity to suppress the decrease in the concentration of n-type charge carriers induced by introduction of acceptor cations; on the other hand, the presence of low-valent cations ensured a better structural tolerance towards La introduction and provided an enhanced level of the ionic conduction. Quite promising results were obtained for Mn-doped $Sr_{0.67}La_{0.33}TiO_{3-\delta}$-based anodes, yielding the polarization resistance as low as 0.45 and 1.2 Ohm×cm^2 at 1173 K in wet H_2 and wet CH_4 fuels, although the information on the anode processing is scarce [12]. Partial replacement of Mn with Ga enables to achieve the R_η of 0.2 Ohm×cm^2 in wet H_2 at 1173 K. Maintaining the anode in hydrogen resulted in a gradual improvement of the performance [540, 541].

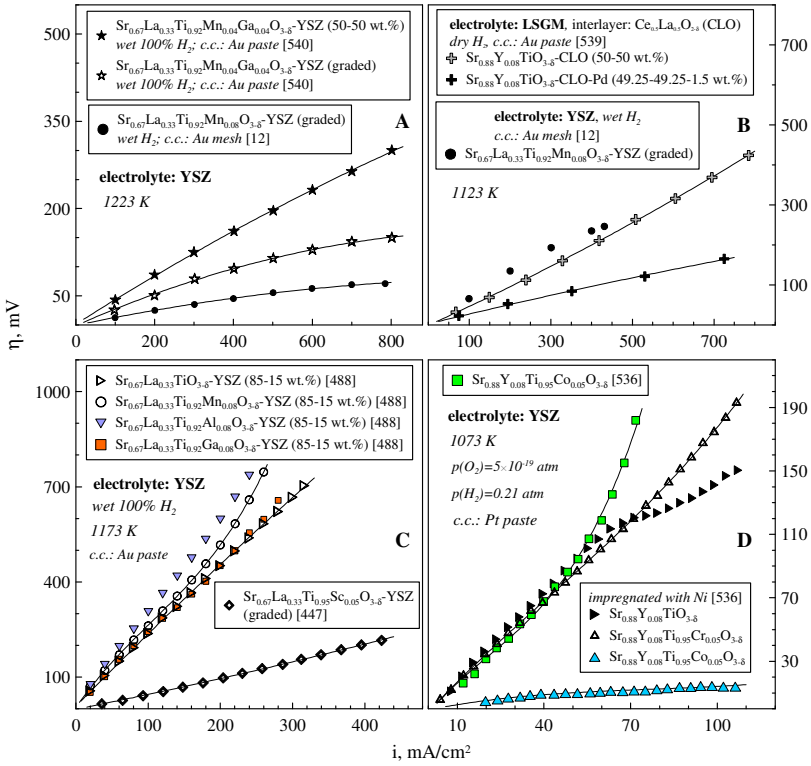

Fig. 1.5.12. Polarization curves of selected titanate-based anodes

A positive impact of Fe-doping into $Sr_{0.67}La_{0.33}TiO_{3-\delta}$ on the anode characteristics has been reported [542, 543]; the optimum performance was found for ~50% of Fe. The polarization resistance of composite anodes varied in the range 1 - 2 Ohm×cm^2 at 1173 K in wet hydrogen; more promising results were obtained for $Sr_{0.92}Y_{0.08}Ti_{0.75}Fe_{0.25}O_{3-\delta}$-based anodes (0.7 Ohm×cm^2 at 1073 K) [528]. Acceptable electrode activity was achieved upon doping with Sc [447], Co [536], Ni [544], consistently with larger amount of oxygen vacancies, higher ionic conductivity and/or catalytic activity towards fuel oxidation processes. Introduction of Cr possessing a low catalytic activity caused large polarization resistances [163, 212, 538] (Fig. 1.5.12).

In accordance with transport and thermomechanical properties, the electrochemical activity of titanate anodes may be improved by preliminary high-temperature reduction [13, 105, 464]. Unfortunately, no literature data on comparative behaviour of preliminary reduced vs. oxidized anode layers are available,

primarily due to peculiarities of the procedure of the cell preparation and operation. In this respect, one may note studies on cone-shaped $Sr_{0.94}Ti_{0.9}Nb_{0.1}O_{3-\delta}$ anode on polarization cycling, where preliminary cathodic polarization accelerates the subsequent electrode processes and reduce the polarization resistance [411]. Similar to the transport and thermomechanical behaviour, most titanate-based electrodes showed a specific feature, associated with fast and in some cases irreversible performance deterioration observable on oxidation. For example, the composite anode $Sr_{0.94}Ti_{0.9}Nb_{0.1}O_{3-\delta}$ - YSZ showed a 2-fold increase in the polarization resistance after exposures to high $p(O_2)$ and subsequent switch to H_2 [411]. $Sr_{0.895}Y_{0.07}TiO_{3-\delta}$ - YSZ - Ni anode showed a satisfactory tolerance towards cycling between H_2, N_2 and air at 1073 K, while a similar procedure at 973 K induced a 35% loss in the power density after 200 cycles [452]. On the other hand, Ni-cermet anode with $Sr_{0.8}La_{0.2}TiO_{3-\delta}$-based support was shown to be capable to endure at least 5 cycles dry H_2 - air, without degradation of the performance; considering a poor tolerance of Ni-based anodes towards oxidation, the presence of titanate layer seems beneficial [545].

Titanate-based electrodes are characterized by a satisfactory chemical compatibility with YSZ electrolyte, although the stability may be deteriorated by Ti diffusion into the electrolyte. No reaction products between $(Sr,Ln)TiO_{3-\delta}$ and YSZ could be observed up to 1623 - 1823 K [247, 377, 416, 537]. The presence of transition metal cations, such as Fe, in the perovskite structure significantly affects the compatibility [501, 528, 531]: in particular, interaction of $SrTi_{1-x}Fe_xO_{3-\delta}$ with YSZ was detected at temperatures above 1273 K, irrespective to Ti:Fe ratio [501]. On the other hand, the interaction may be suppressed by appropriate doping with Ln cations or introduction of A-site cation vacancies [407, 420, 501]. In contrast, studies by Burnat et al. showed a worse compatibility of $Sr_{0.7}La_{0.2}TiO_{3-\delta}$ in comparison with the stoichiometric analogue [546]. Incorporation of Ti into the zirconia lattice is detrimental for the ionic transport ([89, 103] and references cited) which necessitates a search of the optimum cation ratio in the perovskite composition in order to expand the temperature range acceptable for the electrode preparation. Promising results were obtained for $Sr_{0.94}Ti_{0.9}Nb_{0.1}O_{3-\delta}$, chemically compatible with YSZ in air and 9% H_2 - Ar at 1523 K [411]. No secondary phase formation between $Sr_{0.7}La_{0.2}TiO_{3-\delta}$ in contact with CGO10 was detected at 1573 - 1673 K [546].

Summarizing the behaviour of titanate-based electrodes, one may note that addition of titanates in appropriate proportions to ionic conducting and/or catalytically active components significantly widens the applicability of the related electrochemical cells. The main concern, however, remains the low tolerance towards oxidizing atmospheres leading to strong and irreversible changes in the anode microstructure, degradation of the functional characteristics of the electrode constituents, etc.

1.6. Molybdate-based double perovskites as alternative anode materials

Considering the stability under reducing conditions, the choice of potential anode materials may be extended to other perovskite-related structural groups. A remarkable success in terms of electrochemical applications has been achieved with doped molybdates $A_2(Mo,B)_2O_{6-\delta}$ (A = Ca, Sr, Ba, B = Mg, Mn, Fe, Co, Ni) ordered in B-sublattice due to large differences between the charges and/or sizes of molybdenum and

substituent cation. Formation of oxygen-deficient perovskite-like structure becomes possible due to coexistence of highly-valent Mo species ensuring the conservation of oxygen sublattice and the cations in low oxidation states capable to adopt multiple oxygen coordination which stabilizes oxygen vacancies. The ability of Mo to accept electrons and form low-coordinated molybdyl ions is also beneficial for providing the electronic and ionic conductivity [1, 129, 551]. Reasonable activity of Mo-containing compounds towards reforming processes [552-554] is expected to promote the performance of molybdate anodes in natural fuels.

Table 6.1. Total conductivity in reducing atmospheres and thermal expansion coefficients of selected molybdate-based double perovskite materials.

Composition	Total conductivity		Thermal expansion			Reference
	Gas atmosphere or $p(O_2)$, atm	σ_{1073}, S/cm	Gas atmosphere or $p(O_2)$, atm	T, K	$TEC \times 10^6$, K^{-1}	
$CaMoO_{3+\delta}$	5% H_2 - N_2	760	air, N_2, H_2	300 - 1273	11.0	[558, 559]
$Sr_2MgMoO_{6-\delta}$	10^{-17}	0.64				[556]
$Sr_2MgMoO_{6-\delta}$	7×10^{-21}	8.6	0.21	691 - 1074	12.7	[129]
$Sr_{1.4}La_{0.6}MgMoO_{6-\delta}$	5% H_2-Ar	5.0				[557]
$Ba_2MnMoO_{6-\delta}$	dry H_2	1.7	H_2	873 - 1173	15.6	[123]
sintered in 5% H_2 - Ar						
$Ca_2FeMoO_{6-\delta}$	H_2	380				[560]
$Sr_2FeMoO_{6-\delta}$	H_2	220	N_2	300 - 1273	13.9	[560]
$Sr_2Fe_{1.33}Mo_{0.67}O_{6-\delta}$	3% H_2O - H_2	16				[124]
$Sr_2Fe_{1.5}Mo_{0.5}O_{6-\delta}$	H_2	860				[561]
$Ba_2FeMoO_{6-\delta}$	H_2	30	N_2	300 - 1273	13.3	[560]
sintered in 5% H_2 - Ar						
$Ba_2FeMoO_{6-\delta}$	dry H_2	190	H_2	873 - 1173	14.3	[123]
sintered in 5% H_2 - Ar						
$Sr_2CoMoO_{6-\delta}$	5% H_2 - Ar	9.0×10^{-2}				[562]
$Sr_2Co_{1.1}Mo_{0.9}O_{6-\delta}$	H_2	7.5				[125]
$Sr_2Co_{1.15}Mo_{0.85}O_{6-\delta}$	H_2	8.2				[125]
$Sr_2Co_{1.2}Mo_{0.8}O_{6-\delta}$	H_2	3.8	0.21	873 - 1173	15.8	[125]
$Ba_2CoMoO_{6-\delta}$	dry H_2	4.0				[123]
$Sr_2NiMoO_{6-\delta}$	5% H_2 - Ar	1.9				[562]
$Sr_2NiMoO_{6-\delta}$	H_2	53	0.21	300 - 1253	12.1	[563]
$Ba_2NiMoO_{6-\delta}$	dry H_2	2.3				[132]
$Sr_2MgWO_{6-\delta}$	5% H_2 - Ar	4.0×10^{-4}	0.21	300 - 1473	13.2	[564, 565]

Synthesis of $Sr_2MgMoO_{6-\delta}$ is generally accompanied by formation of small amounts of alkali-earth carbonates and $SrMoO_4$; the quantity of the impurities increases in air or in diluted CH_4 atmospheres [555, 556]. The presence of the secondary phases is undesirable for the electrochemical applications and preliminary reduction step is required in order to achieve an acceptable electronic conductivity. Selected functional properties of molybdate-based double perovskites are shown in Table 6.1. The conductivity of the double perovskite $Sr_2MgMoO_{6-\delta}$ and its derivatives after reduction varies in the range 5 - 10 S/cm which is close to the limit acceptable for anode applications, while the material shows reasonable chemical and structural stability and tolerance of the functional characteristics towards moderate oxidation [129, 556, 557].

Pre-reduction of $Sr_2MgMoO_{6-\delta}$ and subsequent annealing in air during the process of the preparation of electrode layers enables to obtain anodes with promising level of the electrochemical activity [126, 129]; in particular, the polarization resistances in the range 0.2 - 1 Ohm×cm^2 were observed, as shown in Table 6.2. The power density of cells with $Sr_2MgMoO_{6-\delta}$ anode (coated with Pt paste) and LSGM electrolyte of 300 μm of the thickness separated with CeO_2-based sublayer achieves 840 mW/cm^2 at 1073 K in dry H_2 [126]. The performance remains on a constant level on introduction of 5 ppm H_2S and shows only a 2.5% drop after 50 cycles (Fig. 6.1). An advantage of molybdate-based anodes is high performance in hydrocarbon fuels amounting to 440 and 350 mW/cm^2 at 1073 K in dry CH_4 and 97% CH_4 - 3% H_2O, respectively [126, 129]. An improvement of the performance with La doping up to 40% was reported, possibly due to generation of additional n-type charge carriers [557]. The power density drop after 50 operation cycles in CH_4-containing fuel achieves 10 - 15% [126, 557].

Application of $Sr_2MgMoO_{6-\delta}$-based materials imposes stringent requirements on the operation conditions, primarily due to formation of $SrMoO_4$ on oxidation. On the other hand, reduction at temperatures above 1173 K is accompanied by decomposition into $Sr_3Mo_2O_7$-based phase, MgO and Mo [555]. High content of alkali-earth cations in both sublattices makes the material susceptible towards the presence of H_2O, CO_2, SO_x in fuel atmosphere, while the presence of molybdenum induces volatilization or surface-diffusion phenomena ([14, 80, 266] and references cited). Another concern relates to insufficient chemical compatibility of $Sr_2MgMoO_{6-\delta}$ with solid electrolytes which necessitates introducing buffer layers [129, 556].

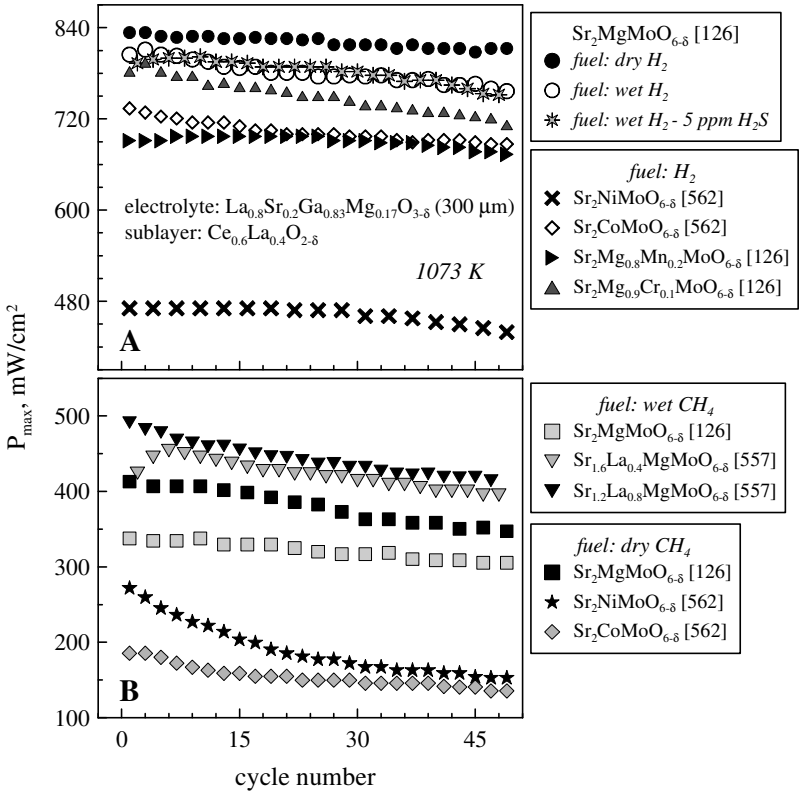

Fig. 6.1. Dependencies of the power densisties exhibited by cells with molybdate-based anodes on redox cycle numbers. Current collectors are the same as in Table 6.2.

Table 6.2. Polarization resistances and polarization values under zero and 500 mA/cm^2 of selected double perovskite molybdate-based anodes.

Composition	Electrolyte	T, K	Gas atmosphere or p(O_2), atm	R_η, Ohm×cm^2	η, mV (i = 500 mA/cm^2)	Reference
$Sr_2MgMoO_{6-\delta}$ *c.c: Pt ink*	$La_{0.8}Sr_{0.2}Ga_{0.8}Mg_{0.2}O_{3-\delta}$	1073	wet 5% H_2 - Ar	0.89		[556]
$Sr_2MgMoO_{6-\delta}$ *c.c: Pt ink*	$La_{10}Si_{5.5}Al_{0.5}O_{26.75}$	1073	wet 5% H_2 - Ar	130		[566]
$Sr_2MgMoO_{6-\delta}$ *c.c: Pt ink*	$La_{10}Si_{5.5}Al_{0.5}O_{26.75}$ with CGO20 sublayer	1073	wet 5% H_2 - Ar	0.87		[566]
$Sr_2MgMoO_{6-\delta}$ *c.c.: Pt paste*	$La_{0.8}Sr_{0.2}Ga_{0.83}Mg_{0.17}O_{3-\delta}$	1073	H_2		71	[126]
			5% H_2S - H_2		95	
			CH_4		200	
$Sr_2Mg_{0.9}MoCr_{0.1}O_{6-\delta}$ *c.c.: Pt paste*	$La_{0.8}Sr_{0.2}Ga_{0.83}Mg_{0.17}O_{3-\delta}$	1073	H_2		110	[126]
$Sr_2Mg_{0.8}MoMn_{0.2}O_{6-\delta}$ *c.c.: Pt paste*	$La_{0.8}Sr_{0.2}Ga_{0.83}Mg_{0.17}O_{3-\delta}$	1073	H_2		140	[126]
$Ba_2MnMoO_{6-\delta}$ *c.c.: Ag paste*	$La_{0.8}Sr_{0.2}Ga_{0.83}Mg_{0.17}O_{3-\delta}$	1073	100% H_2	1.1	250	[123]
$Sr_2FeMoO_{6-\delta}$ *c.c.: not indicated*	$La_{0.9}Sr_{0.1}Ga_{0.8}Mg_{0.2}O_{3-\delta}$ sublayer: CSO82	1123	H_2	0.28		[560]
$Sr_2Fe_{1.33}Mo_{0.67}O_{6-\delta}$ *c.c: Au paste*	$La_{0.8}Sr_{0.2}Ga_{0.83}Mg_{0.17}O_{3-\delta}$	1073	3% H_2O - H_2	0.18		[124]
$Sr_2Fe_{1.5}Mo_{0.5}O_{6-\delta}$ *c.c: Au paste*	$La_{0.9}Sr_{0.1}Ga_{0.8}Mg_{0.2}O_{3-\delta}$	1123	3% H_2O -H_2	0.21		[561]
		1073		0.27		
$Ba_2FeMoO_{6-\delta}$ *c.c: Ag paste*	$La_{0.8}Sr_{0.2}Ga_{0.83}Mg_{0.17}O_{3-\delta}$	1073	100% H_2	0.73	120	[123]
$Ba_2CoMoO_{6-\delta}$ *c.c: Ag paste*	$La_{0.8}Sr_{0.2}Ga_{0.83}Mg_{0.17}O_{3-\delta}$	1073	100% H_2	0.61	180	[123]
$Sr_2NiMoO_{6-\delta}$ *c.c: Ag paste*	$La_{0.9}Sr_{0.1}Ga_{0.8}Mg_{0.2}O_{3-\delta}$	1073	H_2	0.26		[563]

The double perovskite structure enables a partial or complete substitution of Mg in B-sublattice with transition metal cations generating $Mo^{6+/5+}$ and $B^{3+/2+}$ redox couples. In particular, for $A_2FeMoO_{6-\delta}$ double perovskites, decreasing A-site cation radius promotes delocalization of electrons in 2*p*, 3*d* and 4*d* bands of oxygen, iron and molybdenum. This, in particular, leads to increasing conductivity in the order $Ba_2FeMoO_{6-\delta}$<$Sr_2FeMoO_{6-\delta}$<$Ca_2FeMoO_{6-\delta}$ and transition from small polaron to metallic-type behavior [560].

On the other hand, the degree of the ordering and the stability is lower for smaller A-site cations; for example, $Ca_2FeMoO_{6-\delta}$ synthesized in H_2 - Ar atmospheres shows a substantial decomposition into the brownmillerite phase and $CaMoO_4$ on placing into N_2 environments [560]. Introduction of transition metal cations other than Fe into B-sublattice was shown to be less beneficial, primarily due to poor stability. In particular, $Sr_2CoMoO_{6-\delta}$ and $Sr_2NiMoO_{6-\delta}$ showed decomposition in 5% H_2 - Ar at 1073 K [562], although the formation of metallic phases might promote the oxidation processes.

A promising electrode activity was found for $Sr_2FeMoO_{6-\delta}$-based anodes, due to the optimum combination of oxygen vacancy concentration, stability and expansion behaviour. In particular, the power density of dry H_2-fuelled cell achieved 830 mW/cm^2 at 1123 K, exhibiting the drop of 2.7% per 20 hours (Fig. 6.1). In commercial city gas contaminated with H_2S, the power density shows a decrease per initial 3

hours of operation down to 436 mW/cm^2 at 1073 K followed by stable working, without detectable carbon or sulfur deposition [560]. Nevertheless, the overall performance of $Sr_2FeMoO_{6-\delta}$ anodes is inferior in comparison with Mg-substituted analogue.

1.7. Final remarks.

In accordance with literature data on alternative anode materials, most studies have been focused on titanates, chromites and manganites. Briefly, their potential for electrochemical applications may be summarized as follows.

Titanates. $ATiO_{3-\delta}$-based compositions offer a high level of the electronic conductivity at low $p(O_2)$, moderate thermal expansion, stability in reducing atmospheres, contribution of the ionic transfer, chemical compatibility with solid electrolytes, while titanate-based anodes showed a tolerance towards hydrocarbons or S-containing gas species. However, the optimum properties of most titanates can only be achieved after preliminary high-temperature reduction which complicates the procedure of the cell preparation. From this viewpoint, an oxidation often leads to drastic and irreversible chemical or structural transformations with resultant deterioration of mechanical and transport characteristics. Similar features are relevant to other n-type conductors, such as vanadates, niobates, molybdates, etc.

Chromites. $LnCrO_{3-\delta}$ and their derivatives are notable due to their high stability in a wide $p(O_2)$ range, reasonable thermal and chemical expansion, suppressed reactivity with commonly used solid electrolytes. The perovskite structure enables to accommodate a wide range of dopants which allows to tune the functional properties. On the other hand, the low $p(O_2)$ drop of the conductivity makes the issue of the electronic transfer critical for electrochemical applications, while the low level of oxygen transport and catalytic activity necessitates introduction of additional components into the anode. The volatility of Cr-containing species and the tendency towards formation of secondary phases on the surface impose stringent requirements on the gas atmosphere composition and the cell processing conditions.

Manganites. Manganite perovskites possess a high level of the electronic conductivity, which can be kinetically conserved even under anodic conditions, especially if the composition is stabilized with an appropriate dopant. Most authors report an enhanced ionic transport and catalytic activity towards oxidation processes. However, the formation of secondary phases and the conductivity drop under low $p(O_2)$ deteriorates the electrode performance which, in particular, induces degradation of the long-term performance. Manganites exhibit enhanced chemically-induced expansion or contraction; the thermomechanical behaviour is complicated by formation/consumption of cation and oxygen vacancies for the same composition in a wide $p(O_2)$ region. Moreover, high cation diffusivity affects the sintering behaviour which may cause microstructural problems for the electrode layers. High mobility of Mn and reduced stability of the perovskite phase promote the interaction/interdiffusion phenomena at the interface electrode/electrolyte. Similar peculiarities are typical for Fe- or Co-enriched perovskites.

As shown by the examples, no alternative anode composition has been elaborated so far capable to compete with conventional Ni cermets. On the other hand, an appropriate combination of the positive characteristics relevant to the groups presented may offer a possibility to achieve satisfactory electrode

performance and stability. To some extent, such an approach has been realized by preparation of compositions at the joints between the groups i.e. (La,Sr)(Cr,Mn)$O_{3-\delta}$, (La,Sr)(Mn,Ti)$O_{3-\delta}$, (La,Sr)(Cr,Ni)$O_{3-\delta}$, (La,Sr)(Cr,Fe)$O_{3-\delta}$, etc. However, the relationships between chemical composition, functional characteristics and anode properties for most materials are unclear, while promising results have been essentially obtained on composite electrodes, in particular those modified by distribution of metallic phase over the anode layer. With this respect, it would be attractive to reveal the intrinsic properties of the perovskite phases responsible for the polarization behaviour of the corresponding electrodes. The present study will thus evaluate selected derivatives of chromites, manganites as well as complex compositions like (La,Sr)(Cr,Mn)$O_{3-\delta}$ and (La,Sr)(Mn,Ti)$O_{3-\delta}$ in terms of the structural, microstructural, transport and thermomechanical characteristics as well as their electrode activity.

Chapter 2. Experimental

Synthesis and ceramic processing

The conditions of the material processing as well as starting chemicals are listed in Table 2.1. Powders $Zr_{0.85}Y_{0.15}O_{2-\delta}$ (8YSZ), $Ce_{0.8}Gd_{0.2}O_{2-\delta}$ (CGO20) and $(La_{0.9}Sr_{0.1})_{0.98}Ga_{0.8}Mg_{0.2}O_{3-\delta}$ (LSGM) were supplied by Tosoh and Praxair. Synthesis of nano-sized CGO20 was carried out by cellulose-precursor technique; the details can be found in [567].

Most compositions were prepared by the glycine-nitrate process (GNP), a self-sustaining combustion technique which enables to produce submicron-sized homogeneous powder with a large surface area. The method is essentially preferable when the solid state synthesis is stagnated due to kinetic reasons. This technique was employed for the synthesis of perovskite-type $(La_{1-x}Sr_x)_{0.95}Mn_{0.5}Cr_{1-x}Ti_xO_{3-\delta}$ (x = 0 - 0.5), $(La_{1-x}Sr_x)_{0.95}Mn_{0.5}Ti_{0.5}O_{3-\delta}$ (x = 0.15 - 0.75, y = 0 - 0.05), $(La_{0.9}Sr_{0.1})_{0.95}Cr_{0.85}Mg_{0.1}Ni_{0.05}O_{3-\delta}$ and $(La_{0.75}Sr_{0.25})_{0.95}Cr_{1-x}Fe_xO_{3-\delta}$ (x = 0.3 - 0.4). The stoichiometric amounts of the corresponding precursors indicated in Table 2.1 were dissolved in distilled water followed by addition of 1.5-fold excess of glycine. Insoluble TiO_2 was added to the aqueous mixture of other precursors. Irrespective of the initial products, the aqueous mixture was placed into a beaker with the volume of 1 - 2 L, covered with a steel grid and evaporated on a hotplate until autoignition. The resultant foam-like powders were annealed at 1073 - 1273 K for 2 hours to remove organic impurities. Due to low homogeneity of Ti-containing materials, additional annealing steps at 1473 - 1573 K with intermediate regrinding in a planetry ball-mill with zirconia balls were performed. The series $(La_{1-x}Sr_x)_{1-y}Mn_{0.5}Ti_{0.5}O_{3-\delta}$ (y = 0 - 0.03) was synthesized using GNP technique in the Institute of Solid State Chemistry, Chernogolovka, Russia, by A.I. Ivanov and Dr. S.I. Bredikhin.

Synthesis of $SrMn_{1-x}Nb_xO_{3-\delta}$, $CaMn_{0.5}Nb_{0.5}O_{3-\delta}$ and $La_{10}Si_5AlO_{26.5}$ was carried out by a standard ceramic technique. The stoichiometric quantities of precursors indicated in Table 2.1 were mixed, placed into alundum crucibles and heated up to 1073 - 1273 K. Afterwards, the reaction mixture was ground in a ball-mill and subjected to 3 - 5 additional annealing steps in 1073 - 1573 K temperature range, with 5 - 20 hours dwell at the target temperature. The processing of LSGM and $La_{10}Si_5AlO_{26.5}$ solid electrolytes is described in Table 2.2.

The powders obtained by the techniques described were uniaxially pressed into discs (12 - 20 mm in diameter) of various thicknesses. The pellets were sintered in air under conditions indicated in Table 2.1. Heating and cooling was carried out with the rate 2 - 5 K/min, in order to approach to the complete equilibrium with the gas atmosphere. In order to access possible effects of the microstructure on the ionic transport properties, samples of $(La_{0.35}Sr_{0.65})_{0.95}Mn_{0.5}Cr_{0.1}Ti_{0.4}O_{3-\delta}$ were synthesized for 15 or 50 hours.

Ceramic pellets for oxygen permeability measurements were subjected to gas-tightness test. This procedure involved attaching a disc-shaped sample preliminary polished to the necessary thickness to a lateral side of 8YSZ tube (13 mm of outer diameter) with glue (Super Cola 3). After drying the glue, the pellet was immersed into water and the inner volume of the tube was exposed to the pressure of ~2 atm. The quality of the ceramics was checked visually by the absence/presence of air bubbles on the outer surface of the pellet.

Table 2.1. Processing conditions of $(La_{0.75-x}Sr_{0.25+x})_{0.95}Mn_{0.5}Cr_{0.5-x}Ti_xO_{3-\delta}$, $(La_{1-x}Sr_x)_{0.95}Mn_{0.5}Ti_{0.5}O_{3-\delta}$, $(La_{0.75}Sr_{0.25})Cr_{1-x}Fe_xO_{3-\delta}$, $(La_{0.9}Sr_{0.1})_{0.95}Cr_{0.85}Mg_{0.1}Ni_{0.05}O_{3-\delta}$, $SrNb_{1-x}Mn_xO_{3-\delta}$, $CaNb_{1-x}Mn_xO_{3-\delta}$ perovskites.

Composition	Starting component (supplier, purity)	Synthesis technique	Annealing temperature, K	Sintering conditions (compacting pressure, sintering temperature, dwell time)
$(La_{1-x}Sr_x)_{0.95}Mn_{0.5}Cr_{1-x}Ti_xO_{3-\delta}$	$La(NO_3)_3{\times}6H_2O$ (Fluka, ≥99.0%) $Sr(NO_3)_2$ (Aldrich; ≥99%) $Mn(CH_3COO)_2{\times}4H_2O$ (Aldrich; ≥99.0%) $Cr(NO_3)_3{\times}9H_2O$ (Aldrich, 99%) TiO_2 (Aldrich, 99.8%) *preliminary annealed at 973 K for 2 hours* $Fe(NO_3)_3{\times}9H_2O$ (Aldrich; ≥98%) $Ni(NO_3)_2{\times}6H_2O$ (Aldrich; ≥98.5%) $Mg(NO_3)_2{\times}6H_2O$ (Aldrich; ≥99.0%) $C_2H_5NO_2$ (Aldrich; ≥99%)	GNP	1273, 1473, 1573	50 - 100 MPa; 1773 K; 10 - 15 or 50 hours
$(La_{1-x}Sr_x)_{0.95}Mn_{0.5}Ti_{0.5}O_{3-\delta}$			1273, 1373, 1473	60 - 80 MPa; 1623 - 1773 K; 10 - 15 hours
$(La_{0.75}Sr_{0.25})_{0.95}Cr_{1-x}Fe_xO_{3-\delta}$			1273	50 - 150 MPa; 1973 K; 5 hours
$(La_{0.9}Sr_{0.1})_{0.95}Cr_{0.85}Mg_{0.1}Ni_{0.05}O_{3-\delta}$			1273	1873 K, 2 hours
$SrMn_{1-x}Nb_xO_{3-\delta}$	$SrCO_3$ (Aldrich; ≥99.9%) $CaCO_3$ (Lancaster, 99%) Nb_2O_5 (Alfa Aesar, 99.9%) *preliminary annealed at 973 K for 2 hours* $Mn(CH_3COO)_2{\times}4H_2O$ (Aldrich; ≥99.0%)	Solid state synthesis	1273, 1323, 1373, 1423	90 - 130 MPa; 1773 - 1793 K; 10 - 15 hours
$CaMn_{0.5}Nb_{0.5}O_{3-\delta}$			1273, 1323, 1373, 1423	120 - 160 MPa; 1663 K; 15 hours

Table 2.2. Preparation conditions of LSGM and $La_{10}Si_5AlO_{26.5}$ solid electrolytes

Composition	Starting component	Preliminary treatment	Annealing temperatures, K	Sintering conditions (compacting pressure, sintering temperature, dwell time)
$(La_{0.9}Sr_{0.1})_{0.98}Ga_{0.8}Mg_{0.2}O_{3-\delta}$	Commercial powder (supplied by Praxair)		1373	10 – 20 MPa, 1673 K, 4 hours
$La_{10}Si_5AlO_{26.5}$	La_2O_3	1473 K, 2 hours	1373, 1473, 1573	70 - 100 MPa, 1933 - 1943 K, 10-15 hours
	SiO_2	873 K, 1 hours		
	$Al(NO_3)_3 \times 9H_2O$	1073 K, 2 hours		

X-ray diffraction (XRD), thermogravimetric analysis (TGA), Mossbauer spectroscopy studies were carried out on powders obtained by grinding the sintered ceramics. Optionally, the powders were additionally annealed at 1273 - 1573 K prior to the analysis in order to release gaseous species adsorbed from ambient atmosphere. For dilatometric tests and conductivity or Seebeck coefficient measurements, bar-shaped specimens were cut from the pellets using a cut-off machine (Struers) and polished to obtain cuboid-like samples which might be placed and equilibrated on either facet on a flat surface.

X-ray diffraction, Mossbauer spectroscopy

Phase relationships in intermediate and final products were studied using XRD analysis carried out on powdered samples. XRD patterns were collected in atmospheric air on a series Rigaku D/Max-B X-ray powder diffractometer. The scans were obtained in Cu-K_α radiation (λ=0.154178 nm), within 2θ range 10 - 80º. The patterns were collected with scanning rate 3º /min or with 0.02º step with exposition time of 1 - 2 seconds.

In order to evaluate phase changes occurring in the materials upon temperature variations, ceramic samples were quenched from the given temperature into liquid nitrogen. Selected compositions were annealed in Ar or in wet 10% H_2 - N_2 flow with subsequent slow cooling (2K/min) or quenching in the corresponding gas flow. The oxygen partial pressure in the gas atmosphere was controlled using an oxygen sensor placed into the same or a separated furnace. In the latter case, the sensor was connected to the reaction compartment with gas communication systems, while the values of $p(O_2)$ around the sample were calculated from the sensor response corrected for the temperature difference between the corresponding furnaces.

Variations in the crystal structure on heating *in situ* were examined using high-temperature XRD technique. The measurements, carried out at the North Carolina A&T State University by Dr. S.N. Yarmolenko, were performed with AXS-Bruker D8 Discover diffractometer with Cu Kα X-ray radiation source and Eurlean cradle. Parallel beam optics was used to minimize errors associated with sample displacement and surface roughness. Anton Paar H-900 high temperature stage mounted on XYZ-positioning stage was used for measurements at temperatures up to 1173 K. Ceramic samples were polished down to 0.5 mm thick tablet form for better contact with heater. HTXRD scans were performed in the interval 2θ of 20 -

80º with speed 5s/point and step 0.01º. Calculation of the cell parameters of single- or multiple-phase compositions as well as verification of the lattice symmetry was performed using the Fullprof software [568].

Mossbauer transmission studies were carried out in collaboration with Dr. J.C.B. Waerenborgh and Dr. E.V. Tsipis at the Centro de Ciências e Tecnologias Nucleares, Instituto Superior Técnico, Universidade de Lisboa. The spectra were acquired at room temperature and 4 K using a conventional constant-acceleration spectrometer and a 25 mCi ^{57}Co source in Rh matrix. α-Fe foil was selected for velocity calibration. The adsorbers were obtained by pressing the powdered samples into perspex holders. Isomer shifts are related to metallic α-Fe at room temperature. The 4 K spectra were collected using a JANIS bath cryostat (SVT-400), with the sample immersed into liquid He. The spectra were fitted to Lorentzian lines using a non-linear least-squares method [569]. The relative areas and line widths of both peaks in a quadropole doublet and one of the symmetrical peaks constituting a magnetic sextet were constrained to remain equal. The distribution of magnetic splittings was fitted with the histogram method [570].

Microstructural analysis

The microstructural studies of ceramic and powdered samples as well as inspection of the electrode layers were performed by scanning electron microscopy coupled with energy-dispersive spectroscopy (SEM/EDS) on microscopes Hitachi S4100 (Rontec UHV detector, electron beam voltage 25 kV) and SU-70 EDS (Everhart Thornly Secondary Electron Detectors, accelerating voltage 0.5 - 30 kV). Examination of ceramic materials was carried out on fractured or polished surface; in the latter case, mechanical polishing was performed using silicon carbide papers #600-2400 supplied by Struers coated with a small amount of diamond paste ¼ - 9 mkm (Cafro), sequentially decreasing the abrasive roughness. Afterwards, the samples were ultrasonically cleaned in ethanol or acetone and thermally etched for 0.1 - 1 hour in order to remove the organic residues and to visualize the grains. The annealing temperature was selected as 150 - 200 K below the sintering temperature. Obtained ceramics was attached to the sample holder using carbon cement (Gocke) or carbon tape (NEM TAPE). In order to avoid surface charging during microscopic analysis, the samples were covered with a thin layer of carbon using evaporating machine EMITECH K950X.

To observe possible microstructural or compositional changes taking place in the electrode layers during the electrochemical tests, the half-cells subjected to the polarization measurements or duplicates prepared by the corresponding procedure and exposed to the same environments as the cells for the electrochemical studies were attached to the holder by such a manner so as to keep the electrode layer on the top. Another approach involved breaking the half-cell across the electrode and electrolyte layers, perpendicular to the interface, and exposure of the fractured surfaces and the boundary between the half-cell components to the microscopic studies. The latter method allowed to examine the morphology of the electrode layer and detect possible interactions, cation interdiffusion, etc.

TEM analysis was carried out at the University of Aveiro under the supervision of Dr. A.L.B. Lopes with a Hitachi H-9000 microscope (electron beam energy 300 kV). Additional experiments were made at the North Carolina A&T State University by Dr. S.N. Yarmolenko using the microscope Hitachi-H600AB (100 kEv). The procedure of preparation of submicron powdered samples involved their deposition onto copper or

carbon grid holders from ultrasonically-dispersed suspension in ethanol followed by drying and deposition of carbon. The microstructural studies were combined with EDS analysis to control the elemental composition of the regions examined.

Thermal analysis

Dilatometric studies were performed on rectangular bar samples in a vertical dilatometer Linseis L75/N1. Calibration of the dilatometer was carried out on Al_2O_3 bar subjected to the same measurement procedure as the samples studied. Depending on the gas atmosphere and kinetics of equilibration of the material, the data were collected in two regimes. The 1st included continuous heating up to 1373 K and immediate cooling with the rate of 3 K/min down to the ambient temperature; such a procedure was essentially employed during measurements in flowing air. The 2nd approach involved heating (3 K/min) up to 1243 - 1273 K, maintenance at the upper temperature for 2 - 70 hours, with consecutive cooling (2 K/min) and measurements under isothermal conditions in the temperature range 973 - 1273 K with the step of 50 K. Basically, the collection of data on each temperature continued until the complete equilibration; for selected compositions in the series (La,Sr)(Mn,Ti)$O_{3-\delta}$ the stable length could not be attained during a reasonable time period, and the isothermal tests were restricted by 20 - 40 hours. The thermal expansion coefficients and chemically-induced isothermal expansion were evaluated in the flow of air, Ar or CO-CO_2; the latter mixture was formed by preliminary passing CO_2 through an electrochemical oxygen pump where oxygen was evacuated from the gas mixture under fixed current of 300 mA. The oxygen partial pressure was controlled by an oxygen sensor located on the exit from the dilatometer. The isothermal chemical expansion in the corresponding atmosphere with respect to air at a given temperature T was calculated as

$$\varepsilon_C = \frac{1+\left(\Delta L / L_0\right)_{atm,T}}{1+\left(\Delta L / L_0\right)_{air,T}} - 1 \qquad \textbf{(Eq. 2.1)}$$

where $\left(\Delta L/L_0\right)_{atm,T}$ and $\left(\Delta L/L_0\right)_{air,T}$ correspond to relative elongation of the sample on heating from the 300 K up to the temperature T in the corresponding atmosphere or in air, respectively.

Thermogravimetric analysis (TGA) was carried out on a Setaram SetSys 16/18 instruments in a flow of air, Ar or 10% H_2 - N_2 mixture dried with silicagel prior to entering the measuring chamber. Since complete reduction of the materials studied into compositions with a certain stoichiometry could not be achieved under the experimental conditions, the obtained data were analyzed using relative mass changes upon thermal or redox cycling with respect to 573 K in air or, in the case of isothermal measurement, with respect to the mass in air under given temperature. For evaluation of the kinetics of oxygen exchange, transient studies were carried out under isothermal conditions by sequential replacement of air atmosphere by Ar and 10% H_2 - N_2 until the equilibration and in the reverse order. Al_2O_3 powder was used as the reference sample for the calibration of the equipment.

Total conductivity and Seebeck coefficient measurements

The total conductivity of bar-shaped ceramic specimens was measured by 4-probe DC technique. A scheme of the samples for the conductivity and Seebeck coefficient measurements as functions of $p(O_2)$ and temperature is shown in Fig. 2.1. Optionally, in order to ensure a better contact between Pt leads and the sample, the surface region where the contact takes place was preliminary coated with Pt paste (supplied by Heraeus or GEM). For measurements of the conductivity in air, the current leads were pressed to the lateral facets of the bar, in order to provide more uniform current flow through the sample. The activation energy E_a of the total conductivity σ was evaluated using the standard Arrhenius equation:

$$\sigma = \frac{A_0}{T} \exp\left(-\frac{E_a}{RT} \right) \qquad \textbf{(Eq. 2.2)}$$

where A_0 is the pre-exponential factor, T is the temperature, R is the gas constant.

The cell for isothermal measurements of the total conductivity and Seebeck coefficient consists of an electrochemical oxygen pump and sensor (Fig. 2.2) isolated with a glass sealant layer which suppresses a direct impact of current flux through the pump on the signal from the sensor originating from distribution of the current within YSZ. For the thermoelectric power measurements, the sample was fixed between two B-type thermocouples (Fig. 2.1) one end of each also served as a potential probe for measuring thermal e.m.f. of the sample.

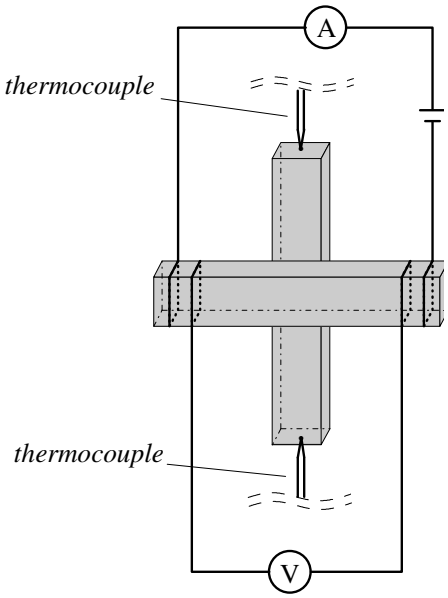

Fig. 2.1. Schematic representation of the contacts between current and potential leads and samples for the conductivity and Seebeck coefficient measurements

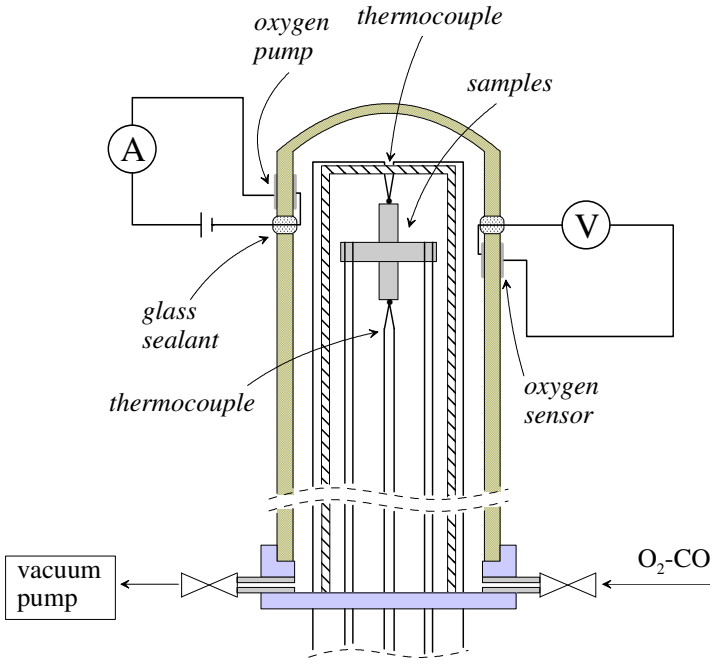

Fig. 2.2. Schematic representation of the cell for the conductivity and Seebeck coefficient measurements

The thermopower was determined under a temperature gradient of 15 - 20 K; the higher potential was formally assigned to a hotter end of the sample. Prior to the tests, the cell was evacuated with a vacuum pump and filled with O_2 - CO_2 mixture. In the process of measurements, the $p(O_2)$ required was adjusted by electrochemical pumping of oxygen in/out of the cell and controlled by the sensor. The studies were performed in 973 - 1223 K. After each reduction run, selected points were re-collected on oxidation in order to control possible structural transitions, phase decomposition or ceramics failure. The equilibration criteria of the sample after a change in either $p(O_2)$ or temperature included the relaxation rates of the conductivity and thermopower less than 0.05%/min and 0.001 μV/K×min, respectively. Due to stagnated gas diffusion and compositional instabilities at $p(O_2)$ in the range 10^{-11} - 10^{-6} atm, and resultant hysteresis phenomena, the data in this region were basically excluded from consideration.

The measured values of the total conductivity and Seebeck coefficient were used for calculation of the concentration of charge carries and their mobility. For the materials with predominant p-type electronic transport, the Seebeck coefficient α is related with the charge carrier concentration p using the Heikes formula [21, 166]

$$\alpha = \frac{k}{e} \cdot \ln \frac{N - p}{p} \qquad \textbf{(Eq. 2.3)}$$

or

$$\alpha = \frac{k}{e} \cdot \ln \frac{\beta N - p}{p} \qquad \textbf{(Eq. 2.4)}$$

where N is the number of states, k is Boltzmann constant, e is the elementary charge and β in Eq. (2.4) is a constant related with spin-degeneracy factor. In Eq. (2.3), any spin-degeneracy phenomena are neglected. The hole mobility (μ_p) was evaluated from the conductivity data as

$$\sigma = ep\mu_p \cdot N_{fu} / V_{uc} \qquad \textbf{(Eq. 2.5)}$$

where N_{fu} is the number of formula units per unit cell, V_{uc} is the unit-cell volume, and p is calculated from Eqs. (2.3) - (2.4) and is related to formula unit. In the case when the exact value of the number of states N cannot be determined, the analysis is carried out operating with the values (p/N) and ($\mu_p \times N$) which are calculated from Eqs. (2.3) - (2.5).

Determination of oxygen permeation fluxes, bulk oxygen tracer diffusion and surface exchange coefficients

The oxygen transport-related parameters were determined only for gas-tight ceramics. The oxygen permeability (OP) through a ceramic membrane is associated with simultaneous migration of oxide ions and electrons induced by a gradient of oxygen chemical/electrochemical potential at the membrane surfaces.

Under the absence of external electrical current, the oxygen flux *j* through a dense mixed conductor of the thickness *L*, placed under the oxygen chemical potential gradient, is given by [571, 572]:

$$j = \frac{RT}{16F^2 L}\int_{\mu_1}^{\mu_2} \frac{\sigma_{ion}\sigma_e}{\sigma_{ion}+\sigma_e} d\mu_{O_2} \qquad \textbf{(Eq. 2.6)}$$

where σ_{ion} and σ_e denote the ionic and electronic conductivity of the membrane material and μ_1 and μ_2 correspond to oxygen chemical potential at the permeate and feed side, respectively. For clarifying the effects of surface kinetics-related limitations, one should introduce the value of specific oxygen permeability $J(O_2)$ [573]:

$$J\left(O_2\right) = \frac{jRTL}{\mu_2 - \mu_1} = jL\left(\ln\frac{p_2}{p_1}\right)^{-1} \qquad \textbf{(Eq. 2.7)}$$

with p_1 and p_2 corresponding to oxygen partial pressures at the membrane permeate and feed sides, respectively. In the case of fast exchange kinetics at the membrane/gas interfaces, the value $J(O_2)$ should be thickness-independent, while the permeation flux is expected to be proportional to reciprocal thickness. When the oxygen transport is determined exceptionally by the rates of the surface processes, the permeation flux is thickness-independent, while the specific permeability linearly increases with the membrane thickness.

The experimental cell for electrochemical measurements of OP is schematically illustrated in Fig. 2.3. The cell consists of an electrochemical oxygen pump and a sensor made of 8YSZ. The contacts between the Pt leads and zirconia surface were ensured by multiple coating and firing Pt paste. In order to eliminate any direct influence of current through the pump on the sensor, an additional zirconia ring was introduced between the electrochemical parts and fixed with glass-ceramic sealant (T_{seal} = 1440 - 1450 K). After sealing the ceramic membrane of the material studied (T_{seal} = 1360 - 1380 K), a series of direct currents I_{pump} was passed through the pump in the direction of elimination of oxygen out of the cell, corresponding to the permeation fluxes in accordance with

$$j = \frac{I_{pump}}{4FS} \qquad \textbf{(Eq. 2.8)}$$

where *S* relates to the active area of the membrane which the permeation flux proceeds through. Under each current, a steady-state gradient of oxygen partial pressures was recorded calculated from the e.m.f. value of the sensor E_{sens}.

$$E_{sens} = \frac{RT}{4F}\ln\left(\frac{p_2}{p_1}\right) \qquad \textbf{(Eq. 2.9)}$$

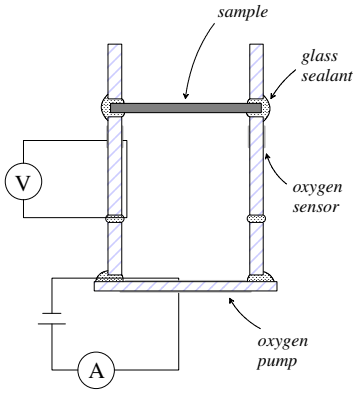

Fig. 2.3. Schematic representation of the cell for oxygen permeability measurements by electrochemical method

The oxygen pressure at the outer side of the membrane (feed side) was fixed at 0.21 atm. In order to assess the parameters responsible for the oxygen transfer across the membrane, the j - p_2/p_1 dependencies obtained were analyzed for membranes with the thickness 0.6 - 1.4 mm in the temperature range 973 - 1273 K. As follows from Eq. (2.6), for materials with dominant electronic conductivity at the absence of the surface-related limitations, the partial oxygen ionic conductivity σ_O may be evaluated from the oxygen flux using the expression [3]:

$$\sigma_O(p_1) = \frac{16F^2 d}{RT}\left(\frac{\partial j}{\partial[\ln p_1]}\right)_{p_2} \qquad \textbf{(Eq. 2.10)}$$

In the case of simultaneous limitations of the surface exchange kinetics and bulk diffusion, their relative roles were estimated using an approximate relationship derived in [320]:

$$\frac{1}{j}\cdot\ln\left(\frac{p_2}{p_1}\right) = \frac{16F^2 d}{RT\bar{\sigma}_{amb}} + k_2^{-1} + k_1^{-1} \qquad \textbf{(Eq. 2.11)}$$

where $\bar{\sigma}_{amb}$ is the ambipolar conductivity (equivalent to the ionic conductivity for materials with dominant electronic transport) averaged over the range p_1 - p_2, and the values k_1 and k_2 relate to the surface exchange rates at the permeate and feed sides, respectively. Solving the system of equations, where each corresponds to Eq. (2.11) with a definite membrane thickness d, yields the values $\bar{\sigma}_{amb}$ and $k_2^{-1} + k_1^{-1}$ under the given gradient p_2/p_1. No attempts to separate k_1 and k_2 were undertaken in the framework of the study.

An alternative technique of OP measurements involved placing the membrane studied under the gradient of flowing air vs. H_2 - H_2O - N_2 gradient. The variations of the oxygen content in the gas atmosphere at the permeate side were evaluated using electrochemical oxygen sensors at the inlet and outlet of the corresponding compartment of the cell. The measurements were carried out by Dr. A.A. Yaremchenko, the details of the method and calculations can be found elsewhere [574].

The bulk oxygen tracer diffusion (D^*) and surface exchange (k) coefficients were assessed using the $^{18}O/^{16}O$ isotopic exchange depth profile method carried out in the Institute of Solid State Physics, Chernogolovka, Russia, by Dr. S.I. Bredikhin and Yu.S. Fedotov. Prior to $^{18}O/^{16}O$ exchange annealing, the polished and cleaned ceramic samples were equilibrated in air of normal isotopic abundance. Afterwards, the chamber was evacuated and labeled oxygen (95 % enriched $^{18}O_2$) was introduced to reach $p(O_2)$ = 0.2 atm. The samples were annealed at 1023 -1223 K for 1 - 45.5 hours followed by quenching. The ^{18}O penetration profiles were determined by time-of-flight secondary-ion mass spectrometry (TOF-SIMS) using a TOF-SIMS.5-100P instrument (ION-TOF GmbH, Germany) operated in the depth profile mode, with a 45° incidence 25 keV Bi^+ primary ion beam and 45° incidence 2 keV Cs^+ sputter ion beam. The crater depth was measured after the SIMS analysis by surface profilometry (Taylor–Hobson Talystep). An example of ^{18}O penetration profile obtained for $La_{0.5}Sr_{0.5}Mn_{0.5}Ti_{0.5}O_{3-\delta}$ is shown in Fig. 2.4.

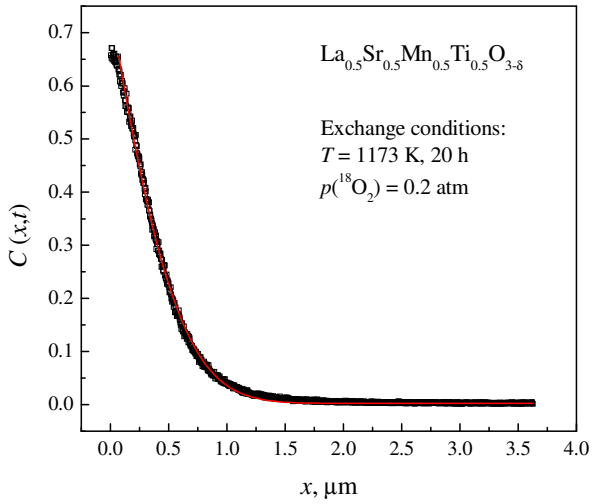

Fig. 2.4. Example of the ^{18}O penetration profile for $La_{0.5}Sr_{0.5}Mn_{0.5}Ti_{0.5}O_{3-\delta}$ at 1223 K.

The rate of isotopic exchange across the gas/solid interface is assumed to be directly proportional to the difference in isotope concentration (C) between the gas and the solid, leading to the boundary condition [337, 575]:

$$-D^* \left.\frac{\partial C}{\partial x}\right|_{x=0} = k\left(C_g - C_s\right) \qquad \textbf{(Eq. 2.12)}$$

where x is the depth, and C_g and C_s are the ^{18}O isotope ratio in the gas phase and in the surface, respectively. Assuming that the isotope concentration in the gas phase is constant, the diffusion equation for this boundary condition and a semi-infinite medium is formulated as [337, 575]:

$$\frac{C(x,t)-C_{bg}}{C_g-C_{bg}} = \mathrm{erfc}\left(\frac{x}{2\sqrt{D^*t}}\right) - \exp\left(\frac{kx+k^2t}{D^*}\right)\times\mathrm{erfc}\left(\frac{x+2kt}{2\sqrt{D^*t}}\right) \qquad \textbf{(Eq. 2.13)}$$

where $C(x,t)$ is the ^{18}O isotope fraction, t is the exchange annealing time, and C_{bg} is the natural background level of ^{18}O (0.20%). D^* and k were obtained by non-linear least squares fitting of the SIMS data to Eq. (2.13).

Preparation of the electrode layers and polarization measurements

Polarization measuremets were performed by electrochemical impedance spectroscopy using 3-electrode configuration. The cell geometry is shown in Fig. 2.5.; such a location of the counter (CE) and reference electrodes (RE) was selected in accordance with [576, 577]. The tests were carried out on cells composed of perovskite, perovskite-based composite or cermet electrodes. Gas-tight pellets LSGM or $La_{10}Si_5AlO_{26.5}$ of 16 - 18 mm diameter and 1.5 - 2.0 mm thickness were used as solid electrolytes. The conditions of the fabrication of the cells with perovskite-based anode and cathodes are listed in Table 2.3. Basically, the deposition of the woring electrode (WE) layers (diameter 5.0 - 6.0 mm) involved preparation of ethanol-based suspension of the material studied followed by paint-brushing the layer onto the substrate with subsequent firing in air. Optionally, a layer of submicron CGO20 powder mixed with 2 wt.% $Co(NO_3)_2 \times 4H_2O$ in ethanol was preliminary applied onto the electrolyte to achieve the surface density of 3 - 5 mg/cm^2 followed by firing at 1473 K in air and subsequent deposition of the electrode layer.

Table 2.3. Composition and preparation conditions of perovskite-based electrode layers

Electrode composition	Sheet density, mg/cm^2	Firing conditions
$(La_{0.75-x}Sr_{0.25+x})_{0.95}Mn_{0.5}Cr_{0.5-x}Ti_xO_{3-\delta}$	7 - 10	1473 K, 2 hours
$(La_{0.75}Sr_{0.25})_{0.95}Cr_{1-x}Fe_xO_{3-\delta}$	5	1473 K, 10 hours
$(La_{0.85}Sr_{0.15})_{0.95}Cr_{0.85}Mg_{0.1}Ni_{0.05}O_{3-\delta}$	10 - 20	1448 - 1473 K, 2 hours
$SrMn_{1-x}Nb_xO_{3-\delta}$	10 - 15	1423 K, 2 hours
$(La_{1-x}Sr_x)_{1-y}Mn_{0.5}Ti_{0.5}O_{3-\delta}$	12 - 14	1323 - 1473 K, 2 hours

Due to strong sinterability of $(La_{0.55}Sr_{0.45})_{0.95}Mn_{0.5}Ti_{0.5}O_{3-\delta}$ powder, the corresponding electrode layers were prepared using various procedures, presented in Table 2.4. All the cells consisted of a LSGM electrolyte preliminary coated with CGO20 sublayer. In order to achieve the optimum adherence of the electrode layer with simultaneous maintainance of the porosity and large surface area, the modification routes involved tuning the electrode firing temperature, grinding and preliminary annealing.

Table 2.4. Preparation conditions of selected electrode layers based on $(La_{0.55}Sr_{0.45})_{0.95}Mn_{0.5}Ti_{0.5}O_{3-\delta}$

Abbreviation	Preparation procedure	Firing conditions
coarse-1473	1. Annealing of as-prepared perovskite powder at 1673 K	1473 K, 2 hours
fine-1473	1. Annealing of as-prepared perovskite powder at 1673 K 2. Grinding	1473 K, 2 hours
fine-1433		1433 K, 2 hours
fine-1373		1373 K, 2 hours
fine-1323		1323 K, 2 hours
passivated-1473	1. Annealing of as-prepared perovskite powder at 1673 K 2. Grinding 3. Annealing at 1573 C 4. Grinding	1323 K, 2 hours

Powder mixtures consisting of a metal (Cu, Ni, Ag) and solid oxide with high oxygen ionic conductivity (CGO20 or 8YSZ) were prepared by mechanical mixing of the precursors or by wet impregnation of one of the phases into the anode layer. The composite powders were mixed with ethanol and applied onto the electrolyte surface using paint-brush technique; the electrode composition and details of the fabrication procedure are listed in Table 2.5. Optionally, a layer of metallic silver was deposited onto the electrolyte surface prior to the electrode application; the corresponding procedure is described in Table 2.6.

Table 2.5. Composition and preparation conditions of metal-ceramics electrode layers

Electrode (abbreviation)	Precursor	Fraction*	Preparation conditions	Sheet density, mg/cm^2
Ni – CGO20	NiO	20 vol. %	1373 K, 30 min	20
	$Ce_{0.8}Gd_{0.2}O_{1.9}$	80 vol. %		
CGO20, Ni-modified	$Ni(NO_3)_2$	approx. 20 vol. %	Firing CGO20 (1473 K, 2 hours) with subsequent impregnation with $Ni(NO_3)_2$-saturated ethanol solution and annealing (773 K, 30 min)	15
	$Ce_{0.8}Gd_{0.2}O_{1.9}$	approx. 80 vol. %		
Ni - 8YSZ - CGO20	NiO	50 wt.%	1253 K, 1 hour	15
	$Zr_{0.85}Y_{0.15}O_{1.92}$	30 wt. %		
	$Ce_{0.8}Gd_{0.2}O_{1.9}$	20 wt.%		
Ni - 8YSZ - CGO20 (La_2O_3-, Ni-modified)	NiO	50 wt.%	1. Firing Ni - 8YSZ - CGO20: 1253 K, 1 hour 2. Impregnation with solution $La(NO_3)_3$ (2 M)+ $Ni(NO_3)_2$ (0.5 M) 3. Annealing at 1173 K, 1 hour	24
	$Zr_{0.85}Y_{0.15}O_{1.92}$	30 wt. %		
	$Ce_{0.8}Gd_{0.2}O_{1.9}$	20 wt.%		
Ag - CGO20	Ag	40 vol. %	1203 K, 0.5 hours	7
	$Ce_{0.8}Gd_{0.2}O_{1.9}$	60 vol. %		
Ni - Ag - CGO20 (16 - 16 - 66)	NiO	16 vol. %	1203 K, 30 min	10 - 15
	Ag	16 vol. %		
	$Ce_{0.8}Gd_{0.2}O_{1.9}$	66 vol. %		
Ni - Ag - CGO20 (10 - 10 - 80)	NiO	10 vol. %	1203 K, 20 min	10 - 15
	Ag	10 vol. %		
	$Ce_{0.8}Gd_{0.2}O_{1.9}$	80 vol. %		
Ni - Ag - CGO20 (5 - 5 - 90)	NiO	5 vol. %	1203 K, 20 min	10 - 15
	Ag	5 vol. %		
	$Ce_{0.8}Gd_{0.2}O_{1.9}$	90 vol. %		
Cu - 8YSZ	CuO	40 vol. %	1223 K, 0.5 hours	6
	$Zr_{0.85}Y_{0.15}O_{1.92}$	60 vol. %		
Cu - CGO20	CuO	40 vol. %	1273 K, 1 hour	5
	$Ce_{0.8}Gd_{0.2}O_{1.9}$	60 vol. %		

**Volume and mass fractions of Ni, Cu and Ag indicated in Table 2.5 correspond to metallic state*

Table 2.6. Composition and preparation conditions of metal-ceramics electrode layers with Ag sublayer

Electrode	Precursor	Fraction	Preparation conditions	Sheet density, mg/cm^2
Ag - CGO20 (40 - 60 vol.%)	Ag (interlayer)		Firing interlayer: 1203 K, 0.5 hours Firing electrode: 1203 K, 0.5 hours	7
	Ag	40 vol. %		7
	$Ce_{0.8}Gd_{0.2}O_{1.9}$	60 vol. %		
Al_2O_3 - Ag - CGO20	Ag (interlayer)		1203 K, 0.5 hours	10 - 15
	Al_2O_3	20 wt. %	1. Al_2O_3 was obtained by mixing equal volumes of 0.1 M solution $AlCl_3$ with 0.5 M solution NH_4OH with subsequent thermal evaporation and annealing at 1073 K for 2 hours 2. After mixing Al_2O_3 with Ag - CGO20, cermet obtained was fired at 1203 K, 0.5 hours	10 - 15
	Ag	80 wt. % of Ag - CGO20 (40 - 60 vol. %)		
	$Ce_{0.8}Gd_{0.2}O_{1.9}$			

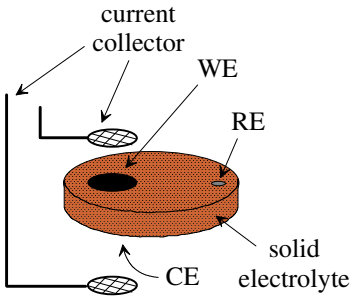

Fig. 2.5. Scheme of the electrochemical cell with 3-electrode arrangement

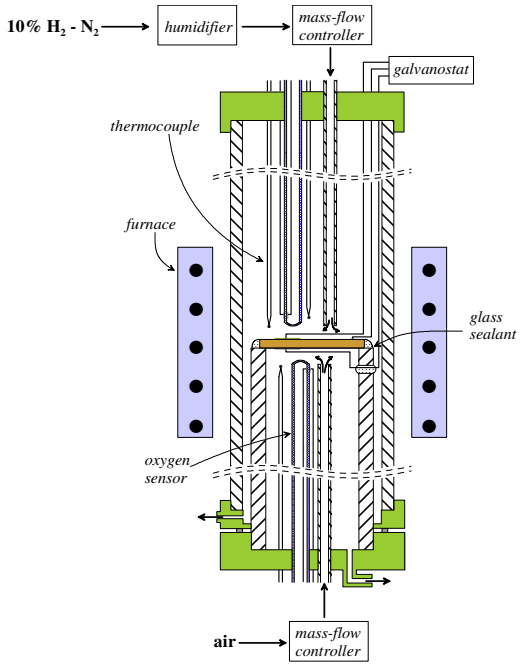

Fig. 2.6. Schematic representation of the set-up for polarization measurement in reducing atmospheres

The CE was applied on the opposite side of the electrolyte membrane symmetrically with respect to the WE. The RE (0.9 - 1.3 mm of diameter) was placed on the distance of 7.0 - 9.0 mm from the nearest edge of the WE; both CE and RE were prepared by coating a thin layer of Pt paste (Heraeus) subsequently fired at 1203 - 1373 K. In order to ensure appropriate current collection, Pt gauze was pressed to the WE and CE. The point contact with the RE was provided by pressing the tip of a thick wire (0.5 mm of diameter). No coverage of the WE with Pt or other metal paste was carried out in order to avoid an interference of additional catalytic effects on the electrochemical properties.

The equipment for electrochemical measurements in reductive atmospheres is shown in Fig. 2.6. The cell was placed onto a tip of an alumina tube (14.5 mm of inner diameter), simultaneously ensuring the contacts between the electrodes and the current collectors, while the lateral surface of the electrolyte was covered with a thick layer of ethanol-based suspension of sealing glass powder (T_{seal} = 1173 - 1223 K). Prior to the measurements, the WE and CE compartments were flushed with humidified 10% H_2 - N_2 (50 ml/min) and air (12.5 ml/min), respectively. The composition of the gas fluxes was settled with Bronkhorst mass-flow controllers and controlled by oxygen sensors. For evaluation of cathode performance, a simplified setup was used, without oxygen sensors and necessity for gas separation.

The electrochemical tests were carried out in galvanostatic mode using Autolab PGSTAT302 Equipment. The impedance data between the WE and RE were recorded in the frequency range from 1 MHz to 1 mHz; the amplitude of the alternating current varied in the range 0.5 - 2.0 mA. The overpotential (η) was calculated as

$$\eta = U - IR_{Ohm} \qquad \textbf{(Eq. 2.14)}$$

where U is the potential difference between the WE and RE, I is the current flowing between WE and CE, and IR_{Ohm} is the ohmic contribution into the total potential drop. In order to estimate the electrode polarization resistance the values of the corresponding ohmic resistance R_{Ohm} were extracted from impedance spectra. The ohmic and polarization resistances were evaluated from the intersection of the high- or low-frequency arcs with the axis Z' in accordance with Fig. 2.7:

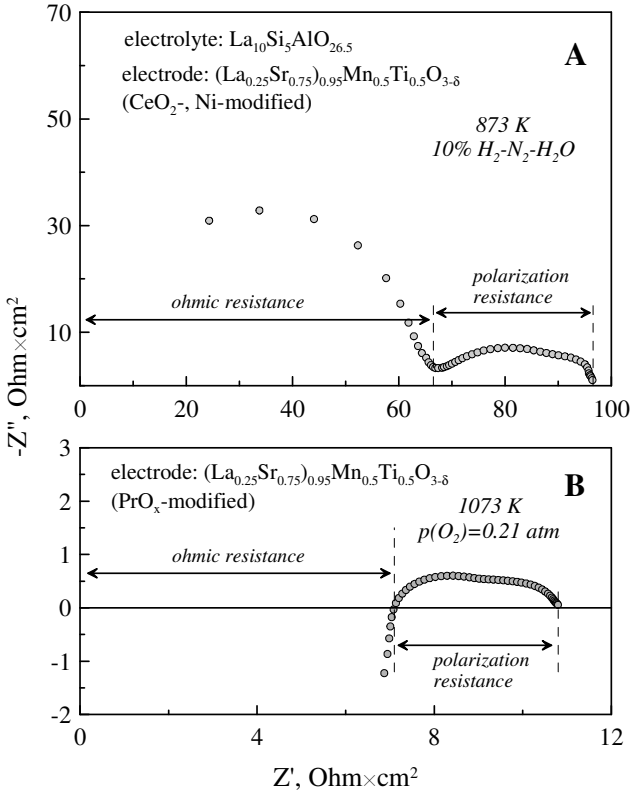

Fig. 2.7. Typical examples of impedance spectra collected for $(La_{0.75-x}Sr_{0.25+x})_{0.95}Mn_{0.5}Cr_{0.5-x}Ti_xO_{3-\delta}$ electrodes and determination of the ohmic constituent in the overall resistance.

Selected electrode layers after electrochemical tests were surface-modified by addition of ethanol-based saturated solutions of catalytically-active components ($Ce(NO_3)_3$ and $Ni(NO_3)_2$ for anodes and $Pr(NO_3)_3$ for cathodes) and the measurements repeated. The decomposition of nitrates proceeded during the heating the system up to the temperature of studies. The cells after the tests as well as as-prepared analogues were subjected to microscopic analysis in order to reveal possible microstructural changes, phase interaction etc.

Chapter 3. Pseudobinary (La,Sr)(Cr,Mn)$O_{3-\delta}$ - $SrTiO_{3-\delta}$ system and alternative $LaCrO_{3-\delta}$-based materials

Chromite perovskites represent a wide group of alternative anode materials possessing high redox stability and acceptable thermomechanical behaviour, while the transport and electrochemical properties may be optimized by an appropriate cation doping [8, 9, 15, 18, 113, 210, 212]. On the other hand, partial or complete replacement of Cr cations is desirable for high-temperature applications, in order to avoid the formation of volatile chromium oxides, hydroxides and other compounds containing high-valent Cr species or to suppress the reactivity with other cell components [44, 82, 139, 142, 285]. In accordance with numerous reports, the systems (La,A)$CrO_{3-\delta}$, (La,A)$MnO_{3-\delta}$ and (La,A)$TiO_{3-\delta}$ exhibit an unlimited mutual solubility provided that B-site doping is accompanied by appropriate variations of the cation ratio in A-sublattice [16, 131, 155-159, 164, 168, 171, 352], while cation modifications in B-sublattice may ensure a promising combination of the functional characteristics such as the tolerance towards a wide range of operation conditions, electronic and ionic transport, thermomechanical properties and catalytic activity [8, 10, 16, 212]. The present section is devoted to studying phase and structural stability, thermal and chemical expansion, mixed electronic and ionic conduction of $(La_{0.75-x}Sr_{0.25+x})_{0.95}Mn_{0.5}Cr_{0.5-x}Ti_xO_{3-\delta}$ and applicability of the title materials for anode or cathode utilizations.

Doping $LaCrO_3$-based compositions with Fe is considered as another approach to reduce the polarization resistance of chromite-based anode layers. However, the literature data on the phase and structural behaviour upon redox cycling, oxidation state of the constituent transition metal cations as well as transport mechanism in Fe-doped chromites are contradictive [9, 17, 44, 178, 179, 191, 206, 212]. The electrode performance of (La,Sr)(Cr,Fe)$O_{3-\delta}$ has been reported to be somewhat lower or comparable to that of (La,Sr)(Cr,Mn)$O_{3-\delta}$ analogues [9, 212, 264], but Fe-doped compositions exhibited an enhanced reactivity with gallate-based electrolytes [9] leading to higher ohmic losses and raising the problem of the long-term stability. This drawback can be to some extent avoided by applying buffer layers between the components of the electrochemical cell. Moreover, the insufficient chemical stability and enhanced chemical expansion may cause long-term degradation of (La,Sr)(Cr,Fe)$O_{3-\delta}$ anodes. In order to clarify the effect of Fe-doping into chromites, the following part concerns functional characteristics of $(La_{0.75}Sr_{0.25})_{0.95}Cr_{1-x}Fe_xO_{3-\delta}$ (x = 0.3, 0.4) perovskites and polarization behaviour of the corresponding anodes in contact with LSGM electrolyte with CGO20 sublayer.

In recent years, much attention has been drawn to a strategy of segregation from the perovskite structure of catalytically active phases, in particular highly dispersed metallic particles [15, 17, 184, 186, 188, 215, 544]. The presence of metal droplets with a large surface area has been reported to accelerate the elementary steps related to gas/solid interface and allow to catalyze the oxidation processes [15, 186, 211, 544]. Cation-stoichiometric perovskites may be thermodynamically intolerant towards simultaneous lowering the amount of B-site cations and oxygen atoms in anionic sublattice leading to separation of lantanide- or alkali-earth metal-enriched secondary phases upon reduction [15, 135]. This issue can be partially resolved by introduction of cation vacancies into A-sublattice. On the other hand, generation of substantial amounts of

the metallic phase and their subsequent agglomeration may lead to performance instability of the anode layers, and the control of the concentration of dopant cations and reduction process is required. The final part of the present chapter is addressed to appraisal of $(La_{0.9}Sr_{0.1})_{0.95}Cr_{0.85}Mg_{0.1}Ni_{0.05}O_{3-\delta}$ perovskites as cathode and anode materials for IT-SOFCs. The presence of Mg is expected to ensure a contribution of the ionic transport and surface exchange into the overall electrode mechanism. Furthermore, even if a slight excess of B-cations in the perovskite causes separation (Mg,Ni)O secondary phase, its presence might promote the formation of dispersed Ni particles upon reduction [578, 579].

3.1. Transport, thermomechanical and electrode properties of perovskite-type $(La_{0.75-x}Sr_{0.25+x})_{0.95}Mn_{0.5}Cr_{0.5-x}Ti_xO_{3-\delta}$ (x = 0 - 0.05)

3.1.1. Phase relationships and structure

XRD analysis showed the continuous solid solution formation in the entire $(La_{0.75-x}Sr_{0.25+x})_{0.95}Mn_{0.5}Cr_{0.5-x}Ti_xO_{3-\delta}$ (x = 0 - 0.5) system under oxidizing conditions, consistently with the phase purity of (La,Sr)(Cr,Mn)$O_{3-\delta}$, (La,Sr)(Mn,Ti)$O_{3-\delta}$ and (La,Sr)(Cr,Ti)$O_{3-\delta}$ materials in a wide compositional range [16, 155, 164, 352]. Selected XRD patterns are presented in Fig. 3.1. The perovskite-type crystal structure of the title compositions was identified as rhombohedrally-distorted (S.G. $R\bar{3}c$), analogously with parent $(La_{0.75}Sr_{0.25})_{0.95}Cr_{0.5}Mn_{0.5}O_{3-\delta}$ and selected representatives of Mn-doped titanates [10, 16, 488]. Table 3.1. lists the unit cell parameters in hexagonal settings and abbreviations used below. The unit cell volume tends to slightly increase with increasing x, as expected from the cation radius variations.

Table 3.1. Abbreviations, unit cell parameters and density of $(La_{0.75-x}Sr_{0.25+x})_{0.95}Mn_{0.5}Cr_{0.5-x}Ti_xO_{3-\delta}$ ceramics

Composition	Abbreviation	a, Å	c, Å	V, Å^3	ρ_{exp}, g/cm^3	Relative density, %
$(La_{0.75}Sr_{0.25})_{0.95}Mn_{0.5}Cr_{0.5}O_{3-\delta}$	LSMCT0	5.4953 (2)	13.3098 (6)	348.08 (4)	5.99	99.3
$(La_{0.55}Sr_{0.45})_{0.95}Mn_{0.5}Cr_{0.3}Ti_{0.2}O_{3-\delta}$	LSMCT2	5.4955 (3)	13.3738 (8)	349.78 (6)	5.74	95.7
$(La_{0.45}Sr_{0.55})_{0.95}Mn_{0.5}Cr_{0.2}Ti_{0.3}O_{3-\delta}$	LSMCT3	5.4992 (1)	13.4138 (7)	351.30 (4)	5.57	95.6
$(La_{0.35}Sr_{0.65})_{0.95}Mn_{0.5}Cr_{0.1}Ti_{0.4}O_{3-\delta}$	LSMCT4	5.4963 (1)	13.4266 (3)	351.27 (2)	5.47	96.4
$(La_{0.25}Sr_{0.75})_{0.95}Mn_{0.5}Ti_{0.5}O_{3-\delta}$	LSMCT5	5.4960 (8)	13.4551 (13)	351.97 (13)	5.18	94.0

Notes:
a, c and V are the unit cell parameters and volume in hexagonal settings, respectively;
ρ_{theor} and ρ_{exp} are the theoretical and experimental density values.

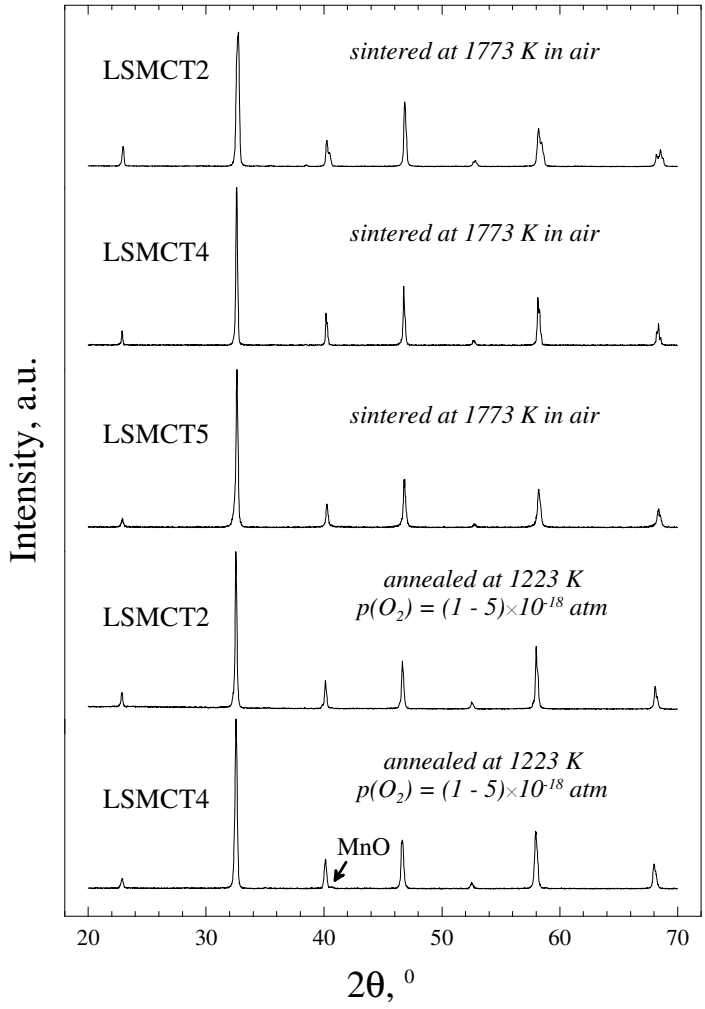

Fig. 3.1. XRD patterns of $(La_{0.75-x}Sr_{0.25+x})_{0.95}Mn_{0.5}Cr_{0.5-x}Ti_xO_{3-\delta}$ after sintering in air at 1773 K and after reduction in flowing 10% H_2 - N_2 gas mixture at 1223 K for 25 hours

Reducing $p(O_2)$ down to 10^{-18} atm does not lead to perovskite decomposition, except for the segregation of minor amounts of MnO. Note that MnO segregation on reduction is typical for most manganite-based compositions even if those are stabilized by B-site doping, as shown in Table 1.3.1. $(La,Sr)(Cr,Mn)O_{3-\delta}$ and $(La,Sr)(Mn,Ti)O_{3-\delta}$ perovskites have been reported to show a transition from the rhombohedral structure into the cubic or orthorhombic symmetry on reduction [16, 113, 177]. No transformations were observed for $(La_{0.75-x}Sr_{0.25+x})_{0.95}Mn_{0.5}Cr_{0.5-x}Ti_xO_{3-\delta}$, although more accurate structural analysis is required to refine the crystal symmetry.

Typical microstructures of $(La_{0.75-x}Sr_{0.25+x})_{0.95}Mn_{0.5}Cr_{0.5-x}Ti_xO_{3-\delta}$ dense ceramics are illustrated in Fig. 3.2. SEM inspection of the ceramic materials showed traces of glassy phases at the grain boundaries, suggesting a liquid phase-assisted sintering process. At the same time, no compositional inhomogeneities were revealed by EDS, within the limit of experimental uncertainty. Introduction of Sr and Ti into the perovskite seems to cause a slight enlargement of the grains, although at high doping levels the effect is less obvious. The ceramics contained no open pores; the density of the ceramic materials was higher than 95%.

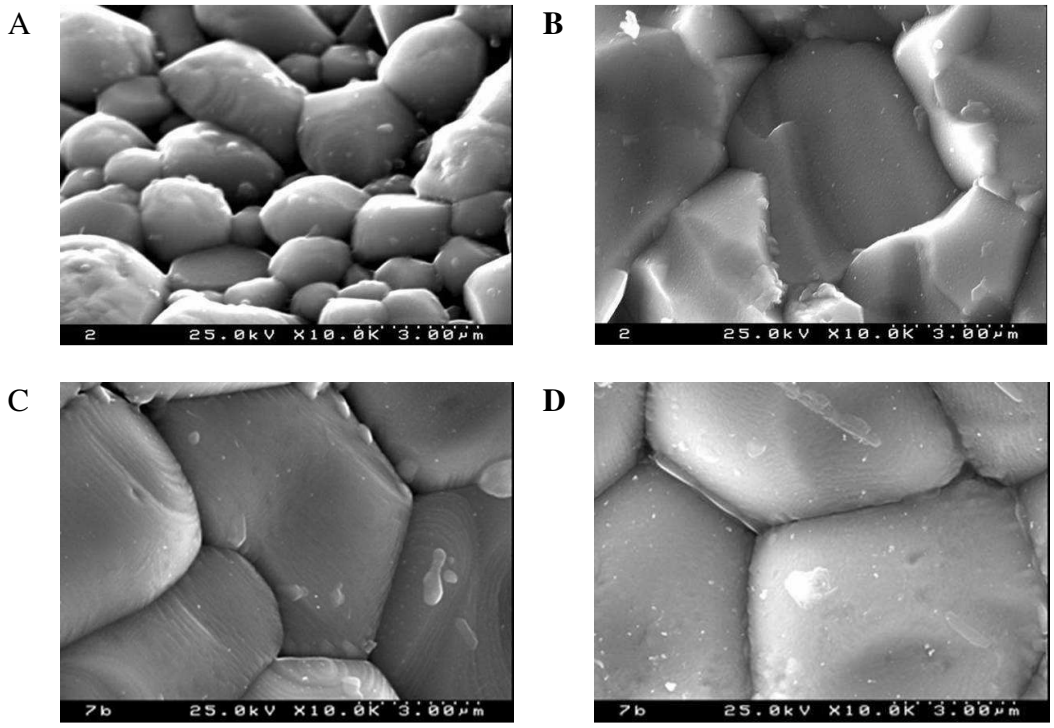

Fig. 3.2. SEM micrographs of fractured (A, B) and polished (C, D) $(La_{0.75-x}Sr_{0.25+x})_{0.95}Mn_{0.5}Cr_{0.5-x}Ti_xO_{3-\delta}$ ceramics sintered during 10 - 15 hours at 1773 K in air: A. x = 0.2; B. x = 0.3; C and D. x = 0.5

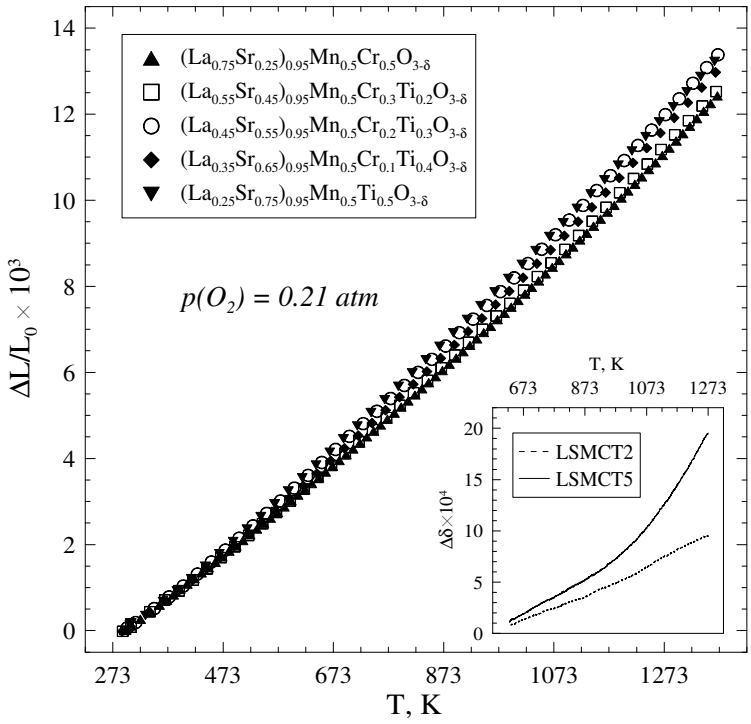

Fig. 3.3. Dilatometric curves of $(La_{0.75-x}Sr_{0.25+x})_{0.95}Mn_{0.5}Cr_{0.5-x}Ti_xO_{3-\delta}$ ceramics in air. Inset compares the oxygen nonstoichiometry variations in LSMCT2 and LSMCT5, collected by TGA on cooling in dry air. L_0 relates to the initial sample length at room temperature.

3.1.2. Thermal expansion

The results of dilatometric measurements are summarized in Figs. 3.3 - 3.4 and Tables 3.2 - 3.5. The average linear thermal expansion coefficients (TECs) of $(La_{0.75-x}Sr_{0.25+x})_{0.95}Mn_{0.5}Cr_{0.5-x}Ti_xO_{3-\delta}$ vary in the range (10.8 - 14.5)×10^{-6} K^{-1}, similar to the other chromite- and manganite-based materials, as shown in Tables 1.2.2. and 1.3.3. Careful examination of the thermal expansion data shows that the TECs tend to a modest increase with strontium and titanium additions. An increase of the TEC with alkali-earth metal content is typical for perovskites [112, 131, 143, 329], while introduction of reasonable amounts of Ti into chromites and manganites is known to suppress the expansion [16, 131, 156, 163, 231].

Table 3.2. Average linear thermal expansion coefficients of $(La_{0.75-x}Sr_{0.25+x})_{0.95}Mn_{0.5}Cr_{0.5-x}Ti_xO_{3-\delta}$ ceramics in air

Abbreviation	T, K	TEC×10^6, K^{-1}
LSMCT0	373 – 923	10.8 ± 0.1
	923 – 1223	12.7 ± 0.2
	1223 – 1523	14.1 ± 0.1
LSMCT2	303 – 923	10.8 ± 0.1
	923 – 1223	12.8 ± 0.1
	1223 – 1373	13.6 ± 0.1
LSMCT3	303 – 923	11.6 ± 0.1
	923 – 1223	13.5 ± 0.1
	1223 – 1373	14.5 ± 0.1
LSMCT4	293 – 923	11.2 ± 0.1
	923 – 1223	13.1 ± 0.1
	1223 – 1373	14.1 ± 0.1
LSMCT5	303 – 923	11.8 ± 0.1
	923 – 1223	13.1 ± 0.1
	1223 – 1373	14.0 ± 0.1

As shown by TGA results (inset in Fig. 3.3), the compositional and temperature trends in TECs correlate with oxygen nonstoichiometry variations, and may be tentatively attributed to decreasing average oxidation state of manganese cations. In particular, all the compositions showed a gradual increase in TECs at elevated temperatures, consistently with the chemical contribution into the overall expansion. At the same time, the oxygen losses on heating in air are minor ($\Delta\delta \leq 0.002$) even for $(La_{0.25}Sr_{0.75})_{0.95}Mn_{0.5}Ti_{0.5}O_{3-\delta}$, and the increase in TEC values with temperature and x observable in Fig. 3.3 and Table 3.2 results primarily from shifting redox equilibria in the perovskite lattice. Namely, co-doping with Sr^{2+} and Ti^{4+} or increasing the temperature seems to promote disproportionation of manganese:

$2Mn^{3+} \Leftrightarrow Mn^{4+} + Mn^{2+}$ **(Eq. 3.1)**

The process leads to raising the concentration of p-type electronic change carriers and facilitates oxygen losses on heating. Moreover, in accordance with ionic radii of Mn^{2+}, Mn^{3+}, Mn^{4+} (0.83 Å, 0.645 Å, 0.53 Å, respectively, suggesting the octahedral coordination and high-spin state of the cations [133]), the disproportionation of Mn^{3+} should indeed result in an overall enlargement of the cation sizes. On the other hand, $Mn^{4/3+}$ and $Cr^{4+/3+}$ species should be interrelated by redox equilibrium

$Cr^{4+} + Mn^{3+} \Leftrightarrow Mn^{4+} + Cr^{3+}$ **(Eq. 3.2)**

and the concentration of the chromium and manganese species is also affected by temperature or the doping degree. The contribution of both processes into the thermal expansion behavior is consistent with chemically-induced expansivity and with the variations of electronic conductivity and Seebeck coefficient, discussed in following sections.

Analyzing the dependence of TECs on $p(O_2)$, one may observe that reduction of $(La_{0.75}Sr_{0.25})_{0.95}Cr_{0.5}Mn_{0.5}O_{3-\delta}$ leads to a decrease of the thermal expansivity (Table 3.3). On the other hand, simultaneous introduction of Sr and Ti gradually reverses this trend; such a behaviour is in accordance with decreasing the chemical expansivity on heating or cooling $(La_{0.75}Sr_{0.25})_{0.95}Cr_{0.5}Mn_{0.5}O_{3-\delta}$ and $(La_{0.25}Sr_{0.75})_{0.95}Mn_{0.5}Ti_{0.5}O_{3-\delta}$, respectively, as demonstrated below.

Table 3.3. Average linear thermal expansion coefficients of $(La_{0.75-x}Sr_{0.25+x})_{0.95}Mn_{0.5}Cr_{0.5-x}Ti_xO_{3-\delta}$ ceramics in air, Ar and CO-CO_2 atmospheres in comparison with data on selected chromite, manganite and titanate-based ceramic materials

Composition	T, K	$p(O_2)$, atm	TEC×10^6, K^{-1}	Reference
$(La_{0.75}Sr_{0.25})_{0.95}Cr_{0.5}Mn_{0.5}O_{3-\delta}$	923 - 1223	0.21	12.7 ± 0.2	This work
		6×10^{-4}	12.5 ± 0.3	
		5×10^{-21} - 3×10^{-13}	11.7 ± 0.2	
$(La_{0.45}Sr_{0.55})_{0.95}Mn_{0.5}Cr_{0.2}Ti_{0.3}O_{3-\delta}$	923 - 1223	0.21	13.5 ± 0.1	This work
		6×10^{-4}	13.5 ± 0.1	
		6×10^{-21} - 4×10^{-13}	12.7 ± 0.3	
$(La_{0.25}Sr_{0.75})_{0.95}Mn_{0.5}Ti_{0.5}O_{3-\delta}$	923 - 1223	0.21	13.1 ± 0.1	This work
		6×10^{-4}	13.3 ± 0.2	
		5×10^{-21} - 3×10^{-13}	14.3 ± 0.1	
$LaCrO_{3-\delta}$	320 - 1270	wet air	8.0	[112]
		wet H_2	8.2	
$La_{0.9}Ca_{0.1}CrO_{3-\delta}$	320 - 1270	wet air	9.0	[112]
		wet H_2	8.5	
$LaCr_{0.9}Mg_{0.1}O_{3-\delta}$	320 - 1270	wet air	8.4	[112]
		wet H_2	8.4	
$La_{0.9}Sr_{0.1}Cr_{0.95}Co_{0.05}O_{3-\delta}$	320 - 1270	0.21	11.4	[153]
		wet H_2	10.6	
$Pr_{0.5}Sr_{0.5}Mn_{0.5}In_{0.5}O_{3\pm\delta}$	970 - 1270	0.21	12.3	[314]
		~10^{-5}	12.5	
$Sr_{0.67}La_{0.33}Ti_{0.92}Mn_{0.08}O_{3-\delta}$	323 - 1123	0.21	12.3	[335]
		5% H_2-Ar	13.8	

Taking into account that the oxygen loss/uptake upon thermal cycling in air increases with Sr and Ti content (the inset in Fig. 3.3), the latter trend might indicate enhanced oxygen nonstoichiometry variations under reducing conditions for Sr, Ti-enriched compositions or shifting the redox equilibrium between $Cr^{4+/3+}$ and $Mn^{4+/3+}$ couples on temperature or $p(O_2)$ variations as well as upon cation doping. Another possibility might relate to a minor mechanical failure of $(La_{0.25}Sr_{0.75})_{0.95}Mn_{0.5}Ti_{0.5}O_{3-\delta}$ on reduction; such a phenomenon has been observed on related compounds [16, 105, 317]. One should note that a slight lowering of TECs at lower $p(O_2)$ is typical for chromite perovskites (Table 3.3) which are characterized by an obvious correlation between the oxygen stoichiometry variations and dimensional changes.

3.1.3. Chemical expansion

As for the parent material, $(La_{0.75}Sr_{0.25})_{0.95}Cr_{0.5}Mn_{0.5}O_{3-\delta}$ [10], the chemically-induced expansion of Ti-substituted compositions on decreasing $p(O_2)$ down to 6×10^{-4} atm is negligible, lower than 0.03% (Fig. 3.4 and Table 3.4). In reducing atmospheres, the lattice expansion increases and achieves almost 0.6% with respect to the atmospheric oxygen pressure (Table 3.5).

Table 3.4. Chemically-induced strain of $(La_{0.75-x}Sr_{0.25+x})_{0.95}Mn_{0.5}Cr_{0.5-x}Ti_xO_{3-\delta}$ ceramics, measured on reducing $p(O_2)$ from 0.21 atm down to 6×10^{-4} atm

Composition	$(L-L^{air})/L^{air}\times10^3$						
	923 K	973 K	1023 K	1073 K	1123 K	1173 K	1223 K
$(La_{0.75}Sr_{0.25})_{0.95}Cr_{0.5}Mn_{0.5}O_{3-\delta}$	0.20	0.23	0.19	0.15	0.14	0.15	0.17
$(La_{0.45}Sr_{0.55})_{0.95}Mn_{0.5}Cr_{0.2}Ti_{0.3}O_{3-\delta}$	0.10	0.11	0.14	0.16	0.13	0.11	0.09
$(La_{0.25}Sr_{0.75})_{0.95}Mn_{0.5}Ti_{0.5}O_{3-\delta}$	0.17	0.20	0.21	0.22	0.20	0.21	0.25

Table 3.5. Chemically-induced strain of $(La_{0.75-x}Sr_{0.25+x})_{0.95}Mn_{0.5}Cr_{0.5-x}Ti_xO_{3-\delta}$ ceramics in reducing atmospheres

T, K	$(La_{0.75}Sr_{0.25})_{0.95}Cr_{0.5}Mn_{0.5}O_{3-\delta}$		$(La_{0.45}Sr_{0.55})_{0.95}Mn_{0.5}Cr_{0.2}Ti_{0.3}O_{3-\delta}$		$(La_{0.25}Sr_{0.75})_{0.95}Mn_{0.5}Ti_{0.5}O_{3-\delta}$	
	$p(O_2)$, atm	$(L-L^{air})/L^{air}\times10^3$	$p(O_2)$, atm	$(L-L^{air})/L^{air}\times10^3$	$p(O_2)$, atm	$(L-L^{air})/L^{air}\times10^3$
923	5×10^{-21}	2.25	6×10^{-21}	4.51	5×10^{-21}	5.21
973	2×10^{-19}	2.30	3×10^{-19}	4.49	2×10^{-19}	5.25
1023	6×10^{-18}	2.21	8×10^{-18}	4.44	6×10^{-18}	5.30
1073	1×10^{-16}	2.12	2×10^{-16}	4.39	1×10^{-16}	5.34
1123	2×10^{-15}	2.08	3×10^{-15}	4.33	2×10^{-15}	5.40
1173	3×10^{-14}	2.04	4×10^{-14}	4.30	3×10^{-14}	5.47
1223	3×10^{-13}	2.01	4×10^{-13}	4.26	3×10^{-13}	5.56

The expansion values in Tables 3.4 - 3.5 are given with respect to the length in air at a given temperature (L^{air}).

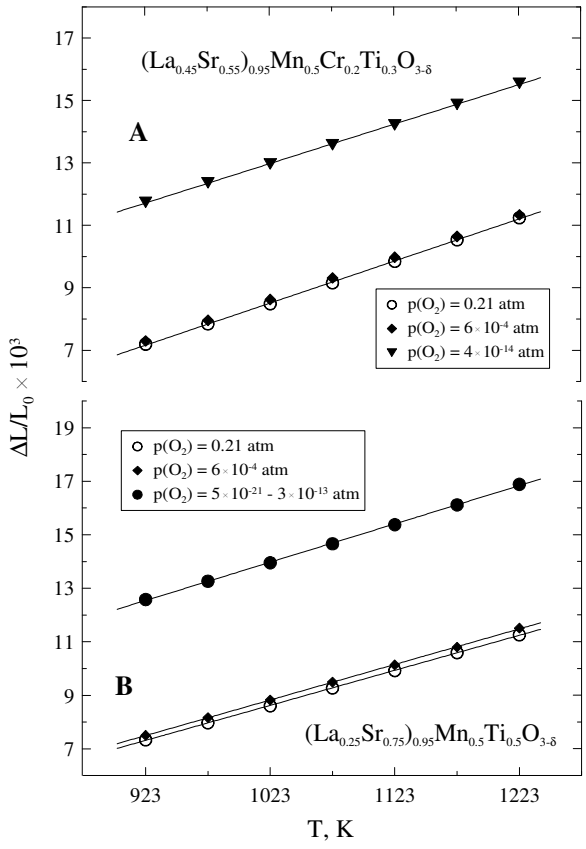

Fig. 3.4. Temperature dependencies of the relative length changes of LSMCT3 (A) and LSMCT5 (B) ceramics in air, Ar and CO-CO_2 atmospheres

In accordance with the model described in Chapter 1.2.4, the $p(O_2)$-induced dimensional changes of perovskite-type materials containing transition metal cations are primarily associated with variations of their oxidation state and ionic radii [193, 196, 234, 236]. The level of the chemical strains indicated in Table 3.5 is close to that observable for $La_{0.8}Sr_{0.2}Mn_{0.5}Al_{0.5}O_{3\pm\delta}$ and $La_{0.4}Sr_{0.6}Mn_{0.6}Ti_{0.4}O_{3\pm\delta}$ perovskites (0.6 - 0.7% upon reduction from air into H_2 - H_2O - Ar atmosphere). Taking into account the high and close Mn concentration in the perovskites indicated and in $(La_{0.25}Sr_{0.75})_{0.95}Mn_{0.5}Ti_{0.5}O_{3-\delta}$ as well as comparatively facilitated reducibility of Mn^{4+} species, one may suggest that the redox couple $Mn^{4+/3+}$ is primarily responsible for the dimension behaviour observed. In particular, extensive oxygen losses on reduction and contribution of the processes described by Eqs. (3.1), (3.2) is confirmed by trends in the total conductivity and Seebeck coefficient with $p(O_2)$, in particular, by the conductivity drop at low oxygen pressures, shown in following sections. Again, the chemically induced expansion of $(La_{0.75-x}Sr_{0.25+x})_{0.95}Mn_{0.5}Cr_{0.5-x}Ti_xO_{3-\delta}$ increases with increasing x, thus confirming that Sr and Ti co-doping promotes oxygen losses and shifts redox equilibria between $Mn^{4+/3+/2+}$ and $Cr^{4+/3+}$ cations.

Irrespective to the compositional trends, the overall level of the thermal and chemical expansion observed in the wide range of conditions is moderate. This makes it possible to use the title materials in contact with solid oxide electrolytes, such as stabilized zirconia, CeO_2-based compositions, LSGM or $La_{10}Si_5AlO_{26.5}$ [30, 227, 580, 581]. Nonetheless, one should still be cautious concerning the strains at elevated temperatures necessary to fabricate electrochemical cells. For example, cooling $(La_{0.25}Sr_{0.75})_{0.95}Mn_{0.5}Ti_{0.5}O_{3-\delta}$ from 1373 to 973 K in air leads to the contraction within $\varepsilon_T \approx -0.54\%$. If

assuming that a relatively thin layer of solid electrolyte with a TEC of 11.1×10^{-6} K^{-1} is fired onto a thick $(La_{0.25}Sr_{0.75})_{0.95}Mn_{0.5}Ti_{0.5}O_{3-\delta}$ substrate, reaching an unstrained condition at 1373 K in air, the expected strain difference after cooling down to 973 K is in the order of $\Delta\varepsilon \approx 0.10\%$. The compressive stresses imposed on the thin solid-electrolyte layer can then be estimated as $\sigma_C \approx \Delta\varepsilon E/(1-\nu) \approx -179$MPa, using typical values of the elastic constants E = 125 GPa and $\nu \approx 0.3$ known for LSGM at 973 K [582]. These low and compressive stresses should be acceptable for applications of the electrochemical cells. However, the thermal and chemical strain components of $(La_{0.25}Sr_{0.75})_{0.95}Mn_{0.5}Ti_{0.5}O_{3-\delta}$ almost compensate each other under reducing conditions, for instance, $(\varepsilon_T+\varepsilon_C) \approx -0.02\%$ at 973 K and $p(O_2) = 10^{-19}$ atm. Under these conditions, the strain difference between the layers becomes $\Delta\varepsilon \approx -0.44\%$, imposing excessive tensile stresses on the thin electrolyte layer (for the above-quoted elastic constants, $\sigma_C \approx 786$ MPa). On the other hand, actual stresses may be significantly lowered when one of the contacting layers is very porous, as for the deposition of a thin porous electrode onto a thicker solid electrolyte support. In the latter case, the stresses under reducing conditions revert from tensile to compressive, thus providing better thermomechanical stability.

3.1.4. Total conductivity

The conductivity in $(La_{0.75-x}Sr_{0.25+x})_{0.95}Mn_{0.5}Cr_{0.5-x}Ti_xO_{3-\delta}$ is predominantly electronic; the oxygen permeation data presented below show that the oxygen-ionic contribution is lower that 10^{-3} %. Fig. 3.5 displays the temperature dependencies of total conductivity (σ) of the ceramic materials studied at atmospheric $p(O_2)$. In air, the conductivity has a thermally-activated character; the activation energies E_a, calculated in accordance with Eq. (2.2), vary within 16 - 30 kJ/mol at 943 - 1263 K (Table 3.6), decreasing on Sr and Ti co-doping.

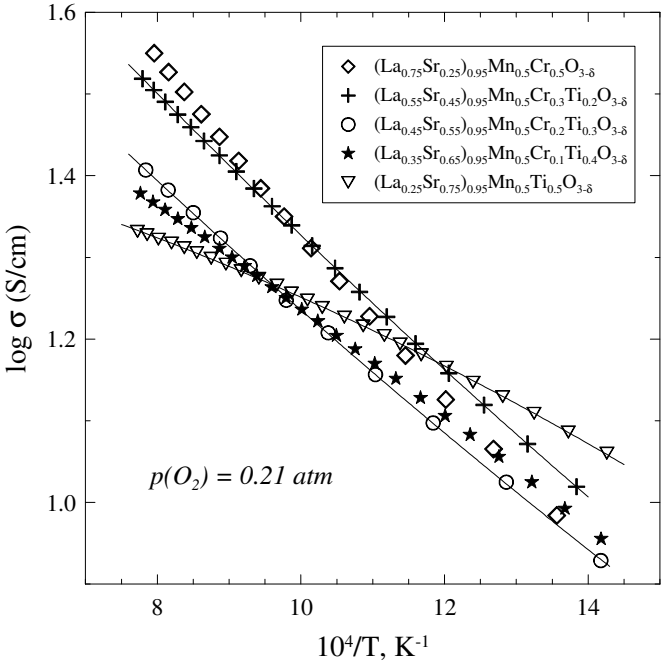

Fig. 3.5. Temperature dependencies of the total conductivity of $(La_{0.75-x}Sr_{0.25+x})_{0.95}Mn_{0.5}Cr_{0.5-x}Ti_xO_{3-\delta}$ ceramics in air

Table 3.6. Activation energies for the total conductivity of $(La_{0.75-x}Sr_{0.25+x})_{0.95}Mn_{0.5}Cr_{0.5-x}Ti_xO_{3-\delta}$ at atmospheric $p(O_2)$

Composition	T, K	E_a, kJ/mol
$(La_{0.75}Sr_{0.25})_{0.95}Cr_{0.5}Mn_{0.5}O_{3-\delta}$	553 - 873	22.6 ± 0.5
	943 - 1263	29.8 ± 0.6
$(La_{0.55}Sr_{0.45})_{0.95}Mn_{0.5}Cr_{0.3}Ti_{0.2}O_{3-\delta}$	553 - 873	20.3 ± 0.4
	943 - 1263	25.6 ± 0.3
$(La_{0.45}Sr_{0.55})_{0.95}Mn_{0.5}Cr_{0.2}Ti_{0.3}O_{3-\delta}$	643 - 903	20.0 ± 0.8
	943 - 1273	24.4 ± 0.8
$(La_{0.35}Sr_{0.65})_{0.95}Mn_{0.5}Cr_{0.1}Ti_{0.4}O_{3-\delta}$	553 - 873	20.2 ± 0.2
	943 - 1263	21.4 ± 0.1
$(La_{0.25}Sr_{0.75})_{0.95}Mn_{0.5}Ti_{0.5}O_{3-\delta}$	553 - 873	15.6 ± 0.1
	943 - 1263	16.1 ± 0.1

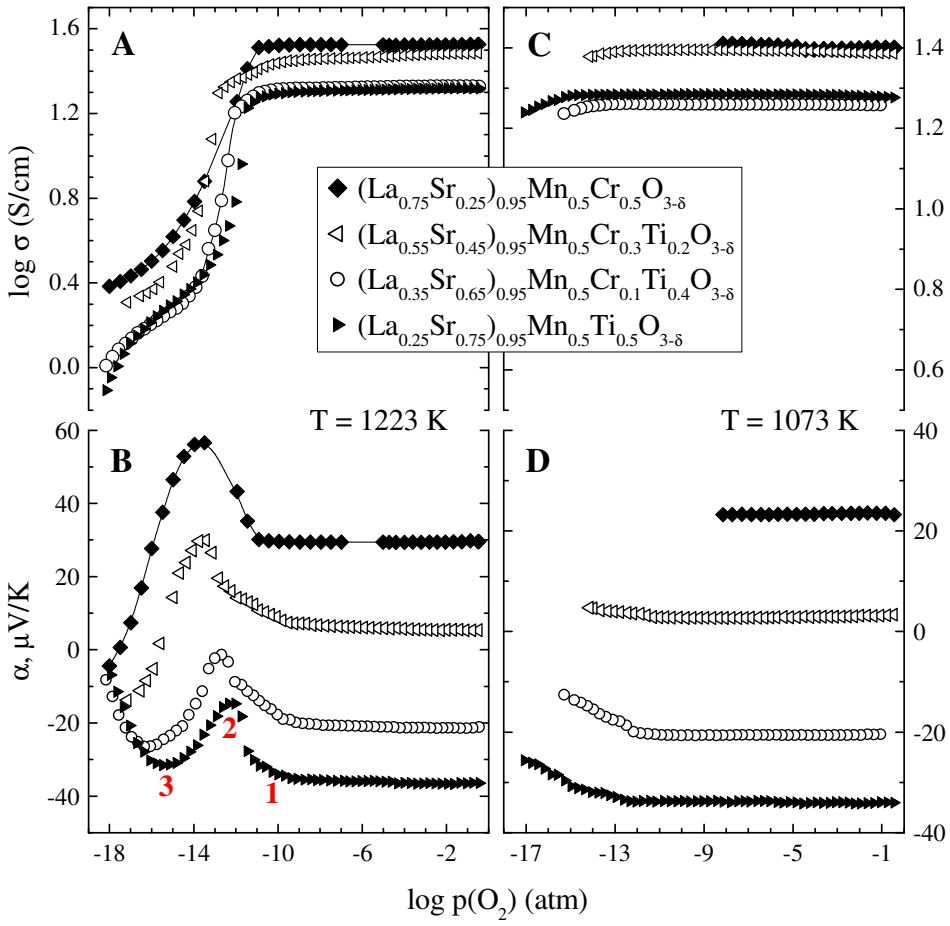

Fig. 3.6. Oxygen partial pressure dependencies of the total conductivity (A, C) and Seebeck coefficient (B, D) of $(La_{0.75-x}Sr_{0.25+x})_{0.95}Mn_{0.5}Cr_{0.5-x}Ti_xO_{3-\delta}$ at 1223 K (A, B) and 1073 K (C, D). The numbers 1, 2, 3 show characteristic conditions corresponding to changes in the redox behaviour (see text)

Introduction of Sr into $LaCrO_{3-\delta}$ or $LaMnO_{3-\delta}$ is known to promote the electronic transport and reduce the activation energy [121, 131, 143]. Moreover, $SrTiO_{3-\delta}$ and $SrMnO_{3-\delta}$-based compositions exhibit broadband conduction mechanism in reductive atmospheres [320, 381, 457, 583], and the reduction of the activation energies might be associated with partial transition in the transport mechanism and corresponding trends in the electronic charge carrier mobility. In turn, temperature dependencies of the charge-carrier concentration should be governed by two factors having opposite effects, namely thermal excitation and increasing oxygen deficiency when temperature increases.

The oxygen partial pressure dependencies of the electrical properties (Figs. 3.6 - 3.7) exhibit a series of specific features typical for $LaMnO_3$- and $LaCrO_3$-based solid solutions [184, 214, 226, 323]. First of all, both the Seebeck coefficient (α) and conductivity are essentially $p(O_2)$-independent in oxidizing and moderately reducing environments, indicating that the oxygen stoichiometry changes are minor. Increasing x lowers the thermopower down to negative values at $x > 0.2$. This trend is not surprising taking into account that strontium titanate exhibits n-type electronic transport. However, reducing oxygen pressure below a certain level, marked as "1" in Fig. 3.6B, gives rise to increasing oxygen deficiency, resulting in increasing Seebeck coefficient and decreasing conductivity. This type of behavior observed for all compositions provides an argument in favor of dominant p-type electronic transport, despite the negative α values for Sr- and Ti-rich materials.

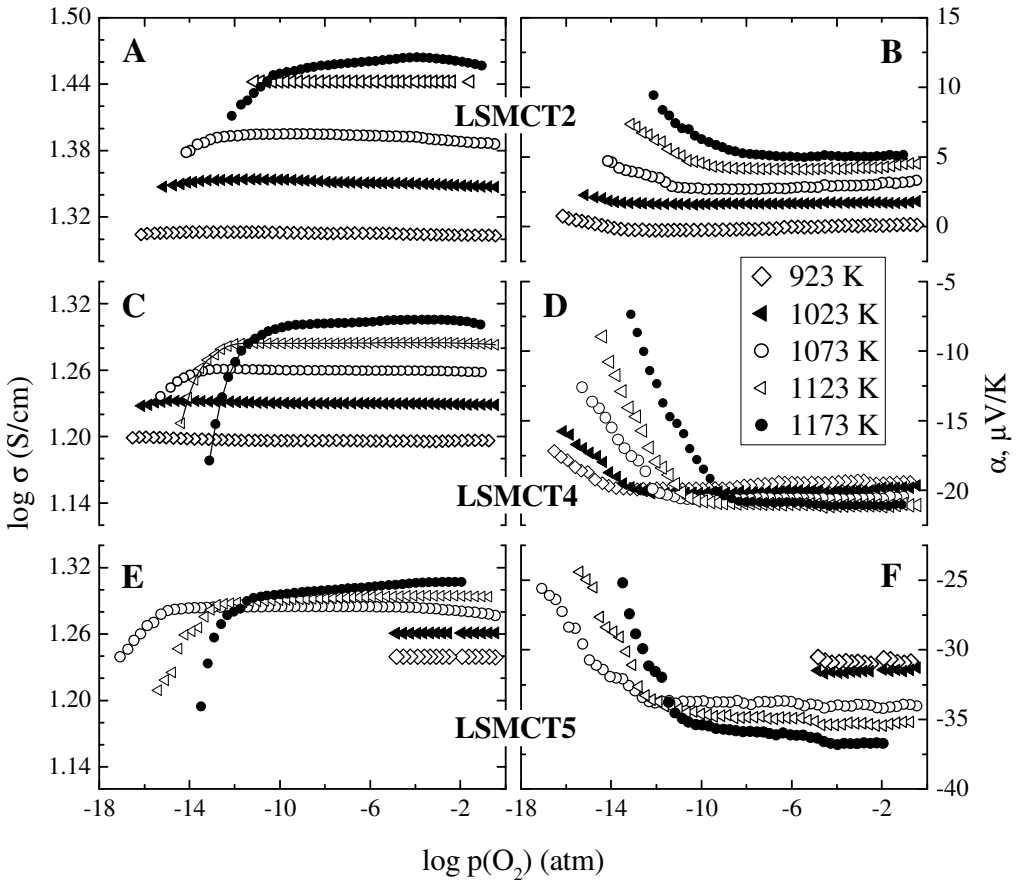

Fig. 3.7. Oxygen partial pressure dependencies of the total conductivity and Seebeck coefficient of LSMCT2 (A, B), LSMCT4 (C, D), LSMCT5 (E, F)

In oxidizing and mildly reducing atmospheres the Seebeck coefficients increase with temperature for the compositions with x = 0 - 0.2, but exhibit a slight opposite tendency when x increases up to 0.4 - 0.5. A possible origin of the thermopower variations in $(La_{0.75}Sr_{0.25})_{0.95}Cr_{0.5}Mn_{0.5}O_{3-\delta}$, associated with shifting the redox equilibrium between Cr and Mn cations towards formation of Mn^{4+} and Cr^{3+} species on heating (Eqs. (3.1), (3.2)) and site-exclusion effects around Cr^{4+} cations, was suggested in [10]. In the case of $(La_{0.75-x}Sr_{0.25+x})_{0.95}Mn_{0.5}Cr_{0.5-x}Ti_xO_{3-\delta}$ (x = 0.4 - 0.5), all titanium cations under oxidizing conditions are expected to have constant oxidation state, 4+; the site-exclusion phenomena near Ti^{4+}, if any, should remain essentially unchanged with increasing temperature. Since the oxygen stoichiometry variations with temperature are much smaller than might be expected from the thermopower changes, the decrease in Seebeck coefficient originates from thermal excitation of p-type electronic charge carriers in accordance with the Heikes formula [26, 166]. The parameters (p/N) and ($\mu_p \times N$) characterizing the population of the electron holes and their mobility were calculated from the data on the conductivity and Seebeck coefficient using Eqs. (2.3) and (2.5); the estimates are shown in Fig. 3.8 - 3.9.

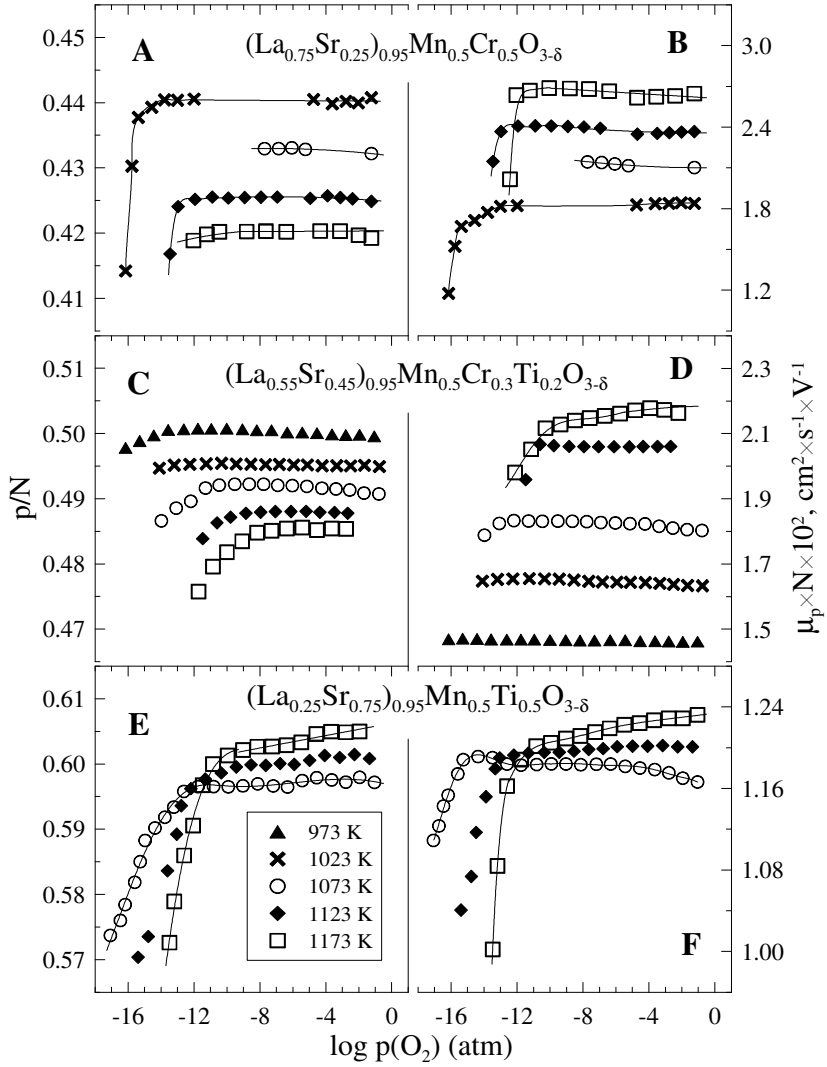

Fig. 3.8. Oxygen partial pressure dependencies of the estimated $\mu_p \times N$ (A) and p/N (B) values for LSMCT0 (A, B), LSMCT2 (C, D) and LSMCT5 (E, F)

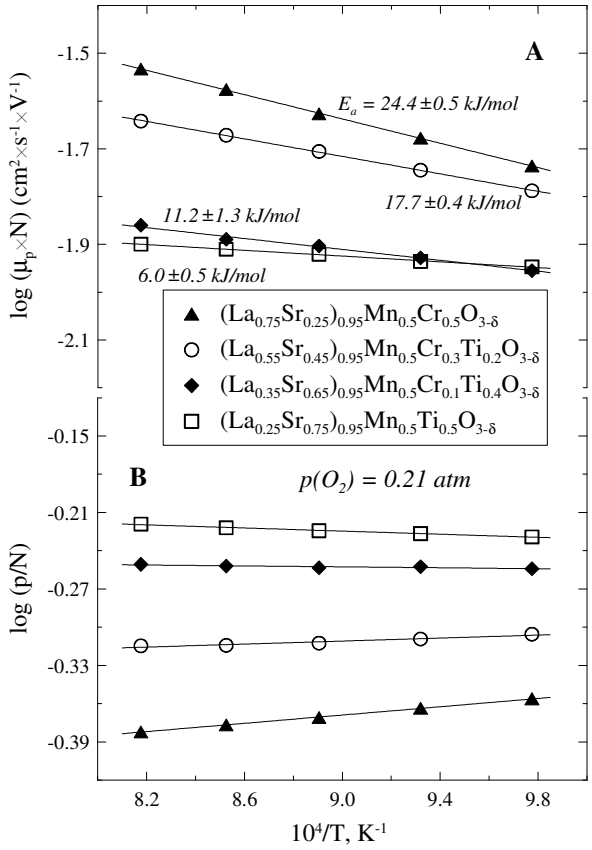

Fig. 3.9. Temperature dependencies of the estimated $\mu_p \times N$ (A) and p/N (B) values at atmospheric oxygen pressure

For all the materials studied, the hole mobility is temperature-activated. This makes it possible to conclude that the small-polaron mechanism is dominant, irrespective of the progressive decrease in the mobility activation energy indicating an increasing role of the broad-band mechanism on doping. In the case of $(La_{0.75}Sr_{0.25})_{0.95}Cr_{0.5}Mn_{0.5}O_{3-\delta}$, the ($p/N$) ratio decreases with increasing temperature as the equilibrium between the B-site cations (Eq. (3.2)) shifts towards Mn^{4+} formation and the site-blocking effects near Cr^{4+} disappear [10]; $(La_{0.25}Sr_{0.75})_{0.95}Mn_{0.5}Ti_{0.5}O_{3-\delta}$ exhibit a modest, but clearly visible opposite trend (Fig. 3.9). If considering the stable oxidation state of Ti^{4+} under oxidizing conditions, rising (p/N) with temperature provides an evidence for progressive Mn^{3+} disproportionation, leading to Mn^{4+} and Mn^{2+} formation (Eq. (3.1)). The increasing Mn^{4+} concentration is responsible for higher oxygen losses and for the larger chemical and thermal expansion observed for Ti- and Sr-rich compositions. The variations in Seebeck coefficient, which becomes negative on co-doping, originate primarily from increasing Mn^{4+} concentration; the occupancy of manganese sites available for hole hopping in $(La_{0.25}Sr_{0.75})_{0.95}Mn_{0.5}Ti_{0.5}O_{3-\delta}$ under oxidizing conditions is higher than 50%. The latter factor contributes also to the relatively low hole mobility which decreases on Ti and Sr co-doping, mainly due to blocking of electronic transfer by the stable Ti^{4+} cations.

Comparison of the oxygen pressures corresponding to the onset of large oxygen losses (point "1" in Fig. 3.6) with the low-$p(O_2)$ stability limits of Cr-, Mn- and Ti-containing oxide phases [26, 39, 46], as shown in Fig. 3.10, suggests that these phenomena are mainly associated with reduction of manganese cations rather than with phase decomposition, in agreement with XRD (Fig. 3.1).

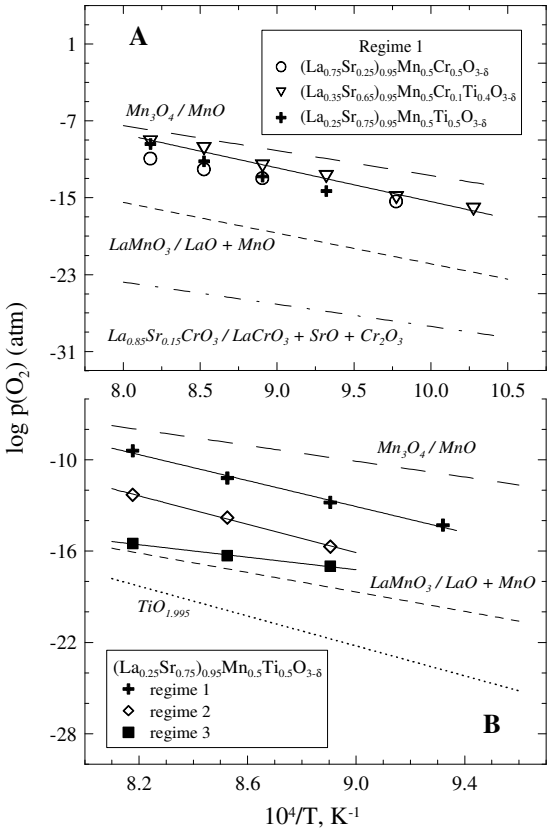

Fig. 3.10. Oxygen partial pressures corresponding to the changes in redox behaviour marked as "1", "2", "3" in Fig. 3.6B. Literature data on the phase stability of Cr- and Mn-containing phases [39, 44, 46] and iso-stoichiometric line for $TiO_{1.995}$ [26] are shown for comparison.

Notice also that the corresponding $p(O_2)$ values are essentially independent of x in $(La_{0.75-x}Sr_{0.25+x})_{0.95}Mn_{0.5}Cr_{0.5-x}Ti_xO_{3-\delta}$, indicating that the electronic transport processes and oxygen deficiency variations are determined by the B sites occupied by manganese, whereas Cr and Ti cations form a redox-stable matrix. Another possibility of the comparable level of the decomposition limits might relate to two opposite effects of Sr and Ti introduction on the stability, with resultant mutual compensation.

At oxygen partial pressures below approximately 10^{-13} atm, the slope of the σ vs. $p(O_2)$ curves decreases (Fig. 3.6A); the Seebeck coefficient of Ti-rich compositions exhibits a maximum and a minimum marked in Fig. 3.6B as "2" and "3", respectively. Most likely, these regimes are associated with rising contributions of the $Mn^{3+/2+}$ and $Ti^{4+/3+}$ redox couples. One should note that the low-$p(O_2)$ process (point "3") is characterized by substantially lower enthalpy in comparison with those occurring in the perovskites studied at higher oxygen pressures (points "1" and "2"), decomposition of Mn_3O_4 or $LaMnO_{3-\delta}$ as well as formation of oxygen vacancies in $TiO_{2-\delta}$. However, due to phase transitions typical for $(La,Sr)(Mn,Cr)O_{3-\delta}$ perovskites on reduction [8, 113] and segregation of MnO traces (Fig. 3.1), quantitative analysis of the electrical properties in this $p(O_2)$ range is problematic. Whatever the microscopic mechanisms, co-doping with Sr and Ti leads to lower conductivity under reducing conditions; this should further increase the role of electronic transport as the electrode performance-limiting factor, characteristic of parent $(La_{0.75}Sr_{0.25})_{0.95}Cr_{0.5}Mn_{0.5}O_{3-\delta}$ [10]. Consequently, the electrochemical activity of $(La_{0.75-x}Sr_{0.25+x})_{0.95}Mn_{0.5}Cr_{0.5-x}Ti_xO_{3-\delta}$ in reductive atmospheres is expected to be lower for Sr- and Ti-enriched compositions.

3.1.5. Oxygen permeability

Despite the small differences in the oxygen stoichiometry at elevated temperatures (the inset in Fig. 3.3), the steady-state oxygen permeation fluxes (*j*) through dense $(La_{0.75-x}Sr_{0.25+x})_{0.95}Mn_{0.5}Cr_{0.5-x}Ti_xO_{3-\delta}$ membranes under a fixed oxygen pressure gradient are quite similar for all the compositions (Fig. 3.11). The activation energies of the permeation fluxes calculated analogously with those of the total conductivity (Eq. 2.2) are also essentially composition-independent and vary in the range 150 - 200 kJ/mol (Table 3.7), close to the corresponding values of oxygen diffusion or ionic conductivity in chromite or manganite-based perovskites [10, 187, 305, 320].

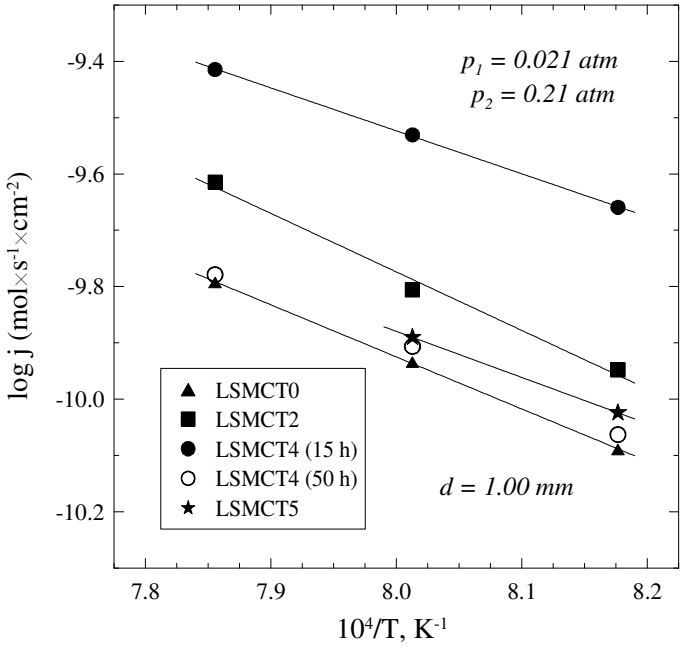

Fig. 3.11. Temperature dependencies of the oxygen permeation fluxes through dense $(La_{0.75-x}Sr_{0.25+x})_{0.95}Mn_{0.5}Cr_{0.5-x}Ti_xO_{3-\delta}$ membranes under a fixed $p(O_2)$ gradient. For LSMCT4, the data on ceramics sintered during 15 and 50 hours are compared. For other materials, the sintering time is 15 hours.

Table 3.7. Activation energies of the permeation fluxes through $(La_{0.75-x}Sr_{0.25+x})_{0.95}Mn_{0.5}Cr_{0.5-x}Ti_xO_{3-\delta}$ membranes under the gradient of 0.21 and 0.021 atm at the feed and permeate side, correspondingly. The membrane thickness is 1.00±0.02 mm.

Composition	T, K	E_a, kJ/mol
$(La_{0.75}Sr_{0.25})_{0.95}Cr_{0.5}Mn_{0.5}O_{3-\delta}$	1223 – 1273	187±29
$(La_{0.55}Sr_{0.45})_{0.95}Mn_{0.5}Cr_{0.3}Ti_{0.2}O_{3-\delta}$	1223 – 1273	209
$(La_{0.35}Sr_{0.65})_{0.95}Mn_{0.5}Cr_{0.1}Ti_{0.4}O_{3-\delta}$ (15 hours)	1223 – 1273	156±32
$(La_{0.35}Sr_{0.65})_{0.95}Mn_{0.5}Cr_{0.1}Ti_{0.4}O_{3-\delta}$ (50 hours)	1223 – 1273	180±102
$(La_{0.25}Sr_{0.75})_{0.95}Mn_{0.5}Ti_{0.5}O_{3-\delta}$	1223 – 1248	167

The similarity between the fluxes suggests that the overall rate of oxygen transport is essentially determined by similar mechanisms, which are not directly related to the intrinsic factors, such as the oxygen vacancy concentration in the bulk or metal-oxygen bonding strength dependent of the cation composition.

The likely limiting factors include, in particular, surface exchange kinetics and oxygen diffusion along the grain boundaries. In order to validate the latter assumption, effects of the grain size on the steady-state oxygen permeation were assessed for $(La_{0.35}Sr_{0.65})_{0.95}Mn_{0.5}Cr_{0.1}Ti_{0.4}O_{3-\delta}$ ceramics sintered during 15 and 50 h (Fig. 3.12); the relevant microstructures are compared in Fig. 3.13.

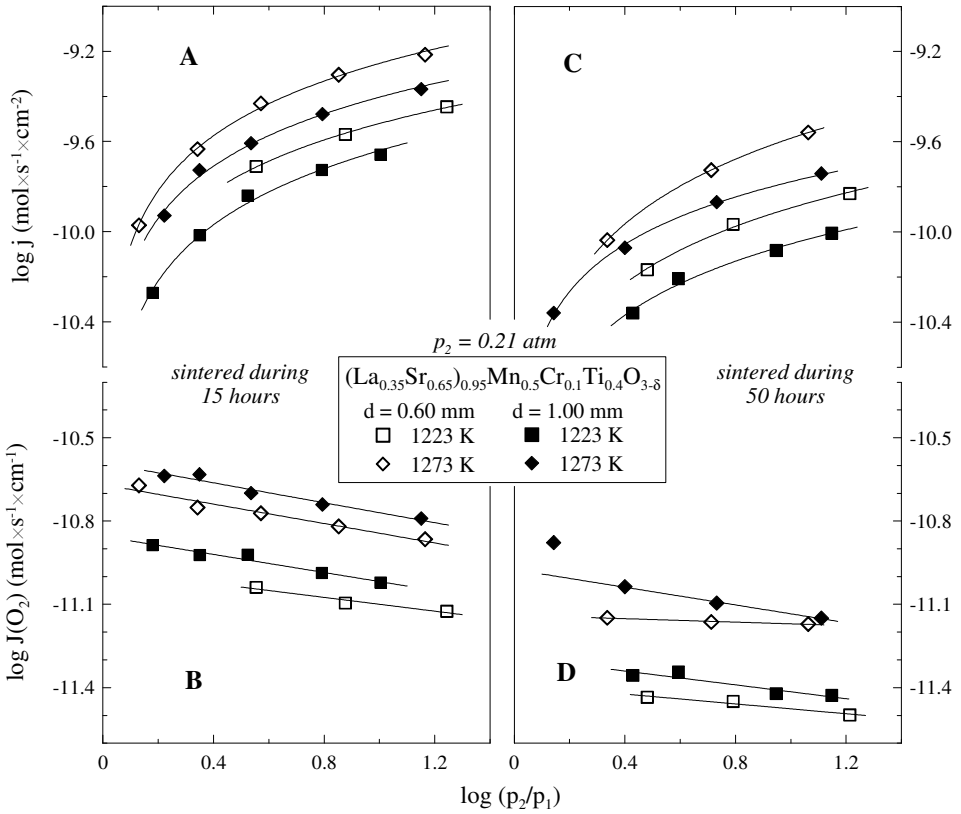

Fig. 3.12. Oxygen permeation fluxes (A, C) and specific permeability (B, D) of LSMCT4 sintered during 15 hours (A, B) and 50 hours (C, D)

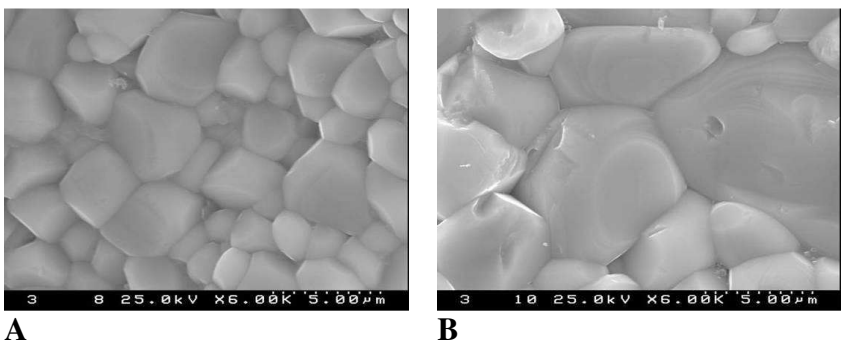

Fig. 3.13. SEM micrographs of LSMCT4 ceramics sintered during 15 hours (A) and 50 hours (B)

The results show that decreasing grain-boundary area causes a significant decrease in the oxygen fluxes, whilst the apparent activation energy remains essentially unchanged. The changes in the permeation fluxes are substantially larger than the level of experimental uncertainties, and are well reproducible for the membranes with different thicknesses. The latter observation is illustrated by Fig. 3.12 (B and D), which compares the values of specific oxygen permeability $J(O_2)$, calculated in accordance with Eq. (2.7). It should also be mentioned that significant grain-boundary contributions to the oxygen ion diffusion are known for $LaCrO_3$-, $LaMnO_3$- and especially $SrTiO_3$-based materials with low oxygen nonstoichiometry [112, 254, 336, 339, 371, 512]. The microstructural features associated with liquid phase-assisted sintering were reported to promote fast ionic conduction along the boundaries [44].

Further inspection of the results shown in Fig. 3.12 shows also a non-negligible role of the surface exchange kinetics. The specific oxygen permeability is proportional to ($j \times d$) and should be thickness-independent when the exchange processes are fast enough [10, 320]. For $(La_{0.35}Sr_{0.65})_{0.95}Mn_{0.5}Cr_{0.1}Ti_{0.4}O_{3-\delta}$ membranes, increasing the thickness leads to lower oxygen fluxes and higher $J(O_2)$ values due to a decreasing role of the interfacial exchange. This complex mechanism makes it impossible to evaluate relative contributions of the grain bulk, grain boundaries and surface-related processes to the overall membrane resistance to oxygen transfer. The oxygem ionic conductivity evaluated using the approach described in Chapter 2 (Eq. 2.11) is as low as $(1 - 5)\times10^{-4}$ S/cm at 1223 - 1273 K which is more than 10 times higher as compared with that for $La_{0.87}Sr_{0.13}Cr_{1.03}O_{3-\tilde{\delta}}$ [198]. Nevertheless, this level of the ionic diffusion is still insufficient to expect any considerable enhancement in the electrochemical reaction zone due to oxygen transport through electrode bulk, as for (La,Sr)MnO_3-based cathodes [324, 584].

3.1.6. Redox kinetics

The low values of the permeation fluxes through $(La_{0.75-x}Sr_{0.25+x})_{0.95}Mn_{0.5}Cr_{0.5-x}Ti_xO_{3-\delta}$ ceramics and resultant large errors in their determination do not allow to make an unambiguous conclusion about the effect of Sr and Ti content on the parameters responsible for the oxygen transport in the perovskites. At the same time, knowledge of the relationships between the composition and transport characteristics is desirable with respect to selection of the optimum composition for the electrochemical applications. In order to compare the rates of the surface exchange processes, mass relaxation studies were carried out on $La_{0.75}Sr_{0.25}Mn_{0.5}Cr_{0.5}O_{3-\delta}$ and $La_{0.25}Sr_{0.75}Mn_{0.5}Ti_{0.5}O_{3-\delta}$ powders under isothermal conditions; an example of the transient behaviour is shown in Fig. 3.14. Both powders were produced by mechanical grinding ceramic samples which should produce the powders with comparable surface area.

The redox kinetics was evaluated from TGA data collected on sequential switches of the atmosphere in the order air - Ar - 10% H_2 - N_2 - Ar - air, in accordance with the model

$$m(t) = m_1 + m_2 \exp\left(-\frac{t}{\tau}\right) \qquad \textbf{(Eq. 3.3)}$$

where m, t, and τ are the mass, time and relaxation time constant, respectively. Note that the right term, $\exp(-t/\tau)$, is common for the description of non-steady-state diffusion and exchange processes and originates from solving the temporal part of the second Fick's law by separation of variables. An exact agreement with Eq. (3.3) corresponds to dominating surface limitations, whereas the solutions for open and partly open boundaries (relatively fast surface exchange) may be represented by a series of exponential terms $\exp(-t/\tau_i)$ with τ_i calculated from the boundary conditions and transport coefficients [575].

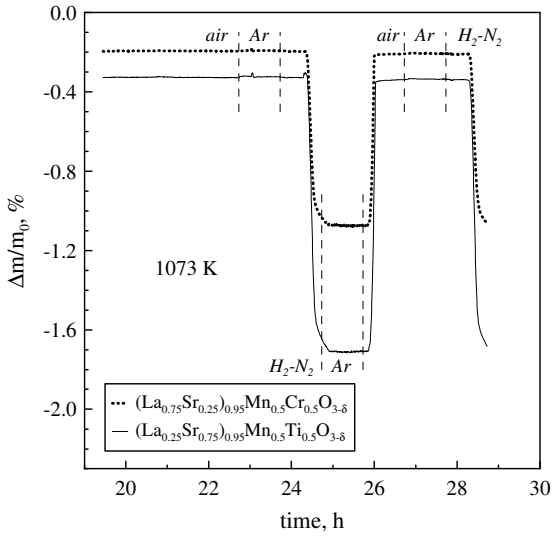

Fig. 3.14. Comparison of relative weight changes of $(La_{0.75}Sr_{0.25})_{0.95}Cr_{0.5}Mn_{0.5}O_{3-\delta}$ and $(La_{0.25}Sr_{0.75})_{0.25}Mn_{0.5}Ti_{0.5}O_{3-\delta}$ on cycling of the oxygen chemical potential in the gaseous phase, measured by TGA. m_0 is the initial weight of the samples equilibrated with atmospheric oxygen at low temperature

The model may be transformed into

$$\frac{m(t\to\infty)-m(t)}{m(t\to\infty)-m(t=0)}=\exp\left(-\frac{t}{\tau}\right) \qquad \textbf{(Eq. 3.4)}$$

and

$$\int_0^\infty \exp\left(-\frac{t}{\tau}\right)dt=\tau \qquad \textbf{(Eq. 3.5)}$$

which can be used to calculate t by numerical integration of the experimental data. Also, deviations from linearity of the term $\frac{m(t\to\infty)-m(t)}{m(t\to\infty)-m(t=0)}$ vs. $\exp(-t/\tau)$ plots enable to identify processes where the number of rate-determining steps is higher than one. The latter situation is indeed observed for the title materials (inset in Fig. 3.15), but the redox kinetics and time constants exhibited by $La_{0.75}Sr_{0.25}Mn_{0.5}Cr_{0.5}O_{3-\delta}$ and $La_{0.25}Sr_{0.75}Mn_{0.5}Ti_{0.5}O_{3-\delta}$ powders are similar within the limits of experimental error.

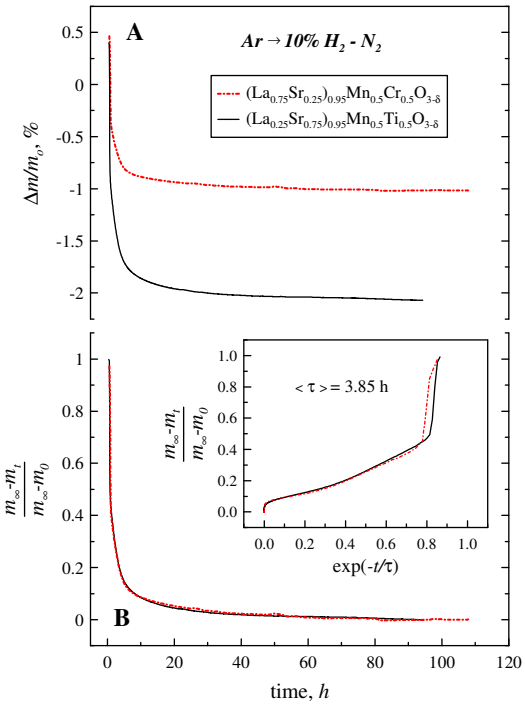

Fig. 3.15. Examples of the relative weight changes of $(La_{0.75}Sr_{0.25})_{0.95}Cr_{0.5}Mn_{0.5}O_{3-\delta}$ and $(La_{0.25}Sr_{0.75})_{0.25}Mn_{0.5}Ti_{0.5}O_{3-\delta}$ powders on reduction after switching the atmosphere from Ar to 10% H_2 - N_2 at 1073 K (A) and reduction kinetics analysis (B)

The similarity between the surface exchange parameters is consistent with a close level of the permeation fluxes exhibited by the perovskites with various Sr and Ti amounts (Fig. 3.11) assuming that the overall kinetics of oxygen permeability is strongly influenced by the surface-related processes. Since the bulk ionic transport in $(La_{0.75-x}Sr_{0.25+x})_{0.95}Mn_{0.5}Cr_{0.5-x}Ti_xO_{3-\delta}$ is rather slow, the low-$p(O_2)$ electrochemical activity should primarily be related with the electronic conductivity of the materials under anodic conditions.

3.1.7. Electrochemical behavior: general trends

Fig. 3.16 shows typical anodic polarization curves obtained on porous $(La_{0.75-x}Sr_{0.25+x})_{0.95}Mn_{0.5}Cr_{0.5-x}Ti_xO_{3-\delta}$-based layers in H_2 - H_2O - N_2 atmosphere. The results demonstrated a good reproducibility for different series of the samples, as shown in the inset. No substantial alterations in the electrochemical behavior were also observed after the current cycling and temperature variations in the range 873 - 1073 K; SEM inspections revealed no significant microstructural degradation after the measurements, both in air and in reducing atmospheres (Fig. 3.17).

In general, increasing x in $(La_{0.75-x}Sr_{0.25+x})_{0.95}Mn_{0.5}Cr_{0.5-x}Ti_xO_{3-\delta}$ system deteriorates the anode performance. This trend correlates with the data on the electrical conductivity in the high-temperature range (Fig. 3.6), indicating that the electrode reaction rate under reducing conditions is strongly affected by the electronic transport. The anodes in contact with $La_{10}Si_5AlO_{26.5}$ showed higher overpotentials and a stronger tendency to limiting currents. The relationships between the functional characteristics of the anode and electrolyte and electrode performance as well as approaches towards optimizing the electrochemical activity of anodes are considered in Chapter 5.

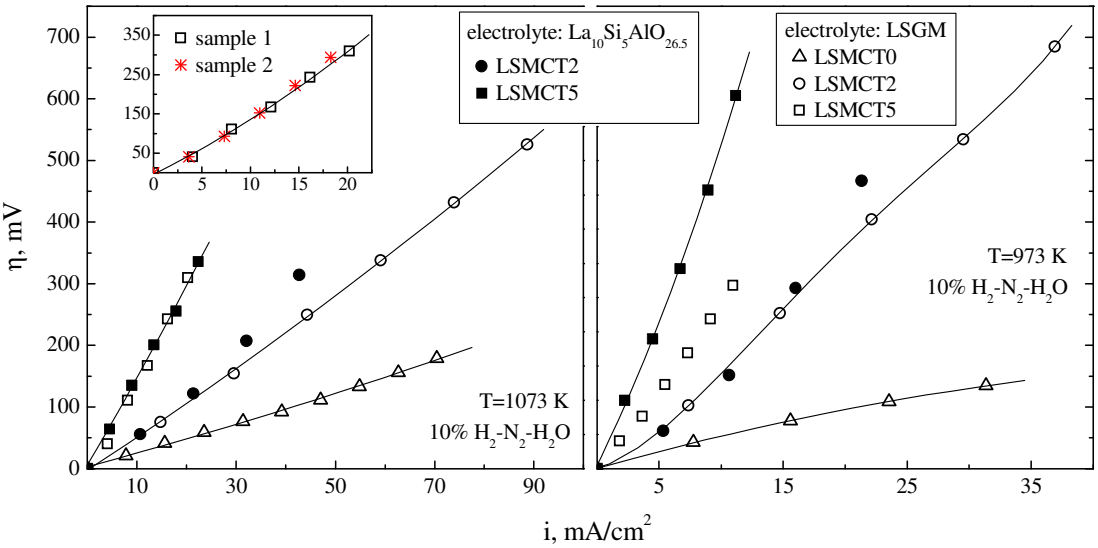

Fig. 3.16. Anodic overpotential vs. current density dependencies for as-prepared LSMCT0, LSMCT2, LSMCT5 electrodes applied onto LSGM and $La_{10}Si_5AlO_{26.5}$ solid electrolytes with CGO20 sublayer. The measurements were performed in wet 10% H_2 - N_2 flow at 973 K and 1073 K. Inset shows an example of the reproducibility tests for 2 various samples of porous LSMCT5 deposited onto LSGM electrolyte.

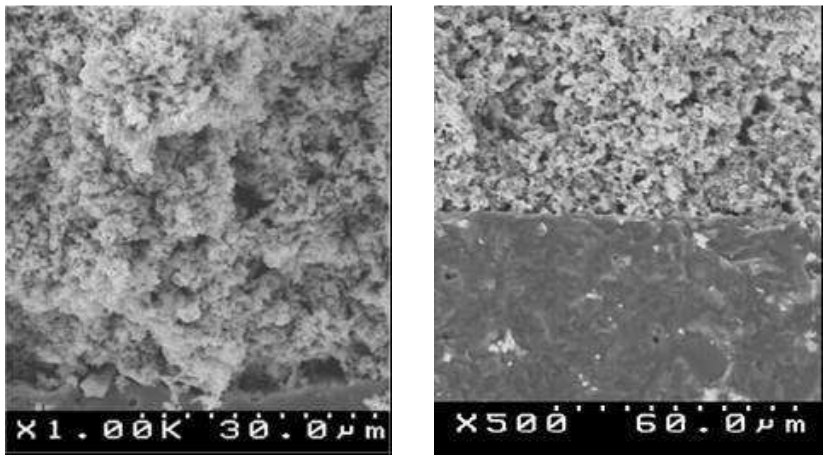

A **B**

Fig. 3.17. SEM micrographs of $(La_{0.75}Sr_{0.25})_{0.95}Cr_{0.5}Mn_{0.5}O_{3-\delta}$ anode applied onto LSGM electrolyte and surface-modified with $CeO_{2-\delta}$ and Ni (A) and $(La_{0.75}Sr_{0.25})_{0.95}Mn_{0.5}Ti_{0.5}O_{3-\delta}$ cathode deposited onto $La_{10}Si_5AlO_{26.5}$ electrolyte and modified with PrO_x (B). The micrographs were collected on half-cells after measurements.

Under oxidizing conditions the conductivity of $(La_{0.75-x}Sr_{0.25+x})_{0.95}Mn_{0.5}Cr_{0.5-x}Ti_xO_{3-\delta}$ is reasonable for the electrochemical utilizations and the electrode performance becomes nearly composition-independent (Fig. 3.18); the polarization curves of as-prepared porous layers follow Tafel-type dependencies. In this situation, the processes at the electrolyte / electrode and electrolyte / gas interfaces are expected to become critical for the overall electrode reaction rate. Similar to the anodes exposed to reducing atmospheres, the

performance of $(La_{0.75-x}Sr_{0.25+x})_{0.95}Mn_{0.5}Cr_{0.5-x}Ti_xO_{3-\delta}$ based cathodes is generally significantly better in contact with LSGM solid electrolyte compared to $La_{10}Si_5AlO_{26.5}$, in correlation with the oxygen-ionic and electronic conductivities of these electrolyte materials.

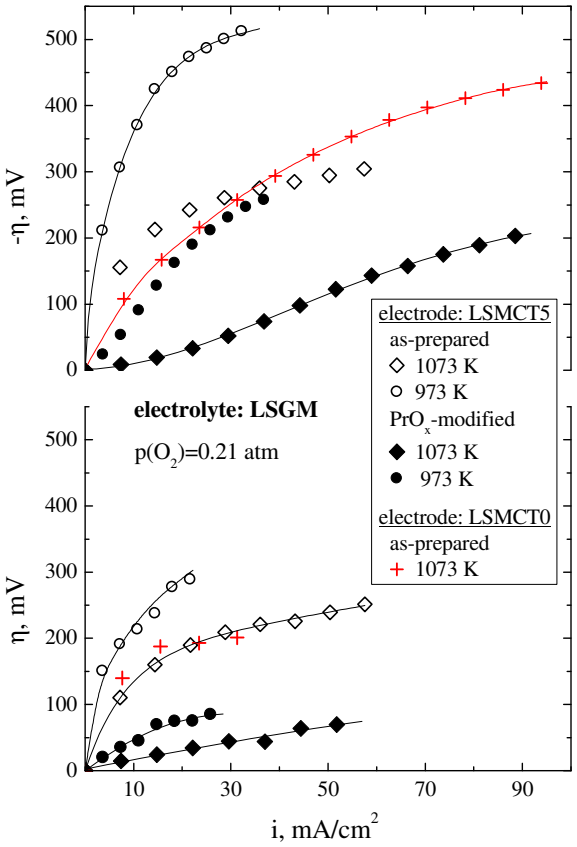

Fig. 3.18. Overpotential vs. current density dependencies of $(La_{0.75-x}Sr_{0.25+x})_{0.95}Mn_{0.5}Cr_{0.5-x}Ti_xO_{3-\delta}$ cathodes in contact with LSGM electrolyte under cathodic and anodic polarization in air

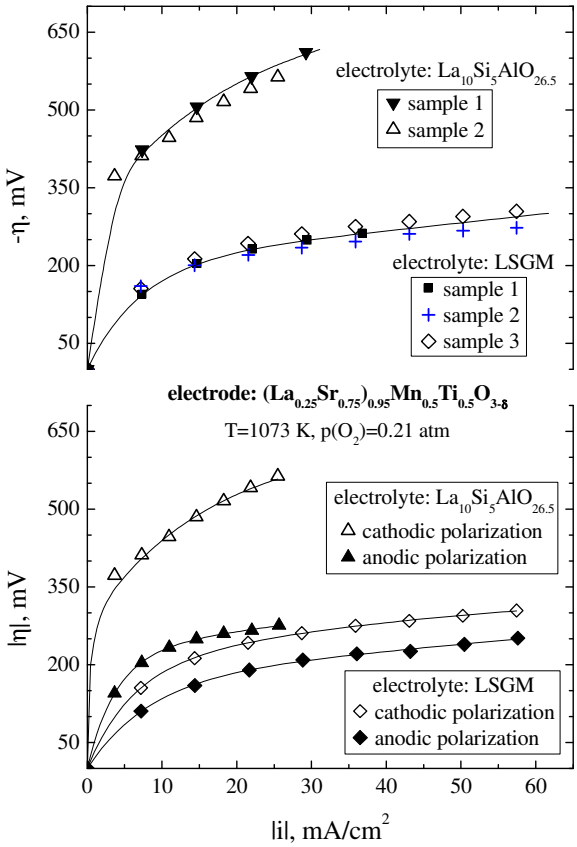

Fig. 3.19. Examples of cathodic polarization curves of $(La_{0.25}Sr_{0.75})_{0.95}Mn_{0.5}Ti_{0.5}O_{3-\delta}$ cathodes in contact with LSGM and $La_{10}Si_5AlO_{26.5}$ solid electrolytes. (A) illustrates the reproducibility of the results obtained for different series of porous electrode samples and (B) shows cathodic and anodic polarization behaviour at 1073 K in air.

Under anodic polarization in air, the influence of solid electrolyte composition becomes less pronounced. The trends under cathodic or anodic currents may partly originate from the incorporation of variable-valence cations into the electrolyte surface during electrode preparation [10, 218]. Anodic polarization raises the oxygen chemical potentials both in the electrode and in the interfacial electrolyte layers, locally increasing the concentration of oxygen species and oxidation state of the variable-valence cations. For the oxygen-hyperstoichiometric silicates where the ionic transport is dominated by interstitial anions [21-24, 585], the interfacial processes related to the oxygen transfer and diffusion should hence be facilitated under anodic polarization and hampered due to cathodic reduction.

Irrespective of the electrolyte composition, the anodic performance of $(La_{0.75}Sr_{0.25})_{0.95}Cr_{0.5}Mn_{0.5}O_{3-\delta}$ and $(La_{0.25}Sr_{0.75})_{0.95}Mn_{0.5}Ti_{0.5}O_{3-\delta}$ in air is significantly higher compared to cathodic (Fig. 3.19). This difference might be attributed to an enrichment of the electrolyte surface with transition metal cations oxidized under anodic currents and resultant increasing p-type electronic conduction or catalytic activity at the electrode/electrolyte interface. In accordance with previous studies, a slight dissolution of transition metal cations in the electrolyte lattice in the region close to the electrolyte/electrode or electrolyte/gas interface has a positive impact on the performance. In particular, the exchange currents for Au cathodes applied onto YSZ preliminary coated with Fe_2O_3 were 2 - 3 orders lower in comparison with a similar cathode deposited onto pure YSZ electrolyte. The effect of iron penetration into the electrolyte was primarily associated with an enhancement of the exchange currents, without variations in the slope of Tafel plots, indicating that the overall mechanism has not been affected by Fe dissolution in the fluorite lattice [586]. Similarly, an activating effect was observed on incorporation of Ce, Mn, Pr, Co into YSZ or Cr, Mn, Ba into LSGM ([584, 587, 588] and references cited).

The mechanism of the improvement is, however, unclear and hardly might be attributed to only electronic conductivity. Although doping of zirconia-based compositions with Mn or Fe indeed increases the electronic contribution, the overall level of the electronic transport still remains rather low to ensure a sufficient current collection [351, 589, 590]. At the same time, isotope exchange studies on Au-coated zirconia showed that the effect of the transition metals in the fluorite lattice relates primarily to catalytic promotion of the oxidation processes; namely, to stabilization of oxygen species adsorbed at Au/YSZ interface [586]. Whatever the particular mechanism of the promotion of the cathodic processes over the electrolyte surface, in the present work a participation of transition metal cations dissolved in the solid electrolyte seems responsible for improved activity under anodic currents. The latter suggestion is, in particular, confirmed by the effect of protective ceria-based layers on the electrode behaviour, as discussed in following sections.

Similar to most oxide electrodes [10, 266, 591], the overpotentials of $(La_{0.75-x}Sr_{0.25+x})_{0.95}Mn_{0.5}Cr_{0.5-x}Ti_xO_{3-\delta}$ cathode layers can be drastically decreased by the infiltration of praseodymia, a result of enhanced exchange currents at both electrode/gas and electrolyte/gas interfaces. Nevertheless, the electrochemical activity of porous $(La_{0.75-x}Sr_{0.25+x})_{0.95}Mn_{0.5}Cr_{0.5-x}Ti_xO_{3-\delta}$ layers in air remains low even after the surface-modification; for example, the cathodic overpotential of $(La_{0.25}Sr_{0.75})_{0.95}Mn_{0.5}Ti_{0.5}O_{3-\delta}$ - PrO_x cathode on LSGM at current density of -80 mA/cm^2 and 1073 K is as high as -190 mV.

In summary, the results show that co-doping of $(La_{0.75}Sr_{0.25})_{0.95}Cr_{0.5}Mn_{0.5}O_{3-\delta}$ by Sr^{2+} and Ti^{4+} makes it possible to decrease chromium content without essential deteriorating effects on the transport properties and electrode performance under oxidizing conditions. The moderate increase of the thermal and chemical expansion, governed by the manganese cations in the B sublattice, may be suppressed by optimizing the acceptor/donor concentration ratio. The same factor, and minor additions of other transition metal cations might be used to increase electronic conductivity and electrochemical activity of the porous SOFC cathodes. However, aliovalent doping with acceptor- and donor-type cations may hardly be expected to suppress the conductivity drop at low $p(O_2)$, which is critical for the anode performance and makes it necessary to incorporate electronically-conducting components in the porous anodes.

3.2. Functional properties of $(La_{0.75}Sr_{0.25})_{0.95}Cr_{1-x}Fe_xO_{3-\delta}$ perovskites

3.2.1. Phase and structural behaviour on redox cycling

Studying the functional properities of $(La_{0.75}Sr_{0.25})_{0.95}Cr_{1-x}Fe_xO_{3-\delta}$ perovkites was carried out in framework of collaborative work with collegues from the Department of Materials and Ceramic Engineering/CICECO, University of Aveiro, and the Nuclear and Technological Institute (presently IST/ITN, Instituto Superior Técnico, Universidade Técnica de Lisboa), involving Dr. M.F. Lue, Dr. E.V. Tsipis, Dr. J.C. Waerenborgh and Dr. A.A. Yaremchenko.

As shown in Fig. 3.20, $(La_{0.75}Sr_{0.25})_{0.95}Cr_{1-x}Fe_xO_{3-\delta}$ (x = 0.3 - 0.4) powders and ceramics prepared in air are single phase perovskites with rhombohedrally-distorted lattice (S.G.: $R\bar{3}c$); the unit cell parameters are listed in Table. 3.8. Note that reducing Sr content and increasing Fe amount in $(La,Sr)(Cr,Fe)O_{3-\delta}$ is known to promote the stabilization of the orthorhombic structure [9, 176, 178]; in particular, rhombohedral symmetry has earlier been reported for $LaSr_2(Fe,Cr)O_{8+\delta}$ [179], whereas $La_{0.75}Sr_{0.25}Cr_{0.5}Fe_{0.5}O_3$ is orthorhombic [178].

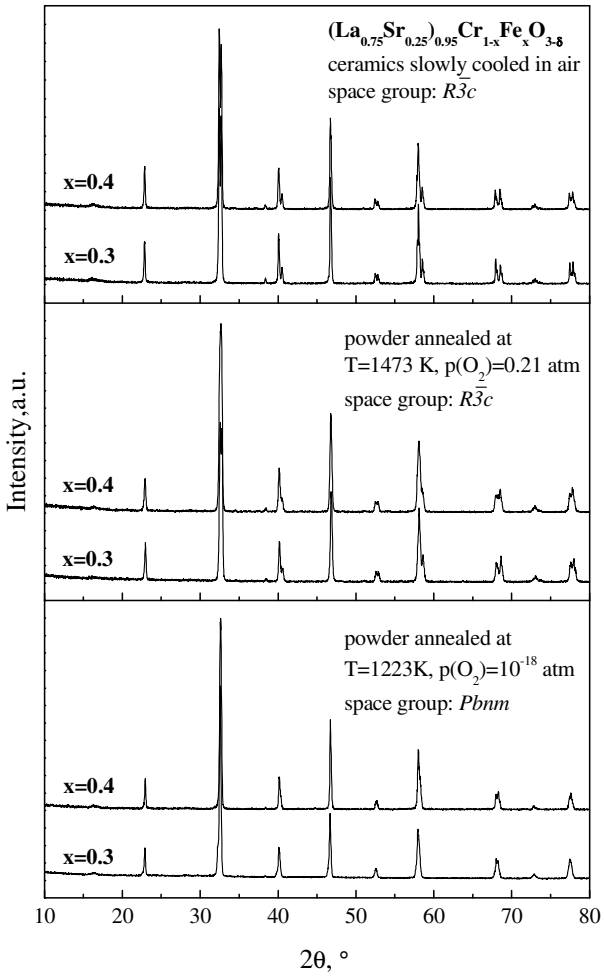

Fig. 3.20. XRD patterns of $(La_{0.75}Sr_{0.25})_{0.95}Cr_{1-x}Fe_xO_{3-\delta}$ after sintering in air at 1973 K, annealing in air at 1473 K and subsequent reduction in wet 10% H_2 - N_2 at 1223 K

Table 3.8. Cell parameters and density of $(La_{0.75}Sr_{0.25})_{0.95}Cr_{1-x}Fe_xO_{3-\delta}$ ceramics

Composition	a, Å	c, Å	V, Å^3	Relative density, %
$(La_{0.75}Sr_{0.25})_{0.95}Cr_{0.7}Fe_{0.3}O_{3-\delta}$	5.5136	13.3514	351.50	95.2
$(La_{0.75}Sr_{0.25})_{0.95}Cr_{0.6}Fe_{0.4}O_{3-\delta}$	5.5170	13.3597	351.15	92.5

Compared to the latter compound, the higher symmetry of oxidized $(La_{0.75}Sr_{0.25})_{0.95}Cr_{1-x}Fe_xO_{3-\delta}$ originates from higher concentration of Cr^{3+}/Cr^{4+} cations having smaller radii with respect to Fe^{3+}/Fe^{4+} [133], thus increasing the perovskite tolerance factor. Moreover, in accordance with the data on electronic transport and Mössbauer spectra discussed below, the average oxidation state of chromium cations is higher than that of iron, again decreasing the average size of B-site cations in the perovskite structure.

In accordance with literature data [178, 191, 212], $(La,Sr)(Cr,Fe)O_{3-\delta}$ are capable to accommodate up to ~25 and 50% Sr and Fe, respectively, with preservation of the single phase down to reduced oxygen pressures. Since the phase boundaries of the perovskites with the compositions similar to those studied in the present section are located close to the anodic conditions, a discrepancy between the reported data on the stability are observed, due to minor differences between the experimental conditions, hindered decomposition kinetics or various sensitivity of the experimental techniques. Selected reports on the stability of iron-doped chromites are summarized in Table 3.9.

Table 3.9. Stability of selected $La(Cr,Fe)O_{3-\delta}$-based perovskites in reducing atmospheres

Composition	T, K	Atmosphere or $p(O_2)$, atm	Stability	Examination method	Reference
$(La_{0.75}Sr_{0.25})_{0.95}Cr_{1-x}Fe_xO_{3-\delta}$ (x = 0.3 - 0.4)	1223	10^{-18}	Stable	XRD, Mossbauer spectroscopy	This work
	1373	10% H_2 - 90% N_2	Stable	TGA	
$LaCr_{0.9}Fe_{0.1}O_{3-\delta}$	1123	1.2×10^{-23}	Start of decomposition	Thermodynamic calculations	[44]
$LaCr_{0.9}Fe_{0.1}O_{3-\delta}$	1173	83% CH_4 - 17% O_2	Stable	XPS, TEM	[17]
	1173	56% CH_4 - 41% Ar - 3% H_2O	Stable		
$La_{0.7}Ca_{0.3}Cr_{0.9}Fe_{0.1}O_{3-\delta}$	1273	10^{-18}	Stable	XRD	[235]
$La_{0.8}Sr_{0.2}Cr_{0.5}Fe_{0.5}O_{3-\delta}$	1173	5% H_2 - Ar	Stable	XRD	[212]
$La_{0.75}Sr_{0.25}Cr_{0.5}Fe_{0.5}O_{3-\delta}$	1173	5% H_2 - Ar	Unstable	XRD	[178]
$La_{0.75}Sr_{0.25}Cr_{0.5}Fe_{0.5}O_{3-\delta}$	1173	10^{-20}	Unstable	XRD, TGA	[191]
$La_{0.33}Sr_{0.67}Cr_{0.33}Fe_{0.67}O_{3-\delta}$	1173	10% H_2 - 90% He	Stable (dissolution of $SrCrO_4$ on reduction)	XRD	[179]
$La_{0.3}Sr_{0.7}Cr_{0.3}Fe_{0.7}O_{3-\delta}$	1073	10^{-20}	Start of decomposition	Neutron diffraction	[169]
	1173	10^{-18}	Start of decomposition		
$La_{0.33}Sr_{0.67}Cr_{0.1}Fe_{0.9}O_{3-\delta}$	1173	10% H_2 - 90% He	Stable	XRD	[179]

No traces of metallic iron or other secondary phases were detected after annealing at 1223 K in wet 10% H_2 - N_2 flow in the present work, in agreement with Mössbauer spectroscopy. This confirms phase stability of the title perovskites in a wide $p(O_2)$ range necessary for the SOFC anode applications. However, the structure of $(La_{0.75}Sr_{0.25})_{0.95}Cr_{1-x}Fe_xO_{3-\delta}$ under low-$p(O_2)$ conditions was identified as orthorhombic (S.G.: *Pbnm*) originating from an enlargement of Cr cations upon reduction which lowers the symmetry.

The Mossbauer spectra collected on samples equilibrated under ambient conditions (Fig. 3.21, Table 3.10) show that Fe is present in the perovskite essentially in +3 state and is octahedrally-coordinated with oxygen. This necessitates generation of Cr^{4+} for charge compensation, while the oxygen content under oxidizing conditions is close to the stoichiometric value, in accordance with TGA studies and the behaviour of Seebeck coefficients with temperature and $p(O_2)$ discussed in the following sections.

One should note that previous reports on the preferential location of electron holes in $(La,A)(Cr,Fe)O_{3-\delta}$-based perovskites are contradictive. In particular, X-ray photoelectron srectroscopy (XPS) studies showed that iron cations in $LaCr_{0.9}Fe_{0.1}O_{3-\delta}$ and $La_{0.7}Ca_{0.3}Cr_{0.9}Fe_{0.1}O_{3-\delta}$ remain essentially in +3 state, analogously to Fe_2O_3 [17, 206]. On the other hand, the data on oxygen nonstoichimetry variations with $p(O_2)$ and temperature were analyzed assuming the constant oxidation state of chromium (+3) and disproportionation of Fe^{3+} species [191]. Electronic transport behaviour of $La_{0.33}Sr_{0.67}Cr_{1-x}Fe_xO_{3-\delta}$ exhibited features typical to ferrite-based perovskites [179], where multiple oxidation states of Fe may coexist in a wide $p(O_2)$ range [114], although the behaviour of chromites with lower Fe content might be quite different.

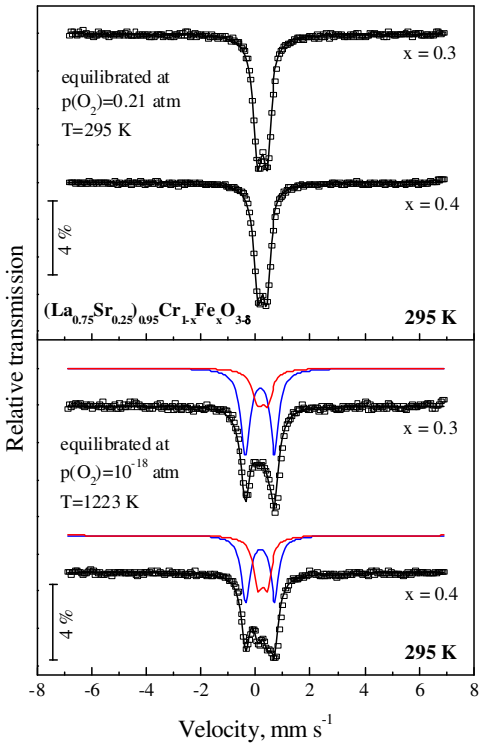

Fig. 3.21. Room temperature Mossbauer spectra of $(La_{0.75}Sr_{0.25})_{0.95}Cr_{1-x}Fe_xO_{3-\delta}$ equilibrated in atmospheric air down to room temperature (top) and reduced in flowing H_2 - N_2 - H_2O gas mixture at 1223 K and $p(O_2)\approx10^{-18}$ atm during 44 hours (bottom). The lines plotted over experimental points are the quadroupole doublet or the sum of two doublets shown shifted for clarity

Table 3.10. Parameters estimated from the Mössbauer spectra of $(La_{0.75}Sr_{0.25})_{0.95}Cr_{1-x}Fe_xO_{3-\delta}$ equilibrated in air and in reducing atmosphere

Composition	Equilibration conditions	Coordination number	Measurement temperature, K	IS, mm/s	QS, 2ε, mm/s	B_{hf} (T)	I, %
$(La_{0.75}Sr_{0.25})_{0.95}Cr_{0.7}Fe_{0.3}O_{3-\delta}$	$p(O_2)$=0.21 atm 295 K	6	295	0.35	0.34	-	100
			4	0.46	-0.02	46.0	100
$(La_{0.75}Sr_{0.25})_{0.95}Cr_{0.6}Fe_{0.4}O_{3-\delta}$	$p(O_2)$=0.21 atm 295 K	6	295	0.35	0.31	-	100
			4	0.48	-0.02	48.0	100
$(La_{0.75}Sr_{0.25})_{0.95}Cr_{0.7}Fe_{0.3}O_{3-\delta}$	$p(O_2)=10^{-18}$ atm 1223 K	6	295	0.36	0.36	-	29
		5		0.27	1.07	-	71
$(La_{0.75}Sr_{0.25})_{0.95}Cr_{0.6}Fe_{0.4}O_{3-\delta}$	$p(O_2)=10^{-18}$ atm 1223 K	6	295	0.36	0.34	-	42
		5		0.28	1.06		58

Analysis of the data on Mössbauer spectroscopy of $La_{0.8}Sr_{0.2}Cr_{0.2}Fe_{0.8}O_{3-\delta}$ revealed ~97% of Fe^{3+}, while further doping with Sr increases the fraction of iron cations in higher oxidation states [592]. It should be noticed that similar discrepancies between the literature data with respect to the oxidation states of transition metal cations were found for Mn- or Co-doped chromites [10, 113, 164-167, 170]. Regardless of the possibility of Fe^{3+} cations to accept additional holes, most authors report that the average oxidation state of Cr species exceeds that of Fe [17, 131, 206, 592], consistently with the current results.

Upon reduction iron cations maintain the state +3, but the formation of oxygen vacancies induces lowering the coordination of Fe^{3+} down to pentahedral. Fig. 3.22 shows changes of oxygen deficiency on reduction in a dry 10% H_2 - 90% N_2 flow, calculated from the TGA results, with respect to the stoichiometry in atmospheric air. The latter reference point was selected as no complete reduction into phase mixtures with definite oxidation states of iron and chromium cations was achieved during TGA experiments up to 1373 K.

Although reduction leads to large nonstoichiometry values, the overall level of oxygen deficiency can still be tolerated by the perovskite lattice. Taking into account that iron cations are trivalent, and assuming $\delta \approx 0$ in air for the sake of comparison, the estimated average oxidation state of chromium in dry 10% H_2 - 90% N_2 tends to asymptotically approach +3.10 for x = 0.3 and +3.01 for x = 0.4 at 1223 K. At 1073 K, these values are +3.16 and +3.14, respectively. Consequently, one may conclude that the redox behaviour and electronic conductivity of $(La_{0.75}Sr_{0.25})_{0.95}Cr_{1-x}Fe_xO_{3-\delta}$ should be primarily governed by $Cr^{3+/4+}$ states in the entire $p(O_2)$ range relevant for the electrode applications.

Despite higher reducibility of $(La_{0.75}Sr_{0.25})_{0.95}Cr_{1-x}Fe_xO_{3-\delta}$ with enhanced iron content (Fig. 3.22), the Mössbauer spectroscopy and thermogravimetric analyses showed no evidence of phase decomposition in mildly reducing atmospheres. In particular, no traces of metallic iron were detected in the Mössbauer spectra after reduction at 1223 K and $p(O_2) = 10^{-18}$ atm, consistently with XRD results. Taking into account that the low-$p(O_2)$ stability limits of iron-containing phases usually exhibit van't Hoff type dependencies on reciprocal temperature [25, 41, 46, 48], an acceptable thermodynamic stability under anodic conditions in the intermediate-temperature SOFCs can be expected. Nonetheless, long-term testing is necessary to access reducibility in pure H_2 at 770 - 970 K, since the low-$p(O_2)$ decomposition of transition metal-substituted chromites may be hindered kinetically [8, 10, 17, 171].

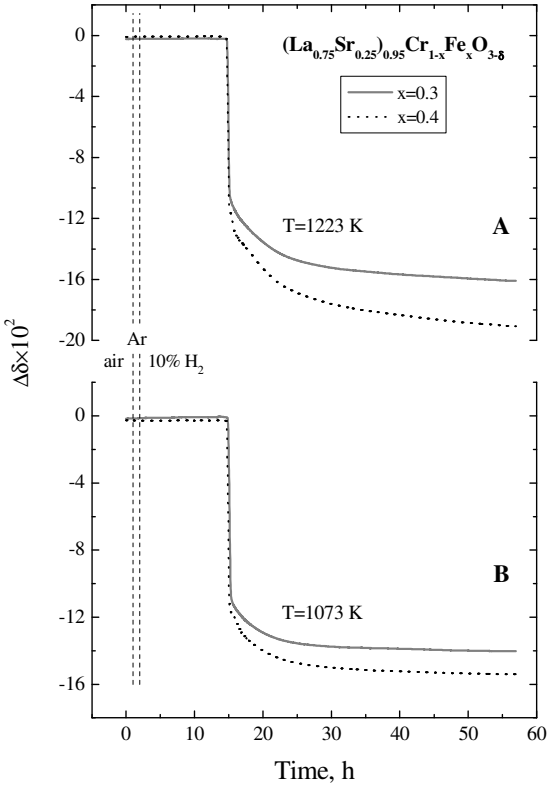

Fig. 3.22. Variations of the oxygen nonstoichiometry of $(La_{0.75}Sr_{0.25})_{0.95}Cr_{1-x}Fe_xO_{3-\delta}$ upon reduction in dry 10% H_2 - N_2 gas mixture at 1223 K (A) and 1073 K (B), calculated from TGA data. The reference points correspond to atmospheric air at a given temperature. The dashed vertical lines show atmospheric changes.

The data on Mossbauer spectroscopy allow to assess a possibility of formation of ordered structures. For hypothetical $(La_{0.75}Sr_{0.25})_{0.95}Cr_{1-x}Fe_xO_{3-\delta}$ where all B-site cations are trivalent, the oxygen vacancy concentration should correspond to approximately 0.19 sites per formula unit ($\delta \approx 0.19$). Assuming a random distribution of the vacancies, approximately 28% penta- and 5% tetra-coordinated B-sites might be predicted from geometrical consideration. The estimated fractions of penta-coordinated Fe^{3+} are, however, substantially higher (Table 3.10), thus indicating a greater energetic favourability for vacancy location near Fe^{3+} in comparison with Cr^{3+}. Moreover, the calculated concentration of penta-coordinated Fe^{3+}, 0.21 - 0.23 cations/f.u., is almost independent of x and is close to the vacancy concentration. As the oxygen nonstoichiometry is low and statistical distribution of Cr/Fe cations in the B sublattice was confirmed by Rietveld refinement of the XRD data, the absence of tetrahedral Fe^{3+} may originate from coulombic repulsion between the randomly distributed oxygen vacancies. Consequently, the low level of oxygen deficiency, comparatively high content of chromium-oxygen polyhedra suppressing the formation of Fe-O-Fe chains as well as the incapability of Fe cations to adopt the tetrahedral oxygen coordination in the present composition, in contrast to the brownmillerite structures, seem responsible for the improved thermodynamic stability of $(La_{0.75}Sr_{0.25})_{0.95}Cr_{1-x}Fe_xO_{3-\delta}$ in the entire $p(O_2)$ range studied. This conclusion is consistent with the results reported in [169, 179], where the compositions with significantly higher quantities of Sr and Fe atoms maintain the disordered perovskite structure.

3.2.2. Thermal and chemical expansion

Fig. 3.23 presents typical dilatometric curves of $(La_{0.75}Sr_{0.25})_{0.95}Cr_{1-x}Fe_xO_{3-\delta}$ ceramics at atmospheric $p(O_2)$ and in flowing CO - CO_2 mixture where the oxygen partial pressure, continuously controlled by an electrochemical oxygen sensor, was 3×10^{-20} atm at 923 K and 2×10^{-12} atm at 1223 K. In both cases the thermal expansion is essentially linear up to 1373 K. When pre-oxidized $(La_{0.75}Sr_{0.25})_{0.95}Cr_{1-x}Fe_xO_{3-\delta}$ is heated in CO - CO_2 atmosphere, a significant chemical contribution to the apparent thermal expansion is observed at 970 - 1220 K due to progressive oxygen losses from the perovskite lattice, similar to $(La_{0.75-x}Sr_{0.25+x})_{0.95}Mn_{0.5}Cr_{1-x}Ti_xO_{3-\delta}$. This effect becomes negligible on cooling back in the same atmosphere, since the low oxygen content in the gas phase does not allow to replenish the losses.

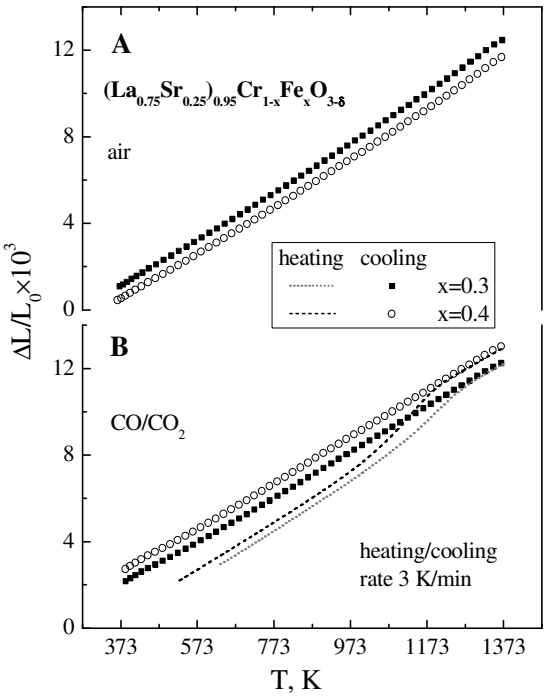

Fig. 3.23. Dilatometric curves of $(La_{0.75}Sr_{0.25})_{0.95}Cr_{1-x}Fe_xO_{3-\delta}$ ceramics in air (A) and CO-CO_2 (B) atmospheres

Table 3.11. Average linear thermal expansion coefficients of $(La_{0.75}Sr_{0.25})_{0.95}Cr_{1-x}Fe_xO_{3-\delta}$ ceramics in air and CO-CO_2 atmospheres

Composition	Atmosphere	T, K	TEC×10^6, K^{-1}
$(La_{0.75}Sr_{0.25})_{0.95}Cr_{0.7}Fe_{0.3}O_{3-\delta}$	Air	470 - 1220	11.3
	CO - CO_2	350 - 1370	10.3
$(La_{0.75}Sr_{0.25})_{0.95}Cr_{0.6}Fe_{0.4}O_{3-\delta}$	Air	470 - 1220	11.1
	CO - CO_2	350 - 1370	10.5

The average TECs of $(La_{0.75}Sr_{0.25})_{0.95}Cr_{1-x}Fe_xO_{3-\delta}$ are relatively low, (10.3 - 11.3)×10^{-6} K^{-1}, and tend to slightly decrease on reduction (Table 3.11), consistently with the common expansion behaviour of chromite perovskites in various atmospheres, discussed in Chapter 3.1.3. The TECs evaluated are close to data for Fe-substituted chromites, with iron content is ≤50% [163, 212], and are substantially lower compared to ferrites or Fe- and Sr-rich (La,Sr)(Cr,Fe)$O_{3-\delta}$ [179, 266], presumably due to the stabilization of Fe^{3+} state, validated by the Mössbauer spectroscopy.

The values of isothermal expansion caused by reduction of $(La_{0.75}Sr_{0.25})_{0.95}Cr_{1-x}Fe_xO_{3-\delta}$ perovskites in CO-CO_2 gas mixtures are presented in Table 3.12. In accordance with the trends exhibited by the oxygen nonstoichiometry variation, Fe-doping substantially increases the chemically-induced strains, up to ~0.2%. Note that the apparent lattice expansivity might also be contributed by the "rhombohedral" - "orthorhombic" structural transition occurring on reduction (Fig. 3.20). Nevertheless, the overall level of the chemical expansion is modest and comparable with the values for B-site doped chromites reported in literature [194, 235, 237] and shown in Fig. 1.2.7. The moderate thermal and chemical expansion is expected to ensure an acceptable mechanical compatibility of the perovskites studied with common solid electrolytes.

Table 3.12. Relative isothermal expansion of $(La_{0.75}Sr_{0.25})_{0.95}Cr_{1-x}Fe_xO_{3-\delta}$ ceramics on reduction in CO-CO_2 atmospheres

T, K	$p(O_2)$, atm	$(L-L_{air})/ L_{air}\times10^3$	
		$(La_{0.75}Sr_{0.25})_{0.95}Cr_{0.7}Fe_{0.3}O_{3-\delta}$	$(La_{0.75}Sr_{0.25})_{0.95}Cr_{0.6}Fe_{0.4}O_{3-\delta}$
923	3.0×10^{-20}	0.51	1.90
973	1.3×10^{-18}	0.45	1.87
1023	4.0×10^{-17}	0.41	1.83
1073	8.9×10^{-16}	0.34	1.79
1123	1.5×10^{-14}	0.28	1.75
1173	2.0×10^{-13}	0.22	1.71
1223	2.1×10^{-12}	0.13	1.63

3.2.3. Mixed electronic and ionic conductivity

The conductivity of $(La_{0.75}Sr_{0.25})_{0.95}Cr_{1-x}Fe_xO_{3-\delta}$ under oxidizing and reducing conditions shows the features typical for p-type electronic conductors and described in Chapter 3.1.4. Examples of $p(O_2)$ dependencies of the total conductivity and Seebeck coefficient are demonstrated in Fig. 3.24. Increasing iron content leads to lower conductivity, consistently with the observation of the constant oxidation state of Fe, since introduction of “inert” iron cations into B-sublattice should reduce the number of available sites for location of holes and diminish the concentration of Cr^{4+} species responsible for the electron transport. On the other hand, previous reports indicate a promotion of the electronic transfer by Fe doping into chromites [131, 179]. One should note that the conductivity behaviour of chromites substituted with 3*d*-cations may be completely different in various compositional ranges, depending on the particular transport mechanism [164-166, 170].

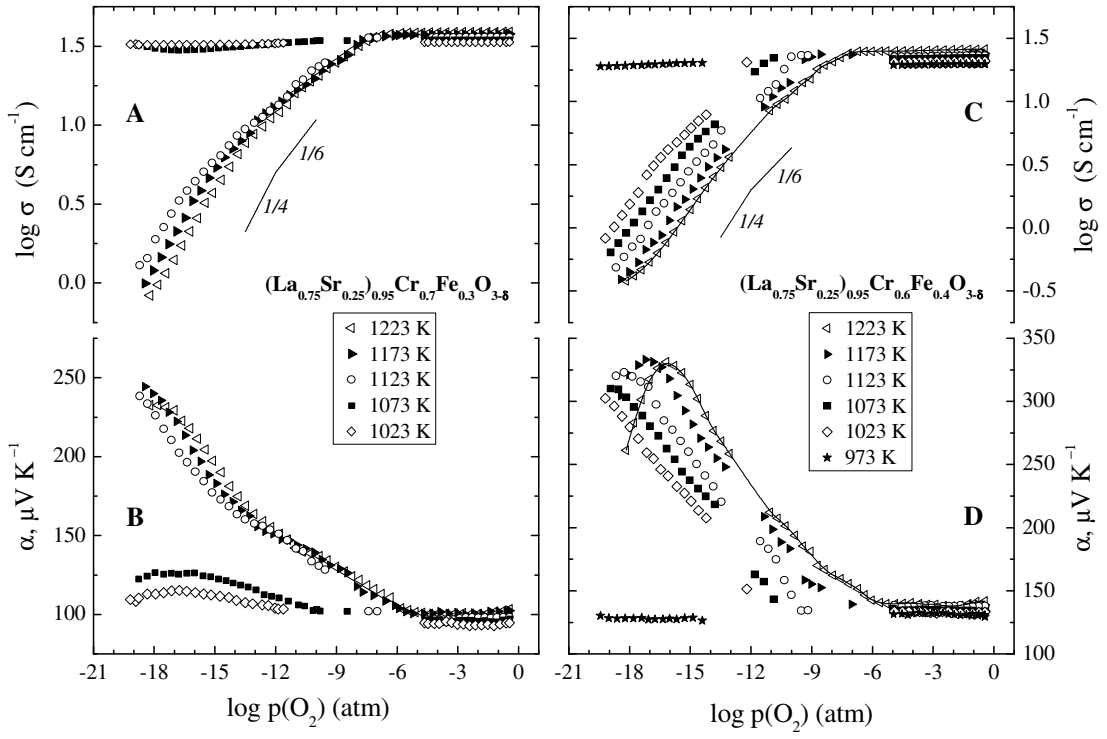

Fig. 3.24. Oxygen partial pressure dependencies of the total conductivity (A, C) and Seebeck coefficient (B, D) of $(La_{0.75}Sr_{0.25})_{0.95}Cr_{1-x}Fe_xO_{3-\delta}$ ceramics

As the oxygen nonstoichiometry variations in oxidizing atmospheres are very minor (Fig. 3.22), the conductivity and Seebeck coefficient in the high-$p(O_2)$ range are essentially independent of the oxygen pressure , as shown in Fig. 3.24. Reduction results in progressive oxygen losses from the perovskite and in decreasing Cr^{4+} concentration, yielding the lower conductivity and higher thermopower. No n-type conductivity branch typical for Fe-enriched perovskites [179, 217] was observed, although a gradual lowering of the slope of the conductivity (Fig. 3.24C) and rapid drop of Seebeck coefficient (Fig. 3.24D) for x = 0.4 occurring on strong reduction might be indicative of a contribution of electronic charge carriers into the overall transport mechanism.

The oxygen permeability measurements were carried out on dense $(La_{0.75}Sr_{0.25})_{0.95}Cr_{1-x}Fe_xO_{3-\delta}$ membranes exposed to flowing air and H_2 - H_2O - N_2 at the feed and permeate sides, respectively. The results indicated that the overall kinetics is governed by the bulk ionic diffusion. Increasing Fe content in perovskite renders higher values of the permeation fluxes indicating a promotion of the ionic diffusion by the presence of iron cations with flexible coordination number. The ionic conductivity estimated in accordance with Eq. (2.10) varies in the range $(5 - 8)\times10^{-2}$ S×cm^{-1} at 1223 K. This level is somewhat lower in comparison with $La_{0.33}Sr_{0.67}Cr_{0.33}Fe_{0.67}O_{3-\delta}$ [179] indicating a positive effect of Sr- or Fe-doping on the oxygen diffusivity due to increasing the oxygen vacancy concentration and weakening metal-oxygen bonds, provided that no structural transformations negatively affecting the ionic transport occur.

3.2.4. Anode properties

SEM analysis of the electrode layers of $(La_{0.75}Sr_{0.25})_{0.95}Cr_{1-x}Fe_xO_{3-\delta}$ deposited onto LSGM electrolyte pellets (preliminary coated with CGO20 sublayer) showed a sufficient porosity and a relatively large surface area (Fig. 3.25), ensuring gas penetration and facile surface exchange processes. The average grain diameter in the electrode layers varied in the range 0.5 - 2 mm. No exfoliation or visible reaction traces between $(La_{0.75}Sr_{0.25})_{0.95}Cr_{1-x}Fe_xO_{3-\delta}$ and CGO20 layers were observed. The polarization tests during over 150 h did not show any significant changes of the electrode grain size.

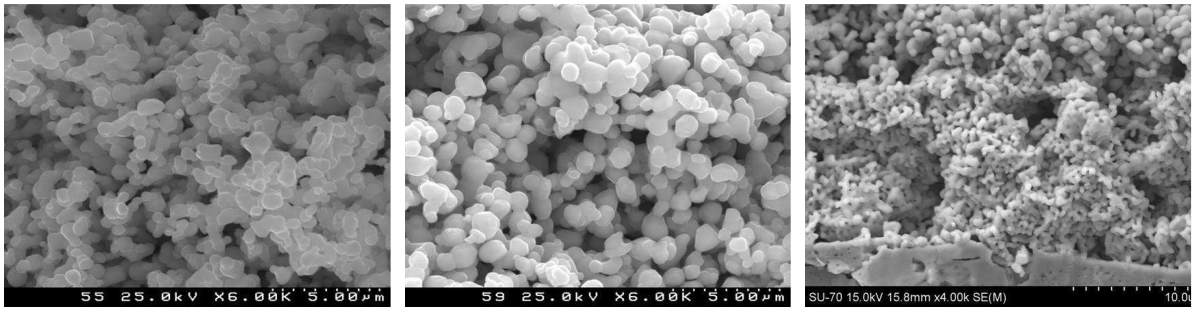

A **B** **C**

Fig. 3.25. Top views of as-prepared $(La_{0.75}Sr_{0.25})_{0.95}Cr_{0.7}Fe_{0.3}O_{3-\delta}$ (A), $(La_{0.75}Sr_{0.25})_{0.95}Cr_{0.6}Fe_{0.4}O_{3-\delta}$ (B) electrode layers and cross-section of fractured $(La_{0.75}Sr_{0.25})_{0.95}Cr_{0.6}Fe_{0.4}O_{3-\delta}$ electrode applied onto CGO20 | LSGM (C) after polarization measurements in wet 10% H_2 - N_2 atmosphere

Typical anodic polarization curves of porous $(La_{0.75}Sr_{0.25})_{0.95}Cr_{1-x}Fe_xO_{3-\delta}$ electrodes with CGO20 interlayers applied onto LSGM solid electrolyte are presented in Fig. 3.26. The electrochemical activity of $(La_{0.75}Sr_{0.25})_{0.95}Cr_{1-x}Fe_xO_{3-\delta}$ tends to moderately decrease with increasing x, in correlation with the electronic conductivity variations. Detailed analysis of the electrode behaviour and comparison of the electrochemical activity with other perovskite-based anode layers is given in Chapter 5.

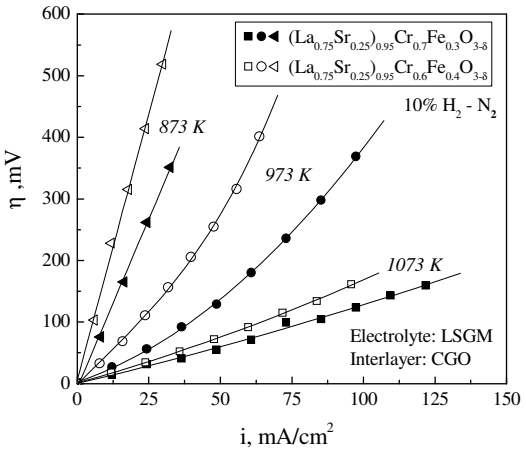

Fig. 3.26. Anodic polarization curves of porous $(La_{0.75}Sr_{0.25})_{0.95}Cr_{1-x}Fe_xO_{3-\delta}$ electrodes with CGO20 interlayer applied onto LSGM solid electrolyte in humidified 10% H_2 - N_2 atmosphere at 873 - 1073 K

3.3. Characterization of $(La_{0.9}Sr_{0.1})_{0.95}Cr_{0.85}Mg_{0.1}Ni_{0.05}O_{3-\delta}$ ceramics and electrodes

As demonstrated in previous sections, anode layers based on $(La,Sr)(Mn,Cr,Ti)O_{3-\delta}$ and $(La,Sr)(Cr,Fe)O_{3-\delta}$ oxides suffer from the drop of the electronic conductivity under reducing conditions and rather low or moderate catalytic activity. In the search of potential alternative anode materials, another approach of optimization of the electrode performance is undertaken related with intentional introduction of Ni cations into the perovskite structure and subsequent precipitation of catalytically-active metallic phase under operation conditions. The choice of the concentration of acceptor-type dopants was selected by such a way so as to incorporate a slightly higher Ni content in comparison with the solubility limit in reducing atmospheres, without formation of any secondary phases capable to deteriorate the activity, and to avoid a substantial decomposition of the perovskite structure which might negatively influence the transport and thermomechanical properties. In particular, the cation content in A-sublattice was taken in a slight deficit in comparison with that of B-site cations, in order to promote the exsolution of Ni particles and avoid a separation of La- or Sr-enriched compounds.

In $LaCrO_{3-\delta}$ substituted with only one type of acceptor-type dopants, at least 40 - 50 % of Mg or Ni may be dissolved in the perovskite structure [131, 142, 181, 183], while the solubility of Sr is assessed to be below 25% [44, 139, 149]. The simultaneous presence of these cations mutually reduces the solubility limits, especially at reduced $p(O_2)$ [151, 184, 185, 265], although one may observe some discrepancy between the reported data. Whatever the trends in the solubility of acceptor-type cations, an excess of Mg and Ni species in the composition may be considered to be beneficial. Since reduction of (Mg,Ni)O oxide or related compounds enables to obtain more dispersed Ni particles in comparison with those produced by reducing metallic Ni, as was demonstrated in [578, 579], even in the case of separation of (Mg,Ni)O phase under ambient conditions, subsequent reduction of the mixture is expected to produce an anode with enhanced catalytic activity. Taking into account the literature data on the dopant solubility in chromites and a preferability of a slight excess of Mg and Ni species, the present part is focused on characterization and evaluation of the electrode activity of $(La_{0.9}Sr_{0.1})_{0.95}Cr_{0.85}Mg_{0.1}Ni_{0.05}O_{3-\delta}$ perovskite.

3.3.1. Phase behaviour and thermal expansion under oxidizing conditions

The characterization of $(La_{0.9}Sr_{0.1})_{0.95}Cr_{0.85}Mg_{0.1}Ni_{0.05}O_{3-\delta}$ powdered and ceramic samples was carried out in framework of collaborative work involving researchers from the Department of Materials and Ceramic Engineering/CICECO, University of Aveiro, and the North Carolina A&T State University. At different stages of this work, important contributions were made by Dr. S.N. Yarmolenko, Prof. J. Sankar, Dr. A.V. Kovalevsky and Dr. Y.V. Pivak. The details of the room- and high-temperature XRD studies, TEM analysis, measurements of the total conductivity and thermal expansion are described in Chapter 2.

An excess of B-cations in the perovskite lattice induced separation of a phase, isostructural to $Mg_{0.4}Ni_{0.6}O$ ($Fm\bar{3}m$), as shown in Fig. 3.30. This phenomenon does not seem to be a drawback, since further reduction of both the perovskite and the (Mg,Ni)O phase ensures segregation of dispersed Ni particles. Moreover, a reasonable oversaturation of the perovskite composition with B-site cations should avoid a

formation of La- or Sr-enriched phases at low $p(O_2)$, detrimental in terms of the transport and electrocatalytic properties.

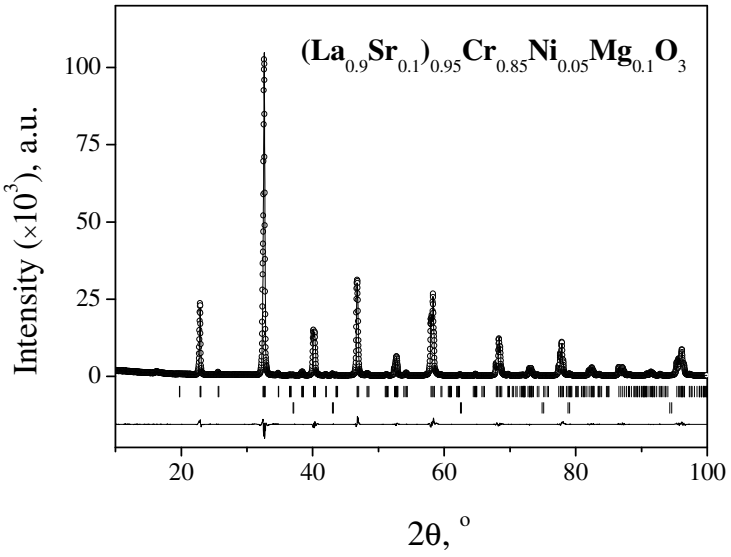

Fig. 3.27. Observed (points) and calculated (top line fit) XRD patterns collected on $(La_{0.9}Sr_{0.1})_{0.95}Cr_{0.85}Mg_{0.1}Ni_{0.05}O_{3-\delta}$ ceramics equilibrated in air. The bottom line is the difference between the observed and calculated data. The vertical bars correspond to Bragg reflections of the perovskite phase (top) and $Mg_{0.4}Ni_{0.6}O$ impurity (bottom).

Fig. 3.28 represents a dilatometric curve of $(La_{0.9}Sr_{0.1})_{0.95}Cr_{0.85}Mg_{0.1}Ni_{0.05}O_{3-\delta}$ ceramics, obtained in the continuous heating regime in air. A drastic change in the expansion behaviour was found at ~370 K, attributable to a structural transition from the low-temperature orthorhombic perovskite (S.G.: *Pnma*) to rhombohedral structure (S.G.: $R\bar{3}c$) at elevated temperatures. More detailed high-temperature XRD studies presented in Appendix A confirmed the transition occurring at 350 - 370 K. One should note that the enlargement of the unit cell volume on heating, calculated from the unit cell parameters of the hexagonal phase and expressed in the linear scale, reasonably correlates with the expansion measured by dilatometry in the corresponding temperature region, as shown in Fig. 3.28.

The transformation of the crystal lattice is in accordance with numerous reports on the structural behaviour of chromite perovskites; in particular, the transition orthorombic - rhombohedral in $LaCrO_{3-\delta}$ was found at 520 - 560 K, shifting to lower temperatures upon Sr doping [112, 131, 183]. The presence of small amounts of Ni in $La(Cr,Ni)O_{3-\delta}$ extends the domain of existence of the orthorhombic perovskites towards higher temperatures [183]. On the other hand, introduction of Ni into $La_{1-x}Sr_xCr_{1-y}Ni_yO_{3-\delta}$ ensures the transition of the orthorombic structure into rhombohedral one occurring at x = 0.2 - 0.25 and y = 0.05 - 0.1 under ambient conditions, as shown in works [176, 181, 187]. In contrast, introducing Mg elevates the transformation temperature [112]. Approximate temperatures corresponding to the structural transformations of chromite-based materials in air are indicated in Table 3.13. The combined effect of the presence of the acceptor cations as well as the A-site cation deficiency in the present composition is the shift of the transition temperature down to 350 - 370 K.

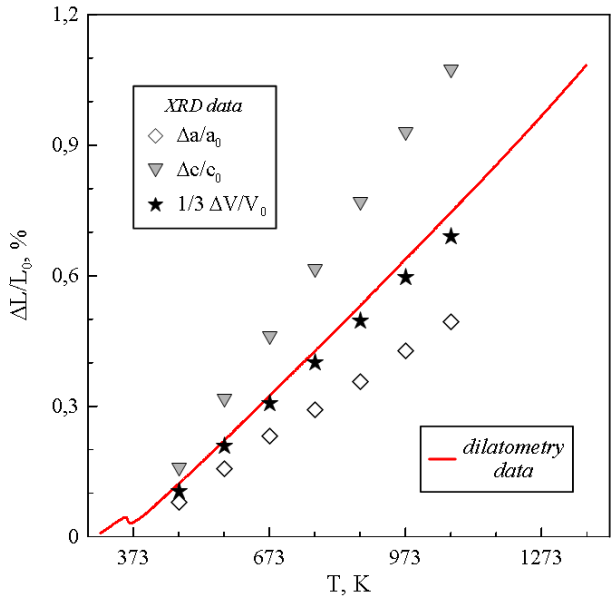

Fig. 3.28. Comparison of the linear thermal expansion of $(La_{0.9}Sr_{0.1})_{0.95}Cr_{0.85}Mg_{0.1}Ni_{0.05}O_{3-\delta}$ in air measured by dilatometry and calculated from the cell parameters at various temperatures. *a*, *c* and *V* correspond to the unit cell parameters and volume in hexagonal settings. L_0 relates to the initial sample length at 300 K (for dilatometric curve) or cell parameters at 373 K (for XRD data) in air.

Table 3.13. Temperatures of the phase transitions in chromites observed on thermal cycling in air

Composition	Low-temperature / high-temperature phase	Temperature or temperature interval of transition, K	Reference
$(La_{0.9}Sr_{0.1})_{0.95}Cr_{0.85}Mg_{0.1}Ni_{0.05}O_{3-\delta}$	Orthorhombic / rhombohedral	350 - 370	This work
$LaCrO_{3-\delta}$	Orthorhombic / rhombohedral	520 560	[112, 183] [131]
$La_{0.9}Ca_{0.1}CrO_{3-\delta}$	Orthorhombic / rhombohedral	580	[112]
$La_{0.9}Sr_{0.1}CrO_{3-\delta}$	Orthorhombic / rhombohedral	340	[112]
$LaCr_{0.9}Mg_{0.1}CrO_{3-\delta}$	Orthorhombic / rhombohedral	600	[112]
$LaCr_{0.8}Mg_{0.2}CrO_{3-\delta}$	Orthorhombic / rhombohedral	620	[112]
$La_{0.75}Sr_{0.25}Cr_{0.5}Mn_{0.5}O_{3-\delta}$	Rhombohedral / cubic	770 - 1370	[177]
$LaCr_{0.9}Ni_{0.1}CrO_{3-\delta}$	Orthorhombic / rhombohedral	640	[183]
$LaCr_{0.8}Ni_{0.2}CrO_{3-\delta}$	Orthorhombic / rhombohedral	670	[183]

Despite the apparently large dimension variations in the vicinity of the phase transformation, further studies of the transport and electrochemical properties revealed no effects associated with mechanical degradation of the material. Above the transition temperature, the dilatometric curve shows almost linear behaviour (Fig. 3.28). For the whole range of oxygen partial pressures studied, the average TECs are relatively low and vary in a narrow range $(10.2 - 11.7)\times10^{-6}$ K^{-1} (Table 3.14). Reduction leads to a decrease of the expansion coefficient, similar for $(La,Sr)(Cr,Mn)O_{3-\delta}$ and $(La,Sr)(Cr,Fe)O_{3-\delta}$ perovskites.

Table 3.14. Average linear thermal expansion coefficients of $(La_{0.9}Sr_{0.1})_{0.95}Cr_{0.85}Mg_{0.1}Ni_{0.05}O_{3-\delta}$ ceramics in various atmospheres determined by dilatometry

$p(O_2)$, atm	T, K	$\overline{\alpha}\times10^6$, K^{-1}
0.21	400 - 923	10.2±0.1
0.21	923 - 1223	10.9±0.1
0.21	1223 - 1523	11.7±0.1
6.3×10^{-4}	923 - 1223	11.0±0.1
4.7×10^{-21} - 3.2×10^{-13}	923 - 1223	10.1±0.2

3.3.2. Total conductivity and phase relationships on reduction

The total conductivity of $(La_{0.9}Sr_{0.1})_{0.95}Cr_{0.85}Mg_{0.1}Ni_{0.05}O_{3-\delta}$ is predominantly electronic with electron holes hopping over B-site cation matrix, and shows the same general trends as $(La,Sr)(Cr,Fe)O_{3-\delta}$ and $(La,Sr)(Mn,Cr,Ti)O_{3-\delta}$ perovskites (Figs. 3.29 - 3.30). However, for Sr-, Mg- and Ni-doped chromites the low-$p(O_2)$ behaviour, among other common factors, may be influenced by formation of nano-sized Ni particles detected by TEM analysis (Fig. 3.31), either precipitated from the perovskite phase or generated by reduction of the (Mg,Ni)O impurity. In the former case, the process should be accompanied by extensive oxygen losses resulting in a decrease of the concentration of p-type charge carriers accompanied with a drop of the electronic conductivity and a raise of the Seebeck coefficient. The formation of metallic Ni was confirmed by XRD inspection of $(La_{0.9}Sr_{0.1})_{0.95}Cr_{0.85}Mg_{0.1}Ni_{0.05}O_{3-\delta}$ ceramics, quenched after reduction at $p(O_2) = 10^{-17}$ atm at 1223 K.

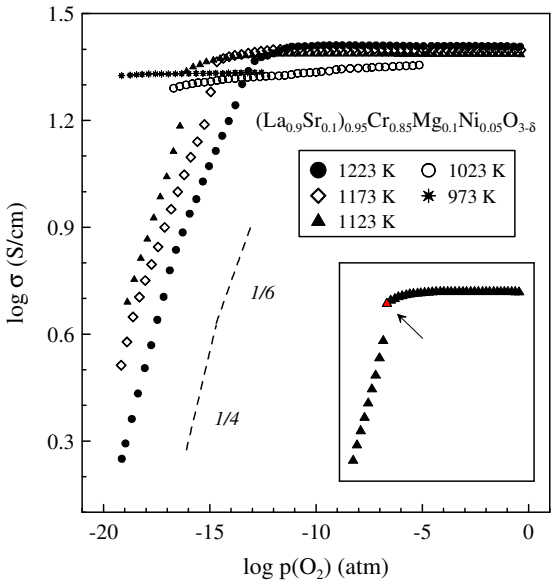

Fig. 3.29. Oxygen partial pressure dependencies of the total conductivity of $(La_{0.9}Sr_{0.1})_{0.95}Cr_{0.85}Mg_{0.1}Ni_{0.05}O_{3-\delta}$ ceramics. Inset shows the criterion of determination of the phase boundaries.

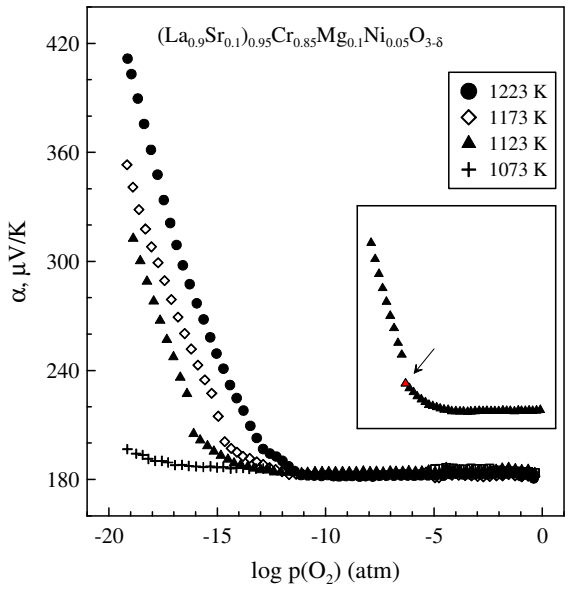

Fig. 3.30. Oxygen partial pressure dependencies of the Seebeck coefficient of $(La_{0.9}Sr_{0.1})_{0.95}Cr_{0.85}Mg_{0.1}Ni_{0.05}O_{3-\delta}$ ceramics. Inset shows the criterion of determination of the phase boundaries.

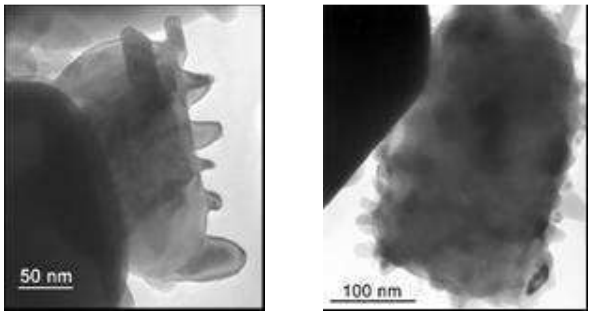

Fig. 3.31. TEM images of $(La_{0.9}Sr_{0.1})_{0.95}Cr_{0.85}Mg_{0.1}Ni_{0.05}O_{3-\delta}$ annealed in H_2-containing atmosphere at 1173 K

Due to the segregation of the metallic phase from $(La_{0.9}Sr_{0.1})_{0.95}Cr_{0.85}Mg_{0.1}Ni_{0.05}O_{3-\delta}$, the phase boundaries of the perovskite are close to those of reduction of NiO into metallic state [41]. This factor indicates that the conductivity drop for the title composition is primarily associated with Ni segregation, although Ni^{2+} cations in the perovskite phase are to some extent stabilized in comparison with the simple oxide. Another particularity of $(La_{0.9}Sr_{0.1})_{0.95}Cr_{0.85}Mg_{0.1}Ni_{0.05}O_{3-\delta}$ relates to comparatively high decomposition enthalpy, possibly attributable to kinetic stabilization of the phase at lower temperatures. This suggestion is consistent with the observation that no conductivity drop was found at the temperatures below 1023 K (Fig. 3.29), which enables to preserve nearly constant total conductivity in the entire $p(O_2)$ region studied, including the anodic conditions.

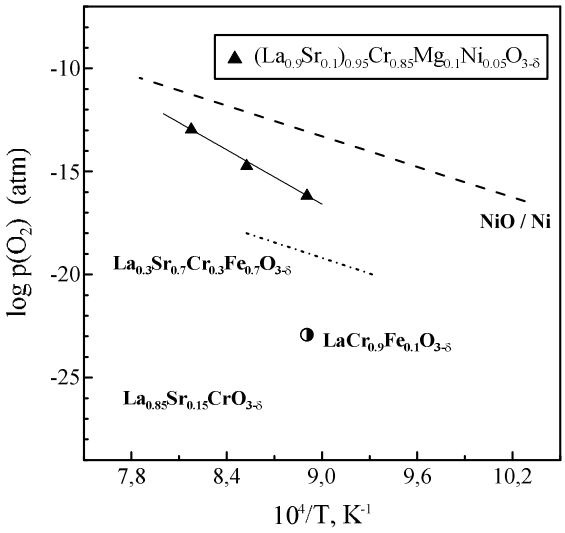

Fig. 3.32. Oxygen partial pressures corresponding to the changes in the transport behaviour of $(La_{0.9}Sr_{0.1})_{0.95}Cr_{0.85}Mg_{0.1}Ni_{0.05}O_{3-\delta}$ estimated as shown in Fig. 3.29 and Fig. 3.30, in comparison with the corresponding data for selected chromite perovskites and NiO/Ni phase boundary [41, 44, 169]

3.3.3. Electrode activity

The present section is devoted to consideration of electrode layers $(La_{0.9}Sr_{0.1})_{0.95}Cr_{0.85}Mg_{0.1}Ni_{0.05}O_{3-\delta}$ applied onto $La_{10}Si_5AlO_{26.5}$ and LSGM electrolytes preliminary coated with CGO20 sublayer. The effect of the presence of the sublayer and detailed characterization of the anode layers is addressed in Chapter 5.

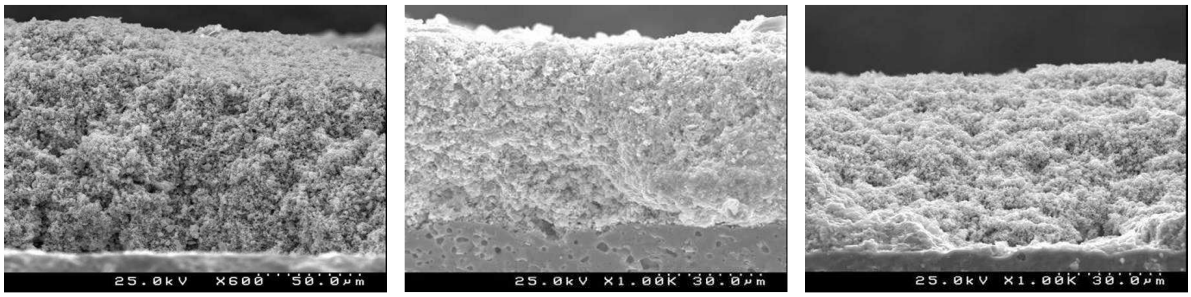

Fig. 3.33. SEM micrographs of as-prepared $(La_{0.9}Sr_{0.1})_{0.95}Cr_{0.85}Mg_{0.1}Ni_{0.05}O_{3-\delta}$ anode layer on $La_{10}Si_5AlO_{26.5}$ electrolyte (A); $CeO_{2-\delta}$- and Ni-modified $(La_{0.9}Sr_{0.1})_{0.95}Cr_{0.85}Mg_{0.1}Ni_{0.05}O_{3-\delta}$ anode on LSGM electrolyte after polarization measurements (B); PrO_x-modified $(La_{0.9}Sr_{0.1})_{0.95}Cr_{0.85}Mg_{0.1}Ni_{0.05}O_{3-\delta}$ cathode on $La_{10}Si_5AlO_{26.5}$ electrolyte after polarization measurements (C).

SEM analysis shown in Fig. 3.33 revealed sufficiently porous electrode layers, with reliable contact between the cell components. The thickness of the layers varied in the range 50 - 80 µm. No substantial microstructural changes were revealed after electrochemical testing the electrodes under reducing or oxidizing conditions, except for formation of agglomerates of catalytically active reagents ($CeO_{2-\delta}$, Ni, PrO_x) introduced during the procedure of the electrochemical testing.

Despite the comparable or even lower level of the total conductivity in oxidative atmospheres, the performance of $(La_{0.9}Sr_{0.1})_{0.95}Cr_{0.85}Mg_{0.1}Ni_{0.05}O_{3-\delta}$ cathodes is significantly better in comparison with $(La,Sr)(Cr,Mn)O_{3-\delta}$ and $(La,Sr)(Mn,Ti)O_{3-\delta}$ perovskites (Fig. 3.34), possibly due the presence of buffer layer in the former case, microstructural peculiarities or participation of (Mg,Ni)O impurity in the electrochemical process, as Ni-containing phases possess an enhanced catalytic activity towards redox processes [578, 593].

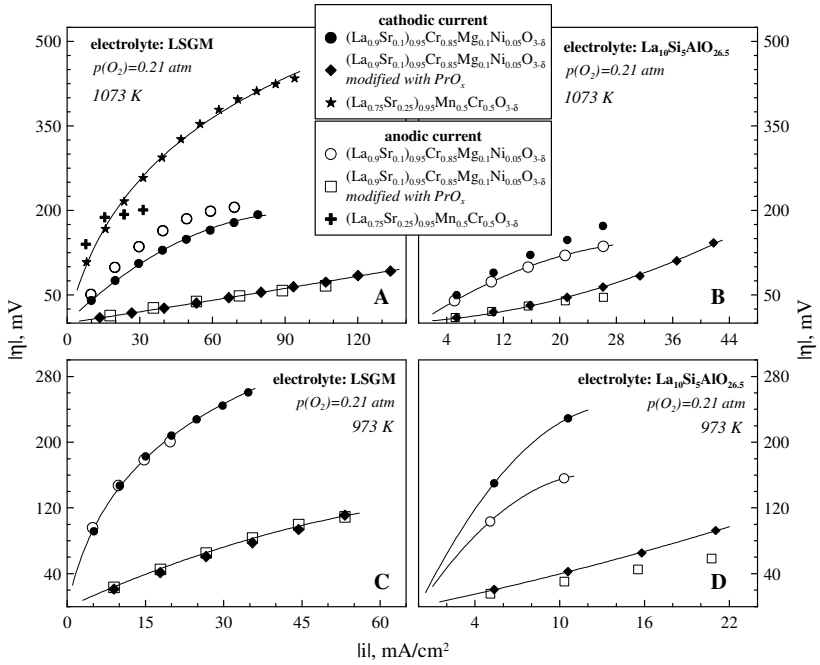

Fig. 3.34. Polarization curves of $(La_{0.9}Sr_{0.1})_{0.95}Cr_{0.85}Mg_{0.1}Ni_{0.05}O_{3-\delta}$ cathodes applied onto CGO20 sublayer in contact with LSGM (A, C) and $La_{10}Si_5AlO_{26.5}$ (B, D) electrolytes at 1073 K (A, B) and 973 K (C, D)

The activity of $(La_{0.9}Sr_{0.1})_{0.95}Cr_{0.85}Mg_{0.1}Ni_{0.05}O_{3-\delta}$ was found to be higher on LSGM electrolyte than on apatite-type electrolytes, in accordance with a poor performance of silicate-based electrochemical cells [566, 591, 594]. Similar to $(La,Sr)(Mn,Cr,Ti)O_{3-\delta}$ cathodes, the polarization resistances may be substantially reduced by distribution of PrO_x phase over the electrode layer, possibly attributable to insufficient activity of the non-modified perovskite phase or microstructure-related improvements. Another particularity of the title cathodes is rather similar polarization behaviour under cathodic and anodic currents; the trend becomes more obvious after addition of PrO_x (Fig. 3.34). As discussed in previous sections, for $(La,Sr)(Mn,Cr,Ti)O_{3-\delta}$ cathodes deposited directly onto the gallate or silicate electrolytes, the anodic polarization is substantially lower in comparison with cathodic one, presumably due to dissolution of transition metal cations in the electrolyte and their influence on the transport characteristics of the latter. In turn, this effect may be governed by current-induced oxidation or reduction of the cations dissolved. The presence of the sublayer in the present case seems to suppress the cation interdiffusion. While $(La_{0.25}Sr_{0.75})_{0.95}Mn_{0.5}Ti_{0.5}O_{3-\delta}$ cathodes applied directly onto apatite electrolyte showed substantially larger polarization values under cathodic polarization, presumably due to formation of additional interstitial oxygen species and promotion of the ionic transport of the apatite phase, for Sr-, Mg- and Ni-doped chromite cathode with CGO20 sublayer the effect of the current direction is less obvious. One should not also neglect a possible direct participation of the ceria-based phase in the electrochemical process with resultant influence on the electrode mechanism, an enlargement of the TPB or minor current-induced microstructural changes.

Apart from the low activity found for cathodes on apatite-type electrolyte, these cells also suffer from a noticeable degradation, as shown in Fig. 3.35. No observable performance loss was found for similar cathodes deposited onto gallate electrolytes, although longer testing is necessary for certain conclusions. As indicated in [566, 580, 594], the apatite phases are prone to segregation of silica and its subsequent spreading along the interfaces or TPB, while the electrolyte material suffers from a degradation of the transport and mechanical properties.

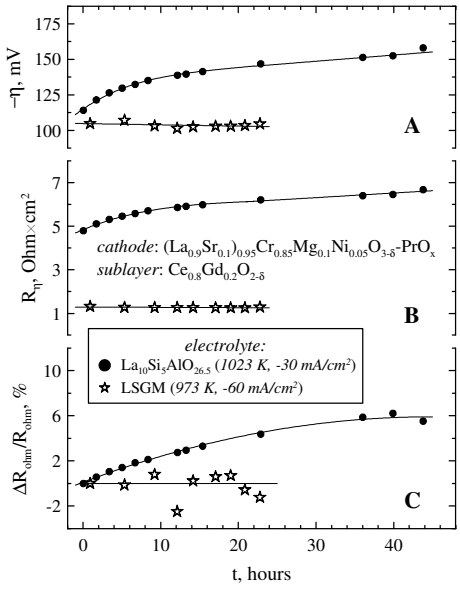

Fig. 3.35. Time dependencies of the polarization (A), polarization resistance (B) and ohmic resistance related to the initial value (C) exhibited by $(La_{0.9}Sr_{0.1})_{0.95}Cr_{0.85}Mg_{0.1}Ni_{0.05}O_{3-\delta}$ cathode applied onto CGO20 sublayer in contact with LSGM and $La_{10}Si_5AlO_{26.5}$ electrolytes. The data were collected in galvanostatic mode.

Fig. 3.36 shows typical impedance spectra collected for a cathode $(La_{0.9}Sr_{0.1})_{0.95}Cr_{0.85}Mg_{0.1}Ni_{0.05}O_{3-\delta}$ in contact with LSGM electrolyte. The impedance arc related to the electrode process is dominated by the process characterized by the frequency domain 0.1 - 100 Hz; the corresponding resistance decreases upon cathodic or anodic polarization. One may observe an additional small semicircle at higher frequencies which seems to grow under anodic currents. Whatever the contributions into the overall electrode mechanism, the polarization resistances evaluated from the impedance spectra are consistent with those found from the slope of the polarization curves, as shown in Fig. 3.37. More detailed analysis of the impedance data is problematic due to poor resolution between the impedance arcs as well as by complexity to prepare identical electrode layers with a good reproducibility of the impedance characteristics by the procedure undertaken in the present study. One should emphasize that no optimization of the electrode fabrication route was attempted here, since the primarily task of the work is related with revealing the relationships between the composition, functional characteristics and performance-determining factors of perovskite-based electrodes.

The polarization resistance of $(La_{0.9}Sr_{0.1})_{0.95}Cr_{0.85}Mg_{0.1}Ni_{0.05}O_{3-\delta}$ cathodes on LSGM electrolyte varies in the range 1- 3 Ohm×cm^2 at 1073 K. Although the performance may further be improved by PrO_x introduction, the overall level of the electrochemical performance is insufficient for the practical utilizations under oxidizing conditions.

Another concern related with the applicability of Cr-enriched materials as cathodes is a strong vaporization of Cr-containing volatile species [82-85] and formation of multivalent chromium-based compounds on the perovskite surface [44, 139], promoted by high oxygen pressure in the cathodic atmosphere. The latter problem becomes even more critical in water vapour-containing environments; therefore, a special equipment is required for preliminary drying of oxidizing gases in order to operate with chromite-based cathodes, which increases the costs and complexity of the electrochemical devices.

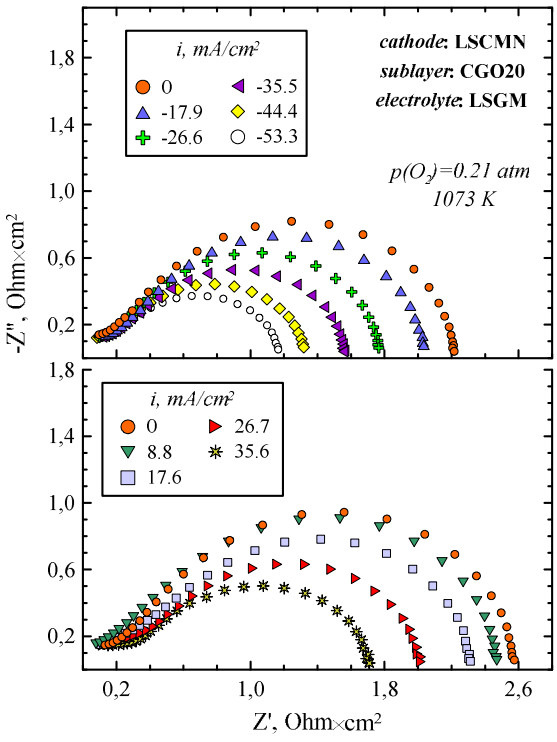

Fig. 3.36. Impedance spectra collected on $(La_{0.9}Sr_{0.1})_{0.95}Cr_{0.85}Mg_{0.1}Ni_{0.05}O_{3-\delta}$ cathode applied onto CGO20 sublayer in contact with LSGM electrolyte collected under cathodic (top) and anodic (bottom) polarization. The spectra were corrected for the ohmic contribution.

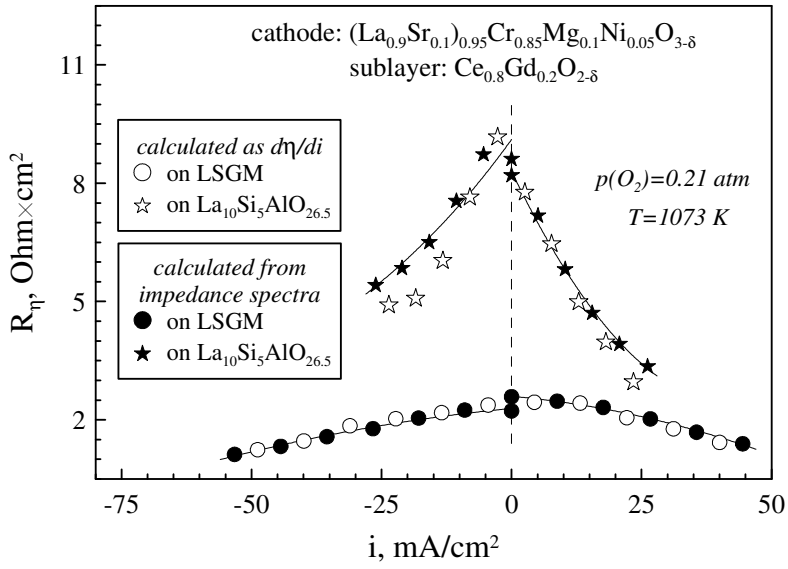

Fig. 3.37. Current density dependencies of the polarization resistance of $(La_{0.9}Sr_{0.1})_{0.95}Cr_{0.85}Mg_{0.1}Ni_{0.05}O_{3-\delta}$ cathodes applied onto CGO20 sublayer in contact with LSGM and $La_{10}Si_5AlO_{26.5}$ electrolytes. The solid symbols correspond to the data calculated from the impedance spectra corrected for the ohmic losses (Fig. 2.7) and empty symbols represent the slopes of the polarization curves shown in Fig. 3.34.

The anode activity of $(La_{0.9}Sr_{0.1})_{0.95}Cr_{0.85}Mg_{0.1}Ni_{0.05}O_{3-\delta}$ in contact with LSGM electrolyte and CGO20 sublayer is also somewhat improved in comparison with $(La_{0.75}Sr_{0.25})Cr_{0.5}Mn_{0.5}O_{3-\delta}$ analogue (Fig. 3.38), possibly due to comparatively high level of the electronic conductivity preserved down to anodic conditions (Fig. 3.29) or participation of reduced Ni particles in electrochemical processes. Nevertheless, the overpotential of ~110 mV shown under current 80 mA/cm^2 at 1073 K for non-modified electrode layer still requires further optimization of the anode composition for the electrochemical applications.

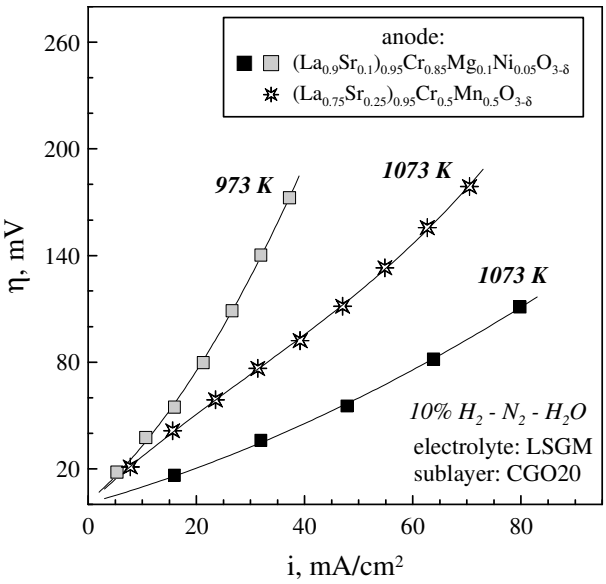

Fig. 3.38. Anodic polarization curves of $(La_{0.9}Sr_{0.1})_{0.95}Cr_{0.85}Mg_{0.1}Ni_{0.05}O_{3-\delta}$ electrodes applied onto CGO20 sublayer in contact with LSGM electrolyte in humidified 10% H_2 - N_2 atmosphere in comparison with $(La_{0.75}Sr_{0.25})_{0.95}Cr_{0.5}Mn_{0.5}O_{3-\delta}$ anode [10]

3.4. Final remarks on chromite-based electrode materials

In the present section three various series of doped chromites were characterized as potential electrode materials. The choice of the compositions was primarily based on a possible modification of the ionic transport and catalytic activity induced by appropriate doping in A- and B-sublattice with simultaneous preservation of the chemical and thermomechanical stability as well as of an acceptable level of the total conductivity in a wide $p(O_2)$ range. Moreover, the amounts of B-site cation dopants were selected as high as possible (i.e. at the limit of phase stability) in order to diminish Cr content and avoid the contamination of the cell components induced by chromium diffusion, vaporization/deposition, etc.

In accordance with literature reports and results shown in the work, most chromites exhibit structural transformations upon thermal or redox cycling; selected examples are demonstrated in Fig. 3.28 and Table 3.13. Although no influence of the transition on the integrity of ceramics or electrode layers was detected, in the case of long-term utilization one should take into account that the electrochemical cell may be exposed to multiple thermal or redox cycles. In accordance with [169, 177], reduction-induced transitions in chromites basically proceed slowly, without any noticeable effects on the overall expansion behaviour. If the issue of the structural transitions cannot be avoided it would be reasonable to focus further efforts on the achieving more gradual transformations to prevent mechanical damages. On the other hand, slow structural rearrangements may be accompanied by hindered equilibration of the transport and dimensional properties and resultant negative influence on the functional characteristics of the materials.

The surface-related processes, presence of the secondary phases, structural transformations, slow equilibration kinetics in the intermediate-$p(O_2)$ range result in hysteresis behaviour of the conductivity observable on the chromite-based materials upon consecutive reduction and oxidation runs (Fig. 3.39).

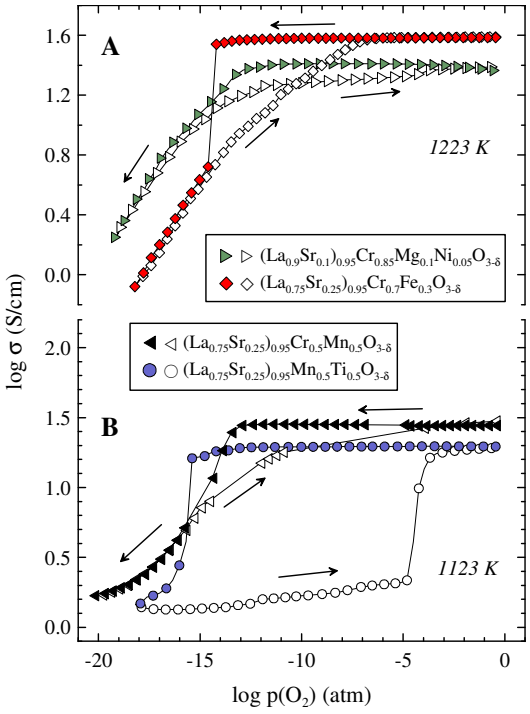

Fig. 3.39. Examples of the hysteresis behaviour observed in $p(O_2)$ dependencies of the total conductivity for selected perovskite materials. Arrows indicate the direction of $p(O_2)$ variations.

Nevertheless, no strong degradation upon redox cycling was observed, as indicated by comparatively small deviations between the reduction and oxidation curves, while the initial level of the conductivity was nearly recovered after a cycle. Such a behaviour is consistent with high chemical and thermomechanical stability of chromites in a wide $p(O_2)$ region and may be regarded to be beneficial compared with $(La,Sr)(Mn,Ti)O_{3-\delta}$ perovskites where the hysteresis is more substantial and the conductivity shows a drastic drop after redox cycling, possibly associated with mechanical failure of the materials.

One of the major problems associated with the processing of Cr-enriched electrode materials relates to the strong tendency of chromites towards surface oxidation under ambient conditions [44, 132, 137, 138]. Fig. 3.40 represents heating behaviour of selected Cr-containing perovskites studied in the present work. One may observe that the most substantial mass changes originating from release of adsorbed oxygen, H_2O or CO_2 gaseous species and resultant strong hysteresis on thermal cycling are relevant to the materials with higher Cr content indicating that these perovskites are more susceptible towards chemical changes at low temperatures in atmospheric air. In terms of the anode applications, the phenomena indicated may induce mechanical failure or loss of activity due to cation redistribution over the material, microstructural degradation, changes in the surface properties, etc. This requires a stringent control of the cell operation procedure and the ambient conditions surrounding the chromite-based anodes. One should note that variations of the chemical state of the surface are also typical for Ti-enriched compositions; an example is demonstrated in Fig. 3.40A.

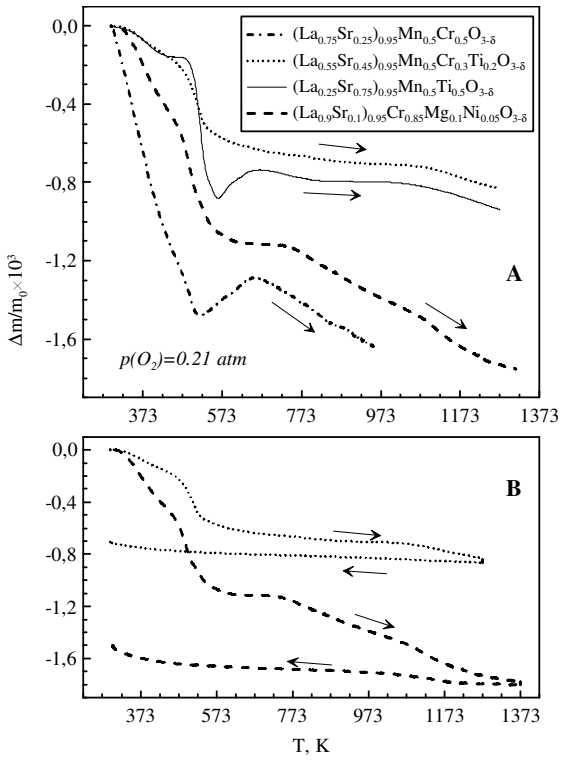

Fig. 3.40. Comparison of the relative weight changes of perovskite-based materials measured by TGA in dried atmospheric air (A). Typical hysteresis behaviour on the thermal cycling (B). Arrows indicate the directions of the temperature changes.

As follows from the trends shown in Fig. 3.40, replacement of Cr with other transition metal cations is desirable in order to provide the tolerance towards the ambient conditions. Furthermore, the intrinsic electrocatalytic activity of chromites is rather low unless improved by additional components which also requires introduction of cations which facilitate the ionic transport and exchange kinetics. However, the results of electrochemical testing showed that reduction of Cr content in $(La_{0.75-x}Sr_{0.25+x})_{0.95}Mn_{0.5}Cr_{0.5-x}Ti_xO_{3-\delta}$ and $(La_{0.75}Sr_{0.25})_{0.95}Cr_{1-x}Fe_xO_{3-\delta}$ leads to lower anode activity, possibly due to suppressed electronic transport (Fig. 3.16 and Fig. 3.26). Therefore, one should find a compromise between the positive effects (oxygen diffusivity, catalytic properties, suppression of the formation of high-valent chromium species) and possible disadvantages (worse chemical and thermomechanical stability and promotion of the conductivity drop) caused by the presence of acceptor-type and/or transition metal dopants the perovskite phase. To some extent, promising combinations of the functional characteristics were demonstrated for $(La_{0.75}Sr_{0.25})_{0.95}Cr_{1-x}Fe_xO_{3-\delta}$ and $(La_{0.9}Sr_{0.1})_{0.95}Cr_{0.85}Mg_{0.1}Ni_{0.05}O_{3-\delta}$ at reduced temperatures (Fig. 3.26, Fig. 3.38); as a result, these groups of anode materials showed the highest potential for further studies which should primarily include the stability of the electrochemical characteristics, since the nearly constant level of the electronic conductivity seems to be associated with kinetic factors.

Although chromite-based compositions are not generally considered as SOFC cathode components due to insufficient activity towards oxygen reduction [587, 595], selected characteristics obtained for cathodes $(La_{0.75-x}Sr_{0.25+x})_{0.95}Mn_{0.5}Cr_{0.5-x}Ti_xO_{3-\delta}$ and $(La_{0.9}Sr_{0.1})_{0.95}Cr_{0.85}Mg_{0.1}Ni_{0.05}O_{3-\delta}$ may have an impact on development of the electrodes for fabrication of symmetrical electrochemical cells. However, the level of the polarization resistances of 1 - 3 Ohm×cm^2 is too high with respect to the requirements for cathode materials, while the problems related with poor chemical stability and contamination of cell components with chromium species necessitate reducing Cr content and make the issue of cathode applications of chromites arguable.

Chapter 4. Transport, thermomechanical and electrochemical properties of manganite-based perovskites

As discussed in Chapter 1.3, recent studies on doped manganites revealed a proper combination of the transport properties and catalytic activity, while the main drawbacks associated with insufficient tolerance towards reductive conditions may be overcome by kinetic stabilization or replacement of Mn with an appropriate amount of high-valent cations [8, 16, 95, 306, 317]. In particular, among chromite- and titanate-based anodes, promising characteristics have been found for (La,Sr)(Cr,Mn)$O_{3-\delta}$ and (La,Sr)(Mn,Ti)$O_{3-\delta}$ compositions, while increasing Mn content in these groups of perovskites was shown to be beneficial in terms of the electrocatalytic properties [16, 210, 352].

One of the most crucial issues related with application of manganites in reducing atmospheres is that stabilization of the perovskite structure by an appropriate B-site substitution basically causes a deterioration of the transport properties and electrode activity (see, in particular, Table 1.3.2). As a result, the optimum combination of the functional characteristics was in most cases found for manganites with minimum substitution degree in B-sublattice [95, 210, 306], despite the facilitated oxygen losses and promoted drop of the conductivity. However, the insufficient thermodynamic stability may induce degradation of the performance in long-term scale, mechanical damage, etc. Therefore, doping strategies should satisfy the following requirements: 1. the sufficient electronic conduction and acceptable electrocatalytic activity relevant to manganites should be preserved; 2. the domain of $p(O_2)$ where the functional characteristics are maintained should be expanded.

Despite a large potential of manganite-based anodes, the number of studies devoted to their applicability under reducing conditions is scarce in comparison with chromite or titanate perovskites. The present section is focused on evaluation of phase, structural, microstructural, thermomechanical, transport and electrochemical behaviour of A(Mn,Nb)$O_{3-\delta}$ (A = Ca, Sr) and (La,Sr)(Mn,Ti)$O_{3-\delta}$ perovskites.

4.1. Perovskite-like $SrMn_{1-x}Nb_xO_{3-\delta}$ and $CaMn_{0.5}Nb_{0.5}O_{3-\delta}$

Nb-doping into perovskites has been regarded as an effective way to stabilize the perovskite structure or expand the phase boundaries of perovskites towards more reductive conditions [20, 130, 596]. Due to extremely low reduction potential, any contribution of $Nb^{5+/4+}$ couple into the overall electronic conductivity may hardly be expected; however, donor-doping into $CaMnO_{3-\delta}$ and $SrMnO_{3-\delta}$ is favourable in terms of excitation of additional n-type carriers. On the other hand, high Nb amount reduces the population of available sites for electronic transport. In the case of large overall content of donor-like cations in the compound, an excess of cation vacancies may be required for the charge compensation which may provoke a transformation of the perovskite lattice into ordered structures. To avoid such a possibility, manganites $CaMnO_{3-\delta}$ and $SrMnO_{3-\delta}$ were selected as parent compositions for assessment of the effect of Nb-doping.

Depending on the oxygen deficiency which may achieve 0.5 per perovskite formula unit, $CaMnO_{3-\delta}$ exists in orthorhombic, tetragonal or cubic structure; the symmetry is higher for oxygen-deficient

compositions [597-599]. As reported by Kruth et al. [600], up to 60% Nb may be introduced into B-sublattice of $CaMnO_{3-\delta}$; further Nb-doping induces separation of $Ca_2Nb_2O_7$-based phases. The orthorhombic lattice symmetry is generally preserved upon doping provided that the oxygen deficiency is below 0.2 [600]. No cation ordering in $Ca(Mn,Nb)O_{3-\delta}$ has been observed [600-602], while at low Nb doping level as well as in parent $CaMnO_{3-\delta}$ formation of oxygen vacancy-ordered superstructures on reduction was reported [600]. The latter information is, however, contradictive [597-600]. The orthorhombic perovskite structure with cation disorder has also been reported for Ta- or Sb-substituted $CaMnO_{3-\delta}$ [601-603]. The studies on $Ca(Mn,Nb)O_{3-\delta}$ concerned mainly their structural characteristics, phase relationships, oxygen nonstoichiometry and low-temperature magnetic and transport properties, while reports on their properties with respect to high-temperature electrochemical applications have not been found.

The perovskite structure of $SrMnO_{3-\delta}$ is stable only at the temperatures above ~1310 K in air; the crystal symmetry is cubic or orthorhombic symmetry depending on the oxygen content [330, 604]. On cooling the lattice adopts four-layers hexagonal structure. In order to stabilize the perovskite lattice, the composition is basically doped with donor-like cations; in particular, introducing 10 - 30% of Ce into A-sublattice was shown to be beneficial for preserving the structure and improving the transport properties [330, 605]. Similar effects might be expected for doping with Nb. At the same time, the reports on the structural behaviour of Nb-doped $SrMnO_{3-\delta}$ are contradictive. No indication of cation ordering have been reported by Lufaso et al. [601, 602], based on neutron diffraction studies. On the other hand, in [19, 20] the structure was identified as cubic perovskite with ordering in B-sublattice. Reduction causes transformation into disordered cubic structure, while the perovskite phase was shown to be stable in 5% H_2 - Ar. The conductivity, however, is rather low, which, in particular, yielded poor cathodic performance [591].

The present section is devoted to evaluation of the effect of A-site cation nature and Mn:Nb atomic ratio on the structural, microstructural, transport and thermomechanical properties of $A(Mn,Nb)O_{3-\delta}$ perovskites.

4.1.1. Phase relationships and structure

$SrMn_{1-x}Nb_xO_{3-\delta}$ with x = 0.2 - 0.5 are single phase perovskites after preparation in air (Fig. 4.1). For x = 0.4, the structure was identified as rhombohedral ($R\bar{3}c$), while the compositions with x = 0.2 and x = 0.5 were refined in cubic symmetry (Table 4.1), although the space groups were identified to be different due to possible B-site ordering for Nb-enriched perovskite. As found by Tao et al [20], ordering between Mn and Nb cations taking place in $SrMn_{0.5}Nb_{0.5}O_{3-\delta}$ under oxidizing conditions may be detected by the appearance of a characteristic peak at $2\theta \approx 37.6^{\circ}$ in XRD pattern. The same peak was found in the present work (inset in the upper pattern in Fig. 4.1) which disappears upon reduction indicating a possible cation disordering. The ordered perovskite structures have also been reported for relative compositions, namely for $SrMn_{0.5}Sb_{0.5}O_{3-\delta}$ [606] and to some extent for $SrMn_{0.5}Ta_{0.5}O_{3-\delta}$ [606]. Although more accurate techniques than XRD are required to detect the formation of superstructures, in the present work the structures of $SrMn_{0.5}Nb_{0.5}O_{3-\delta}$ prepared in air and after annealing in 10% H_2 - N_2 were refined with space group $Fm\bar{3}m$ and $Pm\bar{3}m$,

respectively (Table 4.1). One should separately note that no accent on the structural characteristics was made in this study. This, in particular, is related with the fact that by far no obvious benefit or disadvantage of the cation ordering on the electrochemical characteristics of perovskites has been reported, as both ordered and disordered structures have shown a potential for the electrode applications [8, 16, 126, 129].

Analyzing the behaviour of the cell parameters indicated in Table 4.1, Nb-doping expands the cell volume, referred to the primitive cubic perovskite cell. This trend is expectable, since the ionic radius of Nb^{5+} is larger in comparison with Mn^{4+} (0.64 vs. 0.53 Å) which dominates in the perovskite lattice of the parent $SrMnO_{3-\delta}$. Moreover, introduction of the donor-type cation should induce reducing the oxidation state of Mn species; the cation radius of Mn^{3+} is 0.645 Å, also larger in comparison with Mn^{4+}. The ionic radii are given assuming the octahedral coordination for all the atoms and high-spin state for Mn^{3+} [133]. A similar increase of the cell parameters in orthorhombic settings on Nb doping was observed for $Ca(Mn,Nb)O_{3-\delta}$ series [600].

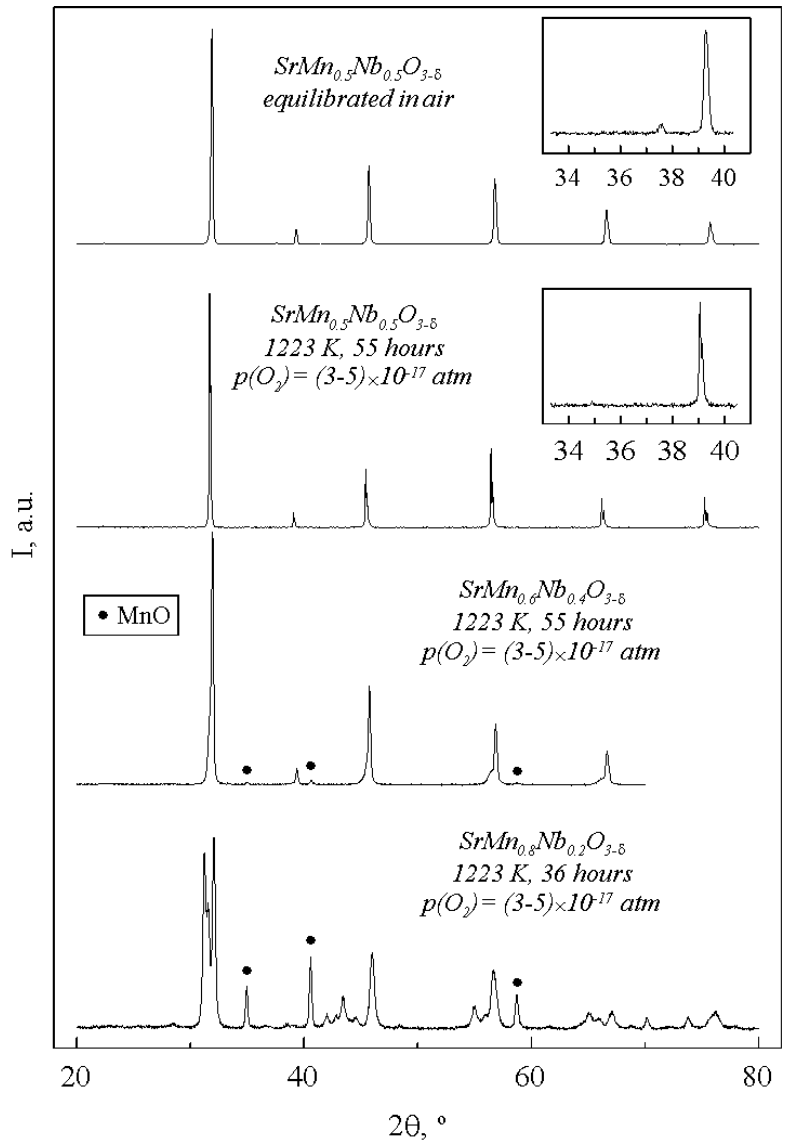

Fig. 4.1. XRD patterns of $SrMn_{1-x}Nb_xO_{3-\delta}$ powders prepared from ceramics. Insets on two upper plots show a magnification of the corresponding patterns in the range of 2θ = 33 - 41°.

Table 4.1. Unit cell parameters and relative density of $SrMn_{1-x}Nb_xO_{3-\delta}$ perovskites

Composition	Processing conditions	S.G.	a, Å	c, Å	$V_{u.c.}/N_{f.u.}$, Å^3	Relative density, %	Reference
$SrMn_{0.8}Nb_{0.2}O_{3-\delta}$	1773 K, air	$Pm\bar{3}m$	3.8713(1)	-	58.019(4)	93.5	This work
$SrMn_{0.6}Nb_{0.4}O_{3-\delta}$	1773 K, air	$R\bar{3}c$	5.5728(2)	13.6446(11)	61.163(9)	92.9	This work
$SrMn_{0.5}Nb_{0.5}O_{3-\delta}$	1788 K, air	$Fm\bar{3}m$	7.9374(2)	-	62.509(5)	86.9	This work
	1223 K, $p(O_2)=(3\text{-}5)\times10^{-17}$ atm	$Pm\bar{3}m$	3.9894(3)	-	63.493(14)	-	
	1223 K, $p(O_2)=(3\text{-}4)\times10^{-21}$ atm	$Pm\bar{3}m$	4.0088(3)	-	64.423(14)	-	
$SrMn_{0.5}Nb_{0.5}O_{3-\delta}$	1673 K, air	$Fm\bar{3}m$	7.9338(3)	-	62.424(7)	-	[20]
	1173 K, H_2-Ar	$Pm\bar{3}m$	4.0022(5)	-	64.106(24)	-	[20]
$SrMn_{0.5}Nb_{0.5}O_{3-\delta}$	1688 K, air, cooling rate K/min	*I4/mcm*	5.6119(6)	7.927(1)	62.412(21)	-	[601]

$V_{u.c.}/N_{f.u.}$ corresponds to the unit cell volume related to the number of formula unit

As can be found from the relative density of sintered ceramics of $Sr(Mn,Nb)O_{3-\delta}$ (Table 4.1) and corresponding SEM images (Fig 4.2), introducing Nb results in a larger volume fraction of pores and smaller grain size, due to suppressed sinterability. Irrespective to the worse quality of $SrMn_{0.5}Nb_{0.5}O_{3-\delta}$ ceramics, the pores seem to be separated from each other, which should not significantly affect the transport characteristics; all the ceramic samples $Sr(Mn,Nb)O_{3-\delta}$ were verified to be gas-tight.

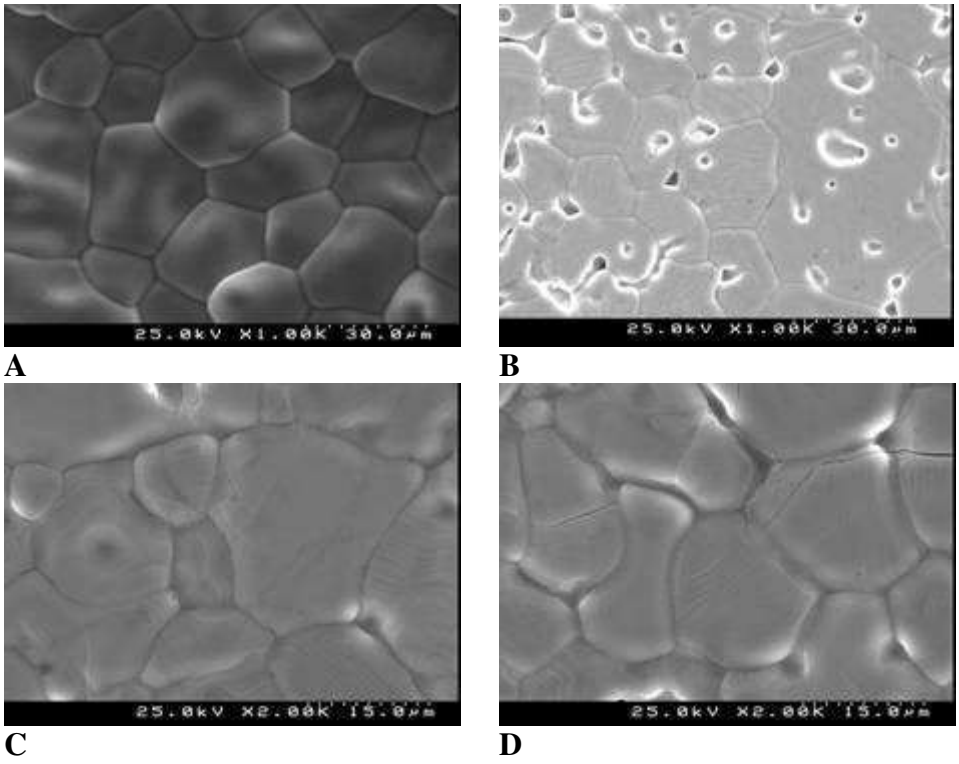

Fig. 4.2. SEM micrographs of polished ceramics $SrMn_{0.6}Nb_{0.4}O_{3-\delta}$; (A), $SrMn_{0.5}Nb_{0.5}O_{3-\delta}$; (B), $CaMn_{0.5}Nb_{0.5}O_{3-\delta}$ (C and D)

On the other hand, Nb-doping improves the stability of the perovskites in reductive atmospheres (Fig. 4.1). After annealing under reducing conditions, single-phase perovskite was only found to form at x = 0.5 (S.G.: $Pm\bar{3}m$); $SrMn_{0.8}Nb_{0.2}O_{3-\delta}$ tends to the complete decomposition, while $SrMn_{0.6}Nb_{0.4}O_{3-\delta}$ forms a mixture of rhombohedral ($R\bar{3}c$) and orthorhombic (*Pnma*) phases with minor MnO impurity alike to $(La,Sr)(Mn,Cr,Ti)O_{3-\delta}$. An example of refining of the 3-phase mixture obtained on reduction of $SrMn_{0.6}Nb_{0.4}O_{3-\delta}$ is demonstrated in Fig. 4.3, while the parameters and fraction of the constituent phases are listed in Table 4.2. The stability of manganites shows a correlation with TGA data in air which demonstrated larger changes of the oxygen nonstoichiometry for Mn-rich materials, as will be discussed below.

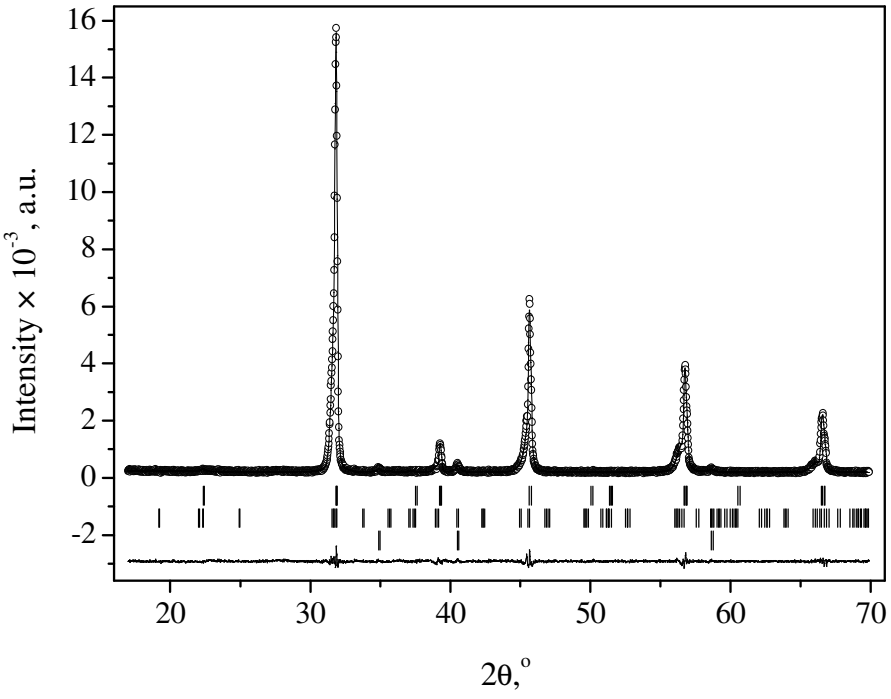

Fig. 4.3. Experimental (open symbols) and refined (upper solid line) XRD patterns obtained for $SrMn_{0.6}Nb_{0.4}O_{3-\delta}$ powder annealed in 10% H_2 - 90% N_2 flow ($p(O_2) = 3\times10^{-17}$ atm) at 1223 K for 55 h. The bottom line is the difference between the experimental and refined data. The vertical bars correspond to Bragg reflections of the phases presented in Table 4.2.

Table. 4.2. Rietveld refinement results for decomposition products obtained after reduction of $SrMn_{0.6}Nb_{0.4}O_{3-\delta}$ powder annealed in 10% H_2 - 90% N_2 flow ($p(O_2) = 3\times10^{-17}$ atm) at 1223 K for 55 h

Phase	S.G.	Mole fraction, %	*a*, Å	*b*, Å	*c*, Å	*V*, Å^3
$SrMn_{1-x}Nb_xO_{3-\delta}$	$R\bar{3}c$	50.2	5.6155(3)	5.6155(3)	13.772(2)	376.11(5)
$SrNb_{1-y}Mn_yO_{3\pm\delta}$	*Pnma*	42.3	5.6196(6)	8.062(2)	5.6435(7)	255.68(8)
MnO	*Fm3m*	7.5	4.4510(8)	4.4510(8)	4.4510(8)	88.18(3)

The cell parameters calculated for $SrMn_{0.5}Nb_{0.5}O_{3-\delta}$ perovskite increase in reducing atmospheres due to increasing radii of B-site cations (Table 4.1), in accordance with generation of large Mn^{3+} or even Mn^{2+} or Nb^{4+} cations. Exposure to mildly reducing conditions causes a ~1.5% increment of the volume cell, while maintenance in dry H_2 at 1223 K yields the volume expansivity of ~3%.

In accordance with previous reports [600, 601], $CaMn_{0.5}Nb_{0.5}O_{3-\delta}$ was refined as orthorhombic perovskite with $GdFeO_{3-\delta}$-like structure (S.G. *Pbnm*); the XRD patterns and corresponding cell parameters are presented in Fig. 4.4 and Table 4.3. The deviations in the lattice parameters observable in Table 4.3. might be attributed to various preparation conditions. Reduction in 10% H_2 - N_2 - H_2O gas mixture leads to a partial decomposition and a loss of crystallinity (Fig. 4.4); the lower stability compared with $Sr(Mn,Nb)O_{3-\delta}$ analogue is consistent with larger oxygen losses in $CaMnO_{3-\delta}$-based composition, as discussed below.

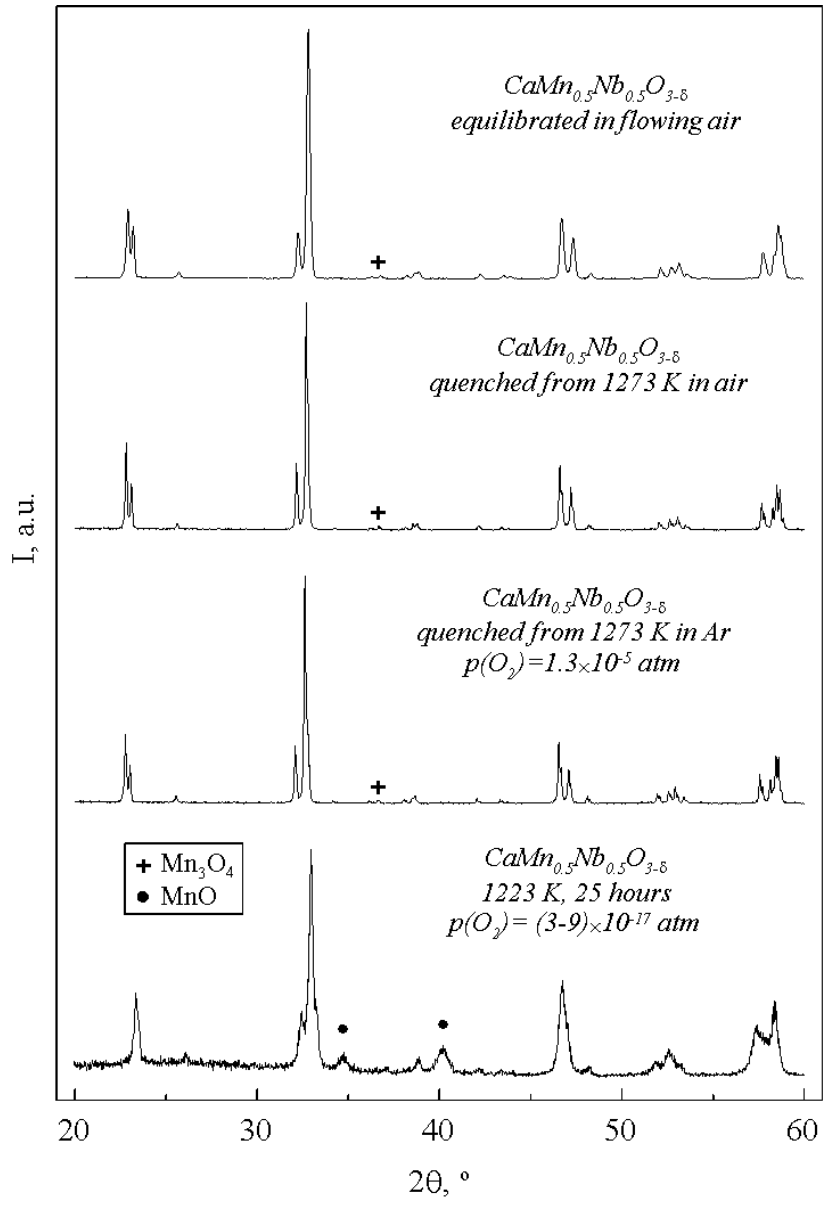

Fig. 4.4. XRD patterns of $CaMn_{0.5}Nb_{0.5}O_{3-\delta}$ powders prepared from ceramics

Table. 4.3. Unit cell parameters of $CaMn_{0.5}Nb_{0.5}O_{3-\delta}$ perovskites.

Preparation conditions*	S.G.	a, Å	b, Å	c, Å	$V_{u.c.}$, $Å^3$	Reference
Annealed at 1273 K and cooled with the rate 1 K/min in air	*Pbnm*	5.5571(2)	7.6847(3)	5.4479(2)	232.65(3)	This work
Annealed at 1273 K and cooled with the rate 5 K/min in air	*Pbnm*	5.5576(3)	7.6883(4)	5.4486(3)	232.81(4)	This work
Annealed at 1273 K in air and quenched into liquid nitrogen	*Pbnm*	5.5575(3)	7.6878(3)	5.4493(3)	232.82(3)	This work
Annealed at 1273 K in argon ($p(O_2) = 1.3\times10^{-5}$ atm) and quenched into liquid nitrogen	*Pbnm*	5.5632(3)	7.7024(4)	5.4482(3)	233.46(4)	This work
Sintered at 1658 K and cooled with the rate 3K/min in air	*Pbnm*	5.5635(4)	7.6996(5)	5.4530(4)	233.59(5)	[689]
Sintered at 1473 - 1673 K and cooled by steps of 50 K (20 hours/step) in air	*Pnma*	5.4527	5.5622	7.7062	233.72	[695]

**In the present work the powder was obtained from ceramics sintered at 1663 K*

No structural transformations were detected after thermal or moderate $p(O_2)$ variations within the accuracy of XRD method; the cell parameters of materials quenched in air or in Ar are listed in Table 4.3. The cell parameters increase during procedures which promote formation of oxygen vacancies, i.e. exposure to high temperature, especially at reduced $p(O_2)$, with subsequent rapid cooling. One may observe a similarity between the parameters obtained for the powders quenched or cooled with the rate of 5 K/min in air from the same temperature demonstrating that the rate indicated is too rapid for achieving the equilibrium. Nevertheless, the variations of the cell parameters upon moderate reduction is not high; in particular, exposure of $CaMn_{0.5}Nb_{0.5}O_{3-\delta}$ to Ar atmosphere with subsequent quenching causes a ~0.3% increase of the cell volume.

4.1.2. Thermal expansion

Nb-doping into $SrMnO_{3-\delta}$ reduces the thermal expansion, as shown in Fig. 4.5 and Table 4.4. This trend is opposite to the behaviour of the cell volume on variation of Nb content calculated at room temperature (Table 4.1), and might primarily originate from suppressed oxygen losses on thermal cycling and resultant decrease of the chemical contribution into the entire expansion for Nb-enriched materials. The latter suggestion is confirmed by an increase of the expansivity on heating (Table 4.4), more pronounced for the $SrMn_{0.8}Nb_{0.2}O_{3-\delta}$, while the perovskites with higher Nb concentration show nearly linear behaviour.

If considering the entire temperature interval studied, replacement of Ca for Sr decreases the average TEC originating from smaller ionic radius of Ca or structural particularities. More detailed analysis shows that the expansion in the high-temperature range is substantially enhanced for $CaMn_{0.5}Nb_{0.5}O_{3-\delta}$ and overcomes the TEC value for Sr-containing analogue, as shown in Fig. 4.5 and Table. 4.4.

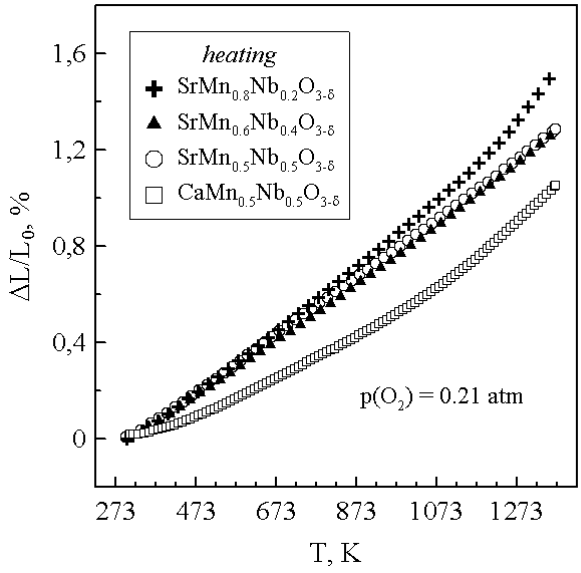

Fig. 4.5. Dilatometric curves of $SrMn_{1-x}Nb_xO_{3-\delta}$ and $CaMn_{0.5}Nb_{0.5}O_{3-\delta}$ ceramics obtained on continuous heating in air with the rate 3 K/min

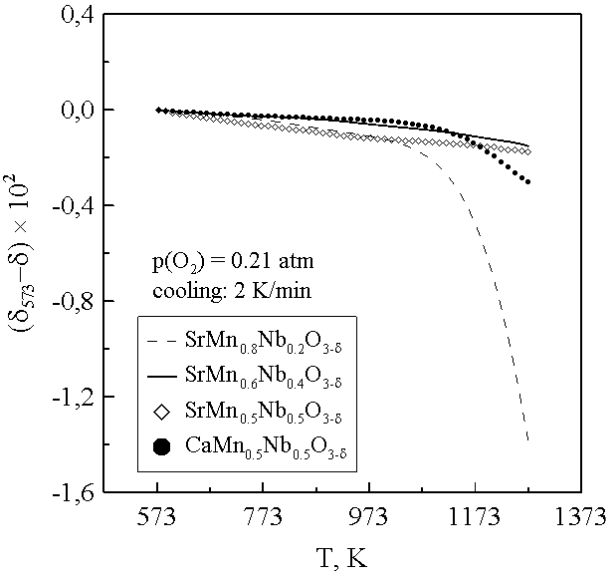

Fig. 4.6. Oxygen nonstoichiometry variations obtained on cooling $SrMn_{1-x}Nb_xO_{3-\delta}$ and $CaMn_{0.5}Nb_{0.5}O_{3-\delta}$ powders in air with the rate 2 K/min

The large difference between the coefficients in the low-and high-temperature intervals combined with the slow equilibration kinetics discussed below might be responsible for accumulation of excessive stresses in $CaMn_{0.5}Nb_{0.5}O_{3-\delta}$ ceramics resulting in formation and propagation of cracks, as shown in Fig. 4.2D. In terms of the thermal expansion behaviour, the materials $SrMn_{1-x}Nb_xO_{3-\delta}$ (x = 0.4 - 0.5) seem more attractive for the high-temperature applications, due to moderate and essentially constant TEC in the whole temperature range.

Table 4.4. Average TECs of $SrMn_{1-x}Nb_xO_{3-\delta}$ and $CaMn_{0.5}Nb_{0.5}O_{3-\delta}$ ceramics in air

Composition	T, K	$\alpha \times 10^6$, K^{-1}
$SrMn_{0.8}Nb_{0.2}O_{3-\delta}$	300 - 800 800 - 1200 1200 - 1370	12.49 ± 0.01 14.03 ± 0.01 21.17 ± 0.07
$SrMn_{0.6}Nb_{0.4}O_{3-\delta}$	300 - 800 800 - 1200 1200 - 1370	11.32 ± 0.01 12.27 ± 0.01 13.53 ± 0.01
$SrMn_{0.5}Nb_{0.5}O_{3-\delta}$	300 - 800 800 - 1200 1200 - 1370	11.59 ± 0.01 11.95 ± 0.02 13.07 ± 0.03
$CaMn_{0.5}Nb_{0.5}O_{3-\delta}$	300 - 800 800 - 1200 1200 - 1370	7.68 ± 0.13 11.21 ± 0.03 14.42 ± 0.03

The expansion behavior of $A(Mn,Nb)O_{3-\delta}$ ceramics is consistent with the changes in oxygen nonstoichiometry observed by TGA (Fig. 4.6) which confirms that the expansivity is strongly contributed by the chemical constituent. In particular, $SrMn_{0.8}Nb_{0.2}O_{3-\delta}$ shows comparatively large oxygen losses (up to 0.015 per perovskite formula unit) above 1000 K; this temperature is close to the point where a pronounced enhancement of the TEC takes place (Fig. 4.5). $CaMn_{0.5}Nb_{0.5}O_{3-\delta}$ also demonstrates an obvious extensive high-temperature oxygen release, unlike Sr-containing analogue, which also correlates with the dilatometric curves. Analyzing the behaviour of $CaMn_{0.5}Nb_{0.5}O_{3-\delta}$ ceramics, one should note a strong hysteresis observable on thermal cycling, and poor reproducibility of the results on subsequent heating and cooling runs (Fig. 4.7). The mass changes obtained by TGA (Fig. 4.8) are affected by cooling rate, while the equilibration of the mass in TGA tests was not achieved for more than 20 hours (inset in Fig. 4.8).

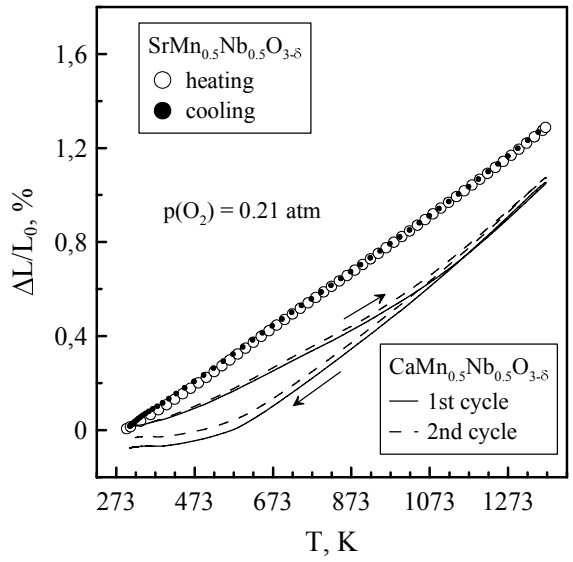

Fig. 4.7. Dilatometric curves of $CaMn_{0.5}Nb_{0.5}O_{3-\delta}$ ceramics obtained on continuous heating and cooling in air

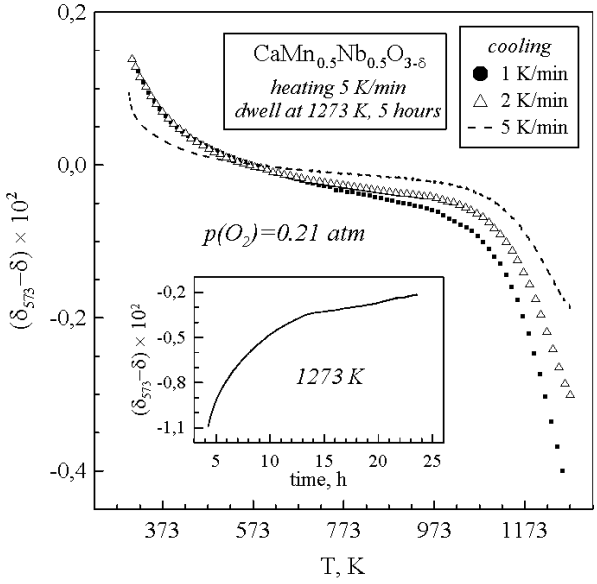

Fig. 4.8. Oxygen nonstoichiometry variations obtained on cooling $CaMn_{0.5}Nb_{0.5}O_{3-\delta}$ powder in air with different rates. Inset shows equilibration of the oxygen nonstoichiometry in air at 1273 K.

In accordance with the data reported in [600], the transformation of the orthorhombic structure of $CaMn_{0.5}Nb_{0.5}O_{3-\delta}$ into cubic was found when δ exceeds 0.2 - 0.25. Assuming the preservation of the single perovskite phase, the transition should occur when the fraction of Mn^{2+} species approaches the total amount of manganese cations, and further oxygen losses from the cubic phase should induce reduction of Nb^{5+} or Mn^{2+} species. Whatever the origin of the structural rearrangement, in the present study the variations in oxygen content in $CaMn_{0.5}Nb_{0.5}O_{3-\delta}$ in air are found to be much smaller, which should exclude any possibility of this transformation. XRD analysis carried out on quenched materials after annealing in air or Ar revealed no significant structural changes except for the increase of the lattice parameters. Nevertheless, taking into account the results of the thermal analysis as well as the slow equilibration kinetics, formation of domains with cubic or other symmetry might be expected, which content is below the sensitivity of XRD

technique. The increase of the cell volume (Table 4.3) confirms the suggestion that the structural variations are induced by oxygen losses. However, further studies are required for elucidation the factors responsible for the slow kinetics in $CaMn_{0.5}Nb_{0.5}O_{3-\delta}$ material.

4.1.3. Total conductivity

Considering the previous reports on the electronic transport in manganites of alkali-earth cations, the parent compositions $SrMnO_{3-\delta}$ and $CaMnO_{3-\delta}$ and their derivatives exhibit polaronic character of the conductivity with dominant n-type charge carriers, although the binding energy of mobile polarons is comparatively small which may induce metallic-like behaviour [330, 583, 595, 608]. The mobile electrons are localized on Mn species, and the concentration of the charge carriers may be quantitatively described via 3-fold charged manganese cations. Generation of Mn^{3+} is associated with oxygen losses from the perovskite structure; the process corresponds to electron transition from half-filled t_{2g} band to the e_g band and may cause comparatively high electron mobility due to a minor occupancy of the latter.

Donor-doping is regarded as another way to increase the concentration of n-type charge carriers. In particular, Ce-doping into A-sublattice of $SrMnO_{3-\delta}$ was shown to promote the electronic transport in the entire solubility domain, although the improvement might also be related with stabilization of the perovskite structure. Appearance of regions with substantially reduced activation energy or even metallic-like temperature dependence of the conductivity has been reported for $SrMnO_{3-\delta}$ [609, 610], $(La,Sr)MnO_{3-\delta}$ [323, 583] or $(Sr,Ce)MnO_{3-\delta}$-based compositions [320, 330, 605], indicative of possible broadband character of the electronic transfer, although the trends might also be attributed to structural transformations or extensive oxygen losses affecting the concentration of mobile charge carriers.

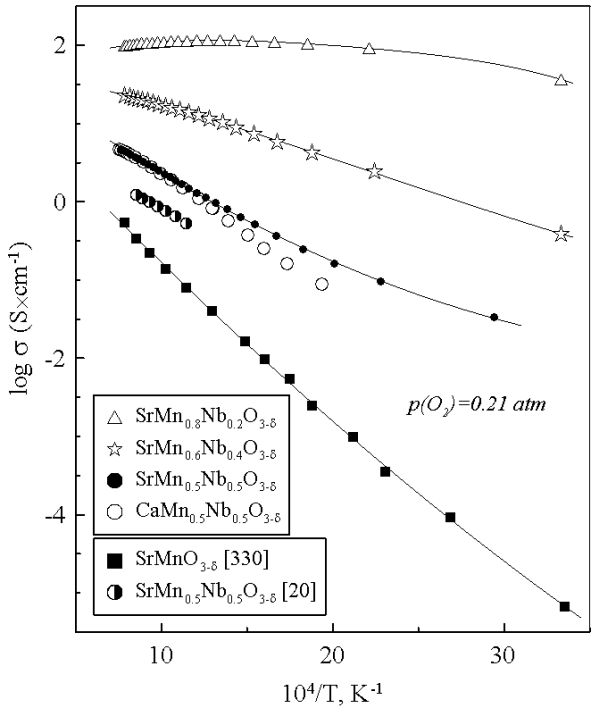

Fig. 4.9. Temperature dependencies of the total conductivity of $SrMn_{1-x}Nb_xO_{3-\delta}$ and $CaMn_{0.5}Nb_{0.5}O_{3-\delta}$ ceramics in air. Data on the conductivity of $SrMn_{0.5}Nb_{0.5}O_{3-\delta}$ [330] and $SrMnO_{3-\delta}$ [20] are given for comparison.

As shown in Fig. 4.9, moderate Nb-doping (up to 20 mol.%) significantly improves the conductivity of $SrMnO_{3-\delta}$, originating from generation of electrons via Nb introduction. The latter effect is qualitatively similar to Ce-doping into $SrMnO_{3-\delta}$ [330], although higher lattice symmetry in comparison with the hexagonal $SrMnO_{3-\delta}$ phase may also contribute to faster electronic transport. On further substitution with Nb, the conductivity substantially drops with simultaneous enhancement of the activation energy, as shown in Table 4.5. $CaMn_{0.5}Nb_{0.5}O_{3-\delta}$ and $SrMn_{0.5}Nb_{0.5}O_{3-\delta}$ exhibit nearly equal conductivity in the high-temperature interval, but the former perovskite is characterized by enhanced activation energy, possibly due to lower structural symmetry.

Table 4.6. Activation energies of the total conductivity and hole mobility of $SrMn_{1-x}Nb_xO_{3-\delta}$ and $CaMn_{0.5}Nb_{0.5}O_{3-\delta}$ in air

Composition	Total conductivity		Hole mobility	
	T, K	E_a, kJ×mol^{-1}	T, K	E_a, kJ×mol^{-1}
$SrMn_{0.8}Nb_{0.2}O_{3-\delta}$	450 - 750	7.1 ± 0.2		
$SrMn_{0.6}Nb_{0.4}O_{3-\delta}$	530 - 1270	19.6 ± 0.1	973 - 1223	19.4 ± 0.2
$SrMn_{0.5}Nb_{0.5}O_{3-\delta}$	650 - 1310	31.5 ± 0.4	973 - 1223	33.4 ± 0.5
$CaMn_{0.5}Nb_{0.5}O_{3-\delta}$	580 - 1320	35.6 ± 0.4		

When Nb fraction in B-sublattice approaches 40 - 50%, Mn^{3+} cations become dominant species and the conductivity exhibits the trends typical for p-type electronic conductors. In particular, large negative Seebeck coefficients observable for $SrMnO_{3-\delta}$, $(Sr,Ce)MnO_{3-\delta}$ or $CaMnO_{3-\delta}$ [330, 598, 611] become close to zero for $SrMn_{0.6}Nb_{0.4}O_{3-\delta}$ with subsequent inversion of the negative sign (Fig. 4.10). Analogously with $(La,Sr)(Mn,Cr,Ti)O_{3-\delta}$ system, this situation may correspond to reduction of the amount of p-type charge carriers below 50% of the overall density of states upon Nb-doping, as shown in Fig. 4.11; the values p/N and μ_p were calculated using Eqs. (2.3) and (2.5) described in Chapter 2, assuming N equal to the overall amount of Mn species in the B sublattice.

Heating induces generation of additional p-type charge carriers; this effect is more pronounced for $SrMn_{0.6}Nb_{0.4}O_{3-\delta}$. Taking into account relatively small variations of the oxygen content (Fig. 4.6), the temperature effect might be primarily attributed to promotion of Mn^{3+} disproportionation. On the other hand, variations of the population of p-type carriers with temperature are rather small, as can be evaluated from the similarity of the activation energies of the total conductivity and hole mobility (Table 4.5).

Substitution of Nb for Mn in $Sr(Mn,Nb)O_{3-\delta}$ substantially decreases the hole mobility and increases the corresponding activation energy. This indicates that apart from diminishing the amount of mobile carriers, the presence of inert Nb cations in the perovskite lattice hampers the electronic transfer, analogously with the trends observed in numerous perovskite systems [111, 306, 320, 596].

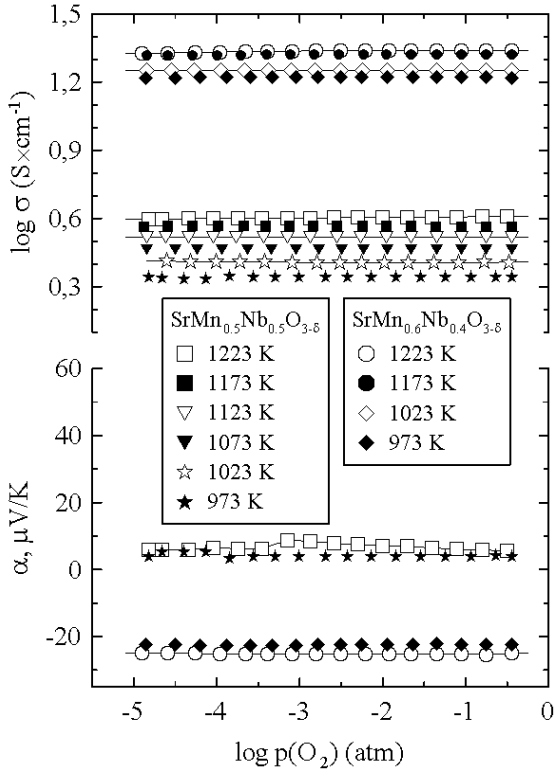

Fig. 4.10. Oxygen partial pressure dependencies of the total conductivity and Seebeck coefficients of $SrMn_{1-x}Nb_xO_{3-\delta}$ ceramics under oxidizing conditions

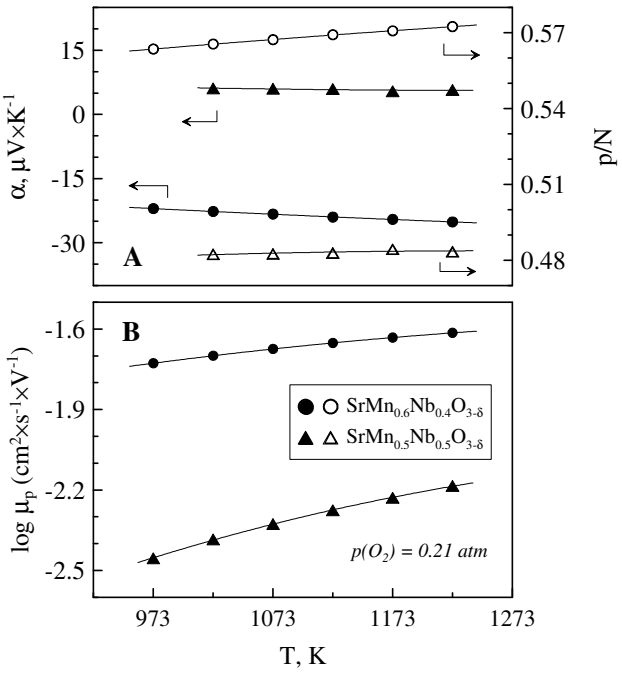

Fig. 4.11. Temperature dependencies of the Seebeck coefficient, fraction of the p-type charge carriers (A) and carrier mobility (B) in $SrMn_{1-x}Nb_xO_{3-\delta}$ ceramics in air

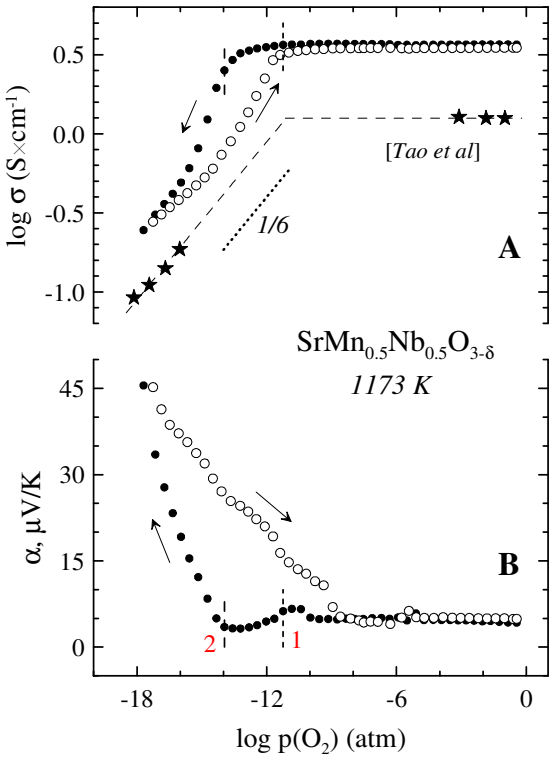

Fig. 4.12. Examples of the hysteresis behaviour of the total conductivity and Seebeck coefficient on redox cycling. Data obtained by Tao et al. [20] are given for comparison

The conductivity and Seebeck coefficient are essentially $p(O_2)$-independent in a wide range of partial pressures (Fig. 4.10). On stronger reduction, the conductivity decreases, as demonstrated in Fig. 4.12. Similar trends have been observed for most manganite-based perovskites stable in a wide $p(O_2)$ range, including $SrMn_{1-x}Nb_xO_{3-\delta}$ (x = 0.5 - 0.6) studied in [19, 20], although the conductivity obtained in the present study is ~3 times higher in comparison with the previously reported data. The conductivity and Seebeck coefficient show hysteresis behaviour on redox cycling; however, the characteristics are reversible which shows that no mechanical degradation occurs on $p(O_2)$ variations and the equilibration of $SrMn_{1-x}Nb_xO_{3-\delta}$ ceramics takes place in a reasonable period.

4.1.4. Oxygen permeability

The level and basic trends of the parameters responsible for the oxygen ionic transport in Nb-doped $SrMnO_{3-\delta}$ ceramics were qualitatively assessed by comparison of the permeation fluxes *j* and specific oxygen permeability $J(O_2)$ through dense ceramics of $SrMn_{0.5}Nb_{0.5}O_{3-\delta}$ with the thickness of 0.60 and 1.00 mm. The behaviour of the permeability characteristics on changing the membrane thickness demonstrated in Fig. 4.13 assumes that the oxygen flux is limited by both bulk oxygen diffusion and surface exchange kinetics, similar to $(La,Sr)(Mn,Cr,Ti)O_{3-\delta}$ series and numerous chromite and manganite perovskites [252, 337, 338]. The activation energy of the fluxes under fixed gradient of the oxygen chemical potential is as high as ~230 kJ/mol, close to the values found for Sr, Ti-doped $(La,Sr)(Mn,Cr)O_{3-\delta}$ ceramics, as shown in Table 3.7.

The effect of the surface exchange limitations over $SrMn_{0.5}Nb_{0.5}O_{3-\delta}$ is especially pronounced at elevated temperatures, where decreasing the membrane thickness has a minor influence on the permeation fluxes. Subsequent cooling induces an enhancement of the difference between the fluxes for various thicknesses which assumes that the activation energy of the ionic diffusion is higher in comparison with the gas/solid exchange kinetics. In the family $(La,Sr)(Mn,Cr,Ti)O_{3-\delta}$ as well as in perovskites characterized by slow ionic transport and hampered equilibration kinetics, the oxygen diffusion was shown to be strongly contributed by the diffusion along grain boundaries [112, 254, 336, 339]; a similar behaviour may be suggested for $SrMn_{0.5}Nb_{0.5}O_{3-\delta}$.

Nb-doped $SrMnO_{3-\delta}$ shows some improvement in comparison with $(La,Sr)(Mn,Cr,Ti)O_{3-\delta}$ series in terms of oxygen diffusivity, as demonstrated by 2-fold increase in the permeation fluxes, shown in Fig. 4.14. Using the model described in Chapter 2 (Eq. (2.11)), the oxygen ionic conductivity was estimated to be as low as 10^{-4} - 10^{-3} S/cm in the temperature interval studied, although any certain calculation is complicated by low values of the permeation fluxes and resultant large errors of the estimation. This level of ionic conductivity and the slow surface rates are too low to expect any extension of the electrochemical zone into the bulk phase of the materials studied. In particular, analogous measurements on $(Sr,Ce)MnO_{3-\delta}$ and $(Sr,Ce)(Mn,Al)O_{3-\delta}$ membranes as well as conductivity studies on $SrFe_{0.6}Nb_{0.4}O_{3-\delta}$ ceramics revealed the ionic conductivity ~1 order of magnitude higher in comparison with $SrMn_{0.5}Nb_{0.5}O_{3-\delta}$ [320, 596, 605]. The results indicate a negative influence of excessive Nb content on the ionic transfer, in accordance with a minor level of the oxygen vacancies (Fig. 4.6) and their reduced mobility in the vicinity of Nb atoms [596].

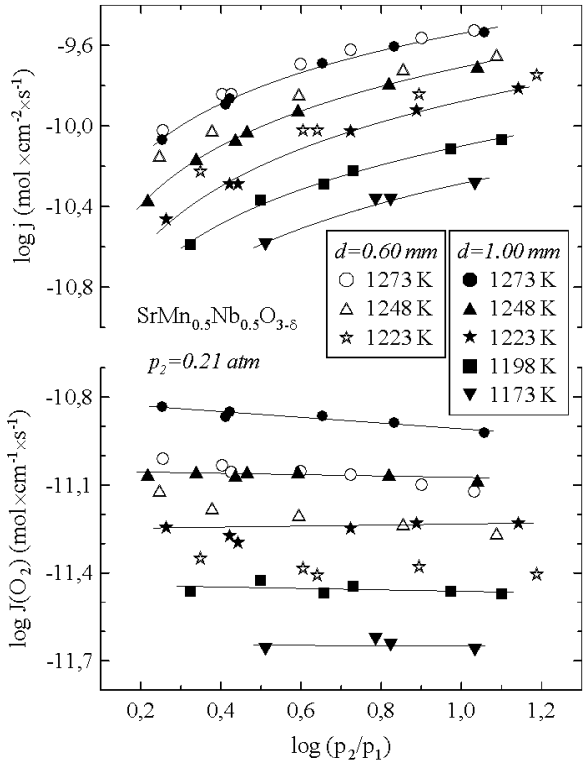

Fig. 4.13. Oxygen partial pressure dependencies of oxygen permeation fluxes and specific oxygen permeability through dense membranes of 1.00 and 0.60 mm thickness of $SrMn_{0.5}Nb_{0.5}O_{3-\delta}$

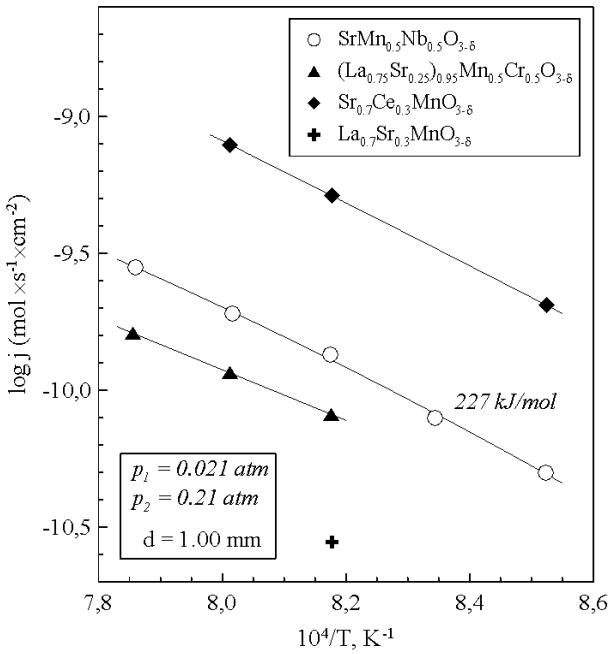

Fig. 4.14. Temperature dependencies of oxygen permeation fluxes through dense membranes of 1.00 mm thickness of $SrMn_{0.5}Nb_{0.5}O_{3-\delta}$ under a fixed $p(O_2)$ drop. Data on other manganite perovskites are given for comparison [10, 320, 612]

4.1.5. Electrode behaviour

As shown in previous sections, the level of the electronic and ionic conductivity in $SrMn_{1-x}Nb_xO_{3-\delta}$ (x = 0.4 - 0.5) is rather low to expect any noticeable electrochemical performance. Indeed, the electrode activity was evaluated to be poor under both oxidizing and reducing conditions. For example, the polarization resistance of the manganites in contact with LSGM electrolyte without especial modifications was evaluated in the range 10 - 20 Ohm×cm^2. Decreasing Nb content slightly improves the anode performance, in accordance with the electronic conductivity behaviour.

Polarization curves for $SrMn_{0.5}Nb_{0.5}O_{3-\delta}$ anode shown in Fig. 4.15 exhibit a slight improvement of the activity upon redox cycling. Possible origins this phenomenon as well analogues in literature will be discussed in Chapter 4.2.5 devoted to $(La,Sr)(Mn,Ti)O_{3-\delta}$ anodes. One of likely activation mechanisms involves current-induced microstructural variations; however, for Nb-doped $SrMnO_{3-\delta}$ the decrease in the polarization resistance is within 15 - 20% and microscopic analysis (Fig. 4.16) does not allow to observe any obvious difference between the microstructures of the electrode layers before and after current application, both in cathodic and anodic direction. Selected approaches towards reduction of the polarization resistance of $SrMn_{1-x}Nb_xO_{3-\delta}$ anodes involving, in particular, surface modifications or optimization of the half-cell composition, are considered in Chapter 5.

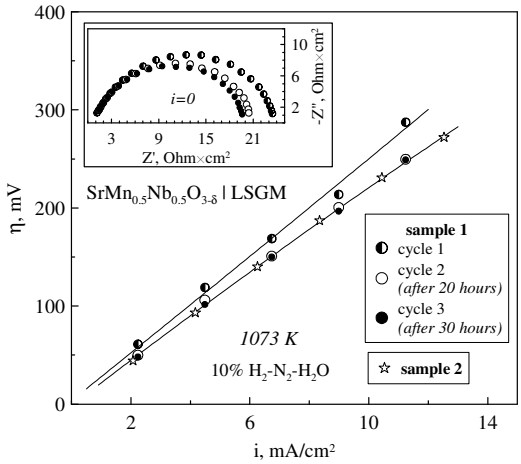

Fig. 4.15. Polarization curves showing the reproducibility between various samples and changes in the electrochemical behaviour after redox cycling for $SrMn_{0.5}Nb_{0.5}O_{3-\delta}$ anode on LSGM electrolyte with CGO20 sublayer. Inset shows the corresponding impedance spectra (corrected for the Ohmic losses and normalized for the electrode area) for "sample 1".

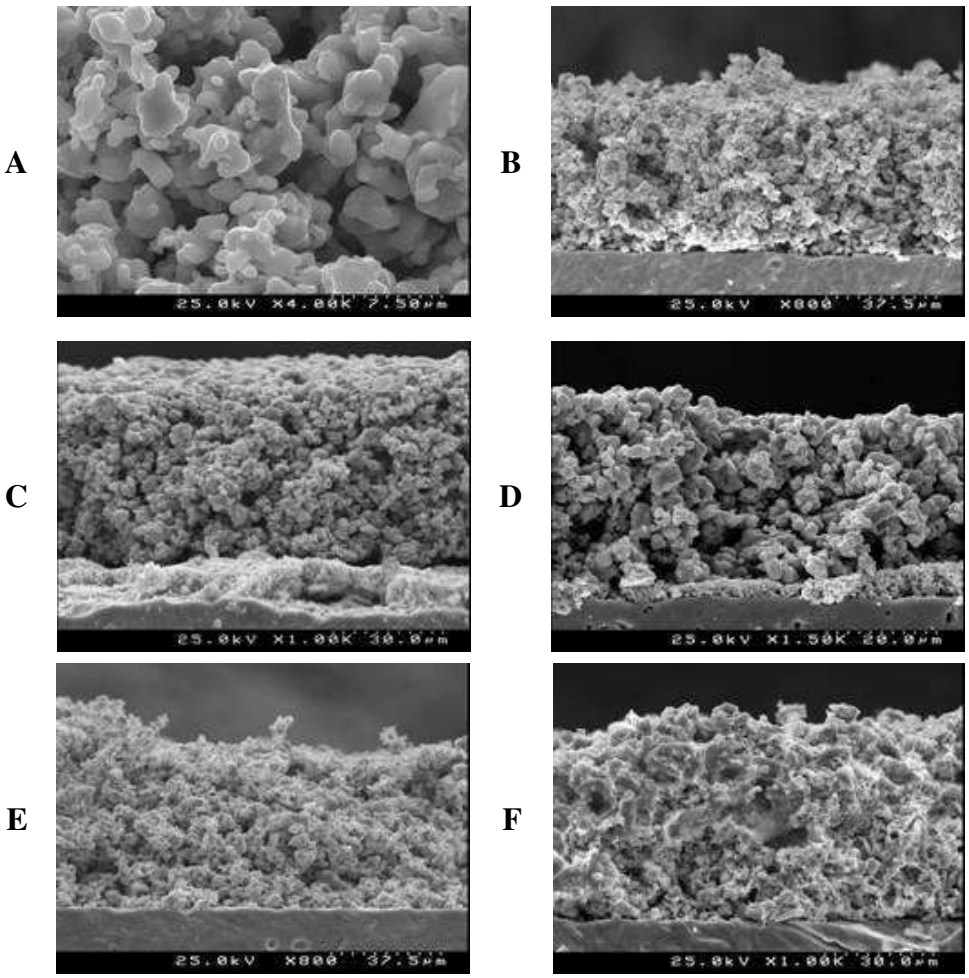

Fig. 4.16. SEM micrographs of $SrMn_{0.6}Nb_{0.4}O_{3-\delta}$ electrode layers: top view of the electrode after cathode measurements (A), cross sections of the electrodes before measurements in contact with $La_{10}Si_5AlO_{26.5}$ (B), $La_{10}Si_5AlO_{26.5}$ with CGO20 sublayer (C) and LSGM with CGO20 sublayer (D). Cross-sections of non-modified (E) and PrO_x-modified (F) electrodes in contact with $La_{10}Si_5AlO_{26.5}$ after cathode measurements.

The cathodic performance of $SrMn_{0.6}Nb_{0.4}O_{3-\delta}$ is somewhat beneficial in comparison with (La,Sr)(Mn,Cr,Ti)$O_{3-\delta}$ series (Fig. 4.17), but still remains too low for practical applications or for any detailed considerations. In particular, the overpotential of non-modified $SrMn_{0.6}Nb_{0.4}O_{3-\delta}$ electrode on LSGM and $La_{10}Si_5AlO_{26.5}$ electrolyte under the cathodic current of 25 mA/cm^2 achieves ~140 and ~410 Ohm×cm^2 at 1073 K, respectively. Corresponding values for $(La_{0.25}Sr_{0.75})_{0.95}Mn_{0.5}Ti_{0.5}O_{3-\delta}$ cathode achieve ~250 and >500 Ohm×cm^2, respectively. Taking into account a comparable level of the total conductivity of $SrMn_{0.6}Nb_{0.4}O_{3-\delta}$ perovskites in oxidizing atmospheres, the improvement might be attributed to slightly higher content of Mn species in comparison with (La,Sr)(Mn,Cr,Ti)$O_{3-\delta}$ series which are responsible for the cathode activity [210, 324, 584]; another possibility relates to ionic transport which is estimated to be slightly better in $SrMn_{1-x}Nb_xO_{3-\delta}$ perovskites, as discussed in Chapter 4.1.4.

Summarizing the general trends shown by the polarization curves under oxidizing atmospheres, one may emphasize the influence of the electrolyte nature and the presence of protective sublayer on both the level of the polarization resistance and on behaviour under cathodic and anodic polarization. The latter factor is in general agreement with the trends exhibited by (La,Sr)(Mn,Ti)$O_{3-\delta}$ and $(La_{0.9}Sr_{0.1})_{0.95}Cr_{0.85}Mg_{0.1}Ni_{0.05}O_{3-\delta}$ cathodes which were evaluated without and with the sublayer, correspondingly. In particular, cathodic currents applied on $SrMn_{0.6}Nb_{0.4}O_{3-\delta}$ layer on LSGM electrolyte induce lower polarization in comparison with the anodic currents.

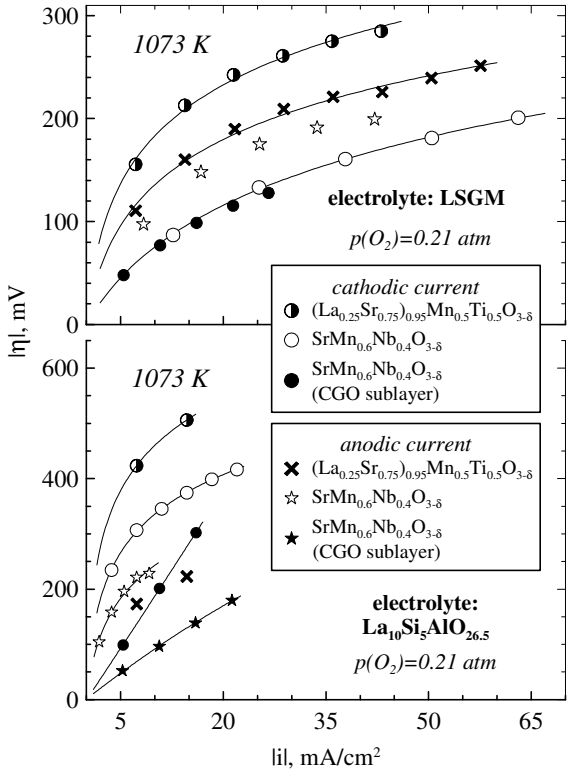

Fig. 4.17. Polarization curves of $SrMn_{0.6}Nb_{0.4}O_{3-\delta}$ and $(La_{0.25}Sr_{0.75})_{0.95}Mn_{0.5}Ti_{0.5}O_{3-\delta}$ cathodes under cathodic and anodic current on LSGM (A) and $La_{10}Si_5AlO_{26.5}$ (B) electrolytes at 1073 K

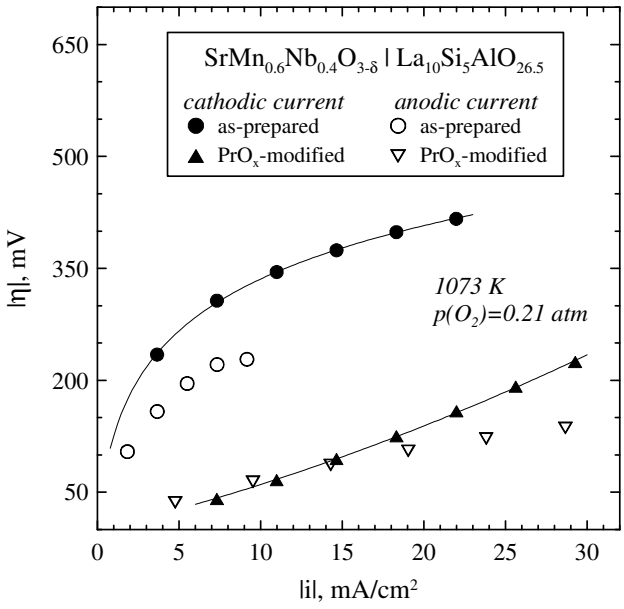

Fig. 4.18. Polarization curves of as-prepared and PrO_x-modified $SrMn_{0.6}Nb_{0.4}O_{3-\delta}$ cathodes under cathodic and anodic current on $La_{10}Si_5AlO_{26.5}$ electrolyte at 1073 K

The opposite trend was detected for similar cells with $La_{10}Si_5AlO_{26.5}$ electrolyte; this behaviour is consistent with various nature of the charge carriers in the gallate and silicate phases (oxygen vacancies and interstitials, correspondingly) which are generated and eliminated under cathodic current, respectively. Such a dependence might indicate that the electrochemical process is governed by a supply/removal of oxygen species from/into the electrolyte phase.

The presence of CGO20 sublayer or introduction of PrO_x into the cathode layer reduces the polarization resistance down to ~7 Ohm×cm^2 at 1073 K on $La_{10}Si_5AlO_{26.5}$ electrolyte and transforms the appearance of the polarization curve from the Tafel-like to nearly linear dependencies (Figs. 4.17, 4.18). Nevertheless, the trends related with the current direction discussed above remain essentially similar.

4.2. Physicochemical and electrode properties of $(La_{1-x}Sr_x)_{1-y}Mn_{0.5}Ti_{0.5}O_{3-\delta}$ perovskites

Due to attractive properties of titanates and manganites, the number of studies on $(La,Sr)(Mn,Ti)O_{3-\delta}$ solid solutions as potential anode materials has been growing in last years. Most works have been devoted to optimization of Mn:Ti ratio. Mn content was demonstrated to favorably influence the conductivity in oxidizing atmospheres (at least up to 60%), while under anodic conditions the effect of Mn fraction in $La_{0.4}Sr_{0.6}Mn_{1-x}Ti_xO_{3-\delta}$ is less obvious. On the other hand, increasing Mn content above 40 - 60% causes phase instability in reducing atospheres [16]. In terms of the electrode microstructure, the presence of Mn is noted to ensure a better wettability of zirconia-based phases and provide higher electrode performance [352]. Whatever the effect of Mn:Ti ratio, the functional properties might also be modified by compositional variations in A-sublattice.

On the other hand, the contribution of metallic phases basically present in the electrode layers into the overall performance is not clear from the available data on the $(La,Sr)(Mn,Ti)O_{3-\delta}$-based anodes. As the technology involving coating a metallic paste over the electrode cannot be utilized in industrial scale, it is necessary to estimate the activity of the anode layers more relevant to practical applications. Moreover, the presence of an additional component obscures the properties of the main electrode phase and does not allow to reveal relationships between the functional characteristics and anode activity of the electrode material, which might be important for further compositional modifications.

As shown in Chapter 3.1, in $(La_{0.75}Sr_{0.25})_{0.95}Cr_{0.5}Mn_{0.5}O_{3-\delta}$ chromium may be partially or completely replaced by Ti with simultaneous equivalent substitution in A-sublattice. However, introduction of Sr and Ti reduces the electronic conductivity down to the level insufficient for the electrochemical applications, especially under anodic conditions while chemically-induced expansion achieves 0.6% for $(La_{0.25}Sr_{0.75})_{0.95}Mn_{0.5}Ti_{0.5}O_{3-\delta}$. Although the latter composition did not exhibit a remarkable cathode or anode performance, further variations of the cation ratios might provide an acceptable combination of the functional properties. The present part is focused on evaluation of the effect of La:Sr cation ratio as well as A-site stoichiometry on the chemical and structural stability, thermomechanical properties, electronic and ionic conductivity and electrochemical performance of $(La_{1-x}Sr_x)_{1-y}Mn_{0.5}Ti_{0.5}O_{3-\delta}$ (x = 0.15 - 0.75, y = 0 - 0.05) anodes in contact with LSGM electrolyte. The studies were partially carried out in the Institute of Solid State

Chemistry RAS, Chernogolovka, Russia, with participation of Dr. S.I. Bredikhin, Dr. V.V. Sinitsyn, Dr. I.N. Burmistrov, A.I. Ivanov, Yu.S. Fedotov, D.A. Agarkov.

4.2.1. Crystal structure

XRD analysis showed formation of single phase perovskites $La_{1-x}Sr_xMn_{0.5}Ti_{0.5}O_{3-\delta}$ (x = 0.4 - 0.5) and $(La_{1-x}Sr_x)_{0.95}Mn_{0.5}Ti_{0.5}O_{3-\delta}$ (x = 0.15 - 0.75) after equilibration in air. The only exception relates to $(La_{0.35}Sr_{0.65})_{0.95}Mn_{0.5}Ti_{0.5}O_{3-\delta}$ where one peak of Mn_3O_4, comparable to the background, might be suspected in the XRD pattern (Fig. 4.19). The crystal structure was refined as rhombohedrally-distorted perovskite (S.G.: $R\bar{3}c$). Similar symmetry has been earlier reported for other representatives of $(La,Sr)(Mn,Ti)O_{3-\delta}$ series, namely, for $La_{0.4}Sr_{0.6}Mn_{1-x}Ti_xO_{3-\delta}$ (x = 0.4 - 0.8) [16], $La_{0.8}Sr_{0.2}Mn_{0.9}Ti_{0.1}O_{3-\delta}$ [238], $La_{0.33}Sr_{0.67}Mn_{1-x}Ti_xO_{3-\delta}$ (0.5<x<0.9) [12].

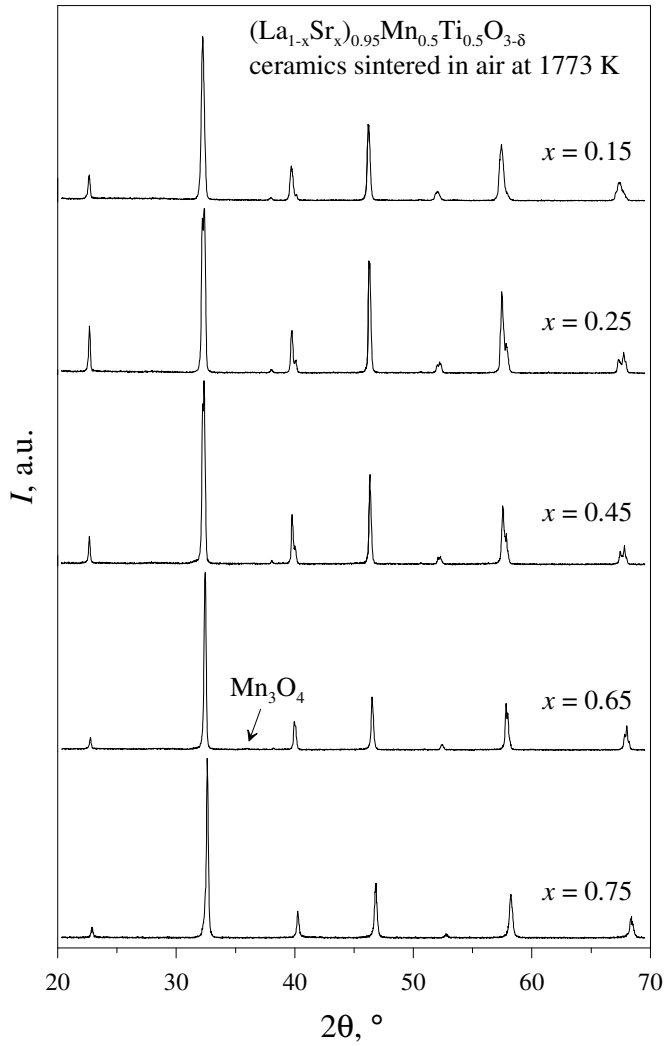

Fig. 4.19. XRD patterns of $(La_{1-x}Sr_x)_{0.95}Mn_{0.5}Ti_{0.5}O_{3-\delta}$ perovskites after sintering in air at 1773 K and slow cooling

The lattice parameters in hexagonal settings of $(La_{1-x}Sr_x)_{1-y}Mn_{0.5}Ti_{0.5}O_{3-\delta}$ are listed in Table 4.6. In general, the unit cell volume of cation-deficient perovskites tends to decrease with increasing x. Taking into account that ionic radius of Sr^{2+} is larger in comparison with that of La^{3+} [133], the trend might primarily be associated with increasing average oxidation state of Mn species and their resultant shrinkage on Sr-doping (suggesting that Ti is completely oxidized). One should note that increasing fraction of Mn^{4+} in Sr-enriched perovskites is consistent with trends observed in electronic conductivity in air, discussed below.

The creation of A-site cation vacancies leads to the unit cell volume expansion (Table 4.6), a result of stronger coulombic repulsion between the oxygen anions [613]. This factor also seems relevant for the La-rich compositions, where the crystal electroneutrality and lattice conservation conditions may lead to the formation of extra cation vacancies instead of Mn^{2+}.

Table 4.6. Unit cell parameters and density of as-prepared $(La_{1-x}Sr_x)_{1-y}Mn_{0.5}Ti_{0.5}O_{3-\delta}$ ceramics equilibrated at atmospheric oxygen pressure (S.G.: $R\bar{3}c$)

Composition	a, Å	c, Å	V, Å^3	ρ_{theor}, g/cm^3	ρ_{exp}/ρ_{theor}, %
$(La_{0.25}Sr_{0.75})_{0.95}Mn_{0.5}Ti_{0.5}O_{3-\delta}$	5.4960(8)	13.455(1)	351.97(8)	5.52	94.0
$(La_{0.35}Sr_{0.65})_{0.95}Mn_{0.5}Ti_{0.5}O_{3-\delta}$	5.5203(6)	13.476(2)	355.67(7)	5.59	91.0
$La_{0.5}Sr_{0.5}Mn_{0.5}Ti_{0.5}O_{3-\delta}$	5.530(3)	13.515(8)	357.96(9)	5.88	97.4
$(La_{0.55}Sr_{0.45})_{0.95}Mn_{0.5}Ti_{0.5}O_{3-\delta}$	5.5471(3)	13.4961(8)	359.64(4)	5.80	93.6
$La_{0.6}Sr_{0.4}Mn_{0.5}Ti_{0.5}O_{3-\delta}$	5.533(2)	13.493(3)	357.87(6)	6.02	96.3
$(La_{0.75}Sr_{0.25})_{0.95}Mn_{0.5}Ti_{0.5}O_{3-\delta}$	5.5578(2)	13.4996(7)	361.13(3)	6.05	88.3
$(La_{0.85}Sr_{0.15})_{0.95}Mn_{0.5}Ti_{0.5}O_{3-\delta}$	5.5633(2)	13.541(1)	362.97(3)	6.15	92.5

No perovskite phase decomposition was observed on reduction in H_2 - H_2O - N_2 atmospheres (Figs. 4.21, 4.22). The traces of MnO observed in the XRD pattern of $(La_{0.35}Sr_{0.65})_{0.95}Mn_{0.5}Ti_{0.5}O_{3-\delta}$ might originate from Mn_3O_4 reduction. Reduction of La-enriched compositions (x = 0.15 - 0.25) leads to structural transformation into the orthorhombic symmetry. Most likely, the transition is associated with extensive oxygen losses from the perovskite structure and generation of large Mn^{2+} and/or Ti^{3+} cations, as follows from the electroneutrality conditions. High quantities of these cations seem to lead to decreasing the tolerance factor, favoring the stabilization of the orthorhombic lattice. In accordance with the cell parameters of reduced perovskites (Table 4.7), the lattice volume of reduced $(La_{1-x}Sr_x)_{0.95}Mn_{0.5}Ti_{0.5}O_{3-\delta}$ (x = 0.45 - 0.65) expands by 1 - 1.5 % with respect to the oxidized phases at room temperature due to lowering oxidation state of the B-site cations, increasing their average radii, and the oxygen vacancy formation promoting cation repulsion. Enrichment of the compositions with La up to 75 - 85% increases the relative difference between the cell volume of the reduced and oxidized phases up to 5 - 6 %, attributable to the structural transformations.

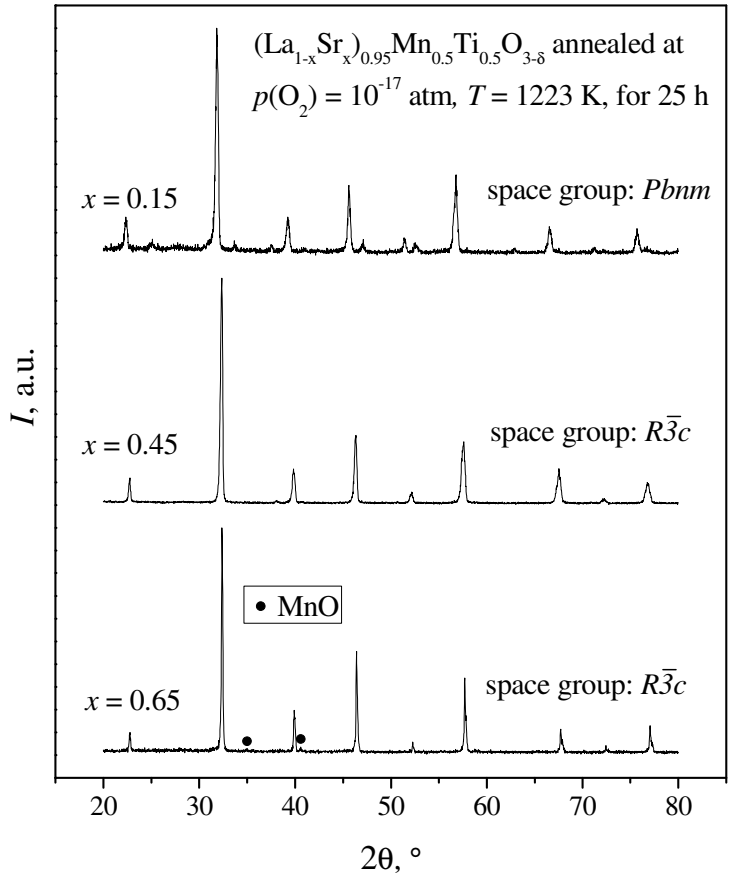

Fig. 4.20. XRD patterns of $(La_{1-x}Sr_x)_{0.95}Mn_{0.5}Ti_{0.5}O_{3-\delta}$ powders after reduction in flowing wet 10% H_2 - N_2 at 1223 K

Table 4.7. Cell parameters of $(La_{0.25+x}Sr_{0.75-x})_{0.95}Mn_{0.5}Ti_{0.5}O_{3-\delta}$ annealed at 1223 K in reducing conditions

Composition	Space group	a, Å	b, Å	c, Å	V, Å^3
$(La_{0.35}Sr_{0.65})_{0.95}Mn_{0.5}Ti_{0.5}O_3$	$R\bar{3}c$	5.5343(8)	-	13.5611(33)	359.71(18)
$(La_{0.55}Sr_{0.45})_{0.95}Mn_{0.5}Ti_{0.5}O_3$	$R\bar{3}c$	5.5571(9)	-	13.6555(24)	365.20(18)
$(La_{0.85}Sr_{0.15})_{0.95}Mn_{0.5}Ti_{0.5}O_3$	*Pbnm*	5.7101(4)	5.6119(3)	7.9426(4)	254.51(4)

Cation-stoichiometric $La_{1-x}Sr_xMn_{0.5}Ti_{0.5}O_{3-\delta}$ (x = 0.4 - 0.5) were shown to remain single phase after annealing in a 20 % H_2 - 80 % N_2 flow containing 5 ppm H_2S during 12 - 24 h at 973 - 1073 K (Fig. 4. 21). This behaviour being reproducible for various compositions indicates a good stability of reduced $(La,Sr)Mn_{0.5}Ti_{0.5}O_{3-\delta}$ in fuel gases, although possible sulfur poisoning surface effects on the electrocatalytic activity require careful investigations.

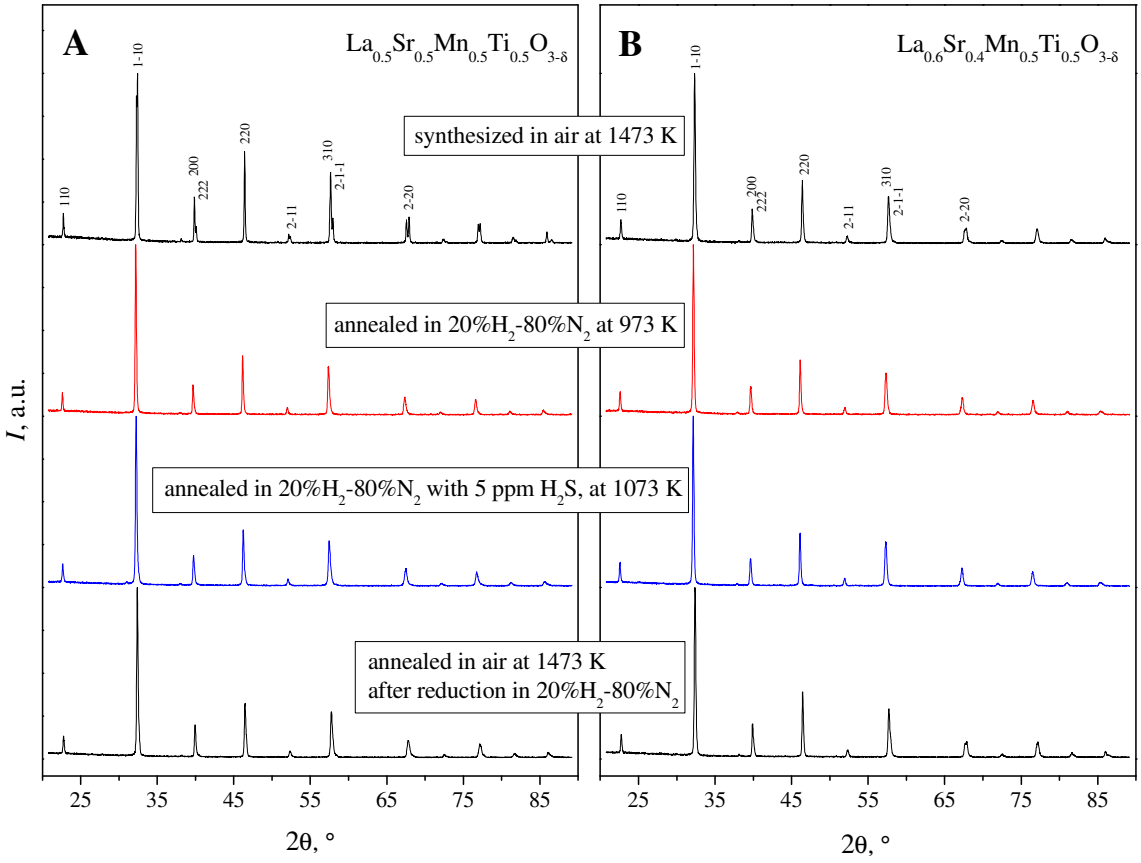

Fig. 4.21. Selected XRD patterns of $La_{0.5}Sr_{0.5}Mn_{0.5}Ti_{0.5}O_{3-\delta}$ (A) and $La_{0.6}Sr_{0.4}Mn_{0.5}Ti_{0.5}O_{3-\delta}$ (B) after preparation, after annealing in H_2-, in H_2S-containing atmospheres and after subsequent annealing in air. Conditions of the thermal treatment are given in legends.

Typical microstructures of $(La_{1-x}Sr_x)_{0.95}Mn_{0.5}Ti_{0.5}O_{3\pm\delta}$ dense ceramics are illustrated in Fig. 4.22. The maximum grain size (50 - 100 μm) was found for the materials with intermediate Sr content in the A-sublattice, i.e. at x = 0.25 - 0.45. Reviewing the literature data on the relationships between the densification of manganites and titanates and their composition, one might observe that increasing Sr content in $La_{1-x}Sr_xMnO_{3\pm\delta}$ up to ~50% leads to smaller grain size. The effect is attributed to larger radius of Sr^{2+} in comparison with La^{3+} hampering the A-site diffusion, as well as suppressed densification at high quantities of Mn^{4+} [614, 615]. One should also take into account that the cation diffusion in manganites and resultant grain growth are promoted by higher A-site cation deficiency [614-616] which decreases upon introduction of Sr into the perovskite [300, 303]. Similar effects might be expected for the $(La_{1-x}Sr_x)_{0.95}Mn_{0.5}Ti_{0.5}O_{3\pm\delta}$ ceramics in the compositional range of $0.25<x<0.75$.

On the other hand, the grain growth taking place on incorporation of donor-like cations into A- or B-sublattice of $ATiO_{3-\delta}$ perovskites (A = Ca, Sr, Ba) is maximum when the substitution is charge-compensated by other factors, such as a simultaneous generation of cation vacancies which enable to prevent a segregation of secondary phases or reduce the stresses in the lattice induced by generation of cations in the oxidation state unfavorable under given conditions (i.e. Ti^{3+}) [247, 617, 618].

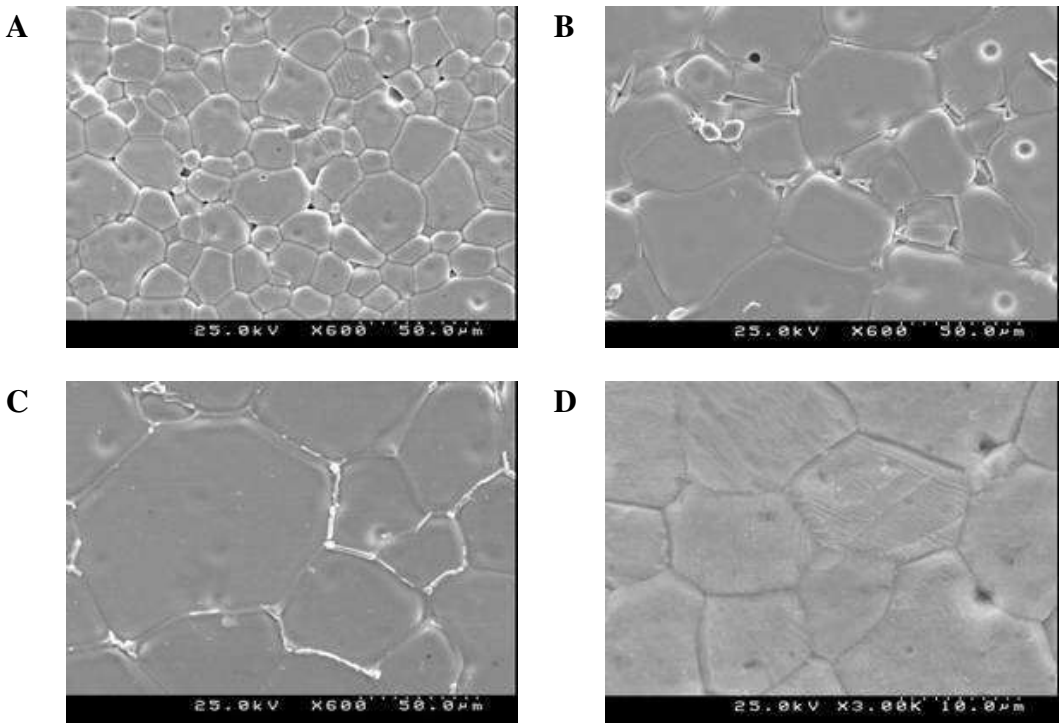

Fig. 4.22. SEM micrographs of $(La_{0.35}Sr_{0.65})_{0.95}Mn_{0.5}Ti_{0.5}O_{3-\delta}$ (A), $(La_{0.55}Sr_{0.45})_{0.95}Mn_{0.5}Ti_{0.5}O_{3-\delta}$ (B), $(La_{0.75}Sr_{0.25})_{0.95}Mn_{0.5}Ti_{0.5}O_{3-\delta}$ (C), $(La_{0.85}Sr_{0.15})_{0.95}Mn_{0.5}Ti_{0.5}O_{3-\delta}$ (D) sintered in air, polished and thermally etched

With respect to the present system, the largest grains should be observed for the perovskites, where the average oxidation state of Mn and Ti species is close to +3 and +4, respectively, while the oxygen content approaches the stoichiometric value. Such conditions should be satisfied for the composition with $x \approx 0.36$, which explains the largest grain size of the nearest neighboring representatives in $(La_{1-x}Sr_x)_{0.95}Mn_{0.5}Ti_{0.5}O_{3\pm\delta}$ series, i.e. for $x = 0.25$ and 0.45.

Considering the possible reasons of the grain growth, one should also take into account a possible segregation of secondary phases in the quantities within the uncertainties of XRD analysis. In particular, as shown by micrographs in Figs. 4.22 B and C, the perovskites with intermediate Sr content showed the presence of another phase at the grain boundaries; the same materials showed the maximum grain growth. EDS analysis showed an enrichment of the impurity particles with Mn atoms. The presence of this phase as well as modest traces of glass-like phase might also contribute to better densification of the compositions with $x = 0.25 - 0.45$. On the other hand, the Mn-enriched impurity might be segregated during the preparation of ceramics for the microscope analysis and not reflect the general sintering behaviour of the materials.

4.2.2. Thermal and chemical expansion

Selected results of the controlled-atmosphere dilatometric measurements performed in the regimes of continuous heating and isothermal dwells with equilibration at 923 - 1223 K are presented in Figs. 4.23 and 4.24, respectively. As for other titanate- and manganite-based materials, the apparent TECs vary in the

range (9.8 - 15.0)×10^{-6} K^{-1}, slightly increasing on heating due to oxygen losses from the lattice (Fig. 4.23; Table 4.8). Introduction of Sr into $(La_{1-x}Sr_x)_{1-y}Mn_{0.5}Ti_{0.5}O_{3-\delta}$, charge-compensated by increasing oxidation states of manganese cations, results in larger oxygen nonstoichiometry variations on heating or reduction. These variations are reflected by higher values of the apparent TECs under similar conditions (Table 4.8) and by larger chemical expansion (Fig. 4.24; Table 4.9). The TECs are essentially unaffected by oxygen partial pressure variations in oxidizing environments and tend to moderately increase in reducing atmospheres, again correlating with the chemically induced strains and conductivity variations discussed below.

Table 4.8. Average linear thermal expansion coefficients of $(La_{1-x}Sr_x)_{1-y}Mn_{0.5}Ti_{0.5}O_{3-\delta}$ ceramics

Composition	Measuring regime	$p(O_2)$, atm	T, K	TEC×10^6, K^{-1}
$(La_{0.25}Sr_{0.75})_{0.95}Mn_{0.5}Ti_{0.5}O_{3-\delta}$	heating 3 K/min	0.21	1223-1373	14.0±0.1
			923-1223	13.1±0.1
			303-923	11.8±0.1
	isothermal dwells	6×10^{-4}	973-1223	13.3±0.2
	(50 K steps)	5×10^{-21} - 3×10^{-13}	923-1223	14.3±0.1
$(La_{0.35}Sr_{0.65})_{0.95}Mn_{0.5}Ti_{0.5}O_{3-\delta}$	heating 3 K/min	0.21	1223-1373	13.5±0.1
			923-1223	12.4±0.1
			303-923	11.4±0.1
$La_{0.5}Sr_{0.5}Mn_{0.5}Ti_{0.5}O_{3-\delta}$	cooling 3 K/min	0.21	1073-1273	13.2±0.1
			473-1073	11.7±0.1
		1×10^{-4}	1073-1273	13.2±0.1
			473-1073	12.0±0.1
		1×10^{-15} - 2×10^{-11}	1073-1273	13.7±0.1
			473-1073	12.2±0.1
	isothermal dwells	0.21	923-1273	12.8±0.1
		1×10^{-4}	923-1273	12.9±0.1
		3×10^{-20} - 2×10^{-11}	923-1273	13.4±0.2
$(La_{0.55}Sr_{0.45})_{0.95}Mn_{0.5}Ti_{0.5}O_{3-\delta}$	heating 3 K/min	0.21	1223-1373	13.4±0.1
			923-1223	12.5±0.1
			303-923	11.0±0.1
	isothermal dwells	9×10^{-5}	973-1223	12.5±0.2
		3×10^{-18} - 4×10^{-12}	973-1223	13.3±0.3
$(La_{0.75}Sr_{0.25})_{0.97}Mn_{0.5}Ti_{0.5}O_{3-\delta}$	heating 3 K/min	0.21	1073-1273	15.0±0.2
			473-1073	11.4±0.1
	cooling 3 K/min	1×10^{-15} - 2×10^{-11}	1073-1273	12.5±0.1
			473-1073	10.8±0.1
$(La_{0.75}Sr_{0.25})_{0.95}Mn_{0.5}Ti_{0.5}O_{3-\delta}$	heating 3 K/min	0.21	1223-1373	13.1±0.1
			923-1223	11.4±0.1
			303-923	10.0±0.1
	isothermal dwells	9×10^{-5}	973-1223	11.8±0.3
		3×10^{-18} - 4×10^{-12}	973-1223	11.6±0.2
$(La_{0.85}Sr_{0.15})_{0.95}Mn_{0.5}Ti_{0.5}O_{3-\delta}$	heating 3 K/min	0.21	1223-1373	12.4±0.1
			923-1223	11.1±0.1
			303-923	9.8±0.1
	isothermal dwells	9×10^{-5}	973-1223	11.4±0.3
		3×10^{-18} - 4×10^{-12}	973-1223	11.8±0.3

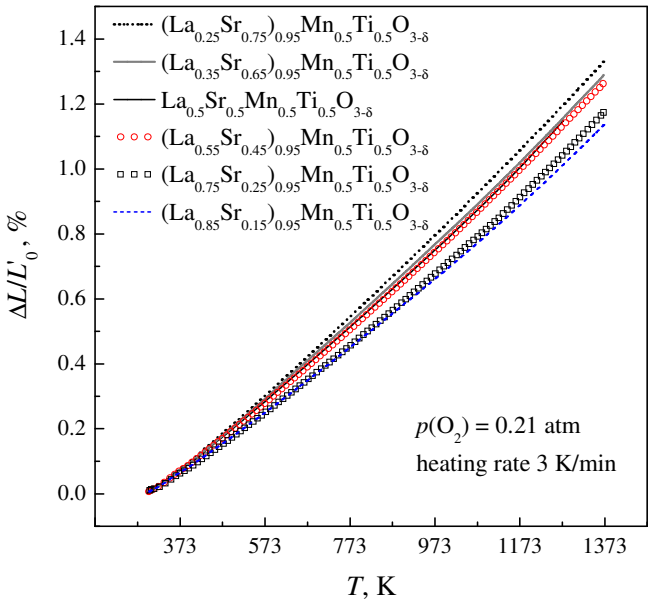

Fig. 4.23. Dilatometric curves obtained on $(La_{1-x}Sr_x)_{1-y}Mn_{0.5}Ti_{0.5}O_{3-\delta}$ ceramics in air collected on continuous heating (3 K/min). L_0' is the initial length at room tempreature in air.

The isothermal lattice expansion on reduction occurs due to lowering average oxidation state and increasing radius of the transition metal cations; the former factor is related to the concentration of electronic charge carriers, determining electronic conductivity and Seebeck coefficient. In accordance with the XRD results, the chemically induced expansion is lower than 0.03 % under oxidizing conditions and achieves almost 0.6 % when $p(O_2)$ is reduced from 0.21 atm down to 10^{-18} - 10^{-12} atm (Table 4.9).

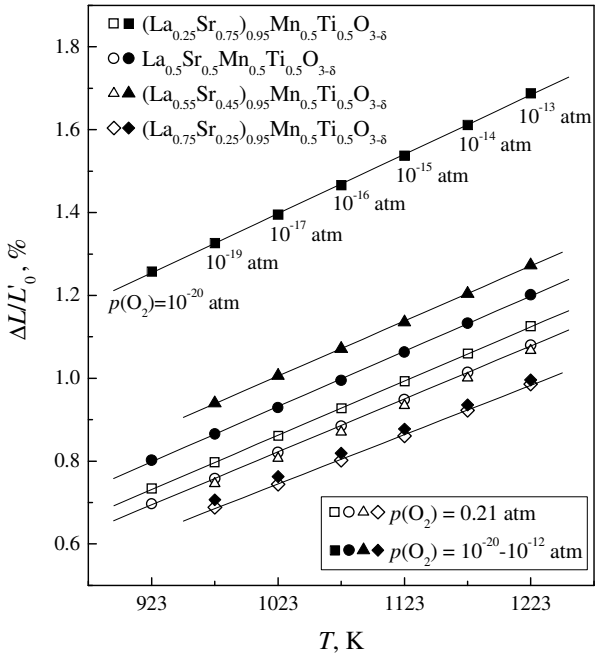

Fig. 4.24. Selected dilatometric data on $(La_{1-x}Sr_x)_{1-y}Mn_{0.5}Ti_{0.5}O_{3-\delta}$ ceramics collected in the regime of isothermal dwells for equilibration at each temperature in air and CO - CO_2. The $p(O_2)$ values in the CO - CO_2 atmosphere are marked for $(La_{0.25}Sr_{0.75})_{0.95}Mn_{0.5}Ti_{0.5}O_{3-\delta}$

Table 4.9. Relative isothermal elongation of $(La_{1-x}Sr_x)_{1-y}Mn_{0.5}Ti_{0.5}O_{3-\delta}$ ceramics on reduction with respect to the length in air (L_0)

Composition	T, K	air → Ar		air → CO-CO_2	
		$p(O_2)$, atm	$\Delta L/L_0$, %	$p(O_2)$, atm	$\Delta L/L_0$, %
$(La_{0.25}Sr_{0.75})_{0.95}Mn_{0.5}Ti_{0.5}O_{3-\delta}$	1223	6×10^{-4}	0.0250	3×10^{-13}	0.556
	1173		0.0207	3×10^{-14}	0.546
	1023		0.0204	2×10^{-15}	0.539
	1073		0.0219	1×10^{-16}	0.534
	1023		0.0214	6×10^{-18}	0.530
	973		0.0196	2×10^{-19}	0.525
$La_{0.5}Sr_{0.5}Mn_{0.5}Ti_{0.5}O_{3-\delta}$	1223	1×10^{-4}	0.0016	2×10^{-12}	0.120
	1173		0.0021	2×10^{-13}	0.118
	1023		0.0017	2×10^{-14}	0.114
	1073		0.0011	1×10^{-15}	0.109
	1023		0.0001	5×10^{-17}	0.107
	973		0.0007	2×10^{-18}	0.107
$(La_{0.55}Sr_{0.45})_{0.95}Mn_{0.5}Ti_{0.5}O_{3-\delta}$	1223		-	4×10^{-12}	0.204
	1173			4×10^{-13}	0.202
	1023			3×10^{-14}	0.199
	1073			2×10^{-15}	0.199
	1023			8×10^{-17}	0.198
	973			3×10^{-18}	0.192
$(La_{0.75}Sr_{0.25})_{0.95}Mn_{0.5}Ti_{0.5}O_{3-\delta}$	1223		-	4×10^{-12}	0.010
	1173			4×10^{-13}	0.012
	1023			3×10^{-14}	0.016
	1073			2×10^{-15}	0.016
	1023			8×10^{-17}	0.018
	973			3×10^{-18}	0.018

L_0 is the length at the same temperature and atmospheric oxygen pressure.

Considering the compositional influence on the expansion behaviour, one should account for possible differences in the equilibration degree of the ceramics. The cation ratio in A-sublattice significantly affects the kinetics of achieving the steady-state properties upon variations of $p(O_2)$ or temperature; selected examples are shown in Fig. 4.25. No equilibrium value of the relative elongation or total conductivity was attained for cation-deficient La-enriched perovskites (x = 0.15 - 0.25) during a reasonable time period. This situation is opposite to the behaviour of the compositions with lower concentrations of La cations or cation-stoichiometric materials, as shown in Fig. 4.26.

Possible origins of such a behavior might primarily relate to the phase transition upon extensive oxygen losses shown by the materials with enhanced La content. As shown in numerous studies [619-621], structural transformations are generally accompanied by a slow lattice recombination with prolonged time scale. Moreover, the presence of high amounts of La cations may induce generation of $Mn^{3+/2+}$ and/or $Ti^{4+/3+}$ redox couples causing a slower diffusion due to defect interactions. One should not also exclude the effects associated with possible oxygen overstoichiometry. As discussed in Chapters 1.3, 1.5, La-enriched manganites have a tendency towards formation of cation vacancies, while $(Sr,La)TiO_{3\pm\delta}$ may incorporate excessive oxygen be generation of Sr-O planes between perovskite-like blocks. Both effects are promoted by higher La content and oxidative conditions [300, 406, 407, 541] and lead to slow equilibration kinetics, which causes large scattering between experimental data [105, 300, 322, 407].

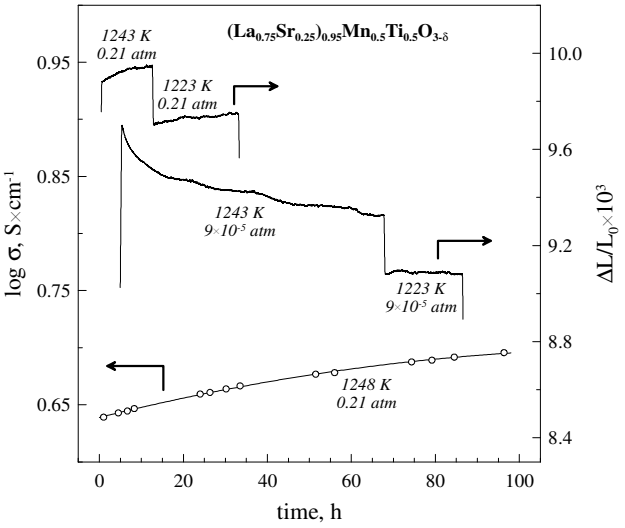

Fig. 4.25. Equilibration curves of total conductivity and relative elongation of $(La_{0.75}Sr_{0.25})_{0.95}Mn_{0.5}Ti_{0.5}O_{3-\delta}$ ceramics in various atmospheres

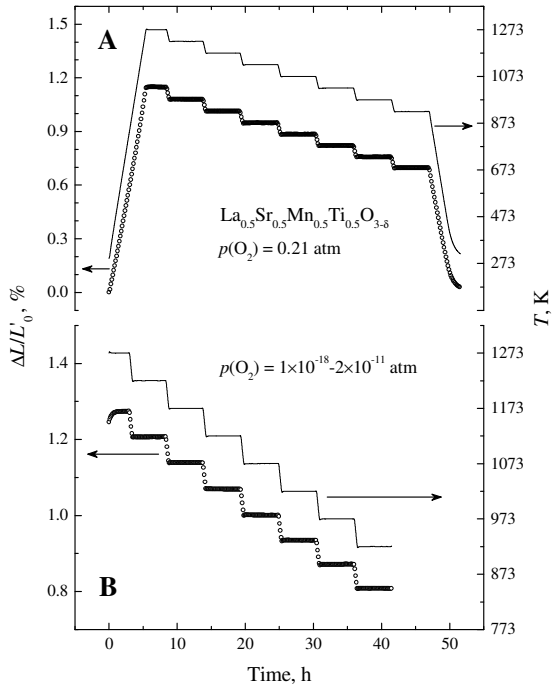

Fig. 4.26. Temperature profiles and equilibration curves of the relative elongations of $La_{0.5}Sr_{0.5}Mn_{0.5}Ti_{0.5}O_{3-\delta}$ ceramics in air (A) and CO - CO_2 (B). *L_0'* is the initial length at room temperature in air

To some extent, similar phenomena might be expected for $(La,Sr)Mn_{0.5}Ti_{0.5}O_{3-\delta}$ with high La amount. For example, assuming that no Mn^{2+} or Ti^{3+} species are formed in atmospheric air and suggesting the phase purity of the compositions (as shown by XRD analysis), the perovskites $(La_{0.75}Sr_{0.25})_{0.95}Mn_{0.5}Ti_{0.5}O_{3\pm\delta}$ and $(La_{0.85}Sr_{0.15})_{0.95}Mn_{0.5}Ti_{0.5}O_{3\pm\delta}$ should accommodate at least 3.05 and 3.1 oxygen atoms per perovskite formula unit. Even if the perovskite structure does not favour an excessive oxygen content (for example, by generation of low-valent Mn or Ti species), the oxygen deficiency and resultant oxygen diffusivity are expected to be minimum for La-enriched materials which also yields a hindered equilibration of the corresponding perovskites.

One should note that preliminary maintenance of the ceramic material at elevated temperatures with subsequent cooling basically accelerates the equilibration processes at lower temperatures, as shown in Fig. 4.25. Although the kinetic factors may affect the general trends in the expansion behaviour as a function of the perovskite composition, it should be separately stressed that the overall level of thermal- and chemical-induced strains, observed in the wide range of temperature and oxygen partial pressure, is still moderate and the title materials are thermomechanically compatible with various solid oxide electrolytes, such as stabilized zirconia, CGO, or LSGM [227, 580, 581, 587].

4.2.3. Electronic transport

As shown in Fig. 4.27, introduction of acceptor-type Sr^{2+} into $(La_{1-x}Sr_x)_{1-y}Mn_{0.5}Ti_{0.5}O_{3-\delta}$ increases the electronic conductivity, in accordance with the p-type charge transfer mechanism, typical for related compositions. For the compositions with x = 0.15 - 0.65, the activation energies are quite similar, varying in a narrow range 29 - 37 kJ/mol at 473 - 1283 K, whilst the E_a of $(La_{0.25}Sr_{0.75})_{0.95}Mn_{0.5}Ti_{0.5}O_{3-\delta}$ is lower, 15 - 16 kJ/mol. (Table 4.10). The latter composition exhibits substantially higher values of the conductivity than the other materials. As discussed in Chapter 3.1.4, such difference in the transport behaviour may indicate a tendency to the transition from small-polaron hopping to broad-band conduction mechanism, caused by rising Mn^{4+} concentration and accompanied by lowering activation energy for the electronic charge carrier mobility. However, the absolute values of the Seebeck coefficient of $(La_{0.25}Sr_{0.75})_{0.95}Mn_{0.5}Ti_{0.5}O_{3-\delta}$ (Figs. 4.28 - 4.30) cannot provide a supporting evidence for such hypothesis.

Regardless of the microscopic mechanisms, the electrical properties of $(La,Sr)Mn_{0.5}Ti_{0.5}O_{3-\delta}$ perovskites are essentially independent of the oxygen chemical potential in oxidizing and moderately reducing atmospheres (Fig. 4.28), thus indicating that the oxygen stoichiometry changes in these environments are very minor. Further reduction induces enhanced oxygen deficiency, which results in higher Seebeck coefficient and lower conductivity, as shown in Figs. 4.29 and 4.30.

Table 4.10. Activation energies of the total conductivity of $(La_{1-x}Sr_x)_{0.95}Mn_{0.5}Ti_{0.5}O_{3-\delta}$ ceramics in air

Composition	Conductivity in air	
	T, K	E_a, kJ/mol
$(La_{0.25}Sr_{0.75})_{0.95}Mn_{0.5}Ti_{0.5}O_{3-\delta}$	553 – 873	15.6±0.1
	943 – 1263	16.1±0.1
$(La_{0.35}Sr_{0.65})_{0.95}Mn_{0.5}Ti_{0.5}O_{3-\delta}$	763-1223	42.5±0.2
$(La_{0.55}Sr_{0.45})_{0.95}Mn_{0.5}Ti_{0.5}O_{3-\delta}$	573-1263	30.1±0.2
$(La_{0.75}Sr_{0.25})_{0.95}Mn_{0.5}Ti_{0.5}O_{3-\delta}$	603-1253	28.9±0.4
$(La_{0.85}Sr_{0.15})_{0.95}Mn_{0.5}Ti_{0.5}O_{3-\delta}$	533-1263	36.5±0.4

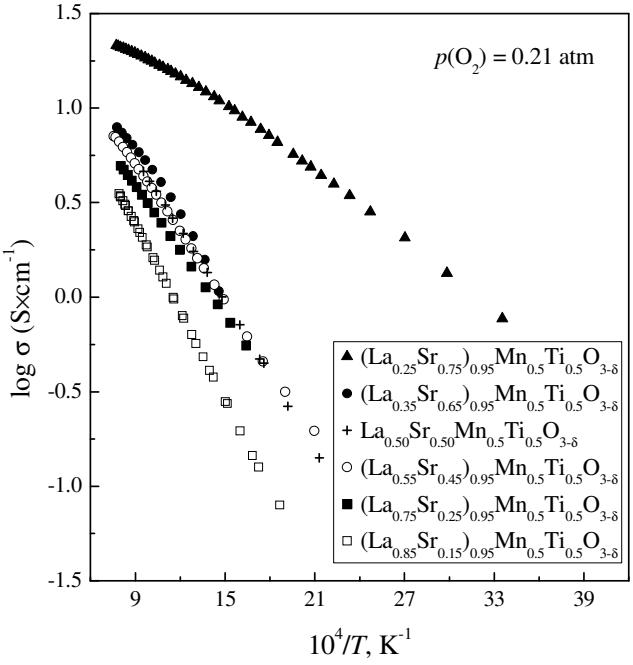

Fig. 4.27. Temperature dependencies of the total conductivity of $(La_{1-x}Sr_x)_{1-y}Mn_{0.5}Ti_{0.5}O_{3-\delta}$ ceramics in air

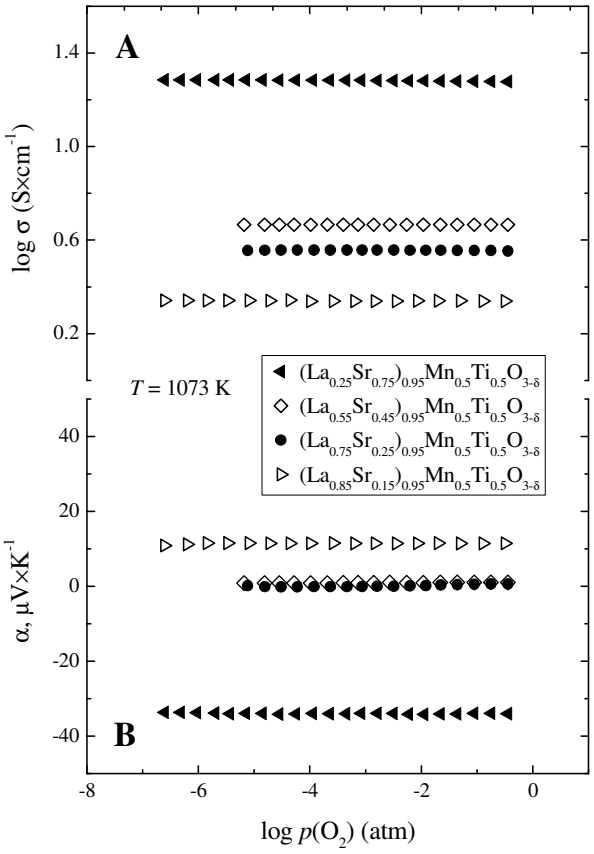

Fig. 4.28. Oxygen partial pressure dependencies of the total conductivity (A) and Seebeck coefficient (B) of $(La_{1-x}Sr_x)_{0.95}Mn_{0.5}Ti_{0.5}O_{3-\delta}$ ceramics in oxidizing atmospheres at 1073 K

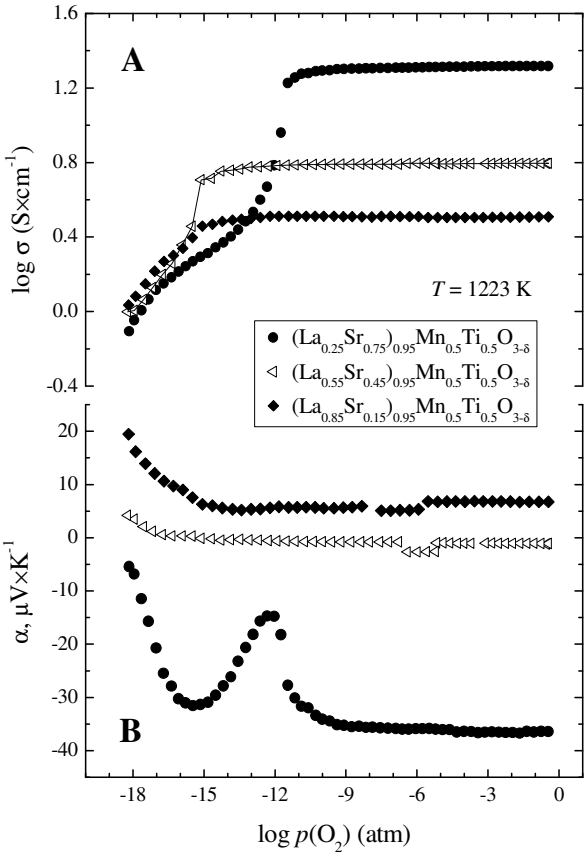

Fig. 4.29. Oxygen partial pressure dependencies of the total conductivity and Seebeck coefficient of $(La_{1-x}Sr_x)_{0.95}Mn_{0.5}Ti_{0.5}O_{3-\delta}$ ceramics at 1223 K

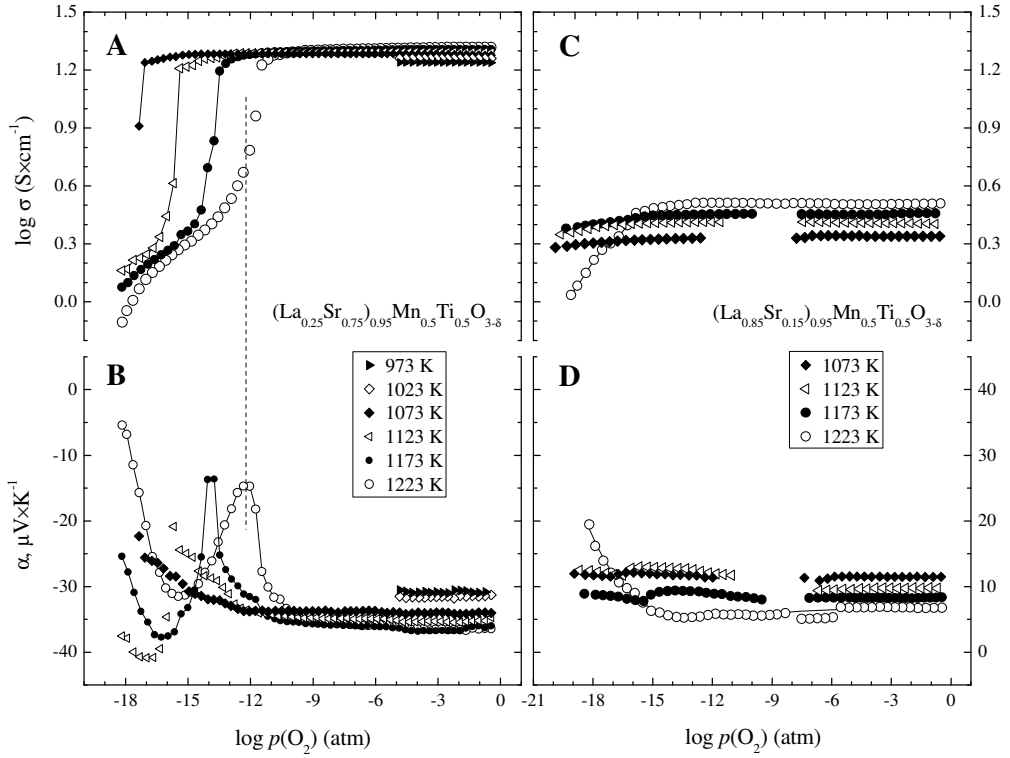

Fig. 4.30. Oxygen partial pressure dependencies of the total conductivity (A, C) and Seebeck coefficient (B, D) of $(La_{0.25}Sr_{0.75})_{0.95}Mn_{0.5}Ti_{0.5}O_{3-\delta}$ (A, B) and $(La_{0.85}Sr_{0.15})_{0.95}Mn_{0.5}Ti_{0.5}O_{3-\delta}$ (C, D)

The trends in the transport-ralated parameters of $(La_{1-x}Sr_x)_{0.95}Mn_{0.5}Ti_{0.5}O_{3-\delta}$ observable upon $p(O_2)$ and temperature variations are similar to those of $(La_{0.75}Sr_{0.25})_{0.95}Cr_{0.5}Mn_{0.5}O_{3-\delta}$ and doped chromites providing another argument in favour of dominant p-type electronic transport. The variations of the conductivity and thermopower are accompanied with strong hystereses on redox cycling (Fig. 4.31), with an apparently irreversible behavior for the La-rich materials. The irreversibility was attributed mainly to the microcrack formation detected on pos-tested samples visually and by optical microscopy inspections; however, kinetics of the orthorhombic - rhombohedral transition, defect reactions involving $Mn^{3+/2+}$ and/or $Ti^{4+/Ti3+}$ redox couples or processes associated with participation of the cation vacancies or ordered structures might also be relevant in the present case. The irreversible drop of the conductivity and mechanical instability restrict the choice of anode material towards the compositions with a modest (<50%) La content.

Another peculiarity of the transport behavior of $(La_{1-x}Sr_x)_{1-y}Mn_{0.5}Ti_{0.5}O_{3-\delta}$ is that increasing Sr amount lowers the thermopower down to negative values. For the compositions with intermediate Sr content, when the average oxidation state of manganese cations is close to 3+, the Seebeck coefficient is expected to be close to zero (Fig. 4.28). If the interaction between $Mn^{3+/4+}$, $Mn^{3+/2+}$, and $Ti^{4+/3+}$ states is strong enough and one type of the electronic charge carriers prevails, the latter situation may take place when the charge carrier concentration corresponds to approximately half of the density of states. In such case, increasing the fraction of Mn^{4+} compensating large Sr^{2+} additions leads to the hole concentration above 50% sites available for their location, shifting the Seebeck coefficient down to negative values; increasing La^{3+} concentration has the opposite effect.

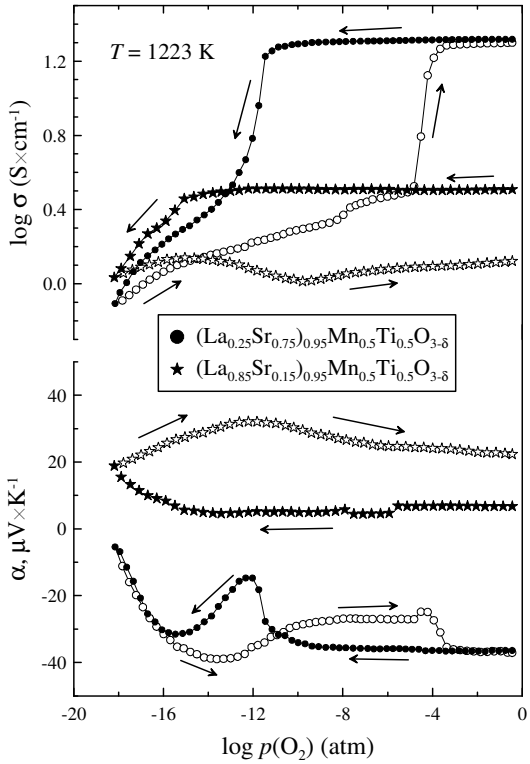

Fig. 4.31. Examples of the hysteresis behaviour of the total conductivity and Seebeck coefficient variations of $(La_{0.25}Sr_{0.75})_{0.95}Mn_{0.5}Ti_{0.5}O_{3-\delta}$ and $(La_{0.85}Sr_{0.15})_{0.95}Mn_{0.5}Ti_{0.5}O_{3-\delta}$ on redox cycling at 1223 K

From a theoretical point of view, an ideal situation in this case could be expected for parent stoichiometric $La_{0.5}Sr_{0.5}Mn_{0.5}Ti_{0.5}O_{3-\delta}$ where the level of thermopower should be primarily determined by the parameters independent of the charge carrier concentration, such as transported heat. For the related compositions with similar La^{3+} and Sr^{2+} concentrations, an analogous behavior may appear if the deviations from ideal [La]/[Sr]=1 ratio are charge compensated by ionic point defects, namely, cation or oxygen vacancies, as for $(La,Sr)MnO_{3\pm\delta}$ with modest strontium content [300, 303]. Such assumptions may explain the fact that the nearly zero thermopower values are observed for the compositions with intermediate Sr^{2+} concentrations, particularly for $(La_{0.55}Sr_{0.45})_{0.95}Mn_{0.5}Ti_{0.5}O_{3\pm\delta}$ and $(La_{0.75}Sr_{0.25})_{0.95}Mn_{0.5}Ti_{0.5}O_{3\pm\delta}$ (Fig. 4.28), with presumably negligible concentration of vacancies (<0.05 - 0.06 per perovskite formula lattice). In the case of charge compensation via the cation vacancy formation, this level of nonstoichiometry may still be tolerated by the perovskite lattice. Although the electronic conduction of these materials slightly increases with Sr content, the overall level of the conductivity is similar for both compositions (Figs. 4.27, 4.28), in contrast to $(La_{0.25}Sr_{0.75})_{0.95}Mn_{0.5}Ti_{0.5}O_{3-\delta}$ and $(La_{0.85}Sr_{0.15})_{0.95}Mn_{0.5}Ti_{0.5}O_{3\pm\delta}$.

Finally, one should mention that the experimentally observed trends cannot completely exclude more complex mechanisms when several types of the electronic charge carriers may be present and low absolute values of the Seebeck coefficient correspond to comparable contributions of the p- and n-type charge carriers, i.e. $t_p\alpha_p \approx t_n\alpha_n$ where t is the transference number. However, no indication of significant n-type contribution can be identified from the conductivity dependencies on oxygen partial pressure and cation composition.

4.2.4. Oxygen permeability and isotope diffusion studies

Measurements of the oxygen permeability through dense membranes $(La_{1-x}Sr_x)_{0.95}Mn_{0.5}Ti_{0.5}O_{3-\delta}$ demonstrated a dominant limiting effect of the oxygen surface exchange kinetics; any estimation of the bulk ionic conductivity was impossible. A similar behavior has earlier been observed for dense $(La_{1-x}Sr_x)_{1-y}MnO_{3-\delta}$ ceramics with x = 0.4 - 0.6 [622]. For example, Fig. 4.32 displays the data on oxygen permeation fluxes through $(La_{0.35}Sr_{0.65})_{0.95}Mn_{0.5}Ti_{0.5}O_{3-\delta}$ membranes with different thicknesses as a function of the oxygen partial pressure gradient expressed via the (p_2/p_1) ratio, where p_1 and p_2 are the oxygen pressures at the membrane permeate and feed sides, respectively. The oxygen fluxes are essentially equal for the 0.60- and 1.00-mm thick ceramics within the limits of experimental error. This tendency unambiguously indicates that oxygen transport is governed by the surface exchange rate, on the contrary to $(La_{0.75-x}Sr_{0.25+x})_{0.95}Mn_{0.5}Cr_{0.5-x}Ti_xO_{3-\delta}$ system where the contributions of interfacial exchange and bulk ionic conduction are significant.

While the behavior of the Cr-containing perovskites made it possible to detect a significant impact of the grain boundary diffusion, no similar conclusions can be drawn for the title system, although the grain boundary mechanism of ionic transport should not be a priori neglected. In particular, the steady-state permeation fluxes through dense $(La_{1-x}Sr_x)_{0.95}Mn_{0.5}Ti_{0.5}O_{3-\delta}$ membranes are, in fact, quite similar to one another due to very low oxygen nonstoichiometry (Fig. 4.33). In these conditions, the role of grain boundary diffusion is expected to increase as for lanthanum manganite [336, 339]. The low oxygen vacancy concentration is also responsible for relatively large scattering in the experimental data. Nevertheless, the oxygen permeability of $(La_{1-x}Sr_x)_{0.95}Mn_{0.5}Ti_{0.5}O_{3-\delta}$ tends to increase with increasing Sr amount, in correlation with the oxygen nonstoichiometry variations revealed by the chemical expansion measurements.

The permeation fluxes through $(La_{1-x}Sr_x)_{0.95}Mn_{0.5}Ti_{0.5}O_{3-\delta}$ ceramics are lower compared to $SrMnO_3$-based phases, such as $Sr_{0.7}Ce_{0.3}MnO_{3-\delta}$ [320, 605], where the oxygen deficiency is substantially higher (Fig. 4.34). The apparent activation energies (Table 4.11) are high, typical for the perovskite compounds with almost stoichiometric oxygen sublattice when the E_a values comprise a large vacancy formation enthalpy contribution [623].

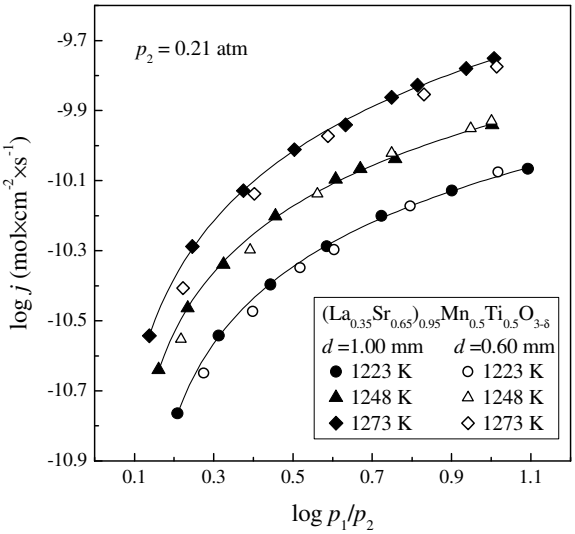

Fig. 4.32. Steady-state oxygen permeation fluxes through dense $(La_{0.35}Sr_{0.65})_{0.95}Mn_{0.5}Ti_{0.5}O_{3-\delta}$ membranes with various thicknesses. The feed-side oxygen pressure corresponds to 0.21 atm

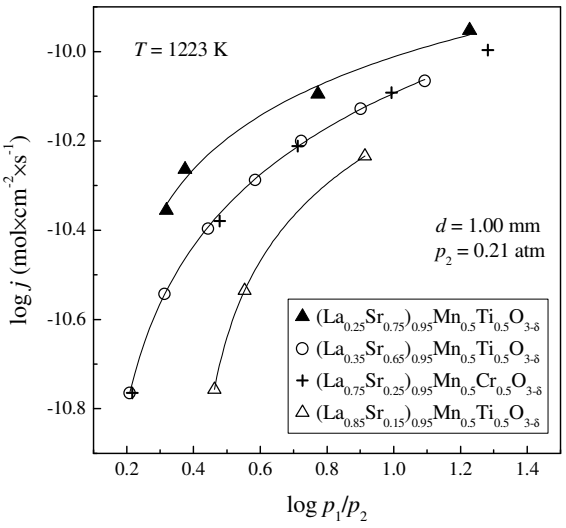

Fig. 4.33. Oxygen permeation fluxes through dense $(La_{1-x}Sr_x)_{0.95}Mn_{0.5}Ti_{0.5}O_{3-\delta}$ ceramic membranes with the thickness of 1.00±0.02 mm at 1223 K

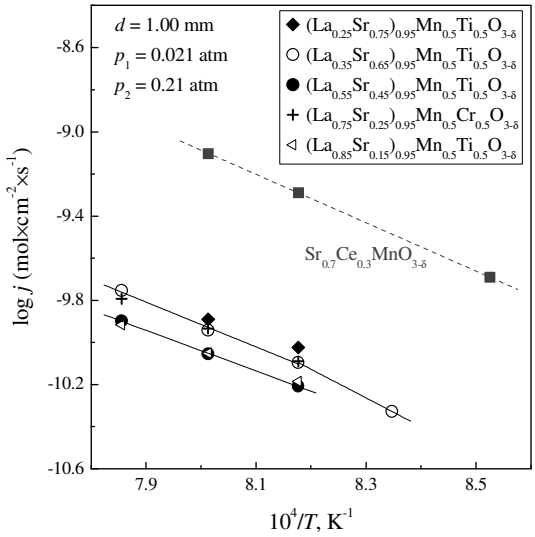

Fig. 4.34. Temperature dependencies of the oxygen permeation fluxes through dense $(La_{1-x}Sr_x)_{0.95}Mn_{0.5}Ti_{0.5}O_{3-\delta}$ ceramic membranes under a fixed $p(O_2)$ gradient. The data on $Sr_{0.7}Ce_{0.3}MnO_{3-\delta}$ [320] are shown for comparison.

Table 4.11. Activation energies for the total electrical conductivity in air, steady-state oxygen permeation fluxes through dense ceramic membranes* and oxygen tracer diffusion coefficients**

Composition	Oxygen permeability		Diffusion coefficient	
	T, K	E_a, kJ/mol	*T*, K	E_a, kJ/mol
$(La_{0.25}Sr_{0.75})_{0.95}Mn_{0.5}Ti_{0.5}O_{3-\delta}$	1223-1248	169		
$(La_{0.35}Sr_{0.65})_{0.95}Mn_{0.5}Ti_{0.5}O_{3-\delta}$	1198-1273	229		
$La_{0.5}Sr_{0.5}Mn_{0.5}Ti_{0.5}O_{3-\delta}$			1073-1223	234
$La_{0.6}Sr_{0.4}Mn_{0.5}Ti_{0.5}O_{3-\delta}$			1123-1223	299
$(La_{0.85}Sr_{0.15})_{0.95}Mn_{0.5}Ti_{0.5}O_{3-\delta}$	1223-1273	170		

** the permeation fluxes correspond to the oxygen pressure gradient of 0.21/0.021 atm and the membrane thickness of 1.00 mm;*

*** the exchange annealing was performed at $p(^{18}O_2)$ = 0.2 atm.*

The results of the isotopic exchange experiments performed in the Institute of Solid State Chemistry RAS, Chernogolovka, for A-site cation stoichiometric $La_{1-x}Sr_xMn_{0.5}Ti_{0.5}O_{3-\delta}$ are summarized in Fig. 4.35. In agreement with the oxygen permeation data, the tracer diffusion coefficients in $La_{0.6}Sr_{0.4}Mn_{0.5}Ti_{0.5}O_{3-\delta}$ and $La_{0.5}Sr_{0.5}Mn_{0.5}Ti_{0.5}O_{3-\delta}$ are very similar to one another, whereas the surface exchange coefficients tend to

increase with acceptor content. The values of D* are lower even with respect to lanthanum-strontium manganites, suggesting that the oxygen anions located near Ti^{4+} are essentially excluded from the migration processes. This assumption is consistent with slower ionic transport in titanates or titanate-doped perovskites, as discussed in Chapter 1.5. If compared to oxygen-deficient $Sr_{0.75}Y_{0.25}Mn_{0.5}Co_{0.5}O_{3-\delta}$ [624] and oxygen-hyperstoichiometric $Pr_2CuO_{4+\delta}$ [625], the difference in the oxygen diffusivity at atmospheric $p(O_2)$ is up to five to eight orders of magnitude. Regardless of the relevant microscopic mechanisms, this level of oxygen ionic transport is insufficient to expect any substantial enhancement of the catalytically-active reaction zone due to a contribution of the electrode bulk diffusion into the electrochemical processes.

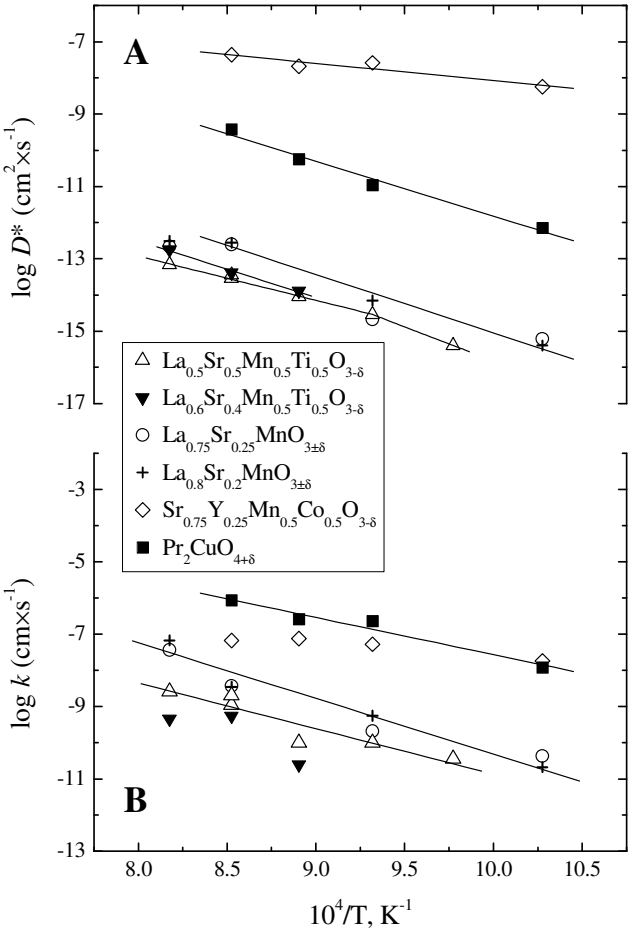

Fig. 4.35. Temperature dependencies of the bulk oxygen tracer diffusion (A) and surface exchange (B) coefficients of dense $La_{0.6}Sr_{0.4}Mn_{0.5}Ti_{0.5}O_{3-\delta}$ and $La_{0.5}Sr_{0.5}Mn_{0.5}Ti_{0.5}O_{3-\delta}$ ceramics compared to the data on $(La,Sr)MnO_{3\pm\delta}$, $Sr_{0.75}Y_{0.25}Mn_{0.5}Co_{0.5}O_{3-\delta}$ and $Pr_2NiO_{4+\delta}$ [624, 625] studied under identical conditions

4.2.5. Electrode behaviour

Summarizing the behaviour of perovskite-type $(La_{1-x}Sr_x)_{1-y}Mn_{0.5}Ti_{0.5}O_{3-\delta}$, one should stress that the chemical and thermal expansion increases with increasing Sr content (Figs. 4.23, 4.24; Tables 4.8, 4.9). The same trend was observed for electronic conduction in oxidizing atmospheres, whereas under reducing

conditions the total conductivity values are essentially similar in the entire compositional range studied in this work (Figs. 4.29, 4.30). The La-rich materials such as $(La_{0.85}Sr_{0.15})_{0.95}Mn_{0.5}Ti_{0.5}O_{3-\delta}$ exhibit smaller oxygen nonstoichiometry variations on reduction and, thus, a more pronounced tendency to $p(O_2)$-independent concentration of the electronic charge carriers and conductivity at temperatures below 1100 K (Fig. 4.30C); however, their reduction is accompanied with strong and apparently irreversible hysteresis phenomena (Fig. 4.31). Although the ionic transport parameters, including the oxygen permeability and surface exchange rate, tend to increase with x (Figs. 4.33, 4.34), the overall level of the ionic conduction is low and no significant influence on the electrode performance may be expected due to minor variations in the these parameters. With respect to the compositional trends in the functional characteristics, the compositions with intermediate strontium concentrations (x = 0.4 - 0.6) seem to provide an optimum combination of the electronic transport and thermomechanical properties.

As will be demonstrated in Chapter 5.3.2, anodes based on cation-deficient $(La_{0.85}Sr_{0.15})_{0.95}Mn_{0.5}Ti_{0.5}O_{3-\delta}$ exhibit a strong tendency towards densification and require specific preparation procedure in order to achieve an adequate porosity and provide a good adhesion to the electrolyte. Moreover, the values of the overpotential are still high for the title anode, presumably due to the microstructural factors.

Therefore, the electrochemical studies were carried out on $La_{0.5}Sr_{0.5}Mn_{0.5}Ti_{0.5}O_{3-\delta}$ anode which may be considered as a compromise composition which reasonably satisfies the requirements in terms of the stability, transport and thermomechanical properties. The electrode layers $La_{0.5}Sr_{0.5}Mn_{0.5}Ti_{0.5}O_{3-\delta}$ exhibit homogeneous porous microstructures where submicron grain size is preserved (Fig. 4.36). No essential microstructural changes were observed after electrochemical testing.

Figs. 4.37 and 4.38 illustrate the behaviour of porous $La_{0.5}Sr_{0.5}Mn_{0.5}Ti_{0.5}O_{3-\delta}$ electrode layers applied onto LSGM at 873 - 1073 K in H_2-containing atmosphere. Analogously to the $(La_{0.75-x}Sr_{0.25+x})_{0.95}Mn_{0.5}Cr_{0.5-x}Ti_xO_{3-\delta}$ electrodes, the rate-determining steps should be related to the electrode surface; the key factors limiting anodic performance are expected to include the interfacial exchange kinetics and electronic conduction. One argument in favour of the non-negligible role of the electronic transport is that the activation energy for electrode conductivity (Fig. 4.38) is significatly lower than E_a values for oxygen permeability, diffusion, and surface exchange (Table 4.11).

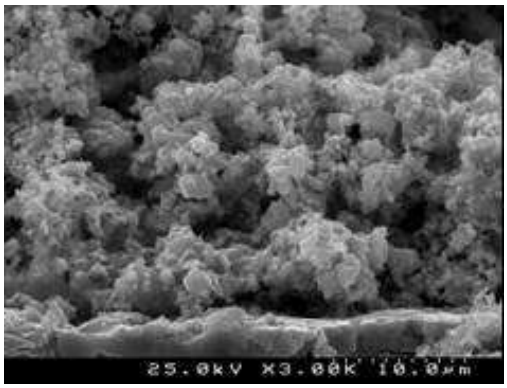

Fig. 4.36. SEM micrograph of a fractured half-cell with porous $La_{0.5}Sr_{0.5}Mn_{0.5}Ti_{0.5}O_{3-\delta}$ anode layer deposited onto LGGM electrolyte with CGO20 sublayer after polarization measurements

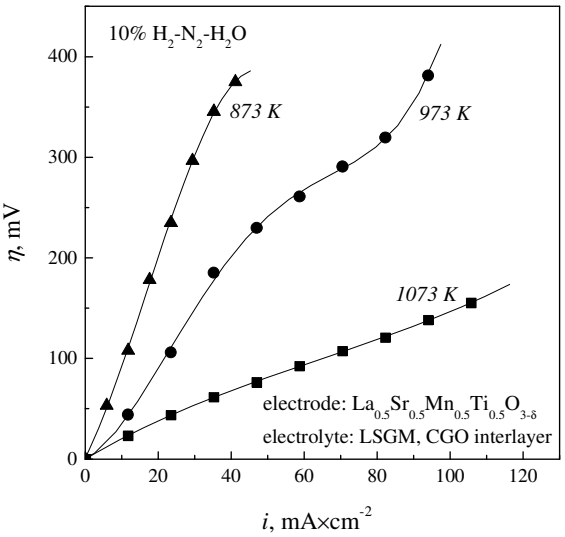

Fig. 4.37. Anodic overpotentials vs. current density dependencies for porous $La_{0.5}Sr_{0.5}Mn_{0.5}Ti_{0.5}O_{3-\delta}$ anode applied onto LSGM electrolyte with CGO20 sublayer in flowing wet 10% H_2 - N_2 at 873 - 1073 K

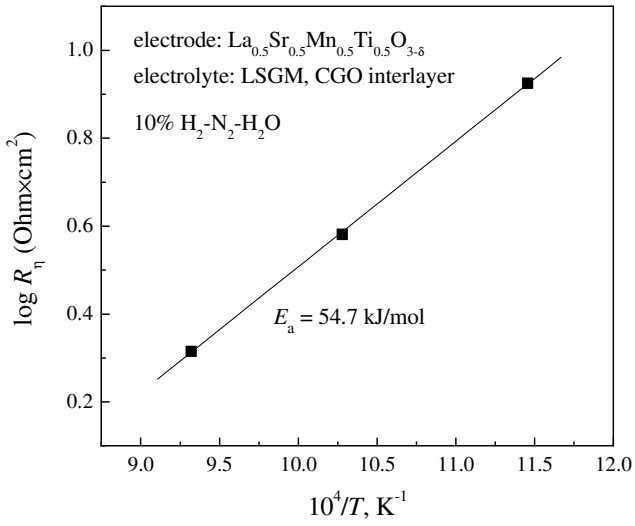

Fig. 4.38. Temperature dependence of the polarization resistance of porous $La_{0.5}Sr_{0.5}Mn_{0.5}Ti_{0.5}O_{3-\delta}$ anode applied onto LSGM electrolyte with CGO20 sublayer under OCV conditions

Whatever the electrode reaction mechanism, the electrochemical activity of $La_{0.5}Sr_{0.5}Mn_{0.5}Ti_{0.5}O_{3-\delta}$ anode layers appears significantly better than that of $(La_{0.75}Sr_{0.25})_{0.95}Cr_{0.5}Mn_{0.5}O_{3-\delta}$ [10] and is close to that of Mn-free $(La_{0.75}Sr_{0.25})_{0.95}Fe_{0.4}Cr_{0.6}O_{3-\delta}$ anodes with similar microstructures. Considering the negative effects associated with the presence of chromium in SOFCs, namely, volatilization of chromium oxides and formation of Cr^{6+}-containing phases in oxidizing conditions at low temperatures, $La_{0.5}Sr_{0.5}Mn_{0.5}Ti_{0.5}O_{3-\delta}$ and its analogues provide significant advantages with respect to the $LaCrO_3$-based electrode materials. The anodic overpotentials of $La_{0.5}Sr_{0.5}Mn_{0.5}Ti_{0.5}O_{3-\delta}$ are, however, still high in comparison with the Ni-containing cermets, thus making it necessary to incorporate the metallic and, possibly, catalytically active components in $(La,Sr)(Mn,Ti)O_{3-\delta}$ based anodes.

4.3. Concluding remarks

Studies on $(La_{1-x}Sr_x)_{1-y}Mn_{0.5}Ti_{0.5}O_{3-\delta}$ and $SrMn_{1-x}Nb_xO_{3-\delta}$ perovskites showed that the stabilization of the single phase manganites at low $p(O_2)$ is an achievable task, although requires comparatively high (up to 50%) amount of high-valent dopant to avoid phase decomposition. One of important features of doped manganites relates to possible structural transformations on thermal or redox cycling, accompanied by slow equilibration kinetics, mechanical failure due to large volume changes, hysteresis phenomena on redox cycling, in some cases resulting in irreversible degradation of the functional characteristics, etc. Such a behaviour was especially pronounced for donor-rich $(La_{1-x}Sr_x)_{0.95}Mn_{0.5}Ti_{0.5}O_{3-\delta}$ and $CaMn_{0.5}Nb_{0.5}O_{3-\delta}$. On the other hand, these effects may be avoided or suppressed by appropriate selection of the composition; in

particular, a relatively rapid equilibration was observed for $La_{0.5}Sr_{0.5}Mn_{0.5}Ti_{0.5}O_{3-\delta}$ and $SrMn_{1-x}Nb_xO_{3-\delta}$ ceramic samples.

The expansivity of $SrMn_{1-x}Nb_xO_{3-\delta}$ (x = 0.4 - 0.5) and $(La_{1-x}Sr_x)_{1-y}Mn_{0.5}Ti_{0.5}O_{3-\delta}$ is moderate and is strongly influenced by chemical contribution arising due to oxygen nonstoichiometry variations. The chemical expansion of $(La_{1-x}Sr_x)_{1-y}Mn_{0.5}Ti_{0.5}O_{3-\delta}$ under reducing conditions is below 0.6% and diminishes on appropriate La-doping into the perovskite.

Donor doping into the title perovskites reduces the concentration of p-type electronic charge carriers. Moreover, for $SrMn_{1-x}Nb_xO_{3-\delta}$ introduction of Nb into B-sublattice negatively influences the mobility of the charge carriers; both factors result in suppressed electronic conductivity upon La or Nb-doping. At the same time, under anode environments, the compositional effect on the electronic transport is less critical which enables to optimize other functional characteristics without substantial degradation of the electronic transport. Taking into account the low values of the conductivity at high $p(O_2)$, La-enriched $(La_{1-x}Sr_x)_{1-y}Mn_{0.5}Ti_{0.5}O_{3-\delta}$ and $SrMn_{0.5}Nb_{0.5}O_{3-\delta}$ are inappropriate for cathode applications. Considering the behaviour of $CaMn_{0.5}Nb_{0.5}O_{3-\delta}$ perovskite, this material can hardly be considered as a component of SOFC anodes or cathodes, due to insufficient stability even under moderately reducing atmospheres, low electronic conductivity, large variations of the TEC upon thermal cycling and a strong tendency towards the hysteresis behavior and slow equilibration.

The ionic transport parameters for heavily-doped manganites are rather low to ensure any substantial enlargement of the electrochemically-active zone and seem to correlate with Mn content in the perovskite. This effect may relate to facilitated Mn reducibility, in particular to a higher flexibility of Mn cations towards changes in the oxygen coordination which enables higher oxygen deficiency in the perovskite structure or promotion of the surface processes by Mn species. Another origin might relate to a negative influence of Ti or Nb species on the oxygen ionic diffusion, in particular by stabilization of oxygen atoms in the vicinity of the donor cation excluding O^{2-} from the transport mechanism.

Due to an acceptable combination of the phase and structural stability, transport and thermomechanical properties as well as microstructural behaviour, the anodes composed of $La_{0.5}Sr_{0.5}Mn_{0.5}Ti_{0.5}O_{3-\delta}$ yield the polarization resistance as low as 1.5 - 2.0 Ohm×cm^2 at 1073 K without a specific anode modification. The level of the electrochemical activity is comparable with that of $(La_{0.9}Sr_{0.1})_{0.95}Cr_{0.85}Mg_{0.1}Ni_{0.05}O_{3-\delta}$ and $(La_{0.75}Sr_{0.25})_{0.95}Cr_{1-x}Fe_xO_{3-\delta}$ (x = 0.3 - 0.4), while the title composition may be advantageous over the chromites in terms of the absence of chromium cations having the tendency towards generation of Cr^{6+} species or formation of volatile compounds with subsequent degradation of the electrode characteristics upon thermal/redox cycling. However, further studies, primarily in terms of the performance stability, are required for all the electrodes studied in order to evaluate the applicability of the materials in SOFC technology.

Chapter 5. Major trends and factors relevant for the SOFC anode performance

In Chapters 3 - 4, selected chromite, manganite and titanate-based groups of anode materials were characterized in terms of their functional properties and general compositional trends observed in the electrode performance. The present part is devoted to comparative studies of the electrochemical properties of the perovskite-like and selected cermet anodes, elucidation of the basic factors affecting the electrode behaviour and search of possible routes to optimize the anode activity.

For fabrication of the electrochemical cells operated in the intermediate temperature range (873 - 1073 K), two types of solid electrolyte materials were selected, namely, $(La_{0.9}Sr_{0.1})_{0.98}Ga_{0.8}Mg_{0.2}O_{3-\delta}$ (LSGM) and $La_{10}Si_5AlO_{26.5}$. The choice of ionic conductors and the particular cation compositions was based on the combination of optimum functional characteristics, primarily in terms of the transport properties, stability under the operation conditions and availability of the precursor materials.

Considering other widely used families of solid electrolytes, zirconia-based solid solutions possess a negligible level of the electronic conductivity, beneficial for the electrolyte application. However, the level of the ionic conductivity in these oxides is 1 - 2 orders lower in comparison with other candidates, such as LSGM, $La_{9.33}Si_6O_{26}$- or CeO_2-based oxides, which makes YSZ more appropriate for applications at higher temperatures rather than in IT-SOFCs. Moreover, some concerns are related with the chemical compatibility of doped ZrO_2 with compositions enriched with rare-earth or alkali-earth cations [30, 329, 626, 627]. Doped ceria suffer from excitation of non-negligible electronic transport and large expansion under reducing conditions, especially promoted by dissolution of transition metal cations penetrated from the electrode phase [5, 30, 237]. This problem imposes severe requirements on the temperature range of applications of CeO_2-based compositions. On the other hand, $CeO_{2-\delta}$ and its derivatives may be successfully utilized as components of the electrode materials or as protective layers between the electrolyte and electrodes.

Lanthanum gallate-based materials seem to be more appropriate for electrolyte applications in the intermediate temperature range in terms of the transport and thermomechanical properties. As discussed below, apatite-type silicates show a worse combination of the functional characteristics, especially in terms of poor stability. However, the availability and low price of the precursor materials as well as large doping possibilities which may to some extent enable to overcome or reduce the concerns indicated also make these materials attractive for further studies. This chapter is devoted to comparative overview of the stability and transport characteristics of $LaGaO_3$- and $La_{9.33}Si_6O_{26}$-based materials and evaluation of the electrode performance of perovskite-like and cermet anodes in contact with the corresponding electrolytes.

5.1. Applicability of lanthanum silicate- and lanthanum gallate-based materials as solid electrolytes: a brief overview.

5.1.1. Stability, transport and thermomechanical properites

As discussed in previous sectons, the electrochemical behavior is strongly influenced by the transport properties and stability of the electrolyte as well as by its compatibility with the electrode material, sublayer or other SOFC components. Therefore, analysis of the electrode properties should involve

consideration of the available data on the oxygen ionic conductivity and long-term behavior of gallate- and silicate-based solid electrolytes.

Temperature dependencies of the total conductivity of selected $LaGaO_3$-based materials in air or moderately reducing atmospheres are presented in Fig. 5.1. Typical for perovskite-type compositions, oxygen vacancies are the dominant ionic charge carriers and the transport properties may be modified by an appropriate acceptor-type doping. The largest conductivity was found for compositions containing La^{3+} and Sr^{2+} cations in A-sublattice, due to minimum lattice strains favorable to the oxygen diffusion [628 - 630]. Among B-site dopants, the maximum ionic transfer was achieved by introduction of an appropriate quantity of 2-fold charged cations (Mg, Co, Fe), due to ensuring a substantial amount and fast mobility of oxygen vacancies [629, 631, 632]. In $(La,Sr)(Ga,Mg)O_{3-\delta}$ series, the largest values of the ionic conductivity were obtained for 10 - 20% of Sr and 15 - 20% of Mg which amounted to 0.10 - 0.17 S/cm at 1073 K with the activation energy of 90 - 110 kJ/mol [581, 629, 631-634]. For comparison, the conductivity of $(Zr,Y)O_{2-\delta}$ oxides varies in the range $(5 - 8)\times10^{-2}$ S/cm at 1073 K [30, 626]. Further addition of the acceptor-type cations into LSGM induces vacancy ordering [635, 636]. The perovskite structure of gallates allows a slight (up to ~2%) A-site cation deficiency; exceeding the limit substantially deteriorates the transport properties [581, 637]. The content of the transition metal cations in B-sublattice should be restricted by 3 - 7% in order to avoid the drop of the ionic conductivity, contribution of the electronic transport or thermomechanical problems ([30] and references cited).

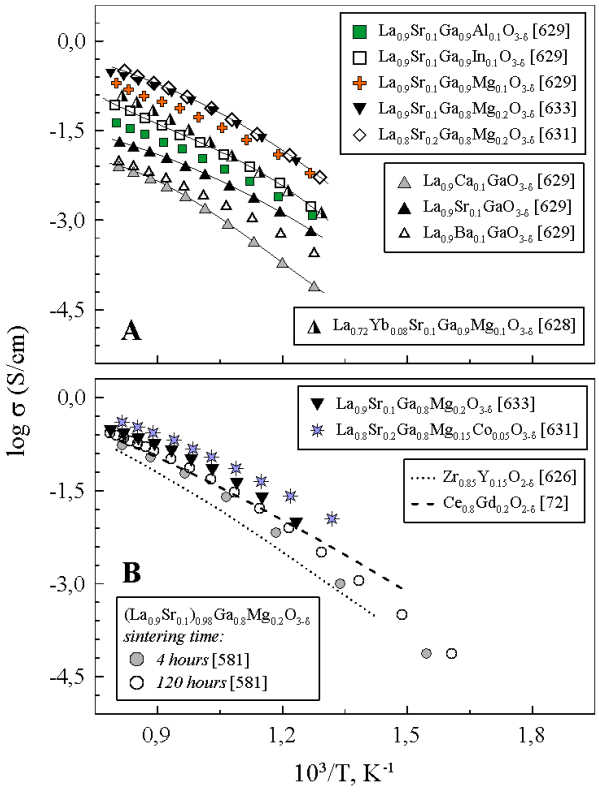

Fig. 5.1. Temperature dependencies of the total conductivity of selected $LaGaO_3$-based compositions. The data in [628, 629, 631] were obtained at $p(O_2)\approx10^{-5}$ atm, other results correspond to the atmospheric oxygen pressure

Analogously with numerous ionic conductors and semiconductors, the functional properties of LSGM are affected by sintering procedure, in particular by the ceramics microstructure and formation of

secondary phases (La_2O_3, $LaSrGaO_4$, $Sr_3Ga_2O_6$ etc.) at the grain boundaries or on the surface. As shown in [581], the presence of the secondary phases as well as an enrichment of the grain boundaries with Sr and Mg may have a hampering effect on the oxygen ionic conductivity and promote the electronic contribution. Nevertheless, the electronic transference numbers in LSGM and related materials do not exceed 0.02, as shown in Table 5.1, which may be considered to be acceptable for utilization this group of materials as solid electrolytes. Increasing the sintering time ensures nearly complete dissolution of the impurities in the perovskite structure; another approach to bind the secondary phases and diminish their negative effects relates to introduction of scavenging agents [478].

Table 5.1. Electronic transference numbers and average TEC values in air of selected materials with dominant oxygen ionic conductivity

Composition	Electronic transference numbers			TEC in air		Reference
	T, K	$p(O_2)$, atm	t_e	T, K	$\alpha\times10^6$, K^{-1}	
$La_{0.9}Sr_{0.1}Ga_{0.8}Mg_{0.2}O_{3-\delta}$	1073	10^{-3}	1.0×10^{-3}	300 - 1473	11.9	[637]
				300 - 1073	10.4	[478]
$(La_{0.9}Sr_{0.1})_{0.98}Ga_{0.8}Mg_{0.2}O_{3-\delta}$	1073	10^{-3}	4.7×10^{-3}	300 - 1473	11.8	[637]
$La_{0.9}Sr_{0.1}Ga_{0.95}Fe_{0.05}O_{3-\delta}$	1073	~0.21	0.86			[635]
$La_{0.9}Sr_{0.1}Ga_{0.95}Co_{0.05}O_{3-\delta}$	1073	~0.21	0.08			[635]
$La_{0.8}Sr_{0.2}Ga_{0.8}Mg_{0.15}Co_{0.05}O_{3-\delta}$	1073	gradient H_2/O_2	2.0×10^{-3}			[631]
$La_{0.9}Sr_{0.1}Ga_{0.76}Mg_{0.19}Co_{0.15}O_{3-\delta}$				300 - 1473	12.7	[644]
$La_{9.83}Si_{5.5}Al_{0.5}O_{26.5}$	1073	0.21	1.8×10^{-3}	373 - 1173	10.0	[21, 580]
$La_{9.83}Si_{4.5}Al_{1.5}O_{26}$	1073	0.21	4.9×10^{-3}	373 - 1173	8.9	[21, 580]
$La_{10}Si_{5.8}Al_{0.2}O_{26.9}$	1073	0.11	1.1×10^{-3}			[640]
$La_{10}Si_5AlO_{26.5}$	1073	0.21	2.5×10^{-3}	473 - 1173	9.1	[21, 580]
$La_{9.83}Si_{4.5}Fe_{1.5}O_{26}$	1123	0.21	8.5×10^{-3}	373 - 1173	9.3	[645]
$La_{9.99}Si_{5.795}Al_{0.2}Fe_{0.005}O_{26.885}$	1073	0.11	2.9×10^{-3}			[640]
$La_{9.83}Pr_6Si_{4.5}Fe_{1.5}O_{26}$	1123	0.21	1.5×10^{-2}	373 - 1173	14.7	[645]
$La_{10}Ge_6O_{27}$	1073	gradient N_2/O_2	4.9×10^{-2}	300 - 1123	11.1	[22, 646]
	1073	gradient H_2/O_2	3.6×10^{-2}			[22]
$Zr_{0.9}Y_{0.1}O_{2-\delta}$	1273	0.21	5.0×10^{-5}			[89]
$Zr_{0.85}Y_{0.15}O_{2-\delta}$				300 - 1273	10.9	[227]
$Ce_{0.8}Gd_{0.2}O_{2-\delta}$	1123	1.0	3.7×10^{-3}	300 - 1273	12.7	[72, 227]

In apatite-type $La_{9.33}Si_6O_{26}$ and its derivatives, the dominant charge carries are interstitial oxygen atoms [580, 585, 638]. An alternative mechanism taking place in oxygen-deficient representatives and involving the transport of oxygen vacancies proceeds much slower [585, 639]. Therefore, the transport properties are promoted by doping strategies leading to formation of overstoichiometric oxygen in comparison with the parent silicate, i.e. by introducing the cations stable in high oxidation state. On the other hand, excessive La or Si content complicates formation of single-phase materials and ceramics densification,

deteriorates the stability, especially in reducing and/or wet atmospheres, induces volatilization of silica species, etc. As a result, the optimum ionic conductivity was found for apatites slightly substituted in B-sublattice and/or possessing a moderate La excess in comparison with the parent composition (Fig. 5.2) [580, 641, 642]. Selected studies have been carried out on germanate-based analogues, but their applicability is limited by high costs and volatilization of GeO_2, tendency towards formation of glassy phase and a phase transition at 1000 - 1100 K shown by lanthanum germanate on heating in air [641, 642].

Promotion of the ionic transport in $La_{9.33}Si_6O_{26}$ was observed by introducing Al, Fe, Mg cations into the apatite lattice, accompanied by a decrease of the corresponding activation energy attributable to formation of a new conduction path due to reduced bonding energy of the metal with oxygen [23, 640, 641]. An increase of the ionic transport was also observed for Nb-doped silicates, due to increasing the amount of the charge carriers with simultaneous preservation of the single phase composition [24].

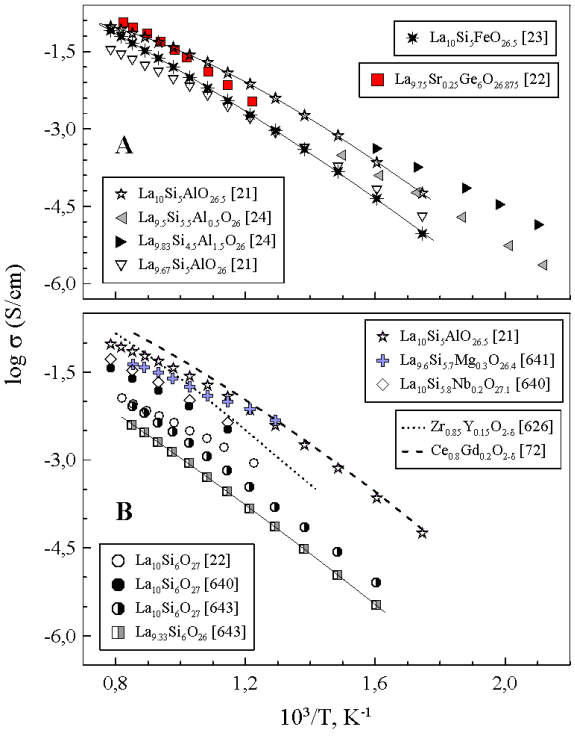

Fig. 5.2. Temperature dependencies of the total conductivity of selected apatite-type silicate and germanate compositions in air

The electronic contribution into the overall conductivity of the apatites basically correlates with generation of excessive oxygen atoms and increases with Al or Fe introduction. This phenomenon is attributed to localization of the electronic defects in the vicinity of the lattice defects with the opposite charge, i.e. oxygen interstitials [580]. The electronic transference numbers in apatites are within 0.01, as shown in Table 5.1.

One of most significant concerns related to both electrolyte materials is associated with insufficient stability towards operation atmospheres and compatibility with other cell components. For LSGM, the main problem is associated with volatilization of gallium oxides and oxyhydroxides, especially pronounced under reducing or wet atmospheres. For cation stoichiometric perovskites, Ga losses may lead to generation of La_2O_3, $LaSrGaO_4$ and other phases enriched with A-cations. Subsequent exposure of La_2O_3 to H_2O or CO_2-

containing atmosphere induces formation of hydroxides or carbonates, with resultant deterioration of the transport properties and degradation of the mechanical integrity. Any contact of LSGM with Pt promotes the depletion of the electrolyte with Ga, due to formation of intermetallic Ga-Pt compounds [633, 637, 581].

In order to avoid separation of the La- or Sr-enriched impurities, a particular interest has been drawn by A-site cation deficient gallates, although an excess of Ga in the perovskite lattice may accelerate the vaporization-related processes. The phenomena indicated impose requirements on the electrolyte processing conditions. On the other hand, LSGM-based materials do not suffer from essential ageing phenomena in the intermediate temperature range, in contrast to zirconia electrolytes [647].

The literature reports on the stability of the apatite-based compounds are contradictory. In particular, a stable conductivity was detected in wet Ar [640], 20% H_2 [648], wet H_2 and wet CO_2 [649]. However, these results relate to comparatively low temperatures, up to 1073 K, while the testing time was limited by 50 - 70 hours. In contrast, long maintaining (1000 hours) of $La_{9.77}Si_6O_{26.655}$ and $La_{10}Si_6O_{27}$ at 1073 K in air resulted in ~5% drop of the conductivity [650], while increasing the operation temperature up to 1173 K revealed ~20% degradation of the total conductivity after 350 hours of reduction of $La_{10}Si_5AlO_{26.5}$ at $p(O_2) \approx 10^{-18}$ atm [21]. Possible origins of the degradation observed seem to be associated with segregation or volatilization of SiO_2 which is accompanied by formation of La_2O_3-based compositions. The separation of the secondary phases deteriorates the transport properties and affects the mechanical integrity of the ceramics. While in the temperature range corresponding to the working conditions of the electrochemical cell the stability seems to be sufficient, any necessity to elevate the ambient temperature (i.e. during the process of the cell preparation or sealing) is detrimental for the functional characteristics of the electrolyte material. Taking into account the reactivity and strong cation interdiffusion between the apatite phase and numerous electrode materials, as discussed below, the issue of the chemical stability is the most critical limitation for the high-temperature application of lanthanum silicate-based materials.

5.1.2. Performance of electrochemical cells composed of gallate- and silicate-based electrolytes

Reviewing the data on the electrochemical performance gallate-based electrochemical cells, one should mention that the basic limitations are associated with the electrode materials rather than with the gallate phase or relate to the problems of the chemical compatibility between the components. As a confirmation of the good applicability of LSGM for the electrochemical utilizations, the polarization resistance of the cathodes and anodes in contact with this electrolyte series may be reduced below 0.1 - 0.5 Ohm×cm^2; examples will be presented in following sections. Promising performances have been obtained for manganite- [651], ferrite- [652], nickelate- [593, 594] and especially cobaltite-based [9, 278, 653] cathodes. Among anodes, acceptable characteristics have been obtained for both conventional cermets [567, 654, 655] and for alternative materials [15, 18, 264, 547, 556]. A reasonable activity towards electrochemical oxidation of hydrocarbon- [116, 230], ethanol- [408], H_2S-containing [116] fuels was observed for cells with LSGM electrolyte. Acceptable performance was obtained utilizing composite electrodes with gallate-based materials

as ionic-conductive components [651, 654], although in this case the issue of the phase interaction becomes critical. One should note that most promising results were collected on the cells containing protective layers between LSGM and electrodes in order to avoid the interaction between the components.

Due to comparatively short period of studies of the apatite-based electrochemical cells and because of their poor performance, the amount of available data on the polarization characteristics of electrodes in contact with lanthanum silicates is extremely few. Among the data reported one may note the results obtained for Ni - CGO, $Sr_2MgMoO_{6-\delta}$, $La_{0.75}Sr_{0.25}Cr_{0.5}Mn_{0.5}O_{3-\delta}$ anodes as well as for $La_{0.8}Sr_{0.2}MnO_{3-\delta}$ and $La_{0.7}Sr_{0.3}FeO_{3-\delta}$ cathodes on $La_{10}Si_{5.5}Al_{0.5}O_{26.75}$ showing the area-specific resistance (ASR) in the range of 0.5 - 1.0 Ohm×cm^2 at 1073 K, while for $La_{0.6}Sr_{0.4}Co_{0.8}Fe_{0.2}O_{3-\delta}$, the corresponding value was obtained as low as 0.04 Ohm×cm^2 [566]. Acceptable performance of the electrodes listed basically necessitates the presence of the buffer layer. One should emphasize that all the electrodes studied were covered with Pt ink. A comparable level of the electrode activity was obtained for platinum or $(La,Sr)(Co,Fe)O_{3-\delta}$-based cathodes deposited onto $La_{9.8}Ge_{5.5}Al_{0.5}O_{26.45}$ [656].

$La_{0.6}Sr_{0.4}CoO_{3-\delta}$ and $La_{0.6}Sr_{0.4}Co_{1-x}Fe_xO_{3-\delta}$ cathodes in contact with $La_{10}Si_{5.8}Al_{0.2}O_{26.9}$ showed the R_η in the range of 0.3 - 1.8 Ohm×cm^2 without any specific optimization, while subsequent introduction of Ag particles by wet impregnation reduced the polarization resistance down to 0.08 Ohm×cm^2 [657]. A cell with $La_{0.6}Sr_{0.4}Co_{0.8}Fe_{0.2}O_{3-\delta}$ cathode, $La_{9.62}Si_{5.79}Al_{0.21}O_{26.33}$ electrolyte and Ni - CGO anode showed the power density of 250 mW/cm^2 at 1073 K [658] which seems to be rather promising taking into account the comparatively thick (720 μm) electrolyte thickness.

On the other hand, conventional anode and cathode materials without any specific modification (which may be too expensive and unreasonable for practical applications) showed extremely large polarization resistances, exceeding 100 - 1000 Ohm×cm^2 [659-661]. Moreover, many electrochemical cells showed a fast and irreversible degradation of the electrode performance which is not surprising taking into account the drop of the total conductivity shown by lanthanum silicates at elevated temperature and strong susceptibility of most electrochemically-active materials towards contamination with silica. Poor electrode characteristics have been found for metal-apatite cermet composites [661], although fabrication of similar composites with other ionic conductors has been found to be beneficial. This, in particular, demonstrates the absence or negligible contribution of any catalytic effect from the silicate-based phases into the electrochemical process.

As shown from the examples, the information on the performance of apatite-containing electrochemical cells is contradictive. Taking into account a poor availability of the experimental results on the anode activity collected from silicate-based cells, more studies on the electrode activity of layers coated onto the apatite-based electrolytes are required in order to clarify their potential for electrochemical applications. The following parts are focused on studying the basic factors responsible for the electrode performance of perovskite-type and cermet anode materials deposited onto apatite-type $La_{10}Si_5AlO_{26.5}$. A particular attention is drawn to the interaction/interdiffusion phenomena and performance degradation. As no special steps were undertaken to modify the electrochemical properties, the polarization values are expected to be rather high, and the work has primarily an investigating nature.

5.2. Electrochemical activity of cermet anodes deposited onto lanthanum silicate-based solid electrolyte

Composite powders consisting of electronic and ionic conducting components (basically, metallic and solid electrolyte phases) are the most studied and widely used materials for SOFC anodes, although the corresponding electrode layers may have some disadvantages in comparison with MIEC anodes, primarily in terms of stringent requirements to their microstructure [1, 2, 7, 662, 663]. Ni is one of the most common components in cermets, although its content should be moderate in order to avoid the problems associated with the sintering of the metallic particles, formation of volatile compounds, large volume changes on redox cycling or anode contamination in C- or S-containing fuels ([1, 7, 266] and references cited).

The present part is devoted to studies of selected cermet anodes in contact with $La_{10}Si_5AlO_{26.5}$ electrolyte. One of particular tasks relates to partial or complete replacement of Ni with other metals without a loss of the electrochemical performance. The technique of preparation of the electrode layers is described in Table 2.5.

SEM analysis carried out on as-prepared half-cells or those after the electrochemical tests revealed an acceptable porosity of the electrode layers and satisfactory connectivity between the cermet electrodes and electrolyte (Fig. 5.3). The thickness of the electrode layers varied in the range 15 - 40 μm. Particles of CGO20 phase showed a tendency towards formation of large agglomerates (up to 10 - 20 μm); nevertheless, the porosity was preserved, although the TPB length might be substantially affected by the poor dispersion. The presence of silver in the anode composition yielded generation of 5 - 10 μm sphere-like domains as shown in Fig. 5.3 C.

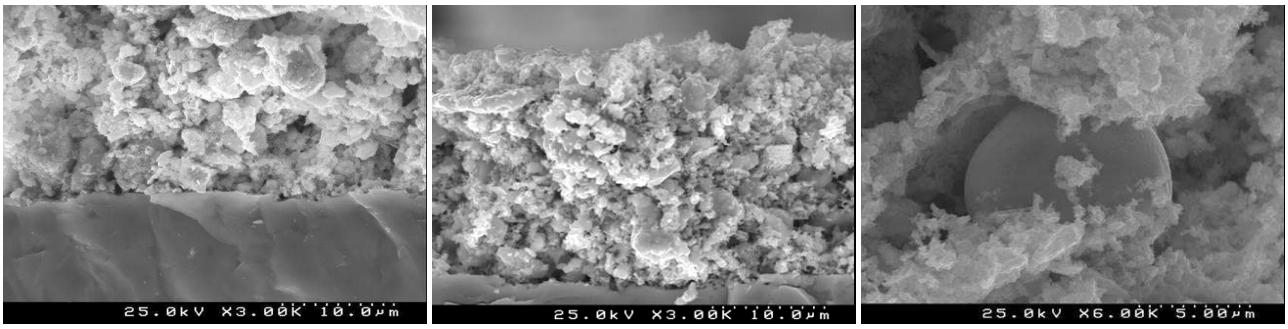

A **B** **C**

Fig. 5.3. SEM micrographs of selected cermet anode layers applied onto $La_{10}Si_5AlO_{26.5}$ electrolyte: A. Cross-section image of Ag - CGO20 (40 - 60 vol.%) anode modified with $CeO_{2-\delta}$ after polarization measurements; B. Cross-section image of as-prepared Cu - CGO20 (40 - 60 vol.%) anode; C. Ag particle in as-prepared Ni-Ag-CGO (20 - 20 - 60 vol.%) anode layer

Selected results on the polarization behaviour of the cermet anode layers in contact with apatite are shown in Table 5.2 and Figs. 5.4, 5.5. The electrochemical performance of the anodes is poor; the corresponding polarization resistances vary in the range 2 - 20 Ohm×cm^2, which is 1 - 2 orders of magnitude larger than required for an adequate operation of a SOFC.

Table 5.2. Polarization resistances at zero current and activation energies of the electrode activity for selected cermet anodes on apatite-type electrolytes

Electrolyte	Anode	Fuel atmosphere	R_η^{1073}, Ohm×cm^2	Activation energy of electrode activity at i = 0		Reference
				T, K	E_a, kJ/mol	
$La_{10}Si_5AlO_{26.5}$	Ni - CGO20 (20 - 80 vol.%)	wet 10% H_2 - N_2	8.3	973 - 1073	96	This work
	CGO20 impregnated with Ni		3.4		139	
	Ag - CGO20 (40 - 60 vol.%)		20		95	
	Ni - Ag - CGO20 (16 - 16 - 66 vol.%)		8.3		74	
	Ni - Ag - CGO20 (10 - 10 - 80 vol.%)		1.6		196	
	Ni - Ag - CGO20 (5 - 5 - 90 vol.%)		4.6		93	
	Cu -YSZ (40 - 60 vol.%)		120		110	
	Cu – CGO (40 - 60 vol.%)		18		83	
$La_{10}Si_{5.5}Al_{0.5}O_{26.75}$	Ni - CGO20 (65 - 35 wt.%)	5% H_2 - Ar	0.59	823 - 1173	99	[566]
$La_{10}Si_{5.5}Al_{0.5}O_{26.75}$	Ni - CGO20 (65 - 35 wt.%) CGO20 sublayer	5% H_2 - Ar	0.57	823 - 1173	93	[566]
$La_9SrSi_6O_{26.5}$	Ni - $La_9SrSi_6O_{26.5}$ (40 - 60 vol%)	5% H_2 - Ar	>1000 *(1023 K)*		-	[661]
$La_{9.8}Ge_{5.5}Al_{0.5}O_{26.45}$	NiO - CGO10 (60 - 40 wt.%)	wet 5% H_2 - N_2	2.2	673 - 1073	75	[656]
with Ag interlayer						
$La_{10}Si_5AlO_{26.5}$	Ag - CGO20 (40 - 60 vol.%)	wet 10% H_2 - N_2	19	973 - 1073	18	This work
	Ag - CGO20 (40 - 60 vol.%) modified by $CeO_{2-\delta}$		2.9		120	
	Al_2O_3 - Ag - CGO20		8.6		77	
	Al_2O_3 - Ag - CGO20 modified by Ni		2.5 *(973 K)*			

In the present work and in [661] Pt mesh was used as current collector. The anode layers in [566, 656] were covered with Pt ink.

The phenomena taking place at the interface anode/electrolyte were qualitatively studied by EDS analysis carried out on fractured half-cells in the regions in the vicinity of the contact between the phases. Selected results collected for Cu - CGO20 and Ag - Ni - CGO20 anode layers are presented in Fig. 5.6 and Tables 5.3, 5.4. Diffusion of La into the cermet, which might be promoted by the apatite phase decomposition, is clearly observable in Fig. 5.6, although the elemental distribution over the anode layer is non-obvious, due to small amount of the contaminant and poor resolution of the technique. Penetration of rare-earth cations from the respective silicates or gallates into the electrodes has been observed in former studies [566, 591]. In the present case, La species might primarily dissolve in fluorite with deterioration of the transport properties and electrochemical activity in comparison with $(Ce,Gd)O_{2-\delta}$ phases [88, 664, 665].

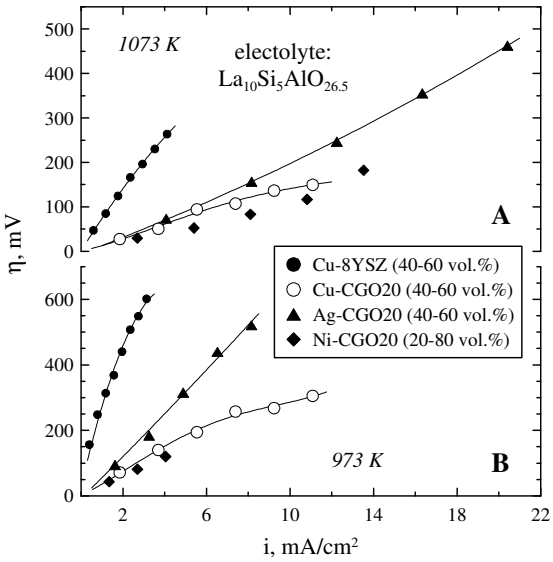

Fig. 5.4. Polarization curves of selected cermet anodes in contact with $La_{10}Si_5AlO_{26.5}$ electrolyte at 973 and 1073 K

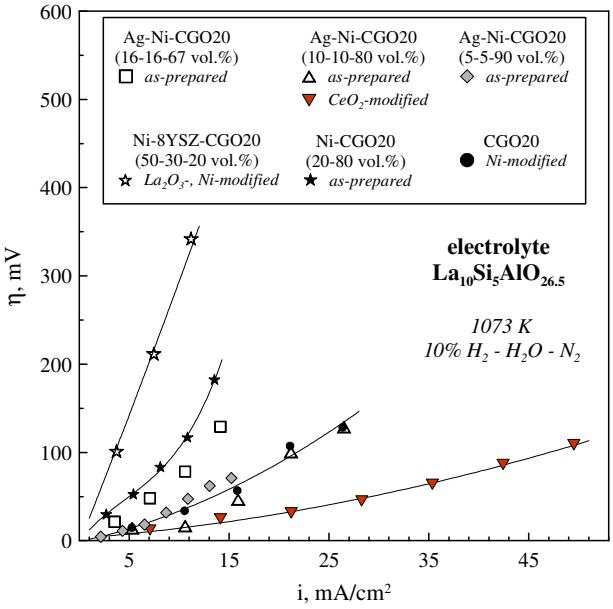

Fig. 5.5. Polarization curves of selected Ni- and CGO20-containing anodes in contact with $La_{10}Si_5AlO_{26.5}$ electrolyte at 1073 K

In turn, the electrolyte layers in the vicinity of the electrode exhibit an accumulation of Ce species, presumably penetrated from the anode, and depletion with Si and Al attributable to diffusion and/or vaporization of the corresponding species; the degree of the changes n the elemental composition correlates with the distance from the electrolyte surface (Table 5.3). The resultant deficiency in Si and Al in the apatite promotes the separation of La_2O_3, with subsequent degradation of the electrolyte transport properties, electrochemical activity of the anode, adhesion between the layers, etc.

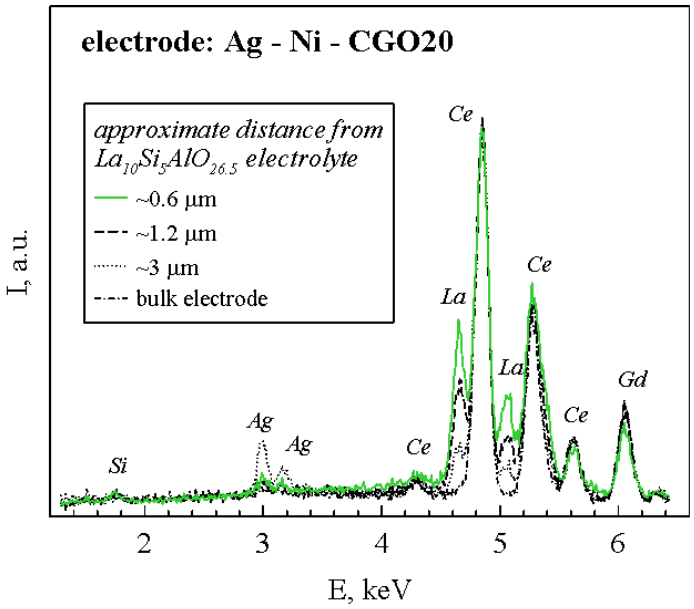

Fig. 5.6. EDS spectra collected from different points of Ag - CGO20 anode at the indicated distances from $La_{10}Si_5AlO_{26.5}$ electrolyte

Table 5.3. Results of EDS analysis carried out on different points of $La_{10}Si_5AlO_{26.5}$ electrolyte at the indicated distance from Cu - CGO20 anode. The molar quantities of the elements are referred to La amount.

Distance from Cu - CGO	Molar ratio Al:Si:La:Ce
20 μm	4.1 : 28 : 100 : 5.3
10 μm	3.7 : 25 : 100 : 5.5
1 μm	2.9 : 20 : 100 : 8.4

Table 5.4. Results of EDS analysis carried out on different points of Cu - CGO20 anode at the indicated distance from $La_{10}Si_5AlO_{26.5}$ electrolyte. The molar quantities of the elements are referred to Ce amount.

Distance from apatite	Molar ratio Si:La:Ce
>10 μm	1.1 : 14 : 100
5 μm	1.6 : 20 : 100
2 μm	4.3 : 39 : 100

As shown in Table 5.4, the relative amounts of Si and La species in Cu - CGO20 layer gradually increases on approaching to the interface, indicating their accumulation at the interface and further penetration of into the anode phase. Despite the apparently low concentration, the presence of silica is detrimental for the electrochemical properties, as indicated in [566, 591, 594]. One should note that the EDS analysis was carried out on half-cells subjected to a single annealing at 1200 - 1300 K in air and one might expect more substantial diffusion or interaction between the cell components even after a short (5 - 10 hours) measurement procedure. Another notion is that the results of EDS analysis do not demonstrate the actual amount of the elements and may be considered only for comparative studies provided that the collection of the data was carried out under similar scanning conditions. In particular, the technique used has a various sensitivity towards light and heavy elements which might infer large deviations in comparison with their absolute content.

In order to bind SiO_2 species in the anode, La_2O_3 phase was introduced into Ni - 8YSZ - CGO20 anode layer by wet impregnation of lanthanum nitrate followed by its subsequent decomposition; however, this approach did not allow to achieve a reasonable performance (Fig. 5.4), possibly due to blocking of the electrochemically active sites, hindering the gas diffusion with lanthanum oxide/silicate formed or negative influence of excessive La amounts in terms of the dissolution in CGO20 phase.

Comparing the performance of the cermet anodes on the apatite-based cells with literature data presented in Table 5.2, the level of the polarization resistances obtained in the present work is significantly lower in comparison with Ni - $La_9SrSi_6O_{26.5}$ cermet (>1 kOhm×cm^2 at 1023 K) [661] but is worse than that of Ni - CGO20 (70-30 wt.%) on $La_{10}Si_{5.5}Al_{0.5}O_{26.75}$ (0.59 Ohm×cm^2 at 1073 K) [566]. The better performance in

the latter reference might originate from differences in the electrode and electrolyte composition, fabrication procedure as well as application of Pt paste on the anode surface.

A noticeable optimization of the anode properties was achieved by addition of silver into the cermets. In particular, moderate quantities of Ag in Ni - CGO20 anode were found to have a positive influence on the electrochemical characteristics (Fig. 5.5), possibly due to a better adhesion of the anode to the electrolyte and between the particles in the electrode layer which ensures a satisfactory percolation of the electron-conductive phase and extended TPB. The promotion of the electrode properties by introducing metallic silver has been demonstrated earlier on $La_{0.5}Sr_{0.4}MnO_{3-\delta}$ [666], $La_{0.6}Sr_{0.4}Co_{0.2}Fe_{0.8}O_{3-\delta}$ [667] $YBaCo_4O_{7+\delta}$ [668], $La_2Ni_{0.8}Cu_{0.2}O_{4+\delta}$ [594], $(La,Sr)(Cr,Mn)O_{3-\delta}$ [10] cathodes as well as on cermet [669, 670] or alternative anodes [367, 671]; the improvement was primarily attributed to enhanced electronic transport over the electrode layer and a contribution of Ag into the catalytic properties.

As shown in Fig. 5.5, the optimum performance is achieved when the total amount of metallic phase is 10 - 20 vol. %; in particular, the polarization resistance of Ag - Ni - CGO (10 - 10 - 80 vol. %) electrode was found as low as ~2 Ohm×cm^2 at 1073 K, substantially increasing under current. The activity may be further improved by distribution of submicron ceria particles over the anode layer using wet impregnation technique. However, increasing the content of CGO20 powder by mechanical mixing has a negative effect, indicating that apart from the composition of the anode layer, the activity is determined by microstructural peculiarities which depend on the preparation route. With respect to the presence of silver in the anode layer, excessive amounts of Ag result in formation of large agglomerates (Fig. 5.3) deteriorating the electrode porosity, while a volatility of Ag [28] sufficiently limits the operational temperature range of the anode.

The presence of CGO20 in the cermet composition seems to be more beneficial in comparison with 8YSZ in terms of the polarization behaviour. Although the literature data on the comparative electrocatalytic activity of ZrO_2- or CeO_2-based conventional Ni cermet anode on commonly used electrolytes (YSZ-, CGO- or $LaGaO_{3-\delta}$-based compositions) are contradictory, the overall level of the performance of cermets containing doped ceria or zirconia may be considered to be comparable [1, 7, 266]. Therefore, the higher performance of Ni - CGO20 in the present work may be attributed to the difference in the preparation process, better electronic percolation in ceria-based anode under reducing conditions or to stronger degradation of zirconia phase in contact with silicates. As shown by previous studies, silica has a tendency towards accumulation at the grain boundaries of zirconia grains, dissolution in the fluorite structure or formation of $ZrSiO_4$ phase, with resultant deterioration of the transport or mechanical properties [672-677]. In turn, segregation of La_2O_3 from the apatite may promote the interaction with ZrO_2-based solutions forming zirconate phases with suppressed ionic conductivity [642]. All these factors result in a strong degradation of the conductivity and electrochemical activity of zirconia-containing electrodes applied onto the apatite electrolytes.

In order to ensure a better adhesion between the electrode and electrolyte layers and provide electronic percolation through the anode, selected electrochemical cells were fabricated applying a layer of metallic silver onto the apatite surface prior to deposition of the electrode layer. The details of the preparation of the corresponding anodes are given in Table 2.6. Selected SEM micrographs collected from the anode layers or from the interface electrode/electrolyte are shown in Fig. 5.7.

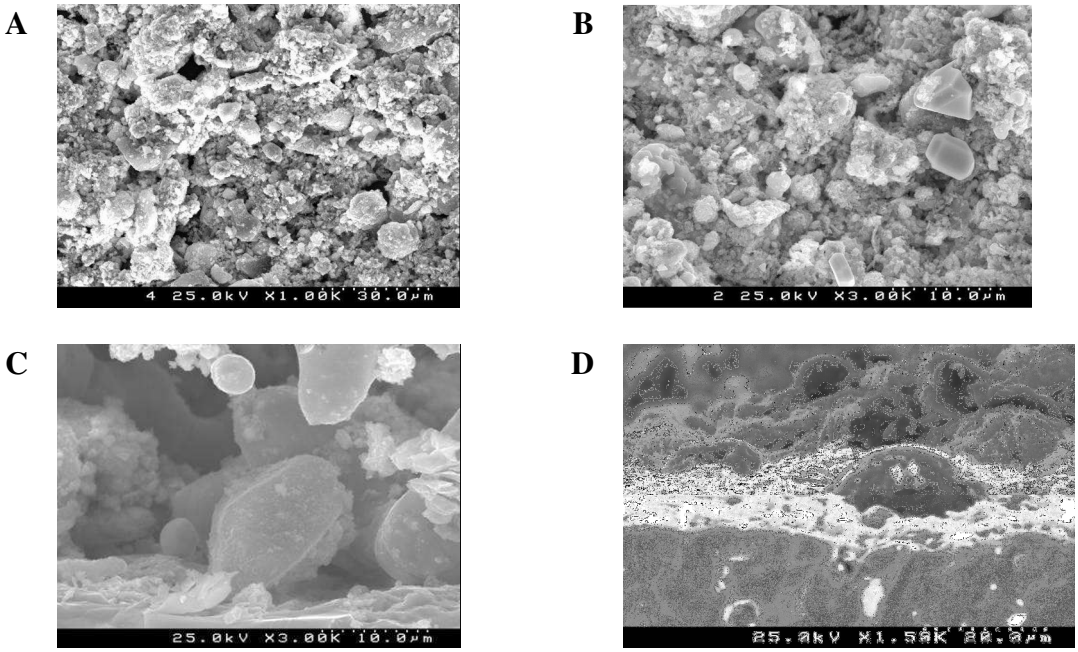

Fig. 5.7. A. As-prepared powder Al_2O_3 - Ag - CGO20; B. Top view of Al_2O_3 - Ag - CGO20 anode after polarization measurements; C. Metallic network formed by Ag particle at the interface between Al_2O_3 - Ag - CGO20 anode and $La_{10}Si_5AlO_{26.5}$ electrolyte with Ag sublayer; D. Electrolyte surface and Ag particles after partial removal of Ni - Ag - CGO20 (16 - 16 - 66 vol.%) anode applied with Ag interlayer.

As follows from the results of the electrochemical studies of the anodes with Ag layer presented in Figs. 5.8 and 5.9, the presence of continuous Ag layer allows to reduce the Ohmic drops, possibly due to a better percolation of the electron-conductive components in the anodes. The lower Ohmic resistance enables to increase the range of currents used for the polarization tests without applying high voltages across the cell.

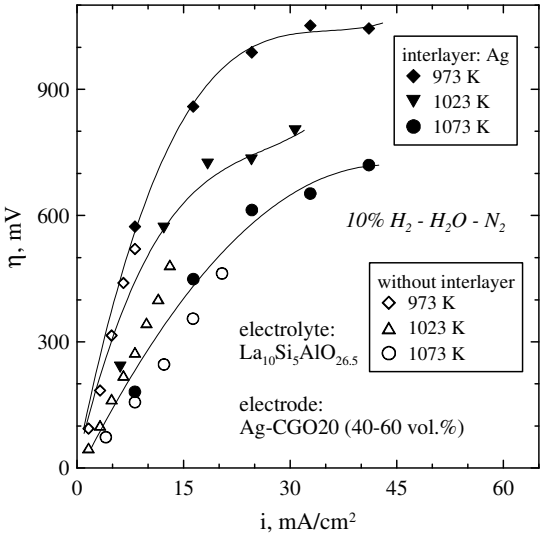

Fig. 5.8. Comparison of polarization curves obtained for Ag - CGO20 (40 - 60 vol.%) anodes in contact with $La_{10}Si_5AlO_{26.5}$ applied with and without Ag interlayer

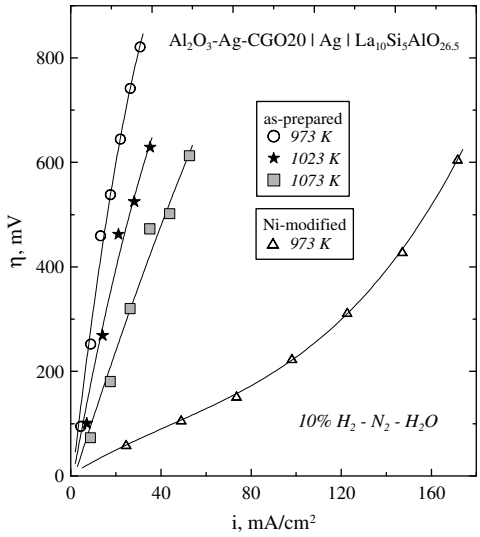

Fig. 5.9. Polarization curves obtained for Al_2O_3 - Ag - CGO20 anodes in contact with $La_{10}Si_5AlO_{26.5}$ with Ag sublayer

On the other hand, the polarization resistance increases after application of the Ag layer (Fig. 5.8), possibly due to reduction of TPB by blocking with Ag particles or worse contact between the apatite and ion-conductive phase in cermet with resultant deterioration of the oxygen exchange between the cell components. Although some oxygen and hydrogen permeability have been reported for pure Ag or Ag-containing alloys [678, 679], this level is obviously insufficient to provide an adequate performance of the anodes.

More promising results were obtained after addition of Al_2O_3 to the electrode and subsequent impregnation with Ni (Fig. 5.9). Since alumina is not expected to demonstrate any contribution into the electronic/ionic transport or catalytic properties [26, 680] of the composites, the effect of Al_2O_3 might relate to formation of a mechanically-stable porous network, while the presence of Ag in the anode provides the connectivity between particles.

The positive effect of application of Ag sublayer on the ohmic losses demonstrates that non-modified cermet anode layers possess insufficient electronic conductivity to ensure a proper current collection, while the improvement of the performance after introduction of Al_2O_3 shows that the parent microstructure does not provide a sufficient gas access to the electrochemically active sites. Optimizing the fraction of the components might enable to achieve a reasonable porosity and large TPB. However, the values of the polarization resistance still remain rather high, which limits the applicability of Ag-containing electrode layers.

Long-term performance tests carried out on Al_2O_3 - Ag - CGO20 cermet deposited onto $La_{10}Si_5AlO_{26.5}$ electrolyte with Ag interlayer showed a continuous degradation of the polarization resistance under galvanostatic conditions which amounts to ~6% per 90 hours, although the data are rather scattered (Fig. 5.10). Even more serious deterioration was detected in terms of the Ohmic resistance; in particular, on initial 10 hours the degradation rate was essentially high, followed by somewhat lower, but still significant (~30% per 90 hours) increase of the Ohmic losses. The latter phenomenon might primarily be associated with reduction of the ionic conductivity of the apatite materials with time [21]; however, the degradation of the transport properties has been found to be negligible at the temperatures below 1073 K [648, 649].

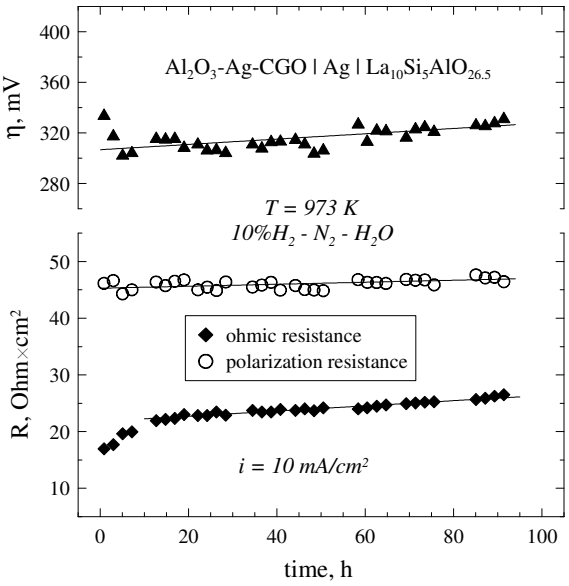

Fig. 5.10. Time dependencies of the overpotential, polarization and ohmic resistance of Al_2O_3 - Ag - CGO20 anodes with Ag sublayer

Other possible origins of the degradation include microstructural features (i.e. detachment of the electrode layer, electrode depletion with Ag due to vaporization, agglomeration of the metallic particles resulting in disruption of the electron-percolative network etc.) or accumulation of silica-based phases at the electrode/electrolyte interface, as confirmed by EDS analysis. All these factors lead to an increase of both polarization and ohmic resistance.

Comparison of SEM micrographs of the Al_2O_3 - Ag - CGO20 electrode powders before and after the electrochemical tests (Fig. 5.7 C and D) does not allow to make certain conclusions on the changes in the cermet morphology, suggesting that the performance deterioration is related primarily with the electrode/electrolyte interface.

Summarizing the results obtained on cermets anodes in contact with $La_{10}Si_5AlO_{26.5}$ electrolyte, one may infer that a reasonable amount in the anode layer of Ni and/or Ag is required in order to achieve an adequate performance. However, both components impose requirements on the operation conditions, primarily in terms of microstructural features, phase stability, dimension behaviour etc. In order to evaluate the potential of silicate-based materials for utilization as SOFC electrolytes, the following investigation is focused on comparative studies of the electrochemical performance of perovskite anodes applied onto $La_{10}Si_5AlO_{26.5}$ and LSGM electrolytes.

5.3. Electrochemical behaviour of oxide anodes in contact with LSGM and $La_{10}Si_5AlO_{26.5}$ solid electrolytes

5.3.1. Comparison of oxide-based anode materials. Correlations of the electrochemical behaviour and transport properties

The basic trends of the structural, transport and thermomechanical properties of selected perovskite-like oxide materials were considered in Chapters 3 - 4, with the primary attention towards the effect of the cation composition on the functional characteristics, mechanism of the electronic/ionic transport, equilibration kinetics, etc. The present part is devoted to a brief summarization and comparison of the properties important for the electrochemical applications for the perovskites which exhibited the maximum potential for utilization as SOFC anodes.

Analysis of XRD patterns under reducing atmospheres (Fig. 5.11) indicates that most perovskite materials may endure redox cycling in terms of the phase stability provided that a sufficient amount of cations with suppressed reducibility (Cr, Ti, Nb) is introduced into the perovskite structure. The presence of minor amounts of MnO phase which accompanies the reduction of manganite-based materials was demonstrated not to affect significantly the transport and electrochemical properties, while the segregation of nano-scaled Ni particles from $(La_{0.9}Sr_{0.1})_{0.95}Cr_{0.85}Mg_{0.1}Ni_{0.05}O_{3-\delta}$ or (Mg,Ni)O secondary phase at low $p(O_2)$ may be beneficial in terms of the catalytic activity. Some precautions should be undertaken with respect to the structural transitions exhibited by La-enriched $(La,Sr)(Mn,Ti)O_{3-\delta}$ and $(La,Sr)(Cr,Fe)O_{3-\delta}$; in particular, a

slow equilibration kinetics and hysteresis behaviour observed on the former family of perovskites leads to mechanical degradation and limits their applicability in the electrochemical cells.

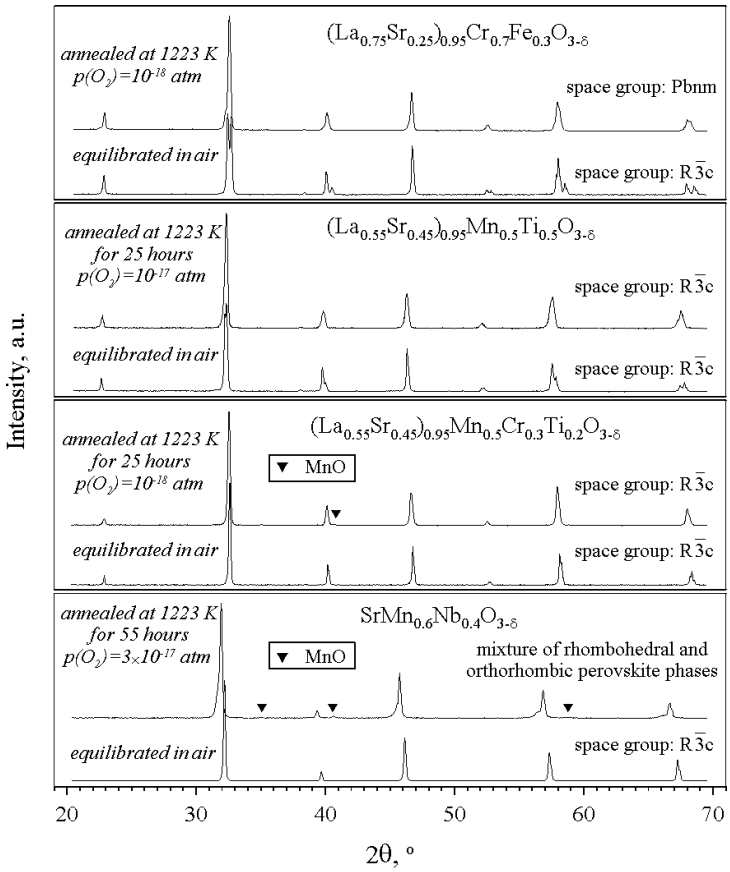

Fig. 5.11. Selected XRD patterns of the oxide anode materials after equilibration in atmospheric air and after reduction. The annealing conditions in reducing atmospheres are given in the legends.

For most studied materials the TEC values vary in the range (11 - 14)×10^{-6} K^{-1} at 923 - 1223 K (Fig. 5.12) and the perovskites are mechanically compatible with LSGM and $La_{10}Si_5AlO_{26.5}$ electrolytes. The compositional trends in the thermal expansivity generally correlate with the reducibility of the corresponding oxides; in particular, increasing strontium and manganese concentrations in the perovskite lattice yields moderately higher thermal expansion, although possible electron exchanges between the reducible species should also be accounted for. For $SrMn_{1-x}Nb_xO_{3-\delta}$ series, the Nb content should exceed 20 - 30 % in order to avoid large expansion and decomposition of Mn-enriched representatives upon reduction.

The isothermal chemically-induced strains of $(La,Sr)(Mn,Cr,Ti)O_{3-\delta}$, $(La,Sr)(Cr,Fe)O_{3-\delta}$ and $(La,Sr)(Mn,Ti)O_{3-\delta}$-based compositions are within 0.6% on reducing $p(O_2)$ down to 10^{-21} - 10^{-12} atm (Fig. 5.13). Decreasing Sr content lowers the chemical expansion as well as TEC values and improves the thermomechanical compatibility with the electrolyte materials. However, even for Sr-enriched $(La_{0.25}Sr_{0.75})_{0.95}Mn_{0.5}Ti_{0.5}O_{3-\delta}$ with maximum strains the chemical expansion of 0.6% is not a critical factor, as discussed in Chapter 3.1.3, which enables to modify the transport and electrochemical properties of this perovskite series without a compromise with the stability or thermomechanical compatibility.

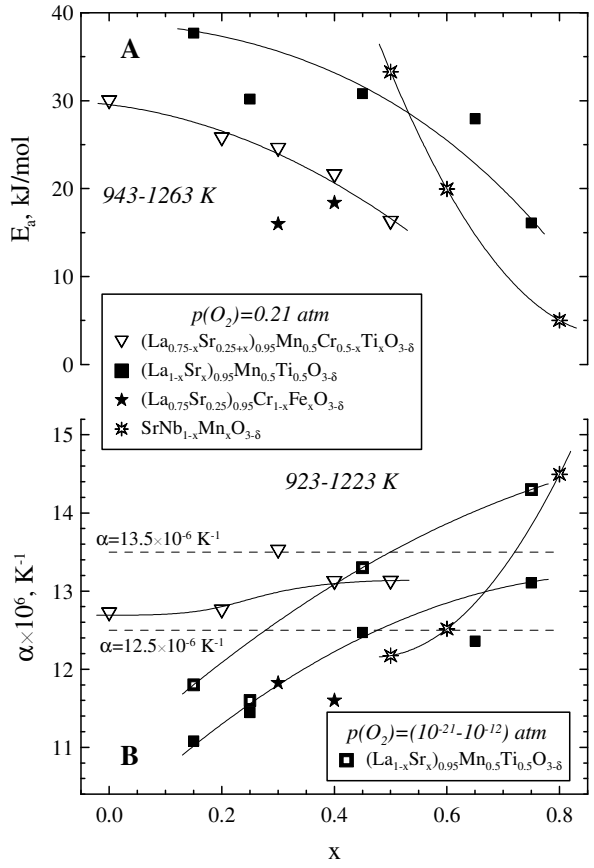

Fig. 5.12. Composition dependencies of the activation energy for total conductivity in air (A) and average TECs measured at atmospheric and low $p(O_2)$ (B). For a more adequate comparison, Nb-doped $SrMnO_{3-\delta}$ is represented as $SrNb_{1-x}Mn_xO_{3-\delta}$.

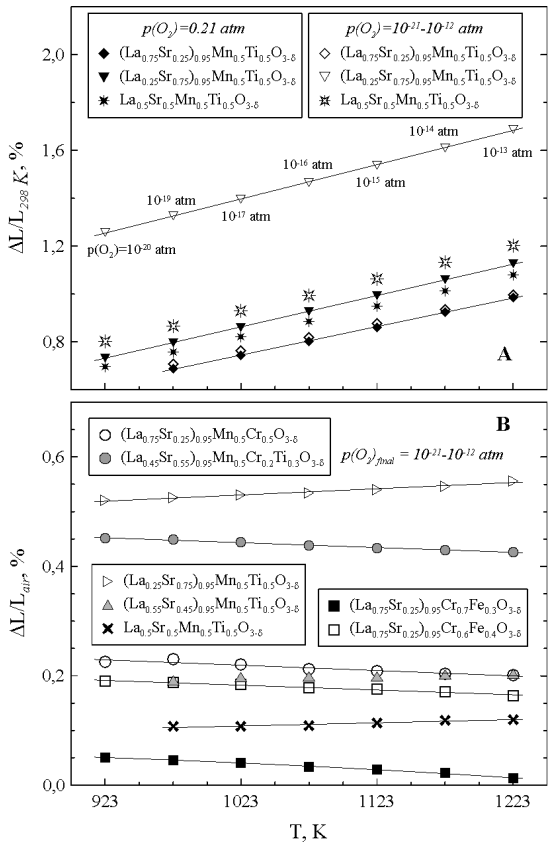

Fig. 5.13. Thermal expansion measured in the regime of temperature cycling with 2 - 5 h dwells at each temperature in air and under reducing conditions (A), and isothermal chemically-induced strain relative to the atmospheric oxygen pressure (B).

The oxygen partial pressure dependencies of the total conductivity (Fig. 5.14) display similar trends for all studied materials. Namely, plateau-like behavior is observed under oxidizing conditions when the variations of the oxygen nonstoichiometry are minor, while the oxygen content is close to stoichiometric value. In accordance with the p-type electronic transport mechanism, in moderately reducing atmospheres the conductivity starts to drop with decreasing $p(O_2)$. As follows from the results of OP studies, the contribution of the ionic transport into the overall conductivity is negligible. The range of the oxygen partial pressures where the conductivity is essentially $p(O_2)$-independent, expands on decreasing temperature as the oxygen nonstoichiometry variations decrease. In some cases, the conductivity at 1073 K is almost constant down to $p(O_2) = 10^{-20}$ atm, though this behavior in the intermediate-temperature range may partly originate from kinetic factors. When considering the major effects of cation composition, it should first be mentioned that incorporation of B-site cations with relatively stable oxidation state, such as Ti or Nb, decreases the hole mobility and conductivity. Taking into account the trends in the stability and expansion behaviour, the optimum concentration of these species in the B-sublattice is within 40 - 60%.

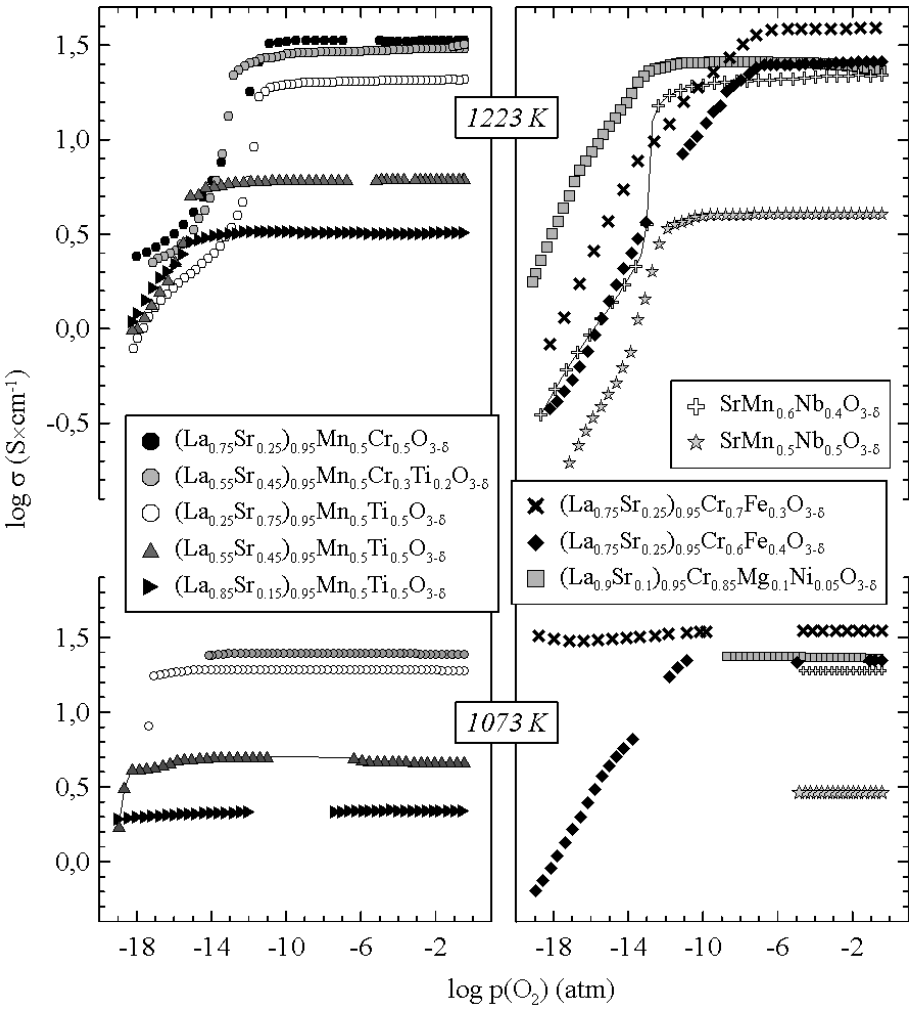

Fig. 5.14. Oxygen partial pressure dependencies of the total conductivity at 1223 K and 1073 K

In accordance with previous studies [190, 195, 300], Sr-doping into the perovskites promotes the reducibility which is reflected by shifting the onset of the conductivity drop to more oxidative conditions. For $(La_{1-x}Sr_x)_{0.95}Mn_{0.5}Ti_{0.5}O_{3-\delta}$ series, La-doping reduces the amount of the electronic charge carries and simultaneously allows to extend the region of $p(O_2)$-independent conductivity to more reductive atmospheres; the resultant effect is that La content has no essential influence of the low-$p(O_2)$ conductivity. The segregation of metallic nickel in reduced $(La_{0.9}Sr_{0.1})_{0.95}Cr_{0.85}Mg_{0.1}Ni_{0.05}O_{3-\delta}$ has no substantial effect on the transport properties as Ni content is small; the total conductivity of this material in reducing atmospheres is comparable to that of $(La_{0.75}Sr_{0.25})_{0.95}Cr_{0.5}Mn_{0.5}O_{3-\delta}$ and $(La_{0.55}Sr_{0.45})_{0.95}Ti_{0.5}Mn_{0.5}O_{3-\delta}$.

The overall level of the conduction of the perovskites is as low as 1 - 30 S/cm in anode atmospheres in the temperature range 973 - 1173 K. An acceptable electronic transport at low $p(O_2)$ may be expected for $(La,Sr)(Cr,Fe)O_{3-\delta}$, $(La_{0.9}Sr_{0.1})_{0.95}Cr_{0.85}Mg_{0.1}Ni_{0.05}O_{3-\delta}$ and selective representatives of $Sr(Mn,Nb)O_{3-\delta}$ and $(La,Sr)(Mn,Cr,Ti)O_{3-\delta}$ with moderate content of Nb or Ti. As for the transport properties in air and, consequently, applicability as cathodes, La-rich $La_{1-x}Sr_xMn_{0.5}Ti_{0.5}O_{3-\delta}$ and Nb-rich $SrMn_{1-x}Nb_xO_{3-\delta}$ perovskites are quite inappropriate for electrochemical utilizations.

The maximum electrochemical activity among the perovskite anodes applied onto LSGM electrolyte with protective CGO20 sublayer was observed for anodes with quite different cation compositions, which include $(La_{0.75}Sr_{0.25})_{0.95}Cr_{0.7}Fe_{0.3}O_{3-\delta}$, $La_{0.5}Sr_{0.5}Mn_{0.5}Ti_{0.5}O_{3-\delta}$ and $(La_{0.9}Sr_{0.1})_{0.95}Cr_{0.85}Mg_{0.1}Ni_{0.05}O_{3-\delta}$. The anodes provide quite similar overpotentials, at the level of ~150 mV under 100 mA/cm^2 current density, which, however, are still higher compared to Ni-containing cermets (Fig. 5.15). The level of the anodic polarization resistance under OCV conditions of the most active electrode materials is as low as 1 - 2.5 Ohm×cm^2 which is quite comparable with the corresponding values reported for perovskite and perovskite-related alternative anode in literature (Table 5.5). The present results are, however, more beneficial as no expensive current collector was applied to improve the electrode performance.

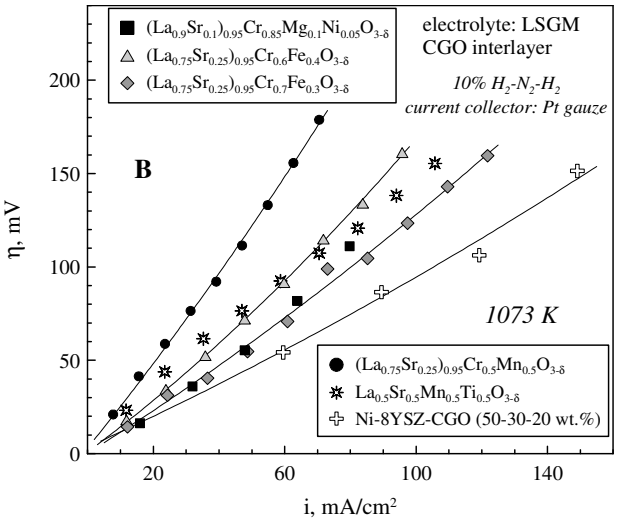

Fig. 5.15. Anodic overpotential vs. current density dependencies for selected half-cells with LSGM and $La_{10}Si_5AlO_{26.5}$ solid electrolytes at 1073 K. Data on Ni - 8YSZ - CGO anode [567] are demonstrated for comparison.

Considering possible origins of the trends in the polarization behavior of the perovskite anodes, one should emphasize the effects of the transport properties of the electrode materials, known from the literature. The effect of the electronic conductivity on the electrode properties has been reported for numerous groups of cathode materials, especially in the case of limited current collection over the electrode layer due to insufficient electronic transport (below 10 - 100 S/cm); this constriction is typical for doped manganites or perovskite-related groups containing “inert” cations in B-sublattice [681, 682]. However, one should take into account that in (La,Sr)$MnO_{3\pm\delta}$ and related systems compositional modifications basically have a multiple and complex influence and may simultaneously affect the stability, electronic and ionic transport, the thermomechanical properties, compatibility with the electrolyte materials, etc [226, 266, 305, 310, 323]. Therefore, elucidating a single performance-determining factor is generally a complex procedure.

Among anode materials studied in literature, the effect of the electronic transport is more difficult to detect, primarily due to low availability of the information on the transport properties of the electrode materials under appropriate conditions. In particular, for Ni - YSZ cermets, an acceptable level of the total conductivity is achieved only when the volume fraction of the metal exceeds the percolation threshold, i.e. 20 - 50 vol. % ([7, 266] and references cited). However, any variations in the content of the constituents in composites are accompanied by non-negligible microstructural changes, and an enrichment of the composite

with metallic phase beyond the optimum level basically leads to a drop of the performance. As shown in Fig. 5.16, increasing Ni content above 30 vol.% in Ni - YSZ results in a gradual decrease of the Ohmic losses which reflects an improvement of the electronic transport of the anode layer. The polarization resistance, however, exhibits a minimum at 40 - 50 vol.% Ni [662]. Similar trends were detected for Cu-perovskite cermets [353]; the observation seems to be associated with strong sintering activity of Cu particles which may hamper the gas access or reduce the TPB in the case of large fractions of the metallic component.

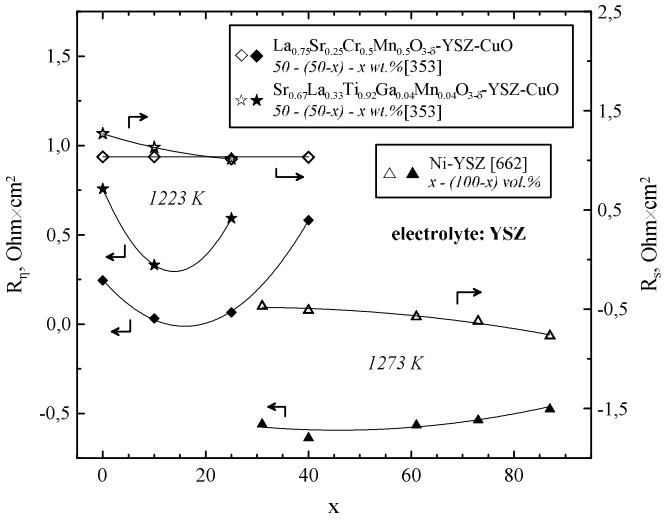

Fig. 5.16. Dependence of the Ohmic and polarization resistance for selected cermet anodes on the content of the metallic phase

More informative with this respect might be studies on oxide-based anodes (in particular, those possessing the perovskite or perovskite-related structure). However, tracing the correlations between the electronic transport properties and electrode performance of such anodes is limited by low availability of the literature data and strong differences between the anode component compositions, microstructure, fabrication route, etc. which does not allow to elucidate the effect of the bulk properties of the electrode material. Comparative studies on various anode materials with perovskite, fluorite, pyrochlore or tungsten bronze structure revealed no obvious correlation between the low-p(O_2) electronic conductivity and polarization resistance, although the Ohmic losses were generally lower for more conductive anode materials [683]. The performance of mixed-conducting anodes not subjected to any specific modifications follows the order $Ce_{0.6}Gd_{0.4}O_{2-\delta}$ > $Zr_{0.71}Y_{0.12}Ti_{0.17}O_{2-\delta}$ > $La_{0.75}Sr_{0.25}Cr_{0.97}V_{0.03}O_{3-\delta}$, irrespective to the trends in the ionic or electronic conductivity of the corresponding materials, and might be improved by addition of small amounts of Ni, in accordance with [684]. Comparison of the polarization behaviour of composite anodes, consisting of $Ce_{0.8}Ca_{0.2}VO_{3-\delta}$, $Gd_{1.86}Ca_{0.14}Ti_2O_{7-\delta}$, $Tb_{0.5}Zr_{0.5}O_{2-\delta}$, $La_{0.9}Sr_{0.1}Al_{0.65}Mg_{0.15}Fe_{0.2}O_{3-\delta}$ as the main mixed-conducting phase, and modified by introduction of ionically and/or electronically conductive components indicated that the performance is governed by numerous factors, primarily by the chemical, thermomechanical and microstructural stability, especially whenever a sufficient level of the electronic conductivity is achieved [107].

Table 5.5. Polarization resistances at zero current, polarization at 60 mA/cm^2 and activation energies of the electrode activity for selected anodes on LSGM electrolytes

Anode	Gas atmosphere	R_η^{1073}, Ohm×cm^2	η^{1073}, mV (i = 60 mA/cm^2)	Activation energy		Reference
				T, K	E_a, kJ/mol	
$(La_{0.55}Sr_{0.45})_{0.95}Mn_{0.5}Cr_{0.3}Ti_{0.2}O_{3-\delta}$ sublayer: CGO20	wet 10% H_2 - N_2	4.7	340	973 - 1073	96	This work
$(La_{0.75}Sr_{0.25})_{0.95}Cr_{0.7}Fe_{0.3}O_{3-\delta}$ sublayer: CGO20		1.2	70	873 - 1073	71	This work
$(La_{0.75}Sr_{0.25})_{0.95}Cr_{0.6}Fe_{0.4}O_{3-\delta}$ sublayer: CGO20		1.6	92	873 - 1073	90	This work
$(La_{0.9}Sr_{0.1})_{0.95}Cr_{0.85}Mg_{0.1}Ni_{0.05}O_{3-\delta}$		5.5		973 - 1073	100	This work
$(La_{0.9}Sr_{0.1})_{0.95}Cr_{0.85}Mg_{0.1}Ni_{0.05}O_{3-\delta}$ sublayer: CGO20		1.4	75	973 - 1073	78	This work
$(La_{0.55}Sr_{0.45})_{0.95}Mn_{0.5}Ti_{0.5}O_{3-\delta}$ sublayer: CGO20		2.2	220	873 - 1073	97	This work
$La_{0.5}Sr_{0.5}Mn_{0.5}Ti_{0.5}O_{3-\delta}$ sublayer: CGO20		2.1	94	873 - 1073	55	This work
$(La_{0.25}Sr_{0.75})_{0.95}Mn_{0.5}Ti_{0.5}O_{3-\delta}$ sublayer: CGO20		12		973 - 1073	80	This work
$SrMn_{0.6}Nb_{0.4}O_{3-\delta}$		12.3		973 - 1073	100	This work
$SrMn_{0.6}Nb_{0.4}O_{3-\delta}$; sublayer: CGO20		12.1		973 - 1073	150	This work
$SrMn_{0.5}Nb_{0.5}O_{3-\delta}$		20		973 - 1073	52	This work
Ni - CGO (95-5 wt.%) sublayer: CGO18	3% H_2O - H_2	0.12	10	873 - 1073	67	[685]
Ni - CSO20 (50 - 50 vol.%)	wet H_2		5.5			[655]
Ni - 8YSZ - CGO20 (50 - 30 - 20 wt.%)	wet 10% H_2 - N_2		55			[567]
$Sr_{0.2}La_{0.8}TiO_{3-\delta}$ - CGO20 (50-50 wt%), impr. with Ni	H_2 - H_2O (97 - 3%)	1.0		873 - 1073	120	[547]
Ni - $Gd_{1.86}Ca_{0.14}Ti_2O_7$ – CGO20	wet 10% H_2 - N_2	0.82	38	873 - 1073	62	[107]
Ni - 8YSZ - $Ce_{0.8}Ca_{0.2}VO_{3-\delta}$ (50 - 30 - 20 wt.%)	wet 10% H_2 - N_2	1.5	72	973 - 1073	42	[107]
$La_{0.75}Sr_{0.35}Cr_{0.5}Al_{0.5}O_{3-\delta}$	wet 5% H_2 - Ar	0.41	32 (+cathode)	973 - 1073	62	[9]
$La_{0.75}Sr_{0.25}Cr_{0.5}Mn_{0.5}O_{3-\delta}$	wet 5% H_2 - Ar	0.28	3.6 (+cathode)	973 - 1073	45	[9]
$(La_{0.75}Sr_{0.25})_{0.95}Cr_{0.5}Mn_{0.5}O_{3-\delta}$ sublayer: CGO20	wet 10% H_2 - N_2	2.8	150	973 - 1073	66	[10]
$La_{0.75}Sr_{0.25}Cr_{0.5}Fe_{0.5}O_{3-\delta}$	wet 5% H_2 - Ar	1.5	130 (+cathode)	973 - 1073	66	[9]
$La_{0.33}Sr_{0.67}Cr_{0.33}Fe_{0.67}O_{3-\delta}$ - CGO10 (50 - 50 wt.%); sublayer: CLO60	wet 100% H_2	0.32			-	[18]
$La_{0.8}Sr_{0.2}Cr_{0.82}Ru_{0.18}O_{3-\delta}$ - CGO10 (50 - 50 wt.%)	wet H_2	0.23 (at 0.5V)			-	[15]
$Sr_2Fe_{1.33}Mo_{0.67}O_{6-\delta}$ sublayer: CSO82	3% H_2O - H_2	0.18		973 - 1073	42	[124]
$Sr_2MgMoO_{6-\delta}$	wet 5% H_2 - Ar	0.89		848 - 1173	77	[556]

The data were obtained on $La_{0.9}Sr_{0.1}Ga_{0.8}Mg_{0.2}O_{3-\delta}$ [9, 15, 18, 547, 655], $La_{0.8}Sr_{0.2}Ga_{0.8}Mg_{0.2}O_{3-\delta}$ [556]; $La_{0.8}Sr_{0.2}Ga_{0.83}Mg_{0.17}O_{3-\delta}$ [124]; $La_{0.88}Sr_{0.12}Ga_{0.82}Mg_{0.18}O_{3-\delta}$ [685]; $(La_{0.9}Sr_{0.1})_{0.98}Ga_{0.8}Mg_{0.2}O_{3-\delta}$ (This work, [10, 107, 567]) solid electrolytes. Pt mesh (This work, [10, 107, 567]), Pt paste/ink [9, 124, 547, 556], Au ink [18] or printed Au grid [15] was used as current collector. In [655, 685] the current collector is not indicated

Analysis of the conductivity and polarization behaviour of the $(La_{1-x}Sr_x)Mn_{0.5}Cr_{1-x}Ti_xO_{3-\delta}$, $SrMn_{1-x}Nb_xO_{3-\delta}$, $(La_{0.75}Sr_{0.25})_{0.95}Cr_{1-x}Fe_xO_{3-\delta}$ and $(La_{0.9}Sr_{0.1})_{0.95}Cr_{0.85}Mg_{0.1}Ni_{0.05}O_{3-\delta}$ anodes allows to reveal a good correlation between the electronic transport and electrochemical properties, as shown in Fig. 5.17, although in some cases the dependence is not strictly linear. Moreover, the obvious trends are observed only within a given perovskite group, while the electrodes fabricated from the representatives belonging to other perovskite series deviate from the correlation. This indicates that the electrode activity is substantially affected by some other factors.

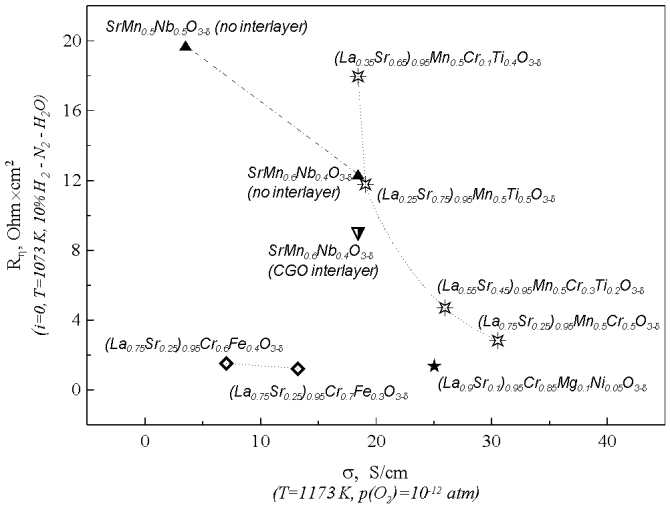

Fig. 5.17. Correlation between the anodic polarization resistance and total conductivity of the electrode materials. All dashed lines are a guide for the eye

In Table 5.6 the data on the linear chemical expansion of the perovskite materials on reduction in $CO-CO_2$ flow and overpotential of the corresponding anodes are compared. The values demonstrate a reasonable correlation, although in some cases the comparison is complicated by differences between the compositions subjected to dilatometric and electrochemical tests (for example, $(La_{0.55}Sr_{0.45})_{0.95}Mn_{0.5}Cr_{0.2}Ti_{0.3}O_{3-\delta}$ and $(La_{0.55}Sr_{0.45})_{0.95}Mn_{0.5}Cr_{0.3}Ti_{0.2}O_{3-\delta}$, correspondingly). Nevertheless, the monotonous behaviour of both the chemical strains and electrochemical activity with Sr doping allows to suggest that the correlation between the thermomechanical and electrochemical properties should be satisfied. As known from previous reports [686-688], for optimum and stable anode operation the linear chemical expansion should be within 0.2 - 0.25% . Among the materials studied, the values of the anode overpotential below 100 mW/cm^2 under current of 60 mA/cm^2 are observed for perovskites with the expansivity lower 0.15 - 0.20%.

Other factors which may influence the electrochemical behaviour include microstructural particularities (in particular, differences in the sinterability behaviour in various perovskite families), ionic transfer, catalytic activity, etc. In particular, for $(La_{0.9}Sr_{0.1})_{0.95}Cr_{0.85}Fe_{0.1}Ni_{0.05}O_{3-\delta}$, the electrode performance may be additionally promoted by the presence of nano-scaled Ni particles on the surface, while comparatively high surface concentration of oxygen vacancies for Fe-doped chromites is also beneficial in terms of the electrochemical properties. Unfortunately, the data on the ionic conductivity or redox kinetics of the perovskites studied only allow to qualitatively estimate an approximate level of possible contribution of the bulk ionic transport or surface exchange into the overall electrode kinetics, without a certain prediction of

the trends under reducing conditions. Nevertheless, taking into account the apparently low level of the total conductivity (0.1 - 10 S/cm) under reducing conditions and the absence of any additives ensuring an appropriate current collection over the anode layer (in contrast to most data on the alternative anode materials reported in literature [8, 9, 16, 201], the electronic transport indeed seems to be a critical parameter responsible for the electrode activity.

Table 5.6. Linear chemical expansion of perovskite materials on reduction in flowing CO - CO_2 with respect to air at 1073 K and overpotentials of the corresponding anodes under current of 60 mA/cm^2.

Composition	Chemical expansion		η^{1073}, mV*
	$p(O_2)$, atm	$\Delta L/L_0^{1073}$, %	(i = 60 mA/cm^2)
$(La_{0.75}Sr_{0.25})_{0.95}Cr_{0.5}Mn_{0.5}O_{3-\delta}$	1×10^{-16}	**0.21**	**150**
$(La_{0.55}Sr_{0.45})_{0.95}Mn_{0.5}Cr_{0.3}Ti_{0.2}O_{3-\delta}$	-	**-**	**340**
$(La_{0.45}Sr_{0.55})_{0.95}Mn_{0.5}Cr_{0.2}Ti_{0.3}O_{3-\delta}$	2×10^{-16}	**0.44**	**-**
$(La_{0.25}Sr_{0.75})_{0.95}Mn_{0.5}Ti_{0.5}O_{3-\delta}$	1×10^{-16}	**0.53**	**500****
$(La_{0.55}Sr_{0.45})_{0.95}Mn_{0.5}Ti_{0.5}O_{3-\delta}$	2×10^{-15}	**0.20**	**220**
$(La_{0.75}Sr_{0.25})_{0.95}Mn_{0.5}Ti_{0.5}O_{3-\delta}$	2×10^{-15}	**0.02**	**-**
$La_{0.5}Sr_{0.5}Mn_{0.5}Ti_{0.5}O_{3-\delta}$	1×10^{-15}	**0.11**	**94**
$(La_{0.75}Sr_{0.25})_{0.95}Cr_{0.7}Fe_{0.3}O_{3-\delta}$	9×10^{-16}	**0.03**	**70**
$(La_{0.75}Sr_{0.25})_{0.95}Cr_{0.6}Fe_{0.4}O_{3-\delta}$	9×10^{-16}	**0.18**	**92**

** Overpotential values correspond to anodes deposited onto LSGM electrolyte preliminary coated with CGO20 sublayer. The measurements were carried out in flowing 10% H_2 - N_2 - H_2O at 1073 K.*
*** The overpotential value was calculated by extrapolation from lower currents.*

5.3.2. Influence of anode layer microstructure on the electrochemical properties

As discussed in Chapter 4.2, the perovskites (La,Sr)(Mn,Ti)$O_{3-\delta}$ with La:Sr ratio close to 1 exhibit an optimum combination of the functional characteristics for application as SOFC anodes. Therefore, a particular attention was drawn by cation-deficient $(La_{0.55}Sr_{0.45})_{0.95}Mn_{0.5}Ti_{0.5}O_{3-\delta}$. However, due to a strong tendency of the perovskite towards grain growth (Fig. 4.22), the procedure of preparation of the electrode layers should be carefully tuned. Micrographs in Fig. 5.18 represent typical microstructures of the electrode layers prepared from $(La_{0.55}Sr_{0.45})_{0.95}Mn_{0.5}Ti_{0.5}O_{3-\delta}$ powders processed in accordance with Table 2.4.

In accordance with the strong sinterability, $(La_{0.55}Sr_{0.45})_{0.95}Mn_{0.5}Ti_{0.5}O_{3-\delta}$ powder without preliminary treatment ("*coarse-1473*") showed formation of large (20 - 30 μm) grains imaged in Fig. 5.18 B. For comparison, much finer microstructure was observed $(La_{0.85}Sr_{0.15})_{0.95}Mn_{0.5}Ti_{0.5}O_{3-\delta}$ powder prepared and deposited under analogous conditions (Fig. 5.18 A). Since large particles are unfavorable in terms of restricted surface area and poor percolation between the particles, the powder morphology was modified by preliminary grinding the electrode powder prior to coating. However, reducing the grain size caused a strong densification of the electrode layer, providing an extremely poor porosity and limited gas access to the electrochemically-active sites, as shown in Figs. 5.18 C and D.

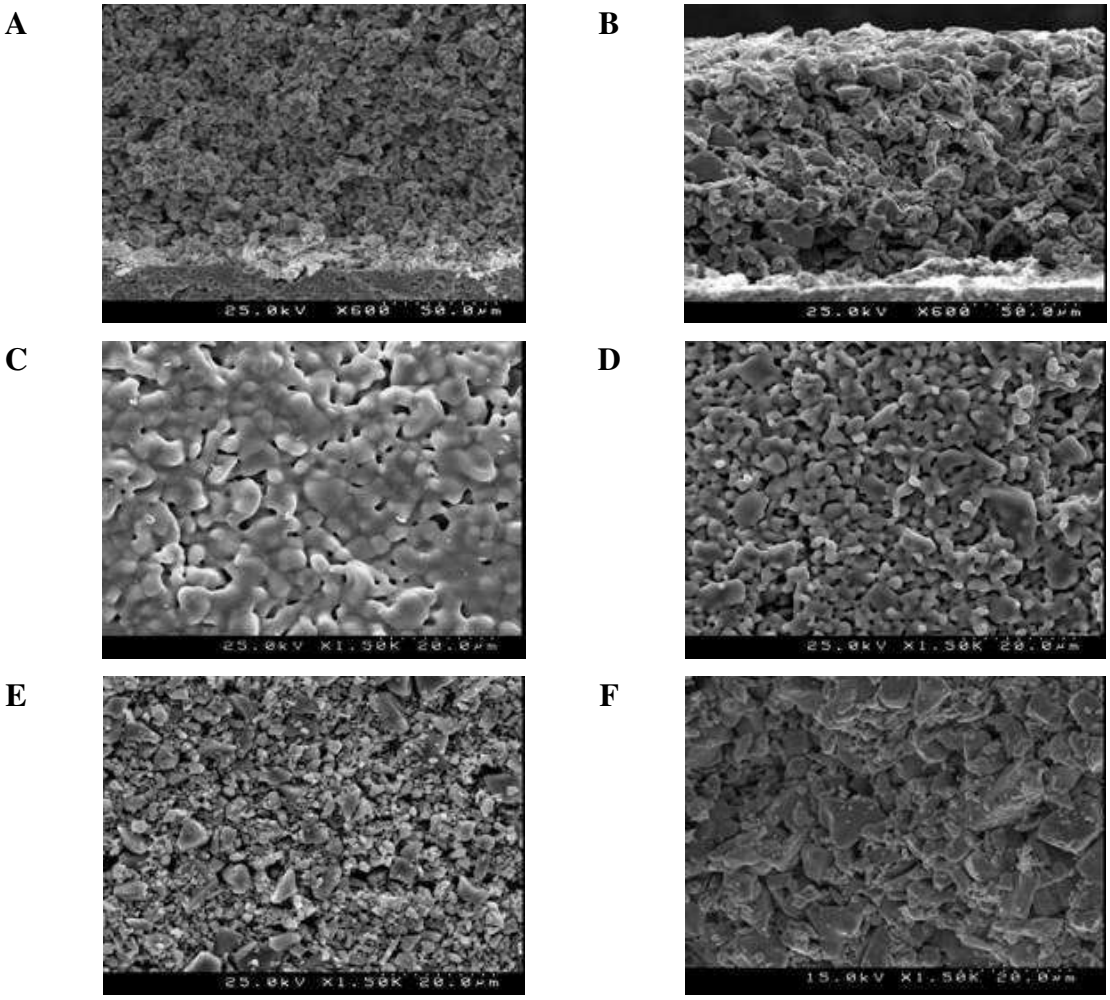

Fig. 5.18. SEM micrographs of as-prepared anode layers deposited onto LSGM electrolyte with CGO20 sublayer: $(La_{0.85}Sr_{0.15})_{0.95}Mn_{0.5}Ti_{0.5}O_{3-\delta}$ fired at 1473 K (A); $(La_{0.55}Sr_{0.45})_{0.95}Mn_{0.5}Ti_{0.5}O_{3-\delta}$ "coarse-1473" (B), "fine-1473" (C), "fine-1433" (D), "fine-1323" (E), "passivated-1473" (F). Abbreviations for $(La_{0.55}Sr_{0.45})_{0.95}Mn_{0.5}Ti_{0.5}O_{3-\delta}$ anode layers are listed in Table 2.4.

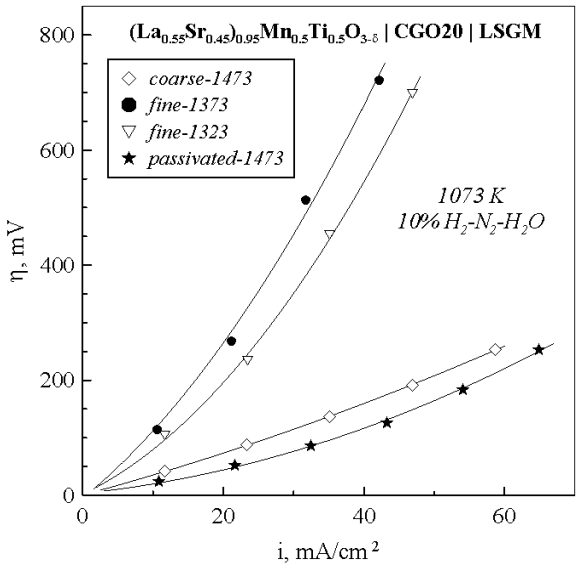

Fig. 5.19. Polarization curves obtained for $(La_{0.55}Sr_{0.45})_{0.95}Mn_{0.5}Ti_{0.5}O_{3-\delta}$ electrodes with various microstructure on LSGM electrolyte with CGO20 sublayer. The preparation procedure and abbreviations for the electrode layers are given in Table 2.4.

Diminishing the firing temperature of the "*fine*" electrodes suppressed the densification of the electrode layer (Figs. 5.18 C, D, E), at the expense of a worse contact between the electrode layer and electrolyte. As a result of the insufficient porosity of the electrode, the overpotential for the anodes prepared from "*fine*" powders enhanced by 4 - 5 times as compared to the "*coarse-1473*" anode layer (Fig. 5.19).

In order to avoid the strong sinterability of the electrode powder, an additional step was included in the procedure of the electrode preparation, defined as "*passivated-1473*" in Table 2.4. Despite a possible deterioration of the surface activity by the additional high-temperature step, the benefit of the preservation of the porosity and at the same time suppressed formation of large grains (Fig. 5.18 F) in comparison with "*coarse-1473*" powder allowed to achieve the maximum electrochemical activity in the series (Fig. 5.19). Nevertheless, the electrochemical activity of the electrodes still remains rather low which requires further optimization of the preparation conditions or modification of the anode composition.

5.3.3. Current-induced activation of anodes

As mentioned in Chapter 4, $Sr(Mn,Nb)O_{3-\delta}$ and $(La,Sr)(Mn,Ti)O_{3-\delta}$-based anodes exhibit an improvement of their electrode activity after polarization cycling. The decrease of the polarization resistance was found to be as high as 35 - 40% for $(La_{0.55}Sr_{0.45})_{0.95}Mn_{0.5}Ti_{0.5}O_{3-\delta}$ anode (Fig. 5.20), which necessitates elucidation of the factors responsible for the improvement. One should note that cathodic current-induced activation has earlier been reported for $(La,Sr)MnO_{3\pm\delta}$-based cathodes, attributable to generation of additional oxygen vacancies at the surface [689, 690] or microstructural effects. In particular, in [691] formation of nanosized pores near the interface electrode/electrolyte after applying the polarization potential of 0.8 V for 3 hours was reported. Jiang et al. [692, 693] detected a transformation of large $(La,Sr)MnO_{3\pm\delta}$ agglomerates into smaller granular-shaped particles with more distinct boundaries taking place at the electrode/gas and electrode/electrolyte interfaces; applying the reverse current did not recover the initial microstructure.

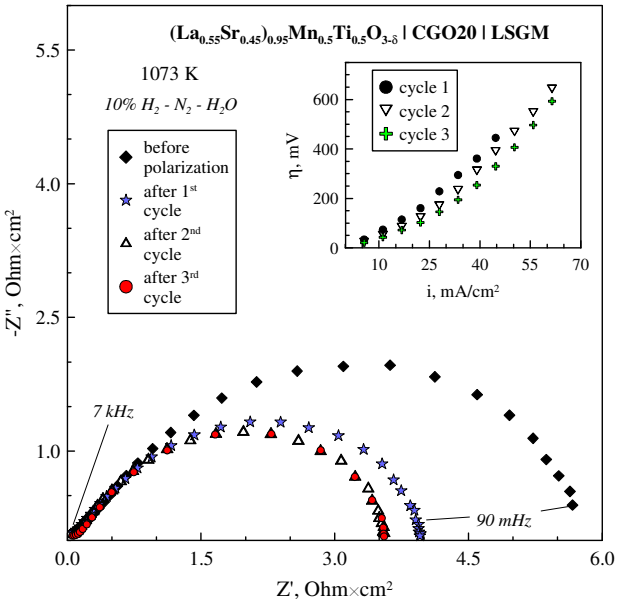

Fig. 5.20. Variations of the impedance spectra (corrected for the Ohmic losses and referred to the electrode area) for $(La_{0.55}Sr_{0.45})_{0.95}Mn_{0.5}Ti_{0.5}O_{3-\delta}$ anode ("*passivated-1473*") applied onto LSGM electrolyte with CGO20 sublayer after polarization cycles. Inset shows corresponding changes in the polarization behaviour

Some variations of the morphology and topography at the interface cathode/electrolyte after polarization were also observed [694]. The activation of (La,Sr)$MnO_{3\pm\delta}$ cathodes might also be related with current-induced dissolution of surface impurities into the perovskite structure; such an improvement might be alternatively caused by preliminary moderate reduction of the cathode or exposure of the surface to dilute acid [311].

In order to elucidate possible microstructural effects on the activation of the electrochemical behaviour of $(La_{0.55}Sr_{0.45})_{0.95}Mn_{0.5}Ti_{0.5}O_{3-\delta}$ anodes, several half-cells composed of "*passivated-1473*" anode layers were fabricated using the technique described in Table 2.4 and subjected to several polarization runs (up to 700 mV) at 1073 K. The electrode morphologies for non-polarized anode layers and after 3 polarization cycles are compared in Fig 5.21.

Although a certain microscopic analysis is complicated due to poor adhesion of pos-tested electrode layers to the electrolyte which does not allow to compare adequately the interface between the cell components, SEM of the non-polarized electrode showed the presence of large agglomerates (up to 15-20 μm) of individual grains (Fig. 5.21 A) which might be responsible for the low electrochemical activity due to their poor percolation, low surface area, etc. After 3 polarization cycles one may observe a substantial reduction of the fraction of agglomerates and an increase of the amount of finer particles (Fig. 5.21 B). Moreover, in the latter case the particle size distribution becomes more uniform, while their form becomes more spherical in comparison with the non-polarized electrode powder, as determined visually. The particles seem to form a more continuous network which ensures a more adequate current collection over the entire electrode layer which might have a great impact on the electrochemical activity, especially taking into account the insufficient electronic conductivity of $(La_{0.55}Sr_{0.45})_{0.95}Mn_{0.5}Ti_{0.5}O_{3-\delta}$ under anode conditions.

At the same time, one should note that the microscopic differences are not distinct, while the polarization effect might be alternatively associated with modifications of the bulk or surface properties of the electrode material. As an assumption, a slight oxidation of the perovskite might induce an enhancement of the electronic conductivity which is stabilized kinetically on subsequent cycles, in accordance with the slow equilibration exhibited by the materials.

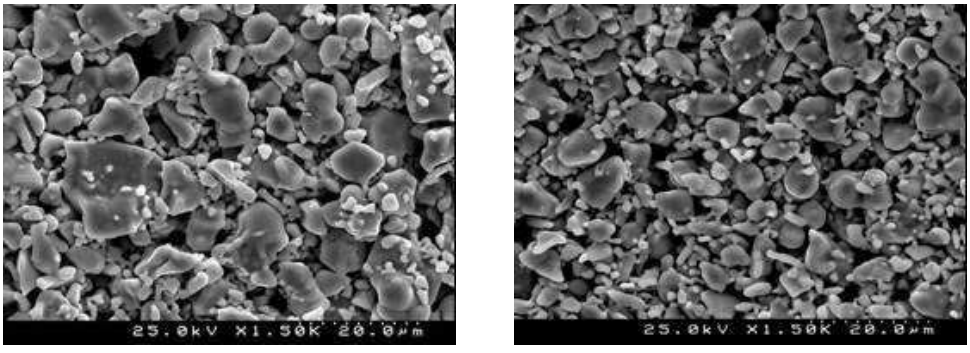

A **B**

Fig. 5.21. SEM micrographs of $(La_{0.55}Sr_{0.45})_{0.95}Mn_{0.5}Ti_{0.5}O_{3-\delta}$ anode powders applied onto LSGM electrolyte with CGO20 sublayer maintained at 1073 K in flowing wet 10% H_2 - N_2 without polarization (A) and after 3 polarization cycles at 300 - 700 mV (B)

5.3.4. Influence of the cation diffusion phenomena on the electrochemical activity. Effect of the solid electrolyte and protective sublayer on the anode behaviour.

Fig. 5.22. represents polarization curves of selected perovskite-based anode materials in contact with apatite and LSGM electrolytes; in both cases a sublayer of CGO20 was applied between the cell components. In accordance with previous studies [591, 594, 660, 661] and with results collected on cermet anodes in Chapter 5.2, the performance of silicate-based electrochemical cells is poor. The same conclusion can be drawn from comparison of the polarization resistance values listed in Tables 5.5 and 5.7. In particular, the polarization resistance of $(La_{0.9}Sr_{0.1})_{0.95}Cr_{0.85}Mg_{0.1}Ni_{0.05}O_{3-\delta}$ which showed the optimum performance among studied perovskite anodes varies in the range 3 - 7 Ohm×cm^2 at 1073 K on the apatite-type electrolyte, as shown in Fig. 5.23. The corresponding values for the same anode obtained on LSGM are as low as 1.0 - 1.5 Ohm×cm^2 (Fig. 5.24).

The effect of the anode material on the polarization behaviour is similar for both electrolytes and qualitatively follows the trends of the electronic conductivity of the corresponding perovskites. The level of the polarization resistance of the perovskite anodes studied is somewhat higher in comparison with earlier reported data (Table 5.5); however, one should note that most previous results have been obtained on mixed-conducting anodes activated by distribution of Pt particles over the electrode surface. This alternatively indicates that the transport and catalytic properties of the anode material have a significant influence on the electrode activity, irrespective of the electrolyte.

Table 5.7. Polarization resistances at zero current and activation energies of the electrode activity at zero current for selected mixed-conducting anodes on apatite-type electrolytes

Electrolyte	Anode	Fuel atmosphere	R_η^{1073} at i = 0, Ohm×cm^2	Activation energy		Reference
				T, K	E_a, kJ/mol	
$La_{10}Si_5AlO_{26.5}$	$(La_{0.55}Sr_{0.45})_{0.95}Mn_{0.5}Cr_{0.3}Ti_{0.2}O_{3-\delta}$ CGO20 sublayer	wet 10% H_2 - N_2	4.0	973 - 1073	81	This work
	$(La_{0.25}Sr_{0.75})_{0.95}Mn_{0.5}Ti_{0.5}O_{3-\delta}$ CGO20 sublayer		12	973 - 1073	92	
	$(La_{0.9}Sr_{0.1})_{0.95}Cr_{0.85}Mg_{0.1}Ni_{0.05}O_{3-\delta}$		22	973 - 1073	67	
	$(La_{0.9}Sr_{0.1})_{0.95}Cr_{0.85}Mg_{0.1}Ni_{0.05}O_{3-\delta}$ CGO20 sublayer		7.0	973 - 1073	120	
	$SrMn_{0.6}Nb_{0.4}O_{3-\delta}$		35	973 - 1073	60	
	$SrMn_{0.5}Nb_{0.5}O_{3-\delta}$		23	973 - 1073	88	
	$SrMn_{0.6}Nb_{0.4}O_{3-\delta}$ CGO20 sublayer		5.6	973 - 1073	170	
$La_{10}Si_{5.5}Al_{0.5}O_{26.75}$	$La_{0.75}Sr_{0.25}Cr_{0.5}Mn_{0.5}O_{3-\delta}$	5% H_2 - Ar	2.0	823 - 1173	110	[566]
$La_{10}Si_{5.5}Al_{0.5}O_{26.75}$	$La_{0.75}Sr_{0.25}Cr_{0.5}Mn_{0.5}O_{3-\delta}$ CGO20 sublayer	5% H_2 - Ar	0.71	823 - 1173	110	[566]
$La_{10}Si_{5.5}Al_{0.5}O_{26.75}$	$Sr_2MgMoO_{6-\delta}$	5% H_2 - Ar	130	873 - 1173	120	[566]
$La_{10}Si_{5.5}Al_{0.5}O_{26.75}$	$Sr_2MgMoO_{6-\delta}$ CGO20 sublayer	5% H_2 - Ar	0.87	823 - 1173	130	[566]
$La_{9.8}Ge_{5.5}Al_{0.5}O_{26.45}$	$La_{0.75}Sr_{0.25}Cr_{0.5}Mn_{0.5}O_{3-\delta}$ CGO10 sublayer	5% H_2 - Ar	2.5	873 - 1073	110	[656]

The results were obtained using Pt mesh (This work), or Pt ink [566, 656] as current collector.

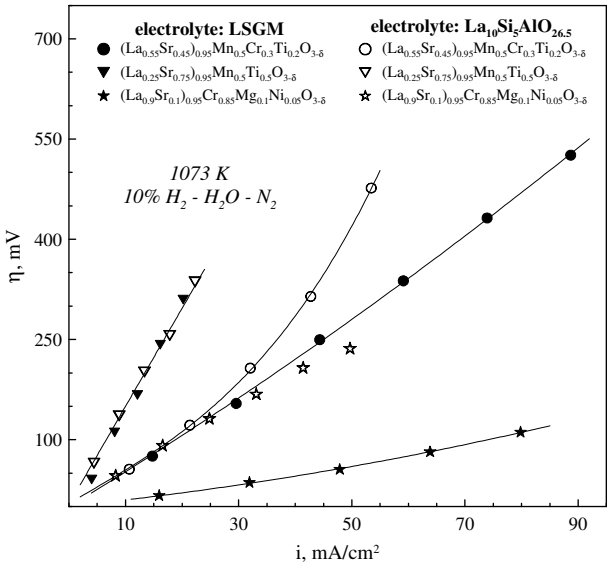

Fig. 5.22. Anodic overpotential vs. current density dependencies for various perovskite-like anode materials applied on LSGM and $La_{10}Si_5AlO_{26.5}$ electrolytes with CGO20 sublayer at 1073 K

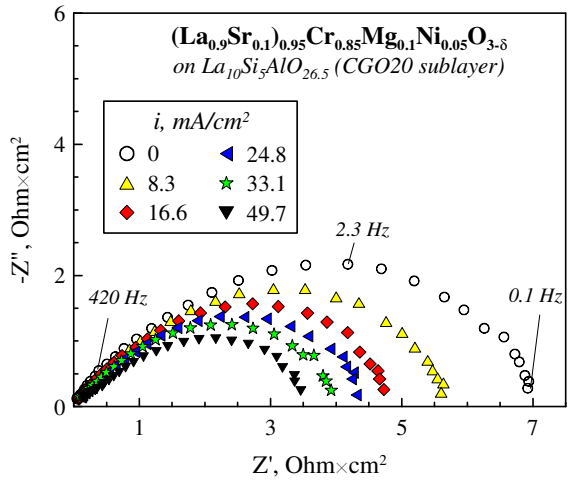

Fig. 5.23. Examples of impedance spectra of $(La_{0.9}Sr_{0.1})_{0.95}Cr_{0.85}Mg_{0.1}Ni_{0.05}O_{3-\delta}$ anode applied onto $La_{10}Si_5AlO_{26.5}$ electrolyte with CGO20 sublayer at 1073 K. The spectra are normalized for the electrode area and corrected for the Ohmic losses

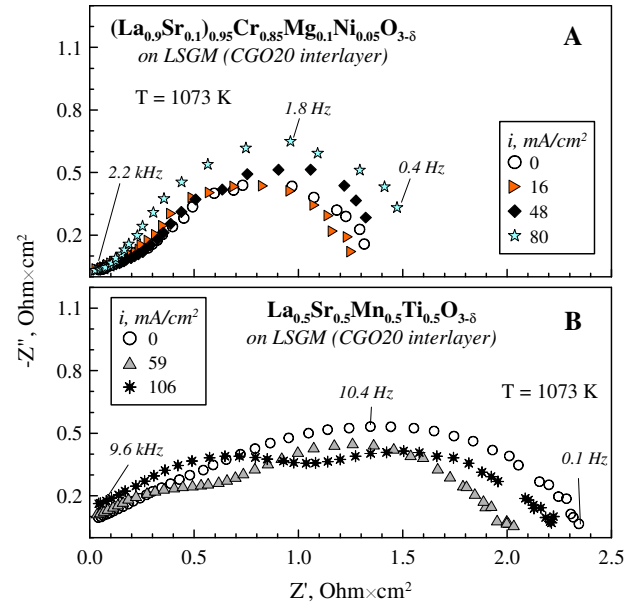

Fig. 5.24. Examples of impedance spectra of $(La_{0.9}Sr_{0.1})_{0.95}Cr_{0.85}Mg_{0.1}Ni_{0.05}O_{3-\delta}$ (A) and $La_{0.5}Sr_{0.5}Mn_{0.5}Ti_{0.5}O_{3-\delta}$ (B) anodes applied onto LSGM electrolyte with CGO20 sublayer at 1073 K. The spectra are normalized for the electrode area and corrected for the Ohmic losses

On the other hand, the maximum difference between the performances of LSGM and $La_{10}Si_5AlO_{26.5}$ electrolyte is observed for more active anode materials, which reflects a strong contribution of additional limitations relevant specifically to the apatite-type materials or related interfaces. One of possible explanations of enhanced activity of the anodes in contact with LSGM might primarily be associated with the transport properties of the electrolyte materials. As observed in numerous studies, the electrode polarization-related parameters show an obvious relationship with the bulk electrolyte resistivity originating from non-uniform current distribution due to discrete contacts between the porous electrodes and solid electrolyte or from an influence of the concentration of ionic and electronic charge carriers at the electrolyte surface on the exchange rate [584, 587, 695-697].

When the surface of the solid electrolyte is exposed to a reducing atmosphere or cation diffusion from the electrode, the enhanced amount of oxygen vacancies may directly contribute into the overall electrochemical process; the latter phenomenon is primarily relevant to $CeO_{2-\delta}$- and $LaGaO_{3-\delta}$-based electrolytes [567, 596, 597]. Another benefit of gallate-based electrolytes may be related with higher contribution of the electronic conductivity in comparison with $La_{10}Si_5AlO_{26.5}$, as shown in Table 5.1. This factor is especially promoted by the dissolution of transition metal cations in the electrolyte matrix, as confirmed by EDS results shown below. Nevertheless, the ionic transport in the electrolyte material cannot be the unique origin of the poor electrochemical characteristics of the cells with $La_{10}Si_5AlO_{26.5}$. For example, relative anodes showed quite acceptable performance in contact with zirconia-based materials [8, 11, 177, 184], contradictive to the trends in the ionic conductivity of the corresponding electrolytes.

As known from the literature [566, 594] and as demonstrated for cermet anodes, a worse activity of the anode applied onto apatite-type electrolyte might relate to segregation and spreading of silica species along the surfaces, grain boundaries of ceramics, interface anode/electrolyte, etc. Analyzing the literature reports on the chemical compatibility between the $La_{10}(SiO_4)_6O_2$-based phases with electrode materials, one may emphasis formation of silicates Sr_2SiO_4 and Nd_2SiO_5 in contact with $(La,Sr)(Co,Fe)O_{3-\delta}$ (annealed at 1173 K) [566] and $Nd_2NiO_{4-\delta}$ (1473 K) [659], respectively. In the latter case, Ni diffusivity caused segregation of additional $La_4Ni_3O_{10+\delta}$ phase. However, most authors indicate that the strong reactivity is generally not typical for apatites in the temperature range corresponding to the cell preparation conditions [566, 591, 594], at least within the uncertainties of XRD analysis.

At the same time, a significant concern is caused by the cation interdiffusion between the cell components; this is especially relevant to migration of Si and La into the electrodes or interlayers or an enrichment of the electrolyte with transition metal or alkali-earth cations. In particular, a low performance and degradation of the electrode properties for $(La,Sr)(Co,Fe)O_{3-\delta}$ [566], $La_{n+1}(Ni,Cu)_nO_{3n+1}$ [591, 594] and $Gd_{0.6}Ca_{0.4}Mn_{0.9}Ni_{0.1}O_{3-\delta}$ [591] cathodes were attributed to the presence of Si in the electrodes detected after the cell preparation or electrochemical tests. Another important issue is associated with La diffusivity resulting from a gradient of the La chemical potential between the cell components. For apatite-type electrolytes, this process is promoted by the presence of La_2O_3-related compounds which often accompany the synthesis process or may be separated due to silica losses [21, 566]. One of concerns relates to penetration of La cations in CeO_2-based phases with formation of $(La,Ce)O_{2-\delta}$ solutions with suppressed transport properties, as has been detected between $La_{10}Si_{5.5}Al_{0.5}O_{26.75}$ and CGO20 at temperatures above

1273 K [566]. Similar to most ionic conductors studied, the apatite structure enables a dissolution of transition metal cations [566, 591, 594, 659]. While in moderate amounts this phenomenon does not seem to be critical, the diffusivity of alkali-earth cations might be undesirable due to a possible decrease of the amount of interstitial oxygen species or formation of $CaO\text{-}SiO_2$ or $SrO\text{-}SiO_2$ blocking layers [591, 698].

Considering the chemical compatibility of gallate electrolytes with electrode materials, one should note that a direct contact of LSGM with materials containing transition metal species, both in metallic or cation state, should be avoided due to a possible cation diffusion and dissolution in the gallate lattice. In particular, penetration of Fe, Co, Ni and to some extent Mn cations into LSGM may induce their substitution for Ga and cause a segregation of $LaSrGa_3O_7$, $LaSrGaO_4$, $LaNiO_{3-\delta}$ or other interfacial phases with poor transport properties [699-703]. Depletion of LSGM with Ga due to the vaporization processes [30, 633], interaction with Pt contacts [581, 633] or Ga diffusion into the electrode phase [700] may also represent a problem in terms of the stability and ionic conduction of the electrolyte material. Large gradients of the chemical potential of La between the cell components may lead to their undesirable enrichment or depletion with La and/or accumulation of the corresponding decompositions products at the interfaces [278, 703]. At the same time, one should note that in the case of adequate fabrication and processing conditions of the cell, the degradation phenomena taking place in LSGM-based cells are not substantial in comparison with those typical for apatite-type electrolytes [21, 594, 659].

In accordance with numerous studies, the problem of the cation diffusivity may be suppressed by preliminary deposition of protective layers onto the electrolyte surface. For this purpose, a wide application has been received by ceria-based layers, preferentially in the porous form in order to provide additional catalytically active centers and extend the electrochemical zone. Table 5.8 represents selected literature data on the effect of the protective layer on the polarization-related parameters of cathodes and anodes. For some electrode/electrolyte couples, the presence of the sublayer reduces the polarization resistance by 1 - 2 orders, although the Ohmic losses may exhibit an increase. This requires reduction of the sublayer thickness down to a definite level (below 5 - 10 μm) which effectively prevents the diffusion processes and provides a minimum Ohmic resistance.

In order to confirm that a contamination of anode layers with silica and/or a possible cation exchange between the cell components are primarily responsible for the electrochemical behaviour observed, the following studies were carried out on the cells composed of similar electrodes/electrolytes; the unique difference being the presence/absence of protective CGO20 sublayer. The electrochemical tests were combined with EDS analysis performed on the layers near the interface. The conditions of the sublayer deposition are described in Chapter 2.

A positive effect of the CGO20 sublayer was demonstrated for anodes/cathodes on LSGM and $La_{10}Si_5AlO_{26.5}$ electrolytes; selected examples of the improved electrochemical behaviour are shown in Fig. 5.25. The improvement was essentially pronounced for Mn- or Cr-enriched perovskites confirming the strong diffusivity of Mn and Cr species, although this phenomenon might be alternatively attributed to enhanced electrochemical activity of the corresponding electrodes and their higher susceptibility towards the modifications.

Table 5.8. Zero-current polarization and series resistance and polarization under 500 mA/cm^2 current of selected electrodes in direct contact with the electrolyte in comparison with similar characteristics obtained with application of CeO_2-based sublayers

Electrode / electrolyte	Sublayer (thickness, μm)	Gas atmosphere or p(O_2), atm	R_η^{1073} or ASR^{1073} Ohm×cm^2	R_s^{1073}, Ohm×cm^2	η^{1073}, mV *(i = 500 mA/cm^2)*	Reference
$La_{0.8}Sr_{0.2}MnO_{3-\delta}$ / $La_{10}Si_{5.5}Al_{0.5}O_{26.75}$	No sublayer	0.21	5.9			[566]
	CGO20 (10 - 15)		0.16			
$La_{0.75}Sr_{0.25}Cr_{0.5}Mn_{0.5}O_{3-\delta}$ / $La_{10}Si_{5.5}Al_{0.5}O_{26.75}$	No sublayer	0.21	3.3			[566]
	CGO20 (10 - 15)		0.61			
$La_{0.8}Sr_{0.2}FeO_{3-\delta}$ / YSZ	No sublayer	0.21	0.34	0.35		[704]
	CGO20 (~6)		0.25	0.52		
$La_{0.6}Sr_{0.4}FeO_{3-\delta}$ / YSZ	No sublayer	0.21	0.26	0.35		[704]
	CGO20 (~6)		0.05	0.25		
$La_{0.6}Sr_{0.4}CoO_{3-\delta}$ / $Zr_{0.81}Sc_{0.18}Ce_{0.01}O_{2-\delta}$	No sublayer	0.21	100			[705]
	CGO10 (2)		1.4			
	CSO20 (>1)		0.04			
$La_{0.6}Sr_{0.4}Co_{0.2}Fe_{0.8}O_{3-\delta}$ / 8YSZ	No sublayer	0.21	120 *(923 K)*	0.61 *(923 K)*		[706]
	CGO20 (~4)		6.2 *(923 K)*	0.82 *(923 K)*		
$La_{0.6}Sr_{0.4}Co_{0.2}Fe_{0.8}O_{3-\delta}$ / $La_{10}Si_{5.5}Al_{0.5}O_{26.75}$	No sublayer	0.21	0.12			[566]
	CGO20 (10 - 15)		4.3×10^{-2}			
Ni-CGO20 (70-30 wt.%) / $La_{10}Si_{5.5}Al_{0.5}O_{26.75}$	No sublayer	wet 5% H_2-Ar	0.59			[566]
	CGO20 (10 - 15)		0.57			
Ni-CSO20 (50-50 vol.%)/ $La_{0.8}Sr_{0.2}Ga_{0.83}Mg_{0.17}O_{3-\delta}$	No sublayer	wet H_2			370	[707]
	CSO20 (~10)				110	
$La_{0.75}Sr_{0.25}Cr_{0.5}Mn_{0.5}O_{3-\delta}$ / $La_{10}Si_{5.5}Al_{0.5}O_{26.75}$	No sublayer	wet 5% H_2-Ar	2.0			[566]
	CGO20 (10 - 15)		0.71			
$La_{0.75}Sr_{0.25}Cr_{0.5}Mn_{0.5}O_{3-\delta}$ impregnated with Cu / $La_{0.8}Sr_{0.2}Ga_{0.83}Mg_{0.17}O_{3-\delta}$	No sublayer	dry H_2			380	[218]
	CLO40				220	
$Sr_2MgMoO_{6-\delta}$ / $La_{10}Si_{5.5}Al_{0.5}O_{26.75}$	No sublayer	wet 5% H_2-Ar	130			[566]
	CGO20 (10 - 15)		0.87			

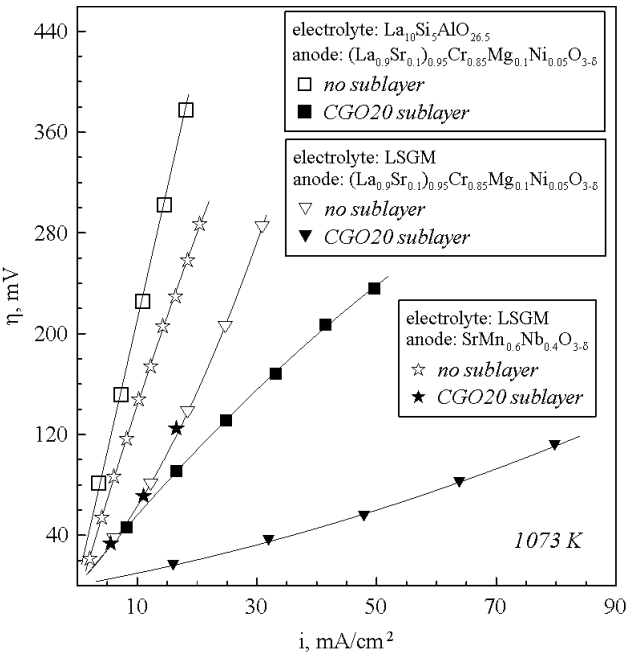

Fig. 5.25. Comparison of polarization curves obtained on $SrMn_{0.6}Nb_{0.4}O_{3-\delta}$ and $(La_{0.9}Sr_{0.1})_{0.95}Cr_{0.85}Mg_{0.1}Ni_{0.05}O_{3-\delta}$ anodes in contact with LSGM electrolyte with and without CGO20 sublayer

In order to check a possible cation exchange, model LSGM - $(La_{0.9}Sr_{0.1})_{0.95}Cr_{0.85}Mg_{0.1}Ni_{0.05}O_{3-\delta}$ and $La_{10}Si_5AlO_{26.5}$ - $(La_{0.9}Sr_{0.1})_{0.95}Cr_{0.85}Mg_{0.1}Ni_{0.05}O_{3-\delta}$ half-cells were prepared by firing in air at 1448 K and the surfaces obtained after fracturing the cell across the interface were examined by SEM/EDS analysis. The experiments were carried out on cells where the electrolyte and electrode layer were subjected to a direct contact or where the protective sublayer was preliminary coated onto the electrolyte. Fig. 5.26 shows the EDS spectra of the apatite and perovskite phases collected in the vicinity (1 - 3 μm) to the interface in comparison with the cation composition of the corresponding phases obtained in more remoted regions where any influence of the cation penetration should be negligible.

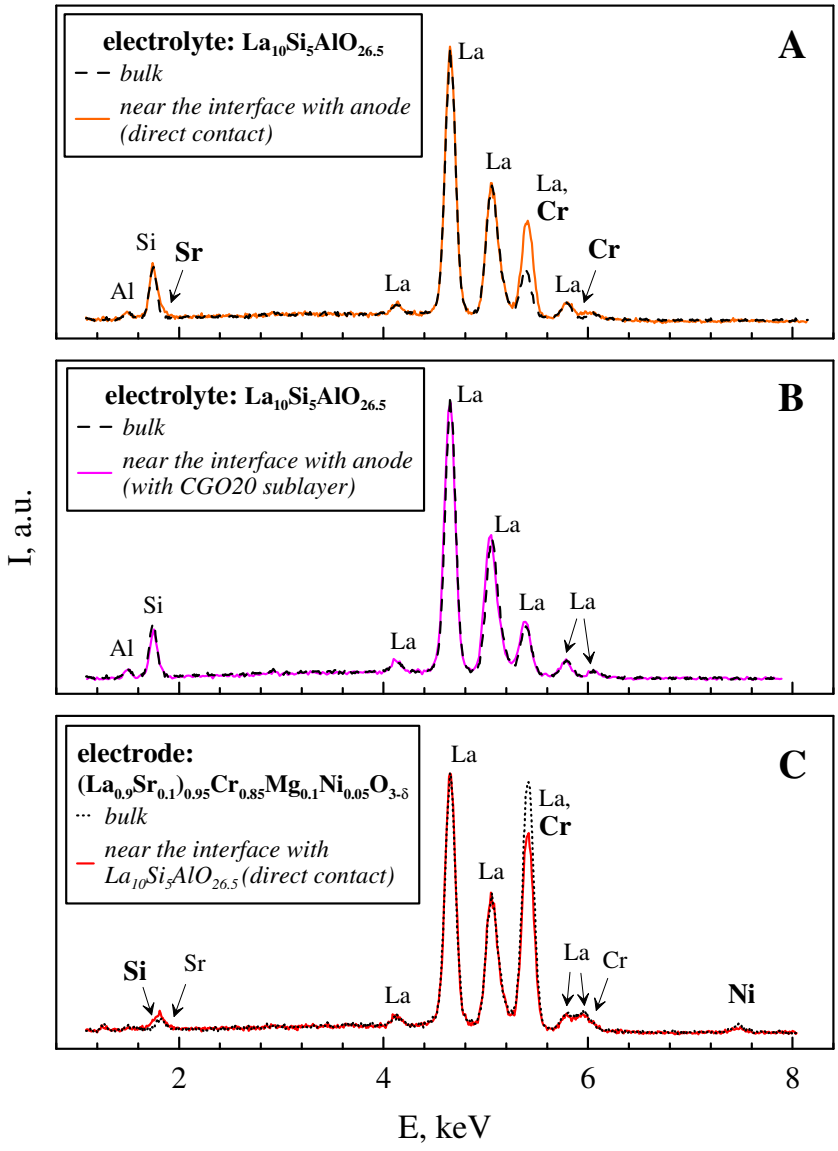

Fig.5.26. EDS spectra of $La_{10}Si_5AlO_{26.5}$ grains (A, B) in the bulk phase and at the interface in direct contact (A) with $(La_{0.9}Sr_{0.1})_{0.95}Cr_{0.85}Mg_{0.1}Ni_{0.05}O_{3-\delta}$ anode and with CGO20 sublayer (B). EDS spectra of $(La_{0.9}Sr_{0.1})_{0.95}Cr_{0.85}Mg_{0.1}Ni_{0.05}O_{3-\delta}$ grains in the bulk phase and at the interface with $La_{10}Si_5AlO_{26.5}$ electrolyte (C).

In the case of the direct contact between the electrode and electrolyte, the most obvious change in the element composition is associated with chromium migration into the apatite phase. As discussed in Chapter 1.2.7, a contamination of cell components with Cr proceeds via bulk/surface diffusion mechanism or involves a participation of volatile $CrO_x(OH)_y$ compositions deposited at the electrolyte surface [82, 83, 285, 288]. As the intensity of the peaks attributable to La and Cr is substantially reduced at the interfacial layers of the electrode, the diffusion mechanism seems to be dominant in the present case, since vaporization-induced chromium losses from the electrode layers contacting with the electrolyte should be comparable or even suppressed in comparison with those at the electrode/gas interface.

Some changes were also found for Ni-related signal. A decrease in its intensity observed for $(La_{0.9}Sr_{0.1})_{0.95}Cr_{0.85}Mg_{0.1}Ni_{0.05}O_{3-\delta}$ phase close to the interface confirms the diffusivity of Ni into the apatite phases, in accordance with [594, 659], although a comparison of the relative depletion of the perovskite with Cr and Ni is complicated due to the low intensity of the Ni peak. No enrichment of the apatite phase with Ni was detected, presumably due to a low Ni content in the parent perovskite. Analysis of Si distribution is complex due to a strong overlapping of Si and Sr peaks. One may observe a change of the symmetry and intensity of the corresponding peak in both contacting phases close to the interface; the character of the changes indicates a possible depletion of the apatite with Si and an enrichment with Sr.

No obvious differences in the cation distribution over the apatite phase were found for the cell containing a protective layer of CGO20 (Fig. 5.26 B) indicating that the differences in the spectra in Fig. 5.26 A and C indeed demonstrate the cation interdiffusion. Although the performance of the cells containing a sublayer applied onto $La_{10}Si_5AlO_{26.5}$ electrolyte is somewhat improved in comparison with analogous cells where the electrode and electrolyte are in the direct contact (Fig. 5.25), the electrochemical activity is still poor. Unfortunately, due to a small thickness and high porosity of the CGO20 layer, no adequate data on the cation distribution over the interface apatite/ceria might be collected from the respective area. In accordance with [566, 594], La and/or Si cations might have a tendency to accumulate in the sublayer or electrolyte layer close to the interface, suppressing the ionic transfer and electrochemical activity.

The results of the elemental analysis, carried out on analogous LSGM-based cells are qualitatively similar to those obtained for the apatite-based cells (Fig. 5.27). In the case of direct contact of LSGM electrolyte with chromite-based electrode, one may observe a strong enrichment of the electrolyte region close to the electrode with Cr and simultaneous reduction of the Cr-related peak on the spectrum of the electrode phase close to the interface in comparison with the bulk (Fig. 5.27 A and C). No presence of Ni species which might be detrimental in terms of the transport properties of the gallate [635, 701] was detected in LSGM phase, although this also might be associated with the small (5%) content of Ni in the electrode phase. Gallium exhibits an accumulation at the electrolyte-contacting layer of the electrode resulted from Ga diffusion or evaporation of Ga-containing species with subsequent deposition.

Application of CeO_2-based sublayer suppresses the interdiffusion between the electrode and LSGM electrolyte; an example is demonstrated in Fig. 5.27 B. No visible differences between the bulk electrolyte phase and the region close to the interface between the cell components were detected, within the uncertainties of the elemental analysis. As for the corresponding changes in the electrode, a certain analysis is complicated due to the porosity of the layer and problems of determination of the distinct boundary between

the CGO20 and $(La_{0.9}Sr_{0.1})_{0.95}Cr_{0.85}Mg_{0.1}Ni_{0.05}O_{3-\delta}$ layers which, in particular, results in appearance of small peaks related to Ce or Gd in the perovskite phase.

As a result of the contamination of the electrode layer with silica and/or cation interdiffusion between the components, the cells containing the apatite as solid electrolyte exhibit a rapid degradation. As shown in Fig. 5.28 A, after exposure of $(La_{0.55}Sr_{0.45})_{0.95}Mn_{0.5}Cr_{0.3}Ti_{0.2}O_{3-\delta}$ anode to polarization cycling under overpotentials of 500 - 800 mV, the polarization and Ohmic resistance exhibit an irreversible increase, equal to~25% and 50%, respectively, despite the presence of the protective CGO20 layer. An application of similar overpotentials on the same cells with LSGM solid electrolyte induces only a ~5% increase of the polarization resistance, without visible changes of the Ohmic losses. One should note that in the latter case the temperature was as high as 1073 K which should promote the degradation processes. The results demonstrate a poor tolerance of the electrochemical cells based on apatite-type electrolytes towards the SOFC operation conditions, in accordance with previously reported data [591, 594, 659-661].

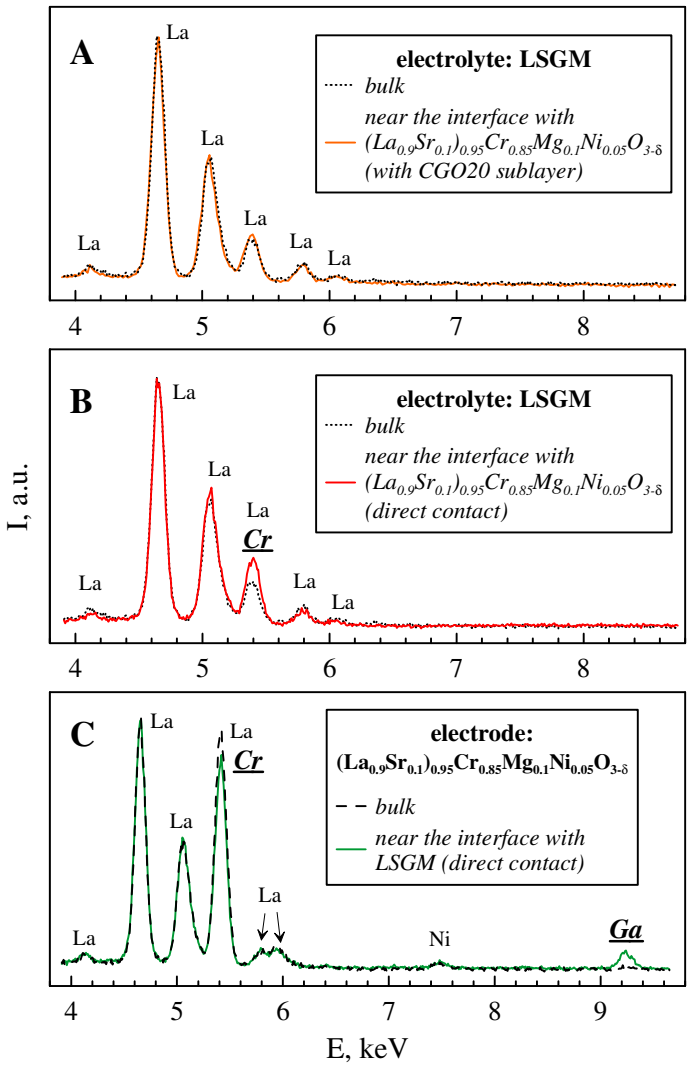

Fig. 5.27. EDS spectra of LSGM grains (A, B) in the bulk phase and at the interface in direct contact (A) with $(La_{0.9}Sr_{0.1})_{0.95}Cr_{0.85}Mg_{0.1}Ni_{0.05}O_{3-\delta}$ anode and with CGO20 sublayer (B). EDS spectra of $(La_{0.9}Sr_{0.1})_{0.95}Cr_{0.85}Mg_{0.1}Ni_{0.05}O_{3-\delta}$ grains in the bulk phase and at the interface with LSGM electrolyte (C).

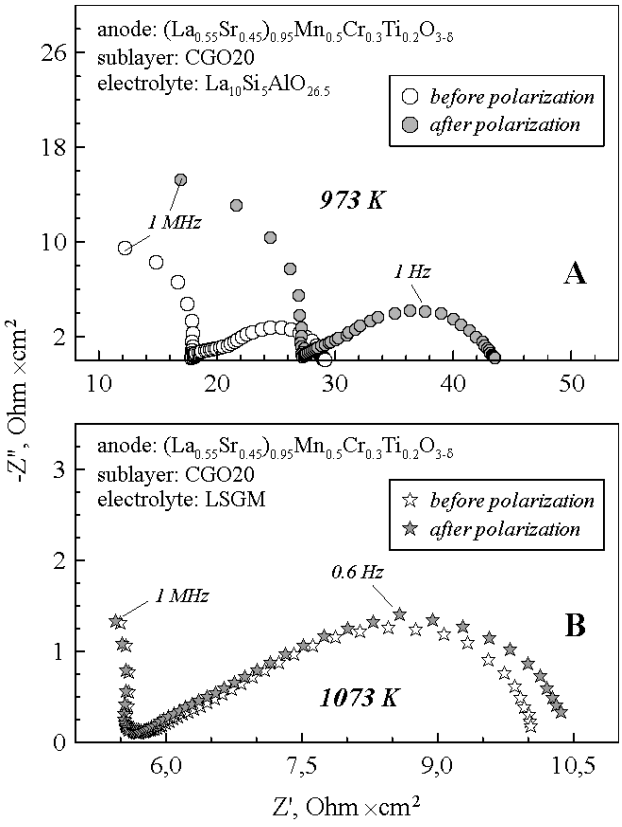

Fig. 5.28. Variations of the impedance spectra of $(La_{0.55}Sr_{0.45})_{0.95}Mn_{0.5}Cr_{0.3}Ti_{0.2}O_{3-\delta}$ in contact with $La_{10}Si_5AlO_{26.5}$ (A), LSGM (B) solid electrolytes and CGO20 sublayer after exposure to anodic overpotentials up to 500 - 800 mV

5.3.5. Impact of infiltrated additives on anode activity

As shown in Table 5.5, the level of the polarization resistance of the perovskite-based anodes exceeds 1 - 2 Ohm×cm^2 at 1073 K which is rather high for electrochemical applications and indicates constrictions related with a non-adequte current collection or insufficient electrocatalytic activity. In order to improve the performances, subsequent optimization steps are required; one of those relates to wet impregnation of the anode layer with catalytically-active additions such as $CeO_{2-\delta}$ and Ni. Fig. 5.29 demonstrates the effect of $CeO_{2-\delta}$ and Ni additions into selected anode layer on their electrochemical behaviour, while the microstrucutures of modified layers are shown in Fig. 5.30. In particular, Figs. 5.30 G, H represent formation of submicron ceria particles inside the porous structure of $SrMn_{0.6}Nb_{0.4}O_{3-\delta}$ anodes.

Impregnation of Ni-containing solutions into the porous $(La_{0.9}Sr_{0.1})_{0.95}Cr_{0.85}Mg_{0.1}Ni_{0.05}O_{3-\delta}$ layer did not demonstrate a substantial activating effect indicating that the amount and distribution of the Ni metallic particles separated from the perovskite lattice at low $p(O_2)$ is close to the optimum level and further additions of Ni is non-effective. On the other hand, the performance may be substantially improved by infiltration of ceria particles into the anode, yielding the current densities as high as ~55 and ~140 mA/cm^2 at 973 K and 1073 K, respectively, under the anodic overpotential of 80 mV (Fig.5.29).

The preferential incorporation of $CeO_{2-\delta}$ phase in comparison with Ni, combined with the reasonable performance observed for "pure" layer of $(La_{0.9}Sr_{0.1})_{0.95}Cr_{0.85}Mg_{0.1}Ni_{0.05}O_{3-\delta}$ allows to suggest that the material possesses a satisfactory electronic conductivity and catalytic activity towards hydrogen oxidation

required for an adequate anode activity, while the ionic transport-related parameters, in particular, the surface concentration of the oxygen vacancies are insufficient; this problem may be overcome by the distribution of ceria particles over the anode surface. In contrast, the low electronic and ionic conductivity as well as poor electrocatalytic activity of representatives of $(La_{1-x}Sr_x)_{0.95}Mn_{0.5}Cr_{1-x}Ti_xO_{3-\delta}$ or $Sr(Mn,Nb)O_{3-\delta}$ series makes it possible to optimize the performance via incorporation of both $CeO_{2-\delta}$ and Ni phases.

The activating effect is similar to additions of praseodimia phase into cathode layers demonstrated in Chapters 3.1.7 and 3.3.3. A positive influence of the wet impregnation or other techniques of incorporating the catalytically-active species has been demonstrated in numerous studies [7, 107, 266, 352, 365, 567]; with respect to the electrode layers studied in the present work, the effect may primarily relate to microstructural optimization, enhanced electrode surface area and TPB, promotion of the transport properties and the catalytic activity of the electrode material, etc.

Considering that the wet impregnation may provide a sufficient and uniform distribution of the electrochemically-active components over the anode layer utilizing comparatively small quantities of the precursors, this approach may also be regarded to be beneficial in terms of reducing the costs of the electrode materials and fabrication techniques in comparison with many other methods of the deposition of the electrode layers, if related to the same power output of the electrochemical cells. However, introduction of dissolved cations into the electrode layers requires an additional high-temperature step which may cause microstructural or thermomechanical problems after thermal/redox cycling. With this respect, preliminary introduction of the electrochemically active components into the oxide matrix and subsequent in-situ generation of the electrochemically active sites might be more beneficial, as shown for $(La_{0.9}Sr_{0.1})_{0.95}Cr_{0.85}Mg_{0.1}Ni_{0.05}O_{3-\delta}$ perovskite in the present study and for Ni- or Ru-doped analogues in literature [15, 186, 544].

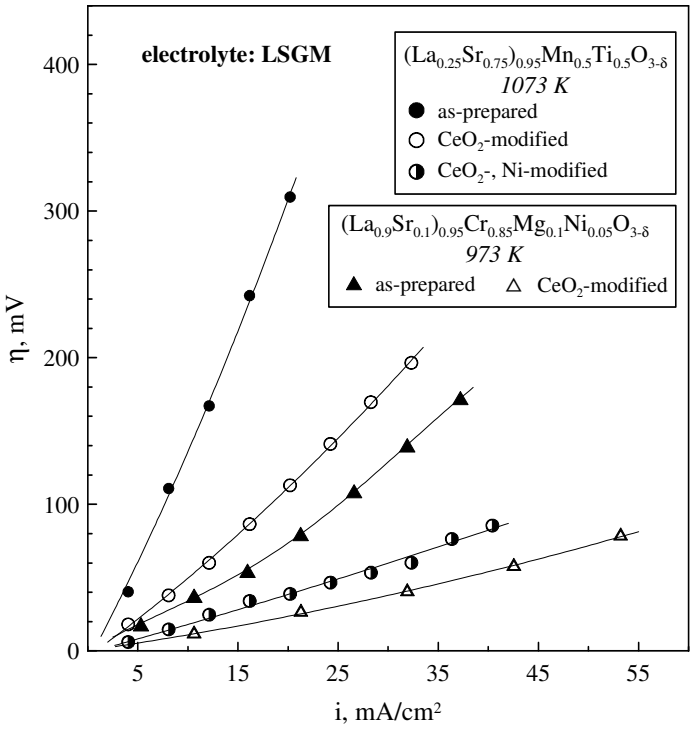

Fig. 5.29. Polarization curves obtained on $(La_{0.9}Sr_{0.1})_{0.95}Cr_{0.85}Mg_{0.1}Ni_{0.05}O_{3-\delta}$ and $(La_{0.25}Sr_{0.75})_{0.95}Mn_{0.5}Ti_{0.5}O_{3-\delta}$ anodes in contact with LSGM electrolyte and CGO20 sublayer before and after the impregnation with $CeO_{2-\delta}$ and Ni

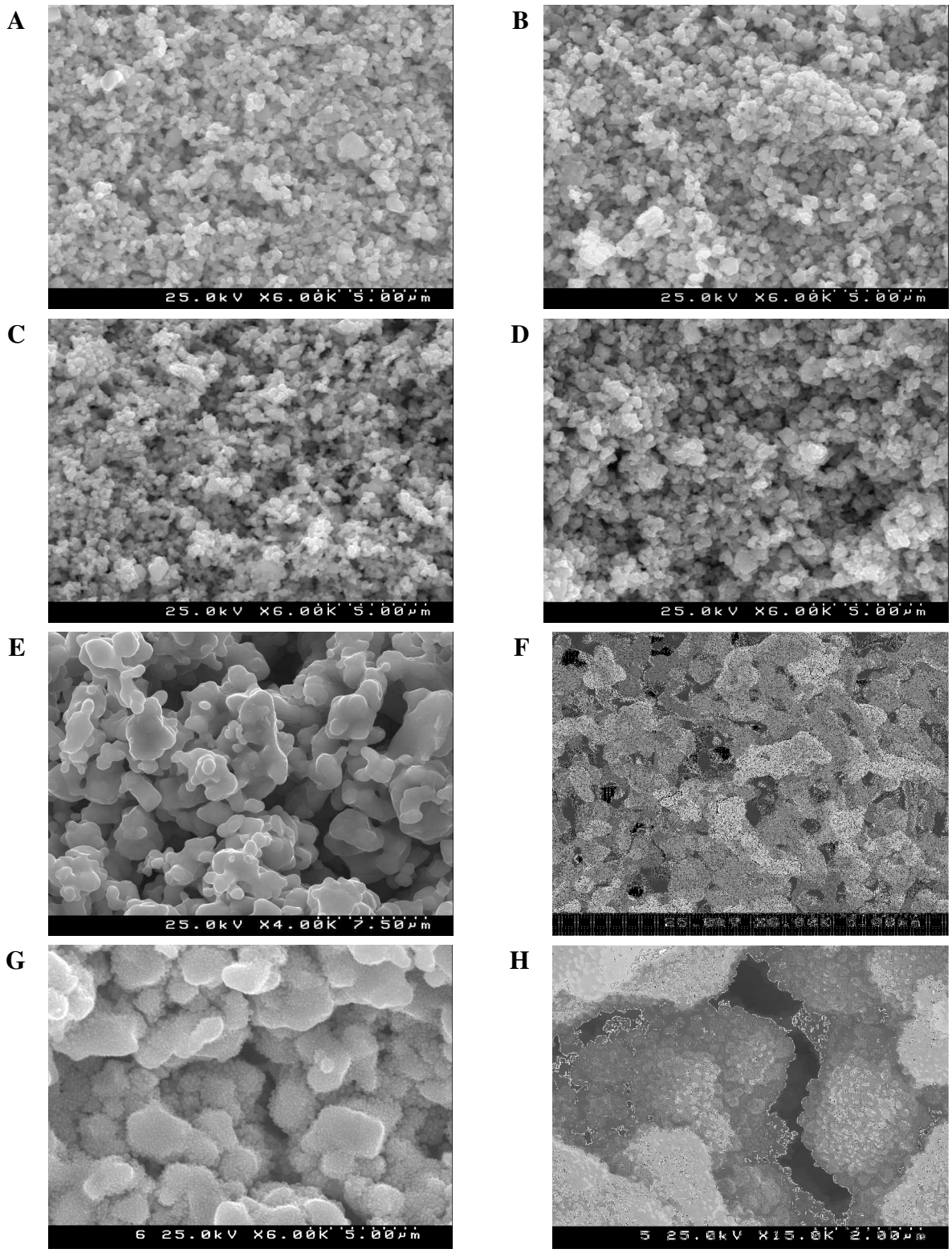

5.30. SEM micrographs of $(La_{0.9}Sr_{0.1})_{0.95}Cr_{0.85}Mg_{0.1}Ni_{0.05}O_{3-\delta}$ (non-modified (A), PrO_x-modified (B), $CeO_{2-\delta}$-modified (C), $CeO_{2-\delta}$- and Ni-modified (D)) and $SrMn_{0.6}Nb_{0.4}O_{3-\delta}$ (non-modified (E), PrO_x-modified (F), $CeO_{2-\delta}$- and Ni-modified (G, H)) electrode layers

5.4. Final remarks

The results obtained on electrochemical cells with gallate- and silicate-based solid electrolytes show that irrespective of their comparable and reasonably high ionic conductivity, the electrochemical performances of the anodes on these electrolytes is quite different. This indicates that the activity is primarily determined by the tolerance of the electrolyte material towards the environmental conditions and compatibility with the electrodes rather than by intrinsic transport properties of the electrolyte composition. In particular, a strong effect of cation interdiffusion was observed, less pronounced at the presence of protective CGO20 layer. With respect to the behavior observed, a serious degradation of the electrochemical properties occurs due to contamination of the electrode surface, catalytically-active sites, etc. with silica in the case of apatite-type electrolyte.

The electrode activity of perovskite-like anodes correlates with the low-p(O_2) electronic conductivity and chemical expansivity of the corresponding materials on redox cycling. Nevertheless, the correlation is not strictly linear and shows significant deviations if comparing the electrochemical properties of various perovskite groups. This indicates that some other factors such as the surface gas exchange kinetics or oxygen vacancy diffusion may be responsible for the anode activity.

The performance of both cermet and perovskite-like electrodes might be considerably improved by infiltration of catalytically active ceria or nickel particles into the electrode layer. The effect is especially pronounced for $CeO_{2-\delta}$ introduction indicating the limitations associated with the catalytic activity of the perovskite anodes or surface vacancy concentration. Nevertheless, even for the most active anodes the performance was obtained insufficient for practical applications. This indicates the necessity of subsequent optimization of the functional characteristics of the electrode and electrolyte materials or cell preparation procedure.

Conclusions

The study was focused on the development of cathode and anode materials based on perovskite-like chromite, manganite and titanate materials. The task indicated involved evaluation of phase and structural relationships, transport, thermomechanical and electrochemical characteristics of the oxide materials studied. Another purpose was related with determination of the principal performance-determining factors and search of approaches allowing to optimize the performance of the electrochemical cells considered. Based on the results obtained, the following conclusion can be drawn from the study:

1. In perovskites $(La_{0.75-x}Sr_{0.25+x})_{0.95}Mn_{0.5}Cr_{0.5-x}Ti_xO_{3-\delta}$ titanium may partially or completely substitute for chromium cations provided that the doping is accompanied by introduction of the equivalent amount of Sr into A-sublattice. The phase and structural stability as well as the transport and electrochemical properties under oxidizing conditions are quite tolerant towards the substitution. Enhanced generation of the oxygen vacancies upon redox cycling, more pronounced for Sr- and Ti-enriched compositions, leads to larger thermal and chemical expansion. However, the main drawback related with the introduction of Sr and Ti refers to the strong drop of the electronic conductivity under the anode conditions resulting in a worse electrochemical behavior.

2. $(La_{0.75}Sr_{0.25})_{0.95}Cr_{1-x}Fe_xO_{3-\delta}$ perovskites possess an enhanced ionic conduction under reducing conditions as compared with most chromite-based materials, which might to some extent be responsible for their promising anode activity. Nevertheless, the electronic conductivity seems have a more pronounced influence on the electrode properties, taking into account the correlation between the low-$p(O_2)$ conductivity and anode performance for the compositions with various Fe content.

3. Insufficient solubility of Ni in $(La_{0.9}Sr_{0.1})_{0.95}Cr_{0.85}Mg_{0.1}Ni_{0.05}O_{3-\delta}$ perovskite and/or the presence of the impurity (Ni,Mg)O ensures the separation of metallic Ni nano-sized particles which promote an enhanced electrochemical performance of the corresponding anodes.

4. Doping $(La_{1-x}Sr_x)_{1-y}Mn_{0.5}Ti_{0.5}O_{3-\delta}$ and $SrMn_{1-x}Nb_xO_{3-\delta}$ with donor-like cations improves their tolerance towards reduction. However, lower concentration of p-type charge carriers in La- and Nb-enriched compositions, respectively, significantly deteriorates their electronic conduction. As a result, the perovskites $SrMn_{1-x}Nb_xO_{3-\delta}$ showed poor cathodic and anodic performance, while the anode based on $La_{0.5}Sr_{0.5}Mn_{0.5}Ti_{0.5}O_{3-\delta}$ oxide, moderately doped with donor-like cations, exhibited an adequate activity without additional modifications. One should note that La-enriched $(La_{1-x}Sr_x)_{0.95}Mn_{0.5}Ti_{0.5}O_{3-\delta}$ (x = 0.75 - 0.85) are characterized by the phase transitions and slow equilibration kinetics upon variations of the oxygen nonstoichiometry resulting in a strong hysteresis, degradation of the transport properties and ceramics integrity which restricts their applicability as anodes.

5. Despite the sufficient and comparable level of the ionic conductivity in LSGM and $La_{10}Si_5AlO_{26.5}$, which exceeds that in ZrO_2-based materials, the electrochemical characteristics of the cells composed of the corresponding electrolytes are substantially different. This indicates that the electrode activity is primarily governed by the stability of the electrolyte material under operation conditions and the compatibility between the cell components. The performance of anodes applied onto the apatite-type electrolyte is poor, presumably owing to the contamination with silica and resultant blocking of the electrochemically-active sites. The

electrode properties may be to some extent optimized by compositional or microstructural modifications, in particular, by impregnation with solutions of catalytically-active species, however the activity still remains inadequate, especially in terms of the long-term performance.

6. The electrochemical behavior is significantly affected by the cation interdiffusion between the cell components, especially in the case of the direct contact, without the application of protective layers. Although the cation exchange is typical for the cells containing both gallate- and silicate-based electrolytes, in the latter case the influence of diffusion on the electrochemical characteristics is more critical. The interdiffusion and interaction phenomena can be reduced by utilization of CeO_2-based sublayer between the electrolyte and electrode rendering an improvement of the electrochemical properties. In particular, the polarization resistance of some perovskite-based anodes may be diminished down to 1 - 1.5 Ohm×cm^2 at 1073 K under zero current.

7. The activity of most perovsite-based anodes generally correlates with the electronic conductivity trends, consistently with the insufficient hole transport under the operation conditions. Another factor that apparently affets the electrochemical properties relates to the chemical expansivity of the anode material on redox cycling. On the other hand, the correlation is not strict and one may observe deviations between various compositional series which indicates the effect of other factors such as surface exchange kinetics, oxygen diffusion-related parameters, etc.

8. The electrode activity may be improved by introducing catalytically-active agents such as $CeO_{2-\delta}$ and/or Ni (for anodes) and PrO_x (for cathodes). The most pronounced effect is observed upon addition of ceria into the anode layer which suggests the electrode limitations associated with the catalytic activity of the perovskites studied, surface concentration of oxygen vacancies, etc. Despite the improvement, the electrode performance still remains on the level, insufficient for practical utilization which requires further optimization of the electrode preparation proceduce, selection of the functional materials, etc.

9. For $La_{10}Si_5AlO_{26.5}$-based electrochemical cells a substantial raise of the ohmic and polarization losses was observed. The degradation was especially pronounced at a large (>500 mV) anode polarization. The electrodes in contact with LSGM electrolyte possess a higher stability, while some manganite-based anode exhibit an improvement in terms of the activity after polarization cycling. However, thermal cycles cause an enlargement of both ohmic and polarization resistance which necessitates an optimization of the contact between the cell components.

List of references

1. J.B. Goodenough, Y.B. Huang, J. Power Sources 173 (2007) 1

2. N.Q. Minh, J. Amer. Ceram. Soc. 76 (1993) 563

3. V. Kharton (Ed.), Solid State Electrochemistry. I. Fundamentals, Materials and their Applications, Wiley-VCH, Weinheim, 2009.

4. B.C.H. Steele, Solid State Ionics 86 (1996) 1223

5. B.C.H. Steele, Solid State Ionics 134 (2000) 3

6. N.Q. Minh, T. Takahashi, Science and Technology of Ceramic Fuel Cells, Elsevier, Amsterdam, 1995

7. S.P. Jiang, S.H. Chan, J. Mater. Sci. 39 (2004) 4405

8. S. Tao, J.T.S. Irvine, J. Electrochem. Soc. 151 (2004) A252

9. J. Pena-Martinez, D. Marrero-Lopez, D. Perez-Coll, J.C. Ruiz-Morales, P. Nunez, Electrochim. Acta. 52 (2007) 2950

10. V.V. Kharton, E.V. Tsipis, I.P. Marozau, A.P. Viskup, J.R. Frade, J.T.S. Irvine, Solid State Ionics 178 (2007) 101

11. B.D. Madsen, S.A. Barnett, J. Electrochem. Soc. 154 (2007) B501

12. A. Ovalle, J.C. Ruiz-Morales, J. Canales-Vazquez, D. Marrero-Lopez, J.T.S. Irvine, Solid State Ionics 177 (2006) 1997

13. Q. Fu, F. Tietz, D. Sebold, S. Tao, J.T.S. Irvine, J. Power Sources 171 (2007) 663

14. E.V. Tsipis, V.V. Kharton, J. Solid State Electrochem. 15 (2011) 1007

15. W. Kobsiriphat, B.D. Madsen, Y. Wang, L.D. Marks, S.A. Barnett, Solid State Ionics 180 (2009) 257

16. Q.X. Fu, F. Tietz, D. Stoever, J. Electrochem Soc. 153 (2006) D74

17. J. Sfeir, P.A. Buffat, P. Mockli, N. Xanthopoulos, R. Vasquez, H.J. Mathieu, J. van Herle, K. Ravindranathan Thampi, J. Catal. 202 (2001) 229

18. M. Gong, D. Bierschenk, J. Haag, K.R. Poeppelmeier, S.A. Barnett, C. Xu, J.W. Zondlo, X. Liu, J. Power Sources 195 (2010) 4013

19. S. Tao, J.T.S. Irvine, Solid State Ionics 154 (2002) 659

20. S. Tao, J.T.S. Irvine, J. Mater. Chem. 12 (2002) 2356

21. A.L. Shaula, V.V. Kharton, F.M.B. Marques, Solid State Ionics 177 (2006) 1725

22. H. Arikawa, H. Nishiguchi, T. Ishihara, Y. Takita, Solid State Ionics 135 (2000) 31

23. A.L. Shaula, V.V. Kharton, J.C. Waerenborgh, D.P. Rojas, F.M.B. Marques, J. Eur. Ceram. Soc. 25 (2005) 2583

24. E.J. Abram, D.C. Sinclair, A.R. West, J. Mater. Chem. 11 (2001) 1978

25. Yu. D. Tretyakov, Chemistry of Nonstoichiometric Oxides, Moscow State University, Moscow 1974 (in Russian)

26. P. Kofstad, Nonstoichiometry, Diffusion and Electrical Conductivity in Binary Metal Oxides, Wiley, NY 1972

27. Solar Atmospheres Inc., Critical Melting Points and Reference Data for Vacuum Heat Treating, Vacuum furnace Redferences Series, №1, V. Osterman, H. Antes (Eds.), Solar Atmospheres Inc., PA 2011
28. R.C. Paule, J. Mandel, Analysis of Interlaboratory Measurements of Vapor Pressure of Cadmium and Silver, Butterworths, London, 1972
29. R.H. Lamoreaux, D.L. Hildenbrand, L. Brewer, J. Phys. Chem. Ref. Data 16 (1987) 419
30. V.V. Kharton, F.M.B. Marques, A. Atkinson, Solid State Ionics 174 (2004) 135
31. B.C.H. Steele, J. Mater. Sci. 36 (1997) 1053
32. M. Suzuki, H. Sasaki, S. Otoshi, A. Kajimura, M. Ippommatsu, Solid State Ionics 62 (1993) 125
33. J. Mizusaki, H. Tagawa, K. Isobe, M. Tajika, I. Koshiro, H. Maruyama, K. Hirano, J. Electrochem. Soc. 141 (994) 1674
34. A. Cantos-Gomez, R. Ruiz-Bustos, J. van Duijn, Fuel Cells 11 (2011) 140
35. V. Roche, R. Karoum, A. Billard, R. Revel, P. Vernoux, J. Appl. Electrochem. 38 (2008) 1111
36. K. Christman, G. Ertl, T. Pignet, Surf. Sci. 54 (1976) 365
37. F.A. Lewis, Platinum Metals Rev. 26 (1982) 20
38. H.E. Bennett, Platinum Metals Rev. 5 (1961) 132
39. W. Hahn, A. Muan, Amer. J. Sci. 258 (1960) 66
40. A.Z. Hed, D.S. Tannhauser, J. Electrochem. Soc. 114 (1967) 314
41. Yu.D. Tretjakow, H. Schmalzried, Ber. Buns. Phys. Chem. 69 (1965) 396
42. C.N.R. Rao, G.V. Subba Rao, Transition Metal Oxides: Crystal Chemistry, Phase Transitions and Related Aspects, U.S. Government Printing Office, Washington 1974
43. I.A. Vasil'eva, E. Yu. Shaulova, Zhurnal Fizicheskoy Khimii 43 (1969) 3047 (in Russian)
44. J. Sfeir, J. Power Sources 118 (2003) 276
45. T. Atsumi, T. Ohgushi, N. Kamegashira, J Alloys Compnd. 238 (1996) 35
46. T. Nakamura, G. Petzow, L.J. Gauckler, Mater. Res. Bull. 14 (1979) 649
47. T. Katsura, K. Kitayama, T. Sugihara, N. Kimizuka, Bull. Chem. Soc. Jpn. 48 (1975) 1809
48. M.V. Patrakeev, I.A. Leonidov, V.L. Kozhevnikov, V.V. Kharton, Solid State Sci. 6 (2004) 907
49. A.N. Petrov, V.A. Cherepanov, A.Yu. Zuev, J. Solid State Electrochem. 10 (2006) 517
50. D.E. Rice, D.J. Buttrey, J Solid State Chem. 105 (1993) 197
51. M. Wakihara, T. Katsura, Metal. Trans. 1 (1970) 363
52. H. Okinaka, K. Kosuge, S. Kachi, Trans. Jap. Inst. Metals 12 (1971) 44
53. S. Zador, C.B. Alcock, J. Chem. Thermodynamics 2 (1970) 9
54. R.A. Rapp, Trans. Met. Soc. AIME 227 (1963) 371
55. F.E. Rizzo, L.R. Bidwell, D.F. Frank, Trans. Met. Soc. AIME, 239 (1967) 1901
56. W.L. Worrell, Thermodynamics, Vienna, IAEA, 1 (1966) 131
57. I.M. Robertson, H.K. Birnbaum, Acta Metall. 34 (1986) 353
58. T. Tabata, H. Birnbaum, Scr. Metall. 17 (1983) 947
59. A. Pundt, R. Kirchheim, Annu. Rev. Mater. Res. 36 (2006) 555
60. J.A. Crawford, R.W. West, J. Appl. Phys. 35 (1964) 2413
61. M.S. Seltzer, Z.E. Hed, J. Electrochem. Soc. 177 (1970) 815

62. B. Fisher, D.S. Tannhauser, J. Chem. Phys. 44 (1966) 1963
63. I. Rom, W. Jantscher, W. Sitte, Solid State Ionics 135 (2000) 731
64. P. Ochin, C. Petot, G. Petot-Ervas, Solid State Ionics 12 (1984) 135
65. E.H. Greener, D.H. Whitmore, M.E. Fine, J. Chem. Phys. 34 (1961) 1017
66. J.F. Marucco, J. Chem. Phys. 70 (1979) 649
67. J.E. Stroud, W.C. Tripp, J.M. Wimmer, J. Amer. Ceram. Soc. 57 (1974) 172
68. J.P. Bonnet, E. Marquastant, M. Onillon, Mater. Res. Bull. 12 (1977) 361
69. K. Naito, T. Matsui, Solid State Ionics 12 (1984) 125
70. S. Gahr, M.L. Grossbeck, H.K. Birnbaum, Acta Metall. 25 (1977) 125
71. C.V. Owen, T.E. Scott, Metall. Trans. 3 (1972) 1715
72. V.V. Kharton, F.M. Figueiredo, L. Navarro, E.N. Naumovich, A.V. Kovalevsky, A.A. Yaremchenko, A.P. Viskup, A. Carneiro, F.M.B. Marques, J.R. Frade, J. Mater. Sci. 36 (2001) 1105
73. O.A. Marina, C. Bagger, S. Primdahl, M. Mogensen, Solid State Ionics 123 (1999) 199
74. H. Tu, H. Apfel, U. Stimming, Fuel Cells 6 (2006) 303
75. H. Inaba, H. Tagawa, Solid State Ionics 83 (1996) 1
76. A. Atkinson, A. Selcuk, Solid State Ionics 134 (2000) 59
77. K. Sato, H. Yugami, T. Hashida, J. Mater. Sci. 39 (2004) 5765
78. P.J. Meschter, E.J. Opila, N.S. Jacobson, Annu. Rev. Mater. Res. 43 (2013) 41
79. D.M. Chapman, Appl. Catal. A 392 (2011) 143
80. S.S. Lin, J. Electrochem. Soc. 127 (1980) 1108
81. M. Farber, O.M. Uy, R.D. Srivastava, J. Chem. Phys. 56 (1972) 5312
82. K. Hilpert, D. Das, M. Miller, D.H. Peck, R. Weiss, J. Electrochem. Soc. 143 (1996) 3642
83. S. Taniguchi, M. Kadowaki, H. Kawamura, T. Yasuo, Y. Akiyama, Y. Miyake, T. Saitoh, J. Power Sources 55 (1995) 73
84. S.P. Jiang, J.P. Zhang, X.G. Zheng, J. Eur. Ceram. Soc. 22 (2002) 361
85. S.C. Paulson, V.I. Birss, J. Electrochem. Soc. 151 (2004) A1961
86. N. Kamegashira, T. Matsui, M. Harada, K. Naito, J. Nucl. Mat. 101 (1981) 207
87. C. Sun, U. Stimming, J. Power Sources 171 (2007) 247
88. V.V. Kharton, A.A. Yaremchenko, E.N. Naumovich, F.M.B. Marques, J. Solid State Electrochem. 4 (2000) 243
89. V.V. Kharton, E.N. Naumovich, A.A. Vecher, J. Solid State Electrochem. 3 (1999) 61
90. A. Holt, P. Kofstad, Solid State Ionics 117 (1999) 21
91. A. Lashtabeg, J.C. Ruiz-Morales, J.T.S. Irvine, J.L. Bradley, Chem. Mater. 21 (2009) 3549
92. C.M. Reich, A. Kaiser, J.T.S. Irvine, Fuel Cells 1 (2001) 249
93. L. Mogni, F. Prado, A. Caneiro, A. Manthiram, Solid State Ionics 177 (2006) 1807
94. M. Al Daroukh, V.V. Vashook, H. Ullmann, F. Tietz, I.A. Raj, Solid State Ionics 158 (2003) 141
95. T. Ishihara, S. Fukui, M. Enoki, H. Matsumoto, J. Electrochem. Soc. 153 (2006) A2085
96. P.R. Slater, J.T.S. Irvine, Solid State Ionics 120 (1999) 125
97. P.R. Slater, J.T.S. Irvine, Solid State Ionics 124 (1999) 61

98. J.L. Kaiser, P.R. Bradley, J.T.S. Irvine, Solid State Ionics, 135 (2000) 519
99. C. Jin, Z. Yang, H. Zheng, C. Yang, F. Chen., Electrochem. Commun. 14 (2012) 75
100. L. Adijanto, R. Kungas, J. Park, J.M. Vohs, R.J. Gorte, Int. J. Hydrogen Energy 36 (2011) 15722
101. S. Wang, Y. Jiang, Y. Zhang, W. Li, J. Yan, Z. Lu, Solid State Ionics 120 (1999) 75
102. D.M. Flot, J.T.S. Irvine, Solid State Ionics 135 (2000) 513
103. M. Mori, Y. Hiei, H. Itoh, G.A. Tompsett, N.M. Sammes, Solid State Ionics 150 (2003) 1
104. S. Boulfrad, M. Cassidy, J.T.S. Irvine, Solid State Ionics 197 (2001) 37
105. O.A. Marina, N.L. Canfield, J.W. Stevenson, Solid State Ionics 149 (2002) 21
106. T. Shimura, K. Suzuki, H. Iwahara, Solid State Ionics 113 (1998) 355
107. E.V. Tsipis, V.V. Kharton, J.R. Frade, J. Eur. Ceram. Soc. 25 (2005) 2623
108. V.V. Kharton, E.V. Tsipis, A.A. Yaremchenko, N.P. Vyshatko, A.L. Shaula, E.N. Naumovich, J.R. Frade, J. Solid State Electrochem. 7 (2003) 468
109. C. Navas, H. K. zur Loye, Solid State Ionics 93 (1997) 171
110. E.V. Tsipis, V.V. Kharton, N.P. Vyshatko, A.L. Shaula, J.R. Frade, J Solid State Chem. 176 (2003) 47
111. A. Aguadero, C. de la Calle, J.A. Alonso, D. Perez-Coll, M.J. Escudero, L. Daza, J. Power Sources 192 (2009) 78
112. M. Mori, T. Yamamoto, H. Itoh, T. Watanabe, J. Mater. Sci. 32 (1997) 2423
113. S.M. Plint, P.A. Connor, S. Tao, J.T.S. Irvine, Solid State Ionics 177 (2006) 2005
114. M.V. Patrakeev, J.A. Bahteeva, E.B. Mitberg, I.A. Leonidov, V.L. Kozhevnikov, K.R. Poeppelmeier, J. Solid State Chem.172 (2003) 219
115. P.Y. Hou, J. Stringer, Mater. Sci. Eng. A 202 (1995) 1
116. B. Ma, U. Balachandran, Mater. Res. Bull. 33 (1998) 223
117. L. Aguiar, S. Zha, Z. Cheng, J. Winnick, M. Liu, J. Power Sources 135 (2004) 17
118. J.C. Fischer II, S.S.C. Chuang, Catal. Commun. 10 (2009) 772
119. S.A. Kramer, H.L. Tuller, Solid State Ionics 82 (1995) 15
120. P. Holtappels, F.W. Poulsen, M. Mogensen, Solid State Ionics 135 (2000) 675
121. Z. Taheri, N. Seyed-Matin, A.A. Safekordi, K. Nazari, S. Zarin Pashne, Appl. Catal. A 354 (2009) 143
122. S. Hui, A. Petric, Solid State Ionics 143 (2001) 275
123. Q. Zhang, T. Wei, Y.H. Huang, J. Power Sources 198 (2012) 59
124. G. Xiao, Q. Liu, X. Dong, K. Huang, F. Chem, J. Power Sources 195 (2010) 8071
125. T. Wei, Q. Zhang, Y.H. Huang, J.B. Goodenough, Mater. Chem. 22 (2012) 225
126. Y.H. Huang, R.I. Dass, Z.L. Xing, J.B. Goodenough, Science 312 (2006) 254
127. N. Danilovic, J.L. Luo, K.T. Chuang, A.R. Sanger, J. Power Sources 192 (2009) 247
128. C. Peng, J. Luo, A.R. Sanger, K.T. Chuang, Chem. Mater. 22 (2010) 1032
129. Y.H. Huang, R.I. Dass, J.C. Denyszyn, J.B. Goodenough, J. Electrochem. Soc. 153 (2006) A1266
130. S. Tao, J.C. Canales-Vazquez, J.T.S. Irvine, Chem. Mater. 16 (2004) 2309
131. V.V. Kharton, A.A. Yaremchenko, E.N. Naumovich, J. Solid State Electrochem. 3 (1999) 303
132. D.H. Peck, M. Miller, K. Hilpert, Solid State Ionics 123 (1999) 47
133. R.D. Shannon, Acta. Crystal. A32 (1976) 751

134. J.W. Fergus, Solid State Ionics 171 (2004) 1
135. N. Sakai, T. Kawada, H. Yokokawa, M. Dokiya, T. Iwata, J. Mater. Sci. 25 (1990) 4531
136. X. Liu, W. Su, Z. Lu, Mater. Chem. Phys. 82 (2003) 327
137. S. Onuma, S. Miyoshi, K. Yahiro, A. Kaimai, K. Kawamura, T. Nigara, T. Kawada, J. Mizusaki, N. Sakai, H. Yokokawa, J. Solid State Chem. 170 (2003) 68
138. J.D. Carter, C.C. Appel, M. Mogensen, J. Solid State Chem. 122 (1996) 407
139. D.H. Peck, M. Miller, K. Hilpert, Solid State Ionics 123 (1999) 59
140. T. Horita, M. Ishikawa, K. Yamaji, N. Sakai, H. Yokokawa, M. Dokiya, Solid State Ionics 108 (1998) 383
141. J. Sfeir, J. van Herle, A.J. McEvoy, J. Eur. Ceram. Soc. 19 (1999) 897
142. M. Mori, T. Yamamoto, T. Ichikawa, Y. Takeda, Solid State Ionics 148 (2002) 93
143. S.P. Jiang, L. Liu, K.P. Wong, P. Wu, J. Li, J. Pu, J. Power Sources 176 (2008) 82
144. L. Zhang, X.B. Chen, S.P. Jiang, H.Q. He, Y. Xiang, Solid State Ionics 180 (2009) 1076
145. K. Hirota, Y. Kunifusa, M. Yoshinaka, O. Yamaguchi, Mater. Res. Bull. 37 (2002) 2335
146. M. Oishi, K. Yashiro, J.O. Hong, Y. Nigara, T. Kawada, J. Mizusaki, Solid State Ionics 178 (2007) 307
147. A.K. Tripathi, H.B Lal, J. Mater. Sci. 17 (1982) 1595
148. S.W. Paulik, S. Baskaran, T.R. Armstrong, J. Mater. Sci. Lett. 18 (1999) 819
149. S.W. Paulik, S. Baskaran, T.R. Armstrong, J. Mater. Sci. 33 (1998) 2397
150. Y. Kunifusa, M. Yoshinaka, K. Hirota, O. Yamaguchi, Solid State Ionics 149 (2002) 107
151. P. Duran, J. Tartaj, F. Capel, C. Moure J. Eur. Ceram. Soc. 25 (2004) 2619
152. J. Mizusaki, M. Hasegawa, K. Yashiro, H. Matsumoto, T. Kawada, Solid State Ionics 177 (2006) 1925
153. M. Mori, N.M. Sammes, Solid State Ionics 164 (2002) 301
154. Z. Zhong, Solid State Ionics 177 (2006) 757
155. V. Vashook, L. Vasylechko, J. Zosel, R. Muller, E. Elhborrn, U. Guth, Solid State Ionics 175 (2004) 151
156. V. Vashook, L. Vasylechko, N. Trofimenko, M. Kuznecov, P. Otchik, J. Zosel, U. Guth, J. Alloys Compnd. 419 (2006) 271
157. V. Vashook, J. Zosel, W. Preis, W. Sitte, U. Guth, Solid State Ionics 175 (2004) 441
158. R. H. Mitchell, A.R. Chakhmouradian, J. Solid State Chem. 144 (1999) 81
159. P. Karen, T. Norby, J. Electrochem. Soc. 145 (1998) 264
160. S.P. Simner, J.S. Hardy, J.W. Stevenson, T.R. Armstrong, Solid State Ionics 128 (2000) 53
161. G.Y. Lee, R.H. Song, J.H. Kim, D.H. Peck, T.H. Lim, Y.G. Shul, D.R. Shin, J. Electroceram. 17 (2006) 723
162. N. Danilovic, J.L. Luo, K.T. Chuang, A.R. Sanger, J. Power Sources 194 (2009) 252
163. G. Pudmich, B.A. Boukamp, M. Gonzalez-Cuenca, W. Jungen, W. Zipprich, F. Tietz, Solid State Ionics 135 (2000) 433
164. R. Koc, H.U. Anderson, J. Mater. Sci. 27(1992)5477
165. S.R. Sehlin, H.U. Anderson, D.M. Sparlin, Solid State Ionics 78 (1995) 235
166. R. Raffaelle, H.U. Anderson, D.M. Sparlin, P.E. Parris, Phys. Rev. B 43 (1991) 7991

167. B. Gilbu Tilset, H. Fjellvag, A. Kjekshus, J. Solid State Chem. 119 (1995) 271
168. Z. El-Fadli, M.R. Metni, F. Sapina, E. Martinez, J.V. Folgado, D. Beltran, A. Beltran, J. Mater. Chem. 10 (2000) 437
169. J.M. Haag, S.A. Barnett, J.W. Richardson, Jr., K.R. Poeppelmeier, Chem. Mater. 22 (2010) 3283
170. R. Koc, H.U. Anderson, J. Eur. Ceram. Soc. 15 (1995) 867
171. L. Deleebeck, J.L. Fournier, V. Birss, Solid State Ionics 181 (2010) 1229
172. E. Loudhiri, A. Belayachi, M. Nogues, M. Taibi, A. Dahmani, M. El Yamani, J. Aride, M.J. Cond. Matter. 3 (2000) 98
173. V.V. Kharton, A.V. Kovalevsky, V.N. Tikhonovich, E.N. Naumovich, A.P. Viskup, Solid State Ionics 100 (1998) 53
174. A. Mineshige, M. Inaba, T. Yao, Z. Ogumi, K. Kikuchi, M. Kawase, J. Solid State Chem. 121 (1996) 423
175. J.A.M. van Roosmalen, P. van Vlaanderen, E.H.P. Cordfunke, W.L. Ijdo, D.J.W. Ijdo, J. Solid State Chem. 114 (1995) 516
176. K.M. Papazisi, S. Balomenou, D. Tsiplakides, J. Appl. Electrochem. 40 (2010) 1875
177. S.W. Tao, J.T.S. Irvine, Chem. Mater. 18 (2006) 5453
178. S. Tao, J.T.S. Irvine, Chem. Mater. 16 (2004) 4116
179. V.L. Kozhevnikov, I.A. Leonidov, J. A. Bahteeva, M.V. Patrakeev, E.B. Mitberg, K.R. Poeppelmeier, Chem. Mater. 16 (2004) 5014
180. M. Stojanovic, R.G. Havenkamp, C.A. Mims, H. Moudallal, A.J. Jacobson, J. Catal. 165 (1997) 315
181. I. Jitaru, D. Berger, V. Fruth, A. Novak, N. Stanica, F. Rusu, Ceram. Int. 26 (2000) 193
182. C.A. Mims, M. Stojanovic, N. Joos, H. Moudallal, A.J. Jacobson, in: U. Stimming, S.C. Singhal, H. Tagawa, W. Lehnert (Eds.), Proceedings of the 4th Int. Symp. on Solid Oxide Fuel Cells (SOFC-V), Proc. Vol. 97, Electrochem. Soc. Series, Pennington, NJ 1997, p. 737
183. H. Hofer, R. Schmidberger, J. Electrochem. Soc. 141 (1994) 782
184. S. Tao, J.T.S. Irvine, Solid State Ionics 179 (2008) 725
185. K.J. Yoon, J.W. Stevenson, O.A. Marina, J. Power Sources 196 (2011) 8531
186. A.L. Sauvet, J. Fouletier, Electrochim. Acta 47 (2001) 987
187. I. Yasuda, M. Hishinuma, Solid State Ionics 80 (1995) 141
188. B.D. Madsen, W. Kobsiriphat, Y. Wang, L.D. Marks, S.A. Barnett, J. Power Sources 166 (2007) 64
189. A. Zuev. L. Singheiser, K. Hilpert, Solid State Ionics 147 (2002) 1
190. S. Onuma, K. Yashiro, S. Miyoshi, A. Kaimai, H. Matsumoto, Y. Nigara, T. Kawada, J. Mizusaki, K. Kawamura, N. Sakai, H. Yokokawa, Solid State Ionics 174 (2004) 287
191. M. Oishi, K. Yashiro, K. Sato, J. Mizusaki, T. Kawada, J. Solid State Chem. 181 (2008) 3177
192. D.K. Lee, H.I. Yoo, J. Electrochem. Soc. 147 (2000) 2835
193. F. Boroomand, E. Wessel, H. Bausinger, K. Hilpert, Solid State Ionics 129 (2000) 251
194. K. Hilpert, R.W. Steibrech, F. Boroomand, E. Wessel, F. Meschke, A. Zuev, O. Teller, H. Nickel, L. Singheiser, J. Eur. Ceram. Soc. 23 (2003) 3009
195. J. Mizusaki, S. Yamauchi, K. Fueki, A. Ishikawa, Solid State Ionics 12 (1984) 119

196. P.H. Larsen, P.V. Hendriksen, M. Mogensen, J. Therm. Anal. 49 (1997) 1263
197. A. Zuev. L. Singheiser, K. Hilpert, Solid State Ionics 176 (2005) 417
198. M. Suzuki, H. Sasaki, A. Kajimura, Solid State Ionics 96 (1997) 83
199. D.P. Karim, A.T. Aldred, Phys. Rev. B 20 91979) 2255
200. T. Akashi, T. Maruyama, T. Goto, Solid State Ionics 164 (2003) 177
201. S. Primdahl, J.R. Hansen, L. Grahl-Madsen, P.H. Larsen, J. Electrochem. Soc. 148 (2001) A74
202. W.J. Weber, C.W. Griffin, J.L. Bates, J. Am. Ceram. Soc. 70 (1987) 265
203. T.R. Armstrong, J.W. Stevenson, K. Hasinska, D.E. McCready, J. Electrochem. Soc. 145 (1998) 4282
204. E. Lay, G. Gauthier, S. Rosini, C. Savaniu, J.T.S. Irvine, Solid State Ionics 179 (2008) 1562
205. Y.P. Fu, H.C. Wang, S.H. Hu, K.W. Tay, Ceram. Int. 37 (2011) 2127
206. O.I. Klyushnikov, V.V. Sal'nikov, N.M. Bogdanovich, Inorg. Mater. 38 (2002) 336
207. A.A. Yaremchenko, A.V. Kovalevsky, V.V. Kharton, Solid State Ionics 179 (2008) 2181
208. K. Hirota, H. Hatta, M. Io, M. Yoshinaka, O. Yamaguchi, J. Mater. Sci. 38 (2003) 3431
209. K.J. Yoon, C.N. Cramer, J.W. Stewenson, O.A. Marina, J. Power Sources 195 (2010) 7587
210. A. El Himri, D. Marrero-Lopez, J.C. Ruiz-Morales, J. Pena-Martinez, P. Nunez, J. Power Sources 188 (2009) 230
211. T. Jardiel, M.T. Caldes, F. Moser, J. Hamon, G. Gauthier, O. Jouber, Solid State Ionics 181 (2010) 894
212. N. Danilovic, A. Vincent, J.L. Luo, K.T. Chuang, R. Hui, A.R. Sanger, Chem. Mater. 22 (2010) 957
213. A.K. Azad, G.G. Eriksson, J.T.S. Irvine, Mater. Res. Bull. 44 (2009) 1451
214. I. Yasuda, T. Hikita, J. Electrochem. Soc. 140 (1993) 1699
215. V. Vashook, J. Zosel, R. Muller, P. Shuk, L. Vasylechko, H. Ullmann, U. Guth, Fuel Cells 6 (2006) 293
216. E.S. Raj, J.T.S. Irvine, Solid State Ionics 180 (2010) 1683
217. J. Yoo, S. Kim, H. Choi, Y. Rhim, J. Lim, S. Lee, A.J. Jacobson, J. Electroceram. 26 (2011) 56
218. J. Wan, J.H. Zhu, J.B. Goodenough, Solid State Ionics 177 (2006) 1211
219. S. Zha, P. Tsang, Z. Cheng, M. Liu, J. Solid State Chem. 178 (2005) 1844
220. M. Liu, L. Zhao, D. Dong, S. Wang, J. Diwu, X. Liu, G. Meng, J. Power Sources 177 (2008) 451
221. T. Xia, Q. Li, J. Meng, X. Cao, Mater. Chem. Phys. 111 (2008) 335
222. E. Lay, G. Gauthier, L. Dessemond, Solid State Ionics 189 (2011) 91
223. X. Zhu, H. Yan, Q. Zhong, X. Zhao, W. Tan, J. Alloys Compnd. 509 (2011) 8360
224. J.O. Hong, S. Miyoshi, A. Kaimai, Y. Yashiro, Y. Nigara, T. Kawada, J. Mizusaki, in T.A. Ramanarayanan, W.L. Worrell, M. Mogensen (Eds.), Proceedings of the 4th international Symposium "Ionic and Mixed Conducting Ceramics", Proc. Vol. 2001-28, Electrochem. Soc., Pennington, NJ, 2001, p. 49
225. N. Sakai, H. Fjellvag, B.C. Haubak, J. Solid State Chem. 121 (1996) 202
226. H. Ullmann, N. Trofimenko, F. Tietz, D. Stoever, A. Ahmad-Khanlou, Solid State Ionics 138 (2000) 79
227. F. Tietz, Ionics 5 (1999) 129
228. H. Hayashi, M. Suzuki, H. Inaba, Solid State Ionics 128 (2000) 131
229. H.E. Hofer, W.F. Kock, J. Electrochem. Soc. 140 (1993) 2889
230. X. Zhu, H. Gu, H. Chen, Y. Zheng, L. Guo, J. Alloys Compnd. 480 (2009) 958
231. M. Gonzalez-Cuenca, W. Zipprich, B.A. Boukamp, G. Pudmich, F. Tietz, Fuel Cells 1 (2001) 256

232. S.P. Simner, J.S. Hardy, J.W. Stevenson, J. Electrochem. Soc. 148 (2001) A351
233. T.R. Armstrong, J.W. Stevenson, D.E. McCready, S.W. Paulik, P.E. Raney, Solid State Ionics 92 (1996) 213
234. A.Yu. Zuev, D.S. Tsvetkov, Solid State Ionics 181 (2010) 557
235. T.R. Armstrong, J.W. Stevenson, L.R. Pederson, P.E. Raney, J. Electrochem. Soc. 143 (1996) 2919
236. S. Miyoshi, J.O. Hong , K. Yashiro, A. Kaimai, Y. Nigara, K. Kawamura, T. Kawada, J. Mizusaki, Solid State Ionics 161 (2003) 209
237. A. Atkinson, T.M.G.M. Ramos, Solid State Ionics 129 (2000) 259
238. M. Mori, Solid State Ionics 174 (2004) 1
239. D. Walbillig, A. Wood, D.G. Ivey, Solid State Ionics 176 92005) 847
240. J. van Herle, D. Perednis, K. Nakamura, S. Diethelm, M. Zahid, A. Aslanides, T. Somekawa, Y. Baba, K. Horiuchi, Y. Matsuzaki, M. Yashimoto, O. Bucheli, J. Power Sources 182 (2008) 389
241. D. Larrain, J. van Herle, D. Favrat, J. Power Sources 161 (2006) 392
242. R.E. Williford, T.R. Armstrong, J.D. Gale, J. Solid State Chem. 149 (2000) 320
243. T. Ishihara (Ed.), Perovskite Oxide for Solid Oxide Fuel Cells, Springer, NY, 2009
244. B.A. van Hassel, T. Kawada, N. Sakai, H. Yokokawa, M. Dokiya, H.J.M. Bouwmeester, Solid State Ionics 66 (1993) 295
245. H. Kruidhof, H.J.M. Bouwmeester, R.H.E. van Doorn, A.J. Burggraaf, Solid State Ionics 63 (1993) 816
246. A. Holt, T. Norby, R. Glenne, Ionics 5 (1999) 434
247. S. Hui, A. Petric, J. Eur. Ceram. Soc. 22 (2002) 1673
248. D. Neagu, J.T.S. Irvine, Chem. Mater. 23 (2011) 1607
249. E.N. Caspi, M. Avdeev, S. Short, J.D. Jorgensen, B. Dabrowski, O. Chmaissem, J. Mais, S. Kolesnik, J. Solid State Chem. 177 (2004) 1456
250. M. Sogaard, P.V. Hendriksen, M. Mogensen, J. Solid State Chem. 180 (2007) 1489
251. I. Yasuda, M. Hishinuma, J. Solid State Chem. 115 (1995) 192
252. T. Ramos, A. Atkinson, Solid State Ionics 170 (2004) 275
253. V.N. Chebotin, Physical Chemistry of Solids, Khimiya, Moscow 1982
254. N. Sakai. T. Horita, H. Tokokawa, M. Dokiya, T. Kawada, Solid State Ionics 86 (1996) 1273
255. J. Yoo, A. Verma, S.Y. Wang, A.J. Jacobson, J. Electrochem. Soc. 152 (2005) A497
256. A. Atkinson, R.J. Chater, R. Rudkin, Solid State Ionics 139 (2001) 233
257. T. Kawada, T. Horita, N. Sakai, H. Yokokawa, M. Dokiya, Solid State Ionics 79 (1995) 201
258. E.S. Raj, J.A. Kilner, J.T.S. Kilner, Solid State Ionics 177 (2006) 1747
259. C.A. Mims, N. Bayani, A.J. Jacobson, P.A.W. van der Heyde, Solid State Ionics 176 (2005) 319
260. C.Y. Park, D.X. Huang, A.J. Jacobson, L. Hu, C.A. Mims, Solid State Ionics 177 (2006) 2227
261. J. Rossmeisl, W.G. Bessler, Solid State Ionics 178 (2008) 1694
262. D. Kek, N. Bonanos, M.Mogensen, S. Pejovnik, Solid State Ionics 131 (2000) 249
263. M. Marwood, C.G. Vayenas, J. Catal. 178 (1998) 429
264. J.M. Haag, B.D. Madsen, S.A. Barnett, K.R. Poeppelmeier, Electrochem. Solid State Lett. 11 (2008) B51

265. A. L. Sauvet, J. T. S. Irvine, Solid State Ionics 167 (2004) 1
266. E.V. Tsipis, V.V. Kharton, J. Solid State Electrochem. 12 (2008) 1367
267. P. Vernoux, J. Guindet, M. Kleitz, J. Electrochem. Soc. 145 (1998) 3487
268. Y. Zhang, Y. Shen, X. Du, J. Li, X. Cao, T. He, Int. J. Hydrogen Energy 36 (2011) 3673
269. J.C. Ruiz-Morales, H. Lincke, D. Marrero-Lopez, J. Canales-Vazquez, P. Nunez, Boll. Soc. Esp. Ceram. Vidrio 46 (2007) 218
270. W. Bao, J. Cheng, Z. Hu, S. Jin, Solid State Ionics 181 (2010) 1366
271. Y. Zhang, Q. Zhou, T. He, J. Power Sources 196 (2011) 76
272. W. Bao, H. Guan, J. Cheng, J. Power Sources 175 (2008) 232
273. Z. Xu, J.L. Luo, K.T. Chuang, A.R. Sanger, J. Phys. Chem. C 111 (2007) 16679
274. B.D. Madsen, S.A. Barnett, Solid State Ionics 176 (2005) 2545
275. T. Yamamoto, T. Itoh, M. Mori, N. Mori, T. Watanabe, N. Imanishi, Y. Takeda, O. Yamamoto, J. Power Sources 61 (1996) 219
276. M. Matsuda, J. Nowotny, Z. Zhang, C.C. Sorrell, Solid State Ionics 111 (1998) 301
277. S.P. Jiang, L. Zhang, Y. Zhang, J. Mater. Chem. 17 (2007) 2627
278. J. Huang, J.H. Wan, J.B. Goodenough, J. Electrochem. Soc. 148 (2001) A788
279. J. Pena-Martinez, D. Marrero-Lopez, J.C. Ruiz-Morales, C. Savaniu, P. Nunez, J.T.S. Irvine, Chem. Mater. 18 (2006) 1001
280. Y. Du, N.M. Sammes, in: S.C. Singhal, J. Mizusaki (Eds.), SOFC-IX, Electrochem. Soc. Proc. Vol. 2005-07, Pennington, NJ, 2005, p. 1127
281. E. Hatchwell, N.M. Sammes, G.A. Tompsett, I.W.M. Brown, J. Eur. Ceram. Soc. 19 (1999) 1697
282. P. Vernoux, M. Guillodo, J. Fouletier, A. Hammou, Solid State Ionics 135 (2000) 425
283. D.M. Bastidas, S. Tao, J.T.S. Irvine, J. Mater. Chem. 16 (2006) 1603
284. X.J. Chen, Q.L. Liu, K.A. Khor, S.H. Chan, J. Power Sources 165 (2007) 34
285. M.C. Tucker, H. Kurokawa, C.P. Jacobson, L.C. De Jonghe, S.J. Visco, J. Power Sources 160 (2006) 130
286. S. Molin, M. Gazda, B. Kusz, P. Jasinski, J. Eur. Ceram. Soc. 29 (2009) 757
287. A.N. Hansson, S. Linderoth, M. Mogensen, M.A.J. Somers, J. Alloys Compnd. 402 (2005) 194
288. M.C. Tucker, J. Power Sources 195 (2010) 4570
289. M.R. Ardigo, M. Perron, L. Combemale, O. Heintz, G. Caboche, S. Chevalier, J. Power Sources 196 (2011) 2037
290. S.P.S. Badwal, R. Deller, K. Foger, Y. Rampakash, J.P. Zhang, Solid State Ionics 99 (1997) 297
291. S.P. Jiang, J.P. Zhang, K. Foger, J. Electrochem. Soc. 147 (2000) 3195
292. S.P. Jiang, S. Zhang, Y.D. Zhen, J. Electrochem. Soc. 153 (2006) A127
293. X. Montero, F. Tietz, D. Stoever, M. Cassir, I. Villareal, J. Power Sources 188 (2000) 148
294. T. Komatsu, H. Arai, R. Chiba, K. Nozawa, M. Arakawa, K. Sato, J. Electrochem. Soc. 154 (2007) B379
295. Q.A. Huang, B. Wang, W. Qu, R. Hui, J. Power Sources 191 (2009) 297
296. M. Brander, M. Bram, J. Froitzheim, H.P. Buchkremer, D. Stoever, Solid State Ionics 179 (2008) 1501

297. A. Holt, P. Kofstad, Solid State Ionics 69 (1994) 137
298. B.C. Tofield, W.R. Scott, J. Solid State Chem. 10 (1974) 183
299. J.F. Mitchell, D.N. Argyriou, C.D. Potter, D.G. Hinks, J.D. Jorgensen, S.D. Bader, Phys. Rev. B 54 (1996) 6172
300. J. Mizusaki, N. Mori, H. Takai, Y. Yonemura, H. Minamiue, H. Tagawa, M. Dokiya, H. Inaba, K. Naraya, T. Sasamoto, T. Hashimoto, Solid State Ionics 129 (2000) 163
301. J.H. Kuo, H.U. Anderson, D.M. Sparlin, J. Solid State Chem. 83 (1989) 52
302. J.A.M. van Roosmalen, E.H.P. Cordfunke, J. Solid State Chem. 10 (1994) 109
303. F.W. Poulsen, Solid State Ionics 129 (2000) 145
304. J. Nowotny, M. Rekas, J. Amer. Ceram. Soc. 81 (1998) 67
305. I. Yasuda, M. Hishinuma, J. Solid State Chem. 123 (1996) 382
306. S. Sengodan, H.J. Yeo, J.Y. Shin, G. Kim, J. Power Sources 196 (2011) 3083
307. V.L. Kozhevnikov, I.A. Leonidov, E.B. Mitberg, M.V. Patrakeev, A.N. Petrov, K.R. Poeppelmeier, J. Solid State Chem. 172 (2003) 296
308. A.N. Petrov, A.Yu. Zuev, I.L. Tikchonova, V.I. Voronin, Solid State Ionics 129 (2000) 179
309. J. Mizusaki, H. Tagawa, K. Naraya, T. Sasamoto, Solid State Ionics 49 (1991) 111
310. T. Atsumi, N. Kamegashira, J. Alloys Compnd. 257 (1997) 161
311. S.P. Jiang, J.G. Love, Solid State Ionics 138 (2001) 183
312. N. Caillol, M. Pijolat, E. Siebert, Appl. Surf. Sci. 254 (2007) 4641
313. Q.H. Wu, M. Liu, W. Jaegermann, Mater. Lett. 59 (2005) 1980
314. J. Richter, P. Holtappels, T. Graule, L.J. Gauckler, Solid State Ionics 179 (2008) 2284
315. Y. Zheng, C. Zhang, R. Ran, R. Cai, Z. Shao, D. Farrusseng, Acta Mater. 57 (2009) 1165
316. C. Su, Y. Wu, W. Wang, Y. Zheng, R. Ran, Z. Shao, J. Power Sources 195 (2010) 1333
317. Q.X. Fu, F. Tietz, P. Lersch, D. Stoever, Solid State Ionics 177 (2006) 1059
318. V. Vashook, D. Franke, L. Vasylechko, J. Zosel, J. Rebello, K. Ahlborn, W. Fichtner, M. Schmidt, T.L. Wen, U. Guth, Solid State Ionics 179 (2008) 1101
319. Q. Fu, X. Xu, D. Peng, X. Liu, G. Meng, J. Mater. Sci. 38 (2003) 2901
320. I.P. Marozau, V.V. Kharton, A.P. Viskup, J.R. Frade, V.V. Samakhval, J. Eur. Ceram. Soc. 26 (2006) 1371
321. K. Nakamura, J. Solid State Chem. 173 (2003) 299
322. J.A. Alonso, M.J. Martinez-Lope, M.T. Casais, J.L. MacManus-Driscoll, P.S.I.P.N. de Silva, L.F. Cohen, M.T. Fernandez-Diaz, J. Mater. Chem. 7 (1997) 2139
323. J. Mizusaki, Y. Yonemura, H. Kamata, K. Ohyama, N. Mori, H. Takai, H. Tagawa, M. Dokiya, K. Naraya, T. Sasamoto, H. Inaba, T. Hashimoto, Solid State Ionics 132 (2000) 167
324. S.P. Jiang, J. Mater. Sci. 43 (2008) 6799
325. Q.X. Fu, F. Tietz, D. Stoever, Solid State Ionics 177 (2006) 1819
326. A.N. Petrov, A.N. Demina, K.P. Polovnikova, A.K. Demin, E.A. Filonova, Inorg. Mater. 42 (2006) 418
327. J.P. Ouweltjes, M. van Tuel, M. Sillessen, G. Rietveld, Fuel Cells 9 (2009) 873
328. F. Chen, M. Liu, J. Solid State Electrochem. 3 (1998) 7

329. Y. Sakaki, Y. Takeda, A. Kato, N. Imanishi, O. Yamamoto, M. Hattori, M. Iio, Y. Esaki, Solid State Ionics 118 (1999) 187
330. S. Hashimoto, H. Iwahara, J. Electroceram. 4 (2000) 225
331. K. Nakamura, K. Ogawa, J. Solid State Chem. 163 (2002) 65
332. T. Grande, J.R. Tolchard, S.M. Selbach, Chem. Mater. 24 (2012) 338
333. S. Miyoshi, A. Kaimai, H. Matsumoto, H. Yashiro, Y. Nigara, T. Kawada, J. Mizusaki, Solid State Ionics 175 (2004) 383
334. S. Miyoshi, J.O. Hong, H. Yashiro, A. Kaimai, Y. Nigara, K. Kawamura, T. Kawada, J. Mizusaki, Solid State Ionics 154 (2002) 257
335. M.J. Escudero, J.T.S. Irvine, L. Daza, J. Power Sources 192 (2009) 43
336. A.V. Berenov, J.L. MacManus-Driscoll, J.A. Kilner, Solid State Ionics 122 (1999) 41
337. R.A. De Souza, J.A. Kilner, J.F. Walker, Mater. Lett. 43 (2000) 43
338. R.A. De Souza, J.A. Kilner, Solid State Ionics 106 (1998) 175
339. S.P.S. Badwal, S.P. Jiang, J. Love, J. Nowotny, M. Rekas, E.R. Vance, Ceram. Int. 27 (2001) 431
340. S. Carter, A. Selcuk, R.J. Chater, J. Kaida, J.A. Kilner, B.C.H. Steele, Solid State Ionics 53 (1992) 597
341. T. Horita, T. Tsunoda, K. Yamaji, N. Sakai, T. Kato, H. Yokokawa, Solid State Ionics 152 (2002) 439
342. I. Yasuda, K. Ogasawara, M. Hishinuma, T. Kawada, M. Dokiya, Solid State Ionics 86 (1996) 1197
343. G.S. Godoi, D.P.F. de Souza, Mater. Sci. Eng. B 140 (2007) 90
344. J.M. Alonso, R. Cortes-Gil, L. Ruiz-Gonzalez, J.M. Gonzalez-Calbet, A. Hernando, M. Vallet-Regi, M.E. Davila, M.C. Asensio, Eur. J. Inorg. Mater. (2007) 3350
345. V. Caignaert, J. Magn. Magn. Mater. 166 (1997) 117
346. I. Gelard, C. Dubourdieu, S. Pailhes, S. Petit, Ch. Simon, Appl. Phys. Lett. 92 (2008) 232506
347. S. McIntosh, M. van den Bossche, Solid State Ionics 192 (2011) 453
348. M. van den Bossche, S. McIntosh, J. Catal. 255 (2008) 313
349. H. Yokokawa, Annu. Rev. Mater. Res. 33 (2003) 581
350. J.H. Kim, D. Miller, H. Schlegl, D. MacGrouther, J.T.S. Irvine, Chem. Mater. 23 (2011) 3841
351. T. Kawada, N. Sakai, H. Yokokawa, M. Dokiya, I. Anzai, Solid State Ionics 50 (1992) 189
352. G. Corre, G. Kim, M. Cassidy, J. M. Vohs, R. J. Gorte, J. T. S. Irvine, Chem. Mater. 21 (2009) 1077
353. J.C. Ruiz-Morales, J. Canales-Vazquez, D. Marrero-Lopez, J.T.S. Irvine, P. Nunez, Electrochim. Acta 52 (2007) 7217
354. S.P. Jiang, X.J. Chen, S.H. Chan, J.T. Kwok, K.A. Khor, Solid State Ionics 177 (2006) 149
355. S. Tao, J.T.S. Irvine, J.A. Kilner, Adv. Mater. 17 (2005) 1734
356. S. Miyoshi, M. Martin, Phys. Chem. Chem. Phys. 11 (2009) 3063
357. S.P. Jiang, J.P. Zhang, Y. Raprakash, D. Milosevic, K. Wilshier, J. Mater. Sci. 35 (2000) 2735
358. S. Tao, J.T.S. Irvine, S.M. Plint, J. Phys. Chem. B 110 (2006) 21771
359. X. Zhu, Z. Lu, B. Wei, K. Chen, M. Liu, X. Huang, W. Su, J. Power Sources 190 (2009) 326
360. G. Kim, S. Lee, J.Y. Shin, G. Corre, J.T.S. Irvine, J.M. Vohs, R.S. Gorte, Electrochem. Solid State Lett. 12 (2009) B48
361. X.C. Lu, J.H. Zhu, Solid State Ionics 178 (2007) 1467

362. S.P. Jiang, Y. Ye, T. He, S.B. Ho, J. Power Sources 185 (2008) 179
363. M. van den Bossche, R. Matthews, A. Lichtenberger, S. McIntosh, J. Electrochem. Soc. 157 (2010) B392
364. N.E. Kiratzis, P. Connor, J.T.S. Irvine, J. Electroceram. 24 (2010) 270
365. R.J. Gorte, J.M. Vohs, S. McIntosh, Solid State Ionics 175 (2004) 1
366. J.C. Ruiz-Morales, J. Canales-Vazquez, J. Pena-Martinez, D. Marrero-Lopez, P. Nunez, Electrochim. Acta 52 (2006) 278
367. J. Liu, B.D. Madsen, Z. Ji, S.A. Barnett, Electrochem. Solid State Lett. 5 (2002) A122
368. B. Huang, S.R. Wang, R.Z. Liu, X.F. Ye, H.W. Nie, X.F. Sun, T.L. Wen, J. Power Sources 167 (2007) 39
369. T. Delahaye, T. Jardiel, O. Joubert, R. Laucournet, G. Gauthier, M.T. Caldes, Solid State Ionics 184 (2011) 39
370. J.C. Ruiz-Morales, J. Canales-Vazquez, B. Ballesteros-Perez, J. Pena-Martinez, D. Marrero-Lopez, J.T.S. Irvine, P. Nunez, J. Eur. Ceram. Soc. 27 (2007) 4223
371. F.D. Morrison, A.M. Coats, D.C. Sinclair, A.R. West, J. Electroceram. 6 (2001) 219
372. J.Y. Kim, K.R. Song, H.I. Yoo, J. Electroceram. 1 (1997) 27
373. C.J. Shin, H.I. Yoo, Solid State Ionics 178 (2007) 1089
374. D.K. Lee, H.I. Yoo, K.D. Becker, Solid State Ionics 154 (2002) 189
375. K. Ueda, H. Yanagi, H. Hosono, H. Kawazoe, Phys. Rev. B 56 (1997) 12998
376. P. Pasierb, S. Komornicki, M. Rekas, J. Phys. Chem. Solids 60 (1999) 1835
377. D. Neagu, J.T.S. Irvine, Chem. Mater. 22 (2010) 5042
378. D.K. Lee, H.I. Yoo, Solid State Ionics 144 (2001) 87
379. M.B. Choi, S.Y. Jeon, H.N. Im, S.J. Song, J. Alloys Compnd. 513 (2012) 487
380. J.W. Fergus, Sens. Actuators B 123 (2007) 1169
381. F. Horikiri, N. Iizawa, L.Q. Han, K. Sato, K. Yashiro, T. Kawada, J. Mizusaki, Solid State Ionics 179 (2008) 2335
382. S. Lee, Z.K. Liu, M.H. Kim, C.A. Randall, J. Appl. Phys. 101 (2007) 054119
383. U. Balachandran, N.G. Eror, J. Phys. Chem. Solids 44 (1983) 231
384. R. Moos, K.H. Hardtl, J. Amer. Ceram. Soc. 80 (1997) 2549
385. R. Meyer, R. Waser, J. Helmbold, G. Borchardt, Phys. Rev. Lett. 90 (2003) 105901
386. J.C.C. Abrantes, J.A. Labrincha, J.R. Frade, Ionics 3 (1997) 16
387. J.C.C. Abrantes, A.A.L. Ferreira, J.A. Labrincha, J.R. Frade, Ionics 3 (1997) 436
388. P. Blennow, K.K. Hansen, L.R. Wallenberg, M. Mogensen, Electrochim. Acta 52 (2006) 1651
389. N.G. Eror, U. Balachandran, J. Solid State Chem. 42 (1982) 227
390. S. Witek, D.M. Smyth, H. Pickup, J. Amer. Ceram. Soc. 67 (1984) 372
391. E. Orhan, P.M. Pontes, M.A. Santos, E.R. Leite, A. Beltran, J. Andres, T.M. Boschi, P.S. Pizani, J.A. Varela, C.A. Taft, E. Longo, J. Phys. Chem. B 108 (2004) 9221
392. M. Ceh, D. Kolar, J. Mater. Sci. 29 (1994) 6295
393. G.H. Jonker, E.E. Havinga, Mater. Res. Bull. 17 (1982) 345

394. H.I. Yoo, S.W. Lee, C.E. Lee, J. Electroceram. 10 (2003) 215
395. D.M. Smyth, J. Electroceram. 9 (2002) 179
396. R.K. Sharma, N.H. Chan, D.M. Smyth, J. Amer. Ceram. Soc. 64 (1981) 448
397. Y.H. Hu, M.P. Harmer, D.M. Smyth, J. Amer. Ceram. Soc. 68 (1985) 372
398. G. Trolliard, N. Harre, D. Mercurio, B. Frit, J. Solid State Chem. 145 (1999) 678
399. M. Yashima, R. Ali, Solid State Ionics 180 (2009) 120
400. X. Liu, C.R. Liebermann, Phys. Chem. Minerals 20 (1993) 171
401. D.S. Filimonov, Z.K. Liu, C.A. Randall, Mater. Res. Bull. 38 (2003) 545
402. K.W. Kirby, B.A. Wetchsler, J. Amer. Ceram. Soc. 74 (1991) 1841
403. J.E. Sunstrom, S.M. Kauzlarich, P. Klavins, Chem. Mater. 4 (1992) 346
404. G.J. Fischer, Z. Wang, S.I. Karato, Phys. Chem. Minerals 20 (1993) 97
405. D. de Ligny, P. Richet, Phys. Rev. B 53 (1996) 3013
406. T. Kolodiazhnyi, A. Petric, J. Electroceram. 15 (2005) 5
407. P. Blennow, A. Hagen, K.K. Hansen, L.R. Wallenberg, M. Mogensen, Solid State Ionics 179 (2008) 2047
408. B.F. Flandermeyer, A.K. Agarwal, H.U. Anderson, M.M. Nasrallah, J. Mater. Sci. 19 (1984) 2593
409. N.G. Eror, U. Balachandran, J. Solid State Chem. 40 (1981) 85
410. S. Hui, A. Petric. J. Electrochem. Soc. 149 (2002) J1
411. P. Blennow, K.K. Hansen, L.R. Wallenberg, M. Mogensen, Solid State Ionics 180 (2009) 63
412. X. Li, H. Zhao, N. Xu, X. Zhou, C. Zhang, N. Chen, Int. J. Hydrogen Energy 34 (2009) 6407
413. S. Hashimoto, F.W. Poulsen, M. Mogensen, J. Alloys Compnd. 439 (2007) 232
414. Q.X. Fu, S.B. Mi, E. Wessel, F. Tietz, J. Eur. Ceram. Soc. 28 (2008) 811
415. U. Balachandran, N.G. Eror, J. Amer. Ceram. Soc. 64 (1981) C75
416. J. Canales-Vazquez, J.C. Ruiz-Morales, B. Ballesteros, D. Marrero-Lopez, J.T.S. Irvine, Bol. Soc. Esp. Ceram. Vidrio 46 (2007) 304
417. S.N. Ruddlesden, P. Popper, Acta Cryst. 11 (1958) 54
418. C.J. Howard, G.R. Lumpkin, R.I. Smith, Z. Zhang, J. Solid State Chem. 177 (2004) 2726
419. P.D. Battle, J.E. Bennett, J. Sloan, R.J.D. Tilley, J.F. Vente, J. Solid State Chem. 149 (2000) 360
420. C.D. Savaniu, J.T.S. Irvine, J. Mater. Chem. 19 (2009) 8119
421. S. Das, A. Poddar, B. Roy, J. Alloys Compnd. 358 (2003) 17
422. D.J. Cumming, J.A. Kilner, S. Skinner, J. Mater. Chem. 21 (2011) 5021
423. V. Vashook, L. Vasylechko, M. Knapp, H. Ullmann, U. Guth, J. Alloys Compnd. 354 (2003) 13
424. Z. Zhang, G.R. Lumpkin, C.J. Howard, K.S. Knight, K.R. Whittle, K. Osaka, J. Solid State Chem. 180 (2007) 1083
425. D.S. Jung, H.Y. Koo, H.C. Jang, Y.C. Kang, Met. Mater. Int. 15 (2009) 809
426. J. Karczewsky, B. Riegel, M. Gazda, P. Jasinski, B. Kusz, J. Electroceram. 24 (2010) 326
427. S. Hui, A. Petric, Mater. Res. Bull. 37 (2002) 1215
428. S. Steinsvik, R. Bugge, J. Gjonnes, J. Tafto, T. Norby, J. Phys. Chem. Sol. 58 (1997) 969

429. J.C. Perez Flores, C. Ritter, D. Perez-Coll, G.C. Mather, F. Garcia-Alvarado, U. Amador, J. Mater. Chem. 21 (2011) 13195
430. V. Vashook, M. Muller, J. Zosel, K. Ahlborn, F. Gerlach, P. Tietz, G. Stover, U. Guth, Ionics 13 (2007) 141
431. D.P. Fagg, V.V. Kharton, A.V. Kovalevsky, A.P. Viskup, E.N. Naumovich, J.R. Frade, J. Eur. Ceram. Soc. 21 (2001) 1831
432. A.A. Murashkina, A.N. Demina, Inorg. Mater. 41 (2005) 402
433. A.A. Murashkina, A.N. Demina, E.A. Filonova, A.K. Demin, I.S. Korobitsin, Inorg. Mater. 44 (2008) 296
434. S. Hashimoto, H. Kishimoto, H. Iwahara, Solid State Ionics 139 (2001) 179
435. L.A. Dunyushkina, V.A. Gorbunov, A.A. Babkina, N.O. Esina, Ionics 9 (2003) 67
436. T.D. McColm, J.T.S. Irvine, Ionics 7 (2001) 116
437. A. Murashkina, V. Maragou, D. Medvedev, V. Sergeeva, A. Demin, P. Tsiakaras, J. Power Sources 210 (2012) 339
438. M. Mori, Z.W. Wang, N. Serizawa, T. Itoh, J. Fuel Cell Sci. Tech. 8 (2011) 051010
439. V.V. Kharton, L. Shuangbao, A.V. Kovalevsky, A.P. Viskup, E.N. Naumovich, A.A. Tonoyan, Mater. Chem. Phys. 53 (1998) 6
440. L.A. Dunyushkina, V.A. Gorbunov, Inorg. Mater. 57 (2001) 1165
441. L.A. Dunyushkina, E.A. Mashkina, I.Yu. Nechaev, A.A. Babkina, N.O. Esina, B.V. Zhuravlev, A.K. Demin, Ionics 8 (2002) 293
442. C.A. McCammon, A.I. Becerro, F. Langenhorst, R.J. Angel, S. Marion, F. Seifert, J. Phys. Cond. Mater. 12 (2000) 2969
443. C.Y. Park, A.J. Jacobson, J. Electrochem. Soc. 152 (2005) J65
444. D.P. Fagg, J.C. Waerenborgh, V.V. Kharton, J.R. Frade, Solid State Ionics 146 (2002) 87
445. A. Feltz, J. Eur. Ceram. Soc. 20 (2000) 2367
446. I. Burn, J. Mater. Sci. 14 (1979) 2453
447. J. Canales-Vazquez, J.C. Ruiz-Morales, J.T.S. Irvine, W. Zhou, J. Electrochem. Soc. 152 (2005) A1458
448. G. Xiao, X. Dong, K. Huang, F. Chen, Mater. Res. Bull. 46 (2011) 57
449. R.H. Mitchell, R.P. Liferovich, J. Solid State Chem. 177 (2004) 4420
450. A. Yamaji, J. Amer. Ceram. Soc. 58 (1975) 152
451. F. Noll, W. Munch, I. Denk, J. Maier, Solid State Ionics 86 (1996) 711
452. Q. Ma, F. Tietz, A. Leonide, E. Ivers-Tiffee, Electrochem. Commun. 12 (2010) 1326
453. K. Lee, J. Destry, J.L. Brebner, Phys. Rev. B 11 (1975) 2299
454. J.G. Bednorz, K.A. Muller, Phys. Rev. Lett. 52 (1984) 2289
455. J.F. Schooley, W.R. Hosler, M.L. Cohen, Phys. Rev. Lett. 12 (1964) 474
456. F. Gervais, B. Cales, P. Odier, Mater. Res. Bull. 22 (1987) 1629
457. H.P.R. Frederikse, W.R. Thurber, W.R. Hosler, Phys. Rev. 134 (1964) A442
458. K. van Benthem, C. Elsasser, R.H. French, J. Appl. Phys 90 (2001) 6156
459. H.W. Gandy, Phys. Rev. 113 (1959) 795

460. R. Moos, K.H. Hardtl, J. Appl. Phys. 80 (1996) 393
461. N.M. Tallan, W.C. Tripp, R.W. Vest, J. Amer. Ceram. Soc. 50 (1967) 279
462. S. Lubke, H.D. Wiemhofer, Solid State Ionics 117 (1999) 229
463. H. Matsumoto, D. Murakami, T. Shimura, S.I. Hashimoto, H. Iwahara, J. Electroceram. 7 (2001) 101
464. P.R. Slater. D.P. Fagg, J.T.S. Irvine, J. Mater. Chem. 7 (1997) 2495
465. C. Ohly, S. Hoffmann-Eifert, R. Waser, J. Electroceram. 13 (2004) 599
466. W. Menesklou, H.J. Schreiner, K.H. Hardtl, E. Ivers-Tiffee, Sens. Actuators B 59 (1999) 184
467. Y. Hu, O.K. Tan, J.S. Pan, H. Huang, W. Cao, Sens. Actuators B 108 (2005) 244
468. R. Waser, Solid State Ionics 75 (1995) 89
469. Y.M. Chiang, T. Takagi, J. Amer. Ceram. Soc. 73 (1990) 3278
470. D.Y. Wang, K. Umeya, J. Amer. Ceram. Soc. 74 (1991) 280
471. R. Hagenbeck, R. Waser, J. Appl. Phys. 83 (1998) 2083
472. W. Heywang, J. Mater. Sci. 6 (1971) 1214
473. K. Hayashi, T. Yamamoto, Y. Ikuhara, T. Sakuma, J. Appl. Phys. 86 (1999) 2909
474. S.A. Howard, J.K. Yau, H.U. Anderson, J. Appl. Phys. 65 (1989) 1492
475. S. Gemming, M. Schreiber, Chem. Phys. 309 (2005) 3
476. M.J. Verkerk, B.J. Middelhuis, A.J. Burggraaf, Solid State Ionics 6 (1982) 159
477. E.H. Greener, W.M. Hirthe, J. Electrochem. Soc. 109 (1962) 600
478. I. Yasuda, Y. Matsuzaki, T. Yamakawa, T. Koyama, Solid State Ionics 135 (2000) 381
479. R. Waser, R. Hagenbeck, Acta. Mater. 48 (2000) 797
480. J. Maier, J. Eur. Ceram. Soc. 19 (1999) 675
481. J. Jeong, E.G. Lee, Y.H. Han, J. Eur. Ceram. Soc. 27 (2007) 1159
482. J.H. Hwang, Y.H. Han, Solid State Ionics 140 (2001) 181
483. U. Balachandran, B. Odekirk, E.G. Eror, J. Solid State Chem. 41 (1982) 185
484. R. Moos, W. Menesklou, H.J. Schreiner, K.H. Hardtl, Sens. Actuators B 67 (2000) 178
485. A. Selcuk, B.C.H. Steele, in G. Gusmano, E. Traversa (Eds.), Proceedings of 4th Conference of Eur. Ceram. Soc. "4th Euro-Ceramic: Electroceramics", Proc. vol. 5, Gruppo Editoriale Faenza Editrice, Italy, 1995, p. 413
486. G. Tsekouras, J.T.S. Irvine, J. Mater. Chem. 21 (2011) 9367
487. V.P. Gorelov, V.B. Balakireva, Russ. J. Electrochem. 33 (1997) 1450
488. D.N. Miller, J.T.S. Irvine, J. Power Sources 196 (2011) 7323
489. M.J. Rampling, G.C. Mather, F.M.B. Marques, D.C. Sinclair, J. Eur. Ceram. Soc. 23 (2003) 1911
490. J.H. Hwang, Y.H. Han, J. Amer. Ceram. Soc. 84 (2001) 1750
491. J. Jeong, Y.H. Han, J. Electroceram. 13 (2004) 549
492. A. Muller, K.H. Hardtl, Appl. Phys. A 49 (1989) 75
493. C.R. Song, H.I. Yoo, Solid State Ionics 120 (1999) 141
494. H.I. Yoo, K.D. Becker, Phys. Chem. Chem. Phys. 7 (2005) 2068
495. H. Iwahara, Solid State Ionics 52 (1992) 99
496. H.I. Yoo, C.E. Lee, J. Amer. Ceram. Soc. 88 (2005) 617

497. S. Shirazaki, H. Yamamura, H. Haneda, K. Kakegawa, J. Moori, J. Chem. Phys. 79 (1980) 4640
498. H. Sasaki, Y. Matsuo, J. Amer. Ceram. Soc. 48 (1965) 434
499. V.V. Kharton, A.P. Viskup, A.V. Kovalevsky, F.M. Figueiredo, J.R. Jurado, A.A. Yaremchenko, E.N. Naumovich, J.R. Frade, J. Mater. Chem. 10 (2000) 1161
500. U. Kiessling, J. Claus, G. Borchardt, R. Waser, in R. Waser, S. Hoffmann, D. Bonnenberg, Ch. Hoffmann (Eds.), Proceedings of 4th Int. Conference on. Electronic Ceram. and Applications "Electroceramics IV", Proc. vol. 2, Verlag der Augustinus Bhg., Aachen, Germany, 1994, p. 827
501. D.P. Fagg, V.V. Kharton, J.R. Frade, A.A.L. Ferreira, Solid State Ionics 156 (2003) 45
502. V.B. Balakireva, V.P. Gorelov, Russ. J. Electrochem. 40 (2004) 530
503. S. Marion, A.I. Bercerro, T. Norby, Ionics 5 (1999) 385
504. H. Iwahara, T. Esaka, T. Mangahara, J. Appl. Electrochem. 18 (1998) 173
505. I.S. Kwak, G.M. Choi, J. Electroceram. 20 (2008) 127
506. J.A. Enterkin, A.E. Becerra-Toledo, K.R. Poeppelmeier, L.D. Marks, Surf. Sci. 600 (2012) 344
507. A.N. Chiaramonti, C.H. Lanier, L.D. Marks, P.C. Stair, Surf. Sci. 602 (2008) 3018
508. T. Bieger, J. Maier, R. Waser, Sens. Actuators B 7 (1998) 763
509. X. Li, H. Zhao, D. Luo, K. Huang, Mater. Lett. 65 (2011) 2624
510. M. Leonhardt, R.A. De Souza, J. Claus, J. Maier, J. Electrochem. Soc. 149 (2002) J19
511. T. Kawada, N. Iizawa, L.Q. Han, K. Yashiro, A. Kaimai, Y. Nigara, J. Mizusaki, in T.A. Ramanarayanan, W.L. Worrell, M. Mogensen (Eds.), Proceedings of the 4th international Symposium "Ionic and Mixed Conducting Ceramics", Proc. Vol. 2001-28, Electrochem. Soc., Pennington, NJ, 2001, p. 297
512. T. Bak, J. Nowotny, C.C. Sorrel, J. Phys. Chem. Solids 65 (2004) 1229
513. V.P. Gorelov, V.B. Balakireva, N.V. Sharova, Russ. J. Electrochem. 35 (1999) 400
514. S. Steinsvik, Y. Larring, T. Norby, Solid State Ionics 143 (2001) 103
515. K.D. Kreuer, Chem. Mater. 8 (1996) 610
516. M. Wideroe, W. Munch, Y. Larring, T. Norby, Solid State Ionics 154 (2002) 669
517. F.W. Poulsen, Solid State Ionics 145 (2001) 387
518. W. Munch, K.D. Kreuer, G. Seifertly, J. Maier, Solid State Ionics 125 (1999) 39
519. N. Sata, K. Hiramoto, M. Ishigame, S. Hosoya, N. Niimura, S. Shin, Phys. Rev. B 54 (1996) 15795
520. E. Matsuhita, A. Tanase, Solid State Ionics 97 (1997) 45
521. K.D. Kreuer, St. Adams, W. Munch, A. Fuchs, U. Klock, J. Maier, Solid State Ionics 145 (2001) 295
522. C.J. Xiao, Z.X. Li, X.R. Deng, Bull. Mater. Sci. 34 (2011) 963
523. R.E. Taylor, in C.Y. Ho (Ed.), Thermal Expansion of Solids, vol. 1-4, ASM Int., USA, 1998
524. G.M. Gladysz, K.K. Chawla, Composites: Part A 32 (2001) 173
525. Y.J. Jiang, R.Y. Guo, A.S. Bhalla, J. Electroceram. 2 (1998) 199
526. M. Munthuraman, K.C. Patil, S. Senbagaraman, A.M. Umarji, Mater. Res. Bull. 31 (1996) 1375
527. D.J. Cumming, V.V. Kharton, A.A. Yaremchenko, A.V. Kovalevsky, J.A. Kilner, J. Amer. Ceram. Soc. 94 (2011) 2993
528. J.S. Yoon, M.Y. Yoon, C. Kwak, H.J. Park, S.M. Lee, K.H. Lee, H.J. Hwang, Mater. Sci. Eng. B 177 (2012) 151

529. Z. Wang, M. Mori, T. Itoh, J. Electrochem. Soc. 157 (2010) B1783
530. B.K. Park, J.W. Lee, S.B. Lee, T.H. Lim, S.J. Park, R.H. Song, W.B. Im, D.R. Shin, Int. J. Hydr. Energy 37 (2012) 4319
531. C.Y. Park, A.J. Jacobson, Solid State Ionics 176 (2005) 2671
532. S.O. Yakovlev, V.V. Kharton, E.N. Naumovich, J. Zekonyte, V. Zaporojtchenko, A.V. Kovalevsky, A.A. Yaremchenko, J.R. Frade, Solid State Sci. 8 (2006) 1302
533. S. Hashimoto, L. Kindermann, P.H. Larsen, F.W. Poulsen. M. Mogensen, J. Electroceram. 16 (2006) 103
534. S. Koutcheiko, Y. Yoo, A. Petric, I. Davidson, Ceram. Int. 32 (2006) 67
535. Y. Takahashi, T. Suzuki, A. Kawahara, Y. Ando, M. Hirano, W. Shin, Solid State Ionics 181 (2010) 1516
536. L. Yang, L.C. De Jonghe, C.P. Jacobsen, S.J. Visco, J. Electrochem. Soc. 154 (2007) B949
537. H. He, Y. Huang, J.M. Vohs, R.J. Gorte, Solid State Ionics 175 (2004) 171
538. C. Bernuy-Lopez, R. Knibbe, Z. He, X. Mao, A. Hauch, K. Nielsen, J. Power Sources 196 (2011) 4396
539. X.C. Lu, J.H. Zhu, Z. Yang, G. Xia, J.W. Stevenson, J. Power Sources 192 (2009) 381
540. J.C. Ruiz-Morales, J. Canales-Vazquez, C. Savaniu, D. Marrero-Lopez, P. Nunez, W. Zhou, J.T.S. Irvine, Phys. Chem. Chem. Phys. 9 (2007) 1821
541. J.C. Ruiz-Morales, J. Canales-Vazquez, C. Savaniu, D. Marrero-Lopez, W. Zhou, J.T.S. Irvine, Nature Lett. 439 (2006) 538
542. J. Canales-Vazquez, J.C. Ruiz-Morales, D. Marrero-Lopez, J. Pena-Martinez, P. Nunes, P. Gomez-Romero, J. Power Sources 171 (2007) 552
543. J.C. Ruiz-Morales, J. Canales-Vazquez, H. Lincke, J. Pena-Martinez, D. Marrero-Lopez, D. Perez-Coll, J.T.S. Irvine, P. Nunez, Boll. Soc. Esp. Ceram. Vidrio 47 (2008) 183
544. C. Arrive, T. Delahaye, O. Jouber, G. Gauthier, J. Power Sources 223 (2013) 341
545. M.R. Pillai, I. Kim, D.M. Bierschenk, S.A. Barnett, J. Power Sources 185 (2008) 1086
546. D. Burnat, A. Heel, L. Holzer, E. Otal, D. Kata, T. Graule, Int. J. Hydr. Energy 37 (2012) 18326
547. K.B. Yoo, G.M. Choi, Solid State Ionics 180 (2009) 867
548. H. Kurokawa, L. Yang, C.P. Jacobson, L.C. de Jonghe, S.J. Visco, J. Power Sources 164 (2007) 510
549. X. Sun, S. Wang, Z. Wang, J. Qian, T. Wen, F. Huang, J. Power Sources 187 (2009) 85
550. R. Kikuchi, N. Koashi, T. Matsui, K. Eguchi, T. Norby, J. Alloys Compnd. 408 (2006) 622
551. J.B. Goodenough, Solid State Ionics 26 (1988) 87
552. J.B. Claridge, A.P.E. York, A.J. Brungs, C. Marquez-Alvarez, J. Sloan, S.C. Tsang, M.L.H. Green, J. Catal. 180 (1998) 85
553. J. Kiwi, K. R. Thampi, M.l Graetzel, P. Albers, K. Seibold, J. Phys Chem. 96 (1992) 1344
554. K.T. Queeney, C.M. Friend, J. Phys. Chem. B 104 (2004) 409
555. C. Bernuy-Lopez, M. Allix, C.A. Bridges, J.B. Claridge, M.J. Rosseinsky, Chem. Mater. 19 (2007) 1035
556. D. Marrero-Lopez, J. Pena-Martinez, J.C. Ruiz-Morales, M. Gabas, P. Nunez, M.A.G. Aranda, J.R. Ramos-Barrado, Solid State Ionics 180 (2010) 1672
557. Y. Ji, Y.H. Huang, J.R. Ying, J.B. Goodenough, Electrochem. Commun. 9 (2007) 1881

558. H.N. Im, M.B. Choi, S.Y. Jeon, S.J. Song, Ceram. Int. 37 (2011) 49
559. H.N. Im, S.Y. Jeon, M.B. Choi, H.S. Kim, S.J. Song, Ceram. Int.38 (2012) 153
560. L. Zhang, Q. Zhou, Q. He, T. He, J. Power Sources 195 (2010) 6356
561. Q. Liu, X. Dong, G. Xiao, F. Zhao, F. Chen, Adv. Mater. 22 (2010) 5478
562. Y.H. Huang, G. Liang, M. Croft, M. Lehtimaki, M. Karppinen, J.B. Goodenough, Chem. Mater. 21 (2009) 2319
563. T. Wei, Y. Ji, X. Meng, Y. Zhang, Electrochem. Commun. 10 (2008) 1369
564. S. Vasala, M. Lehtimaki, S.C. Haw, J.M. Chen, R.S. Liu, J. Yamauchi, M. Karppinen, Solid State Ionics 181 (2010) 754
565. S.J. Patwe, S.N. Achary, M.D. Matthews, A.K. Tyagi, J. Alloys Compd. 390 (2005) 100
566. D. Marrero-Lopez, M.C. Martin-Sedeno, J. Pena-Martinez, J.C. Ruiz-Morales, P. Nunez, M.A.G. Aranda, J.R. Ramos-Barrado, J. Power Sources 195 (2010) 2496
567. E.V. Tsipis, V.V. Kharton, I.A. Bashmakov, E.N. Naumovich, J.R. Frade, J. Solid State Electrochem. 8 (2004) 674
568. J. Rodriguez-Carvajal, Phys. B 192 (1993) 55
569. J.C. Waerenborgh, D.P. Rojas, N.P. Vyshatko, A.L. Shaula, V.V. Kahrton, I.P. Marozau, E.N. Naumovich, Mater. Lett. 57 (2003) 4388
570. J. Hesse, A. Rubartsch, J. Phys. E 7 (1974) 526
571. J. Mizusaki, T. Saito, H. Tagawa, J. Electrochem. Soc. 143 (1996) 3065
572. H.J.M. Bouwmeester, A.J. Burggraaf, Dence ceramic membranes for oxygen separation. In: A.J. Burggraaf, L. Cot (eds.), Fundamentals of Inorganic Membrane Science and Technology, Elsevier, Amsterdam, 1996, p. 435.
573. H.H. Moebius, Oxygen current density coefficient of oxidic materials as a parameter for selection in development of electrodes with solid electrolytes, in: Extended Abstract 37th Meeting of the Int. Society of Electrochemistry, Vilnius, USSR, 1986, vol. 1, pp. 136–139.
574. A.A. Yaremchenko, V.V. Kharton, A.P. Viskup, E.N. Naumovich, N.M. Lapchuk, V.N. Tikhonovich, J. Solid State Chem. 142 (1999) 325
575. J. Crank, The Mathematics of Diffusion, 2nd edn. Oxford Univ. Press, Oxford, 1975
576. R. Jimenez, T. Kloidt, M. Kleitz, J. Electrochem. Soc. 144 (1997) 582
577. F.M. Figueiredo, J.R. Frade, F.M.B. Marques, Bol. Soc. Esp. Ceram. Vidrio 38 (1999)639
578. Y. Shiratori, Y. Teraoka, K. Sasaki, Solid State Ionics 177 (2006) 1371
579. Y. Shiratori, K. Sasaki, J. Power Sources 180 (2008) 738
580. A.L. Shaula, V.V. Kharton, F.M.B. Marques, J. Solid State Chem. 178 (2005) 2050
581. V.V. Kharton, A.L. Shaula, N.P. Vyshatko, F.M.B. Marques, Electrochim. Acta 48 (2003) 1817
582. T. Okamura, S. Shimizu, M. Mogi, M. Tanimura, K. Furuya, F. Munakata, J. Power Sources 130 (2004) 38
583. J. Mizusaki, Solid State Ionics 52 (1992) 79
584. S.B. Adler, Chem. Rev. 104 (2004) 4791
585. J.R. Tolchard, M.S. Islam, P.R. Slater, J. Mater. Chem. 13 (2003) 1956

586. B.A. van Hassel, B.A. Boukamp, A.J. Burggraaf, Solid State Ionics 51 (1992) 161
587. E.V. Tsipis, V.V. Kharton, J. Solid State Electrochem. 12 (2008) 1039
588. P. Bohac, A. Orliukas, L. Gauckler L, in: R. Waser, S. Hoffmann, D. Bonnenberg, Ch. Hoffmann (eds.), Electroceramics IV, vol. II. IWE, University of Technology, Augustinus Buchhandlung, Aachen, 1994, pp. 771–780
589. B.A. Boukamp, T.P. Raming, A.J.A. Winnubst, H. Verweij, Solid State Ionics 158 (2003) 381
590. J.H. Kim, G.M. Choi, Solid State Ionics 130 (2000) 157
591. A.A. Yaremchenko, V.V. Kharton, D.O. Bannikov, D.V. Znosak, J.R. Frade, V.A. Cherepanov, Solid State Ionics 180 (2009) 878
592. M.D. Carvalho, T. Ramos, L.P. Ferreira, A. Wattiaux, Solid State Sci. 12 (2010) 476
593. G. Amow, I.J. Davidson, S.J. Skinner, Solid State Ionics177 (2006) 1205
594. E.V. Tsipis, V.V. Kharton, J.R. Frade, Electrochim. Acta 52 (2007) 4428
595. Y. Takeda, R. Kanno, M. Noda, Y. Tomida, O. Yamamoto, J. Electrochem. Soc. 134 (1987) 2656
596. P.V. Anikina, A.A. Markov, P.V. Patrakeev, I.A. Leonidov, V.L. Kozhevnikov, Solid State Sci. 11 (2009) 1156
597. E. Bakken, T. Norby, S. Stolen, Solid State Ionics 176 (2005) 217
598. E.I. Leonidova, I.A. Leonidov, M.V. Patrakeev, V.L. Kozhevnikov, J. Solid State Electrochem. 15 (2011) 1071
599. L. Rormark, K. Wiik, S. Stolen, T. Grande, J. Mater. Chem. 12 (2002) 1058
600. A. Kruth, U. Guth, A.R. West, J. Mater. Chem. 9 (1999) 1579
601. M.W. Lufaso, P.M. Woodward, J. Goldberger, J. Solid State Chem. 177 (20040 1651
602. P.W. Barnes, M.W. Lufaso, P.M. Woodward, Acta Cryst. B62 (2006) 384
603. M. Retuerto, M.J. Martinez-Lope, M. Garcia-Hernandez, A. Munoz, M.T. Fernandez-Diaz, J.A. Alonso, Mater. Res. Bull. 45 (2010) 1449
604. T. Negas, R.S. Roth, J. Solid State Chem. 1 (1970) 409
605. V.V. Kharton, A.P. Viskup, I.P. Marozau, E.N. Naumovich, Mater. Lett. 57 (2003) 3017
606. T.K. Mandal, V.V. Poltavets, M. Croft, M. Greenblatt, J. Solid State Chem. 181 (2008) 2325
607. A. Kruth, M. Tabuchi, U. Guth, A.R. West, J. Mater. Chem. 8 (1998) 2515
608. H. Taguchi, Phys. Stat. Solidi A 88 (1985) K79
609. K.J. Lee, E. Iguchi, J. Solid State Chem. 114 (1995) 242
610. K. Kuroda, K. Shinozaki, K. Uematsu, N. Mizutani, M. Kato, J. Amer. Ceram. Soc. 63 (1980) 109
611. A. Maignan, S. Hebert, L. Pi, D. Pelloquin, C. Martin, C. Michel, M. Hervieu, B. Raveau, Cryst. Eng. 5 (2002) 365
612. V.V. Kharton, A.A. Yaremchenko, M.V. Patrakeev, E.N. Naumovich, F.M.B. Marques, J. Eur. Ceram. Soc. 23 (2003) 1417
613. A.R. West, Solid State Chemistry and Its Applications. Wiley, 1984, Chichester
614. J.A.M. van Roosmalen, E.H.P. Cordfunke, J.P.P. Huijsmans, Solid State Ionics 66 (1993) 285
615. B.P. McCarthy, L.R. Pederson, R.E. Williford, X.D. Zhou, J. Amer. Ceram. Soc. 92 (2009) 1672
616. J.W. Stevenson, P.F. Hallmann, T.R. Armstrong, L.A. Chick, J. Amer. Ceram. Soc. 78 (1995) 507

617. I. Burn, S.Neirman, J. Mater. Sci. 17 (1982) 3510
618. M. Kahn, J. Amer. Ceram. Soc. 54 (1971) 452
619. Z. Shao, W. Yang, Y. Cong, H. Dong, J. Tong, G. Xiong, J. Membra. Sci. 172 (2000) 177
620. J. Yoo, C.Y. Park, A.J. Jacobson, Solid State Ionics 175 (2004) 55
621. V.V. Vashook, M.V. Zinkevich, Yu.G. Zonov, Solid State Ionics 116 (1999) 129
622. V.V. Kharton, A.V. Nikolaev, E.N. Naumovich, A.A. Vecher, Solid State Ionics 81 (1995) 201
623. J.B. Goodenough, Annu. Rev. Mater. Res. 33 (2003) 91
624. I.N. Burmistrov, O.A. Drozhzhin, S.Y. Istomin, V.V. Sinitsyn, E.V. Antipov, S.I. Bredikhin, J. Electrochem. Soc. 156 (2009) B1212
625. M.S. Kaluzhskih, S.M. Kazakov, G.N. Mazo, S.Ya. Istomin, E.V. Antipov, A.A. Gippius, Yu. A. Fedotov, S.I. Bredikhin, Yi Liu, G. Svensson, Z. Shen, J. Solid State Chem. 184 (2011) 698
626. M. Mori, T. Abe, H. Itoh, O. Yamomoto, Y. Takeda, T. Kawahara, Solid State Ionics 74 (1994) 157
627. T. Ishihara, T. Kudo, H. Matsuda, Y. Takita, J. Electrochem. Soc. 142 (1995) 1519
628. T. Ishihara, H. Matsuda, Y. Takita, Solid State Ionics 79 (1995) 147
629. T. Ishihara, H. Matsuda, Y. Takita, J. Amer. Ceram. Soc. 116 (1994) 3801
630. H. Hayashi, H. Inaba, M. Matsuyama, N.G. Lan, M. Dokiya, H. Tagawa, Solid State Ionics 122 (1999) 1
631. T. Ishihara, H. Furutani, M. Honda, T. Yamada, T. Shibayama, T. Akbay, N. Sakai, H. Yokokawa, Y. Takita, Chem. Mater. 11 (1999) 2081
632. V.V. Kharton, A.A. Yaremchenko, A.P. Viskup, G.C. Mather, E.N. Naumovich, F.M.B. Marques, J. Electroceram. 7 (2001) 57
633. K. Yamaji, H. Negishi, T. Horita, N. Sakai, H. Yokokawa, Solid State Ionics 135 (2000) 389
634. K. Huang, S.T. Tichy, J.B. Goodenough, J. Amer. Ceram. Soc. 81 (1998) 2565
635. V.V. Kharton, A.P. Viskup, A.A. Yaremchenko, R.T. Baker, B. Gharbage, G.C. Mather, F.M. Figueiredo, E.N. Naumovich, F.M.B. Marques, Solid State Ionics 132 (2000) 119
636. A. Skowron, P.N. Huang, A. Petric, J. Solid State Chem. 143 (1999) 202
637. J.W. Stevenson, T.R. Armstrong, L.R. Pederson, J. Li, C.A. Lewinsohn, S. Baskaran, Solid State Ionics 113 (1998) 571
638. S. Nakayama, M. Sakamoto, J. Eur. Ceram. Soc. 18 (1998) 1413
639. V.V. Kharton, A.L. Shaula, M.V. Patrakeev, J.C. Waerenborgh, D.P. Rojas, N.P. Vyshatko, E. V. Tsipis, A.A. Yaremchenko, F.M.B. Marques, J. Electrochem. Soc. 151 (2004) A1236
640. A. Mineshige, Y. Ohnishi, R. Sakamoto, Y. Daiko, M. Kobune, T. Yazawa, H. Yoshioka, T. Nakao, T. Fukutsuka, Y. Uchimoto, Solid State Ionics 192 (2011) 195
641. H. Yoshioka, S. Tanase, Solid State Ionics 176 (2005) 2359
642. E.J. Abram, C.A. Kirk, D.C. Sinclair, A.R. West, Solid State Ionics 176 (2005) 1941
643. S. Tao, J.T.S. Irvine, Mater. Res. Bull. 36 (2001) 1245
644. J.W. Stevenson, K. Hasinska, N.L. Canfield, T.R. Armstrong, J. Electrochem. Soc. 147 (2000) 3213
645. A.A. Yaremchenko, A.L. Shaula, V.V. Kharton, J.C. Waerenborgh, D.P. Rojas, M.V. Patrakeev, F.M.B. Marques, Solid State Ionics 171 (2004) 51

646. M.Yu. Gorshkov, A.D. Neumin, N.M. Bogdanovich, D.I. Bronin, Russ. J. Electrochem. 42 (2006) 737
647. J.B. Goodenough, Solid State Ionics 94 (1997) 17
648. Y.L. Kuo, Y.Y. Liang, Ceram. Int. 38 (2012) 3955
649. T. Nakao, A. Mineshige, M. Kobune, T. Yazawa, H. Yoshioka, Solid State Ionics 179 (2008) 1567
650. M.Yu. Gorshkov, A.D. Neumin, N.M. Bogdanovich, Yu.V. Danilov, L.A. Dunyushkina, Russ. J. Electrochem. 43 (2007) 721
651. T.J. Armstrong, A.V. Virkar, J. Electrochem. Soc. 149 (2002) A1565
652. S. Sun, X. Zhu, Y. Yuan, J. Solid State Electrochem. 14 (2010) 2257
653. T. Horita, K. Yamaji, N. Sakai, H. Yokokawa, A. Weber, E. Ivers-Tiffee, Electrochim. Acta 46 (2001) 1837
654. W. Gong, S. Gopalan, U.B. Pal, J. Power Sources 160 (2006) 305
655. X. Zhang, S. Ohara, R. Maric, K. Mukai, T. Fukui, H. Yoshida, M. Nishimura, T. Inagaki, K. Miura, J. Power Sources 83 (1999) 170
656. D. Marrero-Lopez, P. Diaz-Carrasco, J. Pena-Martinez, J.C. Ruiz-Morales, J.R. Ramos-Barrado, Fuel Cells 11 (2011) 65
657. T. Mitsui, A. Mineshige, T. Funahashi, H. Mieda, Y. Daiko, M. Kobune, H. Yoshioka, T. Yazawa, J. Power Sources 217 (2012) 170
658. A. Mineshige, T. Nakao, Y. Ohnishi, R. Sakamoto, Y. Daiko, M. Kobune, T. Yazawa, H. Yoshioka, T. Fukutsuka, Y. Uchimoto, J. Electrochem. Soc. 157 (2010) B1465
659. S. Chefi, M. Kakhlaoui, A. Inoubli, A. Madani, A. Hammou, Ceram. Int. 39 (2013) 4507
660. C. Bonhomme, S. Beaudet-Savignat, T. Chartier, P.M. Geffroy, A.L. Sauvet, J. Eur. Ceram. Soc. 29 (2009) 1781
661. A. Brisse, A.L. Sauvet, C. Barthet, S. Beaudet-Savignat, J. Fouletier, Fuel Cells 6 (2006) 59
662. H. Koide, Y. Someya, T. Yoshida, T. Maruyama, Solid State Ionics 132 (2000) 253
663. H. Itoh, T. Yamamoto, M. Mori, T. Horita, N. Sakai, H. Yokokawa, M. Dokiya, J. Electrochem. Soc. 144 (1997) 641
664. M. Hrovat, A. Ahmad-Khanlou, Z. Samardzija, J. Holc, Mater. Res. Bull. 34 (1999) 2027
665. H. Hayashi, R. Sagawa, H. Inaba, K. Kawamura, Solid State Ionics 131 (2000) 281
666. V.N. Tikhonovich, V.V. Kharton, E.N. Naumovich, A.A. Savitsky, Solid State Ionics 106 (1998) 197
667. Y. Sakitou, A. Hirano, N. Imanishi, Y. Takeda, Y. Liu, M. Mori, J. Fuel Cell Sci. Tech. 5 (2008) 031207
668. E.V. Tsipis, V.V. Kharton, J.R. Frade, P. Nunez, J. Solid State Electrochem. 9 (2005) 547
669. I. Gavrielatos, D. Montinaro, A. Orfanidi, S.G. Neophytides, Fuel Cells 9 (2009) 883
670. Y. Lin, C. Su, C. Huang, J.S. Kim, C. Kwak, Z. Shao, J. Power Sources 197 (2012) 57
671. X. Zhu, Z. Lu, B. Wei, K. Chen, M. Liu, X. Huang, W. Su, J. Power Sources 195 (2010) 1793
672. S.P.S. Badwal, Solid State Ionics 76 (1995) 67
673. A.P. Santos, R.Z. Domingues, M. Kleitz, J. Europ. Ceram. Soc. 18 (1998) 1571
674. X. Guo, J. Maier, J. Electrochem. Soc. 148 (2001) E121
675. D.A. Neumayer, E. Cartier, J. Appl. Phys. 90 (2001) 1801

676. M. Suzuki, S. Sodeoki, T. Inoue, Mater. Trans. 46 (2005) 669
677. M. Godickemeier, B. Michel, A. Orliukas, P. Bohak, K. Sasaki, L. Gauckler, H. Heinrich, P. Schwander, G. Kostorz, H. Hofmann, O. Frei, J. Mater. Res. 9 (1994) 1228
678. E.N. Kolosov, N.I. Starkovskii, S.G. Gulyanova, V.M. Gryaznov, Zh. Fiz. Khim. 62 (1988) 1309
679. B.A. McCool, Y.S. Lin, J. Mater. Sci. 36 (2001) 3221
680. R. Craciun, W. Daniell, H. Knozinger, Appl. Catal. A 230 (2002) 153
681. J.H. Kim, A. Manthiram, Chem. Mater. 22 (2010) 822
682. Y. Takeda, Y. Sakaki, T. Ichikawa, N. Imanishi, O. Yamamoto, M. Mori, T. Abe, Solid State Ionics 72 (1994) 257
683. P. Holtappels, J. Bradley, J.T.S. Irvine, A. Kaiser, M. Mogensen, J. Electrochem. Soc. 148 (2001) A923
684. S. Primdahl, M. Mogensen, Solid State Ionics 152 (2002) 597
685. S.M. Beresnev, B.L. Kuzin, D.I. Bronin, Russ. J. Electrochem. 43 (2007) 883
686. D. Sarantaridis, A. Atkinson, Fuel Cells 7 (2007) 246
687. Q.X. Fu, F. Tietz, Fuel Cells 8 (2008) 283
688. J. Malzbender, E. Wessel, R. W. Steinbrech, Solid State Ionics 176 (2005) 2201
689. K. Yasumoto, N. Mori, J. Mizusaki, H. Tagawa, M. Dokiya, J. Electrochem. Soc. 148 (2001) A105
690. E. Siebert, A. Hammouche, M. Kleitz, Electrochim. Acta 40 (1995) 1741
691. M. Kuznecov, P. Otschik, P. Obenaus, K. Eichler, W. Schaffrath, Solid State Ionics 157 (2003) 371
692. S.P. Jiang, J.G. Love, Solid State Ionics 158 (2003) 45
693. W. Wang, S.P. Jiang, J. Solid State Electrochem. 8 (2004) 914
694. S.P. Jiang, W. Wang, Electrochem. Solid State Lett. 8 (2005) A115
695. T. Kenjo, Y. Kanehira, Solid State Ionics 148 (2002) 1
696. E.J.L. Schouler, Solid State Ionics 9 (1983) 945
697. H. Uchida, M. Yoshida, M. Watanabe, J. Electrochem. Soc. 146 (1999) 1
698. M. Malki, P. Echegut, J. Non-Crystallline Solids 323 (2003) 131
699. K. Huang, M. Feng, J.B. Goodenough, M. Schmerling, J. Electrochem. Soc. 143 (1996) 3630
700. A. Naoumidis, A. Ahmad-Khanlou, Z. Samardzija, D. Kolar, Fresenius J. Anal. Chem. 365 (1999) 277
701. X. Zhang, S. Ohara, R. Maric, H. Okawa, R. Maric, T. Fukui, Solid State Ionics 139 (2001) 145
702. A. Tsoga, A. Gupta, A. Naoumidis, P. Nikolopoulos, Acta Mater. 48 (2000) 4709
703. J.H. Wan, J.Q. Yan, J.B. Goodenough, J. Electrochem. Soc. 152 (2005) A1511
704. A. Martinez-Amesti, A. Larranaga, L.M. Rodriguez-Martinez, A.T. Aguayo, J.L. Pizarro, M.L. No, A. Laresgoiti, M.I. Arriortua, J. Power Sources 185 (2008) 401
705. M. Shiono, K. Kobayashi, T.L. Nguen, K. Hosoda, T. Kato, K. Ota, M. Dokiya, Solid State Ionics 170 (2004) 1
706. W.H. Kim, H.S. Song, J. Moon, H.W. Lee, Solid State Ionics 177 (2006) 3211
707. K. Huang, J.B. Goodenough, J. Alloys Compnd. 303 (2000) 454
708. S. Yarmolenko, B. Hancock, K. Gordon, V. Kharton, J, Sankar, in ASME, Proceedings of Int. Mechan. Eng. Congress and Exposition, 2007, Seattle, Washington, USA, p. 1.

List of symbols and abbreviations

General abbreviations

approx.	approximately
ASR	area-specific resistance
a.u.	arbitrary units
c.c.	current collector
cermet	metal-ceramics
CN	coordination number
EDS	energy-dispersive X-ray spectroscopy
EMF, e.m.f.	electromotive force
GNP	glycine-nitrate process
impr., impreg.	impregnated
IT-SOFC	intermediate-temperature solid oxide fuel cells
OCV	open-circuit voltage
OP	oxygen permeability
RP	Ruddlesden-Popper
S.G.	space group
redox	reduction-oxidation
SEM	scanning electron microscopy
SOFC	solid oxide fuel cells
TEC	thermal expansion coefficient
TEM	transmission electron microscopy
TGA	thermogravimetric analysis
TPB	triple-phase boundary
WE / CE / RE	working / counter / reference electrode
XPS	X-ray photoelectron spectroscopy
XRD	X-ray diffraction analysis

Chemicals

CGO / CLO / CSO / CGO10	$(Ce,Gd)O_{2-\delta}$ / $(Ce,La)O_{2-\delta}$ / $(Ce,Sm)O_{2-\delta}$ / $Ce_{0.9}Gd_{0.1}O_{2-\delta}$
YSZ / CaSZ / ScSZ / 8YSZ	$(Zr,Y)\ O_{2-\delta}$ / $(Zr,Ca)O_{2-\delta}$ / $(Zr,Sc)O_{2-\delta}$ / $Zr_{0.85}Y_{0.15}O_{2-\delta}$
LnACM	$(Ln,A)(Cr,Mn)O_{3-\delta}$ (Ln = rare-earth element, A = Ca, Sr, Ba)
LSCM	$(La,Sr)(Cr,Mn)O_{3-\delta}$
LSCF	$(La,Sr)(Co,Fe)O_{3-\delta}$

LSGM / LSGMCo / LSGM9182	$(La,Sr)(Ga,Mg)O_{3-\tilde{o}}$ / $(La,Sr)(Ga,Mg,Co)O_{3-\tilde{o}}$ / $La_{0.9}Sr_{0.1}Ga_{0.8}Mg_{0.2}O_{3-\tilde{o}}$
LSM	$(La,Sr)MnO_{3\pm\tilde{o}}$
LSMCT	$(La_{0.75-x}Sr_{0.25+x})_{0.95}Mn_{0.5}Cr_{0.5-x}Ti_xO_{3-\delta}$

Symbols

|	phase boundary where a drop of potential occurs
a, b, c	unit cell parameters, [Å] or [nm]
a_p	unit cell parameter related to simple cubic perovskite, [Å] or [nm]
A_0	pre-exponential factor in the Arrhenius equation, [S×K/cm]
B_{hf}	magnetic hyperfine field, [T]
c_i	concentration of i^{th} species, [mol/cm^3]
c_{i0}	concentration of i^{th} species at the reference state, [mol/cm^3]
D_i	diffusion coefficient of i^{th} species, [cm^2/s]
D_{chem}	chemical diffusion coefficient, [cm^2/s]
D_v	diffusion coefficient of oxygen vacancies, [cm^2/s]
D^*	tracer diffusion coefficient, [cm^2/s]
e	elementary charge, 1.60×10^{-19} C
$e' / h^{\cdot}$	electron / hole
E	elastic constant, Pa
E_a	activation energy, [kJ/mol] or [eV]
E_{sens}	potential difference across the sensor, [mV]
F	Faraday constant, [C/mol]
ΔH_f / ΔH_m / ΔH_a	standard enthalpy change of oxygen vacancy formation / migration / defect association, [kJ/mol]
ΔH_w	standard enthalpy change of dissolution of one mol of water in the material, [kJ/mol]
i	current density, [mA/cm^2]
I	current passing between working and counter electrodes, [mA]
I	intensity of XRD signal, [arbitrary units]
I_{pump}	current passing through the electrochemical pump, [mA]
IS	isomer shift, mm/s
j	oxygen flux through a dense membrane, [mol×s^{-1}×cm^{-2}]
$J(O_2)$	specific oxygen permeability, [mol×s^{-1}×cm^{-1}]
k	Boltzmann constant, 1.38×10^{-23} J/K
k^*	tracer surface exchange coefficient, [cm/s]

*K, K**	equilibrium constant, [dimensionless]
L, d	membrane thickness, [cm]
L, L_0, ΔL	length, initial length and elongation of a ceramic sample, [cm]
m, m_0, Δm	weight, initial weight and weight change, [g]
M	concentration of an aqueous solution, [mol/L]
mol.% / vol.% / wt.%	molar, volume or weight percentage, [5]
n / *p*	electron / hole concentration, [mol/cm^3]
N	density of states, [mol/cm^3]
$N_{f.u.}$	formula unit number
$p(O_2)$ / $p(H_2O)$ / pX / p_i	partial pressure of oxygen / water / X^{th} / i^{th} component in the gas phase, [atm]
P_{max}	maximum power density, [mW/cm^2]
QS	quadrupole shift, [mm/s]
r_i	radius of i^{th} ion, [nm or Å]
R	universal gas constant, 8.314 J×mol^{-1}×K^{-1}
R_{ohm} (R_s)	ohmic (series) resistance, [Ohm or Ohm×cm^2]
R_η	polarization resistance, [Ohm or Ohm×cm^2]
S	membrane or electrode area, [cm^2]
t	time, [hours]
t_o	oxygen ionic transference number, [dimensionless]
T	temperature, [K]
T_{seal}	sealing temperature, [K]
U	voltage across working and reference electrode, [mV]
V, $V_{u.c.}$	unit cell volume, [nm^3 or A^3]
Z', Z"	real and imaginary components of impedance, [Ohm or Ohm×cm^2]

α	thermal expansion coefficient, [K^{-1}]
α	Seebeck coefficient, [μV/K]
α_p / α_n	partial Seebeck coefficients for *p* or *n*-type charge carriers, [μV/K]
β	constant related with spin-degeneracy factor, [dimensionless]
γ_i	activity coefficient of i^{th} species, [dimensionless]
õ	oxygen nonstoichiometry, [dimensionless]
Δõ	change of oxygen nonstoichiometry, [dimensionless]
ε, ε_{ch}	relative chemical expansion, [dimensionless or %]
η	overpotential, [mV]
λ	wavelength, [nm]
μ	chemical potential, [J/mol]
μ_p / μ_n	mobility of *p*-type / *n*-type carriers, [cm^2×s^{-1}×V^{-1}]

ρ_{exp} / ρ_{theor}	ceramics density measured experimentally / calculated from the cell parameters, [g/cm^3]
σ	electrical conductivity, [S/cm]
σ_e / σ_{ion} / σ_O / σ_H	partial electronic / ionic / oxygen ionic / protonic conductivity, [S/cm]
θ	angle, [^{o}]
τ	relaxation constant, [s]

Appendix A. High-temperature XRD studies of $(La_{0.9}Sr_{0.1})_{0.95}Cr_{0.85}Mg_{0.1}Ni_{0.05}O_{3-\tilde{o}}$.

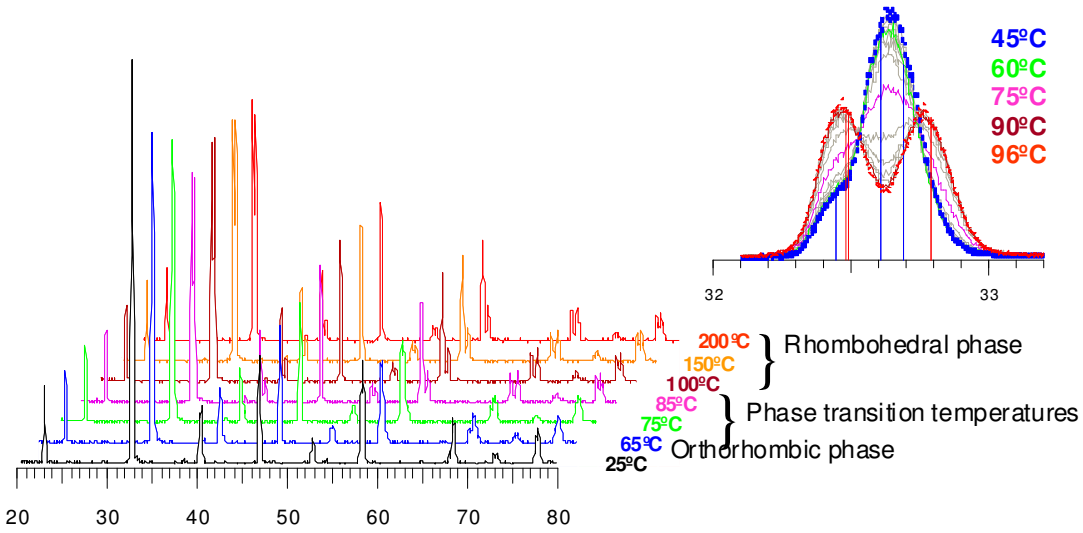

Fig. A1. XRD patterns of $(La_{0.9}Sr_{0.1})_{0.95}Cr_{0.85}Mg_{0.1}Ni_{0.05}O_{3-\tilde{o}}$ ceramics collected at various temperatures. Inset shows XRD at different temperatures for the peaks around 32.5° (blue and red vertical lines correspond to theoretical positions of orthorhombic and rhombohedral phase, respectively).

High-temperature XRD measurements were carried out at the North Carolina A&T State University by Dr. S.N. Yarmolenko and Prof. J. Sankar. The details on the equipment utilized, measuring conditions etc may be found in Chapter 2 or [708].

As noted in Chapter 3.3.1, $LaCrO_3$-based compositions exhibit a transformation of the low-temperature orthorhombic structure into the rhombohedral one stable occurring on heating in air. The transition temperature is governed by the radius of dopant cations; examples are shown in Table 3.13. Fig. A1 demonstrates an evolution of XRD patterns collected on $(La_{0.9}Sr_{0.1})_{0.95}Cr_{0.85}Mg_{0.1}Ni_{0.05}O_{3-\tilde{o}}$ ceramics equilibrated at several temperatures with the step of 3 K in the range 318 - 369 K. Analysis of the XRD data shows that the transition orthorhombic - rhombohedral occurs at the temperatures around 350 K. A close value was observed by dilatometric measurements carried out on continuous heating of a ceramic sample in air, as demonstrated in Fig. 3.28.

On further heating in the range 373 - 1073 K the rhombohedral phase retains, as shown in Fig. A2. The parameters *a* and *c* in hexagonal settings calculated from the patterns linearly increase upon heating, as demonstrated in Fig. 3.28. The average TEC for the parameter *c* is more than twice larger in comparison with that for the parameter *a* (15.3×10^{-6} K^{-1} vs. 7.0×10^{-6} K^{-1}), while the ratio *c/a* gradually increases on heating indicating an anisotropy along [001] direction. The average linear TEC calculated from the high-temperature XRD data is evaluated as 9.8×10^{-6} K^{-1} which is slightly lower in comparison with the value obtained from the dilatometric studies in the same temperature range (10.1×10^{-6} K^{-1}). More details on the structural behaviour of the perovskite $(La_{0.9}Sr_{0.1})_{0.95}Cr_{0.85}Mg_{0.1}Ni_{0.05}O_{3-\tilde{o}}$ may be found in [708].

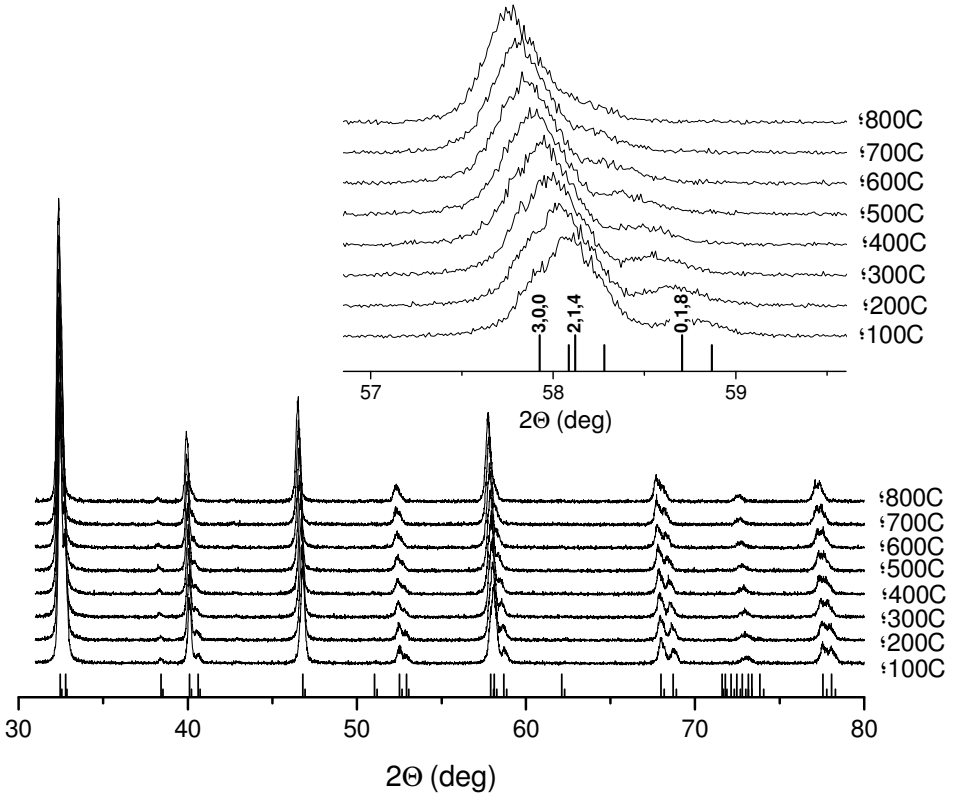

Fig. A2. Typical XRD patterns collected for $(La_{0.9}Sr_{0.1})_{0.95}Cr_{0.85}Mg_{0.1}Ni_{0.05}O_{3-\delta}$ ceramics in the range 373 - 1073 K with 19 peaks used for refinement. Inset shows group of three peaks.